ISSN: 1021-5506

Zoological Studies

Proceedings of **Focus on Microscopy '95**

Vol. 34, Supplement I
April, 1995

Published by the Institute of Zoology
Academia Sinica
Taipei, Taiwan, R. O. C.

Zoological Studies

The publication of *Zoological Studies*, a quarterly, is supported by the Institute of Zoology, Academia Sinica, Taipei, Taiwan 115, R.O.C. Tel: 886-2-7899529, Fax No. 886-2-7858059, E-Mail: ylchen@gate.sinica.edu.tw

This journal is awarded by the National Science Council, Taiwan, R.O.C. This journal is primarily distributed without charge as part of a scientific information exchange program. However, *Zoological Studies* can be available from Wei-Ming Book Co., Ltd., for book dealers and other special interest arrangements. Inquiries should be sent to: Wei-Ming Book Co., Ltd., 10-2 Fl., 149, Roosevelt Road, Sec. 3, P.O. Box 592, Taipei, Taiwan 107, R.O.C. Printed by Enjoy Enterprise Co., Ltd. 10-1 Fl., 293-3, Fuhsing S. Road, Sec. 2, Taipei, Taiwan 106, R.O.C.

Focus on Microscopy '95

立體顯微科技

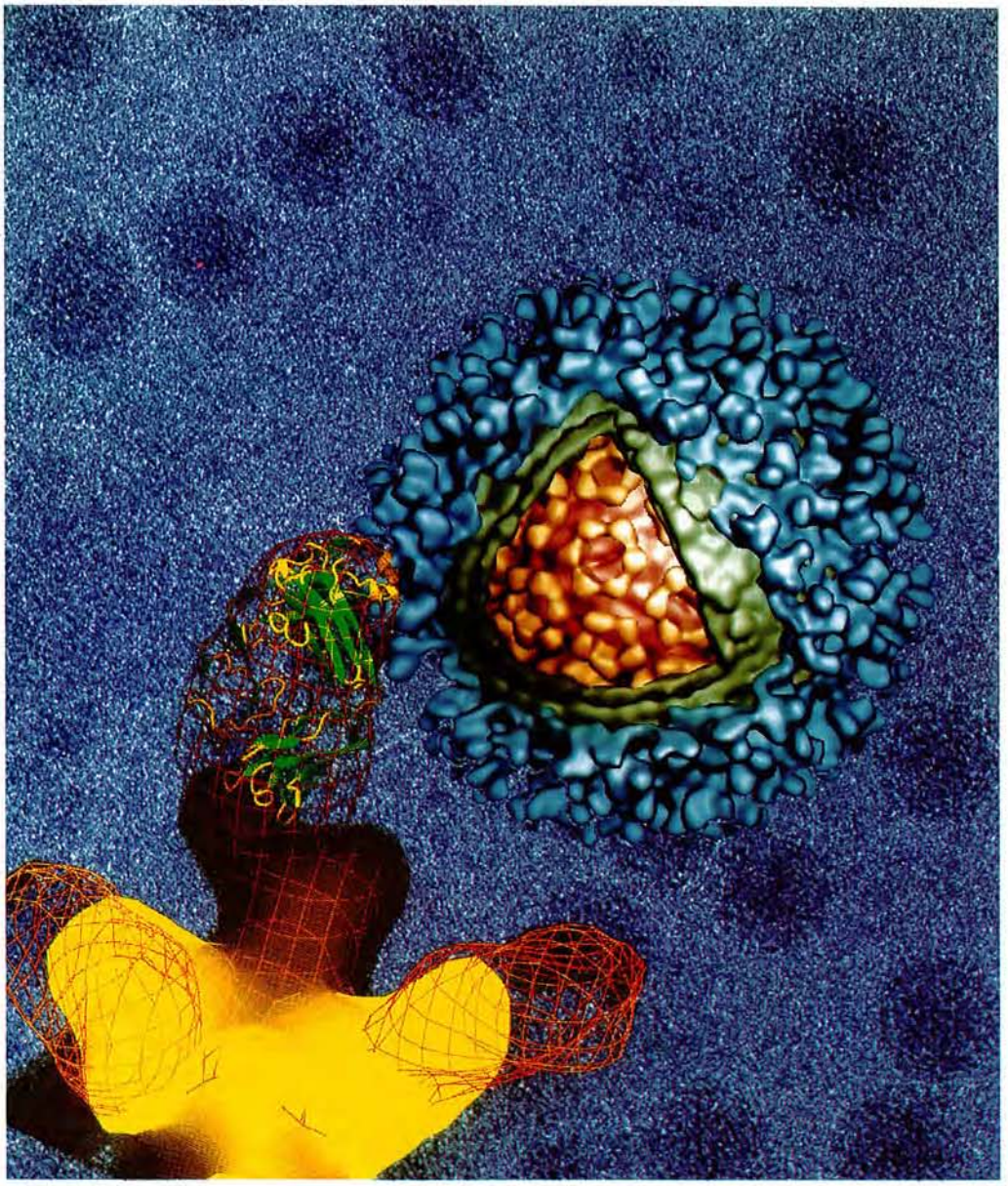

R. Holland Cheng (Purdue University)

April 18-20, Howard Plaza Hotel
Taipei, Taiwan, Republic of China

中華民國・臺北市・福華大飯店仁愛店福華廳

The conference is jointly organized and supported by

Academia Sinica, ROC
Institute of Zoology, Academia Sinica, Nankang, Taipei, Taiwan, ROC
Life Science Research Promotion Center, NSC, ROC
Electron Microscopy Society of China, Taipei, ROC
The Society for 3-D Imaging Sciences in Microscopy (Amsterdam)
AMIL, State University of New York at Buffalo, USA

Organizers

Chang-Po Chen (Taipei)
Chang-Hong Chou (Taipei)
Pung-Pung Hwang (Taipei)
Wen-Yung Lee (Taipei)
Hish-Kan Wu (Taipei)
Jen-Leih Wu (Taipei)
Wen-Lung Wu (Taipei)

G.J. Brakenhoff (Amsterdam)
Ping-Chin Cheng (Buffalo)
Carol J. Cogswell (Sydney)
Min Gu (Sydney)
Vyvyan Howard (Liverpool)
Hyogun Kim (Rochester)

Andres Kriete (Giessen)
C.J.R. Sheppard (Sydney)
D.M. Shinozaki (London, Canada)
E.H.K. Stelzer (Heidelberg)
Tony Wilson (Oxford)

CONTENTS

Session B4 Confocal Microscopy, Image Processing and Restoration

Session B5 Image Processing and Restoration II

Session B6 X-ray Microscopy I

Session B7 X-ray Microscopy II

Session A8 Biological Microscopy V

Session A9 Biological Microscopy VI

Zoological Studies 34, Supplement I (1995)

Zoological Studies

3-D Electron Microscopy of Cells and Organelles by High-voltage EM, Tomography, and Stereopair Analysis

Michael Marko
Wadsworth Center, P.O. Box 509, Albany, NY 12201-0509, USA

MICROSCOPY

3-D electron microscopy is greatly facilitated by the high-voltage EM (HVEM, ca. 1000kV) and the intermediate-voltage EM (IVEM, ca. 200-500kV). Compared to the conventional transmission EM (CTEM, ca. 100kV), the increased penetration of the specimen by the high-energy beam allows the use of thicker specimens without loss of resolution. Thus, there is the potential for more depth information in the images.

For effective 3-D microscopy using stereoscopy or tomography, the thickness of the specimen must be an appreciable fraction of the width of the image field. In the case of CTEM, the specimen thickness is limited to not much more than 100 nm. This means that a final magnification of at least 80-100,000X is required, otherwise the stereo view or tomographic volume has little depth. At such high magnifications, only quite small volumes can be examined. For IVEM, specimens as thick as 300-1000 nm can be used, so magnifications as low as 15-30,000X will provide reasonably deep volumes. For HVEM, specimens of 1000 nm are commonly used, but the instrument is capable of good imaging up to about 10 micrometers, in certain cases. Thus, quite low magnifications can be used with good 3-D results. Clearly, with higher voltage the range of usable thickness and magnification increases.

RECONSTRUCTION METHODS

There are three basic methods by which the 3-D structure of cells and organelles can be obtained using EM: (1) observation of stereopairs, (2) making serial-section reconstructions, and (3) making tomographic reconstructions.

1. *Stereopairs*

Stereopairs can be used for critical observation and analysis when the specimen is not excessively crowded with detail, and when a useful amount of the specimen volume is present within the thickness of the section. Stereopairs are created by tilting the specimen and recording two images. This is still the most common procedure used in HVEM. Within the limits mentioned above, optimum imaging requires that the specimen tilt angle be chosen for the section thickness and magnification used (Beeston 1973). Since the structures seen in EM stereopairs are semi-transparent, excessive over-lapping details limit the useable section thickness for some specimens. For sections much over 1 micrometer in thickness, selective staining is often required.

Stereopairs not only provide a 3-D view, but can be used to make reconstructions and measurements of objects in the specimen. We have developed a computer system which includes provision for drawing parallel depth contours, and 3-D lines, within the 3-D volume of a stereoscopic image. The contours are stored in a database, and used to determine statistics such as length, volume, and surface area. The contours can also be used to create surface-rendered reconstructions. This system is called Sterecon (Marko et al. 1988, 1992).

2. *Serial-section reconstructions*

Serial-section reconstruction is an appropriate technique when the volume of the specimen to be reconstructed is too large to be contained within the thickness of a single section. Although serial sections of 50-100nm thickness can be used with the CTEM, there are advantages to using serial-

section stereopairs of "thick" (about 0.25 to 1.5 micrometers) sections, recorded using the IVEM or HVEM. Fewer but thicker sections can be used, reducing microtomy and microscopy time. The use of Sterecon avoids loss of z-resolution associated with fewer sections, since tracing takes place on several planes within each section (Fig. 1a). The major advantage of using thicker sections is that the 3-D structure of the specimen can be appreciated during tracing. This makes decisions about branching and connectivity of structures much easier and more certain.

For correct serial-section reconstruction, the actual section thickness during microscopy has to be measured and compared to the pre-irradiation thickness. The actual thickness is measured by Sterecon, and the original thickness by interference microscopy or a well-calibrated microtome. The difference is due to mass loss from electron irradiation (Luther 1992). Any incidental tilt of the specimen is measured and corrected by Sterecon during tracing. Alignment between sections is aided by comparison of the contours of the top plane of one section with the structures on the bottom plane of the succeeding section. Fiducial marks independent of the specimen (Bron et al. 1990) are needed for alignment if it is important to find the exact overall shape of the specimen. The contours from all of the sections are combined and grouped to make a reconstruction of the specimen, and to find any desired morphometric parameter.

3. *Electron tomography*

For an important class of objects, such as some cell organelles, HVEM tomography provides the ideal means of high-resolution 3-D study. Any object which can be contained within a single section not thicker than about 2-3 micrometers is a candidate for HVEM tomography. Tomography is required when there is too much information in a stereopair view of the specimen to make a reconstruction by stereoscopic tracing. A tomographic reconstruction (Frank 1992) is created by combining a series of tilted views. The number of views, and the maximum tilt angle, are important resolution-limiting factors (Crowther et al. 1970).

A 3-D resolution of about 6nm is readily obtained by HVEM tomography. The same 3-D resolution cannot be obtained by serial ultrathin sections. The depth resolution of a conventional serial-section reconstruction is limited by the minimum thickness it is possible to cut, and the loss of material between sections due to microtomy and electron irradiation. Thus, depth resolution better than 30-40nm would not be expected. Stereoscopic tracing within serial sections can provide better resolution than this (although not as good as tomography), but only if the specimen is not too complex.

In common practice, a tilt series is recorded around a single axis. It is not possible to tilt sections to 90 degrees (the maximum tilt is often around 70 degrees), so there is a loss of resolution due to incomplete filling of Fourier space during the reconstruction process. We have developed methods to combine tilt series around two axes, thus reducing the missing information (Marko et al. 1994). Compared to a single-tilt reconstruction--even if the same total number of tilt images are recorded in both cases--the 3-D resolution and faithfulness of the reconstruction is increased, and artifacts are reduced (Penczek et al. 1995). We have found that the key to obtaining a good reconstruction is accurate alignment of the tilt-series images, which is only possible if specimen distortion during imaging is controlled or corrected (Marko et al. 1995).

VISUALIZATION METHODS

Visualization of the results of either contour-traced or tomographic reconstruction methods often requires more effort than the reconstruction itself. Reconstructions based on contours are often visualized by surface rendering. The first step is "tiling", in which the points on contour lines at adjacent depth levels are connected to form polygons (often triangles). In the second step, these triangular tiles are shaded and smoothed to produce a realistic surface. Since the contour database provides for grouping contours into objects, display scenes with all objects in the specimen, or only selected objects, can easily be created (Fig. 1b)

Tomographic reconstructions can be volume-rendered by applying voxel density thresholds in an attempt to select or "segment" objects of interest. The opacity of the volume can also be adjusted to make internal structures visible. An example of volume rendering is seen in Fig. 1c. Often, volume-rendering methods work poorly on EM specimens because density segmentation fails due to low contrast. In those cases, we use Sterecon to trace 3-D contours within successive depth regions of the tomographic volume (Fig. 1a). The resulting contours are surface-rendered as above (Fig. 1b). Alternatively, the contours can be used to create a 3-D mask to apply to the volume

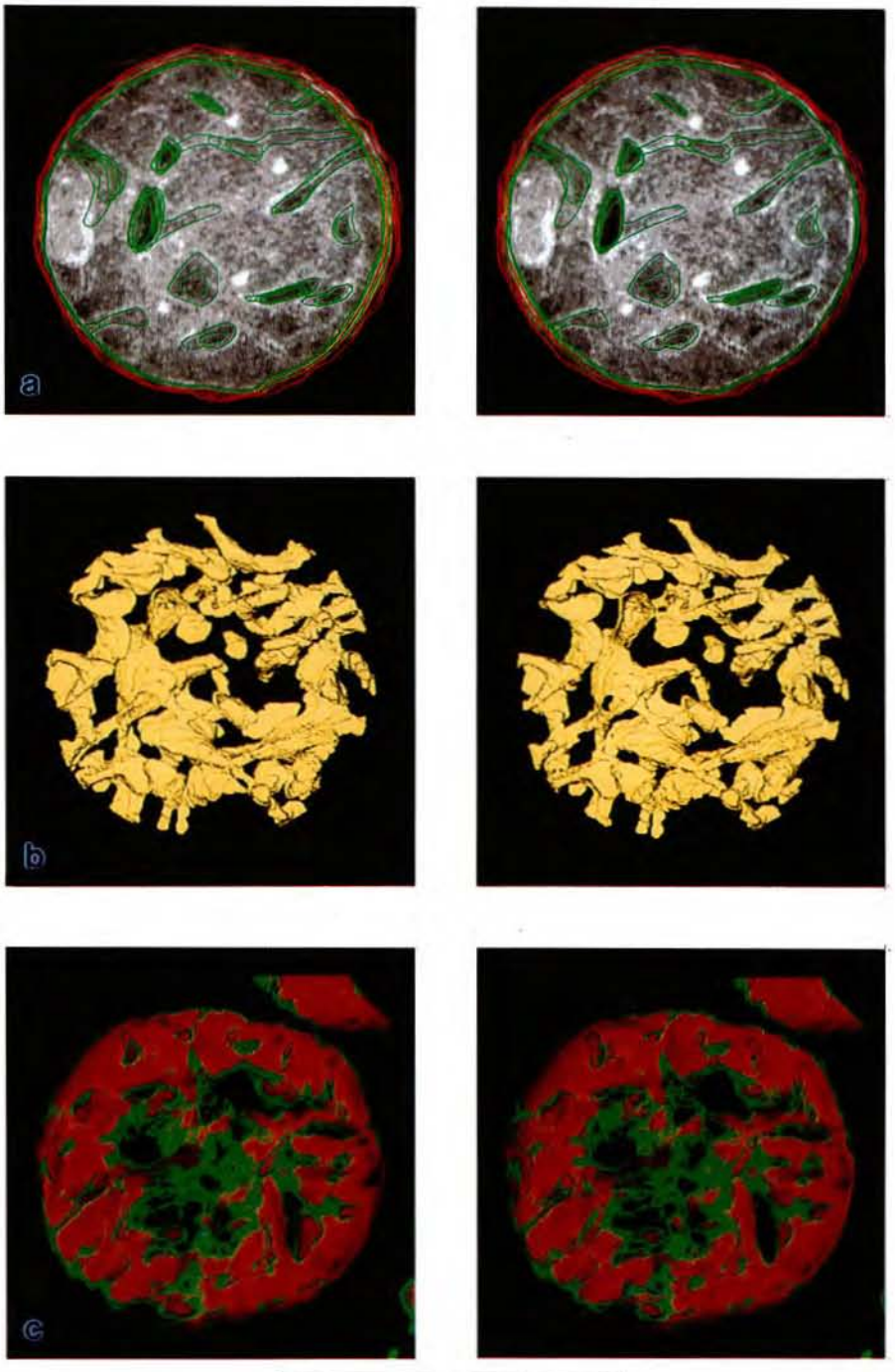

Fig. 1. Stereopair examples of segmentation and rendering techniques, using HVEM tomographic volumes from 0.5-0.7-micrometer thick sections of isolated rat-liver mitochondria (work in progress, Mannella et al. 1995). Scale bar = 1 micrometer, applies to all figures. (a)Segmentation of membranes by contour tracing using Sterecon. A portion of a tomographic volume, with contour lines drawn during stereoscopic viewing. Outer membrane (red) and inner membrane and cristae (green) traced on five depth planes. Same technique used with HVEM stereopairs for serial thick sections. (b)Surface rendering of cristae made from contours traced within a tomographic volume, of which (a) is a portion. About one-half the thickness of the full volume is shown. Inner and outer membranes removed. (c)Volume rendering of a portion of a mitochondrion in the "condensed" state (based on results in Mannella et al. 1994). Membranes (green) and matrix material (red) segmented by setting two density ranges; opacity adjusted to show interior structure. Outer membrane not shown.

for segmentation purposes. The segmented objects can then be volume rendered.

The Albany HVEM is part of the Biological Microscopy and Image Reconstruction Resource, supported in part by NIH PHS grant R01219 (P.I. Dr. Conly Rieder). The Sterecon software, and that used for tomography, a subset of SPIDER, were developed in association with our image-processing lab, supported in part by NSF grant BIR 921 9043 (P.I. Dr. Joachim Frank). The mitochondrial work is supported in part by NSF grant MCB 921 9043 (P.I. Dr. Carmen Mannella).

REFERENCES

Beeston B. 1973. High voltage microscopy of biological specimens: some practical considerations. J. Microscopy **98:** 402-416.

Bron C, P Gremillet, D Launay, M Jourlin, HP Gautschi, HP Baechi, J Schuepbach. 1990. Three dimensional electron microscopy of an entire cell. J. Microsc. **157:** 115-126.

Crowther, RA, DJ DeRosier, A Klug. 1970. The reconstruction of a three-dimensional structure from its projections and its application to electron microscopy. Proc. R. Soc. London **A 317:** 319-340.

Frank J, ed. 1992. Electron Tomography: Three-dimensional imaging with the transmission electron microscope. New York: Plenum Press.

Luther P. 1992. Sample shrinkage and radiation damage. In Electron Tomography, ed J. Frank. New York: Plenum Press, pp. 39-60.

Mannella CA, M Marko, P Penczek, D Barnard, J Frank. 1994. The internal compartmentation of rat-liver mitochondria: Tomographic study using the high-voltage transmission electron microscope. Microsc. Res. and Tech. **27:** 278-283.

Mannella CA, M Marko, A Leith, K Buttle, P Penczek, J Frank. 1995. In preparation.

Marko, M, A Leith, DF Parsons. 1988. Three-dimensional reconstruction of cells from serial sections and whole-cell mounts using multilevel contouring of stereo micrographs. J. Electron Microsc. Tech. **9:** 395-411.

Marko M, A Leith. 1992. Contour-based surface reconstruction using stereoscopic contouring and digitized images. In Visualization in Biomedical Microscopies, ed A Kriete. Weinheim, Germany: VCH, pp.45-73.

Marko M, P Penczek, R Feuerbach, J Frank. 1994. Use of a two-axis tilt series for electron tomography. In Proc. XIII Int. Congress on Electron Microscopy, eds B Jouffrey, C Colliex. Les Ulis, France: Les Editions de Physique, **1:** 505-506.

Marko M, P Penczek, A Leith, K. Buttle, J. Frank. 1995. In preparation.

Penczek P, M Marko, R Feuerbach, K. Buttle, J. Frank. 1995. In preparation.

Zoological Studies 34, Supplement I (1995)

Zoological Studies

Confocal Microscopy of Cyanobacteria in Calcite Speleothems

Guy Cox[1], Anya Salih[1], Julia James[2] and Bill Allaway[3]
[1]*Electron Microscope Unit, University of Sydney, NSW 2006, Australia*
[2]*School of Chemistry, University of Sydney, NSW 2006, Australia*
[3]*School of Biological Sciences, University of Sydney, NSW 2006, Australia*

Speleothems apparently deposited by the action of algae or bryophytes have long been known in caves where some light is present but the environment is protected from atmospheric weathering (Cubbon 1976). These include small tufa-like deposits and small stalactites containing cyanobacteria (Braithwaite and Whitton 1987), but are relatively insignificant in scale. We have recently described (Cox et al. 1989 a, b) an altogether different type of speleothem - massive, ridge-shaped stalagmites which can measure metres in length and height. Cyanobacteria are abundant in the superficial calcite layer and give the stalagmites a deep green colour when they are damp. Both in external appearance and cross section they resemble some stromatolites.

These stalagmites are found in large tunnel-like caves with high roofs and large entrances, open at both ends. Specimens from all known sites share certain distinctive morphological features. They are shaped like a humped ridge, and they have a very characteristic stepped or layered profile. In size they may be anywhere between 200mm long and 100mm high to 2m by 1m.

Scrapings from the surface of the stalagmites reveal predominantly coccoid cyanobacteria, with abundant sheaths, which have been assigned to the genus *Gloeocapsa* (Cox et al. 1989b). Massive stalagmites do not normally form in the relatively dry environment of large cave entrances. For this to happen requires fairly rapid removal of CO_2 from the drip water landing on the stalagmite. Photosynthetic CO_2 fixation by cyanobacteria would provide a mechanism for this, and seems likely to be the major source of calcite deposition in these stalagmites.

Under the microscope the flora of these stalagmites is revealed as an almost pure stand of one or possibly two species of *Gloeocapsa*. This is in striking contrast to nearby pebbles and bedrock surfaces, most of which support a very mixed community of cyanobacteria (filamentous and coccoid) and eukaryotic algae (*Chlorella*, diatoms, dinoflagellates and chrysophytes) often lichenized with fungal hyphae. It would appear that calcite deposition is sufficient to exclude all but those species adapted to it; this further supports our view that these stalagmites are the product of a specific association.

Further investigation requires an understanding of the organization of the cyanobacteria within the speleothem. The confocal microscope is the only tool capable of providing this information. Small (~500μm thick) flakes were taken from the surfaces of some of these speleothems. These were imaged in well slides in the confocal microscope using the red and yellow autofluorescence of the chlorophyll and phycobilins of the cyanobacteria. It proved possible to obtain satisfactory images down to almost 250μm below the surface of these flakes, so that by scanning from both sides virtually the whole volume could be sampled. Clearly there will be some refractive index mismatch but in practice the water-filled porous calcite seems to be sufficiently close in mean refractive index to immersion oil for adequate imaging down to the point at which the lens touches the coverslip.

Fig. 1 shows a Voxel-View reconstruction of a confocal dataset from one of these flakes. A depth of 27μm is sampled from within the flake - cyanobacteria are 'cut' by the optical sections at both the top and bottom of the set. Cyanobacteria are organized in clusters joined by a common sheath, as is typical of *Gloeocapsa*. It is also clear

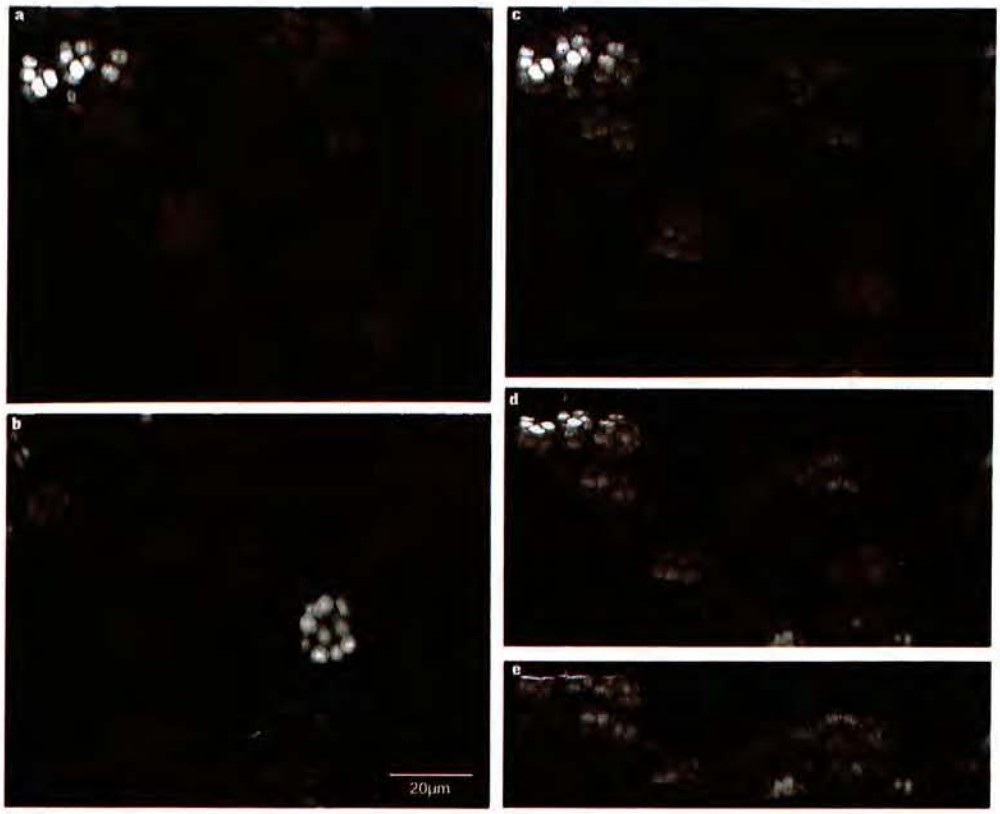

Fig. 1. Views of a confocal flyorescence dataset obtained on a Bio-Rad MRC600 confocal microscope. The original dataset sampled a volume 153×102×27 mm; this was been clipped slightly for volume rendering and pressntation. An oil immersion lens (x100, NA 1.3) was used. (a) Top view, looking straight down on the dataset. (b) bottom view, looking our from the inside of the calcite flake. (c), (d), (e) Tilt series, inclined 35°, 65° and 85° from the top view. In (e) we are looking almost along the plane of the flake.

that the cyanobacteria are overall quite uniformly distributed both laterally and vertically - there is no sign of vertical stratification at this scale, or indeed at the scale of the entire flake. Cell densities and arrangement are not visibly different when looking at either the top or the bottom of a flake. No point is more than 50μm from the nearest clump of cells, implying that the cyanobacteria are well positioned for effective removal of CO_2 from the water surrounding them. The whole pattern of their distribution strongly supports the view that this *Gloeocapsa* is adapted for life in this habitat, and that calcite is being deposited around them while they grow and divide - they are not an opportunistic species simply colonising new bare calcite surfaces.

The combination of confocal microscopy and volume rendering has provided a powerful tool for imaging this unusual bioherm in a way that would have been simply inconceivable a few years ago. Since all of the data is in digital form it is also simple to make it available for numerical analysis. These stalagmites are tens of thousands of years old, and still growing. Understanding the mechanism by which they form will provide the key to the information about past climates which lies buried in their lower layers.

We are very grateful to the management and staff of Jenolan Caves for allowing us to work in Nettle Cave, our study site. This work was supported by an Australian Research Council small grant.

REFERENCES

Braithwaite CJR, BA Whitton. 1987. Gypsum and halite associated with the cyanobacterium Entophysalis. Geomicrobiol. J. **5:** 43-55.

Cox GC, JM James, RAL Osborne, KA Legett. 1989a. Stromatolitic crayfish-like stalagmites. Proc. Univ. Bristol. Spelaeol. Soc. **18:** 339-358.

Cox GC, JM James, KA Legett, RAL Osborne. 1989b. Cyanobacterially deposited speleothems: subaerial stromatolites. Geomicrobiol. J. **7:** 245-252.

Cubbon BD. 1976. Cave Flora, in The Science of Speleology (ed. T.D. Ford and C.H.D. Cullingford). Academic Press, London, New York, San Francisco, pp 423-452.

Zoological Studies 34, Supplement I (1995)

Zoological Studies

Three-dimensional Imaging Approaches and Monte Carlo Simulations: Development of Tools to Study the Morphology and Distribution of Chromosome Territories and Subchromosomal Targets in Human Cell Nuclei

Roland Eils[1,2], Kaan Saracoglu[2], Christian Münkel[1,3], Jorg Imhoff[1,3], Kurt Sätzler[1*,2], Etienne Bertin[4], Steffen Dietzel[5], Evelin Schröck[6], Thomas Ried[6], Thomas Cremer[5] and Christoph Cremer[2,1*]

[1]*Graduiertenkolleg "Modeling and Scientific Computing in Mathematics and Science" at 1*Interdisciplinary Center for Scientific Computing (IWR), University of Heidelberg, 69120 Heidelberg, Germany*

[2]*Institute of Applied Physics, University of Heidelberg, 691.15 Heidelberg, Germany*

[3]*Institute of Theoretical Physics, University of Heidelberg, 69115 Heidelberg, Germany*

[4]*Equipe DyoGen and Lab. TIMC (CNRS URA 1618), Universite Joseph Fourier, Grenoble, France*

[5]*Institute of Human Genetics and Anthropology, University of Heidelberg, 69120 Heidelberg, Germany*

[6]*National Center for Human Genome Research, National Institute of Health, Bethesda, Maryland, USA*

Evidence has been accumulated indicating that the cell nucleus is compartmentalized both structurally and functionally. In particular, it has been demonstrated that chromosomes occupy distinct territories (Cremer et al. 1993). Chromosome territories and subchromosomal regions (e.g. genes) can be visualized by multiple color FISH and optical sectioning with a Leica confocal laser scanning fluorescence microscope. To study their structure in more detail we have developed truly three-dimensional imaging approaches. In addition, we describe Monte Carlo simulations which consider the distribution of such objects under the influence of various geometrical constraints. Such developments are essential in order to establish tools for refined studies of nuclear architecture.

QUANTITATIVE IMAGE ANALYSIS USING THREE-DIMENSIONAL VORONOI DIAGRAMS

The image volume consisting of the whole stack of optical sections is first tessellated into polyhedra providing the Voronoi diagram (Bertin et al. 1993, Eils et al. 1995a). The neighborhood of the polyhedra is described by the dual Delaunay graph. Thereafter painted chromosomes consisting of connected polyhedra are extracted providing a three-dimensional segmentation of the image volume. The geometrical structure of the Voronoi diagram allows the rapid calculation of morphological parameters of segmented objects, such as volume, surface area, length and a shape factor. The construction of the Voronoi diagram for an image volume of a size of 256x256x32 is typically completed within 90 seconds on a Silicon Graphics Workstation (CPU R4000/100 MHz) (Eils et al. 1995a). The localization of subchromosomal targets within chromosome territories is described by two distance parameters. Firstly, the shortest distance d1 between the gravity center of the target and the surface of the tessellated chromosome territory is calculated. Secondly, the shortest distance d2 between the gravity center of the target and an inner line of the territory is territory. This inner line is obtained by the shortest path in the Delaunay graph connecting the two points with maximum distance in the chromosome teritory. The ratio D=d1/d2 provides a rough estimate for the more interior ($D \geq 1$) or more peripheral ($D < 1$) localization of the target within the chromosome territory. All parametrization steps described in this section are performed without any user interaction and typically completed for a given chromoscome territory in less than 10 seconds.

We have applied this technique to study the three-dimensional morphology of chromosome 7 and X territories. Volume ratios calculated for the two chromosome 7- and X-homologs in female human amniotic fluid cell nuclei were similar suggesting that the inactive X chromosome territory (Xi)

was not much more condensed than the active one (Xa). However, the Xi-territory had a ***significantly rounder shape and smaller surface than the Xa-territory (Eils et al. 1995b). These data are consistent with a recently proposed model predicting that the overall genetic activity of a chromosome territory is related to its surface (Cremer et al. 1993, Zirbel et al. 1993). To study the localization of genes within a given chromosome territory the c-myc protooncogene on chromosome 8 was visualized with its respective territory (Fig. 1). Figure 2 provides distance parameters as described above for the localization of this protooncogene in 14 chromosome 8 territories.

ARTIFICIAL NEURAL NETWORKS FOR A CLASSIFICATION OF CHROMOSOME TERRITORIES

Artificial neural networks have been applied in an attempt to distinguish the inactive X-chromosome territory from the active one. 3D microscopic images of the chromosome territories serve as input for these networks. The artificial network consists of a layer of M input neurons and one output neuron. Each input neuron $i \in \{1...M\}$ processes the input data $\underline{b} = (b_1, b_2, ..., b_N) \in \Re_n$ and produces one bit B_i of information (which is then passed to the output neuron):

$$B_i = \Theta\left(\sum_{j=1}^{N} J_{ij} b_j - \vartheta_i\right) \quad i \in \{1 \dots M\}$$

where $\Theta(x)$ is 0 for $x < 0$ and 1 for $x \geq 0$. The synaptic couplings "J_{ij} and the thresholds ϑ_i determine the output functions of the neurons. Equivalently, the one output neuron of the network collects the information of the input layer neurons and produces one output bit of the whole network:

$$B_{out} = \Theta\left(\sum_{j=1}^{N} \tilde{J}_i B_i - \tilde{\vartheta}_i\right)$$

In our case the input string b is a sequentially stored raw image of a X-chromosome territory. The network should decide whether this chromosome is active or inactive ($B_{out} = 0$ or 1, respectively). The network must be trained, i.e. the synaptic couplings and thresholds of the network must be adjusted to fulfill this task as good as possible. Well defined examples of active or inactive X-chromosome-territories (independently defined by Barr body staining) are used in the training algorithm. We have developed a novel training algorithm, called RECOMI (Repeated Correlation Matrix Inversion). RECOMI uses techniques of mathematical optimization theory and is able to optimize the stability of each neuron against noisy input, e.g. background fluorescence. Another major advantage of this algorithm is its high performance speed, since RECOMI does not use the images themselves, but only the image to image correlations. In 80%up to 90% depending on the amownt and set of training examples the network prforms a true

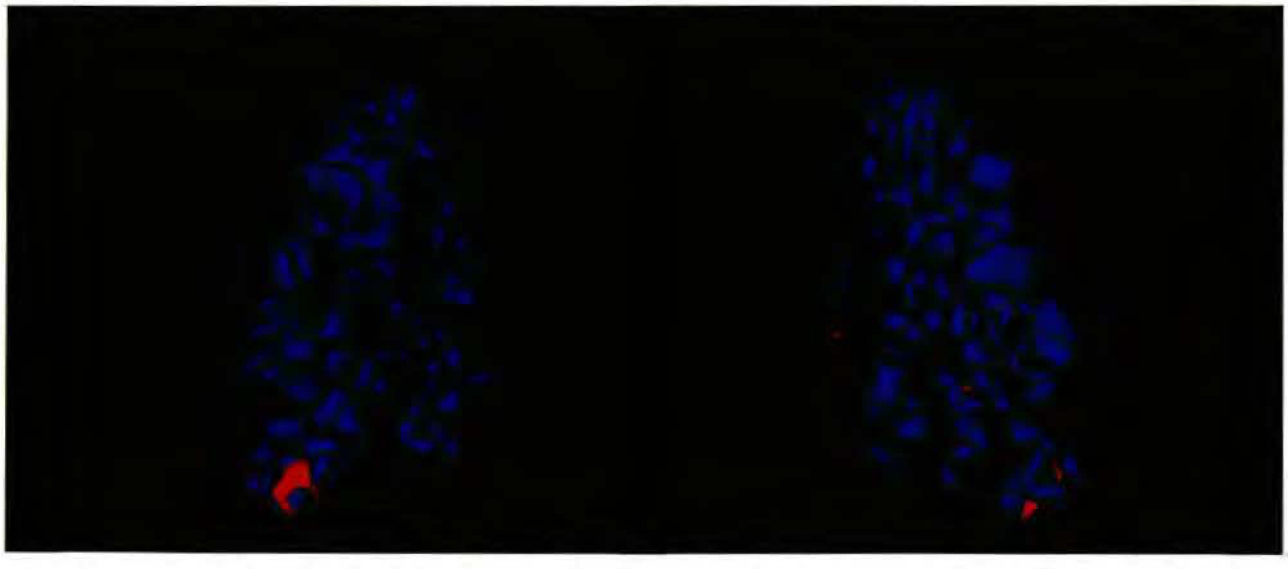

Fig. 1. Computer graphic visualization of a chromosome 8 territory (blue) painted with a chromosome 8 composite probe together with the chromatin domain harboring the c-myc protooncogene (red) hybridized with a phage-contig. The experiment was performed with a cultured, human female ammiotic fluid cell nucleus. The chromosome is shown from two sides (rotation 180 °)

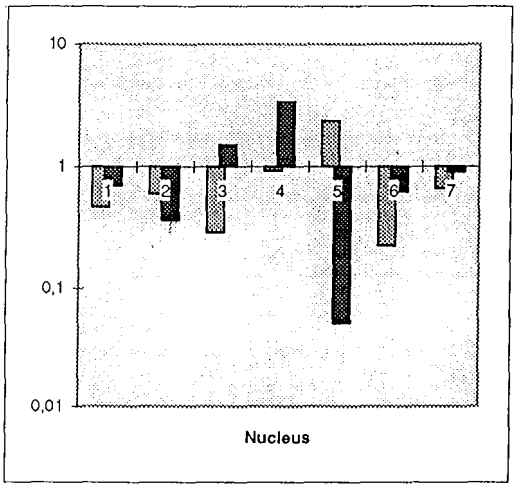

Fig. 2. Position of c-myc in 14 chromosome 8 territories determined by its D = d1/d2 ratio (for further explanation see text) in 7 diploid amniotic fluid cell nuclei (compare Fig. 1). Abscissa: Number of nucleus. Ordinate: Logarithm of the ratio values D. Note, that ratio values D smaller (larger) than 1 indicate a more peripheral (interior) localization of the target within the chromoscome territory.

classification of active or inactive x-chromosomes.

MONTE CARLO SIMULATION OF THE DISTRIBUTION OF CHROMOSOMAL TARGETS IN CELL NUCLEI

The distribution even of "point like" subchromosomal targets in cell nuclei is affected by the spacious extension of chromosome territories. To study such geometrical constraints in a model system chromosome territories and cell nuclei were represented by ellipsoids and spheres. For comparison with experimentally observed distributions of point like targets, various assumptions were made with regard to their location either within or at the surface of model territories. For each assumption the distance between two targets, representing homologous chromosome regions, and between each target and the center of the model nucleus was calculated by Simple Sampling Monte Carlo simulations. Distributions of targets under the various constraints show strong deviations from a model, which assumes that pointlike targets are distributed uniformly and independently from each other within the nuclear space. Experimentally observed distributions of the pericentromeric heterochromatin of chromosome 17 in human lymphocyte nuclei by and large are compatible with the assumption that the respective three-dimensional distributions are solely affected by geometrical constraints. Distributions obtained for chromosome 7 heterochromatin, however, suggest that other than geometrical factors may be involved (Munkel et al. 1995).

To overcome possible drawbacks imposed by the shape rigidity of the geometrical model described above another model was developed which allows flexibility in chromosome territory shape. In this model each territory is composed by some hundred spherical subdomains. In a first step these subdomains are randomly located in a spherical model territory by hybrid Monte Carlo simulation. The volume of these model territories is directly related to the relative DNA-content of the respective chromosome. In a second step the volume of the model chromosome territories is reduced to some 15% allowing all 46 model territories of a diploid human chromosome complement to be placed randomly in the model nucleus. In the third step the volume of the model chromosome territories is increased stepwise by hybrid Monte Carlo simulation till they regain their original size. The simulation is continued to allow relaxation. The last two steps force an originally spherical model chromosome territory to form a more flexible shape. Neighboring territories obtain complementary shapes. The localization of point like targets in the original and transformed territory can also be simulated.

A hybrid Monte Carlo simulation for a nucleus with 46 territories required one day on an up-to-date workstation. To optimize performance, simulation was parallelized (geometrical parallelization and dynamic load balancing). Using four PowerPC (PowerXplorer, PARIX) the calculation time was reduced to approx. seven hours. The mean distance between the gravity center of the transformed chromosome territories and the center of the model nucleus is shown in Fig. 3. The data suggest that larger chromosome territories in comparison with smaller ones should be preferentially distributed toward the nuclear interior. More advanced models which take into account the additional restriction that each territory should be attached to the nuclear envelope are presently under consideration.

REFERENCES

Bertin, E, F Parazza, JM Chassery. 1993. Segmentation and measurement based on 3D voronoi diagram: Application to

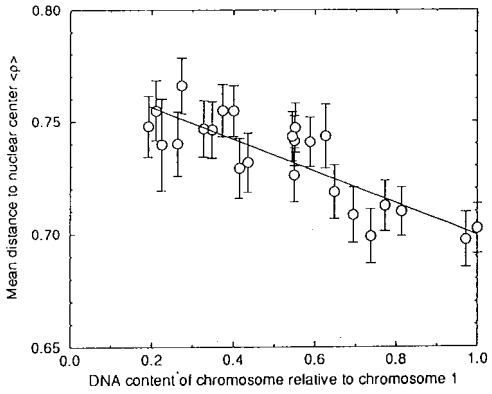

Fig. 3. Ordinate: Mean distances between the gravity center of chromosome territories (1-22, X and Y) and the nuclear center obtained by Monte Carlo simulation for 92 human model nuclei. Abscissa: relative DNA-content of each territory as compared to chromosome 1. Bars indicate mean distances obtained in a series of simulations. The line represents the linear regression curve.

confocal microscopy. Comput. Med. Imaging.Graph **17:** 175-182.

Cremer T, A Kurz, R Zirbel, S Dietzel, B Rinke, E Schröck, MR Speicher, U Mathieu, A Jauch, P Emmerich, H Scherthan, T Ried, C Cremer, P Lichter. 1993. The role of chromosome territories in the functional compartmentalisation of the cell nucleus. Cold spring Harb. Symp. Quant. Biol. **58:** 777-792.

Eils R, E Bertin, K Saracoglu, B Rinke, E Schröck, F Parazza, Y Usson, M Robert-Nicoud, EHK Stelzer, JM Chassery, T Cremer, C Cremer. 1995a. Application of laser confocal microscopy and 3D-Voronoi diagrams for volume and surface estimates of interphase chromosomes. J. Microsc. in press.

Eils R, S Dietzel, E Bertin, E Schröck, MR Speicher, T Ried, M Robert-Nicoud, C Cremer, T Cremer. 1995b. Active and inactive X-chromosome territories can be discriminated by surface and shape but not by volume. submitted.

Münkel C, R Eils, J Imhoff, S Dietzel, C Cremer, T Cremer. 1995. Simulation of the distribution of chromosome targets in cell nuclei under geometrical constraints. submitted.

Zirbel RM, UR Mathieu, A Kurz, T Cremer, P Lichter. 1993. Evidence for a nuclear compartment of transcription and splicing located at chromosome domain boundaries. Chromosome Res. **1:** 93-106.

Zoological Studies 34, Supplement I (1995)

Zoological Studies

High Resolution TEM and Energy Filtering TEM Study of Internal Structure and Composition Distribution in Materials

Fu-Rong Chen[1], L. Chang[2] and J. Y. Wang[3]

[1] *Materials Science Center, National Tsing Hua University, Hsinchu, Taiwan, R.O.C.*

[2] *Division of Engineering, National Science Council, Taipei, Taiwan, R.O.C.*

[3] *Materials R & D Center, CSIST, Lungtan, Taoyuan, Taiwan, R.O.C.*

High resolution transmission electron microscopy (HRTEM) is a very powerful technique to resolve the structure of the materials at atomic level. However, One of the limitations of the HRTEM technique is that it provides little information about the composition in materials. Except for some special case such as the one shown in the Fig. 1, a high resolution image of Al_3Zr precipitate in Al matrix. This image was recorded at the Scherzer underfocus which is about -50 nm for JEOL 4000EX. The Zr atoms are shown as dark contrast and the Al atoms bright dots in the Scherzer focus so that we can see the composition distribution at the atomic level near the interface.

When the high energy electrons pass through the specimen, the electrons are not only scattered elastically but also accompanying the inelastic scattering. Using an imaging filter which is coupled with TEM allows us to select inelastic scattering electrons associated with a particular energy loss which corresponds to a particular element in the materials to form the image. The energy slit locates in the dispersion plane. This technique is very similar to the regular dark field technique, however, it is a dark field technique in the energy space. This technique provides us the information about the distribution of the composition in the materials. Two examples are given below. We have used this technique to study the phase transformation in the Cu-Be alloy and the interlayer characteristics between diamond film and the silicon substrate. Fig. 2 (a) is a bright field image of the γ phase precipitate in the Cu alloy. This γ phase precipitate is about 6 nm in width and exhibits only little contrast due to being not strongly diffracted. However, it shows brighter contrast in the energy filtering image of Fig. 2 (b) which is recorded using Be K edge loss (111 ev) with the width of energy slit 10 ev. This image implies the γ phase precipitate is Be rich.

Diamond film was grown using microwave plasma CVD technique which consists of three steps: carburization, bias and growth. At the bias stage there is an interlayer of 6 nm thick between diamond and silicon substrate . Most of the regions of the interlayer are of amorphous characteristics which presents a barrier to identify the elemental compositions. Fig. 3 (a) and (b) are the Si and C jump ratio maps of the energy selecting images, respectively. The jump ratio maps were obtained by dividing the post-edge loss image by

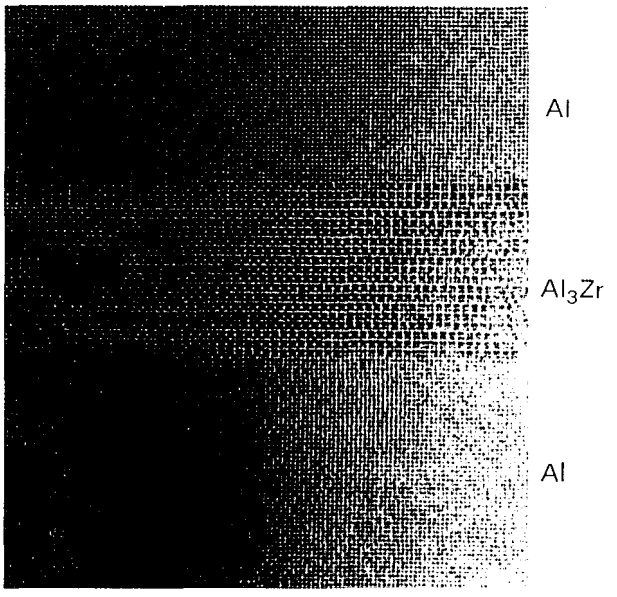

Fig. 1. High resolution image of Al_3Zr precipitate in Al matrix.

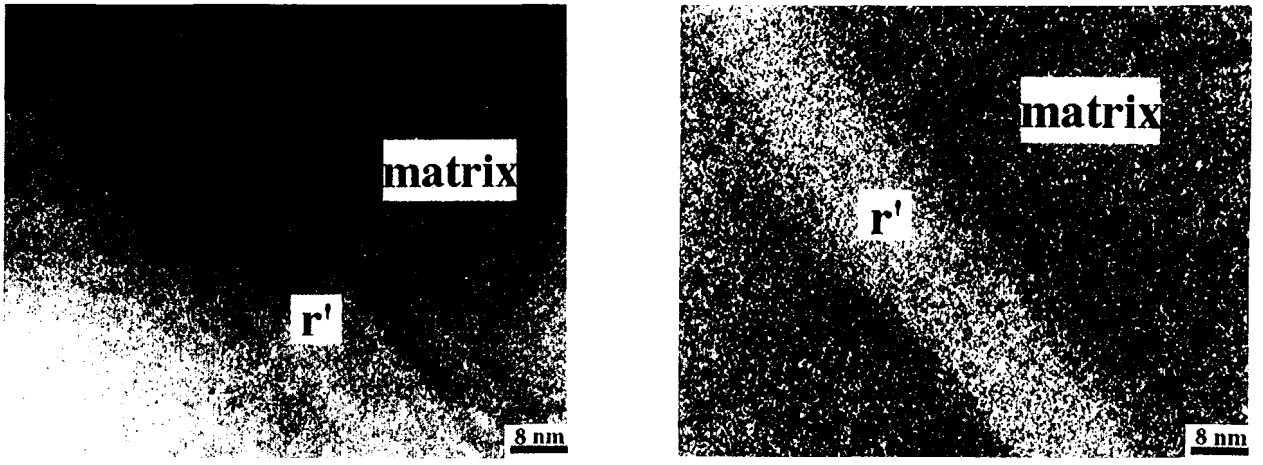

Fig. 2. (a) Bright field image of g precipitate in Cu alloy. (b) The Be K-edge core loss (111 ev) image of (a)

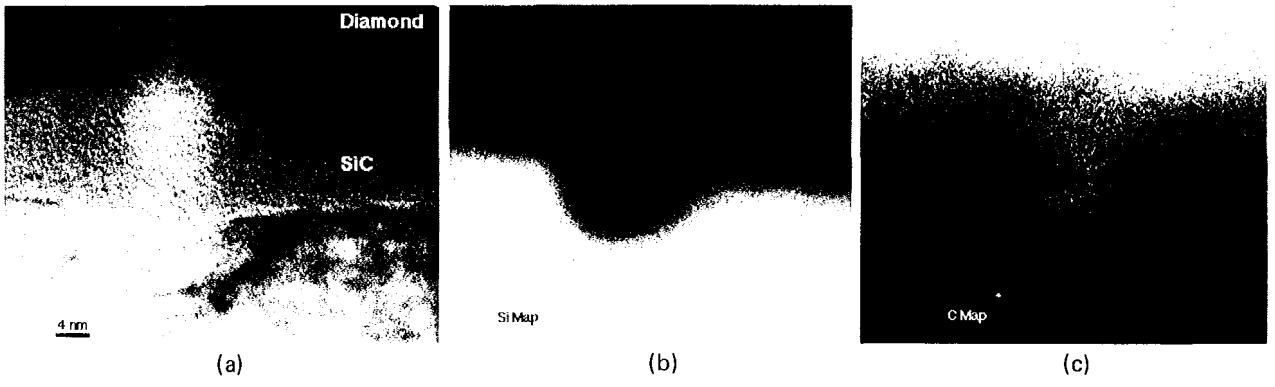

Fig. 3. (a) high resolution image of microwave plasma CVD diamond on silicon. (a) the jump ration map of Si. (b) the jump ration map of C.

the pre-edge image. The post-edge image of Si and C were recorded at the 119 and 303ev, respectively. The pre-edge image were recorded at 79 and 263 ev. The width of the energy slit was set to be 10 ev. There are three contrast levels in both images. It could confirm that the interfacial layer is SiC. We have done the same anaylsis on the specimen in the carburization stage. An amorphous layer consisting of carbon was covered on the Si amorphous layer. It may suggest that the thin interlayer transforms from carbon in the process of carburization to SiC in following bias stage.

With combination of the high resolution TEM and energy filter, we are able to obtain the infiormation of the structure and composition at near atomic level simutaneously. There is, however, still a limitation of detection of the minor elements within the materials due to the low intensity of the inelastic scattering electron and low signal to background ratio of electron source. With the recently developed field emmision TEM, these two techniques will become more powerful from the excellent coherency and the high brightness of the electron source.

Zoological Studies 34, Supplement I (1995)

Zoological Studies

Three Dimensional Analysis of Sea Urchin Mitotic Apparatus with SFP Method

Michio Abe

Department Biology, Tokyo Metropolitan University, Minamiohsawa 1-1, Hachiohji-shi, Tokyo, Japan

Visualization of cytoskeleton in sea urchin embryos is an important process for its developmental analysis on biology. There are many suggestions between the early developmental processes (i.e. nuclear positioning, formation of asymmetric mitotic apparatus and determination of division plane). Despite of the existence of these suggestions, it was very hard to visualize cytoskeleton in whole mounted embryo. One difficulty of visualization was the relatively big diameter of sea urchin egg. The big diameter of sea urchin egg interferes to the normal working distance of conventional immuno fluorescence light microscopy and results low resolution of image unless samples were sectioned or flattened artificially. In fact, most objective lenses with high magnification for conventional fluorescence microscopy have about sixty to eighty μ meter of working distance. So, the whole diameter of sea urchin egg comes to physical limit of objective working distance. Three dimensional visualization of embedded physical sectioned eggs requires very large number of sections. When these images are exported to the computer system for three dimensional visualization, it needs more power of processor and more large area of memories and hard disk for to make the reconstructed image of spatial distribution of cytoskeleton. Optical sliced images are gotten easily without physical sectioning and exported directly to the reconstruction program. One problem of three dimensional reconstruction is the resolution of resulted image. Usually, final 3-D image showed low resolution and "CG like" artificially enhanced view. The solution for this problem is to increase the number of optical sections, which means longer LASER excitation to the samples. To minimize the fading of fluorescence dye, more fast scanning method is required for high resolutional three dimensional analysis. Another problem is the way of expression of the three dimensional objects. The most popular style of visualization is stereo-pair or red-green stereo images. These visualization methods are easy to use but does not show the depth of samples naturally. So, I choose the Simulated Fluorescence Process (SFP) method for the expression of reconstructed three dimensional images. This process makes a rendered realistic image with ray tracing algorithm after the correction of axial distortion. The result of ray tracing is more natural 3-D view than stereo (or red-green) type reconstructions. Cytoskeletons in the mitotic phase embryos were preserved by the optimized isolation medium and fixed. After immuno-stained, confocal images were obtained by the InSIGHT plus-IQ (Meridian Instruments Inc.) equipped on the inverted microscope (IMT-2, Olympus). Embryos were settled on the grass-bottom culture dish and observed with 60X objective (Plan-Apo, NA=1.4). Optical series of sectioned confocal images were obtained for each 0.1micro meter or 0.5 μ meter in depth, and for 100 to 256 in total number. As a result, whole height of mitotic apparatus or embryo is sliced in the confocal sections. Images were analyzed with three dimensional SFP algorithm equipped in InSIGHT plus-IQ system, or exported to the IRIS Indigo (Silicongraphics, Inc.) and rendered with VoxelView system (Vital Images Inc.). Reconstructed SFP images of first mitosis were made through the metapahse to late telophase embryos and streak stake embryos. Projected X-Y image and computer-aided X-Z sectioned images were also made for the whole height of embryos. Animated series of SFP images were also made for the analysis from multi-pointed view.

This work showed the possibility of three dimensional analysis of microtubules in sea urchin embryo with SFP, projection and X-Z sectioning method. With SFP method and enough number of optical sliced images, reconstructed images are free from

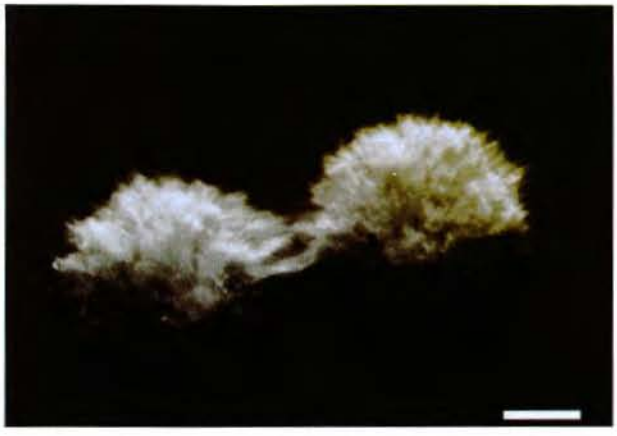

Fig. 1. SFP reconstructed mitotic apparatus of sea urchin *Hemicentrotus pulcherrimus* at the first metaphase. Whole reconstructed mitotic aster and spindle are clearly shown. (Bar=10 μ meter)

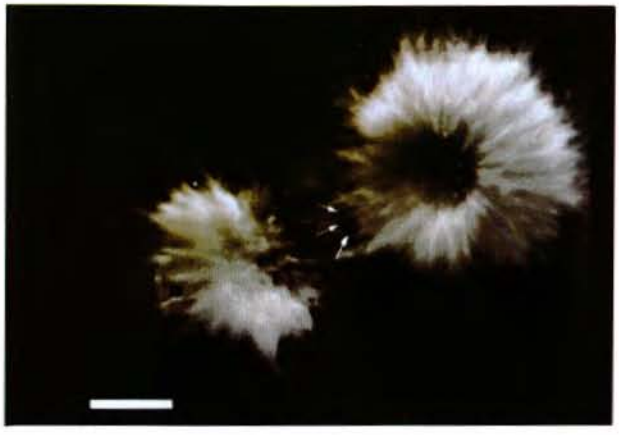

Fig. 2. SFP reconstructed image at the anaphase embryo. Arrows indicated the position of chromosome in the mitotic spindle. (Bar= 10μ meter)

artificial enhancement of microtubule image in the whole height of embryos. These results suggest the usefulness of confocal system for the analysis of the three dimensional distribution of cytoskeleton.

Zoological Studies 34, Supplement I (1995)

Zoological Studies

Generation and Deconvolution of 3-D Voxel Cubes with Leica DM and Optimas

Volker Tympel
Konrad-Zuse-Str. 3 D-7745, JENA, Germany

The new generation of research light microscopes opens the way for an easy interaction with PC-based commercial image processing systems. The DM microscope from Leica used by these work is one of such microscopes with many function controlled via RS232C. In these work z-axis position, light intensity and zoom are used only. The z-axis has a very high precision of 0.1μm per step. The light intensity is controlled by the lamp voltage in the range from 5 to 12 V DC in 256 steps. The zoom can be changed by PC from 0.9x up to 2.5x with a resolution by 0.1x. So it is possible to work with a very high magnification. The camera is a SONY 3chip 1/2" color DXC930P. It is possible to control all camera parameters and functions by PC applicating the 930Control kit. It is also possible to work in the low light field applicating the long time integration mode. Up to 256 normal frames can be integrated directly on the CCD-chips, so that the camera is up to 256 times more sensitive then before. It is possible to acquire color fluorescence images particularly FISH (fluorescence *in situ* hybridization) in a very high quality. A cooling kit with Peltier-element and head sink reduced the noise for image calculation and long time integration. A special image processing filter -called "starkiller"- eliminates really the last pixel defects. Parameter set for special probes and color light temperatures can be saved or loaded, so an optimal adjustment is possible. A color frame grabber CFG from Imaging Technology Inc. digitise the RGB-signals of the CCD camera with a resolution of 768x 512 pixel and 3x 8bit. A normal ISA-bus PC 486/50 was extended in the RAM to 32 MByte to opens the field of application with larger voxel cubes without swapping to the hard disc drive. The systems works under MS-Windows for work groups version 3.11. The image processing software is OPTIMAS from Optimas Inc. version 4.1 extended by Macros written with the ALI- language from OPTIMAS. Functions being critical in time are written as fast C-functions by MS-Visular C++ version 1.5 as Dynamic Link Libraries and are included into ALI. OPTIMAS is an open System with an interface -the Register() and Call() functions- to include fast owner functions. These functions creates voxel cubes in an optimal structure for the i486 processing unit. Using these special structure is possible to the CPU to do a lot of image calculation work directly with dates in the very fast 1. level cache on the CPU. A macro generates multiple layers grabs and fills the voxel cube V with the information from the 2-D image fields (dimensions: sizeX, sizeY) automatically up to sizeZ steps. The first operation is a deconvolution like:

$$Va(x,y,z)=V(x,y,z)+A*V'(x,y,z+1)+B*V'(x,y,z-1)$$

$$V'(x,y,z) =\Sigma V(x+i,y+j,z+k) \quad -1<=i,j,k<=1 \quad 0<=x<sizeX,\ 0<=y<sizeY,\ 0<=z<sizeZ$$

A and B are parameter to describe a simple Point Spread Function with 0>A,B>=-5/90. The results can larger the 8bit and small values are also important to, so it is necessary to scale with a large factor and a non-linear gamma transformation is also necessary to a good D2- field on the display monitor. These operations will be done in some seconds for the full cube. The global result is a new color voxel cube with more details and a broad contrast. The new voxel can be displayed as a sequence of differed cuts ore different projections can be calculated. Also the way for 3-D segmentation is open. The experience from these will be included into a now more powerful version based on fast 300MHz DEC-Alpha RISC processing units with high speed PCI- frame grabber, up to 256MByte RAM and larger 2. level cache based on Windows- NT. The problem of visible digitising noise after the calculation will be reduced by frame integration behind

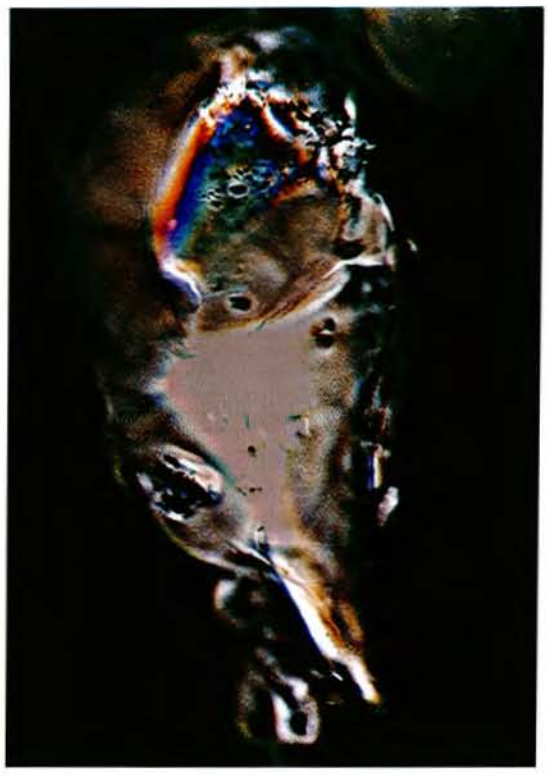

the ADCs and an extension to 10bit input frames ore by cooling the ADCs. This work could be done by the friendly help and support due to the Institute of Molecular Biology of the University Jena especially to Mr. Schwertner.

Zoological Studies 34, Supplement I (1995)

Zoological Studies

Electrofusion of Plant Protoplasts and Three Dimensional Network of Actin Filaments Observed with Confocal Scanning Laser Microscopy

Mieko Taniguchi[1], Naoya Suzuki[1], Tatuo Arii[2] and Takeshi Tangiuchi[3]

[1]*Department of Physics, Faculty of Science, Nagoya University, Chikusa-Ku, Nagoya, 464-01, Japan*

[2]*National Institute for Physiological Sciences, Okazaki, 444, Japan*

[3]*School of Agriculture, Nagoya University, Chikusa-ku, Nagoya 464-01, Japan*

Electrofusion is a powerful tool for studying membrane properties, organization of cytoskeleton and cell motility on the early process of cell fusion. Recently, confocal microscopy have become available for the detection of actin filaments and aggregates in protoplasts (Kobori et al. 1989). The purpose of the present study is to report on the three dimentional structure and dynamical aspects of plant protoplasts during early process of electrofusion. Protoplasts from soybean *(Glycin Max)* and lettuce cotyledons *(Lactuca sativa)* were isolated by using the enzyme solution (Phansiri et al. 1991, Taniguchi and Maeda 1991). Protoplasts aligned in an alternating electric field at frequency of 1 MHz and a field strength of 200 V/cm for 30 s. Fusion was induced by DC pulses of 1,600 V/cm of 50 μs duration using Shimadzu Somatic Hybridizer. Control and AC and /or DC field applied protoplasts were stained by rhodamine-123 for mitochondria (Wu 1987, Chen 1989, Taniguchi, Maeda 1991)· or rhodamine-phalloidin for actin (Taniguchi et al. 1993). The specimens were viewed with a confocal scanning laser microsocpe (Noran Instruments) equipped with a Nikon oil-immersion objective lens with x 100 objective magnification and numerical aperture of 1.3. An argon laser with 488 nm or 529 nm was used to excite for rhodamine- 123 or rhodamine-phalloidin, respectively. Protoplasts were photographed with 20 to 40 parallel optical slices 0.2 to 0.5 μm apart. These images were projected to create a single image in which the specimen was in focus. A series of images was collected at different fcus focus levels (step size 0.05 to 0.5 μm).

When protoplasts from soybean were treated with AC field and stained with rhodamine-123, many yellow-green fluorescence spots (mitochondoria) were observed in the areas of cytoplasm (Fig. 1). In this figure, two protoplasts contact with wide surface areas but in one of two protoplasts mitochondrias are seen to localize in other side. We have also examined the distribution of actin in lettuce and soybean protoplasts. The actin filaments in the dark and light grown protoplasts from lettuce were stained with rhodamine-phalloidin. In control protoplasts, actin located mostly at the periphery of the cells. In AC-treated protoplasts, on the other hand, actin was located at the contact area and at the periphery of nucleus and chloroplasts. After electrofusion we analyzed the

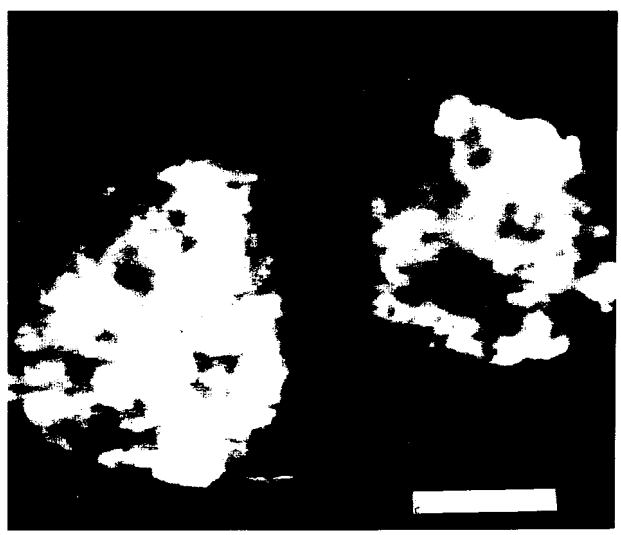

Fg. 1. Confocal microscopic image of soybean protoplasts stained with rhodamine-123, Scale bar, 10 μm.

changes of F-actin organization by time sequential images of confocal micrographs.

Three dimensional observations of protoplasts were also made by a high voltage electron microscope (1 MeV) equipped with a revolving stage to get a pair of stereo-micrographs. Minimum dose and low temperature techniques were used. We discuss these images in detail.

ACKNOWLEDGEMENTS

This work was supported by the Joint Studies Program (1993-1994) of the National Institute for Physiological Science.

REFERENCES

Chen LB. 1989. Fluorescent labeling of mitochondria. Methods in Cell Biology. **29:** 103-123. Acad, Press.

Kobori H, N Yamada, A Taki, M Osumi. 1989. Actin is associated with the formation of the cell wall in rverting protoplasts of the fission yeast *Schizosaccharomyces pombe*. J. Cell Sci. **94:** 635-646.

Phansiri S, T Taniguchi, E Maeda. 1991. Morphological study of soybean protoplasts in early electrofusion process. Jpn. J. Crop. Sci. **60:** 550-557.

Taniguchi T, E Maeda. 1991. Analysis of the fusion process of plant protoplasts by fluorescence microscopy. Plant Tissue Culture **1:** 1-8.

Taniguchi M, N Watanabe, S Aoki, H Kihara, S Phansiri, T Taniguchi, T Arii. 1993. Comparative studies on cultured plant protoplasts using X-ray and optical microscopes and high voltage electron microscope. 4th. Int. Conf. on X-Ray Microscopy. D-8.

Wu FS. 1987. Localization of mitochondria in plant cells by vital staining with rhodamine 123. Planta **171:** 346-357.

Zoological Studies 34, Supplement I (1995)

Zoological Studies

Measurement of Distances in Three-dimensional Dual-colour Confocal Images

Erik M.M. Manders[1]*, R. Hoebe[1], J. Strackee[2], A.M. Vossepoel[3] and J.A. Aten[1]

[1]*Laboratory for Radiobiology, University of Amsterdam, The Netherlands*

[2]*Laboratory for Medical Physics, University of Amsterdam, The Netherlands*

[3]*Faculty of Applied Physics, Delft University of Technology, Delft, The Netherlands*

For the quantitative analysis of the spatial relationship between different biological structures in the same preparation, dual-colour confocal microscopy (Carlsson, 1990) has proven to be a successful technique. The spatial relationship between different objects in a two-colour image can be quantified in several ways, depending on the biological information that has to be abstracted from the image. Measurement of co-localization of objects is one of the relevant quantities that can be determined. The large number of methods to quantify co-localization (Ackner et al., 1991; Manders et al., 1993, Wansink et al., 1994) illustrate that each application needs its individual method. An other important quantity of three dimensional dual-colour images containing a large number of spots is the average distance between nearest neighbouring spots. We have developed an image analysis method to measure the latter quantity. We will present this method and show how it can be applied on dual-colour confocal images of cells that were double-labelled with IdUrd and CldUrd (Manders et al., 1992; Manders et al., submitted) to investigate the dynamics of DNA replication (Fig. 1).

To calculate distances between multiple spots in dual-colour images, an accurate determination of the 3-D positions of these spots is essential. The position of the centroid, as an estimator for the position of a spot, can be calculated on the basis of all voxels that belong the domain of the spot. For this calculation a domain that defines which voxels belong to the spot must be delimited (defining a boundary). To create a boundary for a domain we developed a 3-D image segmentation procedure: the Largest Contour Segmentation (LCS) (Manders et al., submitted). By means of this procedure the position of each spot can be determined accurately and automatically (Fig. 2).

After applying this LCS procedure on both colour-components of a dual-colour image (in the sequel we will mention these components as the red and the green component) and the determination

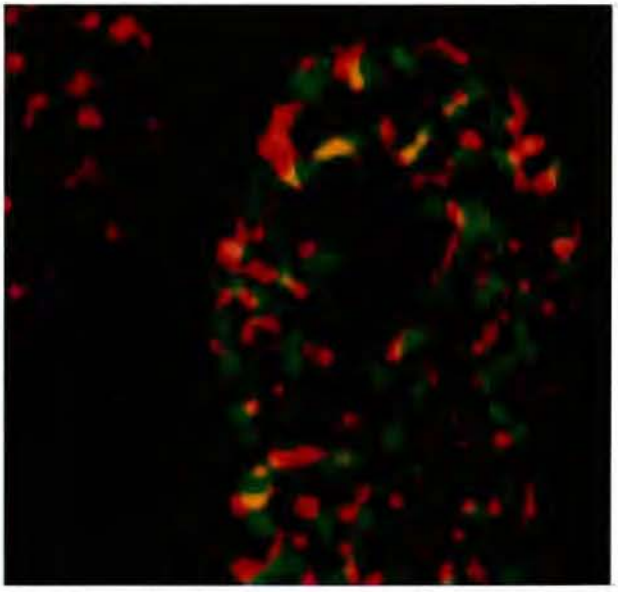

Fig. 1. Preprocessed optical section through the center of a Chinese Hamster cell nucleus, pulse-labelled first with IdUrd (red) and with CldUrd (green) 40 minutes later. After the application of the described method, we measured that the average distance between neighbouring red and green spots is 0.4, μm.

current address: Physics IV, The Royal Institute of Technology, S-10044, Stockholm, Sweden

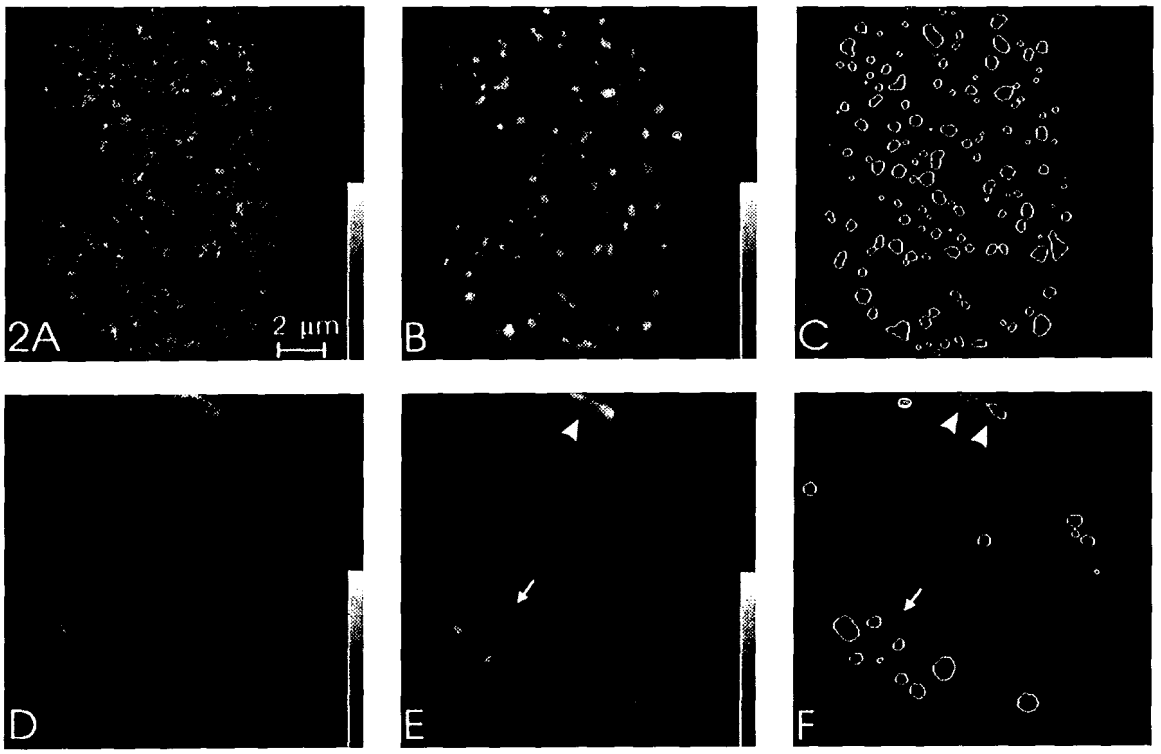

Fig. 2. An optical section through the middle of an early (A) and a late (D) S-phase nucleus as recorded by the confocal microscope. The same 2-D sections (B) and (E) after 3-D image restoration and after 3-D image segmentation (C) and (F). Using the LCS segmentation procedure most domains are detected and their boundaries are defined. However, some are missing (arrows in E and F) and some domains are split into two separate domains (arrowheads in E and F).

of the positions of the spots, the distance between each red spot and each green spot, defined as the distance between their centroids, was computed. Subsequently, pairs of nearest (red-green) neighbours were indicated. A red and a green spot were defined as being paired when there is no other red domain nearer to the green spot and no other green spot nearer to the red one. In that case the inter distance of the pair was listed.

When the average inter-distance of the paired domain is large relative to the accuracy of measurement, the interpretation of the data is simple; the average distance is a direct estimator for the distance that separates the paired red and green spots. When, however, this distance is of the order of the size of the statistical error of measurements, a geometric effect spoils this estimator. The influence of this effect was estimated statistically after which a correction of the data was performed.

This study was supported by the Netherlands organization for Scientific Research (NWO) and SPIN, project 3-D analysis.

REFERENCES

Ackner G, K Mossberg, A Wikström, K Sundqvist, J Gustafsson. 1991. Evidence for co-localization of glucocorticoid receptor with cytoplasmic microtubiles in human gingival fibroblasts, using two different monoclonal antibodies, confocal microscopy and image analysis. *J. Steroid Biochem. Molec. Biol.* **39:** 419-432.

Carlsson K. 1990. Scanning and detection techniques used in a confocal scanning laser microscope. *J. Microse.* **138:** 21-27.

Manders E.M.M, FJ Verbeek, JA Aten. 1993. Measurement of co-localization of objects in dual-colour confocal images. *J. Microsc.* **169:** 375-382.

Manders EMM, J Stap, GJ Brakenhoff, R van Driel, JA Aten. 1992. Dynamics of three dimensional replication patterns during the S-phase analysed by double labelling of DNA and confocal microscopy. *J. Cell Sci.* **103:** 857-862.

Manders, EMM, J Stap, R van Driel, J Strackee, JA Aten. Spatial progression of DNA replication in the cell nucleus. Submitted to *Cytometry*.

Manders EMM, J Strackee, JA Aten. The largest contour segmentation; a tool for the localization of spots in confocal images. Submitted to: *Cytometry*.

Wansink GD, EMM Manders, I van der Kraan, JA Aten, R van Driel, L de Jong. 1994. Transcription by RNA polymerase II is excluded from replication centres: evidence for functional compartimentazation in the S-phase cell nucleus. *J. Cell Sci.* **107:** (in press).

Zoological Studies 34, Supplement I (1995)

Zoological Studies

Fluorescence *in Situ* Hybridization on Human Metaphase Chromosomes Detected by Near-field Microscopy

M.H.P. Moers, A.G.T. Ruiter and N.F. van Hulst

Applied Optics Group, Department of Applied Physics, University of Twente, P.O.Box 217, 7500 AE Enschede, The Netherlands

The high optical resolution and sensitivity of near field scanning optical microscopy (NSOM) promises important applications in biology and biochemistry. In particular fluorescence microscopy, with fluorescent labels as markers for biochemical processes, requires an improvement in resolution. *In situ* hybridization is an example of a technique that demands a higher resolution, especially when used for DNA mapping. With conventional optical microscopes DNA probes can be resolved at distances of about 500 nm. Modern techniques like electron microscopy and atomic force microscopy offer a much better resolution, but give problems with multiple 'color' ISH and with the preparation of the samples.

Near-field scanning optical microscopy (NSOM) might play an important role in the localization of genes on morphologically preserved inter- and metaphase chromosomes: the technique combines the high resolution of scanning probe microscopy with the optical selectivity and sensitivity of optical microscopy. A forthcoming, but important advantage is that a topographic (force) image is obtained simultaneously with the fluorescence image, such that the location of the fluorescence signals can be correlated to the morphology of the chromosome.

The near-field optical microscope used for the detection if *in situ* hybridization signals is integrated on a Zeiss Axiovert inverted microscope: chromosomes are inspected with a high quality epi-fluorescence microscope and preselected for measurements with the near field microscope. The sample is illuminated through a adiabatically tapered, aluminum coated optical fiber with a small aperture at the tip end. The size of the tip, approximately 100 nm, determines the illuminated area of the sample, and thus the resolution. A feedback on shear-force is used for distance regulation.

Fluorescence of the sample is collected by the microscope objective and detected by a photon counting avalanche photo-diode. The sample is raster scanned while both fluorescence and height are measured resulting in a simultaneously obtained fluorescence and topographic map of the chromosome.

The possibility to detect indirectly labeled DNA probes with a near-field scanning optical micrroscope is demonstrated. Both satellite and plasmid probes are accurately localized on human metaphase chromosomes. The fluorescence images show a lot of detail that is not seen with conventional fluorescence microscopy. Optical resolution in the fluographs is better than 100 nm. The fluorescent sites can be correlated to the topography of the chromosomes, which is recorded with a lateral resolution of about 50 nm. Furthermore, two color fluorescence *in situ* hybridization on a single chromosome is shown.

As an example of the results described above, a 7×7 μm image of a human metaphase chromosome 1 is shown. The chromosome is hybridized with dioxygenated p1-79 and immunologically detected with CY-3. We have combined the fluorescence signal and the topography in one image in order to emphasize the simultaneous recording of the signals. The topography of the chromosome is given in grey, and the chromosome structure is clearly recognized. The fluorescence intensity is given in orange. Several signals are observed at the telomer region, giving the location of the p1-79 probe. With conventional microscopy p1-79 usually is observed as a single spot at the telomer, although some sub-structure is recognized. Several other signals are found on the chromosome, which is probably due to non-specific hybridizations.

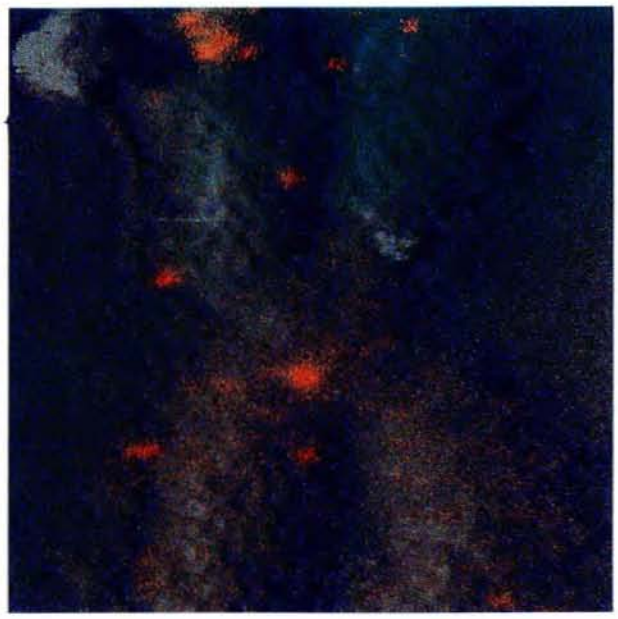

Concluding we clearly demonstrate the possibility and sensitivity to detect fluorescently labeled DNA fragments on human metaphase chromosomes with an optical resolution substantially better than possible with conventional microscopy. Furthermore, a force image of the chromosome morphology is afforded simultaneously.

Zoological Studies 34, Supplement I (1995)

Zoological Studies

High-Resolution Imaging of Human Chromosomes Using Atomic Force Microscope

Ching-Ling Teng[1], Wunshain Fann[2] and Jye-Siung Fang[3]

[1]*Department of Physics, National Taiwan University, Taipei, Taiwan, R.O.C.*

[2]*Institute of Atomic and Molecular Sciences, Academia Sinica, Taipei, Taiwan, R.O.C.*

[3]*Tzu Chi College of Medicine, Hualien, Taiwan, R.O.C.*

We have integrated an atomic force microscope (AFM) with a conventional optical microscope into a system to study the structures of human chromosomes (Fig.1). This integrated system is very convenient for locating objects of interest in the AFM imaging processes. In addition, the system has the capability of directly comparing the chromosome images taken by AFM with those taken by the optical microscope. Though human chromosomes have been extensively studied by other microscopic techniques, such as optical microscopy and electron microscopy, each technique has its disadvantages. The optical microscope has only low power of resolution (around 1 micron), while the electron microscope requires elaborate procedures which may destroy natural states of the sample. It is considered that the structures reflect biochemical characters. Therefore, to understand the nature states of chromosome structures is very important.

The AFM, on the contrary, requires only minimum sample treatment and can give three dimensional surface configurations. It also reveals the chromosome structures at a high resolution around 50nm. However, in general, sample damage is a serious problem by using AFM to study the biological systems. We have tried out tips with four different force constants. The tips with 0.064 N/m force constant were finally selected because they gave better image resolution. In addition, the structures of the chromosomes were quite stable during scanning processes and good quality images can be easily reproduced.

There are four major findings in this study. First, chromosomes are observed with elastic properties, e.g., the images obtained depend greatly on the force applied by the tips. Secondly, AFM

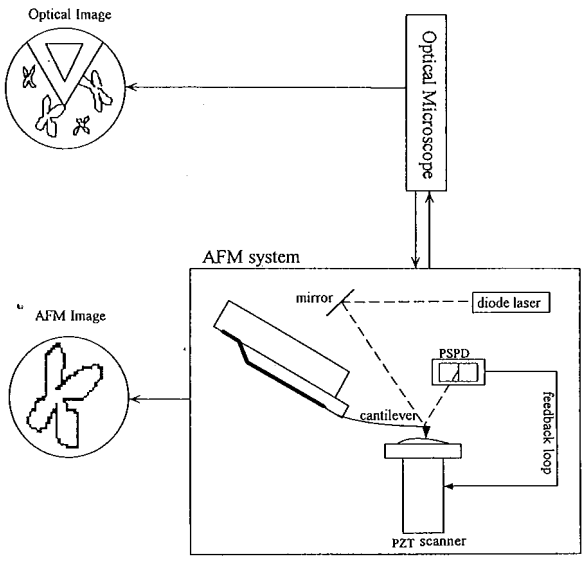

Fig. 1. Illustration showing the integrated optical microscope and the AFM system. From the optical microscope, an image of low resolution is taken. It also provides a sideway to look at the scanning processes. A high-resolution image is obtained by the AFM system.

images reveal the ends of loops of 30nm chromatin fibers, where the fiber reaches the surface and folds back into the body of the chromosome (Fig.2 (A.B)). These results confirm earlier electron microscope observations (Harrison et al. 1981, Adoph et al. 1983). Thirdly, there is a one to one correspondence between the height variations in the AFM image and the banding patterns observed after stained with Giemsa in the optical image. Finally, images of the bivalents isolated from sper-

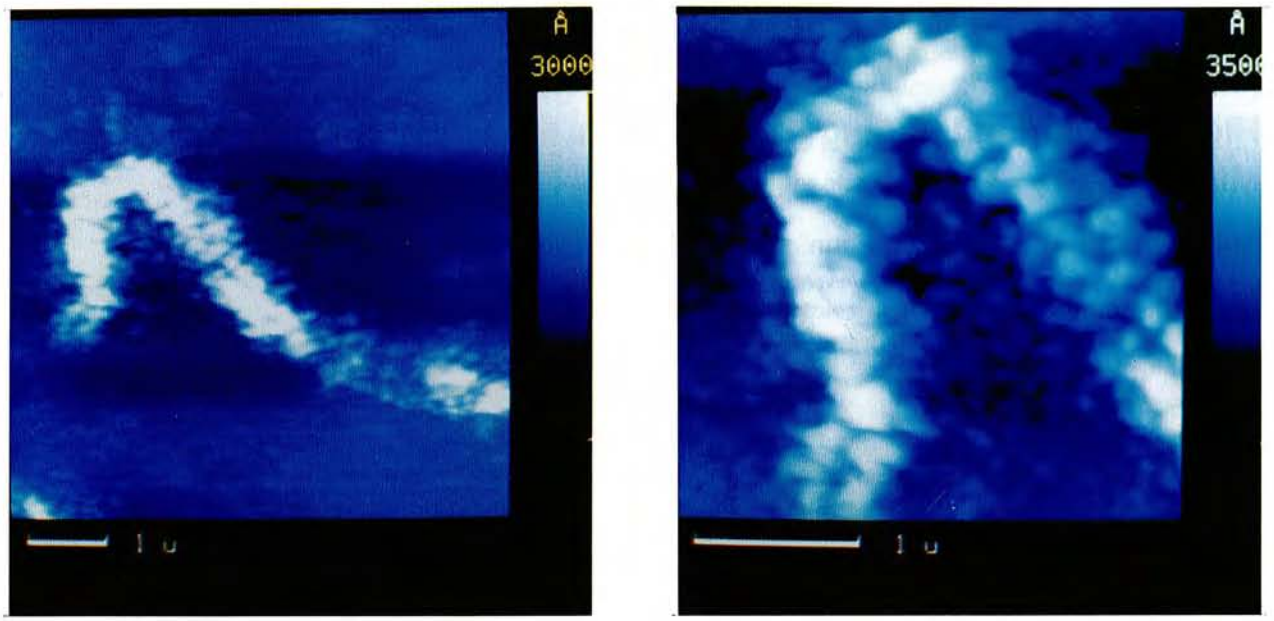

Fig. 2A. A typical AFM image of a human chromosome, with scan size 6.3 × 6.3 μm. **Fig. 2B.** The arc part of the same chromosome with scan size 3 × 3 μm. In these high-resolution images (resolution around 10nm), subunits with sizes in the range between 50nm to 100nm are predominant.

matocytes have shown twisted chromosome configurations which are not apparent in the optical image.

In conclusion, we have demonstrated that AFM is a useful and reliable tool for chromosome studies. This research is partly supported by National Science Council in Taiwan, R.O.C.

REFERENCES

Harrison CJ, M Britch, R Kreisman. 1981. Scanning electron microscope of the G-banded human karyotype. Exp. Cell Res. **134:** 141-153.

Adolph KW, LR Kreisman. 1983. Surface structure of isolated metaphase chromosomes. Exp. Cell Res. **147**: 155-166.

Zoological Studies 34, Supplement I (1995)

Zoological Studies

The Visualization System for Cross Sectional Images

Pei-Wen Liu, Lih-Shyang Chen, Su-Chou Chen and Jong-Ping Chen
Institute of Electrical Engineering, National Chen-Kung University, Tainan, Taiwan, R.O.C.

Recently, the scientific visualization techniques have been widely used in medicine, biology, geography, and many other scientific and technical researches. The scientific visualization exploits sophisticated computer graphics and data processing techniques, such as 3D reconstruction of histological, optical, and tomographical sections, to gain insight and understanding of complex problems characterized by large data sets. In the last couple years, many scientific visualization systems have been developed, such as AVS (Upson et al. 1989), apE (Dyer 1990), and IRIS Explorer (IRIS 1991), and DISCOVER (Chen et al. 1994).

In this paper, we describe a distributed computing system for scientific visualization applications, called "DISCOVER" (a Distributed Interactive Scientific Computing and Visualization Envi Ronment) (Chen et al. 1994). Currently, the system is a medical application framework targeted at physicians in hospitals for clinical applications. The system allows users to interactively display and manipulate the 2D and 3D medical objects, visualize the results, take control of the system computation, and drive the analysis and discovery processes. The system can also be used for the visualization of other scientific data: either numerically computed data, such as the pressure distribution within a fluid reservoir, or empirically measured data, such as tomography radiation measurements or microscopy images.

Our system consists of a virtual host, which consists of one or more personal computers, and one or more workstations, which are the computation servers. Each window in the virtual host is a client of the computation servers. When a command is issued by the user from any window in a host, it is sent to a global command queue and waits for being broadcasted to all the computation servers. After the computation is done, the results will be sent back to the client. In other words, the command queue can be thought of as a single virtual client of the computation servers in the whole system.

In our system, we use MS-windows 3.1 as the underlying window system for the user interface (Fig. 1). Images created by various medical modalities such as CT and MRI are converted into a specific volume data format that is suitable for further processing. The data structure of the volume data, called a quadtree-segment structure, is based on the combination of a quadtree and a run length encoding scheme (Chen et al. 1989). The run length encoding is used along the X direction and a quadtree data structure is used on the Y and Z dimensions to some level. On the bottom level (the leaf of the quadtree), each node is a 16X16 square in size. In other words, an object data consists of a quadtree and a lot of 16X16 node data structures, called boxes, that are pointed to by the leaf node of the quadtree.

There are four different types of windows in the system; a global command window, 2D image windows, 3D image windows, and album windows (Fig. 1). The global command window is used to display and issue the global commands to other three kinds of windows. The 2D/3D image windows are used to display 2D/3D images respectively. The album windows are used to simulate the traditional film-based medical images and the viewing boxes used by the physicians. The medical images, such as CT or MRI images, are displayed in the album window in a row by row, column by column fashion. Images can be moved around inside the album window for comparison just like the photos in an album. The images of interest in the album can be brought to the 2D image windows for more advanced processing.

For the 2D image window, there are three classes

Fig. 1. The graphical user interface of the DISCOVER system. The global command window is on the upper-right corner. The album window is on the lower right corner. The 2D image and 3D image windows under "NCKU DISCOVER" are activated (see the green boxes) and are thresholded simultaneously.

Fig. 2. Some 3D image processing techniques provided by the DISCOVER system. (a) The manipulation with a specified depth (z = 145). (b) The volume surface rendering after the manipulation (a). (c) The volume rendering of the object (b). (d) Another manipulation with a specified depth (z = 190). (e) The volume surface rendering after the manipulation (d). (f) The volume rendering of the object (e).

of tools for image processing: (1). Image manipulation tools, such as zooming and panning, contrast and windowing. (2). Image processing tools, such as high-pass and low-pass filters, histogram equalization, detecting connected components, image combinations, and display of histogram. (3). Image analysis tools, such as density, distance, and angle measurements, coordinates, and drawing region of interest.

For the 3D image windows, there are many 3D visualization and manipulation tools available. The visualization techniques includes surface rendering, volume rendering and volume-surface rendering (Chen et al. 1994) (Fig. 2). The surface rendering method we use is a front-to-back rendering method (Reynolds et al. 1987, Chen et al. 1989). In this method, line segments are used to represent both object and image generated. This method is a fast method to render a complex voxel-based object, such as a medical object. In many clinical applications, there is a need to visualize the spatial relationship between the outer shape of an object and its internal detailed structures. For this purpose, a visualization technique called volume-surface rendering is provided to let user visualize the external and internal structures of medical objects simultaneously. The manipulation processes includes 3D thresholding, cutting the object with a contour specified on the screen, connected component detection, and logical operations such as AND, OR, or XOR, to create new objects.

The DISCOVER system, as it stands today, is in practical use in the Hospital of National Cheng-Kung University in Taiwan for real clinical applications. Physicians can use their desktop personal computers to run the DISCOVER. Due to the fact that the DISCOVER system can process any kind of 2D sectional images and reconstruct them into 3D, we hope that the DISCOVER system can be applied in more research areas in addition to medicine very soon, such as microscopy in neurobiology or cell biology.

REFERENCES

Chen LS, M Sontag. 1989. "Representation, display, and manipulation of 3D digital acenes," Computer Vision, Graphics, and Image Processing, Vol. 48, No. 2.

Chen LS, CP Chen, J Chen, PW Liu, T Shu. 1994. "A Distributed and Interactive Three Dimensional Image System," Computerized Medical Imag and Graphics, Vol. 18, No.5, 1994, pp. 325-337.

Dyer DS. 1990. "A Dataflow Toolkit For Visualization", IEEE CG&A, Vol. 10, No.4, pp.60-69.

IRIS Explorer User's Guide. 1991. Silicon Graphics Inc., Mountain View, CA.

Reynolds RA, D Gordon, LS Chen. 1987. "A dynamic screen technique for shaded graphics display of slice-represented objects," Computer Vision, Graphics, and Image Processing, Vol. 38, No.3.

Upson C, T Faulhaber, Jr., D Kamins, D Laidlaw, D Schlegel, J. Vroom, R Gurwitz, A van Dam. 1989. "The Application Visualization System: A Computational Environment for Scientific Visualization," IEEE CG&A, Vol.9, No.4, pp.30-42.

Zoological Studies 34, Supplement I (1995)

Zoological Studies

Three-dimensional Analysis of Permeability Pathways across Capillary Endothelia

Shih-Chieh Chen[1], Huang-Liang Wei[2] and Roger C. Wagner[3]
[1]*Department of Anatomy, Kaohsiung Medical College, Kaohsiung, Taiwan, R.O.C.*
[2]*Research Center for Occupational Disease, National Institute of Health, Taiwan, R.O.C.*
[3]*School of Life and Health Sciences, University of Delaware, Newark, DE, USA*

Continuous capillaries have very high hydraulic conductivity and provide a partially selective diffusion barrier between the blood and the interstitium. Electron-dense tracers, which are used intravitally to test the conductivity of capillary permeability pathways, are found in the interstitial compartments. It is uncertain, however, whether the tracers have crossed the capillary wall through interendothelial junctions or via the vesicular membranous compartments from two-dimensional electron micrographs. Previous studies (Chen and Wagner 1990, Wagner and Chen 1991) indicate that electron-dense patches of terbium precipitate were often found in regions bounded by pericytes and the abluminal capillary surfaces in the rete mirabile. To answer this question, i.e., whether vesicular pathways are the source of interstitial tracer deposits, three-dimensional information is needed. A reconstruction image from continuous series of thin sections provides a three dimensional map of the areas of dense tracer deposits and any associated pathways via interendothelial junctions or the vesicular membranous compartments across the endothelium.

The rete capillaries were administrated with tracer, fixatives and embedded in British araldite resin as previous reports (Chen and Wagner 1990, Wagner and Chen 1990, Wagner and Chen, 1991). Ribbons of serial thin sections were picked up on slotted grids coated with Formvar film and observed with a Zeiss CEM 902 transmission electron microscope. Sections in the mid-range of a series were examined first. If a patch or dense terbium deposit between a pericyte and endothelial cell was detected, the adjacent sections were examined to determine the distribution of the tracer toward opposite ends of the series. High magnification micrographs (X 30,000) of these regions in all adjacent sections of the series were taken. The negatives of series were sequentially image-registered by Image-I analysis software. Then the registered and digitalized images were exported to the Silicon graphics IRIS workstation. The three dimensional volume visualization system, voxelview, was used to render exterior surfaces and interior structures in sections. The three-dimensional projections of the vesicular system or interend othelial junctions may reveal the permeability pathways across the capillary wall.

When the interstitial plaques were traced through serial sections, the amount of terbium deposits and the plaque areas within mid-series decreased continually to sparse deposits at both ends of the series. In two series, fused vesicular profiles filled with terbium seem to form a continuous channel from the lumen to the interstitium. The three-dimensional reconstruction of membranous compartments showed the continuity of totally electron-dense terbium within a trans-endothelial channel of fused vesicles with the dense interstitial patch deposits. The results indicate that the endothelial vesicular system has provided this transcellular pathway. None of four inter-endothelial clefts formed a paracellular pathway for terbium (Figure 1). Previously, analyses of ultrathin serial sections had not revealed any communications of bound compartments across the endothelial cell (Bundgaard et al. 1979, Frokjaer-Jensen, 1980, Frokjaer-Jensen et al. 1988). The data indicates that communications of membrane compartments might occur by formation of transendothelial channels of fused vesicles or by connection of two close racemose structures on opposite membranes of endothelium.

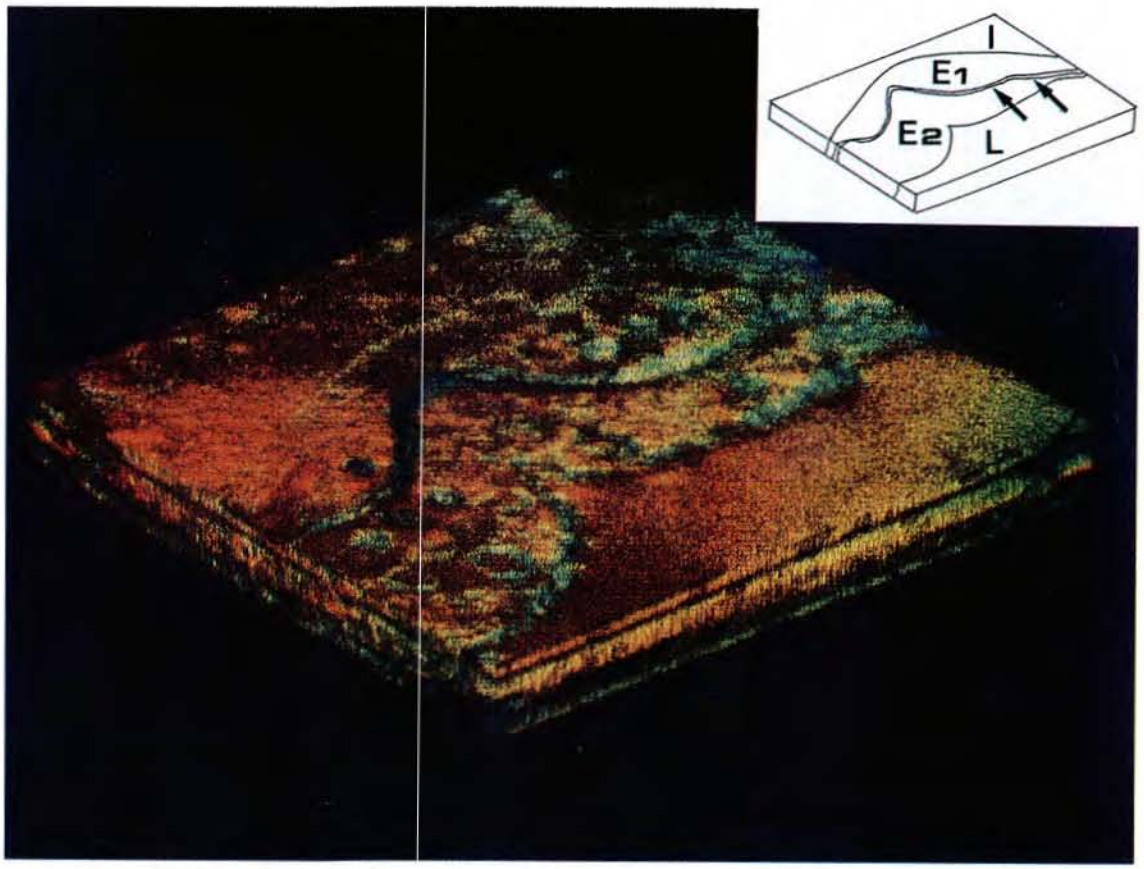

Fig. 1. The three-dimensional projections of the interendothelial junction after reconstruction of eleven sections. The in-terendothelial clefts and adjacent vesicular profiles are filled dense depositions of terbium indicated by blue color. E1 and E2: endothelium, I; interstitium, L: capillary lumen. Arrow: interendothelial junctions between endothelia.

REFERENCES

Bundgaard M, J. Frokjaer-Jensen, C Crone. 1979. Endothelial plasmalemmal vesicles as elements in a system of branching invaginations from the cell surface. Proc. Natl. Acad. Sci. USA. **76:** 6439-6442.

Chen, S-C., RC Wagner. 1990. Improved detectability of capillary permeability tracers by electron spectroscopic imaging. Microvasc. Res. **40:** 439-442.

Frokjaer-Jensen J. 1983. The plasmalemmal vesicular system in capillary endothelium. Conventional electron microscopic (EM) thin sections compared with the picture arising from ultrathin (≈ 140 Å) serial sectioning. Prog. Appl. Microcirc. **1:** 17-34.

Frokjaer-Jensen J, RC Wagner, SB Andrews, P Hagman, TS Reese. 1988. Three-dimensional organization of the plasmalemmal vesicular system in directly frozen capillaries of the rete mirabile in the swim bladder of the eel. Cell Tissue Res. **254:** 17-24.

Wagner, R.C., S-C Chen. 1990. Ultrastructural distribution of terbium across capillary endothelium: detection by electron spectroscopic imaging and electron energy loss spectroscopy. J. Histochem. Cytochem. **38:** 273-282.

Wagner, R.C., S-C Chen. 1991. Transcapillary transport of solute by the endothelial vesicular system: evidence from thin serial section analysis. Microvasc. Res. **42:**139-150.

Zoological Studies 34, Supplement I (1995)

Zoological Studies

Connecting Genomic Architecture and DNA Replication in Three Dimensions

Ronald Berezney, Hong Ma, Chungling Meng, Jagath Samarabandu and Ping-chin Cheng
Departments of Biological Sciences and Electrical and Computer Engineering, State University of New York at Buffalo, Buffalo, NY, 14260, USA

The cell nucleus is the repository for the genetic information of all eucaryotic cells including that of man. Despite enormous progress in defining molecular properties of the genomic functions of DNA replication, transcription and RNA splicing and processing, our knowledge of how these processes are organized and regulated inside the three dimensional structure of the cell nucleus is still in its infancy.

Research in our laboratory employ a dual approach to correlating genomic function and regulation with nuclear architecture. In one series of projects we are identifying, cloning and studying the molecular, genetic and functional properties of the nuclear matrix proteins which compose the three dimensional nuclear architecture. A summary of our recent progress in this area is summarized in a separate abstract in this volume (see Mortillaro et al.).

The second direction of our research uses mulecular labeling, microscopic and computer imaging approaches to visualize in three dimensions sites of genomic organization and function within the *in situ* nuclear architecture and to obtain precise structural and spatio-temporal information about the individual sites where genomic function and regulation occurs. Additionally, our group is investigating the possible arrangement of the functional sites into higher order domains and their relationship to the overall architecture and regulation in the cell nucleus. Our present studies are concentrating on DNA replication and are summarized below.

Fluorescence microscopic analysis of newly replicated DNA has revealed discrete granular sites of replication (RS). The average size and number of RS from early to mid-S phase suggests that each RS contains numerous replicons clustered together. We are using fluorescence laser scanning confocal microscopy (LSCM) in conjunction with multi-dimensional image analysis (MDA) to gain more precise information about RS and their spatio-temporal relationships. Individual RS are optimally visualized following short pulses with BrdU (2 min) in mouse 3T3 fibroblast cells. Using newly improved imaging techniques, we can discriminate over $1x10^3$ RS following a 2 min pulse of cells synchronized in early S phase (Figs. 1 and 2). Preliminary data suggests that the average number of detected sites following a 2

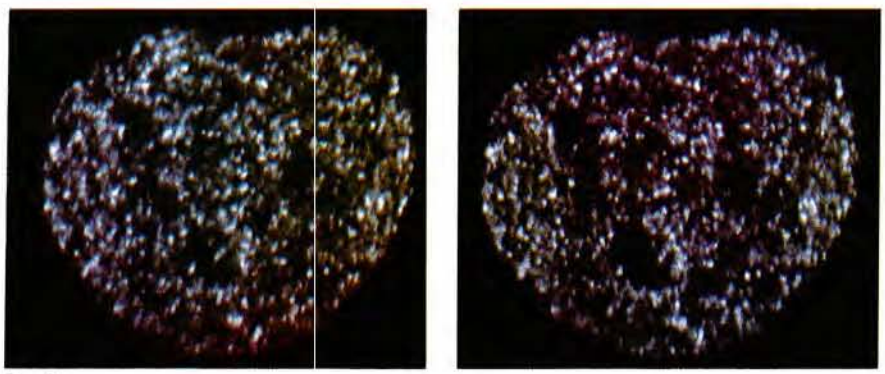

Fig. 1.

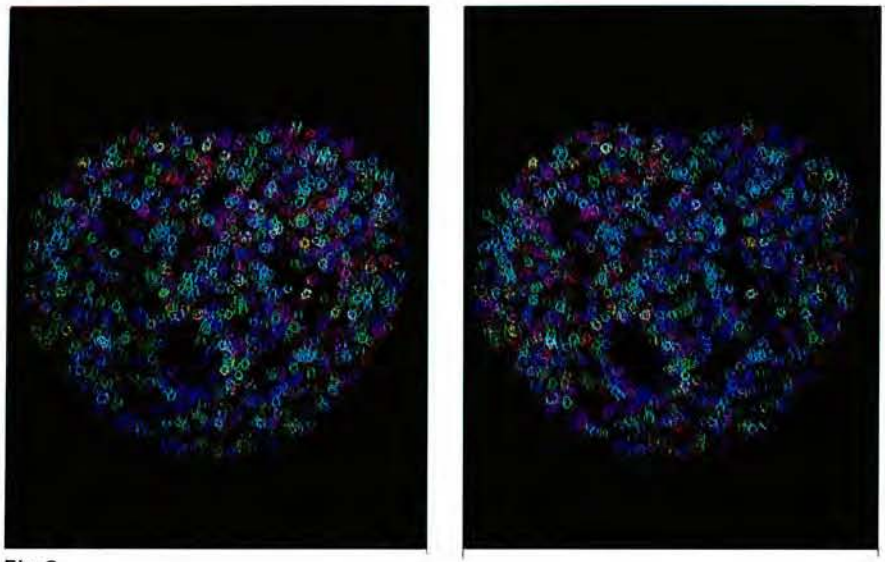

Fig. 2.

min pulse is approximately 600 with each site having an average x or y plane length of about 0.4 microns.

Double labeling experiments performed at two different times (pulse-chase-pulse) enabled us to examine the relationship of early versus later replicated DNA at individual sites. Cells in early S phase were labeled for 2 min with CldU (FITC secondary antibody), chased for different times and pulsed again for 5 min with IdU (Texas Red secondary antibody). As a control, simultaneous pulsing with both CldU and IdU resulted in the virtual complete overlap of all the replication sites with the two probes (yellow replication sites, Fig. 3). Following a 15 min chase, over 50% of the total RS were co-localized and decorated granular RS similar to those observed after a single 2 min pulse (Fig. 4). Later pulsed replication sites (red sites) were consistently observed in juxtaposition to early ones (green or yellow sites). Increasing the chase time between pulses to 1-2 hr resulted in an increasing spatial separation between early and later Rs (Fig. 5).

These results led us to consider the existence of higher order spatial domains of neighboring RS whose replication may be temporally regulated. To investigate this further, we performed long term double labeling (pulse-chase-pulse) experiments, 3T3 cells in early S-phase were pulsed for 1-5 hr with CldU, chased for 0-4 hr and pulsed a second time for 3 hr with IdU. Initial results suggest that a significant portion of the temporally distinct RS occupy separate spatial domains within the nucleus. Arrays of RS in close proximity were often observed within these domains.

We are currently applying pattern recongnition techniques to elucidate the 3-D higher order assembly of individual replication sites. Using a "nearest neighbor" center to center distance of 0.6 microns, we find that the approximately 600 sites with average diameters of 0.4 microns detected after a 2 min pulse, separate into approximately 60 discrete domains (average distance between sites of < 0.2 microns) or about 10 replication sites per domain. The average number of domains per nucleus is reduced to about 30 with a center to center distance of 0.9 microns (< 0.5 micron distance between sites).

In another series of experiments we are following the fate of individual replication sites throughout the cell cycle of 3T3 fibroblasts. Previous studies from our laboratory revealed that the arrangement of replicated DNA into "RS-like" structures persists throughout the cell cycle and subsequent daughter cells. These results may be a consequence of the three dimensional arrangement of chromation into precise domains of clustered loops. We have designed "double pulse - double

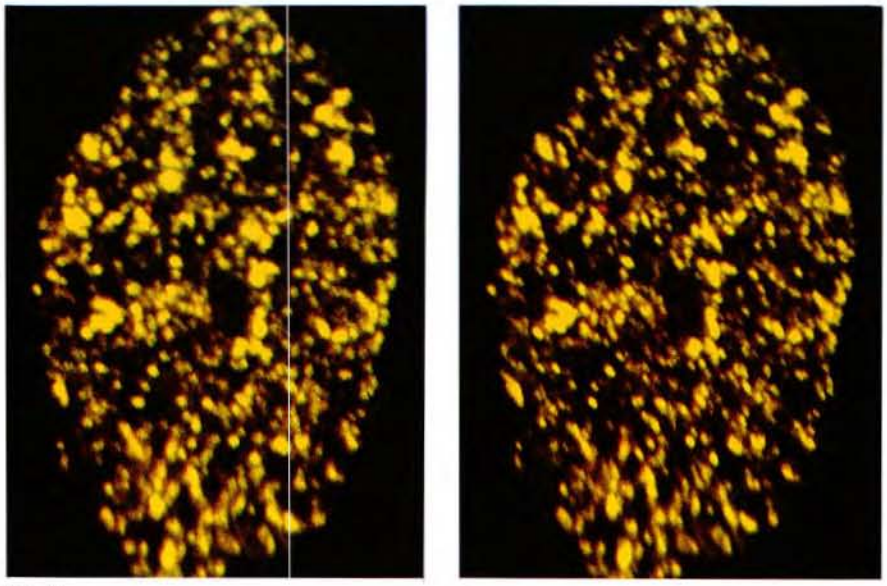

Fig. 3.

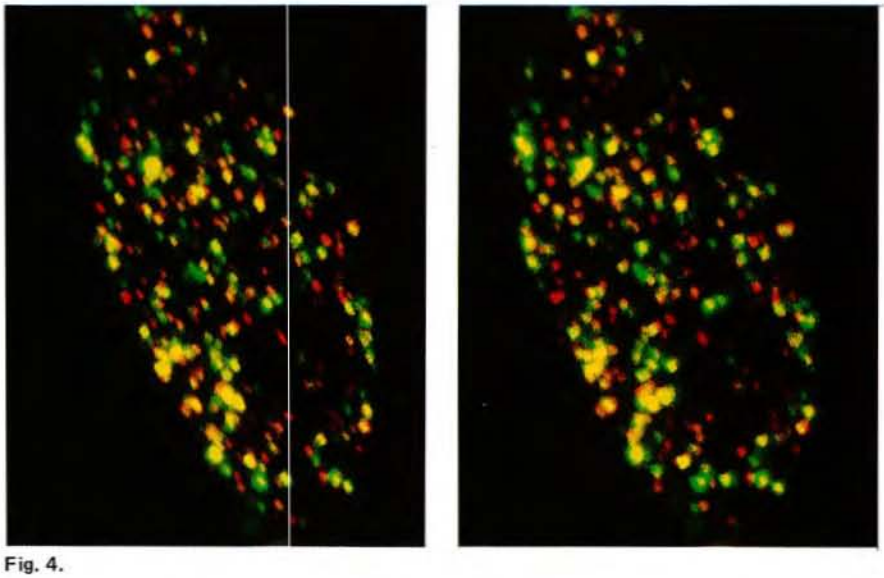

Fig. 4.

chase" experiments to determine whether the DNA sequences replicated at individual RS are precisely maintained as the cell progresses through the cell cycle. RS were labeled in early S (green probe) and two hours later (red probe). Our results demonstrate the maintenance of the temporally distinct replicated DNA into spatially distinct sites (separate green and red labeled sites) throughout the 8 hr S-phase. The G_2-plase, however, was characterized by a significant mixing of DNA between the two populations of sites (~30% yellow sites). The percent of "DNA mixing" between the two populations of sites increased to >50% in subsequent cell generations. In future experiments we will determine the specific genomic sequences (genes) at individual RS and the cell cycle dynamics of these associations.

In summary our combined LSCM-MDA results

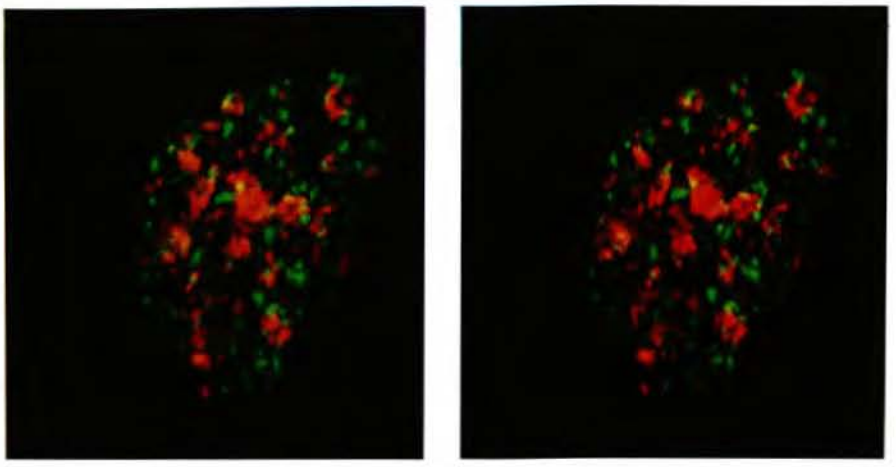

Fig. 5.

indicate that DNA replication occurs on an average of 600 distinct sites at any given time in early to middle S phase. "Pulse-chase-pulse" double labeling experiments reveal that the average RS takes about 1 hr to complete replication. Assuming approximately 4-8x10^4 replicons per nucleus, this suggests that each RS contains an average of 5-10 replicons which are replicated in a relatively synchronous wave. The labeled DNA remains organized in "replication-like sites" throughout the cell cycle and subsequent cell generations. This suggests that the imaged sites are not only sites of replication but are a fundamental aspect of the higher order structure of the genome and its organization inside the cell nucleus. An even higher level of organization was indicated by pattern recognition image analysis which revealed that the individual RS are three dimensionally arranged into a series of higher order domains (approximately 10 RS per domain). (Supported by NIH grant GM-23922)

Zoological Studies 34, Supplement I (1995)

Zoological Studies

Architectural and Molecular Studies of Nuclear Matrix Proteins

Michael J. Mortillaro[1], Jagath Samarabandu[1], Linda Buchholtz[1], Ping-Ching Cheng[2] and Ronald Berezney[1]

[1]*Department of Biological Sciences, State University of New York at Buffalo, NY, USA*

[2]*Department of Electrical and Computer Engineering, State University of New York at Buffalo, NY, USA at buffalo, Buffalo, New York 14260*

Our understanding of the proteins which compose the internal architecture of the nuclear matrix has lagged behind recent progress defining domains of replication, transcription and prem RNA splicing associated with these structures. We are currently focusing our attention on identifying the major proteins which constitute the nuclear matrix. A limited number of interior nuclear matrix proteins, termed nuclear matrins, were previously identified by our lab. In this presentation I will report progress on the analysis of the two nuclear matrins, P-250 and SFA-Cyp. The cDNA encoding, splicing factor associated-cyclophilin (SFA-Cyp), a novel nuclear matrin, will be presented. Antibodies raised against a fusion protein of SFA-Cyp indicate that it is a 103k Da protein which is located in the nucleus and enriched in the nuclear matrix. Also, this antibody stains a series of bright foci in mammalian nuclei which colocalize with splic-

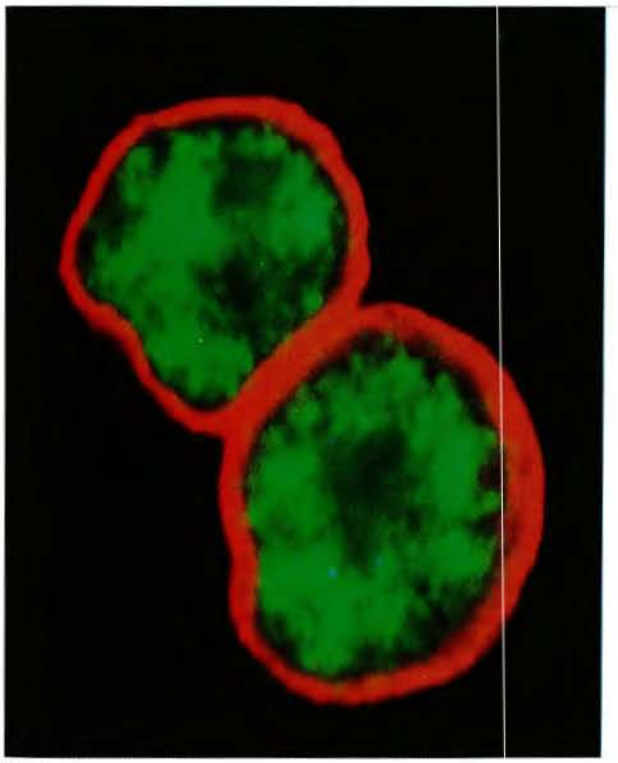

Fig. 1.

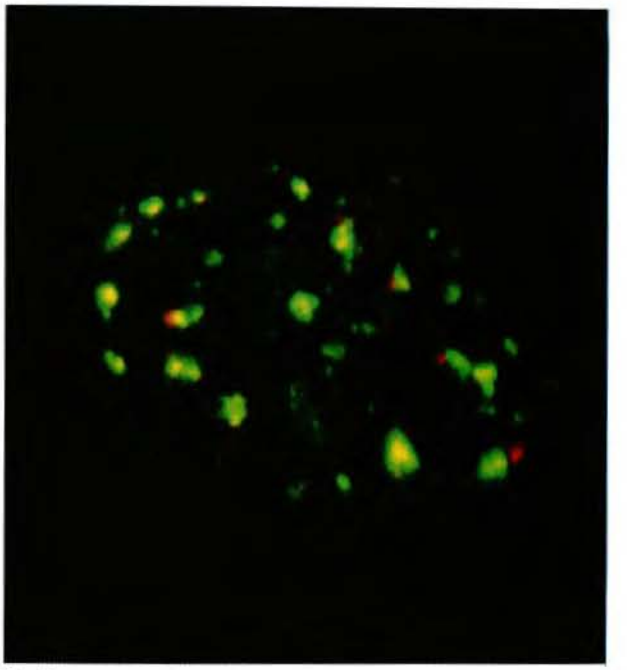

Fig. 2.

ing factors (figure 1 shows anti-lamin A/C (Texas red) and anti-SFA-Cyp (FITC) in primary rat hepatocytes, figure 4 & 5 show human HeLa S3 cells stained with the anti-snRNP antibody Y12 (Texas red) and anti-SFA-Cyp (FITC)). As suggested by its derived amino acid sequence and immunofluorescent pattern SFA-Cyp may chaperone specific proteins to sites of splicesome assembly where it may then assist these proteins to associate with forming splicesomes. A monoclonal antibody raised against nuclear matrices recognizes a protein of 250kDa that is enriched in the nuclear matrix and termed P-250. The protein detected by our antibody was shown by antibody cross reactivity studies not to be a NuMA protein. Laser scanning confocal microscopy of P- 250 visualizes a complex architectural arrangement in the nucleus consisting of several large bright foci and many small, less intensely staining granules. Some of the large bright foci are also stained by splicing factor specific antibodies (figure 2 shows anti-P-250 (Texas red) and anti-SFA-Cyp (FITC) in mouse 3T3 cells). This may indicate an association of P-250 with splicing factors.

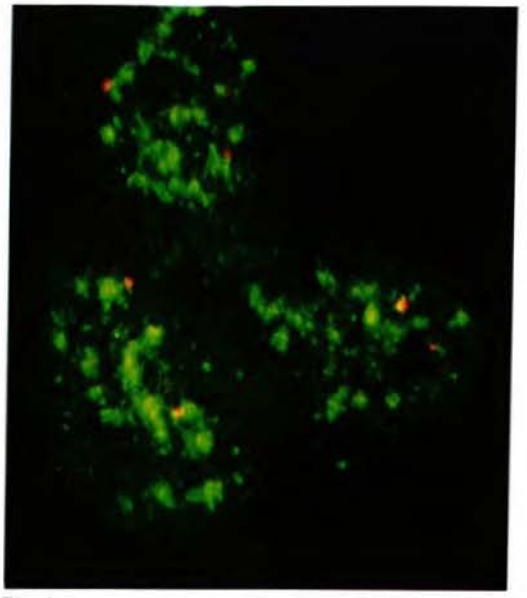

Fig. 4.

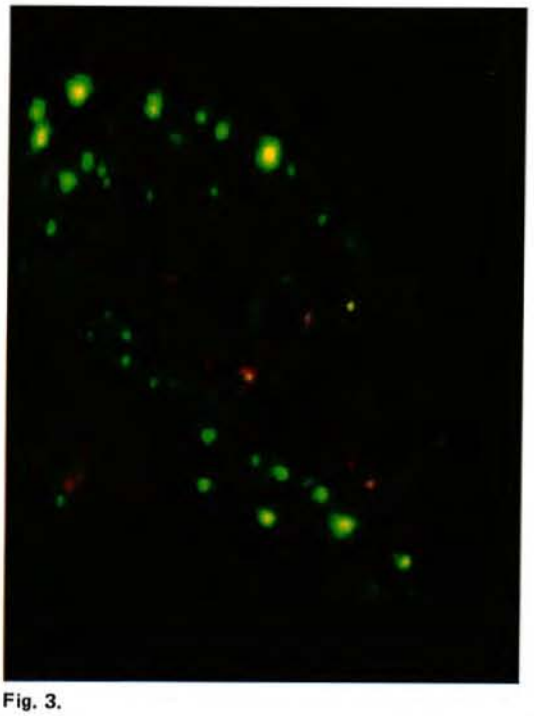

Fig. 3.

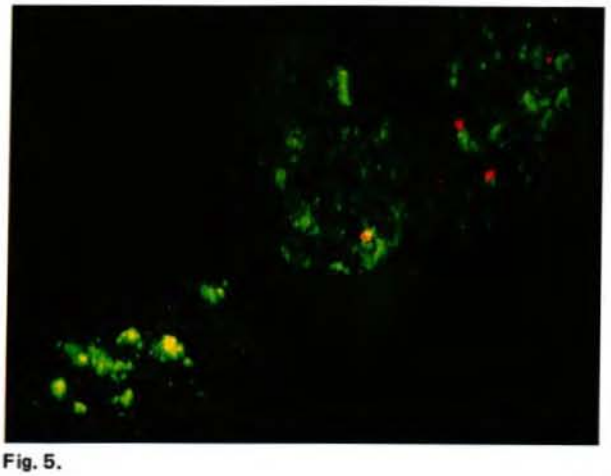

Fig. 5.

Zoological Studies 34, Supplement I (1995)

Zoological Studies

Application of Laser Optics to Plant Cell and Molecular Biology

K. Fukui[1], A. Nomiya[2], M. Nishiguchi[2] and M. Fujishita[3]
[1]*Hokuriku National Agricultural Experiment Station, Joetsu 943-01, Japan*
[2]*National Institute of Agrobiological Resources, Tsukuba 305, Japan*
[3]*Meridian Instruments Far East K. K. Nihonbashi 103, Japan*

Although laser optics has been shown to be an effective tool in the various fields of animal cell and molecular biology, its application and utility to plant cell and molecular biology have been limited. The main reason, besides the number of researchers in the plant fields, is that the plant cell has a characteristic feature of the cell wall. The cell wall interrupts a good sample preparation of chromosomes and prevents the smooth incorporation of antibodies into the cytoplasm. It is also true, in the case of the production of transgenic plants, that the cell wall is a barrier for DNA to be introduced into the cytoplasm and nucleus.

Nevertheless effective applications of laser optics in the plant cell and molecular biology are being explored and some achievements have recently been attained. Three major applications of laser optics, laser microdissection of plant chromosomes, laser poration of plant protoplasts and laser as the optical tweezers in plant cell biology, are reported.

LASER DISSECTION OF PLANT CHROMOSOMES

After establishment of an improved enzyme maceration method to digest and remove cell walls from plant cells (Fukui and Kakeda 1990, Fukui and Iijima 1991), good chromosome sample preparations without cell debris became a routine protocol. Microdissection of defined chromosomal regions of barley and rice chromosomes has been reported (Fukui et al. 1992).

Fig. 1. shows the representative steps of microdissection of barley chromosomes prepared by the improved maceration method. Barley chromosomes, air-dried on a polyester membrane, were subjected to laser microdissection. The 488 nm line from a 5 W argon ion laser through a 100x objective lens dissected the chromosomes by 0.5 μm in width. All the barley chromosomes except for the two pairs of the satellite chromosomes, chromosome 6 and 7, were ablated by using the stronger laser beam. Then the specific regions of chromosome 6 (6p1.5) and chromosome 7 (7p1.1 and 7q1.1) were dissected out from the rest of the chromosomal regions.

Direct cloning of the part of 45S and 5S rDNA from the nuclei cytologically prepared and the dissected chromosomal nucleolar organizing regions have successfully been carried out by using a PCR method. The amplified DNAs were also labeled during the PCR cycle by incorporation of biotinylated dUTP. The fluorescence *in situ* hybridization (FISH) confirmed that the amplified DNAs had been originated from the nucleolar organizing region dissected (Nakamura and Fukui in press). Direct cloning and direct labeling of certain DNA sequences from dissected chromosomes and nuclei becomes a standard chromosome technique. Fig. 2. shows a multi-color FISH of 5S and 45S rDNAs in rice using the probes prepared by the laser dissection method (Ohmido and Fukui in press).

LASER-PORATION OF PLANT PROTOPLASTS

After the establishment of protoplast preparation and culture methods (Takebe et al. 1968), a living plant cell without the cell wall became available in the various experiments. The protoplast system has been used in electroporation for producing transgenic cells and subsequently transgenic plants. Laser-poration has been tested to explore the possibility of developing an alternative

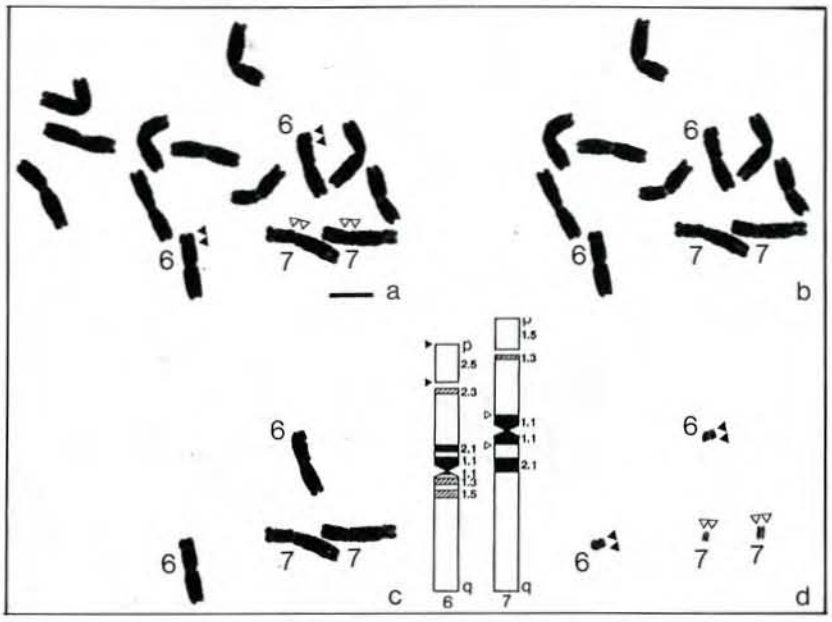

Fig. 1. Representative steps of laser dissection for the defined regions of barley chromosomes.

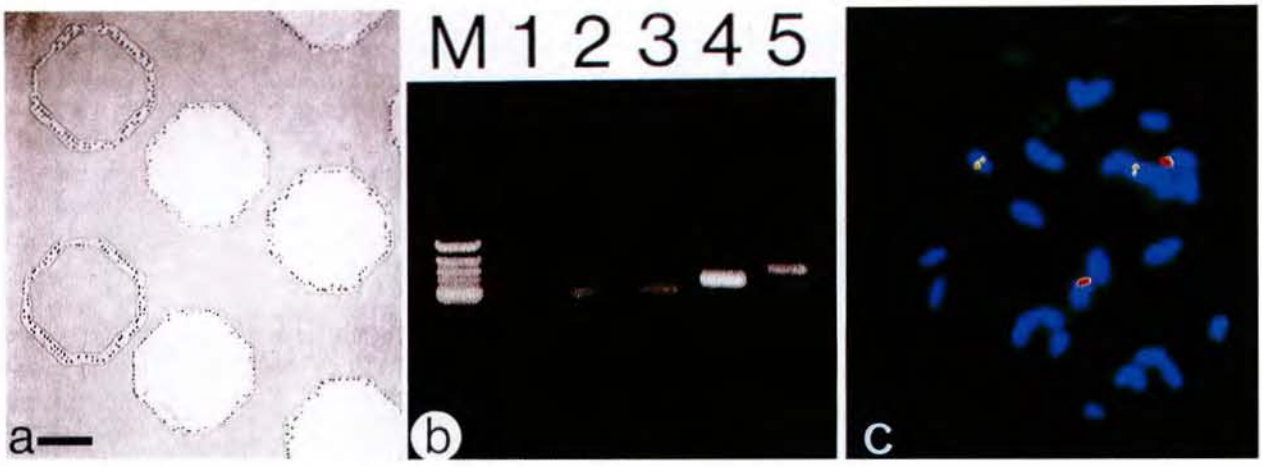

Fig. 2. Multi-color FISH of african rice 5S and 45S rRNA genes using the probes directly cloned and labelled. a) Laser dissection of the membrane with nuclei on the surface. b) Direct cloning and direct labeling of the 5S and 45S rDNAs. c) Multi-color FISH using the probes. Yellow: 5S rDNA. Red: 45S rDNA.

transformation system using protoplasts.

Laser-poration was tested by the incorporation of a dye, Evans Blue, which is not incorporated into living protoplasts. Fig. 3. shows a protoplast before and after optical poration. The living protoplast with green chloroplasts were stained dark blue after laser beam irradiation. It is shown that laser-poration induced the successful incorporation of the dye into the cytoplasms of the protoplasts. Further investigation is needed to clarify the relationship between the strength of the laser beam and the pore sizes for minimizing protoplast damage. The incorporation of DNA/RNA into protoplasts is underway.

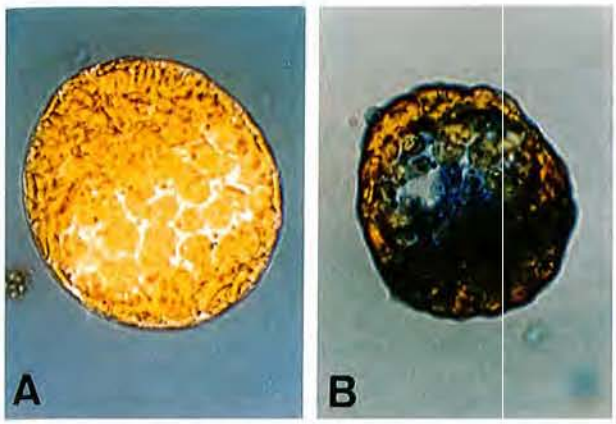

Fig. 3. A protoplast before and after optical poration.

Table 1. Optical tweezers for pollen grains[1)]

Laser power in mW	Laser scan strength (%)[2)]				
	100	80	60	40	20
100	+	+	+	-	-
80	+	+	+-		
60	+-	+-	-		
40	+-	-			
20	-				

1) Glycerol concentration: 20%
2) +: Good movement, +-: Poor movement, -: Not moved

OPTICAL TWEEZERS FOR CHROMOSOME MEDIATED GENE TRANSFER

Chromosome mediated genetic transfer is an alternative method for development of transgenic plants, although the number of reports have been quite limited. The method of random incorporation of the chromosomes and subsequent selection is not an effective way to produce transgenic plants as there is no selection markers for the protoplasts with specific chromosomes.

Thus specific chromosome should be introduced into the plant protoplasts. To meet the objective, flow cytometry is a possible way , although the method needs much more conditions to be refined.

Optical tweezers combined with laser-poration provide an alternative method for chromosome mediated genetic transfer by using a single targeted chromosome and a single cell. To develop the method, the ability of optical tweezers in a viscous solution like cytosol has been examined using cells of *Sacchromyces cereviciae*, pollen grains of Erigeron *annuus*, and nuclei separated from suspension cultured tobacco cells. The optical power of grasping objects was measured by using the combinations of the different laser scan strength and different glycerol concentrations.

Table 1 shows the results of optical tweezing on the pollen grains. In the case of 20% glycerol, pollen grains were easily grasped by the laser beam with 60% or more of the scan strength at 100mW laser power. They could readily be moved around by the movement of the laser beam under the above conditions. As a result the optical tweezers have been showed to have the capacity to pick up and transfer any plant chromosome in viscous solutions like cytosol. Thus it is anticipated that the combination of laser tweezers and laser poration will provide an alternative transgenic system.

As the three types of applications of laser optics described here are all in progress now, there are several areas for refinement. It is, however, clearly demonstrated that the applications of laser optics particularly effective also in the field of plant cell and molecular biology.

REFERENCES

Fukui K, K Kakeda. 1990. Quantiative karyotyping of barley chromosomes by imaging methods. Genome **33:** 450-458.

Fukui K, K Iijima. 1991. Somatic chromosome map of rice by imaging methods. Theor. Appl. Genet. **81:** 597-605.

Fukui K, M Minezawa, Y Kamisugi, N Ohmido, M Ishikawa, T Yanagisawa, M Fujishita and F Sakai. 1992. Microdissection of plant chromosomes by argon ion laser beam. Theor. Appl. Genet. 84: 787-791.

Nakamura M, K Fukui, Chromosome oriented approach for genome analysis of a woodplant, *Sequoiadendron gigaintium* Lindl. Proc. Intl. Union Forest. Res. Org. Cytogenet. Work. Party. 1993. (in press)

Onmido N, K Fukui. Cytological studies of African rice *Oryza glaberrima* steud. Theor. Appl. Genet. (in press)

Zoological Studies 34, Supplement I (1995)

Zoological Studies

Confocal Fluorescence Microscopy for Studying Signal Transduction in Mast Cells and Basophils

Mamoru Nakanishi[1]*, Tadahide Furuno[1] and Reiko Teshima[2]

[1]*Faculty of Pharmaceutical Sciences, Nagoya City University, Tanabe-dori, Mizuho-ku, Nagoya 467, Japan*

[2]*National Institute of Health Sciences, Kamiyoga, Setagaya-ku, Tokyo 158, Japan*

The release of histamine and other inflammatory mediators from mast cells and basophils is the primary event in a variety of acute allergic and inflammatory conditions. The release of granules from these cells is an energy- and calcium-dependent process which is initiated by the receptor crosslinking with antigen. However, it has not been determined yet how the receptor crosslinking induces signal transduction in mast cells and basophils.

Then, we have studied here receptor-mediated calcium signals in rat basophilic leukemia cells (RBL-2H3) and rat mast cells by a confocal fluorescence microscope with an argon ion laser and a He-Cd laser (Nakato et al. 1992, Teshima et al. 1994, Horikoshi et al. 1994). Confocal fluorescence images of fluo-3 loaded RBL-2H3 cells, excited by an argon ion laser (488 nm), became much brighter and more nonhomogeneous than those before antigen stimulation (Fig. 1). Time-dependent fluorescence changes in intensities were abrupt and quite similar to the patterns of the intracellular calcium ion concentration $[Ca^{2+}]_i$ observed by a conventional fluorescence microscope using fura-2. From the morphological patterns of the calcium images, the parts of the bright fluorescence seemed to belong to the nucleus in RBL-2H3 cells. To confirm the above events we measured confocal fluorescence images of the nuclei in RBL-2H3 cells. From the fluorescence images of co-loaded Hoechst 33342 (a DNA-specific fluorescent probe), which was excited by a He-Cd laser (325 nm), the brighter part of the fluo-3 fluorescence intensity was identified to the nucleus in the cell (Fig. 1). These results suggested the possibility that the receptor-mediated calcium signals may transfer not only to the cytoplasm but also to the nucleus (Nakato et al. 1992, Horikoshi et al. 1994). Similar kinds of nuclear calcium signals were also observed in the activation of B lymphocytes, T lymphocytes and mast cells (Yamada et al. 1991, Furuno et al. 1993, Okamoto et al. 1995).

It was said that the nucleus contains an autonomous phosphoinositide signaling system every bit as complex as that at the plasma membrane (Berridge 1993). Then, we have studied the mechanism of the intranuclear calcium signaling pathways using Ba^{2+} and Mn^{2+} instead of Ca^{2+}, because Ba^{2+} and Mn^{2+} entered into these cells through Ca^{2+} channels (Kwan and Putney 1990). We found that Ba^{2+} and Mn^{2+} entered into the cells through Ca^{2+} channels and quenched the fluo-3 fluorescence both in the nucleus and in the cytoplasm. This showed that the increased intranuclear calcium ions after antigen stimulation may come from the cytoplasm not from the nuclear calcium stores (Okamoto et al. 1995).

Next, a confocal fluorescence microscope was used to study the exocytotic secretory processes of mast cells in combination with an fluorescent molecular rotor, 9-(dicyanovinyl) julolidine (DCVJ) (Furuno et al. 1992). DCVJ is known to be a unique fluorescent dye which increases its quantum yield with decreasing intramolecular rotation (Kung and Reed 1989, Iwaki et al. 1993). Here, DCVJ-loaded rat mast cells were stimulated with compound 48/80 and lecithins (Furuno et al. 1992, Nishimura et al. 1994), and their fluorescence images were

*To whom all correspondence should be addressed.

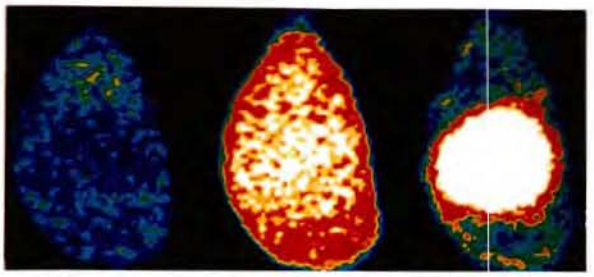

Fig. 1. Confocal fluorescence images of a fluo-3 and Hoechst 33342-loaded RBL-2H3 cell. (left) A fluo-3-fluorescence pseudo-images just before antigen stimulation. (middle) A fluo-3-flyorescence pseduo-images after antigen stimulation at 37°C. (right) A confocal fluorescence iamge of DNA-specific fluorescent probe (Hoeschst 33342)-loaded RBL-2H3 cell which was excited by a He-Cd laser (325 nm).

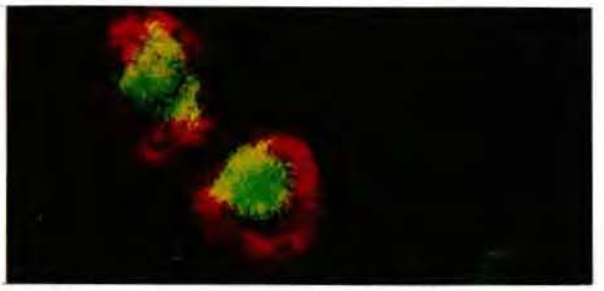

Fig. 2. Confocal fluorescence images of a DCVJ-loaded mast cell after the addition of compound 48/80. DCVJ fluorescence formed a ring-like structure (red color) around the nucleus (yellow color).

Fig. 3. Confocal fluorescence images of the surface expression of CD63 antigen in RBL-2H3 cells. The expression of CD63 antigen was visualized using anti-CD63 antibody and FITC-la-beled anti-mouse antibody on the cell surfaces (yellow color).

compared with fluorescence calcium images of fluo-3-loaded mast cells. Subsequent to transient increases in intracellular free calcium ion concentration, DCVJ fluorescence increased dramatically in the cytoplasm and formed a ring-like structure around the nucleus (Fig. 2), suggesting the possibility that the dye bound to the proteins composing the cytoskeletal architecture. Furthermore, the increases of DCVJ fluorescence intensities were mostly blocked in the presence of cytochalasin D. However, fluo-3 fluorescence intensities still increased after addition of compound 48/80. This suggested that the dye bound to the proteins composing the cytoskeletal architecture and that the molecular movements of proteins and their assembly occurred before the histamine secretion (Furuno et al. 1992, Nishimura et al. 1994).

Lastly, we have investigated the surface expression of CD63 antigen in RBL-2H3 cells and rat mast cells after stimulation of antigen and compound 48/80, respectively. CD63 antigen is located on the basophilic granule membranes in resting basophils, mast cells and platelets (Metzelaar et al. 1991). Activation of basophils and mast cells is thought to induce the fusion of cytoplasmic granules with plasma membranes and to induce the successive release of inflammatory mediators, such as histamine. The surface expression of CD63 antigen was visualized by confocal fluorescence microscopy using anti-CD63 antibody and FITC-labeled anti-mouse antibody (Fig. 3). After antigen stimulation FITC-fluorescence intensities of the membrane surfaces in RBL-2H3 cells became much brighter than those before stimulation. This indicated that the amounts of surface expression of CD63 antigen in RBL-2H3 cells increased after antigen stimulation. The expression of CD63 antigen was maximal between 10 and 20 mins after antigen stimulation (Fig. 3). Time-courses of the surface expression of CD63 antigen were well consistent with the time-courses of the histamine secretion in RBL-2H3 cells. For comparison, we stimulated RBL-2H3 cells with thapsigargin, an in-hibitor of intracellular Ca^{2+} pump. Thapsigargin neither induced the surface expression of CD63 antigen nor the secretion of histamine in RBL- 2H3 cells, although thapsigargin increased intracellular free calcium ion concentration in RBL- 2H3 cells. These result indicated that the surface expression of CD63 antigen is closely related to the histamine secretion in RBL-2H3 cells.

All of the above findings elucidated new insights of the dynamic cellular functions of exocytotic processes in mast cells and basophils.

REFERENCES

Berridge MJ. 1993. Inositol phosphate and calcium signalling. Nature **361:** 315-325.

Furuno T, R Isoda, K Inagaki, T Iwaki, M Noji, M Nakanishi. 1992. A fluorescent molecular rotor probes the kinetic process of degranulation of mast cells. Immunol. Lett. **33:** 285-288.

Furuno T, T Hamano, M Nakanishi. 1993. Receptor-mediated calcium signal playing a nuclear third messenger in the activation of antigen-specific B cells. Biophys. J. **64:** 665-669.

Horikoshi Y, T Furuno, R Teshima, J Sawada, M Nakanishi. 1994. Thapsigargin-induced nuclear calcium signals in rat basophilic leukaemia cells. Biochem. J. **304:** 57-60.

Iwaki T, C Torigoe, M Noji, M Nakanishi. 1993. Antibodies for fluorescent molecular rotors. Biochemistry 32: 7589-7592.

Kung CE, JK Reed. 1989. Fluorescent molecular rotors: A new class of probes for tubulin structure and assembly. Biochemistry **28:** 6678-6686.

Kwan CY, JW Putney. 1990. Uptake and intracellular sequestration of divalent cations in resting and methacholine-stimulated mouse lacrimal acinar cells. J. Biol. Chem. **265:** 678-684.

Mezzelaar MJ, PLJ Wijngaard, PJ Peters, JJ Sixma, HK Nieuwenhuis, HC Clevers. 1991. CD63 antigen; A novel lysosomal membrane glycoprotein. J. Biol. Chem. **266:** 3239-3245.

Nakato K, T Furuno, K Inagaki, R Teshima, T Terao, M Nakanishi. 1992. Cytosolic and intranuclear calcium signals in rat basophilic leukemia cells as revealed by a confocal fluorescence microscope. Eur. J. Biochem. **209:** 745-749.

Nishimura T, T Furuno, M Uchida, M Nakanishi. 1994. An initial signal of activation of rat peritoneal mast cells stimulated by Dutura stramonium: A confocal fluorescence microscopic analysis of intracellular calcium ion and cytoskeletal assembly. Jpn. J. Pharmacol. **66:** 205-211.

Okamoto Y, T Furuno, T Hamano, M Nakanishi. 1995. Confocal fluorescence microscopy for studying thapsigargin-induced divalent cation entry into B cells. Biochem. J. **305:** 1011-1015.

Teshima R, H Ikebuchi, M Nakanishi, J Sawada. 1994. Stimulatory effect of pervanadate on calcium signals and histamine secretion of RBL-2H3 cells. Biochem. J. **302:** 867-874.

Yamada H, J Mizuguchi, M Nakanishi. 1991. Antigen receptor-mediated calcium signals in B cells as revealed by confocal fluorescence microscopy. FEBS Lett. **284:** 249-251.

Zoological Studies 34, Supplement I (1995)

Zoological Studies

Simultaneous Reflection and Transmission Modes Near-field Scanning Optical Microscope

Pei-Kuen Wei[1], Po-Jou Chen[1] and Wunshain Fann[1,2]

[1]*Institute of Atomic and Molecular Sciences, Academia Sinica, Taipei, Taiwan, R.O.C.*

[2]*Department of Physics, National Taiwan University P.O. Box 23-166, Taipei, 10764, Taiwan, R.O.C.*

Near-field optical scanning microscopy (NSOM) has the capability of the conventional optical microscope as well as the high resolution comparable to the scanning electron microscope. In NSOM, a probe with sub-wavelength tip size scans the sample surface with sample/tip separation in 100A length scale. During the scanning period, light emitted by the probe is modulated in accordance with the optical properties of the sample surface. Two configurations can be used to record the light intensity changes, one is to detect the backward scattering light from the surface, the other is to collect the transmission power through the sample. These two images are in opposite contrary and known to be the reflection and transmission mode near-field optical images, respectively. However, due to the configuration, previous NSOM4-7 did not deal with these two images simultaneously. In this paper, we present our new NSOM system that can obtain simultaneous reflection and transmission mode images.

Figure 1 sketches the setup of our NSOM. The system can be divided into two different branches. At the heart of the system is a glass fiber, pulled to form a tapered shape with about 80nm tip size. Some 75nm of alumni are deposited on the tapered fiber's sides to prevent linkage of light. The fiber probe is fixed on a piezoelectric plate, and set into vibration near its resonance. Upon approaching the probe to the sample within 100A scale separation, the distance between sample and probe tip causes an attractive Van-der Waals force. This results in the damping of the tip's vibrational amplitude. The amplitude is recorded and is compared to a preset value. The resulting difference feeds back to the z piezo and maintains the sample/tip separation.

In the above feedback system, how to measure the tip's vibrational amplitude is important. We have used a simple method to measure it. First, an Ne-He laser (15mW at 633nm) is focused near the tip end, then the intensity of the scattered light is detected by a photodetector. By using a lockin instrument, the small AC component in the scattered light is measured. The AC signal contains the message of the vibrational amplitude and can be explained by a simple ray-optics model. The principle of the model is following: Suppose the fiber tip is located at x, part of the incident light (form x to x+a) is scattered to the detector. After probe vibrates with a small amplitude Dx, the incident light which scattered to the detector is little changed. the intensity change can be represented as

$$I_{AC}(x)=\frac{\Delta x}{a}\left|I_{DC}(x+a)-I_{DC}(x)\right| \qquad (1)$$

were I_{AC} is the AC component and I_{DC} is the DC component of detected scattered light. Because only small part of scattered light can reach to the detector, the resultant relation between the amplitude and measured AC component is then represented as

$$I_{AC}(x)=\Delta x \cdot I_{DC}(x) \qquad (2)$$

Above result shows that the measured AC component is the derivative of the DC component, and the vibrational amplitude can be easily obtained by only comparing the DC and AC values. Fig. 2 shows the measured results of the IDC and IAC signals when the vibrational probe moves along x-axis. As shown in Fig. 2, the AC signal is clearly in proportional to the derivative of DC intensity distribution and the vibrational amplitude is calculated to be about 50A.

In the optical branch, another Ne-He laser with green light is coupling to the fiber probe to excite the near-field optical source. It is necessary to use

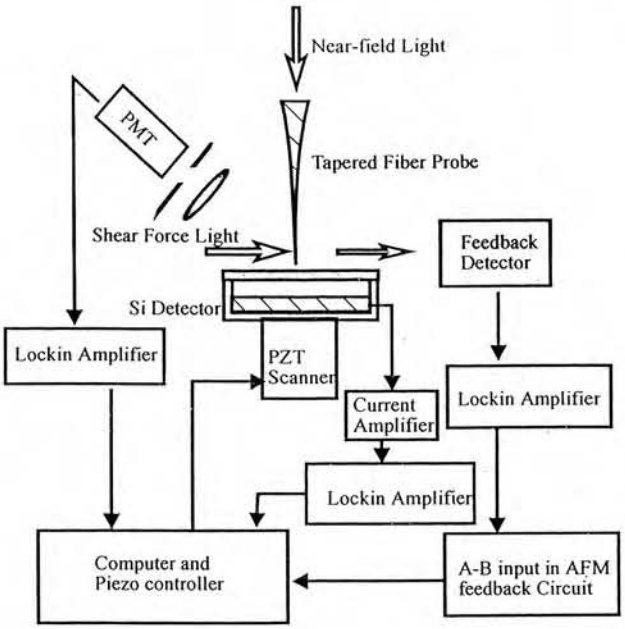

Fig. 1. The schematic of the transmission/reflection near-field optical microsope.

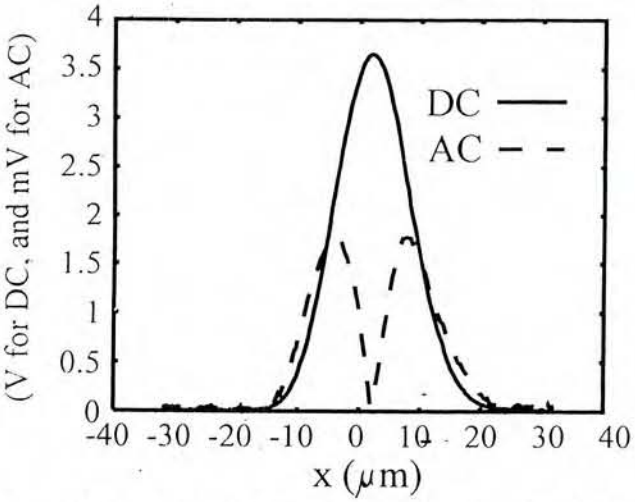

Fig. 2. Measured results of the DC and AC signals of a vibrational probe moving along x-axis.

another wavelength laser because the feedback laser is focused very near onto the tip position that will affect the detection of the near-field power. With another wavelength, we can use a filter to reduce such effect. In the recording of transmission mode image, a planar silicon detector is placed directed below the sample. When near-field light transmitted through the sample, it is collected by the detector.

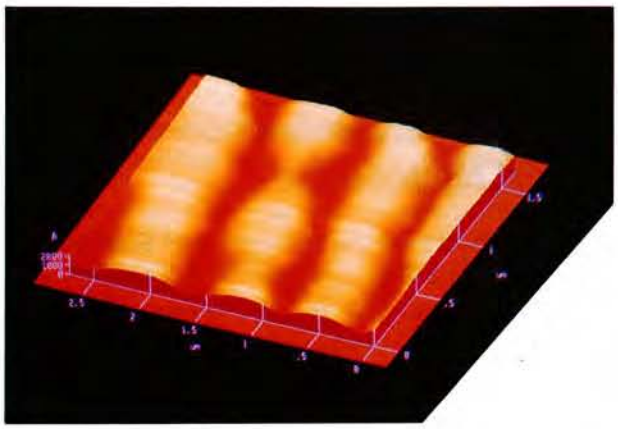

(a)

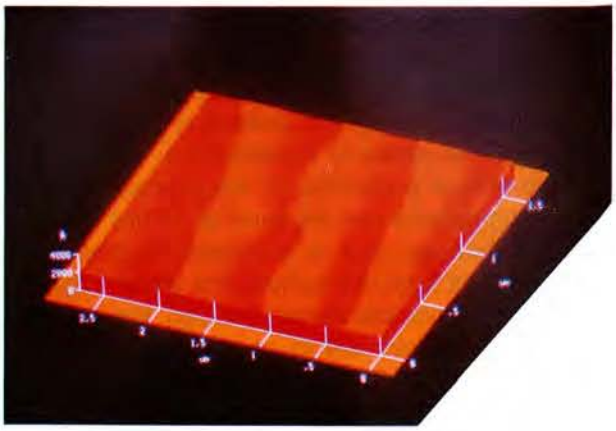

(b)

Fig. 3. Simultaneous transmission(a) and reflection(b) near-field optical images of gold gratings on glass.

At the same time, the scattered near-field power by the sample is focused by an objective lens and then directed on to a photo multiplier tube (PMT). The output of the PMT contains the reflection mode image, and a lockin instrument is used to readout the signal variations.

We have used the system to scan a number of samples of different compositions and structures. In our experiments, the resonance frequency of the fiber probe was 62.5 kHz, the driven voltage to the planar PZT was 0.01V. The NSOM light source was 0.5mW unpolarized He-Ne laser at 540 nm wavelength and optical power from the tip end was measured to be about 1 nW. The preset value was set to maintain the distance between the tip and sample to be about 200nm. To demonstrate our NSOM system with simultaneous reflection and transmission images, a sample of gold grating

on glass was tested. The grating had a period of 1mm, and 2000nm thickness of gold. Fig. 3 shows the simultaneous transmission(a), and reflection (b) NSOM images. These images show good agreement with the sample.

In conclusion, we have presented a scanning probe microscope using attractive-mode force signal to regulate the tip/sample separation, and provided three images of one topographic and two optical images. We believe the system is the first NSOM that can deal these three images simultaneously. Also, we present a new method to measure the small tip's vibrational amplitude for the feedback system. The method is much simpler than others. A simple ray-optics theory can illustrate the mea-surement of vibrational amplitude.

REFERENCES

Betzig E, JK Trautman. 1992. Science **257:** 189.

Betzig E, A Lewis, A Harootunian, M Isaacson, and Kratshmer. 1986. J. Biophys. **49:** 269.

Betzig E, JK Trautman, R Wolfe, EM Gyorgy, PL Finn, MH Kryder, C-H Chang. 1992. Appl. Phys. Lett. **61:** 142.

Fischer UCh. 1986. J Vac. Sci. Technol. **B 3:** 386.

Durig U, DW Phol, F Rohner. 1986. J. Appl. Phys. **59:** 3318.

Betzig E, JK Truman, TD Harris, JS Weiner, and RL Kostelak. 1991. Science **251:** 1468.

Roberts A. 1991. J. Appl. Phys. **70:** 4045.

Zoological Studies 34, Supplement I (1995)

Zoological Studies

Differential Confocal Microscopy for Imaging Surface Microstructures

Jyhpyng Wang, Chau-Hwang Lee, Chun-Hung Lu and Kung-Li Deng

Institute of Atomic and Molecular Sciences, Academia Sinica, and Department of Electrical Engineering, National Taiwan University, Taipei, Taiwan, R.O.C.

The depth resolution of conventional confocal microscopes is limited by the confocal parameter. In the visible spectral range it is possible to make the confocal parameter as small as 0.5 μm. Yet as with any microscopy, one always finds many applications which demand better resolution than available. In this paper we report our development of a new confocal technique, tentatively called differential confocal microscopy, which can be used for imaging and profiling surface structures with depth resolution as large as 20 nm. We demonstrate the potential of this technique by profiling calibrated nanometer semiconductor structures and micrometer optical ridge waveguides, and by imaging a layer of collagen fibers whose diameter is about 100 nm.

In conventional confocal microscopy, the signal light comes mainly from the focal point by fluorescence, reflection, or scattering. Light from outside of the focal region is heavily attenuated by spatial filters. A typical response curve is shown in Fig. 1. The depth resolution is equal to the width of the response curve, which is in the best case equal to the confocal parameter. Although at the focal point the response is largest, in the case that the signal light comes from a reflective surface, placing the sample at the focal point is not the most advantageous. At the focal point the derivative of the response curve with respect to the sample position is zero, which means the response is least sensitive to sample height variation. In contrast, if one places the sample slightly away from the focal point, so that its position is at the slopes of the response curve, the sensitivity is the greatest. At the slopes the sample height variation causes a differential change of the signal. The sensitivity is sufficiently large that the effect can be utilized to profile surface structures with depth resolutions as large as 20 nm.

Our experiments are done in two types of setups. One uses a superluminescent laser diode (Spindler & Hoyer DC25E) in a confocal feedback configuration (Lu et al. 1995). The other uses a He-Ne laser (Melles Griot 05-LHP-121) in a conventional feed-through configuration. The confocal feedback configuration is almost self-aligned, but due to the multi-mode nature of our laser diode, the lateral resolution is not as good as that of the He-Ne laser. Fig. 2 shows the He-Ne laser feed-through configuration. The laser output is focused by a 40× microscope objective onto the sample. The position of the sample at the *z*-axis is controlled by a piezoelectric transducer, and the sample point in the *x-y* plane is set by computer-controlled translation stages. Before the measurements, we first move the sample to the focal point by maximizing the reflected power. Then we raise the sample by about 1/2 confocal parameter, so that the reflection changes linearly with the sample height. Finally we scan the sample in the *x-y* plane and profile the surface structure with great depth resolution.

Fig. 3(a) shows a 3-dimensional image of an H-shaped trench on top of an InGaAs surface. For comparison, we also show in Fig. 3(b) its profile measured with a mechanical contact probe, the Dektak 3030 surface profiler made by Veeco Instruments, Inc. The measurements show that the confocal laser-feedback technique not only has much better lateral resolution, but also contains less noise. It is clear that the sensitivity of our experiments is great enough to see features in depth on the order of 20 nm, even though the lateral resolution is still limited by diffraction.

Unlike with scanning tunneling microscopes, atomic-force microscopes, or the recently developed scanning near-field optical microscopes (Betzig et al. 1992), our experiments are conducted in open loop; no servo control is used to lock the sample distance to a constant value, nor is lock-in detection applied to enhance the signal-to-noise

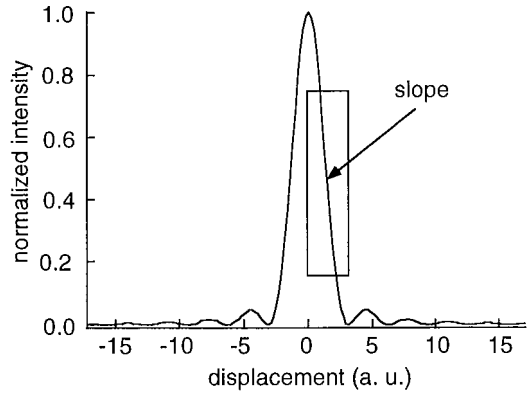

Fig. 1. Axial response of a confocal microscope.

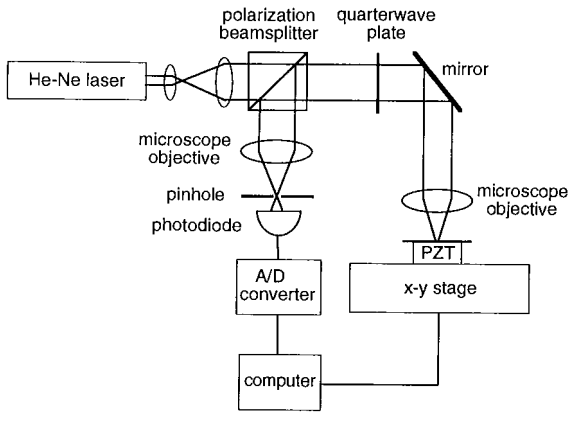

Fig. 2. Experimental setup.

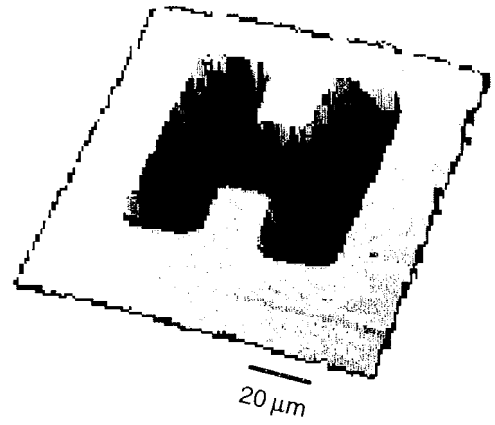

(a)

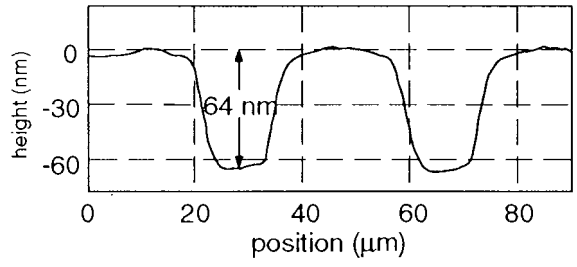

(b)

Fig. 3. (a) The 3-dimensional image of a 60-nm deep H-shaped trench on top of an InGaAs surface, compared with (b) that measured with a Dektak 3030 surface profiler.

ratio. The response time of the detection is limited only by the amplifier and the analog-to-digital converter and the speed of the mechanical translation stages. If electro-optical instead of mechanical scanning is used, we believe that with optimized system components measurements can be performed in the 30 frame/sec video rate.

Fig. 4 shows a 3-dimensional image of a polymethyl-methacrylate optical ridge waveguide on a silica substrate. The measured thickness of the waveguide is by the Dektak 3030 surface profiler. This measurement demonstrates the large linear dynamic range of the technique, which is many times larger than that of interferometric methods. Large linear dynamic range is important for high speed scanning in open-loop measurements because it eliminates the need of shifting the base-height during measurements. With other techniques which have the potential of open-loop measurements but do not have a large dynamic

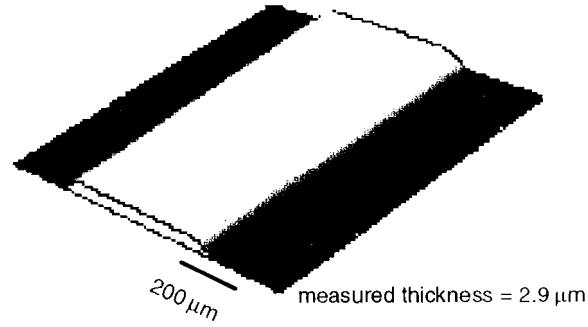

Fig. 4. The 3-dimensional image of a 3-μm high polymethyl-methacrylate optical ridge waveguide.

range, such as interferometric confocal microscopy (Bearden et al. 1993, Juskaitis et al. 1993, 1994), the need of dynamic base-height adjustment greatly reduces the scanning speed when

the sample height variation exceeds a fraction of the wavelength.

The surface profiles shown in Fig. 3 and Fig. 4 cannot be seen under conventional optical microscopes due to lack of contrast mechanism. High resolution nearly contact techniques such as scanning tunneling microscopy, atomic-force microscopy, and scanning near-field optical microscopy can provide much greater lateral resolution, but their measurement speed is much slower than the differential confocal technique due to the necessary close-loop operation mode. Moreover, with the differential confocal technique the distance between the probe head (objective) and the sample can be as large as several millimeters, as compared to nanometers in nearly contact techniques mentioned above. This is important to *in-situ* diagnosis in the fabrication of surface microstructures such as semicon-ductor devices, or in studying the morphology of living biologic samples.

Fig. 5 shows the image of a layer of collagen fibers extracted from bovine skin tissues. Unlike in Fig. 3 and Fig. 4, the measurement was done with the He-Ne laser in the feed-through configuration for better lateral resolution. The diameter of the fiber estimated from pictures taken by scanning electron microscopes is about 100 nm, which is apparently beyond the 0.8-μm lateral resolution of our system. Yet the fiber structure is recognized. The lateral resolution could be further improved by using oil-immersed objectives and shorter wavelength light sources.

In summary, using the concept of differential confocal microscopy, we developed an optical scanning microscope capable of measuring surface microstructures with 20-nm depth resolution and dynamic ranges as large as micrometers. In several respects the technique is complementary to the nearly contact techniques discussed above, yet it costs much less and is much simpler to operate. We believe that this technique has great potential not only in surface diagnosis and metrology needed by the microfabrication industry, but also in biomedical applications in which rapid measurements of living structures are highly desirable.

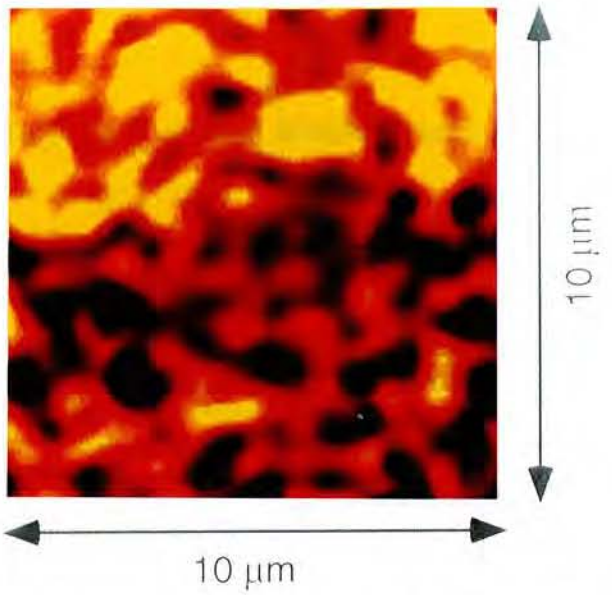

Fig. 5. The scanned image of collagen fibers. The actual diameter of the fiber is about 100 nm.

REFERENCES

Bearden A, MP O'Neill, LC Osborne, TL Wong. 1993. Imaging and vibrational analysis with laser-feedback interferometry. Opt. Lett. **18:** 238-240.

Betzig E, PL Finn, JS Weiner. 1992. Combined shear force and near-field scanning optical microscopy. Appl. Phys. Lett. **60:** 2484-2486.

Juskaitis R, T Wilson, F Reinholz. 1993. Spatial filtering by laser detection in confocal microscopy. Opt. Lett. **18:** 1135-1137.

Juskaitis R, T Wilson, NP Rea. 1994. Compact confocal interference microscopy. Opt. Comm. **109:** 167-177.

Lu J-H, J Wang, K-L Deng. 1995. Imaging and profiling surface microstructures with noninterferometric confocal laser-feedback. Appl. Phys. Lett. To be published.

Zoological Studies 34, Supplement I (1995)

Zoological Studies

On-line Attenuation Compensation in Confocal Microscopy

Wen-Shan Liou, Shan-Jen Pan and Ping-Chin Cheng

Advanced Microscopy and Imaging Laboratory, Department of Electrical and Computer Engineering, State university of New York at Buffalo, Buffalo, NY, USA

The ability to perform optical section with a confocal laser scanning microscope, provides great opportunity to take images at different depths within a sample. But images obtained from deep into the sample will also have longer optical paths, which will have lower signal intensities because of absorption and scattering by the sample 1. This gradual signal attenuation at increasing optical path will reduce S/N ratio and dynamic range of the image stack. The registration of similar structure with reducing intensity will also create difficulty in subsequent analysis such as image segmentation and three dimensional reconstruction. A heuristic method is developed to compensate this attenuation effect.

There is several parameters can be adjusted during the imaging process to get optimal images. The supplied voltage to photomultiplier tube (PMT) is a primary one to control the amplification of incoming signals. Since the gain of a PMT is a function of the supplied voltage, when taking an image stack from a thick sample, it is possible to change the supply voltage of the PMT to modify its amplification, and thus compensate signal attenuation at different depth. The output signal of a confocal microscope can be shown as:

$$I = L \times G\ (\ Vpmt)$$

where L is incoming light detected by the PMT, G is the total amplification of the electronic system, Vpmt is the supplied voltage to PMT and I is the output.

If we add appropriate compensation voltage (Vcom) to the PMT supplied voltage (Vpmt), it will increase or decrease the amplification on detected signals. This will bring output signals from images at difference depth to a similar intensity level. Therefore, the intensity of an image at step i in an image stack can be expressed as:

$$I(i) = L(i) \times G(\ Vpmt + V(i)com\ )$$

Then, the task is to select proper intensity representation of the images, and calculate the compensation voltage base on them. One method to achieve this is to let the microscope user to select similar features (e.g. cell nuclei) in images obtained at different depth, and derive the compensation voltage from the images. Gererally, the features of interest in an fluorescent image are composed of pixels with high signal levels. Therefore, in an automatic approach, the mean of a certain range of bright pixel value can be used to calculate the compensation voltage.

Our heuristic algorithm to compensate attenuation in an imaging stack can be summarized as:

1. The relationship between supplied voltage of the PMT and signal intensity is measured from a homogeneous sample of certain fluorescent dyes such as 0.1% FITC in DMSO solution.
2. At the first slice (the slice closes to the objective) of an image stack, proper illumination intensity and PMT voltage are selected in order to obtain optimal image and with enough adjustment range of the PMT voltage for later compensation. Acquire the image and calculate the mean value of the brightest group of pixels.
3. Move the specimen to the position of last slice (the deepest slice) and repeat step 2 with a proper voltage setting.
4. Use the differences between the mean values from step 2, 3 and data from step 1 to interpolate for compensation voltage.
5. Start the sequence of acquiring a stack of serial optical sections by adjusting the PMT voltage as a function of the sectioning depth based on the interpolated result.

A maize stem, fixed in a1:3 acetic acid/EtOH fixative, dehydrated in EtOH and cleared in winter

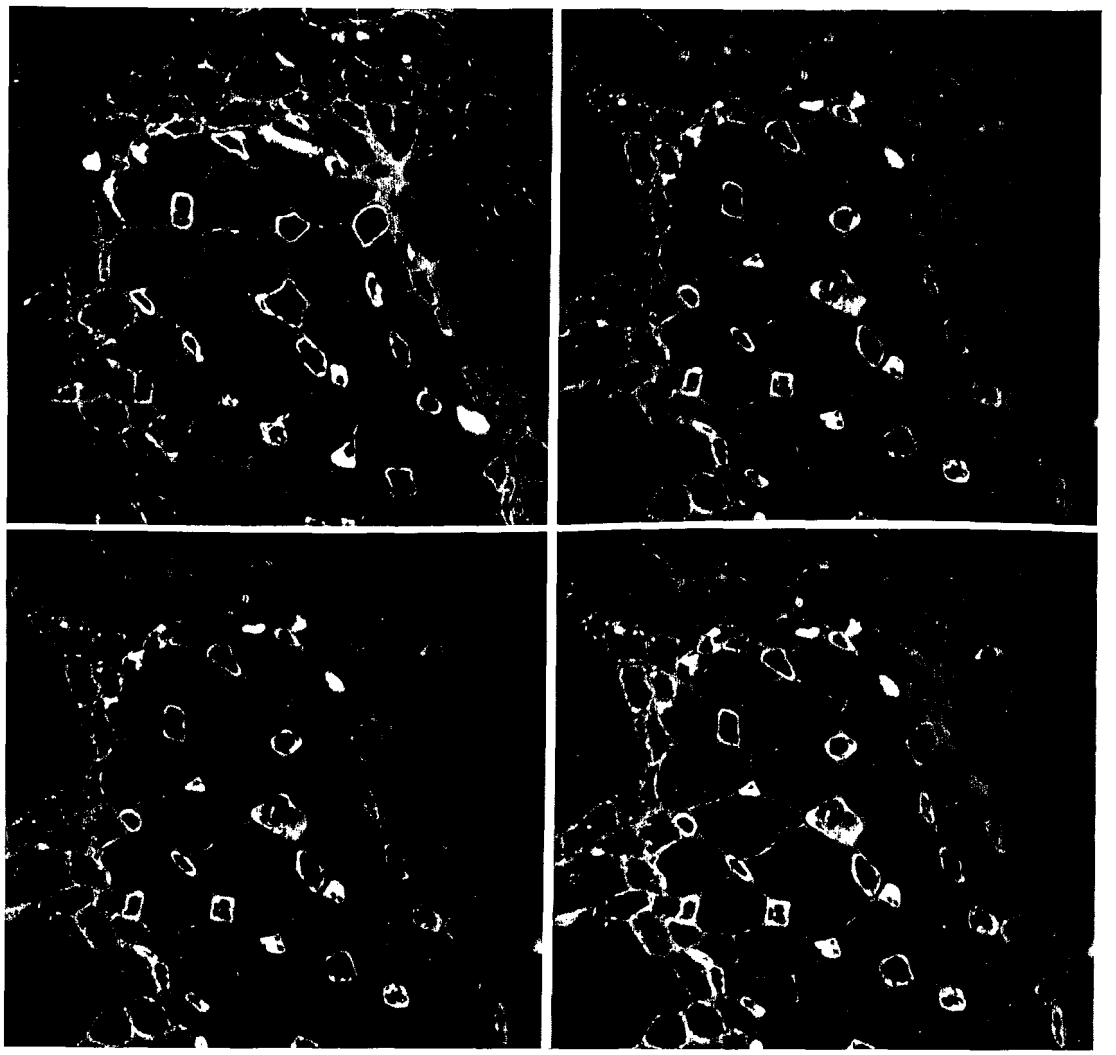

Fig. 1. Cross section of a maize stem. 1A: near the top surface of the sample; 1B: optical section obtained at a depth of 42um from the section shown in 1A; 1C: optical section obtained at the same position as 1B but with proper compensation; 1D: optical section obtained at the same position as 1B but with over compensation.

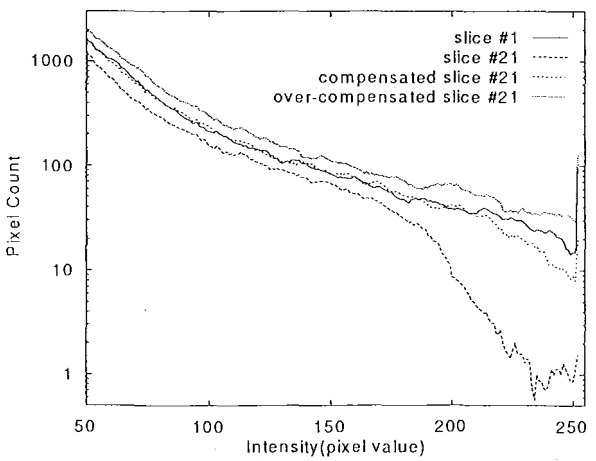

Fig. 2. Intensity histogram of image 1B, 1C and 1D.

green oil, was used as the test sample. The 488nm Ar ion line was used as the excitation wavelength and a 515 nm longpass filter was used in the detecting path. The image in Fig. 1A was taken near the top surface of the sample (first slice). Figure 1B shows the 21st slice which was 42μm deeper than the first slice. Figs. 1C and 1D were also taken at the same position as Figure 1B, but with proper compensation and overcompensation (2X of compensation voltage). The intensity histogram of these four images are plotted in Fig. 2. It clearly demonstrates the compensation method was able to move the histogram of an attenuated image obtained from deeper slice up to a similar level in comparison to the first slice.

This intensity compansation process is incorporated into the control software (developed in our lab at SUNY) for Olympus GR-200 laser scanning confocal microscope running under Microsoft Windows.

REFERENCE

Cheng P.C, and A. Kriete. 1995. Image Contrast in Confocal Light Microscopy. Handbook of Biological Confocal Microscopy, Ch 17, Plenum (in press)

Zoological Studies 34, Supplement I (1995)

Zoological Studies

Segmentation and Analysis Algorithms for Processing Multi-dimensional Images of DNA Replication Patterns in the Mammalian Cell Nucleus

J. Samarabandu, H. Ma, P. C. Cheng and R. Berezney
Department of Biological Sciences, State University of New York at Buffalo, Buffalo, NY 14260 USA

A part from the ability to capture 3D images of microscopic structures, a confocal laser scaning microscope (CLSM) equipped with multiple detectors allows one to add an extra dimension to the data acquisition process by using fluorochromes with different emission spectra. In these studies, position and distribution of microscopic structures such as DNA particles and cell nuclei are of particular importance in studying the morphogenesis of the samples of interest. For double labeling of DNA replication sites, mouse 3T3 cells exponentially grown on cover slips or synchronized at specific times in S-phase were pulsed for brieftimes (2-5 min) with CldU (chlorodeoxyuridune) followed by a chase period and a second labeling with IdU (iododeoxyuridine). The pulsed cells were then fixed (Nakayasu and Berezney 1989) and processed for fluorescence microsocpy using monoclonal antibodies, appropriate extraction conditions and fluorochrome-conjugated secondary antibodies which enabled differential recognition of sites of CldU versus IdU incorporatio into newly replicated DNA (Aten et al. 1992). Under the conditions used, there is no measurable cross reaction between the antibodies for CldU versus IdU labeled replication sites. Figure 1 shows the two channel composite image of a mouse 3T3 nucleus. In an effort to automate the analysis of these microsocpic structures, we developed a host of image processing and analysis techniques to process these multichannel 3D images. These techniques include procedures for leakage correction between channels due to overlapping spectra of the fluorochromes, linear and non-linear filtering methods to reduce the effects of noise and image segmentation algorithms to detect the replication sites (Ma et al. 1994a, Samarabandu et al. 1994b). In this article, we present some of the segmentation and pattern recognition procedures used at different stages.

A three-dimensional imaging system such as a confocal microscope encodes structural information of an object in to a 3D array of gray levels. The task of an image analysis system is to extract structural information from this array of gray levels and present it to the researcher in a form that allows easy access to manipulate and extract morphometrical information (Samarabandu et al. 1991, Samarabandu et al. 1993)

Segmentation is the process of classifying a given pixel as the background or the structure of interest. Once classified, each region needs to be labeled with a unique number to allow interaction with individual structures. In order to take advantage of the regularity of the data,we devised the following

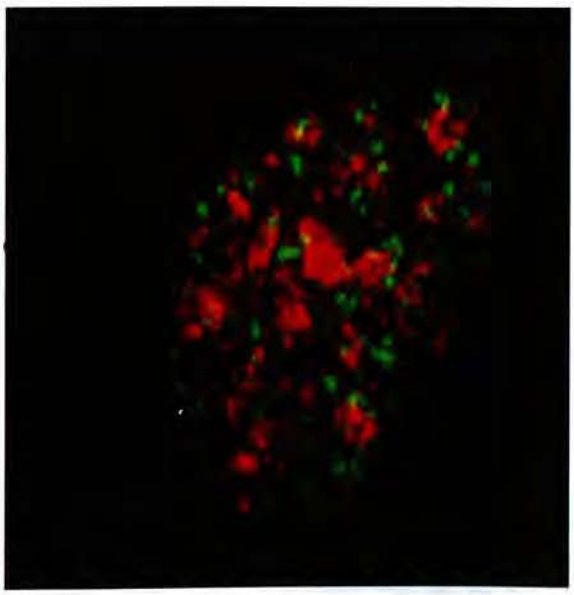

Fig. 1. Two channel composite image of a mouse 3T3 fibroblast. original image was a 768 × 564×15 pixel image.

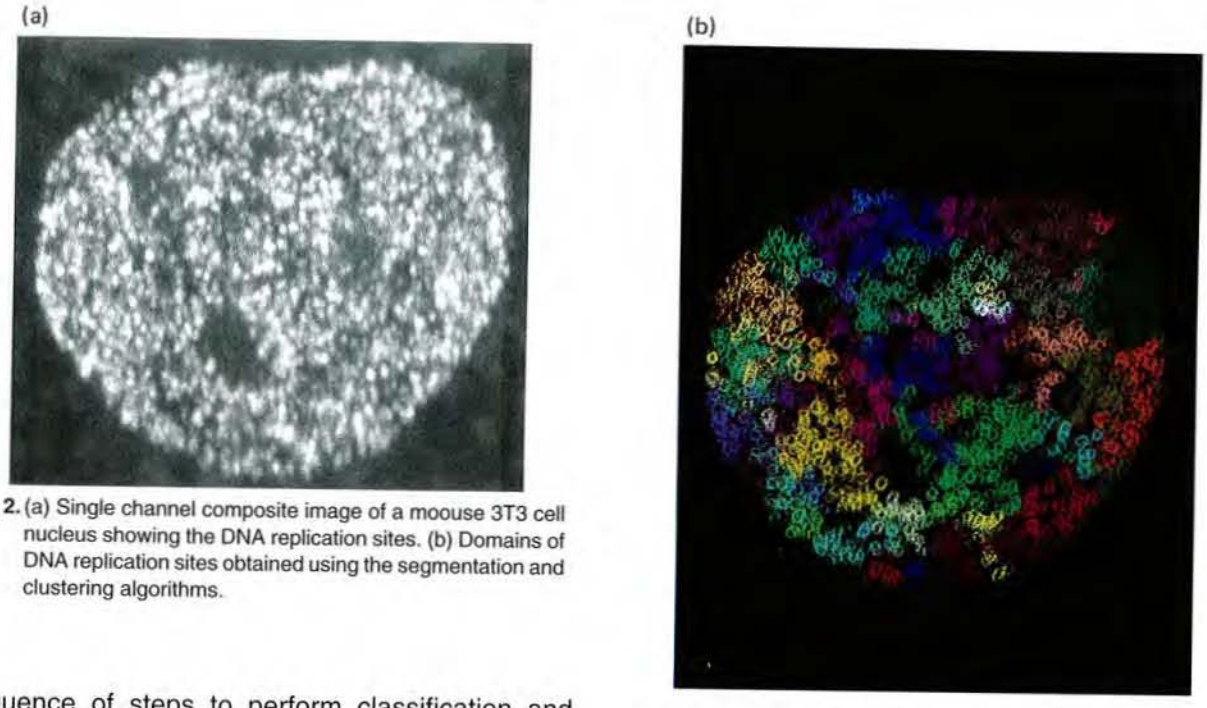

Fig. 2. (a) Single channel composite image of a moouse 3T3 cell nucleus showing the DNA replication sites. (b) Domains of DNA replication sites obtained using the segmentation and clustering algorithms.

sequence of steps to perform classification and labeling.

1.Detection and numbering local maxim

2.Boundary formation

3.Three dimensional connected component analysis

Steps 1 and 2 (detection of local maxima and boundary formation) are performed on individual two dimensional sections of the three dimensional image. Step 3 (three dimensional connected component analysis) uses boundary data on all sections.

The final task of the segmentation process is to form three dimensional objects from individual contours for each section of the 3D image. A unique label for each contour is generated by taking the section number as the two MSB's and the contour number within the section as the two LSB's of a 32 bit number. During the first pass, labels of each contour in one section are propagated to all overlapping contours of the next section. If a contour inherits two or more labels from the previous section, the lesser of them is assigned to it and an equivalence relation is recorded among all the competing labels. During the second pass, each label is examined for any equivalence relations and is replaced by the smaller of the equivalent labels if one exists. During this process, various statistics gathered for each section are accumulated for each object. Details of these algorithms and their performance was presented in a previous article (Samarabandu et al. 1994b).

Determining the position and boundary of the replication sites in three-dimensional space allows us to apply pattern recognitio techniques to further elucidate the 3D higher order assembly of individual replication sites. In one approach, we applied the above segementaiton procedure to each of the two channel images separately and calculated the percentage of overlap for each replication site between the two channels.

The next approach involved clustering the replication sites in to replication domains by grouping them according to the distance between their centers of gravity. The algorithm used in the previous section. Each particle is compared against every other particle and if the distance is less than a pre-set value, they are assigned the same domain number. If the other particle already has a domain number assigned, an equivalence relation is set up between the domain numbers. finally, domain numbers are consolidated with the equivalence relation table. Figure 2 shows such domains for a single channel image.

REFERENCES

Nakayasu H, R berezney. 1989. Mapping replicational sites in the eucaryotic cell nucleus. J. Cell Biol. **108:** 1-11.

Aten JA, JM Baakker, J Stap, GA Boschman, CHN Veenhof. 1992. DNA double labeling with IdUrd and ClDurd for spatioal and temporal analysis of cell prolifcration and DNA replication. Histochem. J. **24:** 251-259.

MA JKSH, X Wei, PC Cheng, R Berezney. 1994. On acquisition and processing of multi-channel confocal images of mammalian cell nucleus. Scanning. (In Press)

Samarabandu J, PC Cheng, R Berezney. 1994. Applicatio of three

dimensional image analysis to the mammalian cell nucleus. in IEEE Regional conference on multidimensional systems (Miami).

Samarabandu J, R Acharya, C Edirisinghe, PC Cheng, H Kim, TH Lin, RG Summers, CE Musial. 1991. Analysis of multi-dimensional confocal images, in Biomedical Image Processing II, vol. 1450 of Electronic Imaging: Science and Technology, SPIE.

Samarabandu J, R Acharya, PC Cheng. 1993. Visualization and interactive exploration of multidimensional confocal images. Computerized Medical Imaging and Graphics. **17:** 183-188.

Zoological Studies 34, Supplement I (1995)

Zoological Studies

Autofluorescence Imaging of Symbiotic Algae in Corals Using Confocal Microscopy - A Potential Tool for Environmental Monitoring

Anya Salih[1], Guy Cox[1] and Rosalind Hinde[2]
[1]*Electron Microscope Unit, University of Sydney, NSW 2006, Australia*
[2]*School of Biological Sciences, University of Sydney, NSW 2006, Australia*

There has been an increasing concern worldwide about deterioration of coral reefs due to natural and anthropogenic environmental perturbations. At present, however, environmental monitoring of coral reefs is limited by difficulties in recognising coral stress, other than by measuring and documenting corals' mortality over time. Mortality generally means that the major deterioration of the coral community has already taken place. Thus, more sensitive means of detection of sub-lethal effects of stress are urgently needed.

Recently, attention has more and more been focussed on the symbiotic relationship of corals and their dinoflagellate algae, commonly known as zooxanthellae. The zooxanthellae release organic nutrients to the coral host, which form the major portion of the animal's nutrition and stimulate its calcification (reviewed by Hinde 1988). The major tropical reef-building coral species are all associated with zooxanthellae, as are some temperate corals, such as *Plesiastrea versipora*, which was the species used in the present study.

Under optimal environmental conditions the coral/algal symbiotic relationship remains stable and only small quantities of zooxanthellae are regularly expelled (Hoegh-Guldberg et al. 1987). However, even relatively small environmental changes can cause an increase in the rate of algal expulsion (e.g. Hoegh-Guldberg & Smith 1989). One sign of acute damage to coral reefs is mass 'bleaching', during which corals actively expel most of their zooxanthellae (e.g. Glynn 1983).

Bleaching can also result from the loss of algal pigmentation (Kleppel et al. 1989, Szmant & Gassman 1990), or more commonly, is a combination of the two factors - loss of algae and loss of photosynthetic pigments (e.g. Szmant and Gassman 1990). In either case, the host appears lighter or even white in colour. The loss of symbionts leads to the loss of organic nutrients which are normally translocated to the coral host, leading to reduced coral growth and often coral mortality (Glynn 1983).

Recently, a number of studies have shown that a change in the rate of algal expulsion is a sensitive response of corals to environmental stress (eg. Muscatine et al. 1991, Gates et al. 1992). In addition, the measurement of specific growth rates of zooxanthellae in corals exposed to sub-lethal effects of stress may also prove to be useful for monitoring environmental impacts on these animals (Brown 1988).

Therefore, the determination of the sizes of algal populations provides a potentially highly effective technique for detecting a reduction in coral vitality well before sustained coral mortalities occur. This study is a preliminary investigation of using Confocal Laser Scanning Microscopy (CLSM) as a tool for monitoring coral health by quantitative assessment of zooxanthella population densities, their division rates and the changes in their morphology.

Algal numbers are generally estimated either by homogenising the whole animal or by macerating a tissue sample and counting the cells on a haemocytometer, while algal division rates are calculated from mitotic indices (ratio of dividing cells to the total number of cells present) measured in such populations (e.g. Hoegh-Guldberg and Smith 1989, Gates et al. 1992). There are, however, no rapid and accurate techniques for determining the changes in algal morphology which may be associated with environmental change. Although electron microscopy can provide an accurate ultrastructural investigation of the algae, chemical

fixation is a lengthy and tedious procedure and frequently results in histological artefacts.

CLSM offers the advantage of high resolution images obtained by optical sections of whole tissues and individual algal cells. The collected images can be stored on computer optical disc and statistically analysed by image analysis software.

Small colonies of the temperate scleractinian coral *Plesiastrea versipora* were used for these experiments. They were maintained in flow-through seawater tanks at 20-25°C. A set of colonies was exposed to artificial light at approximately 80 mmol quanta μm^{-2} s^{-1} (on a 12L:12D photoperiod) and used for confocal imaging of zooxanthellae from unbleached corals. Two other groups of coral colonies were induced to expel large numbers of zooxanthellae by either (i) maintaining the corals in the dark for seven weeks, or (ii) by exposing corals to heat stress (Gates et al. 1992). This was done by increasing the seawater temperature by 7°C for two days and subsequently maintaining them at normal temperatures for the rest of the seven weeks.

Prior to confocal imaging, colonies were narcotised and a piece of tentacle was excised with forceps for microscopic investigations. This was sealed under a cover slip on a well-slide and optically sectioned (oil immersion x100 objective) using a Zeiss epifluorescence microscope. Images were obtained from chlorophyll autofluorescence produced by excitation by light at 488nm from an argon laser and Voxel view software was used to generate three-dimensional (3-D) reconstructions.

Confocal imaging produced detailed images of the distribution of the zooxanthellae within coral tissues, while transverse optical sections through the algae clearly showed which cells were dividing (Fig. 1). This technique, therefore, permits algal population densities and algal mitotic indices to be determined, provided a sufficiently large number of samples are optically sectioned. Additional quantitative information may be obtained by using image analysis software for obtaining such data as cell diameter, volume or numbers of degenerate or irregularly shaped algae.

At high magnification, confocal imaging of the zooxanthellae showed detailed structure of the chloroplasts. The 3-D reconstruction of the optical sections allowed the identiffcation of structural changes associated with the effects of stress not readily apparent when viewed under two-dimensional light or electron microscopy. While chloroplasts of unstressed corals had the normal highly lobed and compact appearance (Fig. 2), the chloroplasts in corals subjected to bleaching showed signs of different degrees of degeneration: a less compact structure, probably a result of dissociation of thykaloid membranes; breakage of chloroplasts into minute fluorescing particles; prominent holes in some chloroplasts; an enlargement of accumulation body and an increased number of crystalline inclusions (Figs. 3 - 6). Similar degenerative changes have been found in senescent zooxanthellae, which form a small percentage of the total algae regularly extruded by corals and anemones (e.g. Steele 1975), but not present in any large numbers within host tissues.

CLSM technique has a number of advantages over conventional microscopy: (1) it is fast, accurate and easy to carry out and does not require complicated staining and chemical fixation; (2) zooxanthellae can be imaged *in hospite*, as this allows their 3-D localisation within host tissues to

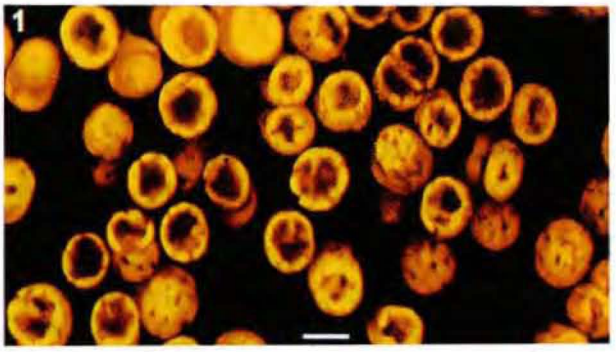

The scale bars for figures 1-3 are equal to 10mm and for figures 4-6 are 5mm.

Fig. 1. A reconstruction from serial, confocal autofluorescence of zooxanthellae within healthy coral tissues. Transverse sections through algae show dividing cells. (30 optical sections at 0.2 μm intervals)

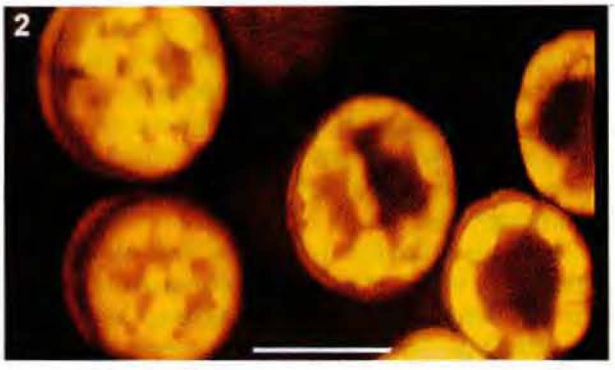

Fig. 2. Reconstruction of unstressed zooxanthellae showing surface and internal structure of chloroplasts. (Reconstruction depth 15 μm)

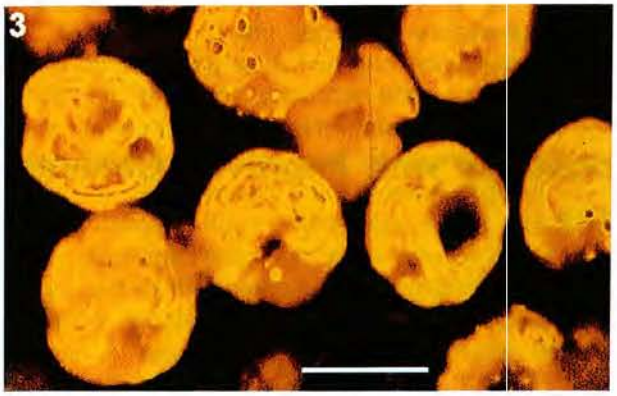

Fig. 3. Degenerate chloroplast structure of zooxanthellae from corals maintained in the dark, showing large holes and dissociation of chloroplast lobes into pieces (25 sections at 0.4 μm intervals).

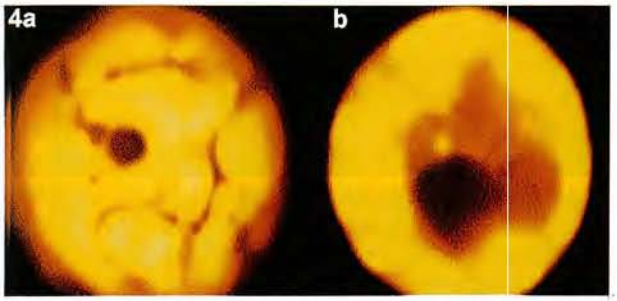

Fig. 4. Zooxanthella in a coral stressed by temperature increase (20 optical sections at 0.4 μm intervals): (a) surface view of reconstruction, showing chlorplast and inclusion bodies; (b) view through mid-section, showing less compact chloroplast appearance and signs of dissociation.

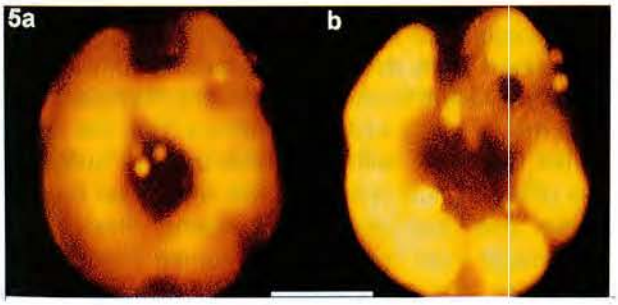

Fig. 5. Zooxanthella from coral at a more advanced stage of bleaching (a) surface view; (b) mid-section showing degeneration and dissociation of chloroplast.

be investigated and prevents the development of various changes associated with the isolation of zooxanthellae from the host; (3) computer reconstruction of the images allows 3-D viewing, manipulation of optical sections, photography and statistical

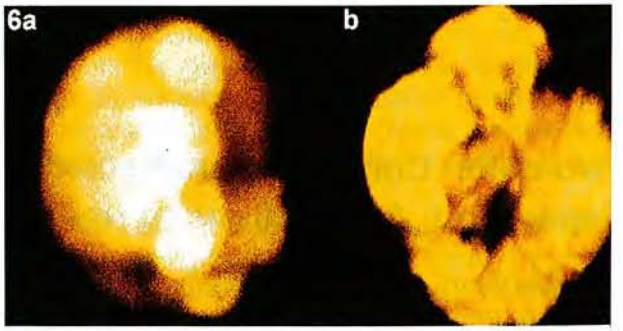

Fig. 6. Reconstruction of algal cells showing highly advanced degeneration of chloroplasts: (a) diffuse structure of chloroplast lobes; (b) final stages of chloroplast degeneration.

analysis; (4) and the technique is relatively inexpensive when compared to other methods used for the assessment of sub-lethal stress on coral reefs.

The results of this investigation show that CLSM provides a novel technique for monitoring algal populations within coral tissues. More importantly, confocal ultrastructural investigations reveal differences between algae from stressed and healthy corals. This represents a valuable avenue for future research in the development of techniques suitable for rapid and accurate appraisal of sub-lethal damage on coral reefs.

REFERENCES

Brown BE. 1988. Assessing environmental impacts on coral reefs. Proc. 6th Coral Reef Symp. 1988, Vol. 1. pp. 71-79.

Gates RD, G Baghdasarian, L Muscatine. 1992. Temperature stress causes host cell detachment in symbiotic cnidarians: implications for coral bleaching. Biol. Bull. **182:** 324-332.

Glynn PW. 1983. Extensive "bleaching" and death of reef corals on the Pacific coast of Panama. Environ. Conserv. **10:** 149-154.

Hinde R. 1988. Symbiotic nutrition and nutrient limitation. Proc. 6th Coral Reef Symp. 1988. vol. 1. pp. 199-204.

Hoegh-Guldberg O, LR McCloskey, L Muscatine. 1987. Expulsion of zooxanthellae by symbiotic cnidarians from the Red Sea. Coral Reefs. **5:** 201-201.

Hoegh-Guldberg O, GJ Smith. 1989. The effect of sudden changes in temperature, irradiance and salinity on the population density and export of zooszanthellae from the reef corals *Stylophora pistillata* (Esper 1797) and seriatopora hystrix (Dana 1846). J. Exp. Mar. Biol. Ecol. **129:** 279-303.

Kleppel GS, RE Dudge, CJ Reese.1989. Changes in pigmentation associated with bleaching of stony corals. Limnol. Oceanogr. **34:** 1331-1335.

Muscatine L, D Grossman, J Doino. 1991. Release of symbiotic algae by tropical sea anemones and corals after cold shock. Mar. Ecol. Prog. Ser. **77:** 233-243.

Steele RD. 1975. Stages in the life history of symbiotic zooxanthellae in pellets extruded by its host *Aiptasia tagetes* (Coelenterata, Anthozoa). Biol. Bull. **149:** 591-601.

Szmant AM, NJ Gassman. 1990. The effects of prolonged "bleaching" on tissue biomass and reproduction of the reef coral *Montastrea annularis*. Coral Reefs. **8:** 217-224.

Zoological Studies 34, Supplement I (1995)

Zoological Studies

Two-color Confocal Fluorescence Microsocpy with Improved Channel Separation; Applications to Neuroscience

Kjell Carlsson[1] and Brun Ulfhake[2]

[1]*Physics IV, The Royal Institute of Technology, S-100 44 Stockholm, Sweden*

[2]*Department of Neuroscience, Karolinska Institute, S-171 77 Stockholm, Sweden*

Intensity-modulated, multiple-beam scanning (IMS) is a new technology that drastically reduces cross-talk between the channels in multi-color confocal fluorescence microscopy (Carlsson et al. 1994). Experiments performed on free fluorophore in solution showed that for FITC (green fluorophore) and Lucifer Yellow (green-yellow fluorophore) no cross-talk at all could be detected when using the IMS method. With conventional detection techniques (i.e. using color filters to separate the light from different fluorophores), these fluorophores produce extensive cross-talk between the detector channels (10-70%). For the red fluorophores TRITC and Texas Red the cross-talk was reduced by an order of magnitude when using IMS. The rationale for application of the IMS technique for use with multi-colored specimens in biology, is that a number of the most useful fluorophores such as Lucifer yellow, FITC and Cyanine-3.18 all are notoriously difficult to separate by using filters only. The aim of the present study was to assess the performance of the IMS method when applied to neuronal tissue specimens, single- or dual-labeled with widely used fluorophores. In the experiments the specimen was simultaneously illuminated by the laser wavelengths 488 nm and 568 nm, modulated at different frequencies in the MHz region. The laser power reaching the specimen was between 0.2 and 0.4 mW depending on the objective used. These light intensities are well below those reported to cause fluorophore saturation problems. Detection was performed by two photomultiplier tubes (PMTs) with filters for the green (515-545 nm) and red (590- nm) wavelength regions respectively. The outputs from the two PMTs were connected to two lock-in amplifiers tuned to the same frequencies as the laser beams. Two different objectives were used, 40/1.0 and 63/1.4, depending on the type of specimen profiles studied. To compare the IMS technique with conventional detection, identical measurements were also performed in the same confocal microscope, but without using the lock-in detection technique.

The studied specimens were from rat spinal cord that was single- or dual-labeled with the fluorophores FITC, Lucifer Yellow (LY), Texas Red (TR), Lissamine Rhodamine (LRSC), and Cyanine-3.18. Labeling was performed by using direct intracellular (IC) injection of the fluorophore and/or by use of indirect immunocytochemistry. Thus, neurons were labeled either IC with Lucifer Yellow or by an antibody that recognizes MAP2, a cytoskeletal protein, that was made visible by a FITC-conjugated secondary antiserum. Axons were labeled with antisera raised against various neuromodulatory peptides (CGRP, enkephalin, substance-P), growth factor GAP-43 and/or the transmitter serotonin (5HT). A variety of secondary sera, conjugated to FITC, Cyanine-3.18, LRSC or Texas Red were deployed to make these markers visible. Comparisons of different fluorophores were made using adjacent sections from the same animal incubated with the same primary antibody. The different fluorophores were evaluated both in single- and dual-labeled specimens. Recordings were made from tissue section series from six experiments. For each fluorophore, or combination of fluorophores, between two and eight recordings were made. In the first experiment single-labeled specimens were studied. In order to work with realistic sensitivities in the two detection channels, we first recorded the corresponding dual-labeled specimens and adjusted the PMT voltages to obtain a similar signal level in both channels. This balance was then retained when recording single-labeled specimens.

Evaluation of the recorded image pairs was done by manually selecting and encircling relevant specimen regions, such as axon-, cell body- or dendritic-profiles. For each region the average light intensities in both detection channels were calculated. In each image pair, several regions (~10) with different light intensities were selected. Thus, the light readings were spread out over a large part of the intensity range 0-255. Linear regression analysis was then carried out for the intensity readings of the two channels in each image pair. The slope of the regression line represents the level of cross-talk between the channels. By calculating the correlation coefficient, we could also assess whether these values were significant with respect to the statistical fluctuations.

Fig. 1 shows examples of images obtained from specimens labeled with FITC and LY. For both fluorophores the IMS technique performs much better than conventional detection - cross-talk is reduced to negligible levels in both cases. Figure 2 shows the regression lines for the images in

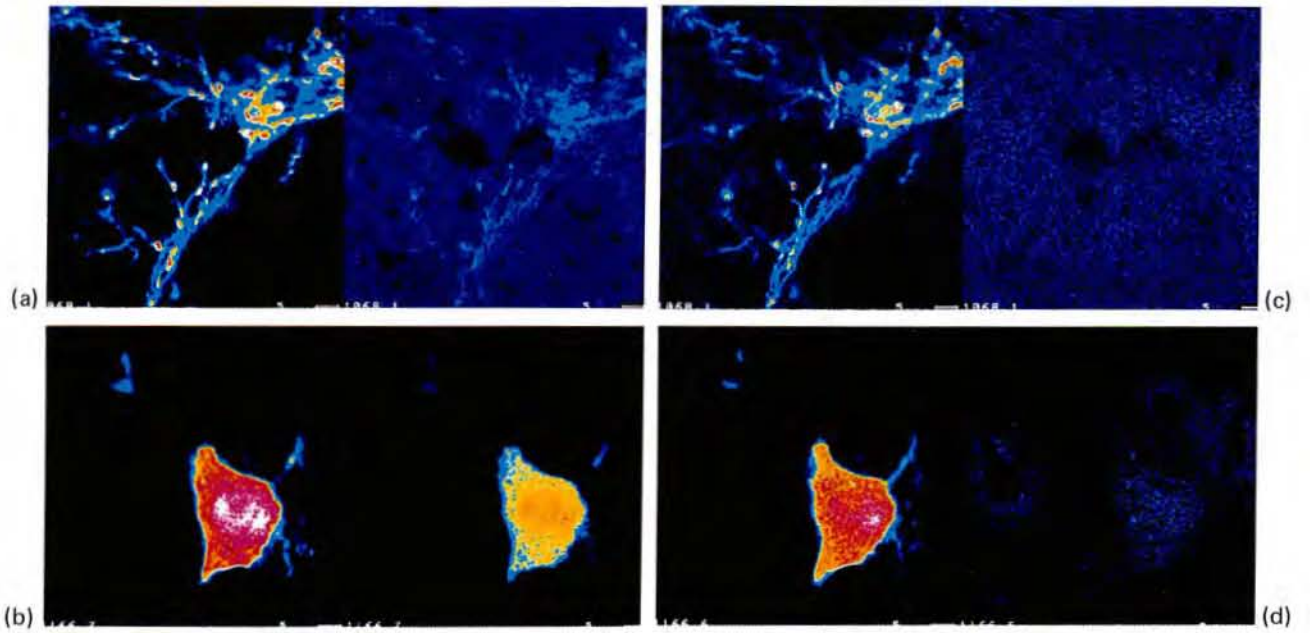

Fig. 1. Examples of single-labeled specimens recorded using non-IMS (i.e. color filters only) and IMS detection methods. In each image pair the left image shows the green channel and the right one the red channel. Pseudo-colors ar used to illustrate the intensity levels. a)FITC-label indicating CGRP-LI in rat spinal cord dorsal horn; non-IMS. b) Same as a), but IMS recording. c) Spinal cord neuron labeled intracellularly with Lucifer Yellow; non-IMS. d) Same as c), but IMS recording. Scale bar = 5 µm.

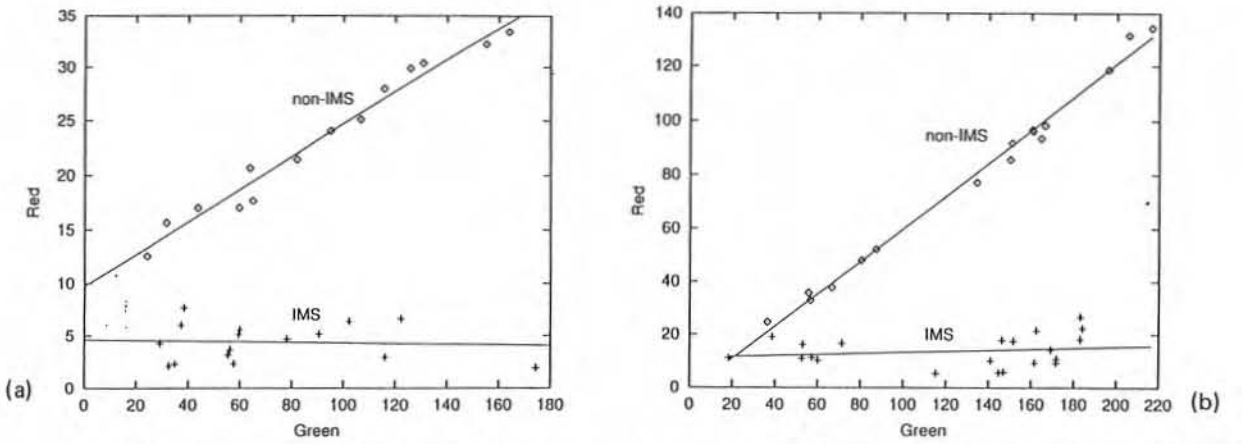

Fig. 2. Regression lines between the two detection channels for the images shown in Fig. 1. a) FITC-labeled specimen. The cross-talk levels are 15 % (non-IMS) and 0 % (IMS). Correlation coefficients of 0.99 and 0.08 respectively were obtained. b) LY-labeled specimen. The cross-talk levels are 61 % (non-IMS) and 2 % (IMS). Correlation coefficients of 1.00 and 0.19 respectively were obtained.

Fig. 1. In Table 1 results from cross-talk measurements on 30 image pairs (six of each for all five fluorophores) of single-labeled specimens are compiled. It can be seen that the cross-talk differs considerably between different recorded images. This is due to the fact that the strengths of the two fluorescent labels in the corresponding dual-labeled specimens display large variations. Since the dual-labeled specimens were used when setting the PMT voltages of the two channels, these variations will affect the level of cross-talk recorded. It is therefore meaningless to talk about one specific cross-talk level - it will depend strongly on the specimen, the labeling technique, and the excitation wavelengths and filters used. Table 1 therefore gives authentic examples of real situations, rather than a standard for cross-talk. It should be mentioned that many of the cross-talk levels given for the IMS method are uncertain because of low correlation coefficients. This is due to the fact that many values are so small as to be difficult to measure; in such cases statistical fluctuations may appreciably influence the results, and even give negative cross-talk values.

The dual-labeled specimens were recorded and evaluated in the same way as the single-labeled ones. However, the results are more varied and difficult to interpret. This is in part due to a varying degree of co-localization for the two fluorophores. Moreover, in specimens labeled with more than one marker there is also a risk for interaction which is not evident in single-labeled specimens and this is particularly a problem when using immunocytochemical labeling techniques.

In summary, we here report that applying the IMS technique to confocal fluorescence microscopy will substantially suppress unwanted cross-talk between labels, thus enabling the use of fluorophore combinations such as Lucifer yellow and Cyanine-3.18.

Table 1. Results of cross-talk measurements (%) in 30 image pairs of single-labeled specimens

Fluorophore	non-IMS		IMS	
	Average	Range	Average	Range
FITC	13.0	6.3-23.7	1.4	-1.4-3.7
LY	36.9	6.8-71.5	3.2	-1.2-11.2
TR	1.2	0.8-1.7	0.3	0.0-0.9
LRSC	1.5	1.0-1.8	0.5	0.1-1.1
Cyanine-3.18	2.2	1.3-2.9	0.4	0.2-0.7

ACKNOWLEDGMENTS

This study was supported by grants from the Swedish Research Council for Engineering Sciences, Knut & Alice Wallenberg Foundation, and The Swedish MRC (proj. 10820).

REFERENCES

Carlsson K, N Aslund, K Mossberg, J Philip. 1994. Simultaneous confocal recording of multiple fluorescent labels with improved channel separation, J. Microsc., **176:** 287-299.

Zoological Studies 34, Supplement I (1995)

Zoological Studies

A Study of the Dynamics of Solid Surfaces and Manipulation of Atoms

Tien T. Tsong
Institute of Physics, Academia Sinica, Taipei, Taiwan, R.O.C.

Understanding the dynamical behavior of solid surfaces and the physical properties of nanometer size material structures as well as developing new methods for producing these structures are becoming more and more important as high-tech materials and devices are getting smaller and smaller every year. Using the atomic resolution field ion microscope and scanning tunneling microscope, we have been studying the atom dynamics of metal and semiconductor surfaces, and methods and principles for creating atomic size structures on these surfaces. The atom dynamics we have studied include random and directional walks of single atoms, the mechanisms of the atomic jump in these walks, surface atomic reconstructions and electronic charge redistributions as a result of quantum confinement effects and electron-phonon coupling or lattice strain, etc. We also find new methods for creating atomic size material structures, study the principles of these methods and the physical properties of these nanometer size structures.

In our study of single atom diffusion, we find that Ir atoms diffuse on the Ir (001) surface by atomic-exchange-displacement mechanism instead of the conventional atomic hopping mechanism. This mode of surface diffusion can occur already at 220 K. For Re adatoms on the same surface, Re-Ir dimer-vacancy complexes can be formed at about 240 K, and diffusion of these complexes can occur at this temperature via different mode of diffusion. Above 280 K, the complex can dissociate. Once it dissociates, the Re atom will substitute into the top surface layer. From earlier studies we know when diffusion adatoms encounter a lattice step, they will either be reflected or will descend the step. The question is when diffusing adatom on a terrace encounter a lattice step, can they ascend the step. Up to now nobody has ever observed the ascending motion of adatoms. We have recently succeeded in observing the ascending motion of Ir atoms at the Ir (111) step. We also successfully measured the activation energy of this ascending motion as well as the dissociation energy of step edge atoms.

In our STM studies, we have found new methods for creating nanometer holes and mounds on Pt and Au surfaces, and clarified the mechanisms for the atom transfer process. In vacuum, we now can create a single atom vacancy on the (7×7) reconstructed Si (111) surface and refill it with an atom from the tip. We can also induce an atomic motion at the sample surface using the probing tip. In air and insulating liquid, holes of 2 to 3 nanometer sizes can be created on the Pt surface by applying a positive voltage pulse of a few volts and width of about 0.1 s. For the Au surface, both hole and mounds can be created but the latter have a much higher probability. We have also observed new periodic image structures which arise from electronic charge redistributions as a result of the confinement effects of domain boundaries and lattice steps. These new structures can be observed only in a very narrow energy window near the Fermi level. They show unique electronic characters, but the structures are also closely correlated to the

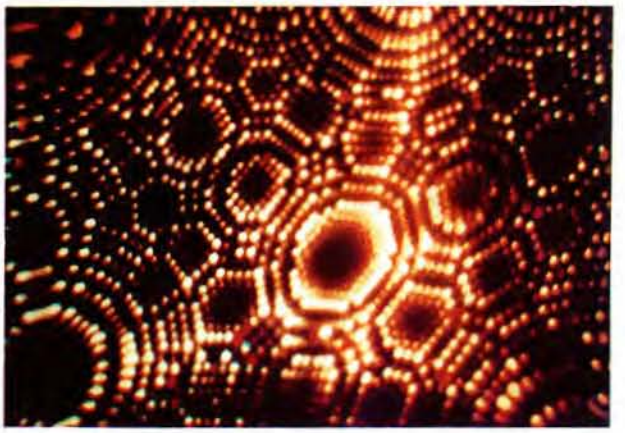

Fig. 1. A field ion image of an Ir tip showing many small crystal faccets.

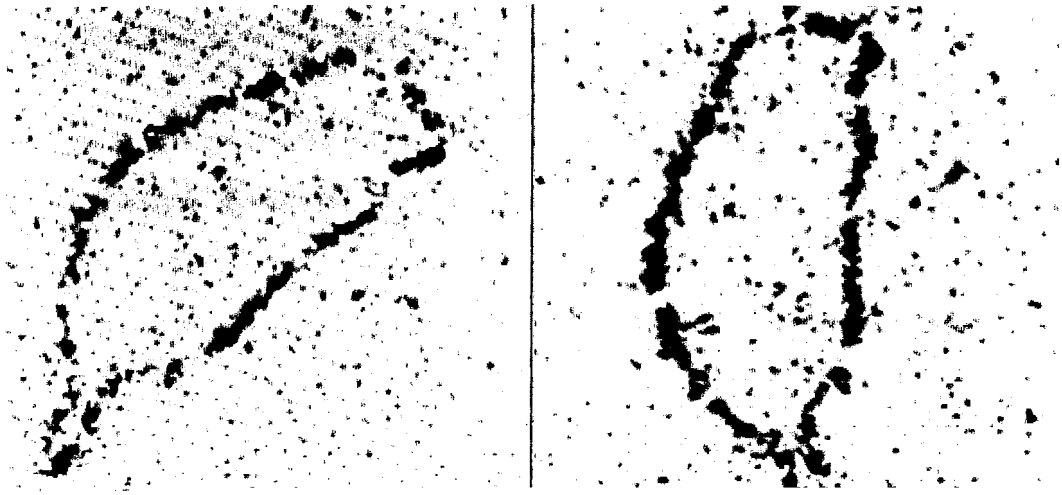

Fig. 2. Two atomic maps of Taiwan created on the Si (111). The size is 70 nm ×70 nm.

original atomic arrangement of the surface. Such structures can also be induced by strain field produced by voltage pulse created nanometer holes plus a domain boundary. These holes can be filled up by surface diffusion. Once the holes are gone, these periodic image structures also disappear.

Thanks are expressed to my coworkers of these works C. L. Chen, Y. R. Tseng, T.Y. Fu, C.S. Chang and W. B. Su, R. L. Lo and T. C. Chang.

REFERENCES

Tsong TT, CL Chen. 1992. Atomic replacement and formation and annihilation of a vacancy on Ir surfaces. Nature **355:** 328-331.

Chang CS, WB Su, TT Tsong. 1994. Field evaporation between a tip and a gold sample in the STM configuration. Phys. Rev. Lett. **72:** 574-577.

Zoological Studies 34, Supplement I (1995)

Zoological Studies

Images of a Membrane-bound Detoxification Enzyme at 4 Å Resolution Obtained by Electron Cryomicroscopy

Hans Hebert[1], Ingeborg Schmidt-Krey[1] and Ralf Morgenstern[2]

[1]*Center for Structural Biochemistry, Karolinska Institutet, Novum, S-141 57 Huddinge, Sweden*

[2]*Institute of Environmental Medicine, Division of Toxicology, Karolinska Institutet, Box 210, S-171 77 Stockholm, Sweden*

INTRODUCTION

The significance of electron microscopy as a tool in structural molecular biology is directly related to the resolution that can be reached. In general, the goal should be to obtain information at a level which allows an accurate spatial localization of all the building blocks of a biological macromolecule such as the amino acids of a protein. Recently, this has been achieved for two membrane proteins (Henderson et al. 1990, Kühlbrandt et al. 1994). A requirement has been that protein molecules be arranged on a lattice forming a two-dimensional crystal. If such an array is sufficiently large and well ordered, averaging can produce significant high resolution information. Thus, it is possible to circumvent one of the fundamental problems in high resolution biological electron microscopy: the conflict between using a sufficient number of electrons to produce significant contrast and protecting the specimen from the dose dependent beam damage.

Electron crystallography is a method which is of particular interest to the study of membrane proteins. Formation of two-dimensional crystals can be induced in a natural membrane environment with phospholipids, and such thin specimens are ideal objects for electron microscopy. In the present work, we have obtained large and well ordered two-dimensional crystals of a membrane-bound detoxification enzyme - microsomal glutathione transferase (molecular weight of the monomer 17.3 kDa). Image data obtained through electron cryomicroscopy and subsequent image processing including compensation for lattice disorder and phase contrast reconstruction has resulted in a projection structure at 4 Å resolution that allows interpretation in terms of secondary structure elements.

MATERIALS AND METHODS

Pure microsomal glutathione transferase was solubilized in 1 % Triton X-100 and mixed with bovine liver lecithin at a lipid to protein molar ratio of approximately three. Slow removal of the detergent was obtained through dialysis. The frequency, size and order of crystalline domains were monitored following negative staining. Image acquisition and on-line Fourier transformation were performed with a Tietz slow scan CCD system attached to a Philips CM120 electron microscope. High resolution images were collected on film at 200 kV with a Jeol 2000EX. The specimens were stabilized in tannin and cooled by liquid nitrogen (Wang and Kühlbrandt 1991). Some of the images were subjected to image processing which included compensation for lattice disorder and phase contrast reconstruction (Henderson et al. 1986). A weight function was applied to the final image amplitude data.

RESULTS AND DISCUSSION

Removal of the detergent resulted in a spontaneous formation of vesicles and membrane sheets. About 20 % of them contained microsomal glutathione transferase arranged on a lattice (Fig. 1a). These 2D crystals often measured about 1 μm in cross section and consisted of a single layer of protein molecules. An R-value test determined the projection symmetry to be pgg and

the unit cell dimensions were a=b=90.5 Å. The scanned areas (4400*4400 pixels at a pixel size on the specimen level of 1.4 Å) contained about 4000 unit cells. The lattice distortions were relatively small as measured by deviations from a perfect least-squares adapted lattice. The Fourier transforms of the images contained significant information extending to 4 Å. The phase residual was typically 20 to 25 degrees for 320 observed reflections.

The unit cell contains four tightly packed protein domains forming a staggered pattern (Fig. 1b). A local three-fold axis relates three molecules into a trimeric structure. The presence of a trimer is consistent with indications from other experiments (Morgenstern et al. 1982, Boyer et al. 1986, Lundqvist et al. 1992). Thus, we conclude that microsomal glutathione transferase is a trimer in the membrane-bound state. The projection structure of each trimer can be described as consisting of two concentric rings (Fig. 1c). The innermost of these has a triangular shape and is subdivided into six strong densities that have a center to center distance of 10 Å. In addition, the Fourier transform has strong reflections at the corresponding spatial frequency. Thus, we interpret the inner core as consisting of six parallel α helices with the helical axes running perpendicular to the plane of the membrane. These helices delineate a central featureless region. The outer ring consists of three elongated domains that do not form a completely closed structure. Since CD spectroscopy measurements have indicated the presence of β structure in microsomal glutathione transferase, this may correspond to β strands running more or less perpendicular to the plane of the membrane as in bacterial porins (Weiss et al. 1991, Cowan et al. 1992).

Interestingly, soluble glutathione utilizing enzymes have a common structural motif consisting of two parallel α helices and four β strands (Dirr et al. 1994). The projection of this conserved domain along the helical axes presents a structure that fits the projection of microsomal glutathione transferase as determined in the present work. This indicates that a similar glutathione binding domain could be present also in this membrane-bound form. In addition, this would mean that the microsomal glutathione transferase consists of both α helices and β structure. This has not been observed in other membrane proteins that have had their structures determined at high resolution (Cowan and Rosenbusch 1994). An alternative interpretation that can be made from the projection data alone is that the elongated outer domain contains one or two slightly tilted helices. The sequence of microsomal glutathione transferase predicts at least three membrane inserted domains. One of these is known to pass through the lipid bilayer (Andersson et al. 1994).

In the present work we have demonstrated the formation of large, well ordered 2D crystals of membrane-bound microsomal glutathione transferase. From electron crystallographic analysis it can be concluded that the protein forms trimers. Each of these consists of two parallel α helices and an elongated domain that could arise from a β sheet or tilted α helices. The projection structure resembles the glutathione binding domain found in soluble proteins with a similar catalytic function. Obtaining a more detailed model of the membrane topology will require the recording of three-dimensional data. This work is now in progress and it is hoped that this will allow localization of all the 154 amino acid residues of the protein

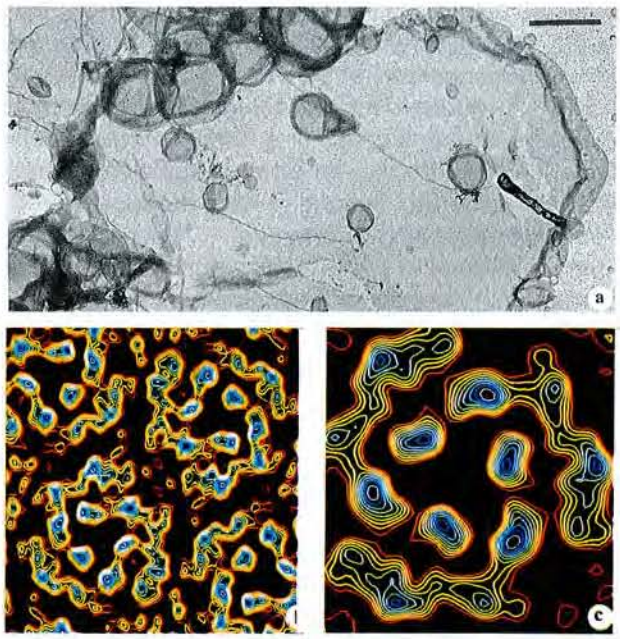

Fig. 1. (a) Electron micrograph of membrane sheets containing two-dimensional crystals of glutathione transferase. The specimen was stained with uranyl acetate. Scale bar 1 μm. (b) Projection map of the unit cell of the microsomal glutathione transferase two-dimensional crystals after image processing including data to 4 Å resolution. The unit cell dimensions are a=90.5, b=90.5 Å and one asymmetric unit contains one trimer of the protein arranged about a local three-fold symmetry axis. (c) The microsomal glutathione transferse trimer after imposing three-fold symmetry. The inner core consists of six parallel transmembrane α helices oriented with their helical axes perpendicular to the plane of the membrane.

monomer. Such a result is of interest, not only for understanding the functional properties of this protein, but also as contributing to the knowledge of membrane protein structure. Since this large, important yet elusive group of proteins is difficult to study with other structural methods, electron crystallography may provide a tool which can be applied more generally. It would be advantageous if the requirement to form large and well ordered cystals of the proteins could be relaxed to some extent since this could still be a limiting factor. Instrumental aspects play a key role in such a development.

REFERENCES

Andersson C, R Weinander, G Lundqvist, JW DePierre, R Morgenstern. 1994. Functional and structural membrane topology of tat liver microsomal glutathione transferase. Biochim. Biophys. Acta. **1204:** 298-304.

Boyer TD, DA Vessey, E Kempner. 1986. Radiation inactivation of microsomal glutathione S-transferase. J. Biol. Chem. **261:** 16963-16968.

Cowan SW, T Schirmer, G Rummel, M Steiert, R Ghosh, RA Pauptit, JN Jansonius, JP Rosenbusch. 1992. Crystal structures explain functional properties of two E. coli porins. Nature. **358:** 727-723.

Cowan SW, JP Rosenbusch. 1994. Folding pattern diversity of integral membrane proteins. Science. **264:** 914-916.

Dirr H, P Reinemer, R Huber. 1994. X-ray crystal structures of cytosolic glutathione S-transferases. Eur. J. Biochem. **220:** 645-661.

Henderson R, JM Baldwin, KH Downing, J Lepault, F Zemlin. 1986. Structure of purple membrane from Halobacterium halobium: recording, measurement and evaluation of electron micrographs at 3.5 Å resolution. Ultramicroscopy. **19:** 147-178.

Henderson R, JM Baldwin, TA Ceska, F Zemlin, E Beckman, KH Downing. 1990. Model for the structure of bacteriorhodopsin based on high-resolution electron cryo-microscopy. J. Molec. Biol. **213:** 899-929.

Kühlbrandt W, DN Wang, Y Fujiyoshi. 1994. Atomic model of the plant light-harvesting complex by electron crystallography. Nature. **367:** 614-621.

Lundqvist G, T Yucel-Lindberg, R Morgenstern. 1992. The oligomeric structure of rat liver microsomal glutathione transferase studied by chemical cross-linking. Biochem. Biophys. Acta. **1159:** 103-108.

Morgenstern R, C Guthenberg, JW DePierre. 1982. Microsomal glutathione S-transferase. Purification, initial characterization and demonstration that it is not identical to the cytosolic glutathione S-transferase A, B and C. Eur. J. Biochem. **128:** 243-248.

Wang DN, W Kühlbrandt. 1991. High resolution eletron crystallography of light-harvesting chlorophyll a/b-protein complex in three different media. J. Molec. Biol. **217:** 691-699.

Weiss MS, U Abele, J Weckesser, W. Welte, E. Schiltz, GE Schultz. 1991. Molecular architecture and electrostatic properties of a bacterial porin. Science. **254:** 1627-1630.

Zoological Studies 34, Supplement I (1995)

Zoological Studies

The Use of Nano-scatterer for Near-field Scanning Microscopy

S. Kawata
Department of Applied Physics, Osaka University, Suita, Osaka 565 Japan

Near field scanning optical microscope (NSOM) is a version of laser scanning microscope (LSM), in which a laser beam and a point detector image is scanned on the sample surface in two or three dimension. The resolution of NSOM is given by the actual size of the probe rather than the wavelength of the light due to diffraction, which is the case of LSM and conventional microscope.

A variety of probes have been designed for NSOM; most of them have small apertures at their tips. The aperture collects the evanescent photons localized near the sample surface, or it illuminates the local area of sample surface with evanescent photons. In this presentation, we describe the use of small scatterers rather than small aperture for observing super-resolving optical near field images. The scatterer converts evanescent photons localized near the sample surface to the propagating ones which can be detected in the far field from the sample. In this presentation, we present two types of probe as photon scatterer and the methods to control the probe position.

Fig. 1 illustrates the optical configuration of NSOM with a scatterer probe. A laser beam focuses on a position of the sample surface and a point detector focuses on the same position where a scatterer probe is placed. This configuration is the same as the LSM configuration except that the scatterer probe exists in the laser-beam spot. Since the probe is placed very near the sample surface, it can scatters evanescent photons produced with the fine structure of sample finer than the wavelength of light. Such evanescent photons do not propagate to the far field from the structure because the spatial wavenumber of evanescent photons normal to the sample surface is imaginary. The photons scattered at the probe tip are detected in the far field with a photodetector.

Fig. 2 shows an example of near field image(10μm×10μm) obtained by scanning a metallic scatterer (Platinum Iridium needle with the apex of 50nm) on the surface of the sample. The

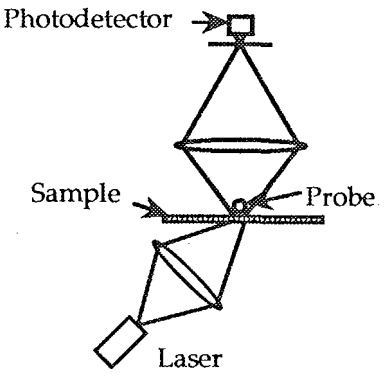

Fig. 1. Illustration of principle of NSOM with scatterer probe.

Fig. 2. NSOM image of murine embryonal myocardial cell. (10μm×10μm)

sample is murine embryonal myocardial cell. The laser used for this experiment was a laser diode of 670 nm (10mW). The beam was incident on the sample which was on a prism with the condition of total internal reflection. The tip of metallic probe shines (scatters photons) when it is inserted in the near field of the sample surface. By vibrating this probe (with the amplitude of 0.5 nm), only the conversion of evanescent photons localized near the sample structure to ordinary photons is detected with lock-in detection technique (Inouye et al. 1994). The distance between the probe and the sample surface is controlled by ~1 nm by regulating the electron tunneling current between the metallic probe and the metal thin film (of the thickness of, for example, 35 nm) coated on the sample (Inouye et al. 1995). This regulation technique results in the STM image detection in addition to the NSOM image detection. Fig. 3 shows the STM image of the same area of Fig. 2.

Since this probe does not contain an optical waveguide inside nor the small aperture at the tip, it could be sharp and small enough to attain ultra-high spatial resolution for both NSOM and STM imaging.

Another method we present here is the use of laser trapping technology for controlling the probe position (Kawata et al 1994). A small dielectric probe isolated from the arm is trapped with a focused laser beam near the sample surface. Fig. 4 show the experimental system of this

Fig. 3. STM image of the same area of the same sample as shown in Fig. 2.

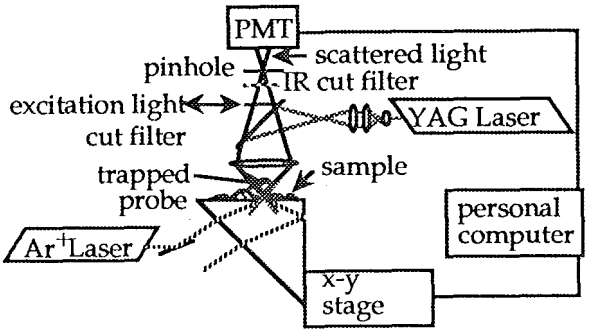

Fig. 4. NSOM with a laser-trapped probe.

NSOM system. The probe is trapped laterally on the optical axis; vertically it is pushed towards the sample surface by setting the focal position of the laser beam at the bottom of the probe.

Fig. 5 (a) and (b) show experimental examples

Fig. 5 (a)NSOM image of a polystyrene sphere in PMMA film. (3.2 μm × 3.2 μm)

Fig. 5(b)NSOM image of aggregated polystyrene spheres in PMMA film. (1.6 μm × 1.6 μm)

obtained with the developed NSOM. The samples are a polystyrene sphere (100 nmϕ; refractive index of 1.59) and its aggregation, respectively. The samples are dispersed in PMMA film (refractive index of 1.49) of the thickness of 100 nm. Since the surface is flat, the image of polystyrene spheres can not be observed either with STM or AFM. Only NSOM gives the optical image of the sample. Fig. 5 (b) shows two-point resolution of 100 nm.

Some more experimental results with the interpretation of NSOM images, such as polarization dependency, nonlinearity, and parameter dependency, will be presented in the presentation.

REFERENCES

Inouye Y, S Kawata. 1994. Near-field scanning optical microscope using a metallic probe tip. Opt. Lett., **19:** 159-161.

Inouye Y, S Kawata, Scanning near-field optical microscope having the scanning electron-tunneling microscope capability using a single metallic probe tip. J. Microscopy (accepted).

Kawata S, Y Inouye, T Sugiura. 1994. Near-field scanning optical microscope with a laser-trapped probe. Jpn. J. Appl. Phys., **33:** L1725-L1727.

Zoological Studies 34, Supplement I (1995)

Theory and Applications of Confocal Theta Microscopy

Ernst H. K. Stelzer[1], Christoph Cremer[2] and Steffen Lindek[1, 2]

[1]*Light Microscopy Group, Cell Biophysics Programme, European Molecular Biology Laboratory (EMBL), Postfach 10 22 09, D-69012 Heidelberg, Germany*

[2]*Institut für Angewandte Physik, Ruprecht-Karls-Universität, Albert-Überle-Str. 3-5, D-69120, Heidelberg, Germany*

INTRODUCTION

The outstanding role of confocal fluorescence microscopy in modern biological research results from its optical sectioning capability, which allows three-dimensional analysis of thick specimens (Shotton 1989). This property is due to the combination of point-like light sources and detectors, such that the illumination and detection volumes are restricted. Only their common volume is relevant to the confocal observation volume. The smaller it is, the better is the resolution. The performance of a confocal microscope is therefore primarily specified by the extent of the confocal point spread function (PSF), which can be determined according to several criteria. Since confocal theta microscopy (Stelzer and Lindek 1994) provides different resolutions along the three axes, it makes sense to introduce a three-dimensional resolution criterion, e.g., the volume enclosed by the isosurface at half maximum of the PSF (VHM - volume at half maximum) (Lindek et al. 1994a). For high-resolution microscopies the VHM is in the range of al (attoliters, 1 al = 10^6 nm^3).

Even with a high numerical aperture (NA) oil-immersion objective lens, illumination and detection are performed over only about 30% of the total solid angle. This gives rise to a PSF that is elongated along the optical axis, which implies that the lateral resolution of any conventional or confocal microscope is better than its axial resolution. Therefore, especially during the past few years a lot of work has been devoted to the improvement of the axial resolution (Sheppard and Gong 1991, Sheppard and Gu 1991, Hell and Stelzer 1992, Bailey et al. 1993, Stelzer and Lindek 1994).

Recently, the development of multi-objective-lens microscopes has revealed new prospects. The 4Pi-confocal microscope (Hell and Stelzer 1992) has an increased aperture due to coherent illumination and/or detection through two opposing lenses. Therefore interference modulates the PSF along the optical axis, and resolution is improved. The confocal theta microscope (Stelzer and Lindek 1994) uses two orthogonally placed lenses to illuminate the sample and to detect the fluorescence light, thereby eliminating the elongation of the PSF along the illumination axis. Both methods have their characteristics and advantages: In 4Pi-confocal microscopy, high-NA oil-immersion objective lenses have to be used to reduce the number of interference maxima (Lindek et al. 1995). This also guarantees high spatial resolution, but will only allow the investigation of thin samples because of the use of interference and because of the short working distance. In confocal theta microscopy, the mechanical arrangement requires the use of objective lenses with a moderate NA (the maximum with water immersion is 0.94). However, water-immersion objective lenses with a long working distance can be used, so no aberrations are induced by a refractive-index mismatch (Hell et al. 1993) and one may work with large biological specimens in an aqueous medium (Stelzer et al. 1995).

A CONFOCAL THETA MICROSCOPE WITH THREE OBJECTIVE LENSES

The idea of confocal theta microscopy is to use a second objective lens to collect the fluorescence light at an angle to the illumination axis. This diminishes the overlap of the illumination and detection PSFs and thus increases the resolution (Fig. 1). The smallest extent of the PSF is reached when the detection axis is orthogonal to the i-

Fig. 1. The idea of confocal theta microscopy. The detection PSF (red) is orthogonal to the illumination PSF (green). Thus, the overlap is restricted to the region close to the geometrical focus, and the confocal theta PSF becomes almost spherical (blue).

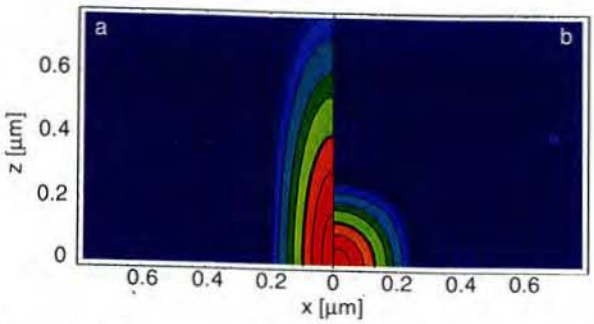

Fig. 2. Contour plots of the confocal (a) and confocal theta (b) PSFs for an orthogonal setup (illumination wavelength 488 nm, detection wavelength 520 nm, NA = 0.94).

Ilumination axis (Fig. 2). In practice the barrel diameter of currently available objective lenses only allows an arrangement with water-immersion lenses of NA =0.75 at an angle of 102°. (Carl Zeiss, Oberkochen, Germany).

However, this has only little influence on the resolution, and a setup with these lenses still has a four times better axial resolution and a three times smaller VHM than a confocal microscope using a lens with the same NA (for an illumination wavelength of 488 nm and a detection wavelength of 520 nm) (Lindek et al. 1994b).

An instrument with three of these objective lenses has been built at the European Molecular Biology Laboratory (EMBL) (Lindek et al. 1994b). It is a stage-scanning instrument set up on both sides of an upright bread-board (Fig. 3). The sample is suck onto a patch-clamp capillary that moves it through the common focus of the objective lenses.

The setup with three lenses is very flexible and allows several microscopies to be realized:

•Three confocal views are possible. With a single-objective-lens microscope different views

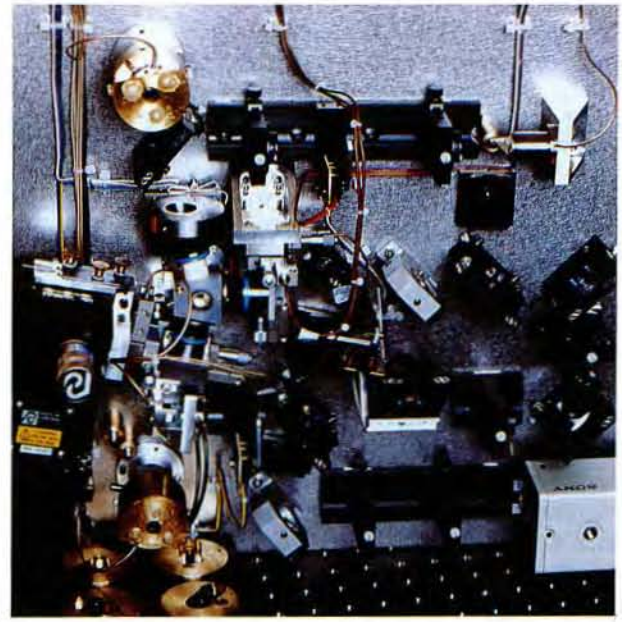

Fig. 3. Photograph of the illumination side of the confocal theta microscope.

are only possible if the sample is rotated (Shaw 1990, Bradl et al. 1992). However, a rotation or a deformation of the sample can cause trouble when evaluating the images. The present instrument has the advantage of allowing observation from three sides without moving the sample.

•Various theta microscopies are possible, since each objective lens can be used for illumination and for detection. The fluorescence intensity is recorded with two photomultipliers, which allows, e.g., the simultaneous imaging of two fluorophores in two different microscopy modes.

•The use of two different lasers (a pulsed tita-nium-sapphire laser that can induce two-photon absorption and an argon ion laser) increases the number of microscopies even further and allows various fluorescent dyes to be excited (Fischer et al. 1995).

APPLICATIONS

The microscope has been designed for biological applications with living specimens and is well suited for developmental biology:

•Since the immersion medium is water, no aberrations are introduced by refractive-index mismatch when biological samples are observed in aqueous media.

•The working distance of moderate-NA water-immersion lenses is quite large, which makes the microscope ideal for the observation of thick samples.

First measurements proved the feasibility and the resolution improvement of confocal theta microscopy (Stelzer et al. 1995). The absence of the elongation along the illumination axis and the better quality of theta images were documented with fluorescent beads. Experiments with a mouse embryo showed that biological material can be handled and that the effect of orthogonal detection also appears clearly when working with biological specimens.

CONCLUSION

Progress in three-dimensional microscopy aims at instruments with a high resolution. This is achieved with the confocal theta microscope, which provides the best resolution ever presented in light microscopy for the investigation of millimeter large biological samples.

ACKNOWLEDGMENTS

The authors would like to thank S. Albrecht, R. Pick, and G. Ritter for their help and Carl Zeiss (Oberkochen, Germany) for providing the objective lenses. S.L. gratefully acknowledges the generous support of the Boehringer Ingelheim Fonds.

REFERENCES

Bailey B, DL Farkas, DL Taylor. F Lanni. 1993. Enhancement of axial resolution in fluorescence microscopy by standing-wave excitation. Nature **366:** 44-48.

Bradl J, M Hausmann, V Ehemann, D Komitowski, C Cremer. 1992. A tilting device for three-dimensional microscopy: application to in situ imaging of interphase cell nuclei. J. Microsc. **168:** 47-57.

Fischer A, C Cremer, EHK Stelzer. 1995. Fluorescence of coumarines and xanthenes after two-photon absorption using a titanium-sapphire laser. Appl. Opt. in press.

Hell S, EHK Stelzer. 1992. Properties of a 4Pi confocal fluorescence microscope. J. Opt. Soc. Am. **A 9:** 2150-66.

Hell S, G Reiner, C Cremer, EHK Stelzer. 1993. Aberrations in confocal fluorescence microscopy induced by mismatches in refractive index. J. Microse. **169:** 391-405.

Lindek S, N Salmon, C Cremer, EHK Stelzer. 1994a. Theta microscopy allows phase regulation in 4Pi (A)-confocal two-photon fluores-cence microscopy. Optik **98:** 15-20.

Lindek S, R Pick, EHK Stelzer. 1994b. Confocal theta microscope wiht three objective lenses. Rev. Sci. Instr. **65:** 3367-3372.

Lindek S, EHK Stelzer, SW Hell. 1995. Two new high-resolution confocal fluorescence microscopies (4Pi, theta) with one-and two-photon excitation. In Handbook of Confocal Microscopy, ed. JB Pawley. New York: Plenum Press in press.

Shaw PJ. 1990. Three-dimensional optical microscopy using tilted views. J. Microsc. **158:** 165-172.

Sheppard CJR, Y Gong. 1991. Improvement in axial resolution by interference confocal microscopy. Optik **87:** 129-32.

Sheppard CJR, M Gu. 1991. Improvement of axial resolution in confocal microscopy using an annular pupil. Opt. Commun. **84:** 7-13.

Shotton DM. 1989. Confocal scanning optical microscopy and its applications for biological specimens. J. Cell Sci. **94:** 175-206.

Stelzer EHK, S Lindek. 1994. Fundamental reduction of the observation volume in far-field light microscopy by detection orthogonal to the illumination axis: confocal theta microscopy. Opt. Commun. **111:** 536-547.

Stelzer EHK, S Lindek, S Albrecht, R Pick, G Ritter, N Salmon, R Stricker. 1995. A new tool for the observation of embryos and other large specimens: confocal theta fluorescence microscopy. J. Microsc. in press.

Zoological Studies 34, Supplement I (1995)

Resolution beyond the Diffraction Limit: 4Pi-confocal, STED, and GSD

Stefan W. Hell[1, 2], Pekka E. Hänninen[1], Martin Schrader[1, 2], Tony Wilson[2] and Erkki Soini[1]

[1] *Department of Medical Physics and Biotechnology Center, University of Turku, P.O. Box 123, 20521 Turku, Finland*

[2] *Department of Engineering Science, University of Oxford, Parks Road, Oxford OX1 3PJ, England*

In far-field light microscopy resolution is determined by diffraction. In a far-field light microscope such as the confocal scanning light microscope, the resolution is governed by the extent of the squared intensity distribution in the focal region. Precise measurements of the confocal PSF (Brakenhoff et al. 1979, Hell et al. Appl Phys Lett, 64, 1994, Schrader et al. 1995) have shown that the axial and lateral resolution of a confocal microscope (NA=1.4 oil, λ= 633 nm) is 520nm and 200nm (FWHM), respectively. At a wavelength of 375nm, this amounts to a resolution of 300 nm (axial) and 120 nm (lateral), obtainable with a confocal microscope of high aperture.

A 3-7 fold increase in axial resolution is achieved with a 4Pi-confocal microscope (Hell 1990, Hell et al. 1992). The 4Pi- confocal micro-scope uses two high numerical aperture objective lenses that are used coherently for illuminating or detecting the same point in the object space. The present paper deals with the latest develop-ments in the field of 4Pi-confocal microscopy. The Optical Transfer Functions (OTF) of 4Pi-con-focal microscopies of type A, B, and C as realised in Oxford are measured and compared with their standard confocal counterpart. The application of the three point deconvolution of Hänninen et al. (Appl Phys Lett, in press) demonstrates an axial resolution of 140 nm (4Pi type A,B and 2-photon excitation type A) of 75nm (4Pi type C) at a (com-paratively long!) wavelength of 633 nm. Furthermore we show that the increased axial bandwidth of the 4Pi-confocal OTF (Gu and Sheppard, JOSA A, 1994) can be used to determine the axial distance between two point objects with a high precision.

Furthermore we discuss STED-fluorescence microscopy which is a concept to overcome the diffraction resolution limit in lateral direction Hell and Wichmann (Opt Lett, 19, 1994). The resolution increase is based on the reduction of the lateral extent of the effective PSF in a scanning fluorescence microscope by preventing exited fluorescent molecules from undergoing spontaneous emission. This is achieved by depleting the excited molecules at the edge of the focus by stimulated emission. The physics of the lateral resolution increase as well as the depletion process is discussed and demonstrated.

An althernate but related concept of depleting the ground state of the fluorophore (Ground State Depletion Microscopy) is introduced.

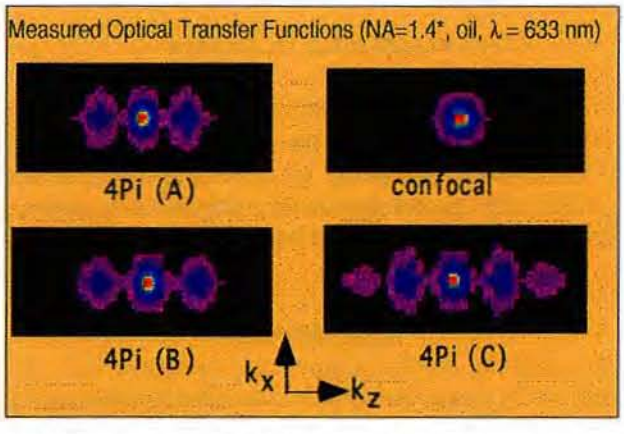

140 nm axial resolution in chromosome sample at an excitation wavelength of 750 nm (!)

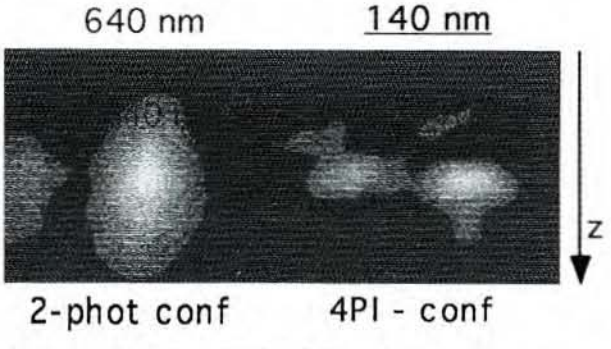

(Fig. Hänninen et al. Appl Phys Lett, in press)

Zological Studies 34, Supplement I (1995)

Conjugated Polymers Studies by Near Field Optical Microscope

W. S. Fann[1], P. K. Wei[1], B. R. Hsieh[2], K. R. Chuang[3], C. I. Chao[4] and S. A. Chen[3]

[1]*Institute of Atomic and Molecular Sciences, Academia Sinica, Taipei, Taiwan, R.O.C.*

[2]*Xerox Corp., Webster Research Center, Webster, NY 14580, USA*

[3]*Department of Chemical Engineering, National Tsing-Hwa University, Hsinchu, Taiwan, R.O.C.*

We have used the near field optical microscope (NSOM) to study the inhomogeneity as well as initiate photochemical processes in conjugated polymer films. A simple transmission-mode near field optical microscope is constructed for these purposes.

Light emitting diode (LED) based on conjugated polymers offers the flexibility of plastic and quantum efficiency approaching the inorganic LED. However the inhomogeneity is a integral part of conjugated polymers film due to the fabrication processes hence NSOM is an ideal tool for such studies at deep sub-micron length scale.

A simple transmission mode NSOM is constructed for such purposes. It is built around a commercial AFM scanning stage and a Si photodetector. The schematic of the microscope is shown in Fig. 1. A special design sample holder is used to mount a 1 cm^2, 250 μm thick Si PN planar photo-detector. This NSOM can provide topographic (AFM) and optical images simultaneously.

Fig. 2a shows the topographic image while Fig. 2b is the NSOM images of thin conjugated polymer, DP-PTV, films. The NSOM image offers the contrast at shear force image does not provide. The bright spot shown in Fig. 3 is due to the π bond breaking by the tapered fiber tip. Hence the NSOM can also be used to initiate the photochemical processes in light emiiting polymer films.

NSOM has also been apply to study the phase separation phenomena in conjugated polymer, polyanilide. Fig. 4a is the topographic and the Fig. 4b is the corresponding NSOM images. It is expected that if the NSOM contrast comes from only the sample thickness inhomogeneity then there should be a one-to one corresponding between the topographic and NSOM images. The place that is high in topographic should also be dark in NSOM images. It is clear that in certain area of the images this relation is not hold. In NSOM images, there is a bright strip, but in shear force image there is no corresponding height variations. bright strip in NSOM image but no corresponding in topographic images. Currently we are investigating the wavelength dependence of the above phenomena.

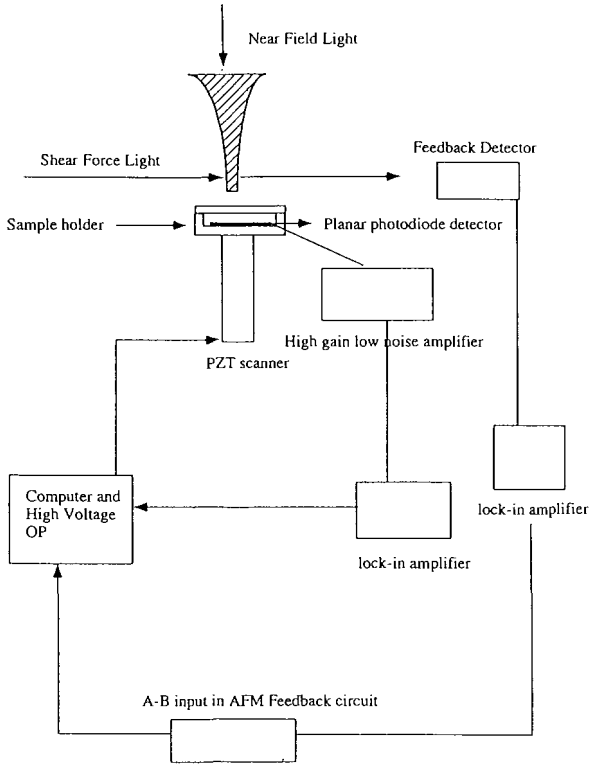

Fig. 1. The schematic of the transmission near field optical microscope.

(a) (b)

Fig. 2. The topographic and NSOM image of conjugated polymer DP-PTV film.

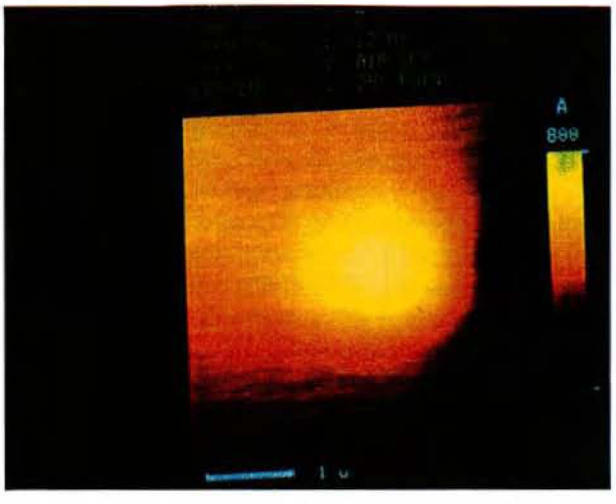

Fig. 3. The photo-chemical processes initiate at DP-PTV film by NSOM.

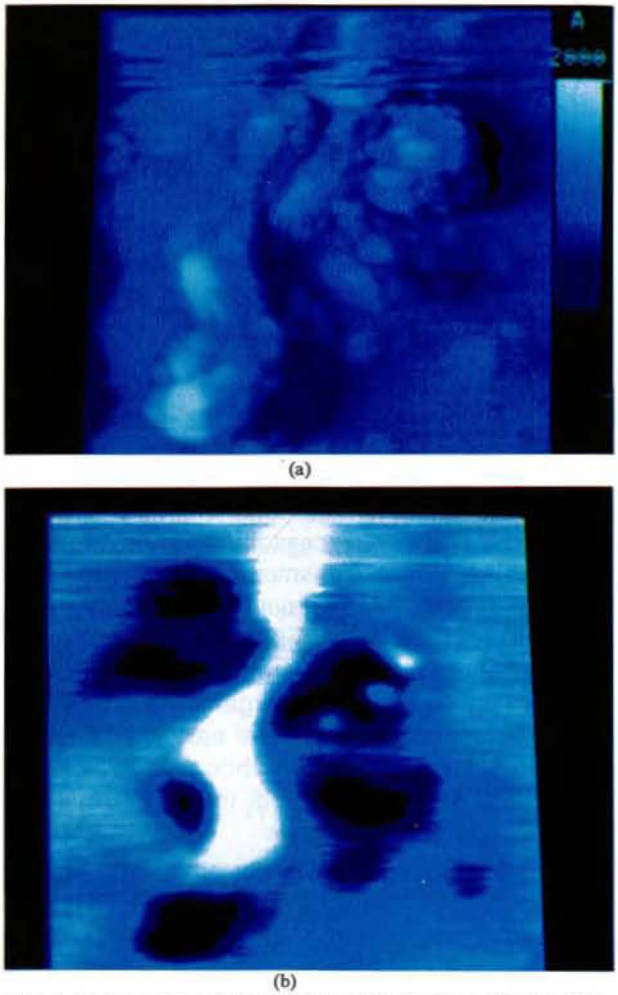

(a) (b)

Fig. 4. (a) the topographic and (b) the NSOM images of polyanilide.

In conclusion, it is demonstrated that NSOM can not only be used to probe the conjugated polymer films but also to modify their properties at sub-micron length scale. It should also be possible to use NSOM to induce elimination reactions in precursor polymer films. This research is partly supported by National Sciences Council in Taiwan, ROC.

REFERENCES

Burroughs LM, DDC Bradley, AR Brown, RM Marks, K Mackey, RH Friend, PL Burns, AB Holmes. 1990. Nature **347:** 539.

Fann WS. 1995. Review of Scientific Instruments, **66:** 1.

Betzig E, JK Trautman, TD Harris, JS Weiner, RL Kostelak. 1991. Science. **251:** 1468.

Betzig E, JK Trautman. 1992. Science **257:** 189.

Zoological Studies 34, Supplement I (1995)

Zoological Studies

The DNA Uptake Mechanism of Transfection Mediated by Cationic Liposomes

Sek-Wen Hui and Ya-Li Zhao

Membrane Biophysics Laboratory, Roswell Park Cancer Institute, Buffalo, NY 14263, USA

Cationic liposomes have become a popular transfection vector for gene delivery in vitro as well as in vivo. Because of their efficiency and ease of production, handling, and quality control, these liposomes provide an excellent alternative mode to viral vectors. Aminolipids such as 1, 2-bis (oleoyloxy)-3-(trimethylamonio)propane (DOTAP) have been used as cationic components of these liposomes. Yet, in spite of wide use of these liposomes, results have not been consistent, mainly because the mechanism of their cellular uptake is not entirely clear, and the factors affecting the uptake efficiency are not known.

In most cases, DOTAP and other cationic lipids work better as a delivery vector when mixed with a non-bilayer-preferring phospholipid such as dioleoloyl phosphatidylethanolamine (DOPE). These liposomes form complexes with negatively charged DNA; the residue positive charges in these complexes facilitate their adhesion to the cell surface. The subsequent fate of these complexes is not well understood. Either the entire complex is phagocytized by the cell, or its lipids fuse with the plasma membrane of the cell, thereby delivering the DNA to the cytoplasm.

We studied the factors affecting the DOTAP-mediated transfection of CHO cells. DOTAP:DOPE (1:1 molar ratio) liposomes were mixed, at a charge ratio of 1:2, with pCMV-β-gal, a plasmid carrying the reporter gene that codes for the enzyme β-galactosidase. 5 mol% of a fluorescent tracer, rhodamine-PE, was added to the lipids to form liposomes used for microscopy experiments. Ethidium bromide was used to label "exposed" DNA in double-labelled experiments. The complexes, when initially formed, were typically 50 nm in size, as measured by freeze fracture electron microscopy and by quasi-elastic light scattering. When added to cell culture media, the complexes aggregated because of polyvalent anions in the media. The fate of DNA-liposome complexes was determined by fluorescence confocal microscopy at various times after adding to CHO cells in different media. We found that the size and formation rate of aggregates were closely related to the uptake of DNA, and therefore the efficiency of transfection.

DNA-liposome complexes aggregated to >1μm almost immediately upon adding to phosphate buffered saline (PBS) or to normal F-10 culture medium containing $NaHCO_3$ (BRL/GIBCO). When added to a special F-10 medium without HCO_3^+ anions, the complex aggregation was much slower, and the terminal aggregate size was much reduced (~380 nm). There was no aggregation when the complexes were added to isotonic sucrose medium containing no anions. The transfection efficiency was measured by counting the number of clones expressing the β-gal gene, using X-gal staining. The subsequent transfection efficiency correlates closely with the size and rate of complex aggregation.

When observed by conventional and confocal fluorescence microscopes, visible aggregates formed immediately after the addition of liposome-DNA complexes to cells in normal F-10 culture medium containing bicarbonates. Most of these aggregates were in suspension and some were adsorbed on the cell surface upon sedimentation (Fig. 1). After 1 hr, many of the aggregated complexes were internalized, and the plasma and cytoplasmic membranes became bright, presumably from fusion with labelled liposome membranes. Figures 2 to 4 represent XY optical sections of a typical cell at 9, 2-5 and 1 μm from the supporting substrate. The XZ section of the same cell is shown in Fig. 5. Aggregated complexes are clearly seen inside the cell. By 3 and 4 hrs (Figs. 6 and 7 representing one out of a series of optical sections of

Fig. 1. An optical section 8-10 μm from the substrate of a cell in normal F-10 medium, immediately after liposome/DNA addition.

Fig. 2. An optical section 9 μm from the substrate of a cell in normal F-10 medium, 1 hour after liposome/DNA addition.

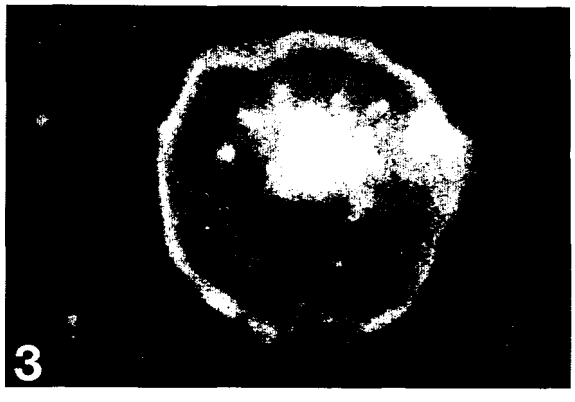

Fig. 3. An optical section 2-5 μm from the substrate, of the same cell in fig. 2.

Fig. 4. An optical section 1 μm from the substrate, of the same cell in fig. 2.

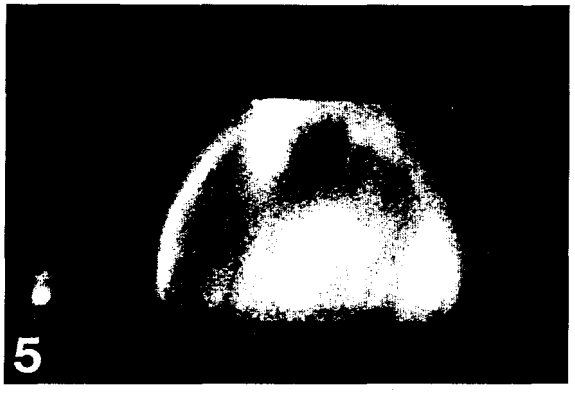

Fig. 5. An XZ optical section of the same cell in fig. 2.

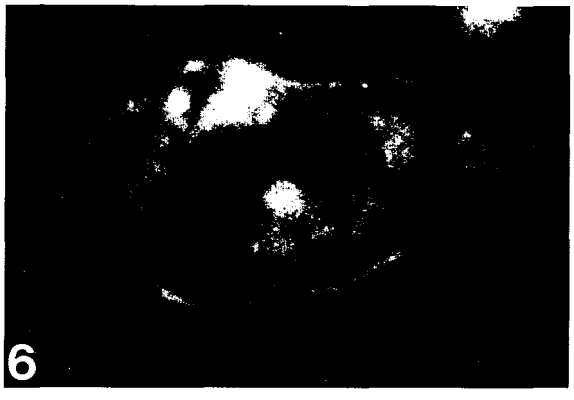

Fig. 6. An optical section 4 μm from the substrate of a cell in normal F-10 medium, 3 hours after liposome/DNA addition.

each cell, respectively), bright aggregates were mostly internalized. The plasma membrane and some cytoplasmic membranes became fluorescent at the same time. On those cells with fluorescent labelled liposome aggregates adhered to their surfaces, these aggregates were often swept to a cap if cells were kept at 37° for over an hour. In contrast, only a few small aggregates were formed an hour after the addition of liposome-DNA complexes to cells in special F-10 media without added bicar-

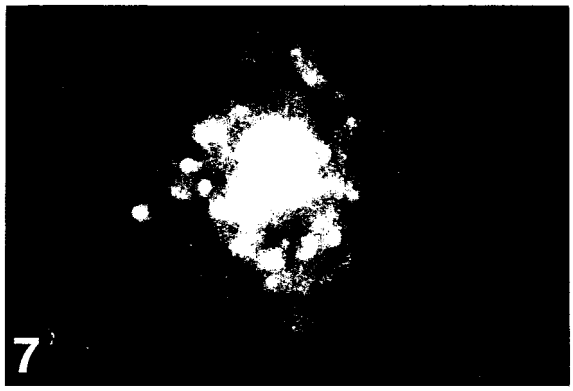

Fig. 7. An optical section 3-5 μm from the substrate of a cell in normal F-10 medium, 4 hours after liposome/DNA addition.

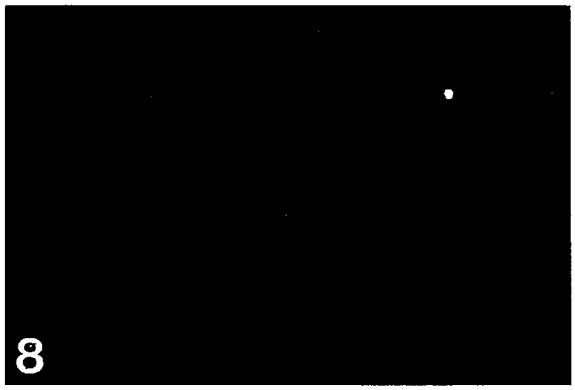

Fig. 8. An optical section 7 μm from the substrate of a cell in bicarbonate-free F-10 medium, 3 hours after liposome/DNA addition.

bonate or other anions, and few are internalized (Fig. 8). Cell membranes were not fluorescent, indicating no significant fusion between liposome and cell membranes. The transfection of cells in media with few aggregates remained at the background level, whereas the transfection levels in cells in media containing large aggregates were high (Table 1).

Our results indicate that the intake mechanism of liposome/DNA is activated by cationic lipid aggregates over a certain size. Aggregates over a certain critical size is needed to trigger phagocytosis and fusion. Without induced aggregation of liposome/DNA complexes by anions in media, fusion and internalization of complexes with cells are limited, hence the transfection efficiency is poor. The mechanism is not unlike that of calcium phosphate induced transfection. This mechanism may explain certain reported transfection inconsistencies when the physical structure of the cationic liposome/DNA complexes was not well defined. From time-dependent, 3-D confocal microscopy studies, we have shown that internalization, and to some degree fusion of fluorescent liposome/DNA complexes to cell membranes is the mechanism of DNA intake, and that the amount of intake is determined by the aggregation of these complexes by anions in the transfection media.

Table 1. Transfection of CHO cells

Transfection medium	Averaged aggregate size (μm)	Number of transfected clones
Normal F-10	1880	155
Sucrose + PBS	1120	50
Sucrose	47	13
HCO_3-free F-10	380	46

REFERENCES

Murray EJ, ed. 1991. Gene Transfer and Expression Protocols, Humana Press, Clifton, New Jersey.

Felgner PL, TR Gadek, M Holm, R Roman, HW Chan, M Wenz, JP Northrop, GM Ringold, MDanielsen, 1987. Proc. Natl. Acad. Sci. USA **84:** 7413.

Alton EWFW, PG Middleton, NJ Caplen, SN Smith, DM Steel, FM Munkonge, PK Jeffery, DM Geddes, SL Hart, R Williamson, KI Fasold, AD Miller, P Dickinson, BJ Stevenson, G McLachlan, JR Dorin, DJ Porteous. 1993. Nature Genetics **5:** 135-142.

Zoological Studies 34, Supplement i (1995)

Zoological Studies

Axial Resolution in Confocal Imaging under Ultrashort Pulsed Beam Illumination

Min Gu, T. Tannous and C.J.R. Sheppard
Department of Physical Optics, University of Sydney, NWS 2006, Australia

A recent development in confocal scanning microscopy is the introduction of an ultrashort pulsed laser beam (Denk et al. 1990, Gu and Sheppard 1994a, Gu et al. 1994, Kempe and Rudolph 1993, Sasaki et al. 1992). The combination of the confocal imaging technique and a pulsed beam promises a number of new imaging methods. One of them is nonlinear confocal microscopy (Denk et al. 1990, Sasaki et al. 1992) including, for example, two-photon fluorescence micrscopy (Denk et al. 1990). Another potential development is time-resolved confocal microscopy (Gu and Sheppard 1994a). It is also possible to perform three-dimensional (3-D) imaging of an object embedded in a highly scattering medium (Andreson et al. 1994). We, in this paper, invesigate axial resolution in confocal microscpy.

We start with the image of a point source. If the point source gives a pulsed beam of a temporal amplitude $U_0(t)$, its Fourier transform, the spectrum of the source, is denoted by $V_0(\Delta\omega)$. For a given frequency component $\Delta\omega=\omega-\omega_0$ with the spectrum $V_0(\Delta\omega)$, the 3-D amplitude point spread function (APSF) h_1 of a circularly symmetric lens can be expressed as (Gu and Sheppard 1994b)

$$h_1(v,u,\Delta\omega)=K\beta^2\exp\{-j\beta u/[4\sin^2(\alpha/2)]\}$$

$$\exp\{j[\Delta\omega\tau'+(\Delta\omega)^2\delta']\}$$

$$\int_0^1 P(r)J_0(r v\beta)\exp[j(\beta r^2 u/2-w r^2)]\,r\,dr \quad (1)$$

where $w=\Delta\omega\tau+(\Delta\omega)^2\delta$ and $\beta=(1+\Delta\omega/\omega_0)$. The definitions of the parameters τ', τ, δ and δ resulting from material dispersion are the same as those given by Kempe and Rudolph (1993). β denotes the normalized fequency of the pulsed beam. Here v and u are radial and axial optical coorrdinates. P(r) is the pupil function of the lens, K is a constant independent of ω, and J_0 is a Bessel function of the first kind of order zero.

Compared with that of Kampe and Rudolph (1993), h_1 in Eq. (1) includes an extra defocus-related phase term

$$\exp\{-\beta u/[4\sin^2(\alpha/2)]\} \quad (2)$$

and an extra amplitude factor β^2. These two frequency-dependent factors can result in a significant effect on 3-D time-resolved imaging in a reflection-mode confocal microscope.

Consider the imaging lenses to be achromatic, so that $\tau=\delta=0$. τ' and δ' can be justified to be zero if a pre-frequency-chirped pulse is used. We assume that the illumination is a Gaussian-shaped pulse given by

$$U_0(t)=\exp(-j\omega_0 t)\exp[-(t/T)^2] \quad (3)$$

where t is the local time coordinate. The pulse width (FWHM) Δt is equal to $2T\sqrt{\ln 2}$. As the paraxial approximation is assumed, we take as an example an objective of numerical aperture $1/\sqrt{2}$ which is approximately the largest value for the paraxial approximation to hold.

The effective 3-D APSF h_e (v, u, $\Delta\omega$) for a confocal non-fluorescence system can be obtained from Eq. (1), which can be used to derive axial resolution for confocal imaging (Gu and Sheppard 1994a). We assume that $\Delta\tau$=10 fs and λ_0=0.8 μm.

The axial responses of a perfect relfector for time-resolved and imaging are shown in Fig. 1, giving a measure of axial resolution in non-fluorescence imaging. It is shown that the half-width of the responses is approximately 2 and 2.65 for time-resolved and time-averaged imaging methods,

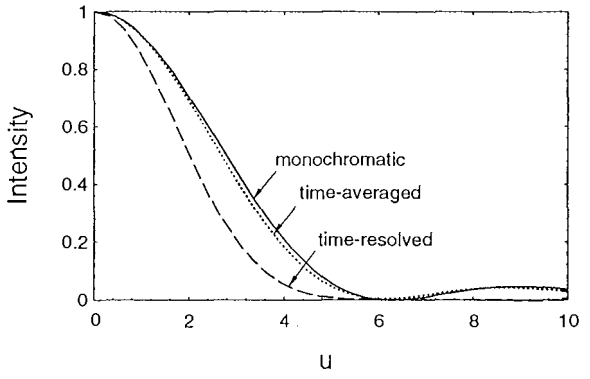

Fig. 1. Axial response of a perfect reflector in time-resolved (dashed) and time-averaged (dotted) non-fluorescence cases ($\Delta\tau$=10 fs). The solid curve represents the axial response under CW illumination.

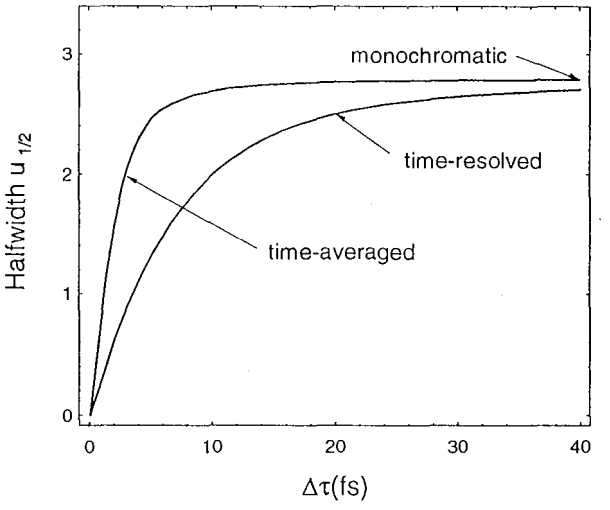

Fig. 2. Half- width of the axial response of a perfect reflector as a function of the pulse width $\Delta\tau$.

respectively, exhibiting that the axial resolution is improved by approximately 28% and 4-5%, respectively, when compared with the value of 2.78 for monochromatic illumination of freuqency ω_0. This conclusion is of importance for time-resolved confocal microscopy because this technique provides not only information on the dynamic behavior of the sample but also its 3-D structure with an axial resolution higher than the current limit in a confocal microscope under CW illumination. The physical reason for resolution improvement in the time-resolved imaging mode results from the phase factor presented in Eq. (2). Because confocal non-fluorescence imaging is a coherent process, the phase resulting from different frequency components contributes in a coherent fashion.

In Fig. 2, the relationship of the half-width of the axial response to the pulse width $\Delta\tau$ is revealed. The axial resolution can be improved dramatically when the pulse width is less than 10 fs. There will be, however, a physical limitation on the shortest pulse width. This shortest pulse will result in the highest axial resolution in practical time-resolved confocal imaging.

For single-photon fluorescence confocal imaging, the contribution from the phase in Eq. (2) can be washed out as the imaging process is incoherent (Gu et al. 1994). Fig. 3 exhibits the comparison of the axial response for pulse and CW illumination (deshed curves) for $\Delta\tau$=10 fs and λ_0= 0.8 μm. The magnitude of the improvement in the former case is approximately 7%. however if the pulse width is shorter than 10 fs, the improvement becomes large (see Fig. 4). For example,

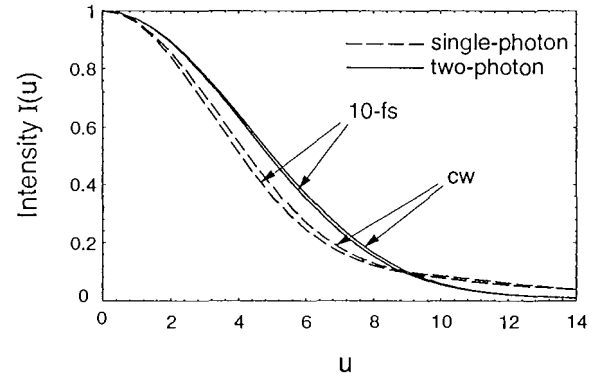

Fig. 3. Axial response of thin single-and two-photon fluorescence layers for pulse ($\Delta\tau$=10 fs) and CW illumination.

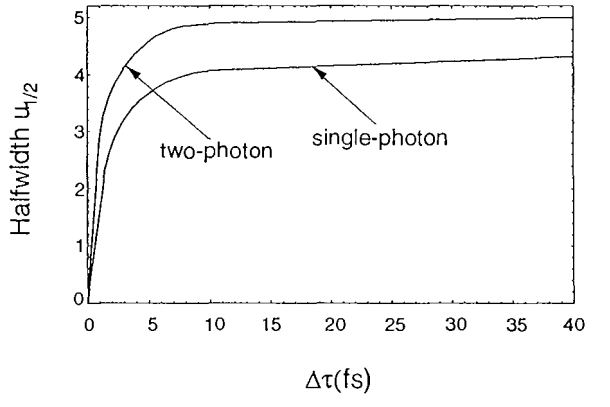

Fig. 4. Half-width of the axial response of thin single-and two-photon fluorescent layers as a function of the pulse width $\Delta\tau$.

when $\Delta\tau$=5 fs, one can improve the axial resolution by 15%. The reason for the improvement is the pre-factor β^2 in the 3-D APSE and the spectral width, and therefore frequencies higher then ω_0 contributes more strongly than those lower.

Another spatially-incoherent confocal imaging method is based on the nonlinear two-photon fluorescence process. For the same reason as in the single-photon fluorescence, the axial resolution may be slightly improved. Fig. 3 gives the axial response (solid curves) of the thin two-photon fluorescent layer. As expected, the improvement is 2% in comparison with CW illumination. Even for a pulse of 5 fs, the change is not pronounced (Fig. 4). The small change is caused by the nonlinear dependence of the fluorescence radiation, which makes the effective spectral bandwidth narrow.

REFERENCES

Anderson GE, F Lui, RR Alfano. 1994. Microscope imaging through highly scattering media. Opt. Lett. **19:** 981-983.

Denk W, JH Strickler, WW Webb. 1990. Two-photon laser scanning fluorescence microscopy. Science. **248:** 73-76.

Gu M, CJR Sheppard. 1994a. 3-D image formation in confocal microscopy under ultrashort laser- pulse illumination. J. Modem Optics. **41:** in press.

Gu M, CJR Sheppard. 1994b. Analysis of confocal microscopy under ultrashort light-pulse illumination - comments. J. Opt. Soc. Am. A. **11:** 2742-2743.

Gu M, T Tannous, CJR Sheppard. 1995. Three-dimensional confocal fluorescence imaging under ultrashort pulse illumination. Opt. Commun. in press.

Kempe M, W Rudolph. 1993. Analysis of confocal microscopy under ultrashort lightpulse illumination. J. Opt. Soc. Am. A. **10:** 240-245.

Sasaki K, M Koshioka, H Masuhara. 1992. Confocal laser-induced absorption microscope. J. Opt. Soc. Am. A. **9:** 932-936.

Zoological Studies 34, Supplement I (1995)

Zoological Studies

Advancements and Applications of Low Temperature Field Emission Scanning Electron Microscopy

William P. Wergin[1], Robert W. Yaklich[2] and Eric F. Erbe[1]
[1]*Electron Microscopy Laboratory, USDA-ARS Beltsville, MD. 20705, USA*
[2]*Soybean and Alfalfa Research Laboratory, USDA-ARS Beltsville, MD. 20705, USA*

In recent years interest in low temperature scanning electron microscopy (SEM) has been revitalized. Much of this interest resulted from the introduction of the field emission (FE) SEM which can be equipped with a new generation of compatible cryosystems that are designed to take advantage of this instrument. This combination of instrumentation provides several advantages that are not available in a conventional SEM operating at either ambient or low temperatures: 1) For biological specimens, observation of frozen hydrated specimens at low temperatures avoids artifacts or physical changes in tissues that commonly result from chemical fixation, dehydration, critical point drying and coating (Beckett and Read 1986, Read and Jeffree 1991, Wergin and Erbe 1989). For example, chemical fixation and dehydration are identified with the extrusion of materials, critical point drying can shrink and distort tissues, and sputter coating with 20-30 nm of metal obliterates fine structural details; 2) For specimens that are soluble in aqueous fixatives and dehydrating agents, for organisms that are tenuously associated, or for tissues that are physiologically active, the cryofixation procedure that is employed for low temperature FESEM preserves features that can not be maintained by conventional chemical fixation; 3) For nearly all types of specimens, the low temperature FESEM can resolve structures that measure less than 10 nm; this attribute easily exceeds that obtained with a conventional low temperature SEM; 4) Finally, a recent technique developed in our laboratory demonstrates that air, water and lipids, components that are commonly present in samples such as foods, cosmetics, pharmaceuticals, soils, as well as most biological specimens, can be easily differentiated using low temperature SEM, whereas they are nearly indistinguishable in most conventionally prepared samples that are viewed at ambient temperatures.

To realize fully the advantages associated with low temperature FESEM, many new techniques had to be modified or developed. For example, the greater resolution of this instrument is capable of resolving grain particles in metallic films formed by the conventional sputter coating technique; therefore, a new generation of cryosystems containing planar magnetron sputter coaters, which have the capacity to produce films with finer grains, were introduced (Müller et al. 1990). This combination of instrumentation, which enables biologists to increase resolution of frozen hydrated samples to less than 10 nm, allows observation of macromolecular particles (Müller et al. 1990, Walther et al. 1990, Wergin et al. 1993). An alternative coating method achieves similar results by using high vacuum evaporation of Pt/C to coat frozen samples for low temperature FESEM (Wergin and Erbe, 1991). Because this method is carried out in a free standing freeze-etch unit on a conventional vacuum evaporator, the frozen, fractured, coated specimen must be subsequently transferred to the cryostage in the FESEM for observation.

Two additional benefits can be gained by mounting samples in hinged gold holders and using high vacuum evaporation to coat the freeze-fractured samples. First, the procedure that is used to evaporate Pt/C is identical to the process that is utilized to make replicas for observation in a transmission electron microscope (TEM). Therefore, after frozen samples are observed at low temperature in the FESEM, they can be removed from the instrument and their Pt/C surface replicas can be recovered for observation in the TEM (Wergin and Erbe 1990). Second, the use of hinged holders provides fractures that reveal complementary faces of the frozen specimens that can be readily observed in the FESEM. Furthermore, if the replicas

from these complementary faces are recovered, they can also be observed and photographed with the TEM (Wergin and Erbe 1992). Consequently, use of high vacuum evaporation in combination with low temperature FESEM provides direct comparison of the same structural features by two distinct electron imaging techniques.

Recently a new preparation procedure has been developed whereby a sample is initially fractured and freeze-etched. Next a portion of the surface of this sample is refractured. Coating the sample then allows observation and comparison of adjacent areas of a frozen sample in which part of the surface of the specimen is freeze-etched and the other portion is merely freeze-fractured. Observation of the sample along the intersect formed by this procedure provides adjacent freeze-etch and freeze-fracture images. These images, which can consist of areas as discrete as the two halves of a single cell, enable one to distinguish and to identify: 1) voids that represent air spaces in the sample; 2) components that are etched denoting free water and; 3) structures that are not etched that include materials such as lipids. This technique assists in more readily determining the sizes and distribution of these components not only in biological samples but in aerosols, emulsions, creams and other liquids as well.

In conclusion, new instrumentation and techniques associated with low temperature SEM allow investigators to observe frozen hydrated samples, to avoid some of the artifacts associated with conventional preparation procedures and to achieve resolution of structures to less than 10 nm. In addition, frozen hydrated specimens can be easily fractured, their complementary faces observed, and the replicas from these fractured faces can be recovered for further analysis and comparison in the TEM. Finally adjacent areas, consisting of a freeze-fractured and a freeze-etched face, can be compared to distinguish between air, free water and lipids.

REFERENCES

Beckett A, ND Read. 1986. Low temperature scanning electron microscopy. In Ultrastructural techniques for microorganisms, eds. HC Aldrich, WJ Todd. New York: Plenum.

Müller T, P Walther, C Scheidegger, R Reichelt, S Müller, R Guggenheim. 1990. Cryo-preparation and planar magnetron sputtering for low temperature scanning electron microscopy. Scanning Microsc. **4:** 863-876.

Read ND, CE Jeffree. 1991. Low temperature scanning electron microscopy in biology. J. Microsc. **161:** 59-72.

Walther P, J Hentschel, P Herter, T Müller K. Zierold. 1990. Imaging of intramembranous particles in frozen-hydrated cells (Saccharomyces cerevisiae) by high resolution cryo SEM. Scanning. **12:** 300-07.

Wergin WP, EF Erbe. 1989. Increasing the versatility of an EMscope SP2000A sputter cryo system on a Hitachi S-570 scanning electron microscope. Scanning. **11:** 293-303.

Wergin WP, EF Erbe. 1990. Use of low temperature SEM and conventional TEM to observe identical areas of fractured membranes from yeast. Scanning. **12:** 69-71.

Wergin WP, EF Erbe. 1991. Increasing resolution and versatility in low temperature conventional and field emission scanning electron microscopy. Scanning Microscopy. **5:** 927-936.

Wergin WP, EF Erbe. 1992. Techniques for obtaining and observing complementary images with a low-temperature field emission SEM and subsequent comparison of the identical cells in freeze-etch replicas viewed with a TEM. Scanning. **14:** 17-30.

Wergin WP, EF Eric, A Robins. 1993. Use of platinum shadowing and magnetron sputter coating in an Oxford Cryotrans System to increase low temperature resolution of biological samples in a Hitachi field-emission scanning electron microscope. Proc. Microsc. Soc. Amer. **51:** 122-123.

Zoological Studies 34, Supplement I (1995)

Zoological Studies

Simple Formulae for Confocal Resolution Parameters: The Full Width Half Maximum (FWHM), the Ellipsoidal Observation Volume (OBSVOL) and the Root Mean Square Spatial Frequency (RMSF)

Kieran G. Larkin

Department of Physical Optics, School of Physics, University of Sydney, NSW 2006, Australia

INTRODUCTION

The need to summarize the overall resolution of an imaging system with a single indicator has led to a variety of resolution parameters. Traditionally measures such as the Rayleigh and Sparrow criteria have been used for the transverse resolution of an axially symmetric optical imaging system. With the advent of confocal microscopy the axial resolution became important too. Although the imaging performance of an isoplanatic system can be fully specified by the 3-D Point Spread Function (PSF), or equivalently, its transform; the 3-D Optical Transfer Function (OTF), there may be some advantage to using a single-valued resolution parameter. One particularly attractive option is the Full Width Half Maximum (FWHM). The idea of using the width of the PSF in one of three orthogonal directions is conceptually simple especially when the width is specified at a point where the system response drops monotonically to half its maximum value. A related parameter called the "observation volume" (OBSVOL) has been proposed for comparisons of multiple objective systems such as the 4Pi confocal theta microscope (Stelzer and Lindek 1994). The OBSVOL, like theFWHM is easily defined. It is, in fact, the volume of an ellipsoid which has each of its three principal axes equal to twice the corresponding FWHM. Unfortunately the analytic calculation of FWHM for systems with large apertures or multiple objectives (for illumination and detection) becomes rather awkward and the simplicity is sacrificed. This, in turn, compromises the apparent simplicity of the OBSVOL. There is, however, a parameter which is very closely related to both the FWHM and the OBSVOL which is easy calculated for all confocal systems and has a simple combination rule which allows elegant extension to more complex systems. This parameter is none other than the root mean square spatial frequency of the transfer function (RMSF). The following sections develop the elementary theory of the RMSF and its relation to the FWHM and OBSVOL.

MOMENT EXPANSION OF THE PSF

The PSF, $p(x, y, z)$, of an isoplanatic imaging system is related to the optical transfer function, $P(\xi, \eta, \zeta)$, by 3-D Fourier

$$p(x,y,z)=\iiint P(\xi,\eta,\zeta)\exp(-2\pi i[x\xi+y\eta+z\zeta])\,d\xi\,d\eta\,d\zeta \quad (1)$$

where (x, y, z) are the Cartesian spatial coordinates in the focal region and (ξ, η, ζ) are the corresponding spatial frequencies (see, for example Gu and Shippard 1994). The PSF is typically the modulus squared of a amplitude PSF and consequently an even function which can be expanded as an even order Taylor series about the origin:

$$p(x,y,z)=p_0\Sigma_{l=0}^{\infty}\Sigma_{k=0}^{\infty}\Sigma_{j=0}^{\infty}a_{2j,2k,2l}x^{2j}y^{2k}z^{2l}. \quad (2)$$

The polynomial coefficient is given by

$$a_{2j,2k,2l}=\frac{1}{(2j)!(2k)!(2l)!}\frac{\partial^{2j}}{\partial x^{2j}}\frac{\partial^{2k}}{\partial y^{2k}}\frac{\partial^{2l}}{\partial x^{2l}}p(x,y,z)|_{x=y=z=0}. \quad (3)$$

Calculation of the FWHM from this expansion

is accurate to better than 1% if $\{j \le 2, k \le 2, l \le 2\}$, which corresponds to a fourth order approximation. If only the second order terms of the above expansion are used, then the estimated FWHM can be as much as 12% in error (for typical forms of the PSF). Equation (2) can be rewritten in terms of the moments of $P(\xi, \eta, \zeta)$ using the Fourier moment-derivative theorem.

$$\frac{\partial^{2j}}{\partial x^{2j}} \frac{\partial^{2k}}{\partial y^{2k}} \frac{\partial^{2l}}{\partial x^{2l}} p(x,y,z)|_{x=y=z=0} = (-2\pi i)^{2(j+k+l)} M_{2j,2k,2l} \quad (4)$$

The moment $M_{2j, 2k, 2l}$ is defined by

$$M_{2j,2k,2l} = \iiint \xi^{2j} \eta^{2k} \zeta^{2l} P(\xi,\eta,\zeta)\, d\xi\, d\eta\, d\zeta. \quad (5)$$

The benefit of this description is that the moments of the system pupil function are easily calculated analytically, even for systems with apodization. Transfer functions can be represented as correlations or convolutions of a few basic pupil functions. Under the operation of convolution or correlation moments add in a simple way. In particular, normalized second order moments are additive.

ESTIMATION OF THE FWHM

The second order approximation to the PSF is

$$p(x,y,z) = p_0 [\, 1 - \mu_{200} x^2 - \mu_{020} y^2 - \mu_{002} z^2 \,]. \quad (6)$$

The normalized moments are

$$\mu_{2j,2k,2l} = \frac{M_{2j,2k,2l}}{M_{0,0,0}} \quad (7)$$

In equation (6) the second order normalized moments are equivalent to the mean square spatial frequencies of the transfer function measured along the three axes. Equation (6) represents a paraboloidal distribution which has ellipsoidal surface contours of constant value (iso-surfaces). Hence an ellipsoid can be defined which contains all values of p greater than some specified proportion of p_0. Generally the proportion specified is one half and the FWHM along the x, y, and z axes arise from the solution of equation (6). As mentioned in section 2, the second order approximation is prone to systematic errors in the predicted FWHM. A fourth order approximation gives an accurate FWHM and a more realistic form of the iso-furface contours. It is worth noting that the iso-surface is no longer (in general) ellipsoidal. This is the source of an inconsistency in the use of an ellipsoidal OBSVOL for a non-ellipsoidal iso-surface. One possible conclusion is that the simple physical ideal of an ellipsoidal volume is incompatible with the precise representation of the PSF. Clearly the ellipsoid no longer has any real physical meaning - it is just a mathematical construct. Such a construct can still be useful if it has some other redeeming feature(s). It can be argued convincingly that the ellipsoid is still a good indicator of the effective OBSVOL. However, a similar argument can be formulated for the volume represented by the second order approximation which has the added advantage that it is easily calculated and extended.

FEATURES OF THE SECOND ORDER APPROXIMATION

Before examining some details of the second order approach it is instructive to consider some general aspects of a second order theory:

Firstly, for any particular PSF form the second order approximation to the FWHM exihibits a fixed error, for example:

sinc()	-5%
sinc () squared	-12%
Airy amplitude	-6%
Gaussian	-17%

The Gaussian is significant because it represents the limit of a PSF which is the product of many individual PSFs as can be shown by the Central Limit Theorem. The peak errors above can be reduced by a consistent rescaling of the estimate, so, for example, the new error could be better than +/-9% in all cases.

Secondly, the concept of an ellipsoidal OBSVOL can be considered to be implicitly second order.

Lastly, the second order approach resembles second order statistics and its familiar concepts of mean and variance which, again, are additive under convolution.

Returning to the main discussion, the most important factor to consider in this section is the relation between the normalized moments and the estimated FWHM. The second order FWHM, w_x, w_y, w_z, are determined from equation

(6) as follows:

$$\frac{1}{2}=\mu_{200}\left(\frac{w_x}{2}\right)^2,\quad \frac{1}{2}=\mu_{020}\left(\frac{w_y}{2}\right)^2,\quad \frac{1}{2}=\mu_{002}\left(\frac{w_z}{2}\right)^2. \tag{8}$$

The normalized moments μ_{200}, μ_{020} and μ_{002} are the mean square spatial frequencies of the transfer function measured along the three principal axes. Consequently:

$$w_x=\frac{\sqrt{2}}{\sqrt{\mu_{200}}}\quad \text{and similarly for } w_y, \text{ and } w_z. \tag{9}$$

Simply stated the FWHM (second order) is inversely proportional to the root mean square spatial frequency (or RMSF) of the transfer function.

The OBSVOL can now be defined in terms of these FWHM. The treatment given here is purely second order so that all confocal systems can be compared in a consistent manner. The usual definition of OBSVOL, V, is as follows:

$$V=\frac{4}{3}\pi w_x w_y w_z \tag{10}$$

In the limit, as the PSF approaches an ellipsoidal Gaussian distribution such a volume encloses almost 85% of the PSF.

The rule for combining FWHM which result from the product of multiple PSFs can be shown to be:

$$\frac{1}{w_x^2}=\sum_n \frac{1}{w_{n,x}^2}\quad \text{and similarly for } w_y \text{ and } w_z. \tag{11}$$

Equation (11) is merely the re-expression of the additive property of variances. The overall OBSVOL is therefore such that:

$$V^2=\frac{\left(\frac{4}{3}\right)^2\pi^2}{\left(\sum_n \frac{1}{w_{n\,x}^2}\right)\left(\sum_n \frac{1}{w_{n\,Y}^2}\right)\left(\sum_n \frac{1}{w_{n\,Z}^2}\right)}$$

$$=\frac{128\,\pi^2}{9\,\mu_{200}\,\mu_{200}\,\mu_{200}}. \tag{12}$$

The product of three orthogonal RMSFs is inversely related to the OBSVOL.

It has been suggested that in confocal systems of the 4Pi type that the FWHM is not a useful parameter because it completely omits the effects of large subsidiary maxima. Instead the variance of the axial PSF has been mooted as a preferred indicator. It is not difficult to show that (for any semi-aperture less than 70 degrees) the variance of the PSF is equal to the variance of the envelope of the axial PSF. The implication is therefore that no improvement is to be inferred from the interference of two juxtaposed objectives. There is also the more serious defiency of real space variances that they are often infinite (especially in conventional imaging systems) so they must be used with great caution, if at all. The simplified methods proposed here only work with variances defined in the spatial frequency domain and FWHM in the space domain. Such variances are always finite because of the limitation upon maximum spatial frequency. With this in mind it is expedient, in 4Pi configurations, to utilize the FWHM of the envelope of the axial PSF. This corresponds to using the transfer function variance of either opposing objective, not both.

DISCUSSION

The three equations (9), (11) and (12) summarize the simple formulae for FWHM, OBSVOL, and RMSF. Obviously a more detailed analysis of the consequences of an explicit versus an implicit second order theory of OBSVOL is needed before either procedure is adopted as a metric by practitioners of confocal microscopy. Ultimately judgement will depend upon demonstration of a one-to-one, monotonic relation between an approximate formulation and the exact formulation. Assuming (presuming!) this to be the case, then the simple formulation presented here could become an attractive alternative to the other currently in use.

REFERENCES

Gu M, CJR. Sheppard. 1994. Three-dimensional transfer functions in 4Pi confocal microscopy. Journal of the Optical Society of America, **A 11:** 1619-1627.

Stelzer EHK, S Lindek. 1994. Fundamental reduction of the observation volume in far-field light microscopy by detection orthogonal to the illumination axis: confocal theta microscopy. Optics Communications **111:** 536-547.

Zoological Studies 34, Supplement I (1995)

Zoological Studies

Appropriate Image Processing for Confocal Microscopy

Guy Cox[1] and Colin J.R. Sheppard[2]
[1]Electron Microscope Unit, University of Sydney, NSW 2006, Australia
[2]School of Physics, University of Sydney, NSW 2006, Australia

Most commercial confocal microscopes today are shipped with software capable of carrying out routine image processing. Typically, matrix convolutions are offered, working with either fixed or user-defined kernels. These allow crispening, smoothing and edge-enhancement operations, usually on square matrices of 3x3, 5x5 or 7x7 pixels. More sophisticated (and processor-intensive) operations such as median filtering may also be offered. All these operations are well known (Gonzales and Wintz 1987, Russ 1990) and are routinely employed where an image can be seen to benefit from the processing. However in current commercial systems they are applied only to two-dimensional images.

Confocal microscopes are generally used to acquire images in three dimensions, and in many cases (where physiological processes are followed through time) in four dimensions. One of the commonest uses of image processing on confocal images is to reduce noise, of which the main component in confocal fluorescence is photon sampling or shot noise. This, by its nature, will be randomly distributed in all 3, and indeed all 4, dimensions. Applying noise-reduction filtering only to individual two-dimensional slices will modify the noise distribution anisotropically, and is clearly not the appropriate procedure.

Effective noise removal requires filtering in as many dimensions as the data set contains (Chen et al. 1990). However, using a conventional square matrix this implies an exponential increase in the number of pixels to be processed at each point as the number of dimensions increases. A 3x3 matrix involves 9 pixels; 3x3x3 involves 27; if we progress to 3x3x3x3 then 81 voxels have to be used in computing each point of the output image. However square matrices are not the only posibility. Cruciform matrices, in which only those pixels adjoining the master pixel at a face are considered, are also often used in 2-D image processing. For 3-D and 4-D processing the cruciform matrix has the tremendous advantage that the increase is linear - each extra dimension adds just 2 more voxels to the number which must be handled at each point. We are therefore currently developing 3 and 4 D cruciform filters for confocal data sets, both matrix smoothing filters and a median filter. These offer the promise of a simple and rational noise removal technique for confocal data sets.

While shot noise is isotropic in all dimensions, other defects of the confocal image are not. The optical resolution, in particular, is isotropic in two lateral dimensions but substantially worse in the axial direction. The effects of this on a three-dimensional biological specimen are seen in Fig. 1 a & b. Because the point spread function of a confocal microscope approximates to an ellipsoid (Brakenhoff et al. 1989, Shaw and Rawlins 1991, Cox and Sheppard 1993), it is logical to apply the conventional tools of image processing in one dimension only - the long axis of the ellipsoid - to improve the perceived appearance of such images. Like all such operations, this will not increase the resolution or the information content of the image, but it will make it possible to extract information which would otherwise be obscured.

This approach was first applied by Cox and Sheppard, 1993. As a test case we used a simple edge-enhancing transform which detected the magnitude of the gradient at a pixel and used that as a weighting factor to modify the intensity of that pixel. It can be represented as:

$$1)\, I_n \leftarrow I_n - (|I_n - I_{n-1}| + |I_n - I_{n+1}|)/s$$

where I is the intensity of a pixel at plane n. The scaling factor s determines what fraction of the gradient is subtracted and must be matched to the degree of over or under sampling in depth. The effect on our biological image is seen in Fig. 1c.

A second transform is a simplification of (1), using only the values of the neighbouring pixels, in the interests of improving speed.

$$2) I_n \leftarrow I_n - (|I_{n-1} - I_{n+1}|)/s$$

This will have the same effect on the slope of the response curve but will behave differently at maxima and minima. In practice, its effect is generally visually indistinguishable from transform (1).

An alternative approach, again applying a classic technique of image processing, is to use an erosion rather than a gradient transform. A constrained erosion is used so that maxima and minima are preserved:

$$3) \text{ IF } I_{n+1} < I_n < I_{n-1} \text{ THEN } I_n \leftarrow I_n - I_{n+1}$$
$$\text{IF } I_{n+1} > I_n > I_{n-1} \text{ THEN } I_n \leftarrow I_n - I_{n-1}$$

If a pixel has one neighbour higher than it and the other lower its value is replaced by that of the lower neighbour. The effect on an image is rather different from that of transforms (1) and (2); background haze is less well removed but the effect on the brighter part of the image is pronounced (Figure 1 d & e). Repeated iterations will 'skeletonise' the image, so that it could be used to find the true positions of multiple superimposed planes in the sample. This is not readily achievable in any other way.

All edge-enhancing transforms are susceptible to noise, so that ideally a noise reducing filter such as a median filter should first be applied to the data set. However applying this in the lateral plane only will be of little use - a 3-D filter is essential. Hence these two techniques, 3-D filtering and 1-D enhancing, are complementary. Providing implementations capable of adequate performance on the type of computers typically used to host confocal microscopes should not be difficult, and indeed some of these processes are already in common use by users of our facility.

The image processing operations presented here are conventional; what is novel is their application in a more rational way to the confocal image. For a 3D or 4D data set the combination of 3D and 1D processing is far more useful than the

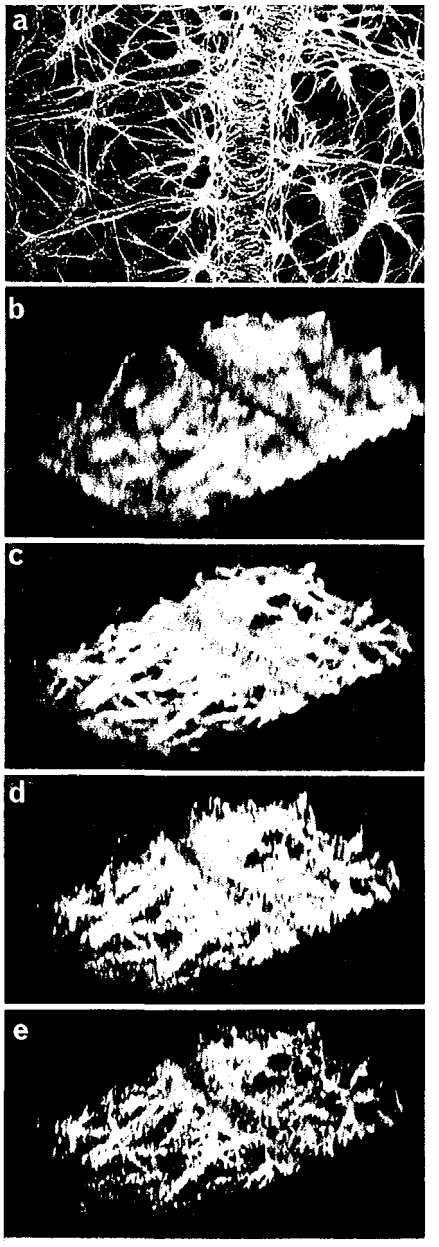

Fig. 1. 3D recontruction of rhodamine-labelled astrocytes around a capillary in the retina of a rat.
(a) Top view, showing good lateral resolution. The branches of the astrocytes are known to be isodiametric, and so should in a perfect image appear the same size in side and oblique views as in this top view.
(b) Oblique view of the original, unprocessed data set. The overall shape is visible but the image appears strongly smeared in the vertical direction; individual astrocyte branches can barely be distinguished.
(c) Processed with transform (1) - the appearance is dramatically improved. Most of the branches visible in (a) can be identified, though their depth still appears too large.
(d) Processed with the erosion transform (3) using one iteration.
(e) Processed with transform (3) using two iterations. The erosion gives more clarity in some areas, but a more 'ragged' overall effect, than transform (1).

2D-only processing offered by microscope manufacturers.

The techniques of image restoration, which also work in three dimensions, represent a different and not strictly comparable approach to the problem. An iterative approach is typically used with the aim of generating a model of the object which would, when operated on by the point spread function of the system, produce the observed image. These techniques were initially applied to widefield images, with the intention of creating optical section data sets without confocal optics (Agard et al. 1989, Carrington et al. 1990, Holmes et al. 1991). Latterly they have also been applied to confocal images, with the aim of creating a data set with enhanced resolution, particularly in the axial direction (Carrington et al. 1990 Shaw and Rawlins 1991, Wilson and Tan, 1993). Image re-storation is ambitious in scope, and demanding in computer power, but limited in its objective - the sole aim is to recreate the original object.

Image processing, by contrast, minimises unwanted information or enhances wanted information in the image. The unwanted information may equally be an artefact of the imaging process or a real part of the specimen; the wanted information may be all the 'real' objects in the image or a subset of them. Even if advances in computer power allow image restoration to become a routine part of confocal microscopy, there will still be uses for simple image processing methods - particularly if they are redeployed in a more appropriate form for the confocal image.

We thank Jonathan Stone for the data set used in Fig. 1.

REFERENCES

Agard DA, Y Hiraoka, P Shaw, JW Sedat. 1989. Fluorescence microscopy in three dimensions. Methods Cell Biol. **30:** 353-377.

WA Carrington, KE Fogarty, L Lifschitz, FS Fay. 1990. Three dimensional imaging on confocal and wide-field microscopes. In: Handbook of Biological Confocal Microscopy (2nd Edition), ed. J.A. Pawley, pp 151 - 168. Plenum Press, New York.

Chen H, JW Sedat, DA Agard. 1990. Manipulation, display and analysis of three-dimensional biological images. In: Handbook of Biological Confocal Microscopy (2nd Edition), ed. J.A. Pawley, pp 141 - 150. Plenum Press, New York.

Cox G, C Sheppard. 1993. Effects of image deconvolution on optical sectioning in conventional and confocal microscopes. Bioimaging **1:** 82-95

Gonzales RC, P Wintz. 1987. Digital image processing (Second Edition). Addison-Wesley, Reading Mass. 503pp.

Holmes TJ, Y-H Liu, D Khosla, DA Agard. 1991. Increased depth of field and stereo pairs of fluorescence micrographs via inverse filtering and maximum-likelihood estimation. J. Microscopy **164:** 217-237.

Russ JC. 1990. Computer Assisted Microscopy. The measurement and analysis of images. Plenum Press, New York. 453 pp.

Shaw PJ, DJ Rawlins. 1991. The point-spread function of a confocal microscope; its measurement and use in deconvolution of 3-D data. J. Microscopy **163:** 151-165.

Wilson T, JB Tan. 1993. Three dimensional image reconstruction in conventional and confocal microscopy. Bioimaging **1:** 176-184

Zoological Studies 34, Supplement I (1995)

Zoological Studies

Investigating Large Microscopic Volumes of Lung by Computer-guided 3-D Image Compositing in Confocal Microscopy

Andres Kriete
Institute of Anatomy and Cytobiology, Image Processing Laboratory, Aulweg 123, 35385, Giessen, Germany

There is a long history of experimental difficulties in the quantitative investigation of the respiratory part of lung, because such studies require imaging of extended volumes at high resolution. Structures like the pulmonary acinus, the ventilatory unit formed of several alveolar ducts, extend to a size of 2000x2000x2000 microns in rat and mouse. They can only be analyzed for their structural organization and branching pattern if all structural details of the lungs parenchyma down to the alveoli are completely resolved. Because of these requirements, only one detailed and complete investigation of an acinus is given in the literature, based on a very time consuming manual performed reconstruction of serial sections with a wax plate technique (Boyden 1971). It was suggested and demonstrated for smaller substructures of the respiratory system, that confocal imaging applied to thick sections and digital image processing might be an alternative way for such investigations (Oldmixon and Carlsson 1993). We describe a computer-guided image acquisition procedure in confocal microscopy, which allows a 9-fold increase of the field of view and an extended imaging in axial direction by scanning aligned thick serial sections.

Histological sections of 50-80 micron thickness (HE stained) of a rat lung are the starting point for our investigation. First the sections are previewed with a low magnifying lens of 5x (such as Plan-Neofluar, NA 0.15). The numerical aperture of this lens is not sufficient for a good axial resolution, but offers a wide field of view. These images are aligned for linear shift and rotation and the approximate region of interest is defined through 3-D visualization of the data stack. When transferred back to the confocal microscope, these corrected images serve for alignment of the histological sections. The goal of the next acquistion step is to sample higher resolved volumes. Variation of the scanning offset, i.e. shifting the scanning beam electronically away from the center in all 8 possible directions at a lateral distance of 600 microns, gives 9 reference images. At a zoom factor of 4 they construct a frame of 1800 um side length (data hold for a Zeiss LSM 410). Switching to a 20x magnifying lens (Plan Neofluar NA 0.5), the field of view at zoom factor 1 can be fitted exactly to that of the individual reference images, so that 9 adjacient, non-overlapping subvolumes can be acquired by optical sectioning within one histological section.

We give an example, where 13 histological sections of 70 micron thickness, each scanned at an axial step size of 10 microns, result in a total of 9x7x13=819 images of 256x256 pixels each. Subsequently these images are fused at every level of optical sectioning, achieving a final volume of 768x 768x 91 voxels being equivalent to 1800x 1800x 910 microns. This volume encloses one complete acinus, but exhibits as well structural details like the alveoli.

In order to visualize such a data volume, various image preprocessing steps have to be performed. The sponge-like character of the lungs parenchyma does not give any insight if a volume rendering algorithm is directly applied, but the structures of insterest have to be segmented and enhanced first. In particular, the intensity of all sections has to be equalized by histogram normalization, before an automatic segmentation of tissue and background can be performed. In order to detect connectivities and to differentiate the structure of the acinus of interest from branches of adjacient acini, the binary volume is seeded at the largest visible diameter of the acinus and binary operations are carried out up and down the data stack, labeling connecting structures.

This procedure is repeated until all connectivities are detected and identified. Once the complete structure of the acinus is defined, volume renditions can take place.

REFERENCES

Boyden EA. 1971. The structure of the pulmonary acinus in a child of six years and eight months. Am. J. Anat. **132:** 275-300.

Oldmixon EH, K Carlsson. 1993. Methods for large data volumes from confocal laser microscopy of lung. J. Microscopy **170:** 221-228.

Zoological Studies 34, Supplement I (1995)

3-D Simulation of Form and Function of Lung

A. Kriete[1], T. Schwebel[1], H.-R. Duncker[1] and M. Marko[2]
[1]*Institute of Anatomy and Cytobiology, Aulweg 123, 35385, Giessen, Germany*
[2]*Wadsworth Center, Department of Health, State University of New York, Albany, New York, USA*

Computer visualization is not only proven to be a valuable tool to interpret data sets coming from from various scanner systems, but also for the investigation of simulated data based on physical, biochemical or mathematical resources. We describe the necessary analytical and computational steps required for a simulation and visualization of a complete lung model of rat or human, based on macroscopical and microscopical measurements for the conductive and respiratory parts of the lung, respectively. To study flow of air and the oxygen uptake, a set of mass transport equation is solved iteratively.

The structure of the mammalian lung is far too complex for a complete analytical investigation of an individual organ, beside the different preparative ways required for studying macroscopical and microscopical aspects. Instead, some basic patterns of the structural organization have to be deduced, which then can be used by the computer to simulate a complete model. The macroscopical, conductive part of the lung is based on studies of corrosion cast models. Stereo images of such models featuring the bronchial tree were analyzed for their branching pattern with the STERECON System, developed at the New York State Department of Health in Albany. Lung segments of interest were traced stereoscopically using a two monitor stereo display system, a digitizer and a 3-D cursor. The end points of the segments, the length, diameters and the angle of branchings can be determined giving a 3-D sceleton of the conductive air-ways. Analyzing the angle/length/diameter relationships gives some basic fractal properties of the branching pattern.

For a quantitative analysis of the respiratory system of the lung, in particular the pulmonary acinus, the imaging of volumes with a computer-guided reference system allows to study the respiratory part of lung, as described in the preceeding abstract (A. Kriete: Investigating large volumes of lung by computer-guided 3-D image compositing in confocal microscopy). The measurement of branching angles and lengths and the overal topology is studied by 3D-TOP, a software developed at our image processing laboratory in Giessen. This software evaluates connectivities between corresponding contours in adjacient sections are connected, based on bijective correspondance analysis. These connectivities form a topological sceleton of the structure and indicate nods and branches that are the backbone to analyze volume and sur-face. These are parameters necessary to describe the function of the respiratory system.

The computer based simulation of the structure of a complete lung starts with the 3-D implementation of the main bronchial segments as measured from the cast model. All daughter branches are added by the computer program, using fractal properties. Such a 3-D computer generated graphical model can be displayed from all sides and the effect of variation of angles and lengths can be easily studied. Typically, such a model of the human lung model features 75000 segments.

Based on the 3-D structural model functional attributes can be added. One example is the flow of air, which is predicted for all segments using the diameter and the dead space relation of daughter branches. To study the oxygen uptake, the mass transport equations have to be solved. Mass transport has to include convection, diffusion and oxygen uptake. Since this set of differential equations can not be mathematically solved, the process of inhalation and exhalation can only be computed iteratively. For a stable solution, up to 10000 time steps have to be calculated for each of the segments. Using a Silicon Graphics

Challenge L computer system with 2xR4400 processors, this takes about 30 hours of computing time. The final oxygen distribution is visualized at the 3-D structural model. We give examples, how the oxyen distribution in human and rat looks like under various breathing conditions.

REFERENCES

Baumann MA, T Schwebel, A Kriete. 1993. Dental anatomy portrayed with microscopic volume investigations. Computerized Medical Imaging and Graphics. **17:** pp 221-228.

Marko M, AD Leith. 1992. Contour-based 3-D surface reconstruction using stereoscopic contouring and digitized images. in: Kriete, A. (ed) Visualization in Biomedical Microscopies. VCH-publisher, Weinheim-New York, pp. 45-73.

Zoological Studies 34, Supplement I (1995)

Zoological Studies

Optical Fibre Probe Microscopy

C.J.R. Sheppard and H. Fatemi

Department of Physical Optics, School of Physics, University of Sydney, NSW 2006, Australia

In the optical fiber probe microscope (Cerre et al. 1991), light is launched into a single mode optical fibre and is incident on the object (Fig. 1). The reflected light is coupled back into the fibre, and after passing through a fibre coupler its intensity measured with a photodiode detector. An image is built up by scanning the fibre tip relative to the object surface. This can be ach-ieved by mechanically moving either the fibre tip or the object itself. The strength of the light coupled back into the fibre depends on the reflectivity of the sample, but also its distance from the fibre (i.e. the surface height) and the tilt of the surface. In practice there is also a reflection of light from the fibre tip, which results in interference fringes being formed as the object is scanned in depth. The interference pattern consists of fringes within an envelope defined by upper and lower parts. Investigation of the details of the interference allows us to extract the various properties of the surface at the particular scan point. In this way it is very similar to the confocal surface profiling methods, except that in the present case there is no peak in intensity because the radiation from the fibre is divergent rather than convergent.

The light emerging from a single mode optical fibre is closely approximated by a Gaussian beam. The variation in intensity along the axis is proportional to $1/(1+(z/z_0)^2)$, where z is the distance from the beam waist, located at the fibre tip, and z_0 is the confocal parameter.

If there is a sample in front of the illuminating fibre tip, a fraction of the light can be reflected from the sample surface back towards the fibre. Part of this light couples back into the fibre, whilst the rest is reflected by the fibre tip back to the sample. Thus multiple reflections are set up, similar to a Fabry-Perot resonator. For the particular case when the normal to the sample surface is parallel to the axis, i.e. when r=0 in Fig. 2, experimental results have been presented previously (Fatemi and Sheppard 1993, Sheppard et al. 1995). It is possible to measure the geometrical parameters of the light emitted from the fibre, e.g. z_0, by observations using a plane mirror as sample.

In the present study, we examine the effects when the surface is tilted, so that $\gamma \neq 0$. We assume that the value of z_0, and thus the far-field angle of divergence, θ, and also the amplitude reflection coefficient γ_0 of the fibre tip, are known. The aim is to measure the amplitude reflection coefficient r of the sample, and the local tilt of the sample surface. The method is valid when the illuminated surface can be assumed locally plane. Spatial resolution is thus limited to about

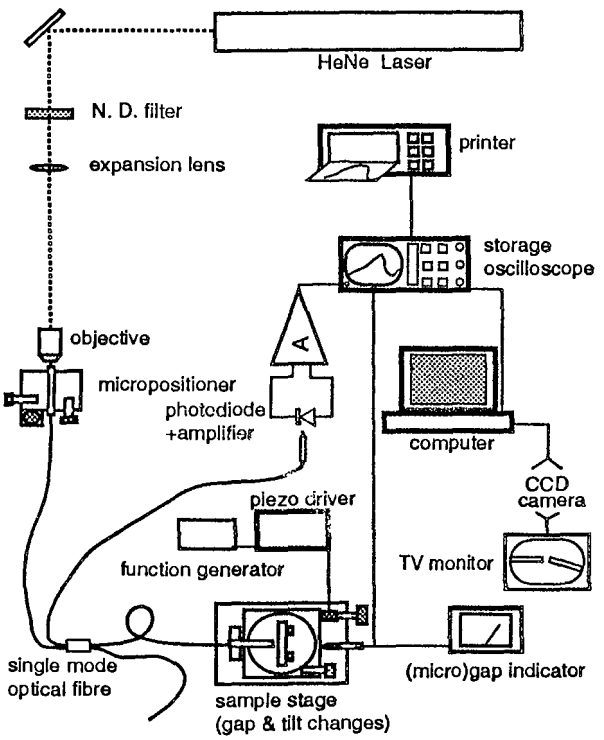

Fig. 1. A schematic diagram of the optical fibre probe microscope.

the fibre spot size, which is around 3 μm in our experiments.

In order to investigate the behaviour of the signal with different sample parameters, we used a tilted mirror as sample.

The fibre tip is viewed and positioned relative to the sample surface (Fig. 2), and can be tracked from side and top views through an image grabbing system. For a given surface tilt the axial position is scanned using a feedback-controlled pie-zoactuator, driven by a sawtooth generator. The signal is digitally accumulatea in a storage oscilloscope and processed using a computer. Fig. 3 shows an example of an experimental plot. The figure covers the lower part of the envelope of the interference fringes, the geometry of which can be used to extract the reflectivity and tilt of the sample. An important property which is observed is the zero of the lower part of the envelope. The existence of this zero limits the measurements to a value of r greater then 0.2. In practice this covers a wide range of industrial and biological samples.

We have also been experimenting with different geomtries of fibre tip, including angled polishing, and the formation of tapers and microlenses.

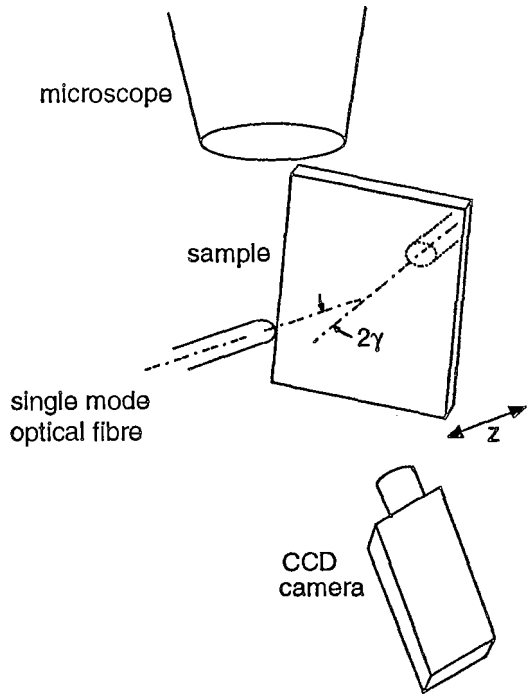

Fig. 2. A close-up of the fibre tip and sample.

REFERENCES

Cerre N, F de Fornel, JP Goudonnet. 1991. Reflection scanning microscopy. Applied Optics. **31:** 903-908.

Sheppard CJR, H Fatemi, Min Gu. 1995. The Fourier optics of near-field microscopy. Scanning. **17:** 28-40.

Fatemi HEG, CJR Sheppard. 1993. Topographic studies of reflecting surfaces by means of a single-mode optical fibre. Australian Conference of Optics, Lasers and Spectroscopy. Melbourne: Proceedings, p.70.

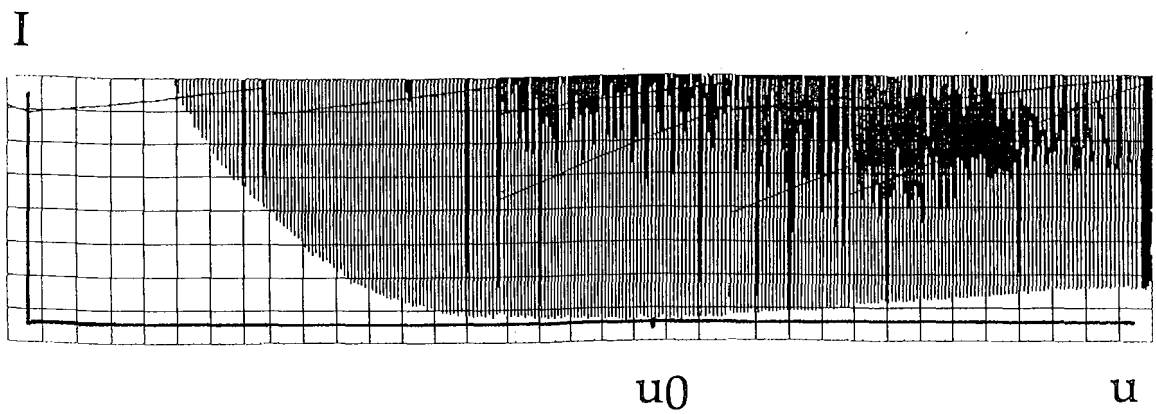

Fig. 3. An example of an interference pattern from a mirror as sample. The lower part of the envelope is shown, depicting a zero in the envelope.

Zoological Studies 34, Supplement I (1995)

Zoological Studies

Surface Profiling and Confocal Microscopy

C.J.R. Sheppard and J.C. Quartel
Development of Physical Optics, School of Physics, University of Sydney, NSW 2006, Australia

There is strong current interest in various approaches for measurement of surface profiles by non-contacting methods. These have application in a wide range of areas including non-destructive testing and industrial inspection. These approaches include various interferometric methods, confocal microscopy, and reconstruction by inverse scattering. The aim of this work is to examine by computer modelling various confocal and interferometric algorithms for surface profiling. In particular we have investigated three methods. The first is the confocal surface profiling method, in which the position of the peak in intensity during an axial scan is recorded (Hamilton and Wilson 1982, Cox and Sheppard 1983). In the second the position of the zero-order fringe in an interferometric image is tracked. This interferometric image can be produced by a range of different forms of interferometric microscope, including those of the Linnik or confocal geometry (Fig. 1). The third method, which is only applicable for surfaces of small RMS surface roughness, is the measurement of phase in a single in-focus image, again using an interferometric microscope.

In each case the two-dimensional image of a one-dimensional rough surface was calculated from scattering data generated using rigorous theory (Wombell and DeSanto 1991). The surfaces were generated to satisfy the statistics of a stationary Gaussian process with Gaussian correlation, and of various degrees of surface roughness. The aims of the study were to investigate the accuracy of the various profiling methods and the effects of system parameters.

The profiling methods can be regarded as nonlinear inverse methods for surface reconstruction based on the Kirchhoff approximation (Sheppard et al. 1993). Thus the methods are expected to tend to break down when the surface roughness is such that the Kirchhoff approximation does not hold. In particular the Kirchhoff approximation assumes that the surface can be taken as locally plane, so that the radius of curvature is large compared with the wavelength. In addition the Kirchhoff approximation neglects multiple scattering effects.

According to the Kirchhoff approximation, the scattering function for a surface of profile $\varsigma(x, y)$ can be expressed in terms of transverse and axial spatial frequencies by (Sheppard et al. 1993)

$$S(m,n,s)=\frac{m^2+n^2+s^2}{2s}\iint_{-\infty}^{+\infty}\exp\{-ik[mx+ny+s\varsigma(x,y)]\}dxdy \quad (1)$$

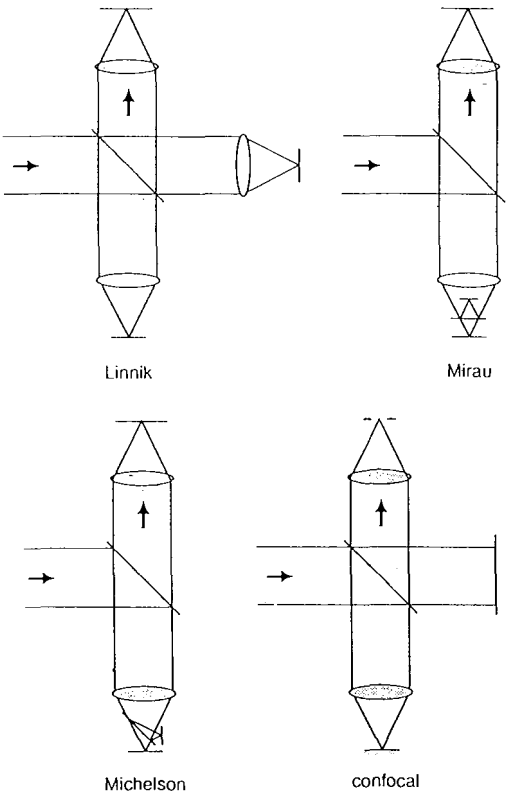

Fig. 1. Different configurations of interference microscope.

where m, n, s are related to the direction cosines of illumination and scattering m_1,n_1; m_2n_2 by

$$m=m_2-m_1$$

$$n=n_2-n_1 \qquad (2)$$

$$s=(1-m_1^2-n_1^2)^{1/2}+(1-m_2^2-n_2^2)^{1/2}$$

Introducing the object function $\delta[z-\varsigma(x, y)]$ for the profile, this can be written in the form of a 3D Fourier transform

$$S(\mathbf{m})=\frac{\mathbf{m}^2}{2\,\mathbf{m}\cdot\mathbf{k}}\iiint_{-\infty}^{+\infty}\delta[z-(x,y)]\exp\{-ik\mathbf{m}\cdot\mathbf{r}\}\,\mathrm{d}\mathbf{r} \qquad (4)$$

where

$$\mathbf{m}=m\mathbf{i}+n\mathbf{j}+s\mathbf{k} \qquad (5)$$

and

$$\mathbf{r}=x\mathbf{i}+y\mathbf{j}+z\mathbf{k} \qquad (6)$$

The amplitude of the 3D image of the surface in the Kirchhoff approximation is then

$$U(\mathbf{r})=\iiint_{-\infty}^{+\infty}c(\mathbf{m})S(\mathbf{m})\exp(ik\mathbf{m}\cdot\mathbf{r})\,\mathrm{d}\mathbf{m} \qquad (7)$$

where $c(\mathbf{m})$ is the 3D coherent transfer function. The form of the coherent transfer function for a confocal microscope has been described elsewhere (Sheppard et al. 1994). However, in practice it is possible to control the value of the transfer function within is passband by apodization or digital image processing. Thus in the following we assume a transfer function

$$c(\mathbf{m})=\frac{2\,\mathbf{m}\cdot\mathbf{k}}{\mathbf{m}^2},\quad \mathbf{m}^2<4 \text{ and } \mathbf{m}\cdot\mathbf{k}>2\cos\alpha$$
$$=0, \text{ otherwise} \qquad (8)$$

where α is the angular semiaperture of the lens, which expression is chosen to exactly cancel the premultiplying factor of Eq.4.

We have investigated surfaces with a correlation lenghth of 1λ, and of RMS surface height, σ, in the range from 0.05 to 0.20 λ.

As examples, in Fig. 2. we show profiles reconstructed using the confocal profiling method for α=60°. It is seen that, although the reconstructions are reasonably good, the reconstruction becomes

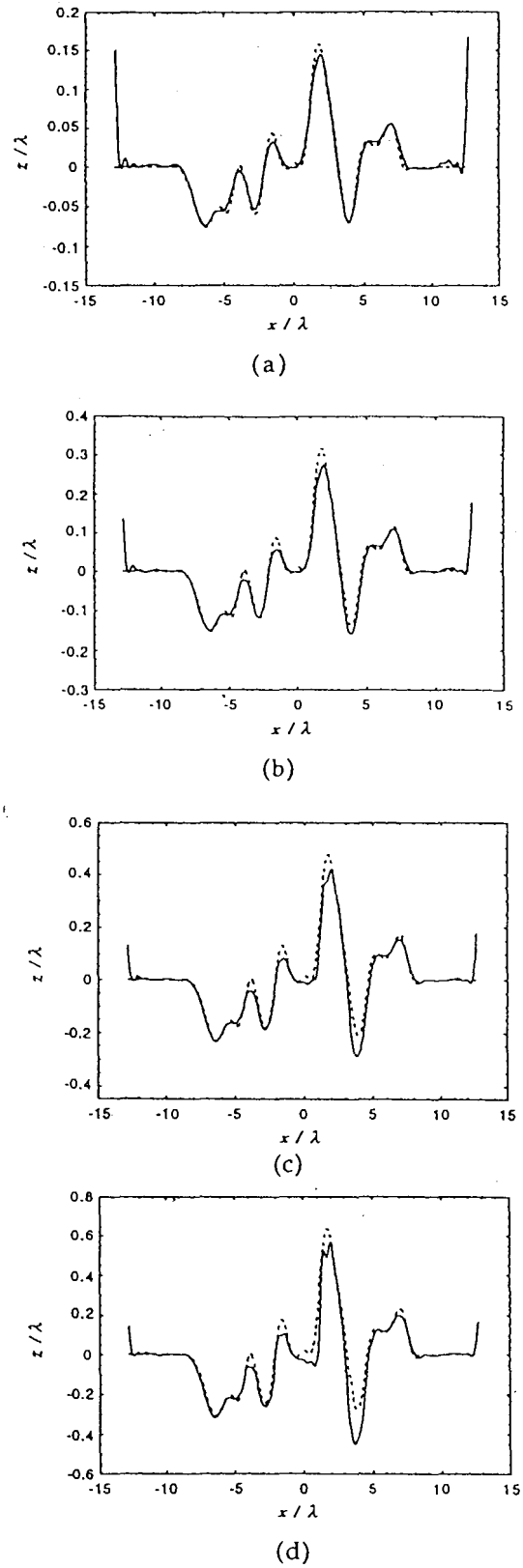

Fig. 2. Profile reconstructions (solid curves) using the confocal profiling method with α=60°. The surfaces (dashed curves) have (a) σ=0.05λ, (b) σ=0.10λ (c) σ=0.15λ (d) σ=0.20λ.

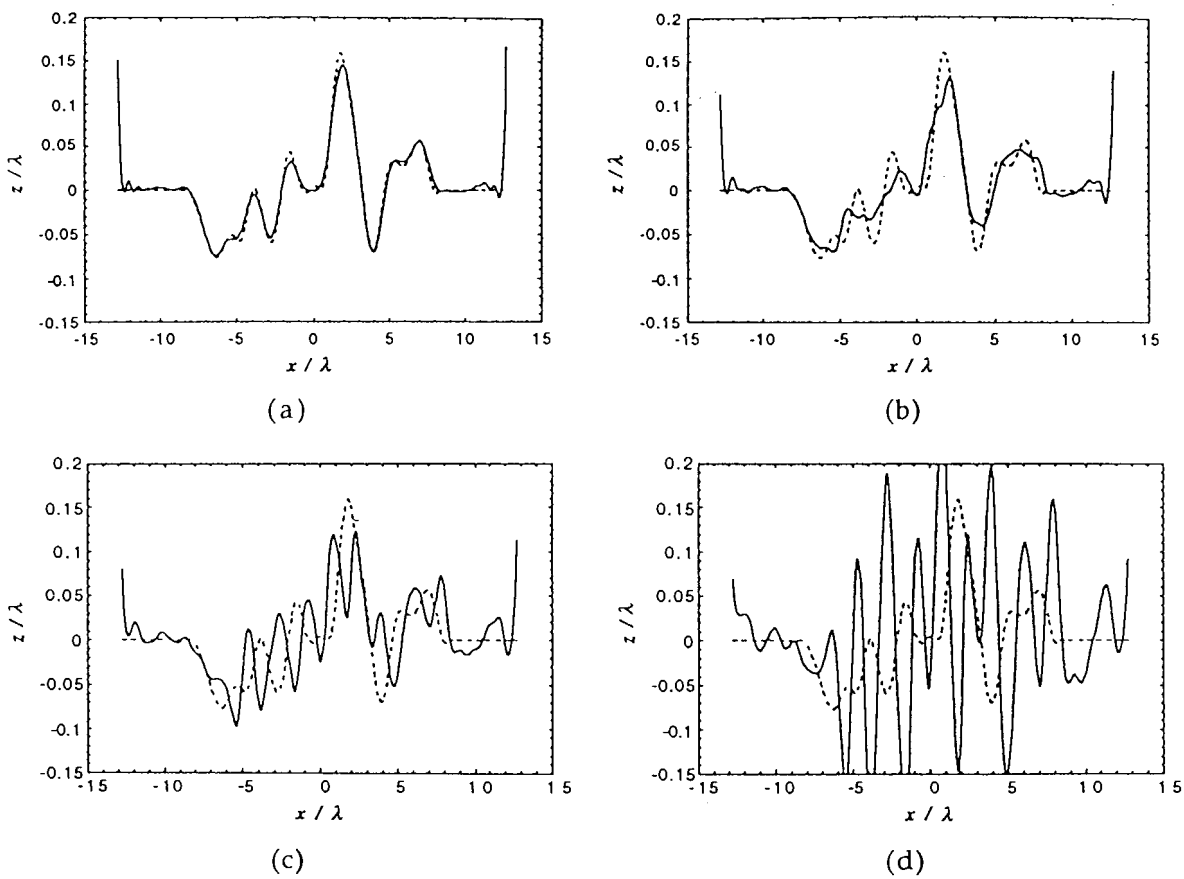

Fig. 3. Profile reconstructions (solid curves) using the confocal profiling method on the surface (dashed curves) $\sigma=0.05\lambda$. (a) $\alpha=60°$, (b) $\alpha=50°$, (c) $\alpha=40°$, (d) $\alpha=30°$.

poorer as the roughness is increased, with the peaks and troughs, where the curvature is greatest, the most likely regions for errors.

In Fig. 3. we show the effect of altering the numerical aperture for a particular surface. It is seen that the reconstruction is poor for α less then about 50°, when the optical system cannot image adequately the transverse spatial frequencies.

Studies of this type can determine the relative performance and limitations in accuracy of the various profiling methods.

ACKNOWLEDGMENTS

The authors thank RJ Wombell and JA DeSanto for providing the scattering data.

REFERENCES

Cox IJ, CJR Sheppard. 1983. Digital image processing of confocal images. Image and Vision Computing, **1:** 52-56.

Hamilton DK, T Wilson. 1982. Three-dimensional surface measurement using the confocal scanning microscope. Applied Physics B, **27:** 211-213.

Sheppard CJR, Min Gu, Y Kawata, S Kawata. 1994. Three-Dimensional transfer functions for high aperture systems. J. Opt. Soc. Amer. a, **11:** 593-598.

Sheppard CJR, TJ Connolly, MIn Gu. 1993. Imaging and reconstruction for rough surface scattering in the Kirchhoff approximation by confocal microscopy. J. Mod. Opt. **40:** 2407-2421.

Wombell RJ, JA DeSanto. 1991. Reconstruction of rough-surface profiles with the Kirchhoff approximation. J. Opt. Soc. Amer. **A,8:** 1892-1897.

Zoological Studies 34, Supplement I (1995)

Zoological Studies

3-D Transfer Function Description for 4Pi Confocal Microscopy

Min Gu and C.J.R. Sheppard
Department of Physical Optics, University of Sydney, NSW 2006, Australia

The three-dimensional (3-D) optical transfer function (OTF) provides a complete description of a fluorescence optical imaging system under the first Born approximation (Sheppard and Gu 1992). It gives the effeciency with which the spatial periodic com-ponents in objects are imaged.

4Pi confocal fluorescence microscopy was described by Hell and Stelzer (1992a) as a means to increase effectively the aperture angle of a confocal system. A problem existing in this system is the appearance of the strong side peaks of the point spread function along the axial direction, degrading the image quality. This issue can be overcome by using two-photon (2-p) fluorescence microscopy (Hell and Stelzer 1992b). There are three imaging modes in 4Pi microscopy: 4Pi-A, 4Pi-B, and 4Pi-C. In this paper, the 3-D OTF for these modes in single-photon (1-p) and 2-p 4Pi confocal fluores-cence microscopy is invesitgated (Gu and Sheppard 1994, 1996).

As the numerical aperture of the objectives in a 4Pi system is large, an imaging theory for a high-aperture system is used to derive the 3-D intensity point spread function (IPSF). Performing the 3-D Fourier transferm of the 3-D IPSF gives rise to the 3-D OTF for the 4Pi confocal fluorescence system.

Let us first consider 1-p 4Pi confocal systems. Fig. 1 gives the 3-D OTFs, normalized to unity at the origin, for a numerical aperture of 71°, which corresponds to the maximum numerical aperture of 1.25 possibly achievable in practice for a water immersion objective. The 3-D OTF for the 4Pi-A confocal fluorescence microscope shows three peaks along the axial direction (Fig. 1a) and is identical to that for 4Pi-B 1-p systmes. The central peak of the 3-D OTF is the 3-D OTF for 1-p non-4Pi confocal imaging. Therefore, axial resolution in the 4Pi-A system is better than that in the non-4Pi system, as expected. The axial resolution can be increased even further if a 4Pi-C 1-p confocal microscope is used. This is because the 3-D OTF (Fig. 1b) for a 4Pi-C system presents five peaks which results in a larger axial extension than that in Fig. 1a. However, the multi-peak 3-D OTF ›lies that there are strong side lobes of the

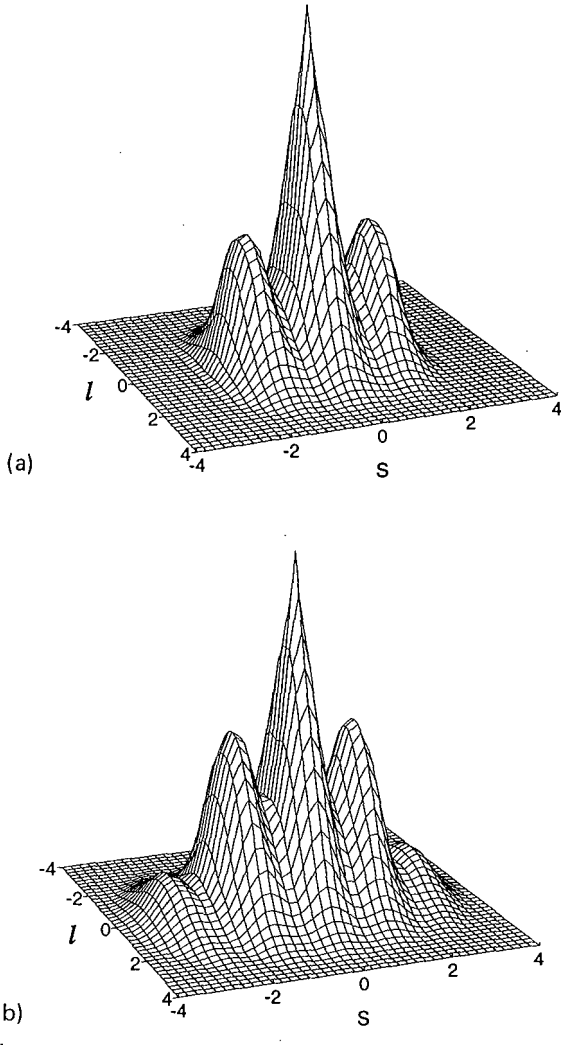

Fig. 1. 3-D OTFs, normalized to unity at the origin, for 1-p 4Pi-A (or 4Pi-B)(a) and 4Pi-C (b) confocal fluorescence microscopes obeying the sine condition for α=71°.

3-D IPSF in the axial direction, which may degrade the axial imaging performance (Hell and Stelzer 1992a).

Fig. 2 shows the calculated 3-D OTFs for 2-p 4Pi confocal fluorescence microscopes with same objectives. For a type-A system, although the 3-D OTF (Fig. 2a) has the same axial extension as that in Fig. 1a, the values of the OTF in the axial direction are increased strongly and there is no pronounced multi-peak structure. These features suggest that high axial resolution may be achieved and that there may be no strong axial side lobes in the 3-D IPSF. It is clear from the 3-D OTF presented in Fig. 2b that the imaging performance in a type-B 2-p system is similar to that in a 1-p type-A (or type-B) system. The difference between Fig. 1a and Fig. 2b is the slope of the central peak. In the case of 2-p microscopy, the slope of the central peak is zero, which is caused by the nonlinear excitation. This feature may result in enhanced images of edge objects (Gu and Sheppard 1995b).

It is important to note that the 3-D OTF for a 2-p 4Pi-C system has excellent behaviours: no multi-peak structure exists and the cut-off axial frequency is larger than that in the transverse direction. We can conclude that the 3-D IPSF for 4Pi-C 2-p confocal fluorescence microscopy has lower axial side lobes and that the central peak of the 3-D IPSF is confined to a small region (Hell and Stelzer 1992b). Therefore high axial resolution can be achieved without degradation of images caused by the side lobes of the 3-D IPSF.

It should be pointed out that when the numerical aperture is increased, the minimum of the multi-peak OTF becomes less pronounced. Eventually, the axial resolution is the same as the transverse resolution in 4Pi-C systems. In the case of a large numerical aperture, the effect of apodization becomes important. In fact, if the objective obeys the uniform angular illumination condition (Gu and Sheppard 1994), the 3-D OTF approaches a symmetric form in the axial and transverse directions for a complete spherical illumination (Gu and Sheppard 1994, 1995).

In conclusion, the 4Pi-C 2-p confocal microscope gives the best axial resolution and its 3-D OTF has the largest information content.

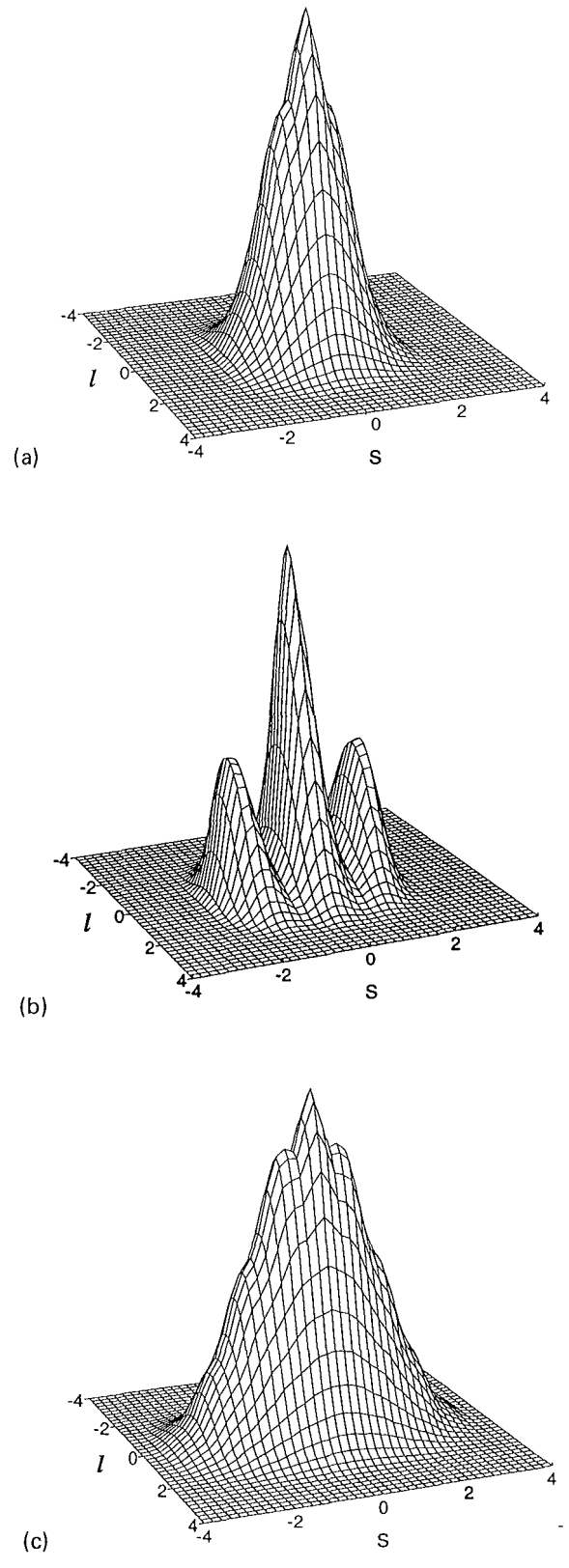

Fig. 2. 3-D OTFs, normalized to unity at the origin, for 2-p 4Pi-A (a), 4Pi-B (b), and 4Pi-C (c) confocal fluorescence microscpes obeying the since condition for α=71°.

REFERENCES

Gu M, CJR Sheppard. 1994. Three-dimensional transfer functions in 4Pi confocal mcroscopes. J. Optc. Soc. Am. A. **11:** 1619-1627.

Gu M, CJR Sheppard. 1995a. Optical transfer function alaysis for two-photon 4Pi confocal fluorescence microscopy. Opt. Commun. **114:** 45-49.

Gu M, CJR Sheppard. 1996. Comparison of 3-D imaging properties between two-photon and single-photon fluorescence microscopy. J. Microscopy. (in press)

Hell S, EHK Stelzer. 1992a. Properties of a 4Pi confocal fluorescence imcriscope. J. Opt. Soc. Am. A, **9:** 2159-2166.

Hell S, EHK Stelzer. 1992b. Fundamental imporvement of resolution with a 4Pi-confocal fluorescence microscope using two photon excitation. Opt. Commun., **93:** 277-282.

Sheppard CJR, M Gu. 1992. The significance of 3-D transfer functions in confocal scanning microscopy. J. Microscopy. **165:** 377-390.

Zoological Studies 34, Supplement I (1995)

Zoological Studies

Fluorescence Lifetime imaging in Bilateral Confocal Microscopy by Double Pulse Excitation

G.J. Brakenhoff[1], M. Müller[1], R.I. Ghauharali[1] and K. Visscher[2]

[1]*Department of Molecular Cytology, University of Amsterdam, Plantage Muidergracht 14, 1018 TV Amsterdam, The Netherlands*

[2]*Department Molecular Biology, Princeton University, Princeton, NJ 08544, USA*

It has been recognised for some time, that the fluorescence lifetime of a molecule not only depends on the internal structure of the molecule itself, but also on its environment. Recently this environmental dependence of the fluorescence lifetime has been introduced as an important contrast parameter in the field of microscopy. An example is for instance the imaging of free cytosolic Ca^{2+} concentrations (Lakowicz and Szmacinski 1993 and the local pH in biological samples (Draxler et al. 1993, Lippitsch et al. 1992].

The use of the fluorescence lifetime as a contrast parameter in microscopy is, among other applications advantageous when the fluorescence lifetime of a probe molecule differs considerably from that of the background radiation or autofluorescence, thus providing an opportunity to suppress the contributions of the latter to the total signal. Also this technique can provide a straightforward alternative to the technique of ratio imaging based on the excitation at two different wavelengths and detection at one fluorescent wavelength or vice versa excitation at one and detection at two, as have been used for the imaging of ion concentrations like Ca^{+} in biological samples.

The principle of the newly developed method of Double Pulse Fluorescence Lifetime Imaging (DPFLIm) is that the fluorescent output from the specimen is collected with excitation by pairs of short pulses having two different timing conditions between the pulses. Each of these pulses is sufficient to drive the fluorescence into saturation or very close to it. If the two pulses of the pair are separated by a time interval which is short with respect to the fluorescence relaxation time then there will be no difference between the fluorescence produced by a single pulse or by the pulse pair. This is because the saturation induced by the first pulse has the effect that the second one cannot induce any further fluorescence. However if the second pulse of the pair is delayed by an interval which is a substantial fraction of the fluorescence lifetime then at the arrival of the second pulse sufficient fluorophore molecules will have decayed to the ground state that additional fluorescence can be induced by the second pulse. This extra amount of fluorescence radiation will be higher for longer delays between the pulses, thus providing a means to determine the fluorescence lifetime from the relative fluorescence in both pulse conditions. These data are collected by separately collecting, on a CCD with the bilateral confocal imaging technique (Brakenhoff and Visscher 1992, 1993) two separate images being illuminated by a stream of pairs of pulses with the indicated different timing conditions. From these images the fluorescence lifetime image can be calculated with an appropriate algorithm.

A theoretical analysis of this new technique for fluorescence lifetime imaging will be presented. Bilateral confocal microscopy and a (cooled) CCD is used for sensitive signal detection over a large dynamic range as required for the calculation of the lifetimes from the image data The sensitivity of the technique is analysed, taking into account: photo degradation, the effect of the laser repetition rate and the effect of non-steady state excitation and the features of the technique are compared to more conventional methods for fluorescence lifetime determination. It is found that under typically experimentally expected conditions, images can be obtained with contrasts corresponding to fluorescence lifetime differences of 10%, when differences in the DPFLIm signal ratio can be resolved within 5%, something which appears feasible (Brakenhoff et al. 1994). One may thus anticipate, that

the DPFLIm technique is as an fluorescence lifetime imaging technique will offer comparative or possible better life time discrimination in comparison with existing techniques, creating new opportunities for using fluorescence lifetime as a contrast parameter in confocal imaging.

Finally we want to emphasize two aspects. First the technique does not require electronic gating of the signal. Rather it relies on an optical gating technique with a time resolution which, depending only on the pulse duration, can be an order of magnitude shorter resulting in the possibillity of imaging with a correspondingly higher time resolution. Second the use of a cooled CCD-camera in the detection - facilitated by the bilateral confocal scanning approach - is essential in this new approach as it provides both the integrating capabilties and the high dynamic range/ signal-to-noise required for the calculation of fluorescent life-time images. As an additional benefit it facilitates fast image collection thanks to parallel speciem excitation and data collection, a practical proposition when operating in the line mode and high excitation powers (Brakenhoff and Visscher 1993).

ACKNOWLEDGEMENTS

This research was financially supported by the Stichting Technische Wetenschappen (STW), Utrecht, The Netherlands, under grant no ANS 33.2941.

REFERENCES

Brakenhoff GJ, K Visscher. 1992. Confocal imaging with bilateral scanning and array detectors. J. Microsc. **165:** 139-146.

Brakenhoff GJ, K Visscher. 1993. Imaging modes for bilateral confocal scanning microscopy. J. Microsc. **171:** 17-26.

Brakenhoff GJ, et al. 1994. Fluorescence bleach rate imaging. J. of Micr. **175:** 154-171.

Draxler S, et al. 1993. Optical pH sensors using fluorescence decay time. Sens. Act. **B 11:** 421-424.

Lakowicz JR, H Szmacinski. 1993. Fluorescence lifetime-based sensing op Ph, Ca^{2+}, K^{+} and glucose. Sens. Act. **B 11:** 133-143.

Lippitsch ME, et al. 1992. Time-domain fluorescence methods as applied to pH sensing. Proc. SPIE **1796:** 202-208.

Muller M, RI Ghauharali, K Visscher, TD Visser, GJ Brakenhoff. 1995. Double Pulse Fluorescence Lifetime Imaging in confocal microscopy, J. Microsc. (in press)

Zoological Studies 34, Supplement I (1995)

Zoological Studies

Measurement of Femtosecond Pulses in the Focal Point of a High NA Lens Using Two-photon Absorption

M. Müller[1] , J. Squier[2] and G.J. Brakenhoff[1]

[1] *Department of Molecular Cytology, University of Amsterdam, Plantage Muidergracht 14, 1018 TV Amsterdam, The Netherlands*

[2] *Center for Ultrafast Optical Science, University of Michigan, 2200 Bonisteel, Ann Arbor, MI 48109-2099, USA*

There has been increasing interest in the application of femtosecond optical pulses in the field of microscopy (Curley et al. 1992). For instance, femtosecond pulses have been used for two-photon absorption (TPA) in microscopy on biological samples (Denk et al. 1990, Piston et al. 1992). The inherent sectioning properties of TPA allows 3D-imaging of biological samples, a facility which has been shown to be of great interest by confocal microscopy (Brakenhoff et al. 1985). It has been recognized that the strong focusing conditions of high NA lenses may distort the shape of the optical pulse (Horvath and Bor 1994). The unique value of the presented two-photon autocorrelation technique is its capability of measuring the actual pulse width at the focal point of a high NA lens, where the interactions determining the two-photon imaging take place. For instance we found that a chirp-free input pulse of 47 femtosecond may broaden by $\approx$ 50% after focusing by a well compensated objective. We show that, with the actual pulse width information obtained by the presented methods, proper pre-chirp compensation can be applied to restore , the actual pulse width in the focus of such a lens system to (almost) its initial value.

The general principle of the autocorrelation technique for the pulse width measurements of ultra short optical pulses is schematically depicted in figure 1. An input beam is split by a 50% beam-splitter into two equal beams. One of the beams passes a variable delay line before it is recombined with the other beam. Moving the delay line changes the optical path of one of the beams with respect to the other. This spatial translation thus translates in a time delay. By mounting the variable delay line on a "shaker" -inducing a periodic change in the delay - the overlap of the pulses at the recombining beamsplitter is periodically varied. If some non-linear response is employed, usually Second Harmonic Generation (SHG) in a BBO crystal, the signal becomes a function of the amount of overlap in time of the two pulses. Note that in principle any non-linear interaction - that is also TPA - will fulfil the requirements for an autocorrelation measurement. We found, as illustrated in this contribution, that TPA autocorrelation can indeed be realised in the focal point of a high NA lens, thus providing a measurement of the temporal envelope of the pulse precisely at the point where the TPA induced fluorescence is generated. For the TPA autocorrelation experiments we used a number of different Rhodamine and Fluoresceine based samples.

Using the TPA autocorrelation response we found that it is not influenced by the specific non-linear medium in which the TPA takes place, indicating the possibility for a general application of this technique. Also it permits the measurement of the characteristic increasing penetration depth in the sample. This behavior is expected by considering the increase in spherical aberration that occurs for larger penetration depth in a medium with a refractive index that does not match that of the objective (Hell et al. 1993). A, not-unexpected but still satisfying observation, was that when the TPA autocorrelation signal is measured as a function of the pre-chirp compensation the minimal pulse width corresponding to the highest peak power, does indeed coincide with the maximum in the fluorescence signal amplitude.

Summarising we may say that the measurements presented in this paper show that it is possible to restore a pulse, broadened by propagation through the microscopic set-up, almost to its original transform limited width, by proper adjustment of the pre-chirp compensation and thus optimise the con-

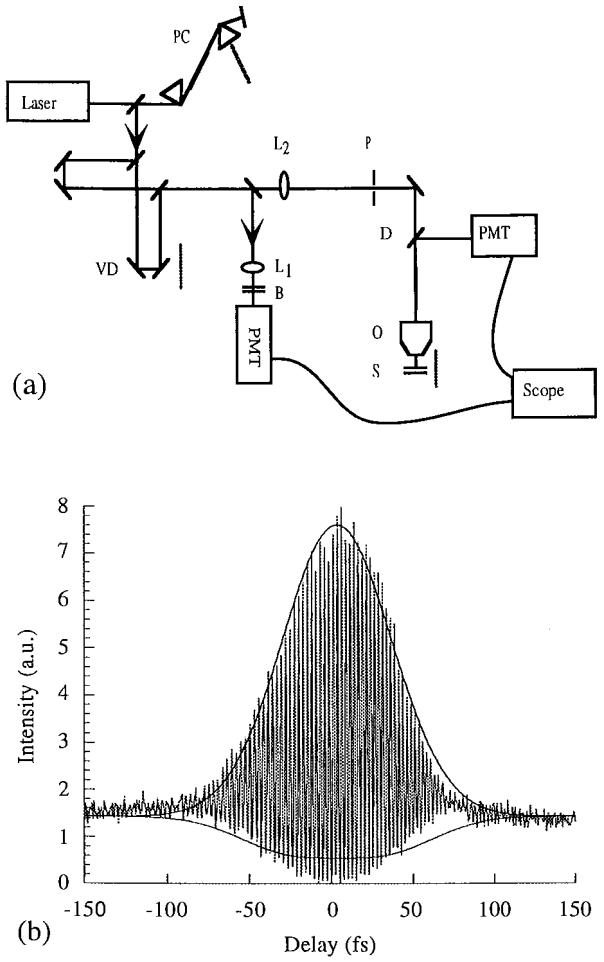

Fig. 1. a) Peinciple of autocorrelation measurement. The input beam is split into two equal parts by a 50% beamsplitter (BS). One of the beams passes a uariable delay line (VD) before being recombined with the other beam on a second - separate but identical -beamsplitter. The variable delay is mounted on a home-built "shaker". By applying a periodic movement of the variable delay, one of the pulses is scanned in time over the other. b) A two-photon autocorrelation measurement of a pulse width of 50.9 ± 1.2 fs in the focus of a high NA objective. The trace was obtained using a 10^{-3} pulse broadening induced by any objective used for a particular application. We observed a strong decrease in signal amplitude for M Rhodamine 6G solution as a medium after optimizing the pre-chirp conditions.

ditions for TPA imaging under the for the imaging relevant conditions.

ACKNOWLEDGEMENTS

The authors thank R. Sprik, B. Gijsbers and T. Norris for assistance. This research was financially supported in part by the Stichting Technische Wetenschappen (STW), Utrecht, The Netherlands, under grant no. ANS 33.2941 and by the National Science Foundation through the Center of Ultrashort Optical Science under STC PHY 8920108.

REFERENCES

Brakenhoff GJ, HTMvd Voort, EAv Spronsen, WA Linnemans, N Nanninga. 1985. Three-dimensional chromatin distribution in neuroblastoma nuclei shown by confocal scanning laser microscopy. Nature **317:** 748-749.

Curley PF, AI Ferguson, JG White, WB Amos, 1992. Application of femtosecond self-sustaining mode-locked Ti:sapphire laser to the field of scanning confocal microscopy. Opt. Quant. Electr. **24:** 851-859.

Denk W, JH Strickler, WW Webb. 1990. Two-photon laser scanning fluorescence microscopy. Science **248:** 73-76.

Hell S, G Reiner, C Cremer, EHK Stelzer. 1993. Aberrations in confocal fluorescence microscopy induced by mismatches in refractive index. J. Microsc. **169:** 391-405.

Horvath ZL, Z Bor. 1994. Behaviour of femtosecond pulses on the optical axis of a lens of a lens. Analytical description. Opt. Commun. **108:** 333-342.

Piston DW, MS Kirby, H Cheng, WJ Lederer, WW Webb. 1994. Two-photon-excitation fluorescence imaging of three-dimensional calcium-ion activity. Appl. Opt. **33:** 662-669.

Piston DW, DR Sandison, WW Webb. 1992. Time-resolved fluorescence imaging and background rejection by two-photon excitation in laser scanning microscopy. Proc. SPIE **1640:** 379-389.

Zoological Studies 34, Supplement I (1995)

Zoological Studies

X-ray Fluorescence Two-dimensional Microanalysis at the VEPP-3 Storage Ring: Aplications in Environmental Science

I.P. Dolbnya and K.V. Zolotarev
Budker Institute of Nuclear Physics, 630090 Novosibirsk, Russia

Some experimental capabilities of the experimental station of X-ray transmission subtraction microscopy and microtomography with the using of the synchrotron radiation (SR) from the 2T wiggler-magnet installed at the VEPP-3 storage ring (2 GeV, 100 mA) (Novosibirsk, Russia) (Dolbnya et al. 1992) in com-bination with X-ray fluorescence (XRF) energy-dispersive registration analysis and fluorescence scanning microprobe technique are presented. The X-ray double-crystal sagittally focusing Si(111) monochromator was employed. The using photon energies range from 7 to 25 keV. The scintillation counters were usually in use as X-ray absorption detectors. We have also employed the ionization chamber filled with nitrogen at normal pressure as the monitoring detector. To register X-ray fluorescence quanta solid state Si(Li) (180 eV at the energy of 5.9 keV, 7 μm Be window in thickness) detector was used. Point-by-point scanning of an object across the properly formed pencil monochromatic beam is used for the X-ray imaging. X-ray transmission imaging enable us to visualize two-dimensional not only an absorption mapping but also the elemental distribution by means of XRF analysis.

There is special interest to study the distribution of elements over the single microparticles in biomedical and environmental aerosol samples. X-ray scanning transmission subtraction microscopy in combination with X-ray fluorescence energy-dispersive registration analysis and fluorescence microprobe technique have been expected to be a promising analytical tool for such investigations.

As a test sample to check the capability of the developed investigation technique, the filter fabricated from the material Whatman-41 was taken. The filter was chosen from the lot of similar filters served as a filters of atmospheric aerosols at the environmental monitoring station near the city Novosibirsk (the large industrial center). The filter under investigation had microparticles with typical mean size of ~7 μm ranging up to ~30 μm. Fig. 1a demonstrates the subtraction roentgenograph (80×80 image points, 8 μm scanning step in horizontal X-direction and 4 μm in vertical) of aerosol filter under study which was taken at Fe K-edge. The coordination cross made from two Mo wires was inserted on a sample as absolute coordinate marker over the image field. This Mo cross is also seen in Fig. 1a. The XRF spectra were taken at photon energies of excitation of 10 and 18.4 keV from the region of different microparticles shown in Figure. For estimation of absolute amount of iron in one particle the information about absorption jump of intensity at Fe K-edge was used from results of the X-ray subtraction imaging of this particle on energies just before and after K-edge. In table 1 the results of measurements and calculations are presented. The detection limit in these measurements is about 1 pikogram for iron.

Using insects as a convenient object for environment monitoring seems to be most promising. Due to the fact that their integuments are not smooth and there are a great deal of a pubescence on their bodies, insects accumulate very well various inclusions from the atmosphere. Moreover, due to their durable flights, sometimes remote migrations, the flying insects are able to give us some information on the state of the atmosphere over rather vast territories, which is very difficult to get by means of conventional control techniques. The available data show that in addition to the elements contained in their food and stored in their organisms, the flying insects can also store different kinds of aerosol particles, being a factor of pollution, in the integuments (Heliovaara et al. 1987).

In further detailed investigations, it seems to be

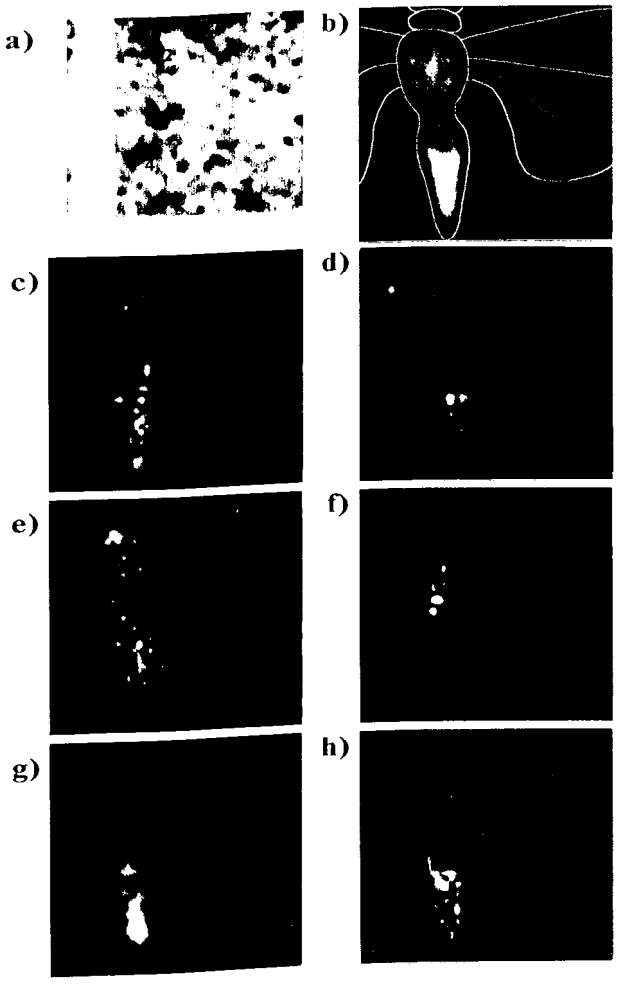

Fig. 1. (a)-subtraction roentgenograph of aerosol filter under study taken at Fe K-edge, 80×80 image points, 8 μm scanning step in horizontal and 4 μm step in vertical; the two-dimensional distribution of different elements under study over the meadow moth, the size of all images is 50 ×46 points, the image pixel is 200×250 μm^2, (b)-general view, the white contours are an art work, (c)-Ca, (d)-Fe, (e)-Ni, (f)-Cu,(g)-Zn,(h)-Br.

important to determine "marking" elements which can be used for reliable biological monitoring. The application of the scanning XRF elemental analysis allows one to determine the distribution of different elements in the body of an individual meadow moth. In this experiment, two moths were examined and the results of the study of one of them are shown in Fig. 1. The images were taken at the photon energy of 14.05 keV corresponding to the position just upper Br K-edge. Analysis of the obtained images has confirmed the hypothesis on the nonuniform distribution of elements in every moth. It is also seen that the major portion of the pollutant elements is concentrated in the body of a moth rather than on its wings. This circumstance permits us to conclude that it is feeding that is mainly responsible for the presence of pollutant elements in moth's bodies. The fraction of pollutant elements which accumulates on the wings from aerosol particles is insignificant.

Table 1. The results of microanalysis of aerosol particles (absolute amounts of elements are in pikograms (10^{-12}g)).

Particle	Ca	Ti	Fe	Cu	Zn
1	20.0	5.41	80.9	0.54	1.12
2	18.9	7.67	82.7	0.69	1.47
3	22.8	1.88	54.1	0.32	0.79
4	43.9	5.79	152.9	0.96	1.23
5	24.9	1.79	45.1	0.42	1.48

Finally, the authors would like to thank V.F. Pindyurin, V.B. Baryshev, P.K. Kotsenogy, V.A. Trounova, I.B. Knor and E.N. Naumova for a kind cooperation.

REFERENCES

Dolbnya IP, NG Gavrilov, NA Mezentsev, VF Pindyurin. 1992. Rev. Sci. Instrum. **63:** 609.

Heliovaara K et al. 1987. Environ Pollut. **48:** 13-23.

Zoological Studies 34, Supplement I (1995)

Zoological Studies

X-ray SR-based Microtomographic Investigation of Microporous Granulated Mercury Catalysts

I.P. Dolbnya[1] and Yu Tanyshev[2]

[1]*Budker Institute of Nuclear Physics, 630090 Novosibirsk, Russia*

[2]*Institute of Catalysis, 630090 Novosibirsk, Russia*

There is the wide class of mercury microporous granulated catalysts having a light matrix (quartz, ceramics and others) with the granule size ranged from ~0.5 mm to ~5 mm, and the typical pore sizes of ~0.5-20 μm. To reveal the internal 3D pore structure of such a catalysts and the level of the filling of the pores by Hg, the X-ray microtomography study of the several granulated Hg-containing catalysts was conducted. For the study, the catalysts with the mean pore sizes of 3-10 μm were chosen. The experiments were carried out at the station of X-ray transmission subtraction microscopy and microtomography with the using of the synchrotron radiation (SR) from the 2T wiggler-magnet installed at the VEPP-3 storage ring (2 GeV, 100 mA) (Novosibirsk, Russia) (Dolbnya et al. 1992). The X-ray double-crystal Ge(111) monochromator was employed. The imaging was performed at two different energies of X-ray quanta 9 keV and 12.3 keV (Hg L_{III}-edge). Point-by-point scanning of an object across the properly formed pencil monochromatic beam is used for the X-ray imaging. The transmission (9 keV) and subtraction (at Hg L_{III}-edge) imageshave been acquired. The space cross-sectional resolution was established to be 2 μm, and the slice height size was ~10 μm. The results of such investigations are presented and discussed.

REFERENCES

Dolbnya IP, NG Gavrilov, NA Mezentsev, VF Pindyurin. 1992. Rev. Sci. Instrum. **63:** 609.

Zoological Studies 34, Supplement I (1995)

Zoological Studies

The SRRC Taiwan Light Source and Scientific Research Programs

Yuen-Chung Liu
Synchrotron Radiation Research Center, No. 1 R&D VI, Hsinchu Science-Based Industrial Park, Hsinchu, Taiwan, R.O.C.

The SRRC 1.3 GeV synchrotron radiation research facility has been operating for one and a half years since its dedication in October 1993. The storage ring is a low emittance, high brightness light source with photon energy ranging from vacuum ultraviolet to soft x-ray. The facility has been opened to the public users to conduct synchrotron radiation experiments starting from April 1994. The overall machine performance of the first year operation as well as its scientific research programs will be presented. Presently, there are three high resolution photon beamlines in use which are dedicated to VUV experiments. In February 27, 1995, SRRC also announced the successful commissioning of its 1.8 Tesla high field wiggler magnet system which is another outstanding accomplishment of the third generation ring. Another three x-ray beamline will be operating in summer 1995. A PESM (photomission spectromicroscopy) beamline, which will be set up at the SRRC-U5 undulator, providing photon energies from 90-400 eV in the first harmonics, is presently under plan.

Zoological Studies 34, Supplement I (1995)

Zoological Studies

Applications of the Confocal Fluorescence Microscopy in the Study of the Centrosomal Proteins

Tang K. Tang and Chieh-Ju C. Tang

Institute of Biomedical Sciences, Academia Sinica, Taipei 115, Taiwan, R.O.C.

During past several years, we have identified and characterized two proteins: NuMA (Nuclear Mitotic Apparatus protein) and protein 4.1 (P4.1). NuMA, originally described as a predominantly nuclear protein, is present in the interphase nucleus and concentrated in the spindle pole of mitotic cells, while P4.1 is an erythrocyte membrane skeletal protein whose function is believed to strengthen red cell morphology. We and others have recently isolated the cDNAs that encoded NuMA and P4.1, respectively. Our results showed that both NuMA (Tang et al. 1993, 1994) and P4.1 (Tang et al. 1990a,b) constitute multiple isoforms heterogeneous in size. The heterogeneity of NuMA (Tang et al. 1993) and P4.1 (Tang et al. 1991, Huang et al. 1993) appears to be arisen by alternative RNA splicing from a single gene.

Confocal fluorescence microscopes have an improved resolution over conventional fluorescence microscopes by producing images in which out-of-focus blur is essentially absent. We have applied the confocal fluorescence microscopy to finely localize the subcellular distribution of NuMA and P4.1. In order to elucidate the localization of various NuMA isoforms, we have developed a transient expression system (Tang et al. 1994). Expression of NuMA-large shows cell cycle-dependent distribution indistinguishable from that of human NuMA; it is present in the interphase nuclei and segregates to the spindle pole during mitosis. However, expression of the two other isoforms (NuMA-medium and -small) shows distinct subcellular localization. NuMA-medium and NuMA-small are distributed in the cytosol and appear to be clustered mainly at the centrosomal region. When cells enter into mitosis, NuMA-medium and -small move into the mitotic spindle pole. In addition, we have mapped the NuMA gene to human chromosome 11q12->q13.5 by a fluorescence in situ hybridization technique. The NuMA DNA was biotin labeled and used as a probe to hybridize the metaphase chromosomes. The chromosome DNA was stained with propidium iodide and the biotinylated probe was detected by FITC-conjugated avidine under a confocal laser-scanning microscope (BioRad MRC 600).

For localization of the large P4.1 isoforms (135 kDa) within the cells, an antibody (anti-5') that specifically recognized the N-terminal end of this large P4.1 isoform was generated. The mouse 3T3 fibroblasts at various cell cycle stages were processed for immunofluorescence with anti-5' and anti-tubulin antibodies. Our results showed that the large P4.1 was mainly detected at the interphase centrosome and formed several large aggregates within interphase nuclei. In prophase stage, the large P4.1 was clearly detected at the separated centrosomes. However, some P4.1 spread within the cytosol. When cells entered metaphase, the large P4.1 was found at the spindle poles and the mitotic microtubules. Finally, in telophase cells, the large P4.1 was located at the midbodies as well as the centrosomes. Interestingly, when we processed the mouse sperms for immunostaining with our anti-5' antibody, the large P4.1 was mainly detected at the basal body complex (centrosomal region) at the base of the sperm tail.

The differential subcellular localization of various NuMA and P4.1 isoforms suggest that some uncharacterized functions of these proteins have not been identified yet.

REFERENCES

Huang JP, C-J Tang, KH Kou, VT Marchesi, EJ Benz, TK Tang. 1993. Genomic structure of the locus encoding protein 4.1:Structural basis for complex combinational patterns of

tissue-specific alternative RNA splicing. J. Biol. Chem. **268:** 3758-3766.

Tang C-J, TK Tang. 1991. Rapid localization of membrane skeletal protein 4.1 gene (EL-1) to human chromosome 1p33->1p34.2 by non-radioactive in situ hybridization. Cytogenet. Cell genet. 57:119.

Tang TK, Z Qin, TL Leto, VT Marchesi, EJ Benz. 1990a. Heterogeneity of mRNA and protein products arising from the protein 4.1 gene in erythroid and non-erythroid tissues. J. Cell Biol. **110:** 617-624.

Tang TK, CE Mazzucco, EJ Benz, VT Marchesi. 1990b. Molecular cloning and nuclear localization of lymphoid membrane skeletal protein 4.1. In Biochemical and Structural Dynamics of the Cell Nucleus, eds. E Wang, JL Wang, S Chien, CW Wu, WY Cheung. San Diego:Academic Press, pp. 43-57.

Tang TK, C-J Tang, Y-L Chen, C-W Wu, 1993. Nuclear proteins of the bovine esophageal epithelium. (II).The NuMA gene gives rise to multiple mRNAs and gene products reactive with monoclonal antibody W1. J. Cell Sci. **104:** 249-260.

Tang TK, C-J Tang, Y-J Chao, C-W Wu. 1994. Nuclear Mitotic Apparatus Protein (NuMA): Spindle association, nuclear targeting and differential subcellular localization of various NuMA isoforms. J. Cell Sci. **107:** 1389-1402.

Zoological Studies 34, Supplement I (1995)

3-D Unbiased Stereological Measurements Using Conventional Light Microscopy, Applied to the Study of Human Intra-uterine Growth Retardation

C.V. Howard, D. van Velzen, P. Sibbons, T. Ansari, Y. Li and N. Pahal
Department of Fetal and Infant Pathology, University of Liverpool, PO Box 147, Liverpool L69 3BX, UK

Design-based, assumption-free, stereological methods guarantee accuracy of estimates of feature volume, surface, length and number (Howard 1990a , b). The precision of these estimates is known and can be 'tuned' by the intensity of the sampling design (Gundersen and Jensen 1987). Those techniques requiring a scanned optical plane for counting objects in 3-D space, such as the 'unbiased brick' (Howard et al. 1985) or 'optical disector' (Gundersen 1986), can be efficiently employed using the confocal microscope and were indeed first demonstrated on such a machine (Baddelcy et al. 1987). However almost all commercially available confocal microscopes operate in epi-illumination mode and therefore the objects of interest have to either reflect or fluoresce. This cuts out much material prepared by conventional histological methods. There are now a number of papers extant in which the measurement of numerical density of cells has been made using the optical sectioning ability of high numerical aperture oil immersion lenses in transmission mode (Braendgaard et al. 1990). The material needs to be embedded in plastic media, such as methyl methacrylate, which do not suffer the shrinkage problems associated with paraffin embedding. Microscopes also need to be fitted with either a microcator to monitor stage movement in the z-axis or a high precision motorised stage.

In developmental pathology it is essential to know the normal growth trajectory of any particular parameter as precisely as is feasible (see Fig. 2). We have shown that Intra Uterine Growth Retardation (IUGR), which affects 20,000 pregnancies per year in the UK, causes permanent stunting of the microanatomy in the kidney, lungs and brain. IUGR infants will have on average only 65% of the normal complement of nephrons (Hinchliffe et al. 1990). This effect has now been shown in a majority of cases studied of Sudden Infant Death Syndrome (SIDS) (Hinchliffe et al. 1930). The number of terminal airways in the bronchial tree has been shown to be reduced in IUGR (Beddoes et al. 1993. Friedman et al. 1993). There appears to be an overall reduction in the total number of cortical brain cells in IUGR infants. These findings indicate that generalised and irreversible developmental damage occurs in IUGR. Epidemiological studies (Barker et al. 1989) show that the life expectancy of low birthweight children is, on average, reduced and that they have an increased incidence of hypertension, ischaemic heart disease and obstructive airways disease in adult life Additionally there is evidence of behavioural abnormality and intellectual impairment in IUGR infants (Ens-Dokkum et al. 1993). The

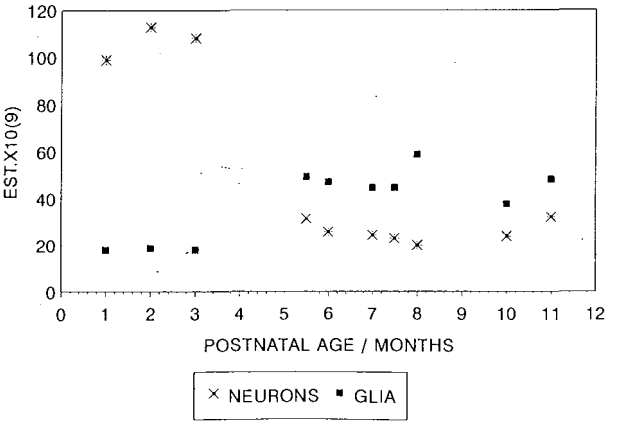

Fig. 1. This shows the postnatal human total neocortical neuronal and glial cell counts, in billions, in the first year of life. Note that there is a vast overproduction of potential neurons which settle down to the adult complement of about 25 billion by the 6the month of postnatal life.

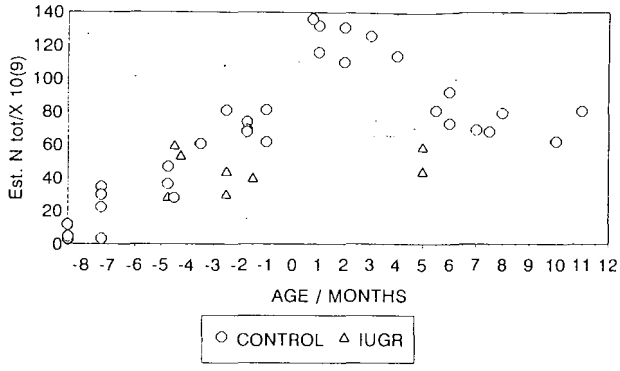

Fig. 2. Demonstrates the difference in the kinetics of total cell complement in the neocortices of normal birth weight (control) (and IUGR cases). By the beginning of the 3rD Trimester the cellularity of the neocortes has fallen behind the control cases.

significance of this in the light of our findings will be discussed.

Examples of the techniques used and the quantitative results will be presented. It is worth noting that these organs have been examined in 2-D microscopy for these conditions in the past. 3-D measurements are invariable more sensitive indices of change. Our findings in IUGR could only have been made with the use of stereological techniques.

REFERENCES

Baddeley A, CV Howard, A Boyde, S Reid. 1987. 3-D spatial statistical anaysis of osteocyte lacunae, using Tandem Scanning Reflected Kight Microscopy. Acta Stereologica, 5 (Suppl II), 87-100.

Barker DJP, PD Winter, C Osmond, B margetts, SJ Simmonds. 1989. Weight in infancy and death fromischaemic heart disease. Lancet Sept 9th **1989:** 577-580.

Beddoes L, CV Howard, PD Sibbons, D Van Velzen. 1993. Terminal duct number in unexplained cot death (SIDS) victims in comparision to airways of infants with intrauterine growth retardation (IUGR) and normal controls. J. Develop. Phys. **20:** 1990201.

Braendgaard H, SM Evans, CV Howard, HJG Gundersen. 190. Total numbers of neurons in human neocortex unbiasedly estimated using optical disectors. J. Microscopy. **157:** 285-304.

Ens-Dokkum M, A schroder, S Veen. 1993. Outcome at five years of age in very pre term and very low birthweight infants in The Netherlands. POPS, Leiden, ISBN 90-9005670-X.

Friedman K, T Takahashi, H Yaegashi, CV howard, PD Sibbons D Van Velzen. 1995. Three dimensional reconstruction of terminal airways in unexplained cot death (SIDS) cases in comparison with intra uterine growth retarded (IUGR) affected infants and normal controls. J. Develop. Phys. **20:** 203-206.

Gundersen HJG. 1986. Stereology of arbitrary particles. A review of unbiased number and size estimators and the presentation of some new ones, in memory of William R Thompson. J. Microscopy **143:** 3-45.

Gundersen HJG, EB Jensen. 1987. The efficiency of systematic sampling in stereology and its prediction. J. Microscopy **147:** 229-263.

Hinchliffe Sa, MRJ Lynch, PH Sargent, CV Howard, D Van Velzen. 1992. The effect of human intrauterine growth retardation on the development of renal nephrons. British Journal of Obstrics and Gynaecology **99:** 296-301.

Hinchliffe SA, CV Howard, MRJ Lynch, PH Sargent, BA Judd D Van Velzen. 1993. Renal developmental arrest in sudden infant death syndrome. Paediatric Pathology **13:** 333-343.

Howard CV. 1990a. The confocal microscope as a geometrical probe. In: 'confocal Optical Microscopy' 2nd Edition. Ed. T Wilson. Academic Press, London pp. 285-302.

Howard CV. 1990b. Measurements in electron microscopy using geometrical probes. In: 'Electron Microscope Imaging and Analysis for Biologists' Eds PW Hawkes U Valdre. Academic Press, London. pp. 479-508.

Howard CV, S Reid, A Baddeley, A Boyde. 1985. Unbiased estimation of particle density in th Tandem Scanning Relected Light microscope. J. microsce. **138:** 203-212.

Markova Y, CV Howard, D Van Velzen. 1995. Structural abnormalities of Substantia Nigra neurons in unexplaned cot death (SIDS) cases in comparison with intra uterine growth retarded (IUGR) affected infants and normal controls. J. Develop. Physiol. **20:** 227-231.

Zoological Studies 34, Supplement I (1995)

Zoological Studies

Photobleaching Kinetics of Fluorescein in Quantitative Fluorescence Microscopy

Loling Song[1,2], I. Ted Young[2] and Hans J. Tanke[1].

[1]*Department of Cytochemistry and Cytometry, Faculty of Medicine, Leiden University, Wassenaarseweg 72, 2333 AL Leiden, The Netherlands*

[2]*Department of Pattern Recognition, Faculty of Applied Physics, Delft University of Technology, 2628 CJ Delft, The Netherlands*

INTRODUCTION

Photobleaching is a dynamic process in which fluorochrome molecules undergo photo-induced chemical destruction upon exposure to excitation light and thus lose their ability to fluoresce. The photobleaching phenomenon has been the basis of many fluorescence measurement techniques developed and successfully applied since the 1970's.

The mechanisms of photobleaching in biological objects are not yet well-understood. In microscopy, fluorochrome molecules are chemically bound to targets of interest (such as DNA, RNA, protein, or other cellular components) in which the chemical micro-environment is very complex, often differs from one specimen to another, and is very difficult to control. Although a single-exponential (or first-order) process is often used as a basis for the photobleaching techniques in microscopy, the experimental data from many studies deviate from a pure single-exponential function $I = Be^{-kt}$ (Benson et al. 1985, Koppel et al. 1989, and Rigaut et al. 1991).

The study reported here is aimed at a systematic analysis of photobleaching kinetics in microscopy. It focuses on the photobleaching process of fluorescein alone.

PHOTOCHEMICAL AND PHOTOPHYSICAL BACKGROUND

Lindqvist and co-worker (Lindqvist 1960 and Kasche et al. 1964) demonstrated that the triplet excited state fluorescein molecules became depopulated via two major pathways: the reaction between a triplet and another triplet or a ground state dye molecule (Dye-Dye mechanism); and the reaction between a triplet dye molecule and an oxygen molecule (Dye-Oxygen mechanism). These reactions, in turn, were shown to produce the transient semi-reduced and semi-oxidized forms of the dye triplet, and then became non-fluorescent photo-product or were reverted back to the ground state molecules.

To study the photobleaching behavior of fluorescein, all of the photochemical reactions from the studies of Lindqvist and Kasche are incorporated into a model described by the following six coupled differential equations:

$$\frac{d}{dt}[N_s(t) = [k_d N_{s*}(t) + k_1 N_{T*}(t) + k_2 N_{T*}^2(t) + k_3 N_{T*}(t) N_s(t) + k_6 N_{T*}(t) N_x(t) + k_7 N_{T*}(t) N_R(t) + k_8 N_{T*}(t) N_{o2}(t)] - [k_a N_s(t) + k_5 N_{T*}(t) N_s(t)]$$

$$\frac{d}{dt}[N_{s*}(t) = k_d N_s(t) - [k_d N_{s*}(t) + k_{isc} N_{s*}(t)]$$

$$\frac{d}{dt}[N_{T*}(t)] = k_{isc} N_{s*}(t) - [k_1 N_{T*}(t) + k_2 N_{T*}^2(t) + k_3 N_{T*}(t) N_s(t) + 2 k_4 N_{T*}^2(t) + k_5 N_{T*} N_s(t) + k_6 N_{T*}(t) N_x(t) + k_7 N_{T*}(t) N_R(t) + k_8 N_{T*}(t) N_{o2}(t) + k_9 N_{T*}(t) N_{o2}(t)] \quad \text{Eq. 1}$$

$$\frac{d}{dt}[N_x(t)] = k_4 N_{T*}^2(t) + k_5 N_{T*}(t) N_s(t) + k_9 N_{T*}(t) N_{o2}(t)$$

$$\frac{d}{dt}[N_R(t)] = k_4 N_{T*}^2(t) + k_5 N_{T*}(t) N_s(t)$$

$$\frac{d}{dt}[N_{o2}(t) = -k_9 N_{T*}(t) N_{o2}(t)$$

where S, S*, T*, X and R refer to the singlet ground, singlet excited, triplet excited, semi-oxidized and semi-reduced state of fluorescein, respectively, and N refers to the molecular population. In this system, k_1 to k_9 are those derived by Lindqvist and Kasche (Lindqvist 1960, Kasche 1964) for the pH range in the current study. The non-linearity introduced by the bimolecular processes makes it extremely difficult to find an analytical solution for the system in Eq. 1. Instead, an efficient iterative numerical method has to be used to study the photobleaching kinetics of fluorescein.

MATERIALS AND METHODS

Study of Kinetics by Mathematical Simulation

The photobleaching kinetics was monitored by numerically solving the system of ODE's using the highly-efficient software package "Livermore Solver for Ordinary Differential Equations" (LSODE) (Hindmarsh 1983) and was customized for the current study. A strategy of a dynamically adjusted step size took into consideration the drastically different time scales originating from the nanosecond singlet excited state lifetime and micro- to milli-second triplet state lifetime (a so-called stiff problem).

Simulation of the photobleaching process of free fluorescein in solution and bound fluorescein in microscopy was accomplished by setting the appropriate initial conditions and recording the population change of each energy state over time. For the simulation, only the excitation intensity and fluorochrome concentration were varied to closely resemble the experimental conditions, and all other rate constants are intrinsic to fluorescein for the pH used in the present study, and were quoted directly from Lindqvist.

Free Fluorescein in Solution

A fluorescein sodium solution of 0.01 μM was then placed in three cuvettes: (1) control sample, which was not bleached, (2) air-saturated sample, and (3) deoxygenated sample, from which oxygen was purged by flushing argon gas for 15 minutes. A Leitz DM epi-fluorescence microscope with a 100W mercury arc lamp and a 450-490 nm excitation filter block was used as a bleaching light source.

Bound Fluorescein in Microscopy

Fluorescein surface-labeled microspheres were centrifuged onto standard microscope slides. The slides were air-dried in the dark and embedded in PBS in the absence of anti-fading agents.

Ficol-isolated human lymphocytes on glass slides were *in situ* hybridized and fluorescein molecules were directly (without antigen-antibody complex or spacer molecules) attached to probes specific for the centromeric region of chromosome 1. The preparation was embedded under a cover slip in PBS.

RESULTS AND DISCUSSIONS

The experimentally derived bleaching curves and simulated kinetic curves demonstrated that the simulation very closely resembled the bleaching behavior observed in the actual experiment, both for free and bound fluorescein. For simulated air-saturated fluorescein solution, the ground state depletion was completely described by a single-exponential function with the least-square residual very close to zero. The build-up of the bleached dye population was largely due to the D-O mechanism.

For both the experimentally-derived and the simulated conventional fluorescence microscopy case, the kinetic curve of the ground state depletion deviated significantly from a single-exponential function. The build-up of the bleached dye population was predominantly due to the D-D mechanism.

Since the D-O mechanism consists of only one pseudo-unimolecular reaction leading to the bleached dye molecules, the bleaching behavior will be a single-exponential process in the absence of all D-D reactions. In the simulation of fluorescein in solution, where N_S is low and $N_S << N_{O2}$, the probability of a reaction between dye molecules is very low. This probability is governed only by the concentration (or the intermolecular distance) of the reacting molecules, since the rate of reaction is constant at a given temperature. The photobleaching in this case is primarily caused by the reaction between a dye molecule and an oxygen molecule, since the intermolecular distance between an oxygen molecule and a dye molecule is smaller than that between the dye molecules. Photobleaching then shows a single-exponential behavior.

On the other hand, in microscopy where fluorescein molecules are bound to targets of a very small surface area or volume, the average in-

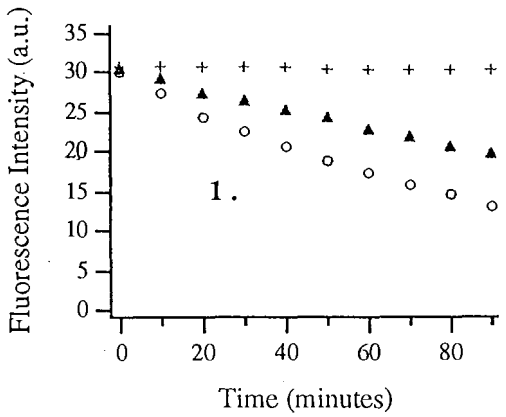

Fig. 1. The photobleaching curve of free fluorescein solution.

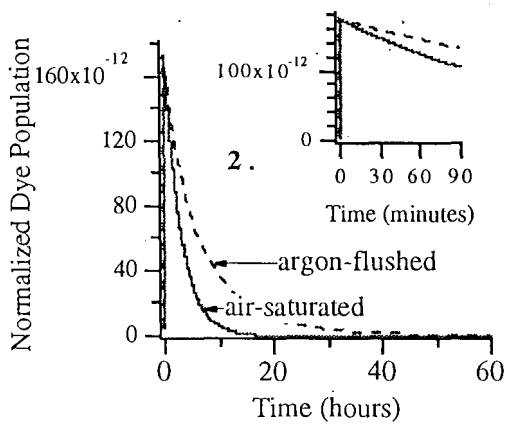

Fig. 2. Simulation for free fluorescein in air-saturated and argon-flushed solutions.

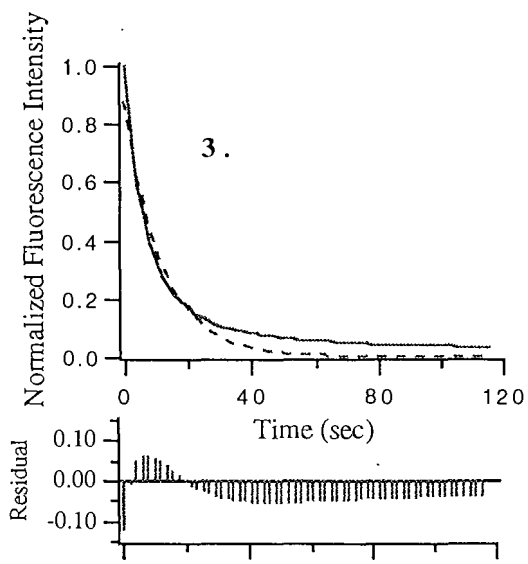

Fig. 3. The photobleaching curve of the centromeric region of chromosome 1 in a human lymphocyte. (– data, --- single-exponential fit)

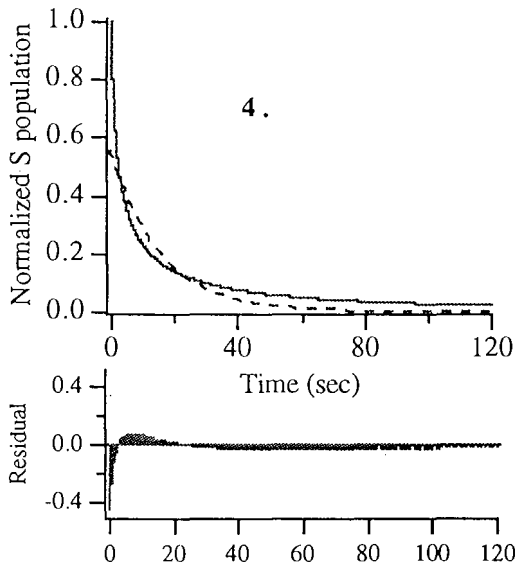

Fig. 4. Simulation for bound fluorescein in conventional fluorescence microscopy. (– simulated data, --- single-exponential fit.)

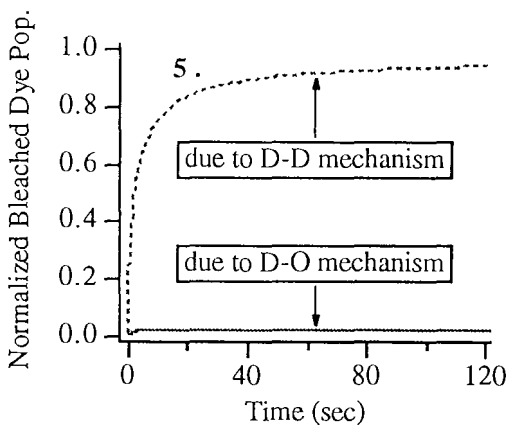

Fig. 5. Formation of the bleached molecules due to the different bleaching mechanisms (for the same case as in Fig. 4.)

termolecular distance of fluorescein molecules is smaller than the distance between a fluorescein molecule and oxygen. A triplet dye molecule is therefore more likely to react with another dye molecule than in solution. The high local density of fluorescein molecules promotes the proximity-induced D-D reactions. Since the D-D mechanism involves more than one bimolecular reaction (and thus more than one exponential term) leading to the bleached dye molecules, the bleaching behavior will not be single-exponential even in the absence of the D-O reactions.

CONCLUSION AND WORK IN PROGRESS

The present study has addressed a fundamental question about the photobleaching mechanism of fluorescein in microscopy. It has demonstrated through both experimental and theoretical methods that the single-exponential behavior is only a special case of the bleaching process when the average intermolecular distance of fluorescein is significantly greater than the average distance to oxygen, and that the photobleaching process of bound fluorescein in microscopy is in general not a single-exponential process. Further studies are being carried out to provide additional photophysical evidence for the role of the triplet in the photobleaching of fluorescein in microscopy, the results of which will be presented at the conference. The improved understanding of photobleaching mechanism in microscopy will have a direct application in quantitation of fluorescence emission.

REFERENCES

Benson DM, J Bryan, AL Plant, AM Gotto, Jr., L. C. Smith. 1985. Digital imaging fluorescence microscopy: Spatial heterogeneity of photobleaching rate constants in individual cells. *J. Cell Biol.* **100:** 1309-1323.

Hindmarsh AC. 1983. ODEPACK, a systematized collection of ODE solvers. *In:* Scientific Computing. RS Stepleman, editor. North-Holland, Amsterdam. 55-64.

Kasche, V, L. Lindqvist. 1964. Reactions between the triplet state of fluorescein and oxygen. *J. Phys. Chem.* **68:** 817-823.

Koppel DE, C Carlson, H Smilowitz. 1989. Analysis of heterogeneous fluorescence photobleaching by video kinetics imaging: the method of cumulants. *J. Microsc.* **155:** 199-206.

Lindqvist L. 1960. A flash photolysis study of fluorescein. *Arkiv för Kemi* **16:** 79-138.

Rigaut JP, J Vassy. 1991. High-resolution three-dimensional images from confocal scanning laser microscopy. Quantitative study and mathematical correction of the effects from bleaching and fluorescence attenuation in depth. *Analyt. Quant. Cytol. Histol.* **13:** 223-232.

Usui Y, K Itoh, M Koizumi. 1965. Switch-over of the mechanism of the primary processes in the photo-oxidation of xanthene dyes as revealed by the oxygen consumption experiments. *Bull. Chem. Soc. Japan* **38:** 1015-1022.

Zoological Studies 34, Supplement I (1995)

Zoological Studies

Recent Developments in Non-linear Laser Microscopy Illuminated by Two Photon Excitation

Watt W. Webb

Applied Physics and Developmental Resource for Biophysical Imaging and Optoelectronics, Cornell University, Ithaca, N.Y. 14853, USA

Non linear laser microscopy responds to the challenge of fundamental problems in biological science by providing the means for microscopic imaging of the dynamical microchemistry and for microscopic pharmacology in functional tissues and cells.

Simultaneous interaction of two low energy long wavelength (deep red) photons with a chromophore molecule adds their energies to excite molecular transitions that ordinarily absorb ultraviolet or visible light. The 100 femto second pulses of a strongly focused mode locked laser beam provide high peak intensity in the focal volume for a localized source of virtually simultaneous photons at about 10^{22} photons per second. Because two photon excitation is intrinsically limited to the focal volume there is no out of focus background, photobleaching or photodamage. Photoactivation of caged bioeffector molecules, such as neurotransmitters, can be localized to a submicron focal volume and released on microsecond to millisecond time scales for dynamical micropharmacology experiments. Because two photon excitation eliminates the need for confocal and ultraviolet optics it allows sharp, high efficiency fluorescence imaging deep within thick preparations such as 100μm thick hippocampal brain slices that strongly scatter light of short wavelength.

Ratio imaging of the calcium indicator Indo 1 using visible light of ~ 695 nm wavelength has routinely provided 3-dimensional (3-d) resolved imaging of cytoplasmic calcium at 4 images per second, and 3-d resolved linear scans at 1000 per second. True video rate 3-d resolved fluorescence imaging at 30 images per second has recently been obtained using two photon line illumination.

Instrumentation for two photon excitation laser scanning microscopy has been developed to a stage ready for adaptation to industrial production. The two photon excitation cross sections and spectra of many familiar fluorophores have been measured for the first time with the pleasing result that the optimum two photon excitation wavelengths are frequently far shorter than twice the one photon excitation wavelength as the simplest models had suggested. Therefore many, if not most, fluorescent markers and indicators that are commonly used in biological research can be excited within the convenient range of the commercially available titanium sapphire mode locked femtosecond pulsed lasers. However shorter wavelengths are preferred for some photochemical applications. The emission spectra of these fluorophores are essentially the same with two photon excitation as with one photon excitation.

Applications of two photon excitation in laser scanning microscopy that will be illustrated as time allows include dynamical 3-d resolved imaging of (1) cytoplasmic calcium waves, sparks and signals in several tissues, (2) neurotransmitter receptor function on cell surfaces by spatially resolved release of caged neurotransmitters, (3) nuclear distribution during embryonic development, (4) chromosome arrangements during meiosis, (5) NADH imaging of metabolic state, and others, Quantitation methods for micro pharmacology including localized calcium release, caged neurotransmitter release and 3-d diffusion measurements will be illustrated.

Some recent publications on biological applications of two photon excitation are listed for further reference to relevant literature.

REFERENCES

Denk W, DW Piston, WW Webb. 1994. Two-photon molecular excitation in laser scanning microscopy. Handbook of Biological Confocal Microscopy, ed. by J. Pawley (Plenum 1995)

Denk W, JH Strickler, WW Webb. 1990. Two-photon laser scan-

ning fluorescence microscopy. Science **248:** 73-76.

Denk W. 1994. Two-photon scanning photochemical microscopy: Mapping ligand-gated ion channel distributions , Proc. Natl. Acad. Sci. **91:** 6629-6633.

Denk W, KR Delaney, A Gelperin, D Kleinfeld, BW Strowbridge, DW Tank, R Yuste. 1994. Anatomical and functional imaging of neurons using 2-photon laser scanning microscopy. Journal of Neuroscience Methods **54:** 151-162.

Piston DW, MB Kirby, H Cheng, WJ Lederer, WW Webb. 1994. Two-photon fluorescence excitation in laser scanning microscopy images calcium ion activity in three dimensions. Applied Optics **33:** 662-669.

Piston DW, DR Sandison, WW Webb. 1992. Time-resolved fluorescence imaging and background rejection by two-photon excitation in laser scanning microscopy. SPIE. **1640:** 379-390.

Strickler JH, WW Webb. 1991. Three-dimensional optical data storage in refractive media by two-photon point excitation. Opt. Lett. **16:** 1780-82.

Strickler JH, WW Webb. 1991. Two-photon excitation in laser scanning fluorescence microscopy. SPIE. **1398:** 107-117.

Webb WW. 1990. Two photon excitation in laser scanning fluorescence microscopy. In transactions of the royal microscopy Society, New Series Volume 1: MICRO 90, ed. H. Y. Elder (Adam Hilger, Bristol 1990), pp. 445-450.

Williams RM, DW Piston, WW Webb. 1994. Two photon molecular excitation provides intrinsic three dimensional resolution for laser-based microscopy and microphotochemistry. FASEB Journal **8:** 804-813.

Zoological Studies 34, Supplement I (1995)

Zoological Studies

Contrast, Resolution, Bleaching and Statistics in Confocal Microscopy

James B. Pawley
Department of Zoology, University of Wisconsin, Madison, 53706, USA

Although those using the transmission electron microscope (TEM) have long been accustomed to thinking of the resolution of their instrument as being usefully defined only in terms of contrast, until quite recently it was common for those involved in biological light microscopy to speak of the resolution of their instruments in some sort of absolute sense. In part, this due to the fact that, as spherical aberration cannot be corrected in the TEM, the contrast transfer function (CTF) of the TEM varies with defocus in a complex manner: oscillating in sign across the zero-contrast line as one proceeds to higher spatial frequencies. In practice, the absolute TEM information-limit is set not by diffraction but by the limited coherence of the source and by electro-magnetic instabilities which combine to cause the "envelope function" of the CTF to decline steadily at higher spatial frequencies. This complexity forces the user to explicitly consider the CTF in order to interpret high-resolution TEM images.

In contrast, when operated with absorption or epi-fluorescence contrast, the CTF of a diffraction-limited light microscope goes obediently to zero in a fairly simple manner that holds few surprises and, for most purposes, is adequately summarized by the Rayleigh Criterion. At the other extreme, the many biological applications of high-resolution LM imaging often involve interference effects such as differential-interference contrast (DIC) and are used in combination with video-based image enhancement techniques. The CTF of such a complex system is perhaps too complicated to encourage theoretical analysis.

Unfortunately, this general lack of attention to the relationship between contrast and resolution in LM has tended to obscure a simple but important fact: that the contrast produced by small features is transmitted to the detector much less efficiently than that of larger features. (i.e. that small features inevitably appear in the image with low contrast.) The purpose of this paper is to focus on the way this fact interacts with signal level and photobleaching to place a practical limit on resolution in fluorescence confocal imaging.

Although contrast is an essential ingredient in our ability to "see" a feature, the signal-to-noise ratio (S/N) of the data is equally important. These two factors were first combined to produce a measure of "visibility" by Rose (1948) who quantified the relationship between the minimum size that a feature in a television image must have in order to be seen as different from its surroundings, δ, the contrast and S/N. A similar analysis was later applied to TEM images by Glaeser (1971, 1975) who was trying to image molecules that were damaged by the electron beam illuminating the specimen. He wanted to calculate the minimum dose of illumination necessary to produce a useable image and derived the equation, $\delta = A/C_i(f \bullet n)^{1/2}$ where n is the average of number quanta/unit-area (q/pix), at the specimen and these are utilized to form the image with a fractional efficiency, f. C_i is the contrast (in %) intrinsic to the interaction between the specimen and the impinging radiation, as transmitted by the microscope. This formulation assumes that the only source of noise is the statistical variation in **n** as described by Poisson statistics. A is a constant that must be ~ 5 for a single pixel to be "seen" above the local background by a human observer but which is smaller for larger image features.

In practice, this equation shows that in an image with only 2 gray levels (feature and background), the intensity of a feature one pixel in size must be >25q/pix in order to be dis-tinguishable from a background of 1 q/pixel. In other words, the staining ratio would have to be at least 25:1 even if the microscope did not reduce the contrast of the feature at all. However, if the contrast be-

tween two adjacent point features were reduced to that of the Rayleigh Criterion (~25% darker at the midpoint between the features), the peak brightness would have to be about 400 q/pix to separate the 75% signal from the 100% peaks by 5x the statistical noise level. This represents a 16x increase in signal that must be acquired and, hence, in the dose of illumination applied to the specimen. Dropping the contrast to 10% (making the dip in the intensity between the peaks only 90% of the peak value) implies a 100x increase in dose.

Now that confocal-fluorescence microscopy is beginning to approach diffraction-limited resolution, it is easy to demonstrate the importance of this relationship. Fig. 1 shows a series of confocal images made with only a few photons/ pixel, of part of a test specimen consisting of a metal-film-on-glass pattern over a "sea" of fluorescent oil (Centonze and Pawley 1995). As the average peak signal level varies from (a): 2, (b): 4, (c): 8 to (d): 16 counts/pixel, the visibility of the bars in the smaller patches improves. This happens not because the optical resolution changes but because by we are now counting enough particles to permit such low-contrast features to be recognized above the noise level. Unfortunately, in confocal fluorescence microscopy, both fluorescence saturation and photobleaching prevent an arbitrary increase in the signal level.

This analysis emphasizes again the importance of increasing the quantum efficiency (QE) of the detector in the confocal microscope above its present level of 3-20%. It also points to the crucial importance of S/N in any effort to compare the relative photon efficiency for 3D-microscopical imaging of confocal/fluorescence microscopy vs. the widefield/deconvolution technique. While the CCD detector used with the latter technique has a clear edge in QE, the contrast produced in the recorded data is greatly reduced if highly stained features are located above or below the

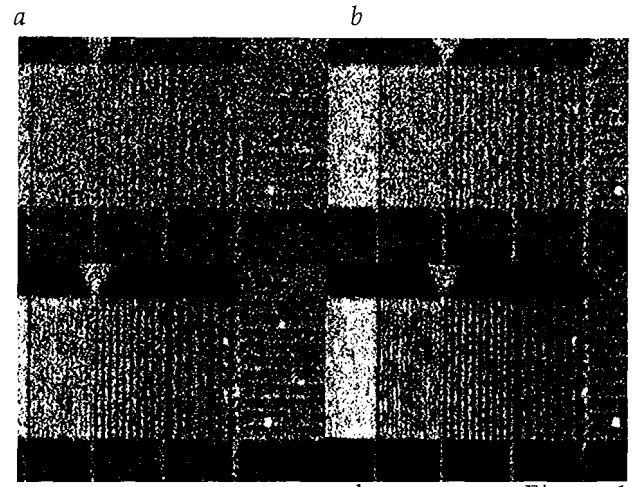

Figure 1

plane of focus. It is as yet unclear where in the range of staining sparcity, what is gained by the widefield method in terms of QE (and hence improved S/N) becomes more important than that which is lost by the reduced contrast of the recorded data. (i.e. the stain contrast as modified by the point-spread function of the microscope). What is clear is that it is most important to increase the "use factor," f, as much as possible and, in the case of confocal-fluorescence microscopy, this means increasing detector quantum efficiency.

REFERENCES

Rose A. 1948. Television pickup tubes and the problem of noise. Adv. Electron **1:** 131. Glaeser, RM 1971. Limitations to significant information in biological electron microscopy as a result of radiation damage. J.Ultrastruct.Res. **36:** 466.

Glaeser RM. 1975. Radiation damage and biological electron microscopy. In: Physical Aspects of Electron Microscopy and Microbeam Analysis, edited by Siegel, B.M and Beaman, D.R. NY: Wiley and Sons, 205-230.

Centonze V, J Pawley. 1995. "Tutorial on practical confocal microscopy and use of the confocal test specimen" in Handbook of Biological Confocal Microscopy, 2nd Edition. (Ed. J. Pawley) Plenum Press, NY 549-569.

Zoological Studies 34, Supplement I (1995)

Zoological Studies

Three-Dimensional Structure of Calcium Release Channel from Skeletal Muscle by Electron Cryomicroscopy and Angular Reconstitution

Irina Serysheva[1], Elena V. Orlova[1,3], Wah Chiu[1], Michael B. Sherman[1], Susan L. Hamilton[2] and Marin van Heel[3]

[1]*Department of Biochemistry, Baylor College of Medicine, One Baylor Plaza, Houston, Texas 77030, USA*

[2]*Department of Molecular Physiology and Biophysics, Baylor College of Medicine, One Baylor Plaza, Houston, Texas 77030, USA*

[3]*Fritz Haber Institute of the Max Planck Society Faradayweg 4-6, D-14195 Berlin, Germany*

Electron cryomicroscopy has been advanced to be a unique tool to study macromolecular assemblies which cannot be readily tackled by X-ray crystallography and NMR (Chiu 1993). The reliability of the technique has been illustrated by a number of examples which the X-ray structures of the individual components are known (Jeng et al. 1989, Wang et al. 1992). For the examination of biological structures at different functional or chemical states, advantages of using ice-embedded specimens have been well established (Chiu 1986). For reconstructing the 3-dimensional structures of single particles, the approach of Frank's group is based on the assumption that the particles in the electron images would have the same orientations and their method has been applied to study a variety of specimens (Penczek et al. 1992, Radermacher et al. 1994). An alternative approach of performing three-dimensional reconstruction with particles at random orientations called angular reconstitution has been proposed by van Heel (van Heel 1987, van Heel et al. 1992). This paper reports the first biological application of the angular reconstitution to determine the three-dimensional structure of the Ca^{2+} release channel from rabbit skeletal muscle in a closed state (Serysheva et al. 1995).

The calcium release channel is located in the gap between the transverse tubular system and the junctional membrane of the terminal cisternae of SR. It contains a membrane spanning region and a soluble region with 4 homotetramer of total molecular mass of 2.4 million daltons. The Ca^{2+}-release channel is solubilized and purified from rabbit skeletal muscle (Hawkes et al. 1989). The Ca^{2+}-release channel protein was driven towards its closed state by depleting the Ca^{2+} with 1 mM EGTA in 300 mM KCl, 10 mM MOPS (pH 7.4). Figure 1 shows an electron image of the ice-embedded Ca^{2+}-release channel with a moderate contrast. Although a good number of the channel proteins are oriented with its square shape face perpendicular to the plane of the grid, we have found single channel proteins in all possible orientations.

The 3D structure of the Ca^{2+} release channel seen from two different directions is shown in Figure 2. The view of the channel protein facing the SR lumen side shows an outer square and an inner square, which are rotated with respect to each other over an angle of ~ 40° (top panel). The view of the protein, facing the cytoplasm towards the transverse tubule, shows a central opening of ~ 50 Å in diameter (bottom panel). The rim of the central channel forms a continuous network that extends to the peripheral mass. At the corners of the peripheral mass is a most characteristic domain shaped like a closed laboratory clamp with four fingers. "Handles" or "bridging domains"

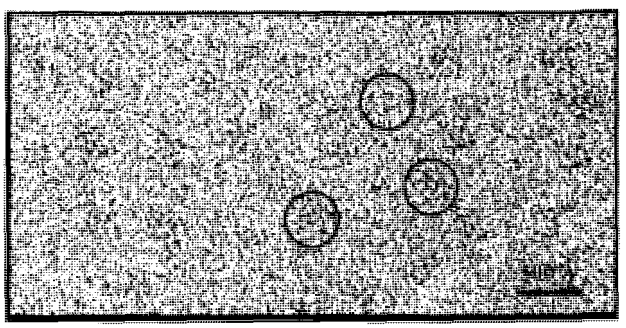

Fig. 1. 100 kV electron image of Ca^{2+} release channel embedded in ice. Several images of the individual channel proteins are circled and appear to have different orientations.

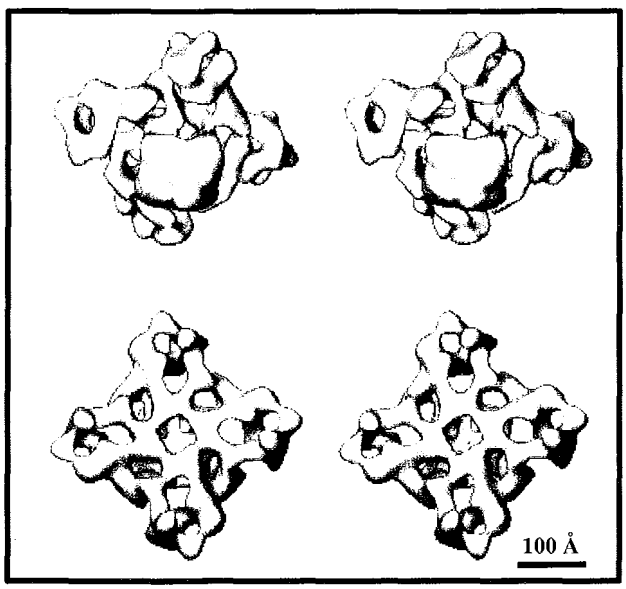

Fig. 2. Stereo views of the 3D structure of ice-embedded Ca^{2+}-release channel in closed state as viewed from the SR lumen side (top panel) and from the cytoplasmic side (bottom panel). The volume of the reconstruction at the chosen density threshold level corresponds to a mass of 2.4 million daltons assuming a protein density of 1.35 g/cm^3. It is a homotetramer with a membrane and a cytoplasmic region. The image reconstruction was carried out with IMAGICS software as following: The selected particle images were aligned by iterative multi-reference alignment techniques, and sorted into homogeneous classes of similar images by automatic multivariate statistical classification procedures. All molecular images belonging to the same class were averaged to produce noise-free class averages or characteristic views. The class averages were assigned to angles by angular reconstitution technique. The 3D reconstruction was computed and used for realignment to improve the image statistics and accuracy in angular determinations. The final 3D map was computed from 150 class averages with a sufficiently uniform distribution of Euler angles to attain 30 Å isotropic resolution. The resolution of the structure was estimated to be ~30 Å based on the Fourier shell correlation coefficients of two independent

interconnect the four clamps. Each of these features may represent distinct domains of the protein. As would be expected for a closed channel, there is no obvious opening of the Ca^{2+}-release channel on the lumenal side of this membrane protein.

This research has been supported by grants from the NCRR of NIH, the W. M. Keck Foundation, and the R. Welch Foundation to W. C.; NIH and Muscular Dystrophy Association to S. L. H. and DFG to M.vH.

REFERENCES

Chiu W. 1993. What does electron cryomicroscopy provide that X-ray crystallography and NMR spectroscopy cannot? Ann. Rev. Biophys. Biomol. Struct. **22:** 233-255.

Jeng TW, RA Crowther, G Stubbs, W Chiu. 1989. Visualization of alpha-helices in tobacco mosaic virus by cryo-electron microscopy. J. Mol. Biol. **205:** 251-257.

Wang G, C Porta, Z Chen, T Baker, JE Johnson. 1992. Identification of a Fab interaction footprint site on an icosahedral virus by cryoelectron microscopy and X-ray crystallography. Nature **355:** 275-278.

Chiu W. 1986. Electron microscopy of frozen, hydrated biological specimens. Ann. Rev. Biophys. Biophys. Chem. **15:** 237-257.

Penczek P, M Radermacher, J Frank. 1992. Three-dimensional reconstruction of single particles embedded in ice. Ultramicroscopy **40:** 33-53.

Radermacher M, V Rao, R Grassucci, J Frank, AP Timerman, S Fleischer, T Wagenknecht. 1994. Cryo-electron microscopy and three-dimensional reconstruction of the calcium channel/ryanodine receptor from skeletal muscle. J. Cell Biol. **127:** 411-423.

van Heel M. 1987. Angular reconstitution: A posteriori assignment of projection directions for 3D reconstruction. Ultramicroscopy **21:** 111-124.

van Heel M, H Winkler, E Orlova, M Schatz. 1992. Structural analysis of ice-embedded single particles. Scanning Microscopy Suppl. **6:** 23-42.

Serysheva II, EV Orlova, W Chiu, MB Sherman, SL Hamilton, M van Heel. 1995. Electron cryomicroscopy and angular reconstitution to visualize the skeletal muscle calcium-release channel. Nature Structural Biology **2:** 18-24.

Hawkes MJ, M Diaz-Munoz, SL Hamilton. 1989. A procedure for purification of the ryanodine receptor from skeletal muscle. Membrane Biochemistry **8:** 133-145.

Zoological Studies 34, Supplement I (1995)

Zoological Studies

The Wigner Distribution Function, and the Special Affine Fourier Transform: Signal Processing and Optical Imaging

S. Abe[1] and J. T. Sheridan[2]

[1]*College of Science and Technology, Nihon University, 7-24-1 Narashinodai, Chiba 274, Japan*

[2]*European Commision, Joint Research Centre (JRC), Institute for Systems Engineering and Informatics, (ISEI), Ispra (VA), I-21020, Italy*

Signal analysis is usually performed in the space (time) or spatial-frequency (frequcncy) domains through the classical Fourier transformation (FT) (Goodman 1994, Stremler 1982). Since these two domains are orthogonal to each other, information on the spatial position is completely lost when working in the spatial-frequency domain, or vice versa. However, there are situations in which it is still desirable to get information simultaneously on the position and spatial frequency of a signal. Such information is limited by the uncertainty principle.

The Wigner distribution function (WDF) (Wigner 1932) offers the representation of a signal function in terms of position and spatial-frequency variables, called the phase-space variables. (x , k) simultaneously.

Recently the concept of the fractional Fourier transformation (FRT), (Namias 1980, McBride and Kerr 1987) has been introduced to the area of optical signal processing, (Lohmann 1993, Ozaktas et al. 1994, Dorsch et al. 1994). It has been pointed out that a GRIN medium can be used to directly produce the FRT of an input field by varying its length. The FRT corresponds to the rotation of the WDF in the phase space, (Lohmann,1993).

Geometrically, in phase space, the classical FT is given by a (Pi)/2 rotation. Since the FRT allows an arbitrary rotation angle, it can avoid the above mentioned difficulty concerning the orthogonality between the two domains. Recent investigations on signal analysis based on the FRT shows how effectively the noise filtering can be realized, (Ozaktas et al. 1994, Dorsch et al. 1994). Optical generations of the FRT, using free space propagation and a lens (es) has also been proposed, (Lohmann 1993).

Here we first wish to discuss a more general class of the Fourier-type transformations. We consider the special affine transformation in the phase space, (i. e., the most general power-conserving linear transformation) and present the corresponding integral transformation of the signal function. It is referred to as the special affine Fourier transformation (SAFT), (Abe and Sheridan 1994a, Abe and Aheridan 1994b, Abe and Sheridan 1994c, Abe and Sheridan 1995). In this formulation, the FRT is the simple transformational sub-case of the rotation.

Then we apply the SAFT to standard operations in geometric optics. We show the SAFT interrelates geometric optics operations and the corresponding wave-function transformations. The operations of lens, free-space propagation, magnification, and the FRT are seen to be he Abelian subgroups of the SAFT, (Abe, Sheridan, 1994b). Next we apply the SAFT to an optical system which has small imperfections, to establish the concept of the almost-Fourier and almost-Fresnel transformations, (Abe and Sheridan 1994c).

We briefly discuss the filtering problem based on the SAFT. Such a mathematical formalism can offer an unified approach to local signal analysis. In particular, we show that the wavelet and windowed Fourier transformations are included as special cases.

Finally the FRT has also been shown to provide a new means of interpreting and analysing afocal imaging systems, (Bernardo and Soares 1994). Once again the SAFT allows more general ideas to emerge in this area.

REFERENCES

Abe S, JT Sheridan. 1994a. Generalisation of the fractional Fourier

transformation to an arbitrary lineatr lossless transformation: An operator approach. J. Phys. A, Math. Gen. **27:** 4179-4187.

Abe S, JT Sheridan. 1994b. Optical operations on wave functions as the Abelian subgroups of the special affine Fourier transformation. Opt. Lett., **9:** 1801-1803.

Abe S, JT Sheridan. 1994c. Comment on "The fractional Fourier transformation in optical propagation problems". J. Mod. Opt., Submitted and under review.

Abe S, JT Sheridan. 1995. The almost-Fourier and almost-Fresnel transformations, Opt. Comm. **133:** 358-388.

Bernardo L M, ODD Soares. 1994. Fractional Fourier transforms and imaging, J, Opt. Soc. Am. **11:** 2622-2626.

Dorsch RG, AW Lohmann, Y Bitran, D Mendlovic, HM Ozaktas, 1994. App. Opt. **33:** 7599.

Goodman JW. 1994. Introduction to Fourier optics, 2nd Edition, McGraw-Hill Co., Inc.

Lohmann A. 1993. Image lotation, Wigner rotation, and the fractional Fourier transform. J. Opt. Soc. Am. A. **10:** 2181.

McBride AC, FH Kerr. 1987. On Namias's fractional Fourier transform. Inst. Math Appl. J. Appl. **25:** 159-179.

Namias V. 1980. The fractional order Fourier transform and its applications to quantum mechanicw. J. Inst. Math. Appl. **25:** 241-165.

Ozaktas H M, B Barshan, D Mendlovic, D Onural. 1994. Convolution, filtering and multiplexing in fractional Fourier domains and their relation to chirp and wavelet transforms. J. Opt. Soc. Am A. **11:** 522-559.

Stremler FG. 1982. Introduction to communication systems, 2nd Edition, Addison-Wesley, Reading, Massachusetts.

Wigner E. 1932. On the quantum correction for the thermodynamic equilibrium. Phys. Rev. **40:** 749-759.

Zoological Studies 34, Supplement I (1995)

Zoological Studies

Sensitive Low Frequency Optomechanical Sensor

C. Th. Coutsomitros, M. Whelan and J. T. Sheridan

European Commission, Joint Research Centre, Institute for Systems Engineering and Informatics, Ispra (VA), I-21020 Italy.

In this poster recent work on the development of an optomechanical detector for weak, low fequency (0.1 - 20Hz) mechanical vibrations is presented. The device is patented, (Coutsomitros, 1993, Cousomitros and Franchi 1994), and some earlier results have previously been presented at international conferences (Coutsomitros 1994, Cousomitros et al. 1994a and b).

The detector is essentially a dynamical interferometer, coupled to and air floated optical table, Critically balanced vertical glass plates, in a set of geometries, produce between them a Fabry-Perot type interferometer, The resulting dynamical interference pattern between the two inner vibrating surfaces is then examined. The mechanical properties of the plates and the effects of the layer between the plates produce a system which is sensitive to weak low frequency mechanical excitation. The introduction of holographic gratings onto the surfaces of the plates has been found to strenghten the observable interference fringes. The device works at room temperature and pressure, is robust, and has been shown to give reproduceable results (in terms of sensitivity). Increased sensitivity with decreased temperature has also been noted.

The development of such a device requires the modelling and examination of the behaviour of optical tables and isolation equipment, at frequencies for which they are in general not designed. It also requires careful analysis of the mechanical properties of the system, including contributions due to surface tension, electrostatic charges, contact forces, thermal and mechanical properties of the glass plates, and fluid flow between the plates, A mechanical model based on these effects and assuming the existence of multiple non-resonant cavities is currently being developed.

The detector, as it currently appears, is non-optimised. Despite this fact a comparison with commercially available accelerometers show that the system appears competitive in performance and potentially cheeper to manufacture, Currently work to produce a more controlled device is being carried out.

Correlation between the variations of the interference fringes produced by the detector and a periodic mechanical excitation system, made using a rotating mass of 4Kg at distances of up to 25m, has been established. Using a high speed CCD camera and signal analysis software developed at the Department of Applied Optics of Strassbourg University further evidence for this correlation has recently been found. (Miehe, 1993, Miehe, 1994).

Other experiments involving the use of a mechanical shaker as a normalieed vibration source are also being carried out. Measurements of the transfer of the resulting vibration into the modes of the table, using ESPI and piezoelectric based accelerometers, allows an examination of the transfer of vibration between the table and the plates to be carried out.

It has also been found that the interference pattern from the parallel plate arrangement can also be stimulated into varying synchronously with an incident modulated low power (>1mW) light source. In this mode the system has characteristics in many ways analogous to those of one manufactured with a material which exhibates bulk non-linear optical Kerr effect, as the optical pathlength in the layer appears proportional to the incident intensity.

Such an arrangement offers the possibility of optically modulating an optical signal. (Coutsomitros, 1993, Coutsomitros et al. 1994a). By coating the plates with metal it might also be possible to modulate the resulting capacitors capacitance using the input optical beam. In relation to the

vibrational sensor this work makes available an alternative method to measure and test the mechanical response of the device. In this way thermal, and mechanical effects can be more carefully examined.

The use of a hypersensitive form of this dynamical interferometer to detect Newtonian graviational gradients and the forces arising due to light radiation pressure on the plates are also being examined. (Coutsomitros 1994b, Coutsomitros et al. 1994b). The sensor may also find use in seismic studies.

REFERENCES

Coutsomitros C Th. 1993. Modulateur Optique, patent n. 88184 Luxembourg 28/10/1992 and also international patent n. PCTPE93/02977, 27/10/93.

Coutsomitros C Th, M Franchi. 1993. Detecteur de arations d'une grandeur physique, patent n. 88197, 3/11/1992, Luxembourg and also international patent n. PCTPE93/02978, 27/10/93.

Coutsomitros C Th. 1994a. Dispositif de detection de microvibrations de tres faible amplitudes, patent n. P/2390 Luxembourg, 15/1/1993, and also international patent n. PCTEP94/00050, 10/1/94.

Coutsomitros C Th. 1994b. Compact hyper-sensitive interferometric sensor for gravitation measurements, First Edoardo Amaldi Conference on Grvitation Wave Experiments, Frascatti, Rome, June.

Coutsomitros C Th., A Lucia, G Volta. 1994a. All optical interferometric modulator, Frontiers in Information Optics, Kyoto, April, International Commission for Optics.

Coutsomitros C Th., A Lucia, G Volta. 1994b. Hypersensitive interferometric sensor for radiations flux measurements, Optical Methods in Bio-Medical and Environmental Sciences, Tokyo April, International Society of Optics Within Life Sciences, OWLS III.

Miehe G. 1993. Assistance Technique dans le cardre du programme Europeen "Value", Rapport de Fin d'Etude, Contract No. 5588-93-11 PC ISP F, Groupe D'Optique Appliquee, CRN Strasbourg, Universite Louis Pasteur.

Miehe G. 1994. Caracterisation d'un detecteur d'interaction de gravitation, Memoire No. 791/94, Groupe D'Optique Appliques, CRN Strasbourg, Universite Louis Pasteur.

Zoological Studies 34, Supplement I (1995)

Zoological Studies

Membrane Specializations in Skeletal Muscle Cells

H. Benjamin Peng[1], A. Afshan Ali[1], David F. Daggett[1] and Lauren P. Baker[2]

[1]*Department of Cell Biology and Anatomy, University of North Carolina, Chapel Hill, NC 27599, USA*

[2]*Department of Pharmacology, University of Washington, Seattle, WA 98195, USA*

The neuromuscular junction (NMJ) and the myotendinous junction (MTJ) are two important membrane specializations of vertebrate skeletal muscle cells. At the NMJ, acetylcholine receptors (AChRs) are clustered in response to motor innervation. This clustering of AChRs ensures the rapid transmissions of signals from nerve to muscle to elicit contraction. The AChRs are stabilized at the postsynaptic membrane by a complex of cytoskeletal proteins. The MTJ, on the other hand, is the interface between the contractile apparatus and the extracellular matrix in the form of the tendon apparatus. The sarcolemma at the MTJ exhibit extensive membrane invaginations, which distribute contractile force to a large membrane area. Thus, the MTJ is structured to ensure the integrity of the sarcolemma during force transmission from the myofibrils to the tendon. This specialization is also marked by an extensive array of cytoskeletal proteins.

Our lab has been interested in the cellular and molecular mechanisms involved in the development of these specializations. Using light microscopy, including conventional and confocal fluorescence microscopy, a number of proteins have been localized to these specializations, These include both structural proteins, such as talin, vinculin and dystrophin, and proteins with enzymatic activities,

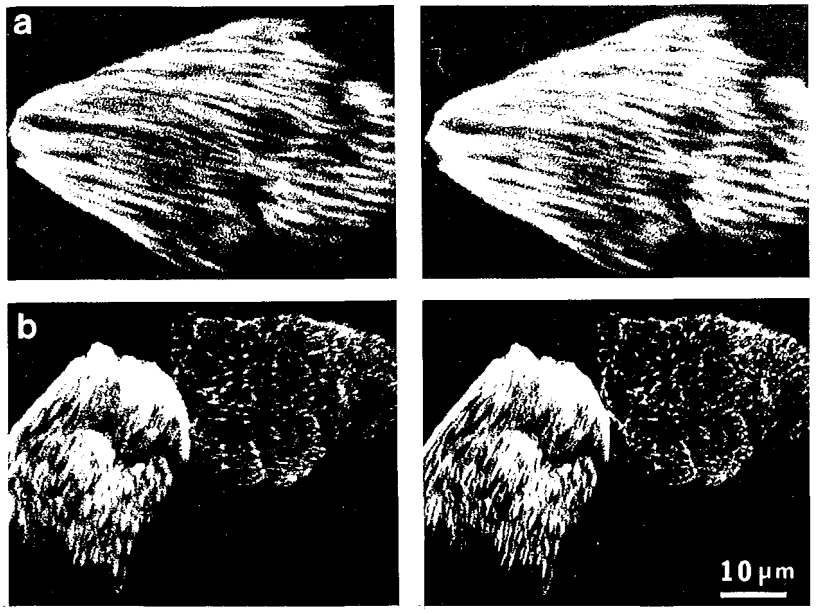

Fig. 1. Confocal stereo views of the myotendinous junction (MTJ). Dissociated single *Xenopus* myotomal muscle fibers were labeled with an antibody against dystrophin which is highly concentrated along membrane invaginations at the MTJ. These invaginations are seen as longitudinal streaks at the end of muscle fiber. (a) A longitudinal view. The sample was optically sectioned at 2 μm intervals and a stack of 23 images were superimposed. (b) Longitudinal and end-on views. The sample was optically sectioned at 1 μm intervals and the stack contained 41 images.

such as focal adhesion kinase (FAK). However, the distribution of these proteins at these two specializations is often non-overlapping. For example, FAK is localized at the MTJ but not at the NMJ. On the other hand, AChRs and the postsynaptic 43K protein are only clustered at the NMJ. Thus, these proteins can be used as markers for these two types of specializations.

To understand the development of these specializations, we have experimented with non-cellular stimuli to induce their formation. One of the most effective stimuli to induce NMJ and MTJ is latex beads. Using cultured Xenopus muscle cells as a model, we found that both NMJ-type specialization, as evidenced by clustering of AChRs, and MTJ-type specialization, as evidenced by FAK localization, can be induced at bead-muscle contacts. By coating beads with different endogenous and exogenous molecules, we were able to make inference into the signal transduction processes. Beads coated with heparin-binding growth factors, such as basic fibroblast growth factor and the newly discovered heparin-binding growth-associated molecule (HB-GAM), were most active in inducing AChR clustering. Heparan-sulfate proteoglycan (HSPG) is a ubiquitous component of the basement membrane of a variety of cell types. Recent studies have shown that an important function of the HSPG is to serve as storage sites for certain growth factors. Factors that are bound to the HSPG are essentially immobile and thus are ideal candidates for pericellular signaling. In fact, our confocal microscopy on cultured *Xenopus* muscle cells has demonstrated that HB-GAM is localized at the cell surface in association with HSPG. This suggests that extracellular matrix-associated molecules may be the endogenous ligands for the induction of these membrane specializations. Our results are consistent with the notion that these matrix-bound ligands are locally presented to the muscle cell surface to effect the development of NMJ and MTJ.

Since the receptors for these growth factors are usually receptor tyrosine kinases (RTKs). We used phosphotyrosine antibodies to probe the signal transduction process initiated by bead presentation. Our results have shown a concentration of phosphotyrosine labeling at bead-muscle contacts as one of the earliest detectable changes. This is consistent with the notion that beads induce the local activation of RTKs at the contact site, leading to tyrosine-specific phosphorylation of substrate proteins. To identify RTKs and their substrates, we have begun to isolate specializations that are induced by beads. By removing beads from muscle cell surface, pieces of membrane with their associated specializations are often isolated in high purity. This is evidenced

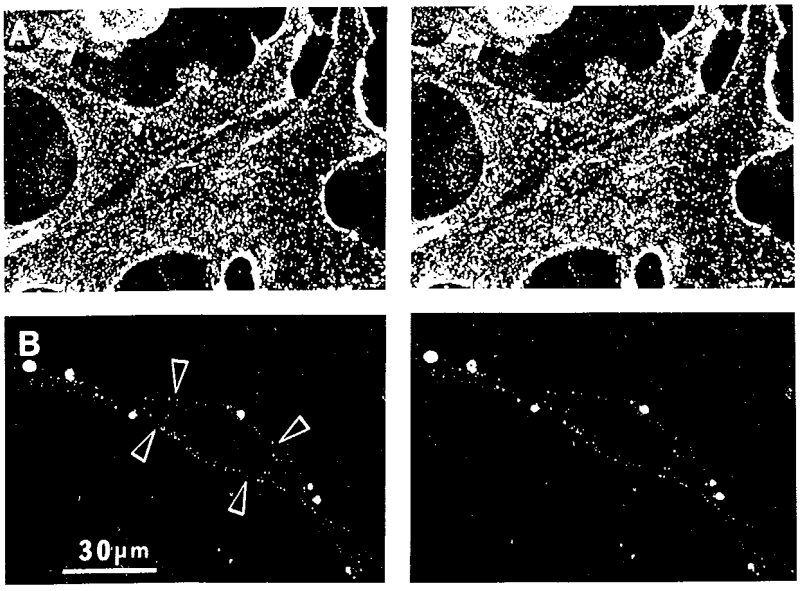

Fig. 2. Confocal stereo images of HB-GAM distribution on the surface of cultured *Xenopus* myotomal muscle cells before (A) and after (B) heparinase treatment. HB-GAM is present on the entire cell surface. Heparinase removes a significant amount of this protein from the cell surface. The arrowheads in B point to residual HB-GAM staining after enzymatic treatment. The large fluorescent objects around the cell periphery are autofluorescent yolk granules released from damaged cells during dissociation.

by fluorescence microscopy of AChR patches that are left on beads upon their removal from cells. When these bead-associated membrane patches are subjected to biochemical analysis, We found both structural proteins, Such as AChR and syntrophin, and kinases, such as mitogen-activated protein kinase, are components of the bead-associated specialization. We are hopeful that this analysis may lead us into the identification of essential components of the signal transduction complex in the induction of these sarcolemmal specializations in skeletal muscle cells.

Zoological Studies 34, Supplement I (1995)

Zoological Studies

Application of Rigorous Numerical Techniques to the Calculation of Images in Scanning Optical Microscopy

J. F. Aguilar and E. R. Méndez

División de Física Aplicada Centro de Investigación Científica y de Educación Superior de Ensenada Apdo Postal 2732 Ensenada, Baja California, México.

The standard approach to describe the process of image formation in optical microscopy is based on scalar wave theory and on approximate models for describing the interaction of the optical field with the structure of the object. The validity of this approach becomes questionable when the object contains features comparable to the wavelength, and when the structures are optically thick.

In this work, we consider the problem of image formation in scanning optical microscopy. Under the assumption that the sample is one-dimensional and assuming also a one-dimensional optical system, we have developed a fairly rigorous approach to describe the image formation process. By one dimensional we mean a sample whose properties, when referred to a cartesian coordinate system, may present changes along, say, the x direction and are constant along the y one. We divide the process of image formation in the scanning optical microscope into three parts: We first need a mathematical description of the field incident on the sample. In the second stage, we need an accurate model to describe the interaction between this field and the sample. This is essentially a scattering problem, and there is no simple way of solving problems of this kind. The main feature of our work is that this aspect of the problem is approached in a fairly rigorous manner. In the third stage, the reflected light is propagated back through the optical system toward the detector. The angular size and position of the detector can be rather arbitrary and in fact define the mode of image formation. The image is formed on a point-by-point basis by scanning the sample under this point spread function. Various modes of image formation have been considered, including coherent, partially coherent, dark field and confocal. The sample is normally assumed to be a surface relief object ruled on a homogeneous material characterized by its complex refractive index, but calculations with layered objects have also been performed.

To illustrate the method, and for brevity, we restrict the discussion here to the case of a perfectly conducting surface illuminated by s-polarized light. As mentioned, we first need to provide an adequate description of the beam incident on the surface. For an s-polarized beam the only non-zero component of the electric field is its y component. We assume that the lens is diffraction limited and, thus, that the complex amplitude associated with the incident field on the plane z=0 is a "sinc" function. This in-cident field is propagated to out-of-focus planes using angular spectrum techniques. It results in the following expression (Aguilar and Méndez, 1994):

$$E_i(u,v)=\exp[-i(\frac{u}{\alpha_m^2}+\frac{v^2}{2u})]\sqrt{\frac{\pi}{4u}}\,[f(\sqrt{\frac{u}{\pi}}+\frac{v}{\sqrt{u\pi}})+f(\sqrt{\frac{u}{\pi}}-\frac{v}{\sqrt{u\pi}})], \quad (1)$$

where

$$f(x)=\int_0^x \exp(i\frac{\pi}{2}\xi^2)\,d\xi, \quad (2)$$

the optical coordinates v and u are given by

$$u=k\alpha_m^2 z,$$
$$v=k\alpha_m^2 x,$$

$k=2\pi/\lambda$ is the wavenumber, and the constant α_m

represents the numerical aperture of the system.

Due to our assumptions, after interacting with the surface, the field remains s polarized, and this simplifies matters considerably; throughout the whole process of image formation we then only have to deal with the y component of the electric field. The surface profile is represented by the function $z=\zeta(x)$, and using Green's integral theorem, one can express the total field above the surface as the sum of the incident and scattered fields:

$$E(x,z)=E_i(x,z)+\frac{1}{4i}\int_{-L/2}^{L/2} H_0^{(1)}(k[(x-x')^2 + (z-\zeta(x))^2]^{1/2})F(x')dx', \quad (3)$$

where

$$F(x')=[-\zeta'(x')\frac{\partial}{\partial x'}+\frac{\partial}{\partial z'}]E(x',z'). \quad (4)$$

Here, $H_0^{(1)}$ represents a Hankel function of the first kind and order zero, and L represents the length of the surface. The second term on the right hand side of Eq. (3) represents the scattered field, which is determined by the source function F(x), related to the normal derivative of the field on the surface.

By taking the limit $(x,z) \rightarrow [x_0,\zeta(x_0)]$, and using the fact that the total electric field on the surface must vanish, it is possible to write an integral equation that determines the source function F(x). We find that

$$E_i(x_0)=\lim_{\eta\rightarrow 0}\int_{-L/2}^{L/2} L_0(x_0,x',\eta)F(x')dx', \quad (5)$$

where

$$L_0(x_0,x',\eta)=-\frac{1}{4i}\int_{-L/2}^{L/2} H_0^{(1)}(k[(x-x')^2 + (z-\zeta(x))^2]^{1/2})F(x')dx', \quad (6)$$

with $\eta>0$.

The integral equation expressed by Eq. (5) was first converted into a matrix equation and then, to find F(x), the matrix equation was solved employing standard numerical techniques. The intensity reaching the detector can then be calculated for a given geometry. This provides the signal associated with a particular position of the surface along the x direction.

Rigorous images can be calculated in this fashion. Effects such as multiple scattering and changes in the state of polarization of the scattered light are taken into account. We have found that for steplike objects the Kirchhoff approximation gives images that are in good agreement with those obtained with the integral equation approach. A similar conclusion has been reached for the case of ridgelike structures. However, for the case of groovelike structures, multiple scattering is possible and this makes the Kirchhoff approximation inadequate to describe the image formation process. This effect is more pronounced in partially coherent modes of image formation.

The confocal scanning optical microscope, with its depth discrimination property, can also be used to estimate the profile of highly reflecting samples. In the profilometer mode of operation the sample is scanned along the z direction, and the position at which the maximum intensity is reached is associated with the relative height of the surface at that particular position of the sample along the x axis. For this case, we have found that the instrument can successfully estimate a given surface profile when:

i) - The local surface slope does not exceed a given maximum value.

ii) - The surface can be considered locally flat.

Concerning the first statement, we have proposed a criterion for the upper limit in the local slope. The second conclusion implies that the lateral resolution of the instrument is much worse when used as a profilometer than when used as an imaging system. It is also worth mentioning that unresolved features introduce spurious details in the estimated profile.

REFERENCES

Aguilar JF, ER Méndez. 1994. Imaging optically thick objects in scanning microscopy: perfectly conducting surfaces. J. Opt. Soc. Am. **A 11:** 155-167.

Zoological Studies 34, Supplement I (1995)

Zoological Studies

Cryo-electron Microscopy, Antibody Labeling, and Image Analysis Reveals Macromolecular Interactions in Enveloped Alphaviruses

R. Holland Cheng, Norman H. Olson, Timothy S. Baker, Richard J. Kuhn and Thomas J. Smith
Department of Biological Sciences, Purdue University, West Lafayette, IN 47907, USA

Electron microscopy is an excellent tool for visualizing hydrated structures of biological specimens (Stewart and Vigers 1986), especially viruses and complexes of viral-cellular macromolecules that are too large to study with current X-ray crystallographic methods (Baker 1992). With low temperature, low dose, and image analysis procedures, cryo-electron microscopy (cryoEM) has proven to be an effective means to reveal both external and internal features of biological specimens (Cheng et al. 1994) including enveloped viruses (Cheng et al. 1995). Aid with monoclonal antibody labeling, two alphaviruses were used as a model system of enveloped viruses to study virus: host recognition.

Ross River virus (RR) and Sindbis virus (SIN), members from the SF and the SIN groups respectively, were chosen for antibody binding studies since both native structures were known (Cheng et al. 1995, Strauss and Strauss1994). The 27 closely-related, icosahedral, positive strand RNA viruses are subdivided into three major groups with an extremely wide host range. Three-dimensional structures of RR and SIN, complexed with antibody Fab fragments, were determined to a resolution of about 2.7nm with cryoEM and image reconstruction. Two structures clearly show that the Fab fragments bind to the extreme apexes of the trimeric glycoproteins (Fig. 1). This region of the spike appears to be composed of E2 glycoprotein since the epitopes that antibodies recognize are on E2. Moreover, the binding domains of the neutralizing antibodies were shown to be involved in virus; receptor binding (Vrati 1988, Stanley 1986). The overlap of the antibody foot-prints in two of the three type groups suggests that the tip region of the spikes is conserved for host recognition in alphaviruses.

Knowledge of the virus structure allows us not only to model the atomic structure of the capsid protein into a monomeric packing arrangement inside the viral envelope (Fig. 1), but also to map the host protein into a monomeric packing arrangement inside the viral envelope (Fig. 1), but also to map the host recognition sites on the surface of the glycoprotein (Chemg et al. 1995, Choi et al. 1991, Liu et al. 1994). On the basis of our model-building studies, the protein residues that are predicted to be involved in protein: protein, protein: RNA, and protein: glycoprotein contacts in the nucleocapsid, can now be probed with site-directed mutagenesis and X-ray crystallography to investigate viral assembly and uncoating.

We thank Drs. Stephen Fuller, Jim Strauss, Hokkin Choi, and Michael Rossmarm for helpful discussions. This work was supported by NSF (TSB) and NIH grants, and also a program project grant from NIH to TSB, RIK, and TJS. Research was also supported by a grant from the Lucille P. Markey Charitable Trust for the development of structural studies at Purdue University.

REFERENCES

Stewart M and G Vigers. 1986. Nature **319:** 631-636.
Baker TS. 1992. Electron Microscopy **3:** 275-279.
Cheng RH. et al. 1994. Structure **2:** 271-282.
Cheng RH. et al. 1995. Cell 80, 621-630.
Strauss J and E Strauss. 1994. Microbiol. Rev. **58:** 491-562.
Vrati S. et al. 1988. Virology **162:** 346-353.
Stanley J. et al. 1986. J.Virol. **58:** 107-115.
Choi H. et al. 1991. Nature **354:** 37-34.
Liu H. et al. 1994. J. Mol. Biol. **240:** 127-137.

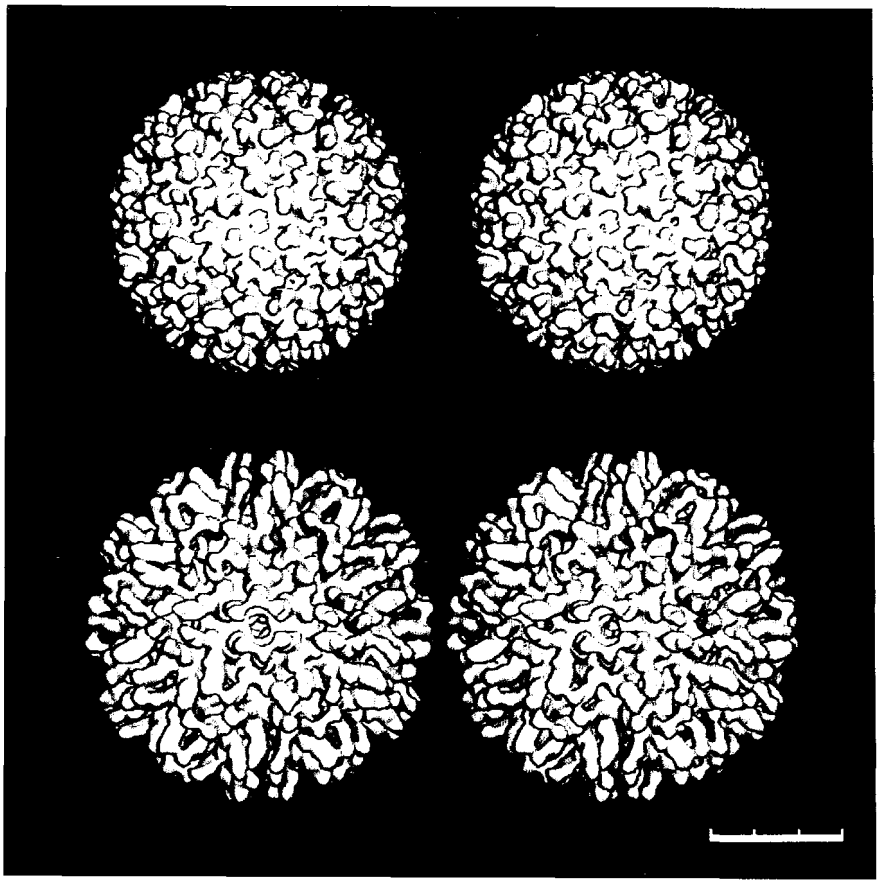

Fig. 1. Stereo pairs of surface rendered three-dimensional reconstructions reveal the structures of Ross River virus in a native and an antibody-bound conformation. The reconstruction was computed at 2.7 nm resolution with 68 and 42 independent particle surface-shaded representations are viewed along an icosahedral twofold axis. Comparison of the surface features of Ross River virus between its native particle and its complex form attached with monoclonal antibodies reveals the locations where the 240 Fab fragments binds the 80 copies of spikes. Binding domain of these antibodies also suggests to be a region in which the virus engages in the host recognition. The fact that the footprint of the antibody in Sindbis virus (data not shown) is nearby the one in Ross River virus suggests that the host recognition site may be conservative in alphaviruses. Bar=30 nm.

Zoological Studies 34, Supplement I (1995)

Zoological Studies

Applications of Electron Microscopy to Materials and Earth Sciences — Dislocations, Shape and Orientation Changes and Interdiffusion

Pouyan Shen

Institute of Materials Science and Engineering, National Sun Yat-sen University, Kaohsiung, Taiwan, R.O.C.

Interactions of solid materials with liquids, vapors or other solids are of concern in earth sciences, especially the diagenesis, weathering and metamorphic processes which involve the compositional, structural and morphological changes down to nanometers scale. The electron microscopy, SEM, TEM, HRTEM and AEM have been used to study some materials with emphasis on: (i) dislocations, (ii) shape and orientation changes and (iii) composition variation due to interdiffusion. The formation mechanism of the materials can then be inferred as outlined below.

TEM was used to characterize the defect microstructures of chromium spinel and pyrite in the serpentinized chromitite occurrence of the Kenting melange, southern Taiwan (Hwang et al. 1988). Dislocations arranged as dipoles, tangles and subgrains boundaries were found in chromium spinel and pyrite indicating that they were plastically deformed and polygonized later. The deformation episodes of the Hengchun chromitite were then inferred from the known creep behavior of analogue spinel materials and pyrite. In the other case, the disloca-tion outcrops revealed by optical microscope and SEM were found to be useful indicator of directional dissolution rate as demonstrated in the acidic dissolution of willemite, Zn_2SiO_4, an important phase for Zn source, crystalline glaze and phosphorous applications (Lin and Shen 1993a).

In the second category dealing with shape and orientation, the optical and SEM images of curved etch hillocks on the (0001) plane of willemite showed the role of screw axis on dissolution (Lin and Shen 1993b). Thus, lattice diffusion of minerals may be significant in some weathering processes under ambient temperature. Shape and orientation are also of concern in composite materials. For example, TEM indicated that the shape and orientation of the intragranular NiO particles have surprisingly aligned with those of the zirconia matrix when the NiO/ZrO_2 (alloyed with 10 mol.% Y_2O_3) composites were annealed for 300 h at 1600°C (Chen and Shen). Similar behavior is expected for the mineral assemblages in the interior of the earth. Surface features and the shape of a living organism can also be used as indicator of its behavior. For example, frictional bars and eroded areas of the coral-boring bivalve Lithophaga nigra were revealed by SEM, suggesting that this organism is a mechanical borer rather than a chemical borer, as previously believed (Fang and Shen 1988). However, the debris at the bottom of the burrow may dissolve chemically when metabolism reduces the pH. Near the carbonate compensation depth, the level at which the complete supply of carbonates is dissolved, the calcareous particles may become nanometers in size, and the size effect on dissolution (Lin and Shen 1994) may become important.

Finally, interdiffusion was known to cause disordering of atoms in some diffusion couples of metal alloys, and recently in aluminized coatings on Inconel 600, a Ni based alloy (Chen et al.). A drastic concentration gradient at interface may account for such changes. As for ceramic system, preliminary AEM study of the annealed yttriumiron garnet (YIG)/ZrO_2 composite showed that diffusion-induced amorphization (DIA) occurred within the lattice of YIG rather than at the YIG/ZrO_2 interface. These results have following implications: *(1)* previous determination of interdiffusion coefficient may have overlooked the fact that an intermediate phase exists at interface, *(2)* the diffusion path of a diffusion couple may be different from previous versions if phase and composition changes are considered at nanometers scale, and *(3)* DIA is expected in minerals assemblages such as in metamorphic rocks.

It is expected that future studies on surface changes of samples immersed in wet medium and spiked with poisons should improve the current knowledge of the diagenesis and weathering processes. Confocal microscopy should help to some extent in this regard. STM and AFM have been useful to reveal surface reconstruction and electronic structure of the atomic planes of some materials. However, the exact nature of an interphase interface remains to be explored theoretically and experimentally. Hopefully, the variation of the equation of state toward an interface can be considered in the future simulation of HRTEM images.

Acknowledgments: I thank Prof. A.C. Su for inspiring discussions and reading the abstract.

REFERENCES

Hwang SL, P Shen, HT Chu, RC Jeng. 1988. Bull. Minéral., **111:** 457-469.

Lin CC, P Shen. 1993a. Geochimica et Cosmochimica Acta, **57:** 27-36

Lin CC, P Shen. 1993b. Geochimica et Cosmochimica Acta, **57:** 1649-1655.

Chen JN,P Shen, in prep.

Fang LS, P Shen. 1988. Mar. Biol. **97:** 349-354.

Lin CC, P Shen. 1994. Geochimica et Cosmochimica Acta, **58:** 3583-3593.

Chien A, D Gan, P Shen, sumbitted to Mater. Sci. Eng. (A).

Zoological Studies 34, Supplement I (1995)

Zoological Studies

Differentiation-associated Modifications of Ultrastructures in Human Cervical Carcinoma SIHA Cells

Hwan-Wun Liu[1], Yung-Fu Yang[2], Su-Ping Teng[1], Yaw-Wen Guo[1] and Chung-Faye Chao[1]

[1]*Department of Biology and Anatomy, National Defense Medical Center, Taipei, Taiwan, R.O.C.*

[2]*Department of Obstetrics and Gynecology, Tri-Service General Hospital, Taipei, Taiwan, R.O.C.*

Differentiation is one of the most important cell processes and has been extensively studied for decades. However, modifications of ultrastructures during the differentiation are not well defined. This communication reported differentiation-associated modification of ultrastructures in human cervical carcinoma SIHA cells treated with a variety of differentiation promoting reagents. Cell cycle analysis and cell survival (MTT) assay showed that differentiation status of SIHA cells was modified by these reagents. Since keratins are epithelium-specific markers, and expression of keratins are closely related to differentiation status of epithelial cells and carcinoma derived from epithelial cells. Keratin filaments of SIHA cells were investigated by immunofluorescent staining with AE1/AE3 monolclonal antibodies. In control cells (Fig. 1a), keratin filaments were evenly distributed in the cytoplasm. Aggregation of keratin filaments were found in the cells treated with retinoid acid (Fig. 1b). In the cells treated with arabinosyl cytosine (ara-C), cell size were increased, and distribution of keratin filaments were more extensive. Cell sizes and distributions of keratin filaments were not apparently altered in the cells treated with phorbol diester (TPA). Electron microscopic observation, however, revealed autophagosomes containing mitochondria (Fig. 2). These results indicate that keratin filaments and mitochondria are modified during differentiation of SIHA cells. However, their roles in cell differentiation needs to be determined.

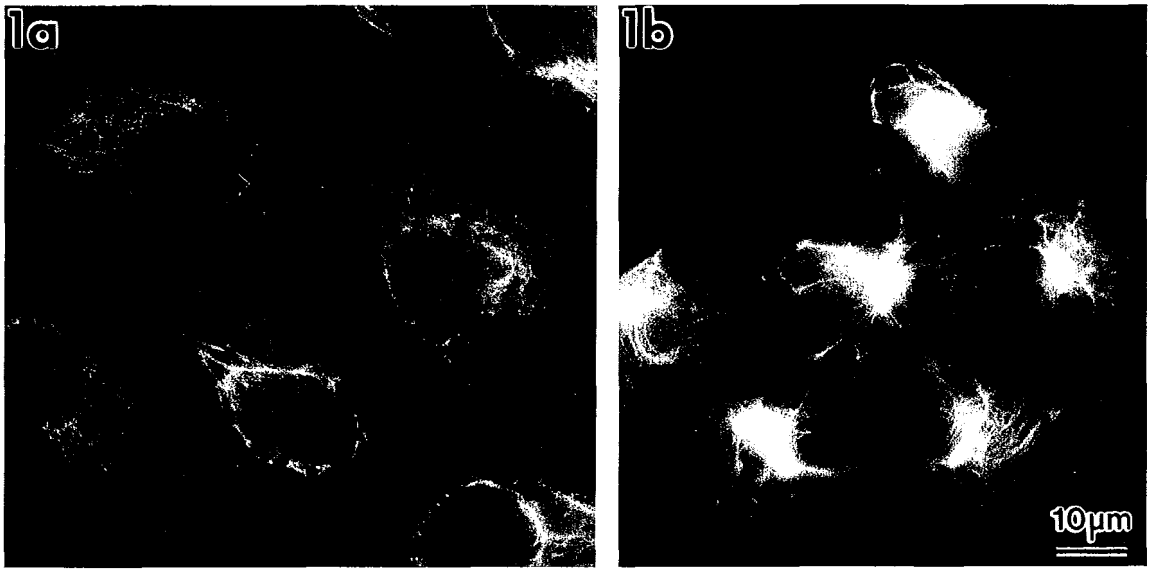

Fig. 1. Immunofluorescent staining showed that keratin filaments were evenly distributed in cytoplasm of control cells (a). In cells treated with retinoic acid (b), keratin filaments aggregated in center of the cell.

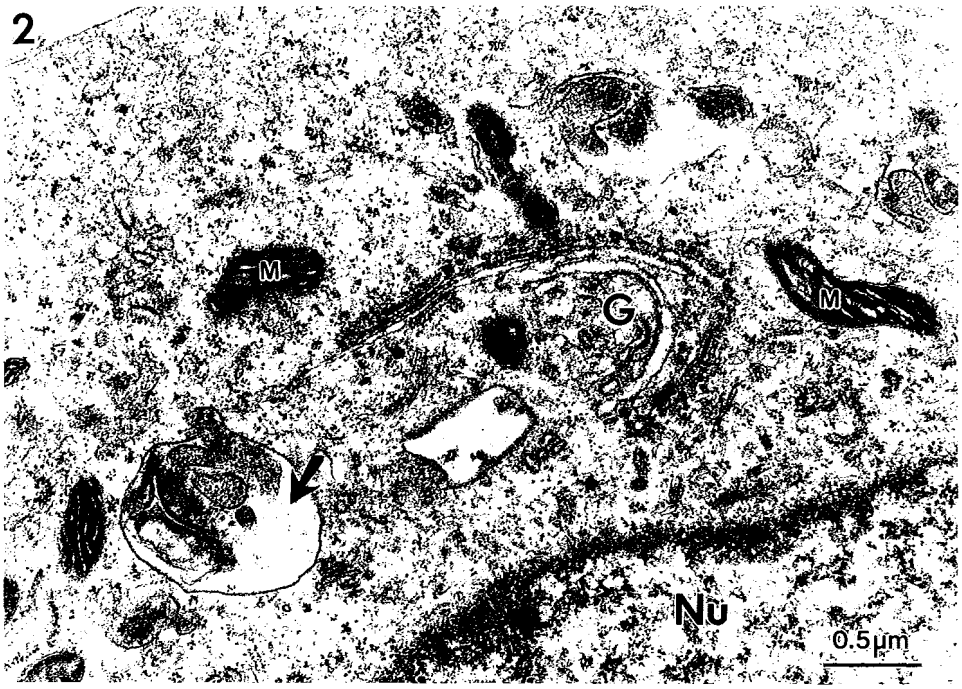

Fig. 2. In SIHA cells treated with TPA, autophagosomes containing mitochondria (arrow) were found. Morphology of mitochondria (M), golgi apparatus (G) and nucleus were apparently normal.

Zoological Studies 34, Supplement I (1995)

Zoological Studies

Polarisation Contrast in Scanning Microscopy

T. Wilson, R. Juškaitis, S. Shatalin and J.B. Tan

Department of Engineering Science, University of Oxford, Parks Road, Oxford OX1 3PJ, UK

We will begin by discussing the differences between polarisation contrast imaging in conventional and confocal systems and show that because of the fundamentally different imaging properties of the two systems, the extinction coefficient is finite in a conventional system even with perfect polars, whereas an "infinite" extinction coefficient is to be expected in a confocal system.

We will then discuss the axial response of high numerical aperture systems and show that a polarisation effect leads to an asymmetric response when the objective lens numerical aperture is greater than the refractive index of the specimen. The effects are reminiscent of spherical aberration but occur even with the best corrected lenses.

In order to take advantage of polarisation effects to enhance the contrast due to a particular object property it is necessary to realise that the optical field reflected from the specimen contains all the information about the object that can be included in the image. The optical imaging system then determines how this field is compressed into a single pixel brightness value. The conventional microscope imaging system performs this compression by essentially integrating the intensity in the exit pupil of the objective lens over the area of the exit pupil whereas the confocal system ef-fectively integrates the amplitude over the pupil area. In both cases the information from the object is the same but the imaging system has caused it to be "averaged" over the pupil in a different way. This inevitably causes a good deal of information about the object to be obscured. This drawback can be overcome if we modify the imaging system to obtain images whose contrast is determined by the form of the field at the exit pupil of the objective lens. In its simplest form we could form an image of the exit pupil which is ,of course, the basis of conoscopy.

In order to illustrate our approach we will concentrate on a variety of planar thin film structures. The conoscopic patterns in these cases are particularly sensitive to polarisation effects and variations in film thickness. Indeed if we consider a simple system consisting of a layer of silicon dioxide deposited on a silicon substrate it is relatively easy to use a curve fitting approach to determine the film thickness. In this case it is only necessary to analyse the data corresponding to the s or p polarised beams. If we consider other angles within the conoscopic pattern then it is possible to extract the full ellipsometric data about the specimen. In effect the conoscopic system is acting as a photometric or micro-ellipsometer.

Since the intensity in conoscopic pattern depends only on the Fresnel reflection coefficients r_s or r_p along mutually perpendicular diameters and on a combination of the two along other diameters that the pattern will, in general, not be angularly symmetric. We may take advantage of this to enhance image contrast. In a conventional system the asymmetry integtates out and an image intensity proportional to $|r_s|^2+|r_p|^2$ results. We will demonstrate a polarisation difference imaging technique which enhances the asymmetry and leads to and image where variation in film thickness are clearly visible.

We will further consider imaging between crossed and parallel polars and suggest a variety of spatial filters which may be inserted into the optical system to enhance specific image contrast. The role and choice of wavelength and objective lens numerical aperture will also be discussed.

Zoological Studies 34, Supplement I (1995)

Zoological Studies

3D X-ray Microscopy: High-resolution Stereo-imaging with the Göttingen X-ray Microscope at BESSY

Johannes Lehr

Forschungseinrichtung Röntgenphysik, University of Göttingen, Geiststra ße 11, D-37073 Göttingen, Germany

A multiple-angle viewing stage has been built at the Forschungseinrichtung (FE) Röntgenphysik (University of Göttingen) and was implemented at the Göttingen x-ray microscope at BESSY (Schmahl et al. 1993). First TXM (transmission x-ray microscope) stereo images have been taken of sheaths of mineral accumulating bacteria *Leptothrix Ochracea* and diatoms. It results that the three-dimensional structure of these specimens can be revealed at high resolution. For the studies a microzoneplate with an outermost zonewidth of about 40 *nm* was used at a wavelength of λ=2.4 *nm*. Structures of 40 *nm* size can clearly be seen.

INTRODUCTION

The aim of x-ray microscopy is to study specimens in a natural environment at resolutions far beyond those of visible light microscopes. Image-formation is based on the natural contrast of the specimen-structures against the surrounding media. Currently this technique is applied to various fields of interest including biology, medical research and soil science. The investigated specimens typically have a thickness of up to 10µm, which is similar to the size of the image-field of the Göttingen TXM. It is therefore obvious that the three-dimensional structure of the objects must be considered. As reflection at interfaces is neglegibly small in the soft x-ray domain, it is possible to look into thick specimens that are opaque for visible light. The TXM is therefore an ideal tool for the study of three-dimensional specimens. When using a TXM in the traditional way, the information about one dimension is lost. Since the depth of focus of the TXM is of comparable size as the thickness of the objects, an appropriate approach to recover this information is to apply the technique of stereoscopy to the TXM. First stereoscopy-experiments with resolutions beyond those of visible light methods have been performed by the Lawrence Berkeley Laboratory (Loo et al. 1992), using the scanning transmission x-ray microscope (STXM) at the National Synchrotron Light Source, Brookhaven National Laboratory.

EXPERIMENTAL

The optimum tilt angle for stereoscopic images can be estimated from the classical parallax equation, which relates the parallax ΔY to the angle of tilt, the magnification M and the vertical separation Δh of two points in the object at the angle midway between the two tilts.

$$\Delta Y = 2\Delta h M \sin(\Theta/2) \qquad (1)$$

For a good three-dimensional impression, the parallax ΔY should be in the range between 3 and 5 *mm* (Hudson and Makin, 1970), when stereo-pairs are viewed at a distance of 25 *cm* from the eyes. Assuming a total magnification of *M*=4000 and an object thickness of 5 µm, optimum tilt angles Θ between 5 and 15 degrees can be calculated. At the Göttingen TXM the maximum tilt angle is too small for stereo-views, if a conventional specimen holder with large dimensions in the direction perpendicular to the rotation axis is used. To solve this problem without major changes to the microscope, a multiple-angle viewing stage with a specimen-support of 0,5 *mm* width was constructed. Currently, tilt angles of about 40 degrees can be achieved with this modification.

RESULTS

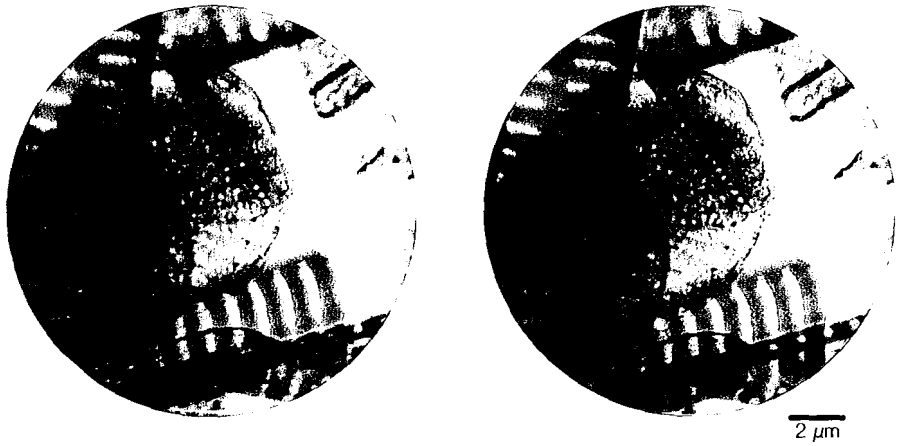

Fig. 1. Stereo-pair images of sheaths of the mineral accumulating bacteria *Lepothrix Ochracea*. The stereo angle is 12.5 degrees.

Fig. 2. Stereo-pair images of diatoms at a stereo angle of 5 degrees.

In a first series of experiments images of sheaths of mineal accumulating bacteria *Leptothrix Ochracea* (Fig. 1) and diatoms (Fig. 2) were taken from various viewing angles. The exposure times were around 2 seconds. From measurements of the object-thickness it can be seen that the range of depth that contributes to the three-dimensional image is much bigger than the depth of focus. In Fig. 1 for example, the obect-thickness is 9 µm, whereas the depth of focus is about 1.5µm. It is therefore very likely that stereo-images can be taken at even higher resolution, even if the depth of focus is less than 0.5 µm, when a microzoneplate with an outermost zonewidth of 20 *nm* is used. Stereoscopy combined with x-ray microscopy proofs to be a powerful technique for studying the three-dimensional structure of specimens from biology and soil science, as the results show. For future applications of this technique it will be advantageous to combine it with the cryo-preparation method, which is also under development at the FE Rontgenphysik (Schneider and Niemann 1994). The range of specimens, which can be examinated will be extended to objects in aqueous medium and further applications in biology and medical research will be enabled.

REFERENCES

Schmahl G, D Rudoph et al. 1993. X-Ray Microscopy Studies Optik **93:** pp. 95-102.

Loo jr, BW, S Williams, S Meizel, XS Rothman. 1992. X-Ray stereomicroscopy: High resolution 3-D imaging of human spermatozoa in aqueous suspension with natural contrast. Journal of Microscopy, Vol. **166:** Pt 2, May pp. PR5-PR6.

Hudson B, MJ Makin. 1970. The optimum tilt angle for electron stereo-microscopy Journal of Physics E: Scientific Instruments Volume **3:** p 311.

Schneider G, B Niemann. 1994. Cryo-X-Ray Microscopy: First Images of Specimens at Low Temperatures X-Ray-Science (Newsletter of the Kings College, London), Issue 2, Summer.

Zoological Studies 34, Supplement I (1995)

Zoological Studies

Energy Filtering and Exit Surface Wavefront Reconstruction of Thick Biological Specimens - Technical Development for Three Dimensional Electron Microscope Tomography

Karen F. Han, John W. Sedat and David A. Agard

Graduate Group in Biophysics, Howard Hughes Medical Institute, Department of Biochmistry and Biophysics, University of California San Francisco, CA 94143, USA

High resolution studies of cellular organellse and nuclear structures are often investigated by using transmission electron microscopy (TEM). Three dimensional (3D) reconstruction is essential to elucidate high resolution substructures of these macromolecular assemblies. There are two main approaches to obtain 3D reconstructions in TEM: serial thin sections and tomography. Our laboratory uses the latter technique which has the advantage of nearly isotropic resolution in 3D with the reconstruction resolution to be much higher than the former. 3D tomography is the reconstruction of an object by combining multiple projection views of the object at different tilt angles. In order to accurately reconstruct these structures, it is essential to understand the relationship between the TEM image intensity and specimen mass density. Due to the natural dimensions of these structures, they are considered thick (0.3-1.0μm at high specimen tilt angles) for TEM studies. Compared with thin specimens (0.1 μm), the imaging of thick specimens are additionally complicated by multiple scattering which gives rise to the incoherent and partially coherent components that degrade the images. Two techniques were used to analyze the mechanism of image formation for thick specimens: electron energy-loss spectroscopic imaging (ESI), and the exit wavefront reconstrction using a through focus series. We showed that: 1) there is a significant amount of coherent transfer in thick specimen imaging, 2) the coherent component in the images are contributed almost exclusively by elastically scattered electrons, 3) the incoherent component are mostly contributed by multiple elastic and inelastic scattering, and 4) exit wavefront reconstruction can act in part as an energy filter.

Electron-specimen interactions include single and multiple, elastic and inelastic scattering. Multiple and inelastic scattering events give rise to nonlinear imaging effects which complicates the interpretation of the images collected. In addition, due to the chromatic aberration of the TEM's objective lens, multiply scattered indlastic electrons cause a blurring of the image due to an effective broadening of the focus spread. We have shown previously that when imaging our typical thick specimens at 200 keV, only the elastic (zero-loss) and plasmon (single inelastically scattered) electrons contribute to high resolution images. Most inelastically scattered electrons are multiply scattered and contribute to low resolution images.

The coherent component of the image can be extracted in a three-dimensional power spectrum of a through focus series. The coherent information in the opwer spectrum lies on a parabola which is the Ewald sphere4-6. In such restroations, the components which are not mutually coherent through focus are naturally excluded, including multiple and inelastic scattering. By analyzing the 3D power spectrum of a through focus series, one can quantify the relative amount of coherent and imcoherent components. Figrue 1 shows a few representative cross-sections of the Ewald sphere from the unfiltered esit wavefront of a 0.5μm specimen (epon embedded, stained with uranyl acetate and lead citrate) at 200 keV. As the schematic diagram shows, the coherent component is on the outer circle, and the noise or

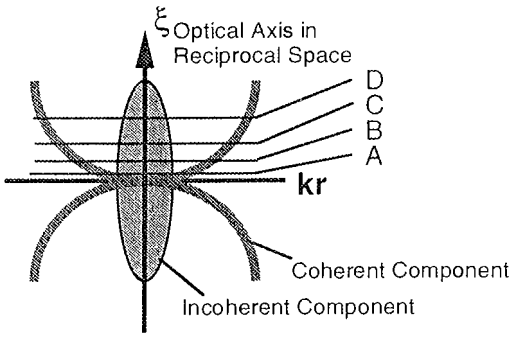

incoherent component is at the center. Contrary to common assumption, coherent transfer is significant in these thick specimens. Ehen the same analysis was done on the thuough focus series of only slastically scattered electrons (or zero-loss filtering), we found that the coherent component is greatly enhanced (Fig.2). The central component is still quite prominent perhaps due to multiple elastic scattering. When normalized by total counts, the central component is reduced in the filtered series. Images from the plasmon electrons (25 eV-loss) contain very weak parabola component and a large central component, while all images from other energy ranges contain only the central (incoherent) component. An analogous study was done on a 0.7 μm specimen where we showed that only the zero-loss filtered series contain the parabola (coherent) component (data not shown). We conclude that the coherent component of thick specimen TEM images are contributed by elastically scattered electrons, and the incoherent component contains mostly multiple inelastic and some multiple elastic electrons.

From the results above, we showed that restored specimen esit wavefront from and unfiltered through focus series effectively 'filters' out the inelastically scattered electrons. This applies for thick specimens because most inelastically scattered electrons are multiply scattered and therefore contribute very little to the coherent component of the images. By virtue of excluding the multiple scattering component, the restored images displayed enhanced contrast with higher resolution. Thus in thick specimen imaging. the combined use of energy filtering and through focus reconstruction is optimal to recover the exit wave (Fig.3). The interpretation of the aberration corrected images are proposed as follows: the amplitude component coming from the absroptive effect

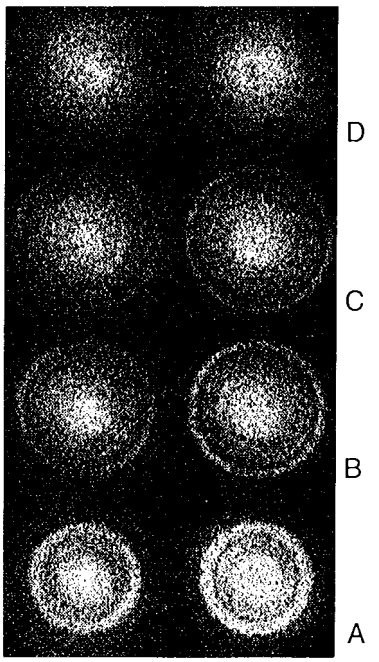

Fig. 1. Fig. 2.

Fig. 1. Selected cross sections through the Eeald Sphere of 0.5mm thick specimen, unfiltered, at 200keV, displayed in order of increasing reciprocal z. (Eesolution limit is 2.4nm^{-1})

Fig. 2. Selected cross sections as in Figure 1, but from the zero-loss filtered series, demonstrating an enhanced coherent component. (Resolution limit is 2.4nm^{-1})

has a logarithmic relation to the mass density of the specimen, and the high resolution phase component is linearly related. This has direct implications to the three dimensional reconstructions of these specimens where aberrations were not corrected and a simple direct relationship was assumed.

ACKNOWLEDGMENTS

The authors thank A. J. Gubbens for the use of the Gatan Imaging Fliter and M. Braun feld for the specimens used in this study. K.F.H. is supported by the Howard Hughes Medical Imstitute Predoctoral Fellowship in the Biological Scienced. This work is supported by grants from the National Institutes of Health (GM 31627 for D.A.A.; GM25101 for J.W.S.) and by Howard Hughes Medical Institute.

REFERENCES

Reimer L, R Rennekamp, I Fromm, M Langenfeld. 1991. Contrast in the electron spectroscopic imaging mode of a TEM. IV.

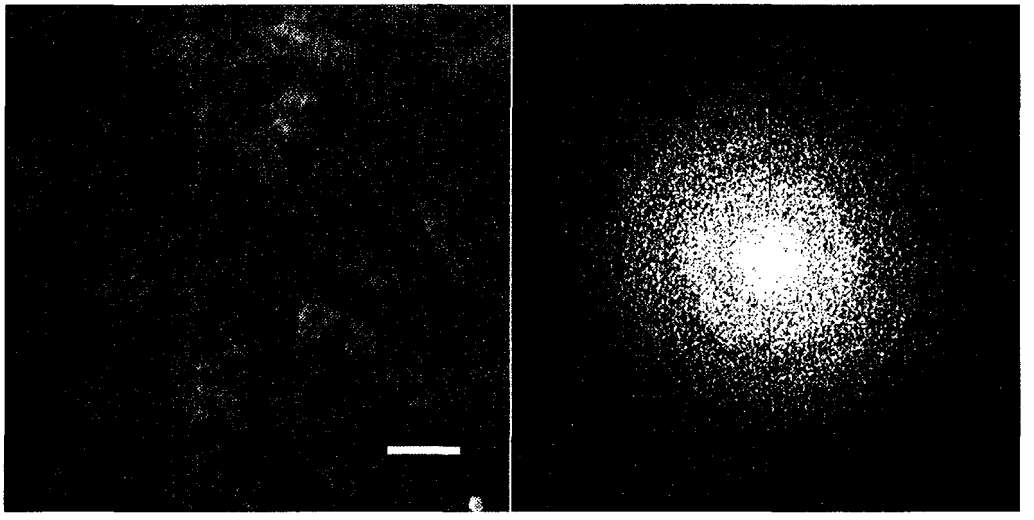

Fig. 3. Reconstruction of the projected specimen mass-density combined from the amplitude and phase components of the restored exit wavefront. Diffractogram resolution limit is 2.4nm $^{-1}$. Scale bar: 50nm. The specimen is eponembed-ded microtubules from an in vitro centrosome preparation.

Thick specimens imaged by the most-probable energy loss. Journal of Microscopy, **162:** 3-14.

Han K, A Gubbens, A Koster, M Braunfeld, J Sedat, D Agard, 1993. Analysis of electron-specimen interactions of thick biological specimens in transmission electron microscopy at 200 keV. Proc. 52nd Ann Microscopy Society of America, 204-205.

Han K, J Sedat, D Agard. 1995. Mechanism of Image Forma- tion for Thick Biological Specimens: Exit wavefront reconstruction and electron energy-lwss spectroscopic imaging. Journal of Microscopy, April (in Press).

Van Fyck, D. Op de Beeck, M. 1990. New direct methods for phase and structure retrieval in HREM. Proc. of 12th Int'l Congress for Electron Microscopy, 26-17.

Taniguchi Y, T Ikuta, R Shimizu. 1991. Assessment of image formation by three-dimensional power spectrum in transmission electron microscopy. Journal of Electron Microscopy, **40:** 5-10.

Coene W, G Janssen, Op de Beeck, M. Van Dyck, D. 1992. Phase retrieval through focus variation for ultra-resolution in fiele - emission transmission electron microscopy. Physical Review Letters, **69:** 3743-3746.

Zoological Studies 34, Supplement I (1995)

Zoological Studies

In Situ Localization of Plant Viral Genes and Gene Products in Infected Cells

Na-Sheng Lin[1], Gunn-Guang Liou[1], Chin-Chieh Chen[1] and Ban-Yane Chang[2]

[1] *Institute of Botany, Academia Sinica, Taipei, Taiwan 115, R.O.C.*

[2] *Agricultural Biotechnology Laboratories, National Chung Hsing University, Taichung 400, R.O.C.*

In situ hybridization and immuno cytochemical staining have been the powerful tools for localization of specific nucleic acids and proteins in tissue sections for the studies of cell biology, development and genetics. In this study, bamboo mosaic virus (BaMV) was used as a model virus to demonstrate ultrastructural locations and movement of BaMV RNA and the proteins it encoded in infected cells. BaMV has a single-stranded, plus-sense RNA genome with five conserved open reading frames (ORFs). Young leaves of green bamboo (Bambusa oldhamii) showing systemic mosaic symptom were harvested for electron microscopy. Leaf tissue pieces were fixed with glutaraldehyde and embedded in Lowicryl HM20. Immuno- and *in situ* hybridization electron microscopy was performed. BaMV capsid protein and masses of virions were detected in the cytoplasm and vacuoles of infected cells by antiserum to BaMV capsid protein followed by gold-labelled goat anti-rabbit IgG complexes. At the early stage of infection, BaMV capsid protein was also detected within the nuclei, especially in the nucleoplasm of the rolled young leaf samples (Fig. 1). However, the electron-dense crystalline bodies (EDCBs) were not labelled with antiserum to BaMV capsid protein. On the other hand, EDCBs were detected by using anti-ORF2 serum in the cytoplasm as well as in the nuclei (Fig. 2) whereas the BaMV virions were not labelled. In addition, digoxigenin (Dig)-labelled riboprobe, corresponding to the 173 nts at the 3' end of BaMV RNA, was used to hybridize the viral nucleic acids in tissue sections. The hybrids were subsequently reacted with sheep anti-Dig antibody followed by immunogold. BaMV RNA was specifically detected within chloroplasts, motochondria and nuclei of infected cells at all stages of infection. BaMV virions and 'BaMV-specific EDCBs were also labelled (Fig. 3).

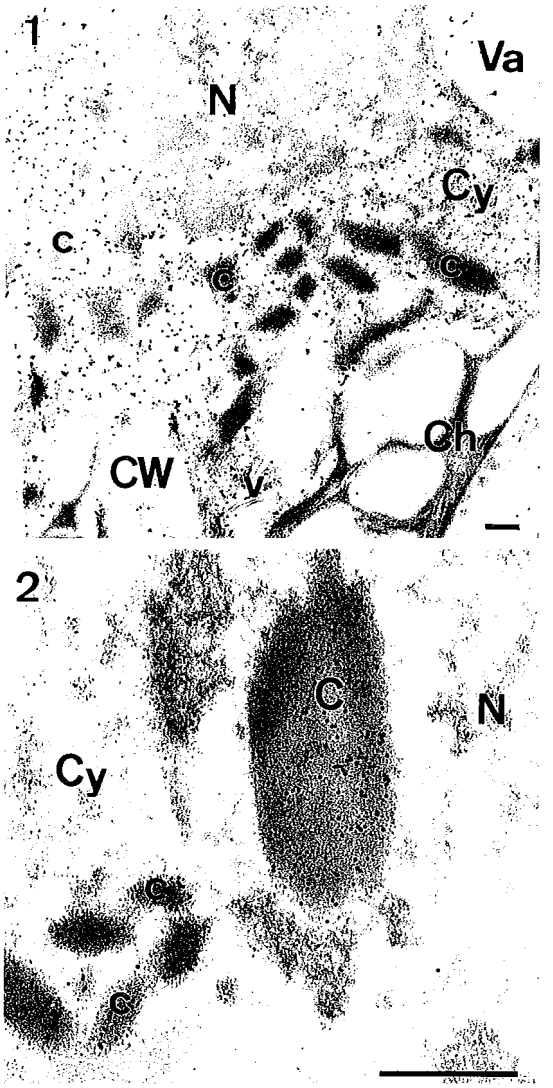

Fig. 1-2. Immunological detection of BaMV capsid protein and 28 kDa protein in glutaraldehyde-fixed, Lowicryl HM20-embedded and BaMV-infected green bamboo leaves. Thin sections were first stained with dilute anti-BaMV-CP serum (1) or anti-ORF2 serum (2), followed by gold-labelled goat anti-rabbit IgG complexes.

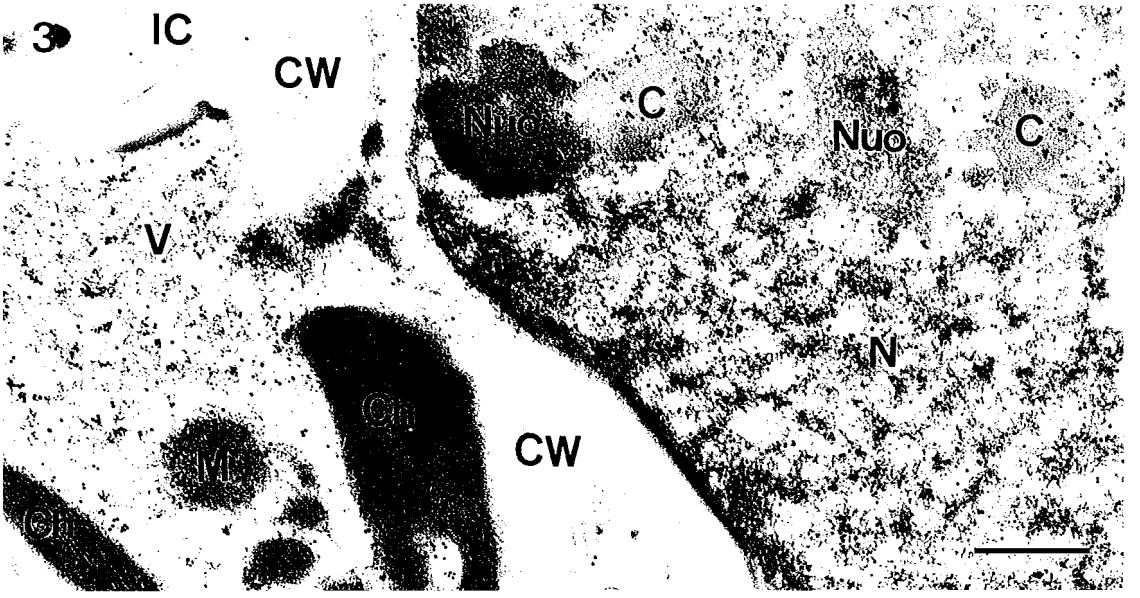

Fig. 3. *In situ* hybridization of BaMV RNA in BaMV-infected green bamboo leaves. Thin sections were hybridized with Dig-labelled riboprobe and detected with immunogolds.
C, electron-dense crystalline bodies; Ch, chloroplast; CW, cell wall; Cy, cytoplasm; IC, invtercellular space; M, mitochondria; N, nucleus; Nuo, nuleolus; Va, vacuole; V, virion. Bars = 500 nm.

The *in situ* localization of BaMV RNA and BaMV-encoded proteins provide important information about BaMV pathogenesis and gene expression.

REFERENCES

Lin NS, FZ Lin, TY Huang, YH Hsu. 1992. Phytopathology **82:** 731-735.

Lin NS, BY Lin, NW Lo, CC Hu, TY Chow, YH Hsu. 1994. J. Gen. Virol. **75:** 2513-2518.

Lin NS, CC Chen. 1991. Phytopathology **81:** 1551-1555.

Lin NS, CC Chen, YH Hsu. 1993. J. Histochem. Cytochem. **41:** 1513-1519.

Zoological Studies 34, Supplement I (1995)

Zoological Studies

Asymmetric Cell Division and Cell Determination in Plant Development

Bai-Ling Lin
Institute of Molecular Biology, Academia Sinica, Nankang, Taipei, Taiwan 11529, R.O.C.

The term "asymmetric cell division" is used here to refer to any cell division in which the two derivatives assume different paths of development and have distinct cell fates. Therefore, the asymmetry does not necessarily lie in the size difference of the derivatives, although the difference in cell size often provides a marker and even has been proposed as a driving force of differentiation (Treinin and Feitelson 1993). Asymmetric cell division provides a mechanism to generate cell diversity in all organisms. Numerous examples of asymmetric cell division exist during the development of a plant. Because plant cells are confined to rigid cell walls and do not undergo morphogenetic movement, the orientation of cell division plane and the direction of cell expansion are key determinants in plant morphogenesis, and thus are tightly regulated. In many cases, differentiation starts from an unequal cell division, in which the small cell forms a specialized structure, either by itself or by further concerted unequal cell divisions in surrounding cells. While in others, the size difference is not as obvious immediately following the cell division, but later, one of the derivatives becomes distinctly larger and is committed to an altered path of development. Here I discuss one example for each type of these asymmetric cell divisions.

Trichome development starts from the small cell delineated by an unequal cell division in the protodermal layer, which then elongates away from the surface into a defined shape. Three classes of mutations in trichome development have been studied in *Arabidopsis* (Marks et al. 1991). Among them, one is devoid of trichomes, and the isolated gene encodes amino acid sequences highly homologous to the protooncogene *myb* (Oppenheimer et al. 1992). Myb protein contains a DNA binding domain and a region participating in protein-protein interactions (Sakura et al. 1989). It does not fit the configuration for a transmembrane signaling molecule, and therefore could be a downstream molecule in the signaling cascade of cell determination.

Stoma differentiation is similar to trichome development in several aspects but involves concerted asymmetric cell divisions in the neighboring cells. Stomata are surface pores anchored by derivatives of the protodermal layer, resulted from unequal cell divisions, and distributed throughout the epidermis in variable densities, without direct contact of each other. Following an unequal cell division in an epidermal cell, the small cell becomes the guard mother cell (GMC). The nuclei in the surrounding epidermal cells migrate toward the sides of GMC, and further un-equal cell divisions occur with precise orienta-tions in these cells and the GMC to produce the stomatal complex, which is highly specialized and distinct from ordinary epidermal cells.

Lateral root initiation in ferns provides evidence for the action of both induction and lateral specification (Greenwald and Rubin 1992). The entire lateral root structure originates from a single cell within the endodermis, which is a single layer of cells surrounding the vascular cylinder along the axis of the main root. The lateral root initial (LRI) is always the distal derivative of a cell division. The asymmetry of the cell division may not be distinct prior to the completion of division, but the cell destined to become LRI expands rapidly. It first enlarges to reach approximately 20-fold the volume of its sister cell or any ordinary endodermal cell, then undergoes a series of cell divisions in precise sequences and orientations within the contour of the cell. Transversely, LRI always arises from the endodermal initial facing the protoxylem of the vascular cylinder. Thus in diarch fern roots, only two longitudinal files of endodermal cells, each facing one protoxylem pole, are potentially capable of generating LRIs through establishing cell polarity and asymmetric cell division.

REFERENCES

Greenwald I, GM Rubin. 1992. Making a difference: the role of cell-cell interactions in establishing separate identities for equivalent cells. Cell **68:** 271-281.

Marks MD, J Esch, P Herman, S Sivakumaran, D Oppenheimer. 1991. A Model for cell-type determination and differentiation in plants. Symp. Soc. Exp. Biol. **45:** 77-87.

Oppenheimer DG, PL Herman, S Sivakumaran, J Esch, MD Marks. 1991. A *myb* gene required for leaf trichome differentiation in Arabidopsis is expressed in stipules. Cell **67:** 483-493.

Sakura H, C Kanei-Ishii, T Nagase, H Nakagoshi, TJ Gonda, S Ishii. 1989. Delineation of three functional domains of the transcriptional activator encoded by the *c-myb* protooncogene. Proc. Natl. Acad. Sci. USA **86:** 5758-5762.

Treinin M, DG Feitelson. 1993. Unequal cell division as a driving force during differentiation. J. Theor. Biol. **160:** 85-95.

Zoological Studies 34, Supplement I (1995)

Zoological Studies

Powerful Tools for 3D Microscopy Image Analysis, Processing and Visualization Based on 2D and 3D Fourier Transforms

Carol J. Cogswell, Kieran G. Larkin and Matthew R. Arnison
Department of Physical Optics, School of Physics, University of Sydney, NSW 2006, Australia

In recent years we have developed an experimental confocal microscope that can acquire images in confocal transmission modes, such as transmission brightfield and transmission Nomarski differential interference contrast (DIC) (Cogswell et al. 1994, Cogswell and O'Byrne 1992, Dixon and Cogswell 1995). We have configured the microscope with point-like laser illumination, with two photomultiplier detectors (PMTs) in the transmitted image (detection) path, and have used a beam splitter to direct half of the light to each PMT. When a pinhole spatial filter is placed in front of one PMT detector, this portion of the microscope behaves as a confocal transmission system. If the second PMT is left as a large-area detector (i.e. no pinhole is inserted) then it produces images similar to a conventional transmission microscope. Using both detectors provides us the opportunity to obtain both a conventional and a confocal transmission image simultaneously, for each plane of focus within the specimen, which is essential for precise comparison and evaluation of the two modes.

Initial experimental results with this microscope system show, particularly when using DIC optics, that the confocal configuration helps reject flare from out-of-focus scattering objects as compared to the conventional large-area-detector microscope configuration. In addition, the confocal transmission DIC mode appears to give an improvement in the ability of the system to delineate the edges and surfaces of objects in the axial direction as compared to a conventional DIC microscope. However, in the two-dimensional (2D) optical sections of a confocal focus series, these improvements appear as well-illuminated features that go out of focus more rapidly than in the conventional transmission DIC microscope. Thus the images are rather different from a typical confocal reflection mode in which out-of-focus features contribute little to the image and therefore appear dark.

Because of the non-typical appearance of the confocal transmission DIC images produced in our experiments, our initial attempts to apply standard confocal image processing and 3D visualization techniques to analyze the conventional versus confocal DIC images, or to extract and display image features, were unsuccessful. In order to help alleviate these problems, we have begun to investigate alternative methods for image analysis using Fourier transform techniques. In this paper, we describe a digital 3D fast Fourier transform (FFT) method for measuring and displaying the spatial frequencies which comprise our 3D image volumes. This 3D spatial frequency information can then be used to evaluate the axial and transverse resolution of our confocal versus conventional transmission images. The 3D FFT was developed by our group as a subroutine to expand a 2D FFT algorithm in a commercial software package (Vital Images VoxelMath) so that it would produce a 3D FFT of the full image volume. Besides evaluating resolution, the 3D FFT procedure is useful for determining if small shifts in registration have occurred between successive 2D sections in a 3D image stack.

In addition to the 3D FFT analysis, we also show that digital Fourier transform methods, such as the Hilbert transform (Oppenheim and Schafer 1989), can be successfully employed to overcome the difficulty of visualizing differentially-shaded phase objects, in 3D, that are typical of images acquired using transmission DIC optics. The Hilbert transform has the property of inverting one side of the differential shading gradient while at the same time maintaining the high spatial frequencies of the original DIC image (Cogswell et al. 1995). This is in contrast to a standard (directional) integration algorithm which tends

to act as a low pass filter, removing the high spatial frequency information (i.e. fine detail) in the image at the same time as it removes the shading gradient of features typical of DIC. The Hilbert transform algorithm allows us to extract object features from our 2D transmission Nomarski DIC image slices, in such a way that they can be further processed with a high boost axial filter, and then clearly visualized as a full 3D volume.

REFERENCES

Cogswell CJ, KG Larkin, MR Arnison, JW O'Byme.1995. 3D Fourier analysis methods for digital processing and 3D visualization of confocal transmission images. SPIE **2412:** (in press).

Cogswell CJ, KG Larkin, JW O'Byrne, MR Arnison.1994. High-resolution. multiple optical mode confocal microscope: I. System design, image acquisition and 3D visualization. SPIE **2184:** 48-54.

Cogswell CJ, JW O'Byrne.1992. A high resolution confocal transmission microscope: I. System design. SPIE **1660:** 503-511.

Dixon AE, CJ Cogswell. 1995. Confocal microscopy with transmitted light. In Handbook of Biological Confocal Microscopy, 2nd edition, ed. JB Pawley. New York: Plenum, (in press).

Oppenheim A, R Schafer.1989. Discrete-time signal processing. New Jersey: Prentice-Hall.

Zoological Studies 34, Supplement I (1995)

Zoological Studies

Transport Pathways of Lipoproteins across the Arterial Endothelial Cells

Cheng-Heng Kao[2], Jan-Kan Chen[2], Jong-Shung Kuo[3] and Vie Cheng[1]

[1]*Department of Biology, Tunghai University, Taichung, Taiwan, R.O.C.*

[2]*Department of Physiology, Chung Gung College of Medicine and Technology, Lin-Kou, Taiwan, R.O.C.*

[3]*Department of Medical Research, Veterans General Hospital, Taichung, Taiwan, R.O.C.*

Endothelial injuries in the artery have long been considered as an initial event in the pathogenesis of atherosclerosis. Increasing arterial endothelial permeability can cause low density lipoproteins (LDL) to filtrate and accumulate in the intima (Ross 1993). However, the nature of the initial damage to the arterial wall is not fully understood. Our previous studies showed that the endothelial ultrastructure of the branched regions of aortic arch was quite different from that of the unbranched regions (Kao et al. 1994). In this study, we use fluorescein
(DiL) labeled LDL to compare the distribution of LDL in the different regions of the arteries in the hypercholesterolemic rats. We also use colloidal gold labeled LDL to investigate *in situ* the transport pathways of LDL across the arterial endothelium at the branched regions of the arteries. Rat or human LDL was separated from pooled plasma by differential centrifugation. Then, LDL was coupled to DiI or colloidal gold (diameter =10 nm). Male Sprague-Dawley rats, weighing approximately 250 gm were fed high-cholesterol diet over a period of 1 year. At 1, 3, 6 and 12 months after feeding, three to five animals were anesthetized. The thoracic and the abdominal aorta, the right and the left femoral arteries were cannulated with polyethylene tubings. After the vascular bed was cleared with PBS at 37°C, the tubings between the thoracic aorta and the left ventricle and the tubings between the femoral arteries and the abdominal aorta were connected with peristaltic pump to form two closed circuits. Then, the colloid gold-LDL or DiI-LDL was infused. The animal was then perfused through the left ventricle with the fixative. The aorta, carotid artery, abdominal aorta and their branched regions were collected and prepared for quantitative electron microscopy. The adhesion and penetration of mononuclear cells into the intima occurred after 1-3 months of high cholesterol diet treatment. The fatty streak started to appear in the intima at 6 months, whereas the endothelium still kept intact. More LDL-DiI accumulated in the branched regions than those in the unbranched regions of the arteries. LDL-gold conjugates were observed in the plasmalemmal vesicles, multivesicular bodies and in the subendothelial space in both the branched and the unbranched regions. Quantitative study revealed that the volume densities of plasmalemmal vesicles which contained the LDL-gold particles in the branched regions of aortic arch were significantly ($P<0.05$) higher than the density value in the unbranched regions. The incidence of open junctions was significantly increased in the branched regions of aortic arch whereas no open junctions were observed in the unbranched regions. Moreover, the LDL-gold conjugates were present within most of these open junctions (Fig. 1). These results indicated that the major visible routes for transport of the LDL across the endothelium in the branched regions of the arteries are open junctions as well as plasmalemmal vesicles. The region-associated permeability changes might account for the incidence of atherosclerosis in the branched areas of arteries.

REFERENCES

Ross R. 1993. The pathogenesis of atherosclerosis: a perspective for the 1990s, Nature **362:** 801-809.

Kao CH, JK Chen, VC Yang. 1994. Ultrastructure and permeability of endothelial cells in branched regions of rat arteries. Atherosclerosis **105:** 97-114.

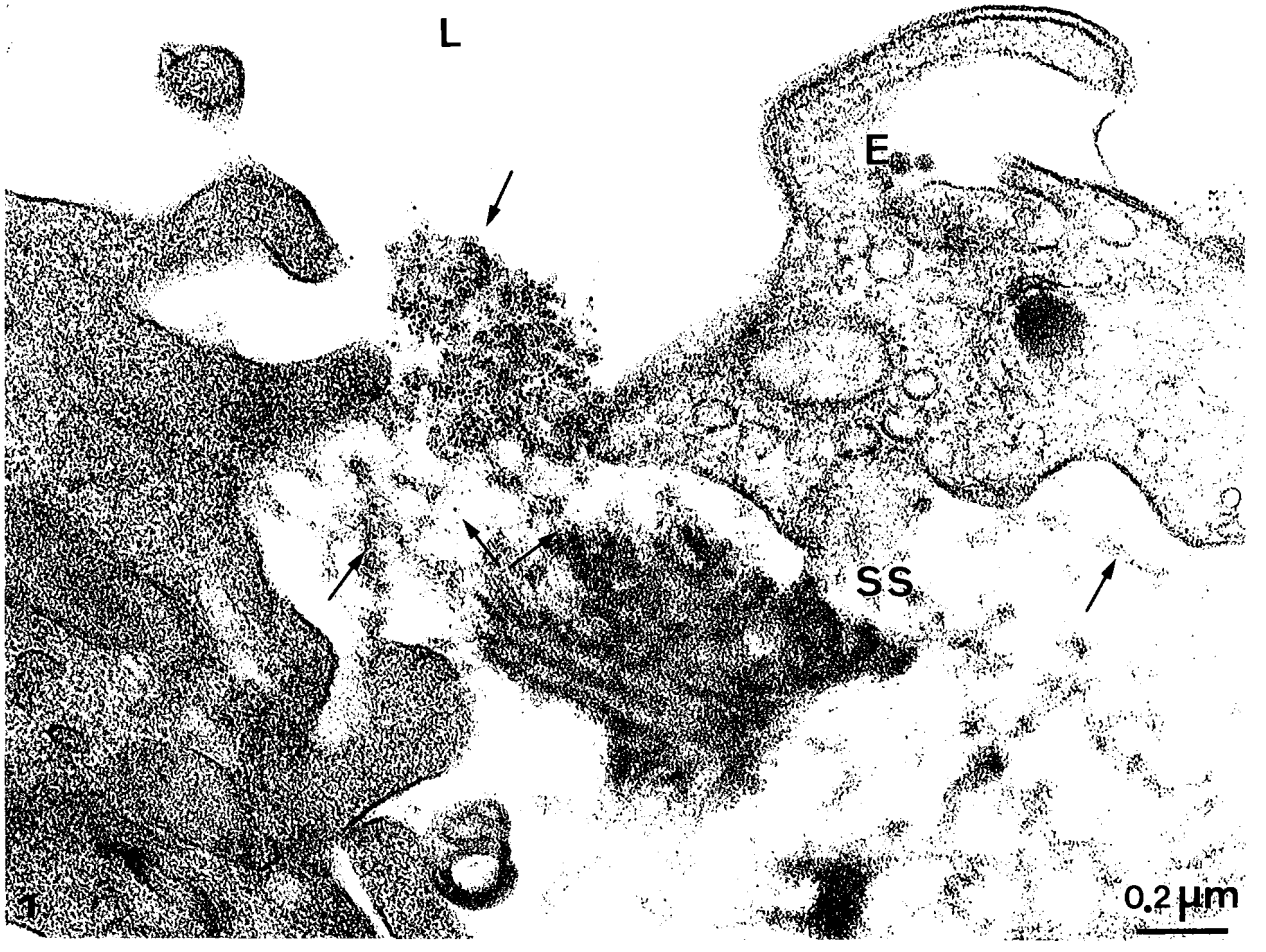

Fig. 1. Endothelial cells (E) of rat aortic arch after 6 months on the high-cholesterol diet. LDL-gold particles (arrow) are seen within the open junctions as well as in the subendothelial space (SS).

Zoological Studies 34, Supplement I (1995)

Zoological Studies

Morphological Changes of Rat hipposampal Neurons after Noradrenergic Depletion

Hwa-Min Hwang[1], Yi-Pin Lee[2], Pei-Li Ho[1], Shu-Chen Weng[1] and Hsin-I Kao[1]
[1]*Department of Anatomy, Chang Gung College of Medicine and Technology, Taoyuan, Taiwan, R.O.C.*
[2]*Department of Neurobiology, Northeastern Ohio University College of Medicine, USA*

In developing rodent brain, the noradrenergic projections are among the earliest to be formed (Lauder et al. 1974, Seiger et al. 1973). The adult pattern of noradrenergic innervation in all areas of the hippocampus was shown to be established by the postnatal 10th day (Loy et al. 1980). During this early postnatal period, the existence of an intact noradrenergic system is believed to be associated with developmental plasticity (Kasamatsu et al. 1979). Early manipulation of noradrenergic projections significantly alter the normal course of neuronal development. Neonatal treatment with either 6-hydroxydopamine (6-OHDA) or N-(2-Chloro-ethyl)- N-ethyl-2-bromobenzylamine (DSP-4) causes a permanent noradrenergic hypoinnervation of forebrain regions an a hyperinnervation of the brain stem (Gustafson et al. 1987). In the present study we investigated the effects of noradrenergic depletion by neonatal injection of DSP-4 on the hippocampal neurons by electron microscopy.

Neonatal pups of Long Evans hooded rats were given subcutaneously DSP-4 in a dosage of 100 μg/g, dissolved in 0.9% saline, once within 12 hr after birth. Some litermates were used as control animals receiving an equal volume/body weight of saline. Animals were sacrificed and processed for immunohistochemistry to reveal noradrenergic innervation and for electron microscopy to examine ultrastructural changes in the hippocampus 4-6 months after injection.

By applying a polycolonal antiserum made to dopamine β-hydroxylase, an synthetic enzyme for norepinephrine and a reliable marker of noradrenergic innervation, immunohistochemical staining revealed a substantial decrease of noradrenergic fibers in the hippocampus. At the light microscopic level, heavily stained neurons were found in the dentate gyrus, the hilar region and the hippocampal CA1 area, but rarely seen in the CA1 area, after toluidine blue-staining of 1 μm epoxy sections. These neurons had a dark appearance of both cytoplasm and nucleus and were termed "dark cells" in contrast to the light staining of normal neurons. Electron microscopic examination revealed a gradient of neuronal darkness, from normal light, grayish, gray, to completely dark. The increased darkness were due to an accumulation of fine granules in both cytoplasm and nucleus (Fig. 1). Compared with normal neurons, the dark cells barely maintained typical processes. In addition to the increase of fine granules and shrunk shape, certain cytological changes were also noted. The nuclear envelope of dark cells was rich in invagination (Fig. 2). Stacks of mostly smooth endoplasmic reticulum and polyribosomes did not aggregate to form Nissl bodies. Instead, they appeared to be abundant and distributed over the neuronal soma (Fig. 3). Even in the primary dendrites, while the normal neurons did not have many organelles, the dark cells were found to be packed with mitochondria, ribosomes and cisternal structures (Fig. 4).

Most of dark cells had an invaginated nucleus containing a normal nucleolus with increased fine granules but no increase of heterochromatin (Fig. 2). They either had stacks of long slender endoplasmic reticulum (Fig. 3) or were packed with short tortuous and enlarged reticulum (Fig. 5). In addition to abundant free ribosomes, mostly polyribosomes, many lysosomes were found to be in the form of lipofuscin granules (Figs. 3 and 5). Enlargement of several membranous structures, including Golgi apparatus, endoplasmic reticulum and nuclear envelope, and enrichment of polyribosomes and residual bodies were typical features in these cells.

Based on these ultrastructural characteristics, the dark cells appeared to be metabolically active. The morphological features of their soma are similar to those of chromatolytic perikarya induced

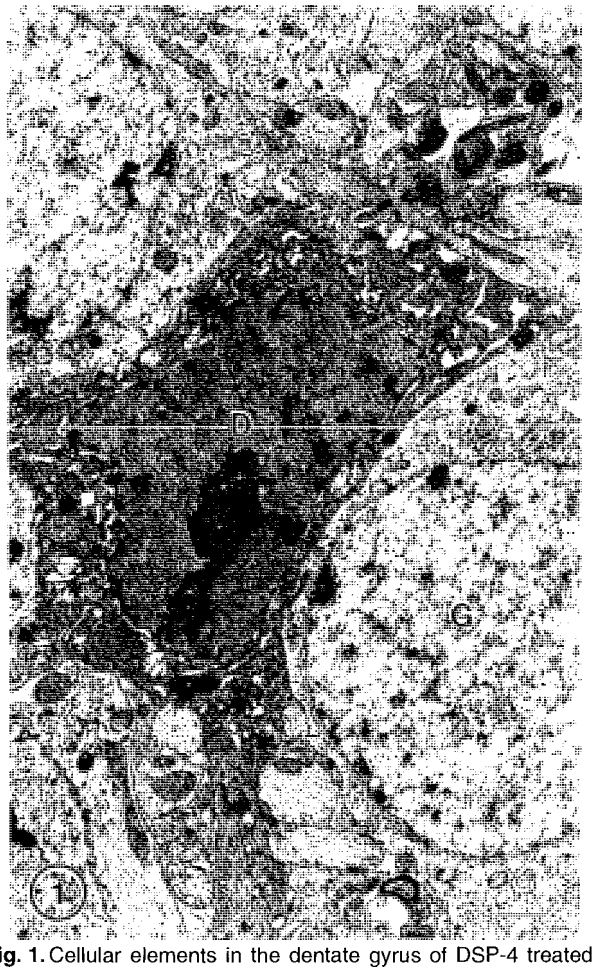

Fig. 1. Cellular elements in the dentate gyrus of DSP-4 treated rats. Normal granule cells (G) reveal light appearance of nucleus and cytoplasm. A dark cell (D) within tie granule cell layer is characteristic of intensive electron density throughout nucleus, cytoplasm and processes except enlarged cisternal structures. Scale bars: 1 μm.

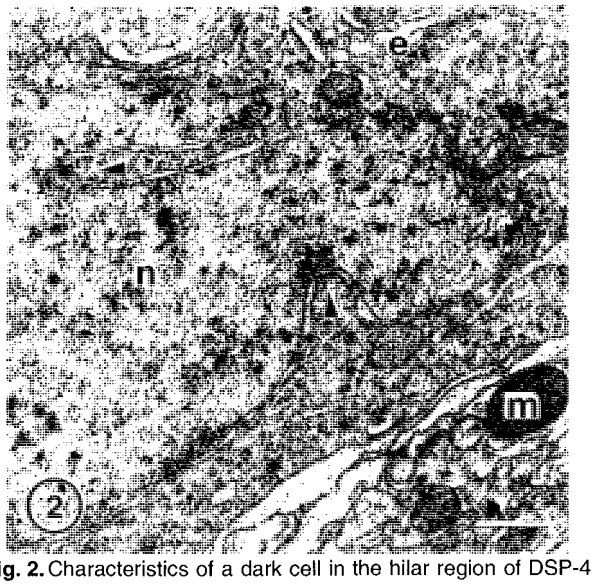

Fig. 2. Characteristics of a dark cell in the hilar region of DSP-4 treated rat. Note the increase of invagination (arrowheads) of the nucleus (n), polyribosomes, endoplasmic reticulum (e), mitochondria (m), and abundance of fine granules in both nucleus and cytoplasm. No increase of heterochromatin was seen. Scale bars: 0.5 μm.

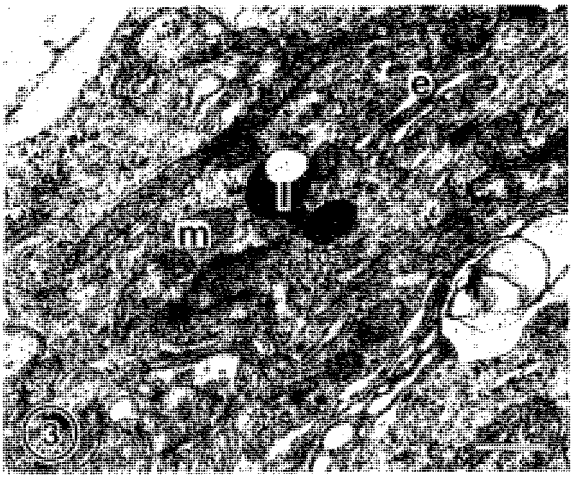

Fig. 3. Cytoplasm of a dark cell in the hilar region of DSP-4 treated rat. Except the increased polyribosomes, endoplasmic reticulum (e), mitochondria (m) and fine granules, more lysosomes (l) were seen as a form of residual body containing lipofuscin granules. Scale bars: 0.5 μm.

by axotomy. Electron microscopic studies of chromatolytic neurons have shown fragmentation of Nissl bodies in which the aggregates of granular endoplasmic reticulum decreased markedly in size with a concomitant increase of polyribosomes (Lieberman 1974). Because of the appearance of invaginated nuclear envelope, an enlarged Golgi apparatus and increased numbers and complexity of lysosomes, the chromatolytic response to axonal damage was considered to be rather a restorative process aimed at reconstituting the neurons than a degenerative phenomenon (Mathews et al. 1972). Similarly, the dark cells could be in an active state of cytoplasmic protein synthesis. The accumulation of fine granules in the nuclei and the cytoplasm could have resulted from an increased nuclear RNA synthesis, as observed in the cytochemical analysis of chromatolytic perikarya (Watson 1965 1978). Since the amount of lipofuscin granules had increased in the dark cells, accumulated fine granules could

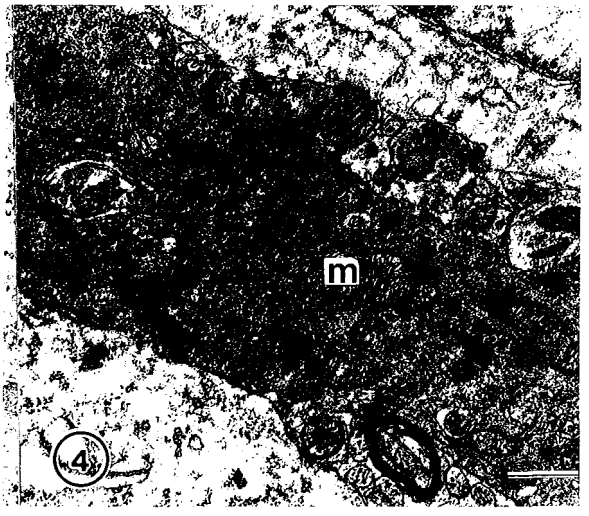

Fig. 4. Primary dendrite of a dark cell in the hilar region of DSP-4 treated rat. Like the soma, the dendrite is packed with great amount of polyribosomes, mitochondria (m) and fine granules. Scale bars: 0.5 μm.

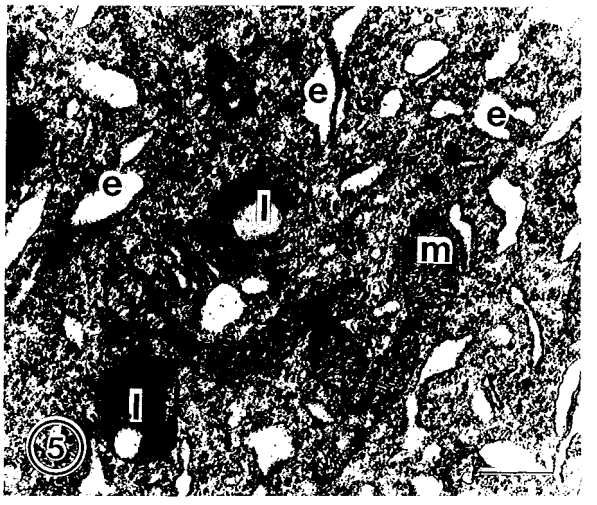

Fig. 5. Enlarged cisternae in the cytoplasm of a dark cell in the hilar region of DSP-4 treated rats. Some dark cells, like the one shown here, have enlarged cisternae (e) distributed with abundant polyribosomes, mitochondria (m), lysosomes (l) and fine granules. Scale bars: 0.5 μm.

also be a different pattern of lipofuscin accumula-'tion as found in pyramidal neurons of the aging brain (Braak 1984).

Concerning cytotoxic or neurotoxic effects of DSP-4 on developing brain, noradrenergic neurons and even other monoaminergic neurons degenerate or undergo plastic changes after drug treatment. In noradrenergic target areas, there was a dispute about neuronal loss in the neocortex after 6-OHDA injection (Ebersole 1981, Onteniente et al. 1980). Despite the presence of few disintegrated cells, no neuronal loss was observed in the hippocampus 4-6 months after injection in the present study. No ultrastructural features indicating degeneration processes, such as pyknotic cells and profiles of dense or lamellar bodies, were seen in the dark cells. Thus, most, if not all, of the dark cells are unlikely too be in a process of degeneration. Examination of specimens from drug-treated animals at several time points after injection revealed that no significant amounts of dark cells were present at light and electron microscopic levels until 2-3 months after injection. No significant changes in neuronal numbers of the hippocampal areas were found even in one-year-old norepinephrine-depleted rats. Furthermore, deep toluidine blue-stained pyramidal cells and granule cells have been reported in the early postnatal hippocampus of developing Long-Evans hooded rats before the postnatal 7th day (Fuh et al. 1990). Like the dark cells in this study, they contained fine granules in both nucleus and cytoplasma dn had a gray and dark appearance. These dark cells developed gradually into normal neurons of light appearance within a week after birth. In other system, particularly in the reproductive organs, cells of dark appearance are believed to be germ cells having mitogenic potency or newly formed cells from stem cells (Clemont et al. 1976, Cormack 1987). Although a significant increase in granule cells in the ventral dentate occurred 4 months after DSP-4 injection, no evidence of cell division was seen in the current observation. Nevertheless, dark cells may represent a population of neurons at a physiological status different from other cells.

In conclusion, neonatal injection of DSP-4 caused a substantial reduction of noradrenergic fibers and the appearance of dark cells in the hippocampus of rats aging between 4-6 months. The dark cells may have occurred as a result of long-term noradrenergic deficiency instead of direct cytotoxic or neurotoxic actions of DSP-4 on hippocampal neurons. The nature of the dark cells and their functional significance in norepinephrine-depleted rats are still unclear and require further investigation.

REFERENCES

Blue M, JG Parnavelas. 1982. The effect of neonatal 6-

hydroxydopamine treatment on synaptogenesis in the visual cortex ofthe rat. J. Comp. Neurol. **205:** 99-205.

Braak H. 1984. Architectonics as seen by lipofuscin stains. In Cerebral Cortex Vol. 1, Cellular Components of the Cerebral Cortex, eds. A Peters, EG Jones. New York: Plenum Press, p. 59-104.

Clermont Y, L Hermo. 1976. Spermatogonial stem cells and their behaviour in the seminiferous epithelium of rats and monkeys. In Stem Cells of Renewing Cell Population, eds. AB Cairnie, PK Lala, DG Osmond. New York: Academic press.

Cormack DH. 1987. Ham's Histology. London: J. B. Lippincott.

Dunwiddie TV, AL Mueller, PC Bickford, NR Zahniser. 1983. Electrophysiological and biochemical sequelae of the destruction of hippocampal noradrenergic afferents by DSP4. Brain Res. **269:** 311-317.

Ebersole P, JG Parnavelas, M Blue. 1981. Development of the visual cortex of rats treated with 6-hydroxydopamine in early life. Anat. Embryol. **162:** 489-492.

Fuh YS, HM Hwang. 1990. Developmental changes in hippocampal CA1 area of Long-Evans hooded rat. Symp. Assoc. Anat. R.O.C. **2:** 10-11.

Gustafson EL, RY Moore. 1987. Noradrenaline neuron plasticity in developing rat brain: effects of neonatal 6-hydroxydopamine demonstrated by dopamine hydroxylase immunocytochemistry. Devel. Brain Res. **37:** 143-155.

Jaim-Etcheverry G, LM Zieher. 1980. DSP-4: A novel compound with neurotoxic effects on noradrenergic neurons of adult and developing rats. Brain Res. **188:** 513-523 .

Jonsson G, H Hallman, E Sundstrom. 1982. Effects of the noradrenaline neurotoxin DSP-4 on the postnatal development of central noradrenaline neurons in the rat. Neurosc. **7:** 2895-2907.

Kasamatsu T, JD. Pettigrew. 1979. Preservation of binocularity after monocular deprivation in the striate cortex of kittens treated with 6-hydroxydopamine. J. Comp. Neurol. **185:** 139-162.

Lauder JM, FE Bloom. 1974. Ontogeny of monoamine neurons in the locus coeruleus, raphe nuclei, and substantia nigra of the rat. I. Cell differentiation. J. Comp. Neurol. **155:** 469-482.

Lieberman AR. 1974. Some factors affecting retrograde neuronal responses to axonal lesions. In Essays on the Nervous System, eds. R Bellaris, EG Gray. London: Oxford University Press, pp. 71-105. Loy R, DA Koziell, JD Lindsey, RY Moore. 1980. Noradrenergic innervation of the adult rat hippocampal formation. J. Comp. Neurol. **189:** 699-710.

Maeda T, M Tohyama, N Shimizu. 1974. Modification of potential development of neocortex in rat brain with experimental deprivation of locus coeruleus. Brain Res. **70:** 515-520.

Mathews MR, G Raisman. 1972. A light and electron microscopic study of the cellular response to axonal injury in the superior cervical ganglion of the rat. Proc. R. Soc. Ser. **B 181:** 43-79.

Onteniente B, N Konig, J Sievers, S Jenner, HP Klemm, R Marty. 1980. Structural and biochemical changes in rat cerebral cortex after neonatal 6-hydroxydopamine administration. Anat. Embryol. **159:** 245-255.

Seiger A, L Olson. 1973. Late prenatal ontogeny of central monoamine neurons in the rat: fluorescence histochemical observations. Z. Anat. Entwickl.-Gesch **140:** 137-141.

Sharma VK, SI Hanik, R Busto, SP Banerjee. 1981. Effects of noradrenaline depletion on adrenergic and muscarinic cholinergic receptors in the cerebral cortex, hippocampus and cerebellum. Exp. Neurol. **72:** 179-194.

Wendlant S, TJ Crow, RV Stirling. 1977. The involvement ofthe noradrenergic system arising from the locus coeruleus in the postnatal development of the cortex in theratbrain.BrainRes. **125:** 1-9.

Yasuda RP, TV Dunwiddie, NR. Zahniser. 1986. The acute effects of 6-hydroxydopamine treatment on noradrenergic function in the rat hippocampus in vitro. BrainRes. **367:** 121-127.

Zahniser NR, GR Weiner, T Worth, K Philpott, RP Yasudo, G Jonsson,TV Dunwiddie. 1986. DSP4-induced noradrenergic lesions increase ,-adrenergic receptors and hippocampal electrophysiological responsiveness. Pharmacol. Biochem. Behav. **24:** 1397-1402.

Zoological Studies 34, Supplement I (1995)

Zoological Studies

The Video-enhanced Light Microscope: A Renaissance Tool for Quantitative Live-cell Microscopy

Charles E. Bracker
Department of Botany and Plant Pathology, Purdue University, West Lafayette, IN 47907-1057, USA

The in vivo dynamics of living cells, organelles, and other moving objects on a microscopic scale are especially amenable to study and quantitative analysis by video enhancement and real-time digital image processing of high magnification light microscopic images. Dynamic events in cell growth or other processes can be tracked and measured with unprecedented precision and efficiency. Videotaped images of cells growing in thin slide culture chambers are spectacular, and the results dramatically bring to life developmental processes at high resolution that are impossible to imagine, interpret, or accurately quantitate from still images. The processing of these images permits them to be measured precisely and analyzed. The magnification required as the resolution limit of the microscope is approached is in the range of 5,000 x to 20,000 x on video display monitors. While such magnifications necessarily involve empty magnification, the enlargement is essential for detecting positional changes in the 1-2 pixel range between video frames when using a microscaler or the digital measuring function of an image processor.

Images obtained through a video camera are processed before they are displayed on a monitor or recorded on magnetic storage media. Real-time digital image processing simulates the video-enhanced contrast championed by Robert Allen for DIC microscopy of living cells, microtubules, etc. and permits the ready detection and display of delicate objects that are well below the size range for Abbe resolution. This processing allows background equalization to remove optical irregularities, enables brightness control, provides gamma control and contrast stretching to optimize image contrast for parts of the object that are of greatest interest, and it permits pseudocoloring to discriminate specific gray levels. Real-time application of digital filters also allows special effects to be recorded in real time. Videotaped images can be analyzed frame by frame to precisely locate and plot the displacement rate, trajectories, and motion patterns of objects that are either moving or changing size and shape during a video sequence. Successive freeze-frame images obtained through a frame grabber can be subtracted from each other to reveal difference images which reveal patterns of dynamic change during a particular time interval.

Traditionally performed with differential interference contrast optics (DIC), video enhancement is especially effective with phase contrast images of living cells. Phase contrast often reveals more information about the specimens than does DIC because it reveals differences and dynamic changes in refractive index, and it displays information in shades of gray that are related to differential refractive index within the specimen. Thus, images that are otherwise revealed as undifferentiated "pseudo bumps and depressions" in DIC images, appear distinct from each other for more precise identification and characterization when phase contrast optics are used. Delicate objects in living cells, which may appear undetectable to the human eye in DIC images, can be seen, tracked, and measured with enhanced phase contrast. To take best advantage of phase contrast optics, cells should be mounted or grown in a medium with its refractive index adjusted to a value similar to that of the specimen, to minimize the distracting phase haloes at the boundaries of cells.

Measurements of motion or growth near the limits of optical detectability require appropriate compromise among competing variables to assure that true displacement is being measured and that artifacts of the measurement technique have been avoided. This requires attention to ac-

ceptable noise levels in digital images, and selecting appropriate time intervals between measurements in relation to pixel size and displacement rate. Without such precautions, non-linear displacement patterns can be corrupted artifactually to disclose artifactual changes in displacement rate or suppression of rate changes, both of which lead to erroneous conclusions about motion or growth.

The detection limits in low-noise images approach single pixels which represent image units as small as 30 nm. When gray-scale images are converted to pseudocolor, the positions of specific gray-scale values are obvious to the unaided eye and can be used as objective markers for locating and measuring positions of an object in successive images. This is especially evident for living fungal hyphae whose growth can now be measured at one-second intervals, roughly two orders of magnitude faster than was practical with prior methodology.

This advantage has permitted measurements that reveal cell elongation in altemating fast-slow pulses with periods ranging from 3 to 30 seconds depending on the organism and its overall cell elongation rate. Individual organelles can be tracked, their motion plotted, and dynamic processes interpreted from the displayed data in ways that were not previously possible.

One of the problems encountered in video microscopy is the potential image distortion caused by electronic devices in the chain of components leading from the original optical image created by the objective lens to the final image that is displayed or printed (e.g. frame grabbers, video monitors, printers, image processors, cameras, etc.). Further, because of the nature of video imaging, point-to-point resolution in a final image may differ from that obtainable by the optical system alone and will differ in the X and Y axes. Microfabricated test targets are being developed to: a) routinely record and measure resolution in X, Y, and Z axes, b) to judge detection capability in X and Y, c) to measure image distortion, and d) to establish accurate size calibration, by recording phase and/or amplitude test objects from the test targets onto videotapes under specific conditions of microscope alignment and operation. An angled ramp with microfabricated resolution patterns etched onto its surface yields a simple and direct measure of depth-of-field under any conditions of microscope alignment. This provides a simple means of accurately measuring the thickness of in-focus optical sections when it is necessary to acquire images of specimens at known focal intervals for three-dimensional reconstructions without overlap or missing information. These targets will function as routine calibration tools and as test targets for critically evaluating the capabilities of optical and electronic devices used in the total microscope technology package.

Another problem important to quantitative studies is artifactual drift, or creep, of the specimen image. This is caused by thermal drift of microscope parts as the instrument warms up after the illuminator and other electrical elements are turned on. Typically, the rate of drift is greatest in the Z axis (reaching more than 30 μm in 2 hrs.) and least in the X axis, and is influenced by the construction, design, and brand of the microscope as well as the time when the illuminator was turned on. Thermal drift declines to a minimum about two hours after the illuminator is turned on but still continues at a measurable rate that cannot be controlled with conventional microscope design. A robotic auto-tracking stage can be programmed to track several objects within the image independently, and when the drift of stable markers is automatically subtracted from the total motion of target objects, net displacement due to true motion or growth of the object can be plotted.

A recent development, which will be available in the near future, is a robotic motion and/or cell growth tracking stage for light microscopes that will automatically track moving objects in real time, in three dimensions, by analyzing the trajectories of objects identified in successive video images. The concept instrument will provide focus tracking as well as automatic X-Y tracking and data recording for displacement of the target objects. This technological advance turns the microscope stage from a relatively simple mechanical device for adjusting the position and focus of the object, into a sophisticated analytical tool for studying quantitative aspects of cellular dynamics at a level of accuracy, and with a response time, that lie beyond the capability of human control of a manual or motor driven stage. By tracking object(s) over a coordinate field that is many times larger than the window in view at any one time, tracking is seamless, and continuous data streams are not corrupted when the stage translates to track an object as it moves from one field of view to another.

The convenience and power of the modern video-enhanced microscope system has made it possible to quantitatively analyze patterns of cell morphogenesis as they are influenced by behavior of subcellular structures. These include coordination between the positions and migration rates

of secretory vesicles in fungal cells and sites of localized cell expansion and wall growth. But the technique is applicable to any object which changes its position, orientation, or size during observation. This approach has also provided an unprecedented opportunity to merge microscopy of real cell dynamics with computer simulations created by computer-driven cell growth models and to quantitatively compare predictions of the models with actual images of growing cells.

Zoological Studies 34, Supplement I (1995)

Zoological Studies

Distribution of Taste Pores and Ultrastructural Organization of Gustatory Cells in Gerbil Vallate Taste Buds

Kuo-Shyan Lu[1], Ming-Huei Chen[1] and Ko-Kaung Liao[2]

[1]*Department of Anatomy, College of Medicine, National Taiwan University, Taipei, Taiwan, R.O.C.*

[2]*Chung-Shan Dental and Medical College, Taichung, Taiwan, R.O.C.*

The gerbil, a desert animal, is different from other rodents such as rat, mice and others, because it can survive under extremely dry conditions due to its great capacity to conserve water. In a recent review, Schiffman and Gatlin (1993) proposed that the sense of taste conveys the attractive properties of foods (five primary taste properties: salty, sour, sweet, bitter and umami) that promote and maintain food intake. They also inferred that taste not only play a role in protection against harmful substance but also contribute significantly to nutritional status as well as to the quality of life. Consequently, it is reasonable to expect that the ultrastructure of gerbil's taste bud may different from that of other rodents. However, to our knowledge so far, we retrieved only one abstract concerning the ultrastructure of the gerbil taste bud in fungiform papilla (St. Joer and Kinammon 1987) and no other previous reports have been published. Moreover, the quantification on the distribution of the taste bud in the gerbils is lacking. In order to extend our knowledge about the taste capacity and the ultrastructure of the taste bud in gerbils, we determined to analyze the surface ultrastructure and distribution of taste pores by scanning electron microscopy and to characterize the ultrastructure of gustatory cells by transmission electron microscopy in the gerbil vallate papilla.

In the gerbil, a single vallate papilla was located on the midline of the tongue root. It comprised two separated trenches (about 800) μm in length and 300μm in depth), which were separated more widely at the rostral end than at the caudal end. The lingual epithelium on the dorsal surface of the papilla is parakeratinized and that on the trench wall is nonkeratinized or slightly keratinized.

Transmission electron microscopy revealed that the taste pore of the gerbil vallate taste buds was populated by a tuft of microvilli (equivalent of taste hairs at light microscopic level) among which an electron-dense material filled all the intervillous spaces. Four types of taste cells were identified by their ultrastructural characteristics: type I, II, intermediate and basal cells, and each type comprised about 78%, 14%, 5% and 1-2% of the total taste cell population, respectively (Fig.1).

Taste buds distributed randomly on both lateral and medial sides of the trench wall in roughly equal number as estimated by the number of taste pores on the exposed trench wall surface (Fig.2). The

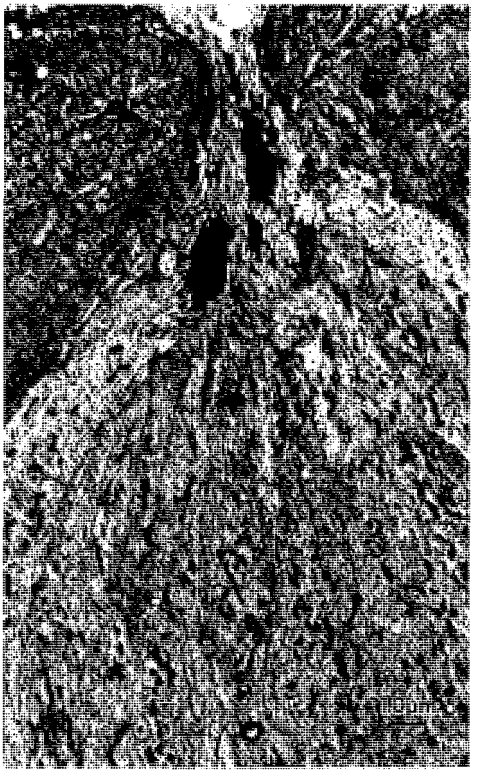

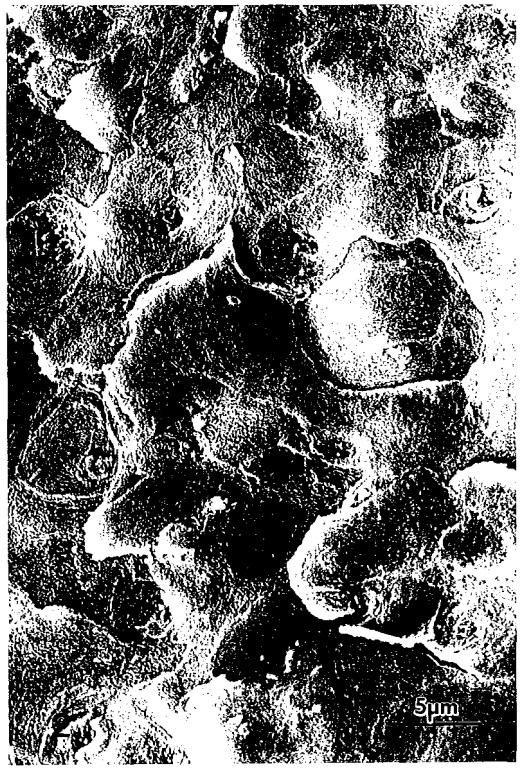

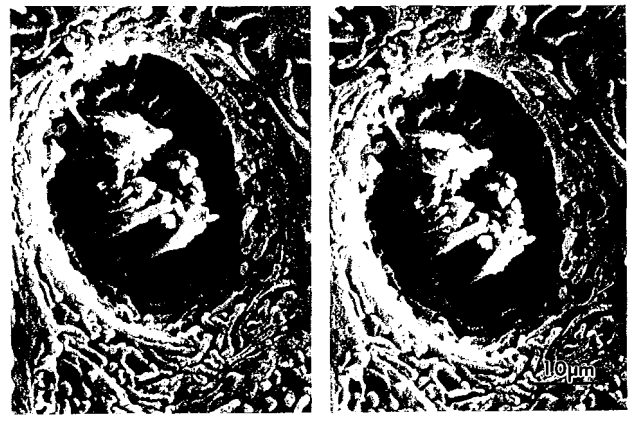

total number of taste pores observed is 342 from four different vallate papillae with an average of 85±1.67 (mean ± standard error of mean) taste pores per papilla (N=4). The distribution density on the trench wall is 1.89 ± 0.5 taste pores per 1000 μm^2 (N=8; from either medial or lateral wall of the trenches in five papillae). There were more numerous taste pores on the caudal end than on the rostral end. Figure 3 is a stereopair electron micrographs of a rather clean taste pore demonstrating a tuft of microvilli of taste cells underneath the pore. It is revealed that the taste pore was surrounded by layers of parakeratinized epithelial cells characterized by numerous microridges (microfolds or microreplicas) on the free surface. Frequently, the taste pore was so deep and hindered by the secretory material of the taste bud and the mucus of the oral mucosa, and therefore, no definite structures were identified.

This is the first report to reveal the ultrastructural organization and to demonstrate quantitatively the distribution of taste pores in gerbil vallate papilla. The present data will provide a firm basis for future comparative, immunocytochemical and neurological studies involving the gustatory system. Further studies on taste pore organization by freeze-fracture to investigate their intercellular junctions and the possible mechanism of gustatory neural transmission are in progress.

Supported in part by grants Nos. NSC-81-0412-B002-558 and NSC-82-0412-B002-407 from National Science Council, Taiwan, ROC.

REFERENCES

St. Joer VL, JC Kinnamon. 1988. Assoc. Chemorecp. Sci. **9:** 84 (abstract)

Schiffman SS, CA Gatlin. 1993. Ann. Rev. Nutri. **13:** 405-436

Zoological Studies 34, Supplement I (1995)

Feldkamp-type Cone-beam Reconstruction: Revisited

Ge Wang[2] and Ping-Chin Cheng[1]

[1]*Advanced Microscopy and Imaging Laboratory (AMIL), Department of Electrical and Computer Engineering State University of New York, Buffalo, NY 14260, USA*

[2]*Mallinckrodt Institute of Radiology, Washington University, School of Medicine, Saint Louis, Missouri 63110, USA*

The cone-beam approach is desirable for faster data collection, higher image resolution, better radiation utilization and easier hardware implementation, therefore it attracts more and more attention in biological, medical and material studies (Smith 1990, Gulberg 1992, Cheng et al. 1993). Despite important progress in exact cone-beam reconstruction (Tuy 1983, Smith 1985, Grangeat 1991, Danielsson 1992, Axelsson and Danielsson 1994), approximate cone-beam formulas remain practically important. Feldkamp-type formulas are popular in approximate cone-beam reconstruction (Feldkamp et al. 1984, Gullberg 1992, Wang et al. 1991, 1992, 1993a, 1993b, 1994).

The advantages of approximate cone-beam reconstruction are as follows. First, incomplete scanning loci can be used. The completeness condition for exact reconstruction rquires that there exist at least a source position on any plane intersecting an object. This condition cannot be satisfied in cone-beam X-ray microtomography when planar or dashed-line helical scanning loci are used (Wang et al. 1991, 1939a). Second, partial detection coverage is permissible. In exact cone-beam reconstruction, the cone-beam is assumed to cover the entire object from any source position. Unlike emission tomography, complete detection coverage is impossible in cone-beam X-ray microtomography, since most specimens are either rod-shaped or planar instead of spheric. Third, computational efficiency is high. Because of the second advantage, approximate reconstruction involves much less raw data, especially in reconstruction of rod-shaped and planar specimens. The computational structure of Feldkamp-type reconstruction is straightforward, highly parallel, and hardware supported. Feldkamp-type formulas are particularly fast in reconstructing a limited number of slices or small regions of interest. The linogram idea (Edholm and Herman 1987) used in exact fourier cone-beam reconstruction (Danielsson 1992, Axelsson and Danielsson 1994) may also be adapted to Feldkamp-type reconstruction. Fourth, image noise and ringing artifacts are less. With the direct Fourier method (Axellson and Danielsson 1994), it was found that exact cone-beam reconstruction produces more ringing as compared to the Feldkamp method. We hypothesize that this is inherent to all exact cone-beam reconstruction formulas that take the second derivative of data. In most of the cone-beam literature synthetic noise-free data are used, therefore this problem did not look too serious. Further evaluation and comparison would be valuable

Feldkamp-type cone-beam formulas were derived by modifying the convolution and back projection fan-beam formula. To reconstruct a voxel, fan-beams tilted horizontally and passing through the voxel are used. To Compensate for the tilted fan-beam geometry, both the source-to-origin distance and the angular differential were modified, and incremental contributions integrated. In this paper we will formulate Feldkamp-type reconstruction in a manner that is clearer in terms of plausibility.

Let the $\vec{x}$ coordinate system be the cone-beam reconstruction system, where $\vec{x}=(x, y, z)^t$, $(.)^t$ denotes the transpose of a vector. A specimen $s(\vec{x})$ is supported in the cylindrical region $x^2+y^2 \leq 1$. A scanning locus is described as $\vec{\phi}(\beta)=(\rho(\beta)\cos\beta, \rho(\beta)\sin\beta, h(\beta))^t$, $\rho(\beta)>1$, where β is the X-ray source rotation angle around the z axis counterclockwise. A scanning turn is obtained by restricting β in $[0, 2\pi)$. Cone-beam projection data, $R(p, \zeta, \beta)$, or $R(\vec{\alpha}, \beta)$, are recorded on an imaginary detector plane passing through the z axis and facing the X-ray source, where p and ζ are horizontal and longitudinal coordinates of the detector system, and $\vec{\alpha}=(\alpha_1, \alpha_2, \alpha_3)^t$ specifies

the direction of an X-ray.

Let us consider δ and c functions: $\delta(\vec{x}-\vec{x}_0)$ models a 3-D point object located at $\vec{x}_0$, $c(\vec{x})$ is defined as being independent of z, that is, $c(\vec{x})=c(x, y)$.

Longitudinally projecting $\vec{\phi}(\beta)$, $\beta\in[0, 2\pi)$, onto the $z=z_0$ plane. We have another scanning locus: $\vec{\phi}^*(\beta)=(\rho(\beta)\cos\beta\ \rho(\beta)\sin\beta\ z_0)^t \quad \beta\in[0, 2\pi)$. It can be shown that exact fan-beam data $R^*(p, 0, \beta)$ in the $z=z_0$ plane can be obtained by multiplying a horizontal profile of cone-beam projection $R(p, \zeta, \beta)$ with the cosine of the X-ray tilting angle, $\frac{\sqrt{\rho^2(\beta)+p^2}}{\sqrt{\rho^2(\beta)+p^2+\zeta^2}}$. Note that in the case of $\delta(\vec{x}-\vec{x}_0)$ ζ should be the longitudinal coordinate of projected $\delta(\vec{x}-\vec{x}_0)$.

Under the moderate conditions we proved a derivative-free noncircular fan-beam reconstruction formula (Wang et al. 1993a):

$$g(x,y)=\frac{1}{2}\int_0^{2\pi}\frac{\rho^2(\beta)}{(\rho(\beta)-s)^2}\int_{-\infty}^{\infty}F(p,\beta)f\left(\frac{\rho(\beta)t}{\rho(\beta)-s}-P\right)\frac{\rho(\beta)}{\sqrt{\rho^2(\beta)+\rho^2}}dpd\beta, \quad (1)$$

where $F(p, \beta)$ represents fan-beam data,

$$t=x\cos\beta+y\sin\beta \text{ and } s=-x\sin\beta+y\cos\beta,$$

f is a reconstruction filter. Hence, applying the derivative-free noncircular fan-beam reconstruction formula with $R^*(p, 0, \beta)$ will produce exact reconstruction o the $z=z_0$ plane.

As δ and c functions represent typical cases of sharp and smooth variation, it is reasonable to apply the same cone-beam data correction scheme generally to approximate transaxial fan-beam data. By doing so, we immediately obtain the generalized Feldkamp cone-beam reconstruction formula (Wang et al. 1993b):

$$g(x,y,z)=\frac{1}{2}\int_0^{2\pi}\frac{\rho^2(\beta)}{(\rho(\beta)-s)^2}\int_{-\infty}^{\infty}R(p,\zeta,\beta)f\left(\frac{\rho(\beta)t}{\rho(\beta)-s}-p\right)\frac{\rho(\beta)}{\sqrt{\rho^2(\beta)+p^2+\zeta^2}}dpd\beta, \quad (2)$$

where

$$\zeta=\frac{\rho(\beta)(z-h(\beta))}{\rho(\beta)-s}.$$

It becomes clear that the essential step in Feldkamp-type cone-beam reconstruction is to modify cone-beam projection data so as to achieve exact transaxial reconstruction for any δ and c functions,. Correction is done by multiplying cone-beam data with the cosine of the X-ray tilting angle. Consequently, Feldkamp-type reconstruction can be decomposed into two steps: cone-beam to fan-beam data conversion and fan-beam reconstruction.

With arguments similar to those described above, cone-beam reocnstruction can also be achieved via correcting cone-beam data to fan-beam data in an inclined plane under the condition that a projected scanning locus stays outside a projected specimen support, the projection direction being defined by the normal of the tilited plane. It was previously established that the longitudinal integral of an reconstructed image volume by Feldkamp-type algorithms is exact (Feldkamp et al. 1984, Wang et al. 1992). We similarly proved that Feldkamp-type reconstruction with respect to a tilted longitudinal axis produces the exact 2-D parallel projection along the tilted longitudinal axis. This finding updates our earlier result that 2-D parallel-beam projections can be aproximately computed from cone-beam data (Lin et al. 1993). In practice, full 3-D information is often not useful, several stereo projection image pairs may be sufficient in some applications. Hence, exact 2-D parallel-beam projection pairs are the most desirable.

Our derivative-free noncircular fan-beam formula utilizes full-scan data, which consist of two complete projection data sets. Actually, fan-beam reconstruction can also be performed with either half-scan or double full-scan projection data. Accordingly, half-scan and double-helix-scan cone-beam algorithms can be formulated. The above discussion with one scanning turn can be extended to half- and double-helix-scan cases, respectively. With the same progection data correction, exact transaxial reconstruction can be achieved for $\delta(\vec{x}-\vec{x}_0)$ and $c(\vec{x})$ with half-or double-helix-scan data. In the half-scan case, the angular range involved in a transaxial slice reconstruction is substantially reduced. As a result, half-scan cone-beam reconstruction (Wang et al. 1994) may improve longitu dinaltemporal resolution. In the double-helix-scan case, a transaxial slice is reconstructed with consine-corrected and linearly com-

bined projection data from twins of scanning turns. Double-helix-scan cone-beam reconstruction is exact for a specimen with linear longitudinal variation.

REFERENCES

Axelsson C, PE Danielsson. 1994. Three-dimensional reconstruction from cone-beam data in O ($N^3 \log^N$) time. Phys. Med. Biol. **39:** 477-491.

Cheng PC, TH Lin, G Wang, DM Shinozaki, HG Kim, SP Newberry. 1992. Review on the development of cone-beam X-ray microtomography. Proc. of the 13th International Congress on X-ray Optics and Microanalysis: 559-556, Manchester, UK.

Danielsson PE. 1992. From cone-beam projections to 3D Radon data in O ($N^3 \log^N$) time. Proc. IIEEE Medical Imaging Conference: 1135-1137.

Edholm PR, GT Herman. 1987. Linograms in image reconstruction from projections, IEEE Trans. Medical Imaging **6:** 301-307.

Feldkamp LA, LC Davis, JW Kress. 1984. Practical cone-beam algorithm. J. Opt. Soc. Am. **A1:** 612-619.

Grangeat P. 1991. Mathematical framework of cone-beam 3D reocnstruction via the first derivative of the Radon transform. Mathematical Methods in Tomography (Lecture Notes in Mathematics) ed. Herman GT, Louis AK and Natterer F.

Gullberg GT, GL Zeng, FL Datz, PE Christian, CH Tung, HT Morgan. 1992. Review of convergent beam tomography in single photon emission computed tomography. Phys. Med. Biool. **37:** 507-534.

Lin TH, G Wang, PC Cheng . 1993. Reconstruction of orthogonal views from cone-beam projections. Journal of Scanning Microscopy **15** (Suppl III): 61-63.

Smith BD. 1985. Image reconstruction from cone-beam projections: necessary and sufficient conditions and reconstruction methods. IEEE Trans. Medical Imaging **4:** 14-28.

Smith BD. 1990. Cone-beam tomography: recent advances and a tutorial review. Opt. Eng. **29:** 524-534.

Tuy HK. 1983. An inversion formula for cone-beam reconstruction. SIAM J. Appl. Math. **43:** 546-552.

Wang G, TH Lin, PC Cheng, DM Shinozaki, HG Kim. 1991. Scanning cone-beam reconstruction algorithms for X-ray microtomography. Proc. of SPIE **1556:** 99-113.

Wang G, TH Lin , PC Cheng, DM Shinozaki. 1992. Point spread function of the general cone-beam X-ray reconstruction formula. Journal of Scanning Microsocpy **14:** 187-193.

Wang G, TH Lin, PC Cheng. 1993a. A derivative-free non-circular fan-beam reconstruction formula. IEEE Trans. Image Processing **2:** 543-547.

Wang G, TH Lin, PC Cheng, DM Shinozaki. 1993b. A general cone-beam reconstruction algorithm. IEEE Trans. Medical Imaging **12:** 486-496.

Wang G, Y Liu, TH Lin, PC Cheng, DM Shinozaki. 1994. Half-scan cone-beam X-ray microtomography formula. Journal of Scanning Microscopy **26:** 216-220.

Wang G, PC Cheng. 1995. Rationale of Feldkamp-type cone-beam CT, Proc. of the 4th International Conference for Young Computer Scientists (in press).

Zoological Studies 34, Supplement I (1995)

Zoological Studies

Cytoskeletal and Nuclear Behavior During Female Gametophyte Development and Fertilization in Angiosperms

Bing-Quan Huang[1], William F. Sheridan[1] and Scott D. Russell[2]
[1]*Department of Biology, University of North Dakota, Grand Forks, ND 58202, USA*
[2]*Department of Botany and Microbiology, University of Oklahoma, Norman, OK 73019, USA*

INTRODUCTION

The basic events of embryo sac development and fertilization have been extensively studied using classical techniques in light microscopy and electron microscopy. The megaspore mother cell produces four megaspores after meiosis. Only one chalazal megaspore survives and then goes through three mitotic divisions giving rise to a 7-celled embryo sac. However, the information concerning nuclear positioning and anchoring, nuclear division, cell wall and filiform apparatus formation and its correlation to the changes of mcirotubular cytoskeleton is still scarce due to the inaccessibility of megasporocyes and megagametophytes.

In most of the species studied, the prominent features during fertilization include the degeneration of one of the synergids, its subsequent penetration by the pollen tube, and release of the male gametes which subsequently migrate and fuse with the female target cells. The elements of this fertilization system are well described, but the organization and possible involement of the cytoskeleton of the embryo sac have only recently been examined. The exclusion of the sperm cytoplasm before fusion is not yet completely understood.

To obtain a better understanding of the microtubular and nuclear behavior during the embryo sac development and the involvement of cytoskeleton during fertilization, we have characterized the changes of oganellar DNA and the role of the microtubular cytoskeleton during megasporogenesis and megagametogenesis in maize and structural and cytoskeletal changes during fertilization in *Nicotiana tabacum*.

RESULTS AND DISCUSSION

Embryo sac development is initiated by the meiotic divisions of the megaspore mother cell. The cytoplasmic organelles are predominantly distributed in the chalazal region of the megasporocyte reflecting the early polarity of the cell which confirm the previous reported premeiotic establishment of megas-porocyte polarity. After meiosis I the two nuclei of the megasporocyte migrate to the opposite poles of the cell which elongates to a large extent. By the completion of meiosis, the megasporocyte has produced four megaspores, among which only the chalazal-most megaspore survives while the three other megaspores degenerate. The organellar DNA of the megaspore is mainly perinuclear. The first mitosis of the surviving megaspore gives rise to the two-nucleate embryo sac. The polarization of he microtubules and organellar DNA becomes conspicuous. Dense microtubule bundles in the perinuclear region of the mcropylar end of the embryo sac form an anastomosing network extending from the nucleus to the cell cortex. The micropylar nucleus is surrounded by a dense accumulation of organellar DNA and perinuclear microtubules, while those in the chalazal end are present to a lesser extent. Although the precise function of the these perinuclear microtubules is unclear, it is likely that each pole of microtubules claims a region of cytoplasm in which the microtubules extend and maintain one pattern of polarity. The polarity of DNA-containing organelles is apparently established in the late two-nucleate embryo sac with the DNA-containing organelles predominantly surrounding the micropylar nucleus. Because the young egg cell con-

tains a significant number of the DNA-containing organelles after cellularization of the embryo sac, it appears that this early event in the determination of the reproductive cells occurs in the two-nucleate stage, although cellular differentiation is delayed until cytokinesis at the eight-nucleate stage.

The initiation of the second mitosis is followed by simultaneous nuclear divisions at both the micropylar and chalazal poles. At telophase of the second mitosis the phragmoplast at the micropylar end is oriented parallel to te long axis of the embryo sac and is nearly perpendicular to the transverse orientation of the chalazal phragmoplast. Consequently, the plane of alignment of the pair of sister nuclei at the micropylar pole is nearly a right angle to that of sister nuclei at the chalazal pole. Simultaneous nuclear division also occurs in the four nuclei at the third mitosis. At cytokinesis of the third mitosis phragmoplasts ar simultaneously formed between the eight nuclei at the micropylar and the chalazal poles, indicating the location of future cell walls . The disturbance of the positioning of the female gametophyte nuclei and their spatial relationship during cell formation and differentiation embryo sacs carrying the maize indeterminate gametophyte (ig) mutation results in the formation of unanticipated cell types. This suggests that the positioning of the nuclei by control of mitotic spindle orientation and by control of unclear migration is fundamentally related to the determination of cell fate and cell differentiation in the developing embryo sac. After cellularization, two synergids and one egg cell form at the micropylar pole, three antipodal cells form at the chalazal pole, and the central cell occupies the center of the embryo sac. Numerous longitudinally aligned microtubule bundles are localized at the synergids and the antipodal cells, while sparse transverse microtubule arrays are seen in the central cell, mainly at the cortical region. The antipodal cells continue to divide and produce variable numbers of cells at the chalazal pole until embryo sac maturity.

Before fertilization, the synergid is a highly polarized cell with dense longitudinally aligned arrays of microtubules adjacent to the filiform apparatus at the micropylar end of the cell associated with major organelles. However, it is evident upon examination of cryofixed material that one of the synergids displays a dramatic morphological change after pollination, which begins to degenerate before pollen-tube arrival with breakdown of the plasma membrane and the larger chalazal vacuole delayed until the penetration of the pollen-tube. The electron density of cytoplasmic organelles increases and the nucleus becomes distorted. Abundant electrondense material extends from the degenerated synergid into intercellular spaces at the chalazal end of the synergid and between the synergids, egg and central cell. Rhodamine-phalloidin and immunogold labeling revealed that this electron-dense material contains abundant actin. Actin in the synergid becomes locally intense and particularly conspicuous at the chalazal end of the dengerated synergid, forming two "corona"-like bands at the inter-faces between the egg, central cell and synergid. The location of myosin-like proteins in pollen tube and on the surfaces of generative cells and vegetative nuclei presents the possibility that actomyosin interactions act as a controlling factor in the deposition, positioning and fusion of male gametes during fertilization. The sperm cell, which are believed to lack actin, may therefore be passively conveyed by means of the superficial myosin of the sperm cells and the actin coronas of the embryo sac. This actin is part of a mechanism in the egg apparatus which apppears to precisely position and facilitate the access of male gametes to the egg and central cell for fusion.

Upon pollen-tube arrival, the male gametes are released through a terminal aperture into the degenerate synergid. Cellular organelles remain largely intact after polen tube discharge. This suggests that the onset of synergid degeneration occurs before the arrival of the polen tube, but the breakdown of the cell occurs only after pollen tube penetration. Unfused sperm cells within the degenerate synergid appear to be strongly modified by their passage in and discharge from the pollen tube. The exterior of the sperm cell is delimited by a single membrane. Apparently once pollen tube discharge occurs, the inner pollen tube plasma membrane is stripped off and releases the sperm and vegetative nucleus triggering the disassociation of the male germ unit and allowing the gametes to separate and follow their respective fates. Before the gametic fusion, a few heritable organelles, apparently mitochondrial, are evident in the cytoplasm of the sperm, but these appear to be enclosed within ER inclusion. Dictyosomes, ER, and a rounded nucleus are

also prominent features prior to gametic fusion. Vacuolization and the "rounding" of sperm cells occur only after the sperm cells are deposited in the degenerate synergid, but not during normal growth within the pollen tube. The exclusion of sperm cyto-plasm and explosion of its single membrane may represent a crucial phase in the preparation of the sperm for fusion.

Zoological Studies 34, Supplement I (1995)

Zoological Studies

Fast Confocal Beam Scanning Laser Fluorescence Microscope for Single-photon and Two-photon Excitation

Ernst H.K. Stelzer, Nicholas J. Salmon and Clemens Storz

European Molecular Biology Laboratory (EMBL), Light Microscopy Group, Cell Biophysics, Programme Postfach 10.2209, Meyerhofstrasse 1, D-69012 Heidelberg, Germany

A fast confocal fluorescence microscope which is based on the following technologies was designed and built at EMBL:

(1) conventional inverted fluorescence microscope as the basic unit
(2) Argon ion laser as primary light source for single-photon excitation
(3) Titanium sapphire laser as light source for two-photon excitation
(4) resonant galvanometer for fast movement of beam along first axis
(5) conventional galvanometer for slow movement of beam along second axis
(6) piezo-electrically mounted objective lens for focusing
(7) photomultipliers operated in counting mode
(8) multiple processors to record and process the data

The instrument was built for applications in modern cell biology. One of its specific interests is the analysis of processes such as mitosis,endocytosis, exocytosis, and phagocytosis as a function of time not only in two (as e.g. in video microscopy) but in three dimensions. A prerequisite is that the object provides a specific contrast. This is accomplished by vital fluorescent markers that are incorporated into the cell body. At least one marker is specific for the problem that is investigated. The other marker is usually less specific and provides a view of the cell body, the plasma membrane or the nucleus.

The three-dimensional dye distribution is observed as a function of time using two photomultipliers that register the fluorescence emissions of two different dyes. The fast scanner is capable of producing 8000 lines per second which results in about 15 frames (two channels) per second assuming an image size of 512 lines and 512 picture elements per line. The photomultipliers can resolve up to 200 million counts per second. This means, that at most 8 photons will be registered per picture element. The number of photons per picture element is recorded by a computer, stored in main memory during the recording process and finally copied to disk. Effectively the instrument is able to record a complete 15-sections-deep data set every 4 seconds.

For an evaluation of the instrument's performance, latex beads immersed in water were observed to determine their diffusion rate. Diffusion might not be an efficient way for distributing e.g. proteins inside cells (low group velocity), but individual particles tend to move quite a large distance within a short period of time. Being able to determine the diffusion rate of a single particle will therefore provide us with an upper limit for the speed that can be recorded with this instrument.

A biological application is the determination of phagocytic pathways in macrophages. These experiments are an extension of similar experiments performed with video microscopy: phagocytosed fluorescent latex beads are observed in three dimensions while they move through the cell. The experiments determine the transport rate and the exact paths of the beads. The main goals of these investigations are the determination of the different steps of phagocytosis and of the involved intracellular compartments.

All of these experiments have been performed using single-photon and two-photon excitation. Naturally, two-photon excitation is less efficient and results in a lower resolution than single-photon excitation when used with the same dye. However, it does not require the use of a pinhole and the high excitation wavelength is less likely to affect the viability of the biological system that is observed

in the microscope.

The instrument has not been designed to produce "pretty pictures". Although an image can be averaged 16 or more times to increase the dynamic range the goal is to use three-dimensional fluorescence-intensity distributions that have been acquired at high speed. High speed means that the sample does not change while the data is being recorded. Effectively the difference in age between the top left and lower right picture element is reduced as far as possible. The three-dimensional data set will then provide a flash view of the specimen.

An important question in high speed confocal fluorescence microscopy is, how many photons are required to produce an image? Another question is, how relevant are the intensity variations in fluorescently labeled specimens? Are they relevant or are they just an artifact of the labeling process? Our instrument is designed to provide the answer to a very simple question: "Is a fluorophore at this location, Yes or No?" By recording three-dimensional intensity distributions as a function of time we are able to observe changes in the distribution and by careful analysis assign a function to the changes.

Zoological Studies 34, Supplement I (1995)

Zoological Studies

Calculation and Measurement of the Axial Forces Exerted by Photonic Tweezers

Arne Rosin[1,2], Thorsten Wohland[1,3] and Ernst H.K. Stelzer[1]

[1]*Light Microscopy Group, Cell Biophysics Programme, European Molecular Biology Laboratory (EMBL), Postfach 10 22 09, D-69012 Heidelberg, Germany*

[2]*Institut für Angewandte Physik, Ruprecht-Karls-Universität, Albert-Überle-Str. 3-5, D-69120 Heidelberg, Germany*

[3]*Physikalisches Institut, Ruprecht-Karls-Universität, Philosophenweg, D-69120 Heidelberg, Germany*

INTRODUCTION

Although photonic tweezers are used regularly in biological research (Block, et al. 1990, Finer et al. 1994, Perkins et al. 1994), the forces they exert on transparent particles with radii larger than half the laser wavelength are still not well characterized. Commonly accepted theories are an electromagnetic model (Barton et al. 1988, Wright and Sonek 1993, Wright et al. 1994) for bead radii smaller than half the laser wavelength and a ray-optics model (Ashkin 1992, Roosen 1979, Wright et al. 1990) for beads much larger than the laser wavelength ($r \geq 5\ \lambda$). The electromagnetic model has been used to calculate radiation forces for particle radii up to 0.5 μm in water (Wright and Sonek 1993). The same theory has been applied to 2.5 μm-radius water droplets in air (Barton et al. 1988) and to 20 μm-radius micro spheres with a refractive index of 1.2 in vacuum (Visscher and Brakenhoff 1991). No such theoretical studies have been published for latex beads of that size in water. An extension of the geometrical-optics model to particle radii below 8λ has been attempted using the properties of a Gaussian beam (Bakker-Schut et al. 1991), but the validity of this approach could not be shown. Another promising calculation for particles with a radius of $5\ \lambda$ has been compared to an indirect measurement (Wright et al. 1990). In this case the trapping region was investigated experimentally but no direct force measurement has been performed to compare theoretical and experimental results. This extended geometrical-optics model (Wright et al. 1990) has not been applied to particles with radii between $1/2\ \lambda$ and $5\ \lambda$.

In this contribution axial trapping forces exerted by photonic tweezers on dielectric latex micro spheres are investigated theoretically and experimentally for particles with radii between 0.25 μm and 3 μm ($1/4\ \lambda$ and $3\ \lambda$). Currently discussed theories have either not been validated thoroughly by experiments or fail to predict forces for particles of this size. Using the results of a theoretical approach that uses the properties of Gaussian beams and takes the size of the micro sphere and its sub-microscopic interaction with the surrounding medium into account an analytical phenomenological expression is developed that describes the axial forces as a function of the particle radius. For micro spheres with radii ≥ 1 μm the theoretical results of a sub-microscopic theory (Fig. 1) agree well with the measured forces. The phenomenological theory (Fig. 2 and 3) describes all experiments excellently. Since the axial force is smaller than the lateral force we assume that

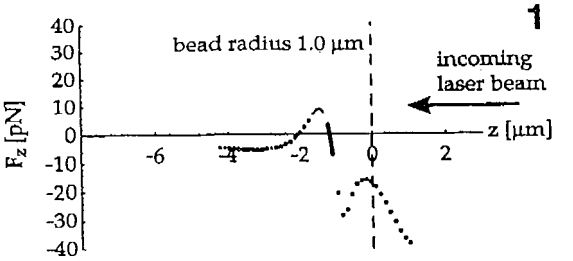

Fig. 1. Calculated axial forces for a particle (η=1.57) with a radius of 1 μm at various positions along the optical axis. The assumptions are: wavelength 1064 nm, power 160 mW, and an oil-immersion microscope objective lens (NA = 1.3) with an ideal beam waist radius of 0.43 μm. The geometric focus (z = 0) is indicated by the dashed lines. The region with positive axial forces is the trapping region. The transition from positive to negative forces at $z \approx (r + 0.2$ μm) is the equilibrium position.

experiments based on loosing particles from photonic tweezers are sensitive for the axial force.

EXPERIMENTS

The basic idea of the experiments is to capture a latex sphere of radius (r) and to move it against the forces of friction through a solution of known viscosity (η). The bead is gradually accelerated until it drops out of the photonic trap. At this maximum velocity (v_{max}) the frictional force is greater than or equal to the axial force of the photonic tweezers. This is a direct force measurement, since Stokes' law for viscous media (Landau & Lifschitz 1981, p.73)

$$F_{max}=6\pi\eta r v_{max} \qquad (1)$$

directly relates the drag force (F) and the velocity (v_{max}) of a spherical particle. It should be noted, that a particle dragged through a viscous medium has no significant macroscopic momentum. As soon as the photonic tweezers loose their influence on the particle movement is dominated by diffusion.

Theory

The phenomenological theory provides a formula that can be fitted to the data if we assume that the force is proportional to the radiation pressure and that the lateral forces cancel each other along the optical axis:

$$F_z(r)=\frac{n_{med}\cdot P}{c}\cdot q(n_p,n_{med})\cdot \frac{\left(W_0\cdot B\cdot Exp\left[\frac{2r^2z_0^2}{W_0^2B^2}\right]\cdot\left(\frac{\pi}{2}\right)^{\frac{1}{2}}\cdot Erf\left[\frac{\sqrt{2}\,r\,z_0}{W_0B}\right]-2\,r\,z_0\right)}{W_0\cdot B\cdot Exp\left[\frac{2r^2z_0^2}{W^2B^2}\right]\cdot\left(\frac{\pi}{2}\right)^{\frac{1}{2}}} \qquad (2)$$

Erf is the error function, $B=(r^2+z_0^2)^{\frac{1}{2}}$, P is the power of the incoming light, c is the speed of light, and n_p and n_{med} are the refractive indices of the particle and the medium respectively. r is the variable, W_0 and z_0 are related. Thus only W_0 and q remain unknown. The parameters were the forces as a function of the bead radius. The curve was therefore fitted non-linearly to the experimental data set (Fig. 2).

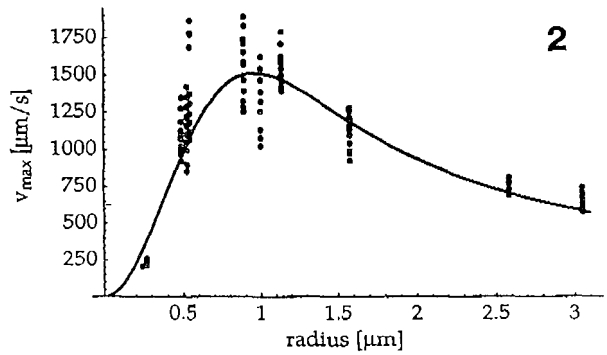

Fig. 2. Measured maximum velocities of latex spheres (η=1.57) with radii between 0.24 µm and 3.05 µm as a function of the spheres radii. The curve summarizes 237 experiments with 2 different materials and 11 different particle radii. The calculated fitting curve is obtained from Eq. 2. The fitting parameters were the lateral extent (W_0 = 0.92 µm) of the Gaussian focal point and the factor $q(n_p,n_{med})$ = 0.04.

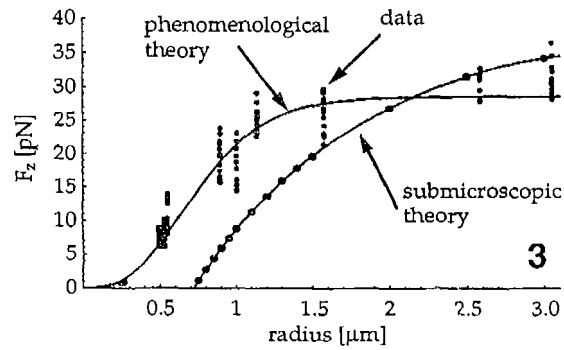

Fig. 3. Comparison of forces derived from velocity measurements as shown in Fig. 2 and calculated forces. The experimental values were obtained using Eq. 1.

DISCUSSION

The sub-microscopic theory is an explicit calculation of a scattering cross-section and thus tells us a lot about the behavior of latex beads and probably of every other transparent object caught in an photonic trap (Fig. 1). Looking at Fig. 2 which shows escape velocities as a function of the particle radius one can distinguish three different regions. Latex spheres with a size of approximately the extent of the microscope's point spread function at a wavelength of 1064 nm are captured most effectively. Above this size, beads are moved slower since the increase in radius dominates the low increase in of axial force. The velocity and thus the force for beads smaller than the extent of the point spread function rapidly approaches

zero. The steep slope for small particles results from a r^3-increase of the light intensity that interacts with the volume of the micro sphere (see Eq. 2). This volume effect for small particles is typical for a scattering problem and has been observed previously (Wright and Sonek 1993).

Although in the experiment the trapped particles were moved in the x/y-plane the escape velocity is related to the axial forces and not to the lateral forces as done by some authors (e.g., Sato et al. 1991). Our interpretation is in agreement with other theoretical results, which state that lateral forces are much stronger than axial forces (Ashkin 1992, Malmqvist and Hertz 1992).

ACKNOWLEDGMENT

We thank Prof. Christoph Cremer and Prof. Gisbert zu Putlitz. S. Lindek critically reviewed the abstract.

REFERENCES

Ashkin A. 1992. Forces of a single-beam gradient laser trap on a dielectric sphere in the ray optics regime. Biophys. J. **61:** 569-582.

Bakker-Schut TC, G Hesseling, BG de Grooth, J Greve. 1991. Experimental and theoretical investigation on the validity of the geometrical optics model for calculating the stability of optical traps. Cytom. **12:** 479-485

Barton JP, DR Alexander, SA Schaub. 1988. Internal and near-surface electromagnetic fields for a spherical particle irradiated by a focused laser beam. J. Appl. Phys. **64:** 1632-1639.

Block SM, LS B Goldstein, BJ Schnapp. 1990. Bead movement by single kinesin molecules studied with optical tweezers. Nature **348:** 348-352.

Finer JT, RM Simmons, JA Spudich. 1994. Single myosin molecule mechanics: piconewton forces and nanometer steps. Nature **368:** 113-119.

Landau LD, EM Lifschitz. 1981. Lehrbuch der theoretischen Physik. Hydrodynamik. 4th Ed. Akademie-Verlag. Berlin.

Malmqvist L, HM Hertz. 1992. Trapped particle optical microscopy. Opt. Comm. **94:** 19-24.

Perkins TT, DE Smith, S Chu. 1994. Direct Observation of Tube-Like Motion of a Single Polymer Chain. Science **264:** 819-822.

Roosen G. 1979. La levitation optique de spheres. Can. J. Phys. **57:** 1260-1279.

Sato S, M Ohyumi, H Shibata, H Inaba. 1991. Optical trapping of small particles using a 1.3-mm compact InGaAsP diode laser. Opt. Lett. **16(5):** 282-284.

Visscher K, GJ Brakenhoff. 1991. Single beam optical trapping integrated in a confocal microscope for biological applications. Cytom. **12:** 486-491.

Wright WH, GJ Sonek, Y Tadir, MW Berns. 1990. Laser trapping in cell biology. IEEE J. Quant. Electr. 26:2148-2157.

Wright WH, GJ Sonek. 1993. Radiation trapping forces on microspheres with optical tweezers. Appl. Phys. Lett. **63:** 715-717.

Wright WH, GJ Sonek, MW Berns. 1994. Parametric study of the forces on micospheres held by optical tweezers. Appl. Opt. **33:** 1735-1748.

Zoological Studies 34, Supplement I (1995)

Zoological Studies

TEM Study of Carbon Nanotubes

Sumio Iijima
R & D Group, NEC Corporation, 34, Miyukigaoka, Tsukuba, 305, Japan

INTRODUCTION

High resolution transmission electron microscopy (HRTEM) has been intensively used in characterization of crystalline defects, and it can provide 3-D structural information in some cases. For example structural instability of nanometersized metal particles were found in the real time VTR observation at the atomic level resolution (Iijima et al. 1986). Such low dimensional structures are of rccent interest among solid state scientists who expect novel properties not found in bulk forms. More recently discovery of C_{60}, or the fullerene, has brought a great excitements in interdisciplinary fields of science and technology (Kroto et al. 1985). The individual C_{60} molecule, which is a graphitic shell structure consisting of 60 carbon atoms, and 0.7nm in diameter, can be imaged without difficulty be HRTEM. Many of fundamental problems with the molecule however are not solved by HREM. On the other hand, carbon nanotubes, a family of fullerenes and discovered serendipitously by the present author (Iijima 1991), are an ideal subject for the HRTEM investigation and in fact their structures can only be analyzed by this technique. The present talk is concerned with carbonaceous materials and nanotubes with an emphasis of unique use of the HRTEM.

GRAPHITIC STRUCTURES OF CARBON

Three forms of carbon, namely, diamond, graphite and amorphous carbon, are well known and their structures have been studied intensively be HRTEM. Graphitic structures vary from an amorphous state to a perfect graphite crystal depending upon their thermal treatments during the specimen preparation. Partially graphitized carbon is familiar to electron microscopists for the microscope resolution test specimen (c-spacing 0.34nm). The present author found spherical graphite particles of a nanometer size in a vacuum deposited amorphous carbon films (Iijima 1980). The particle consists of nesting spherical shells of graphitic sheets (Fig. 1). The most inner shell is about 0.7nm in diameter and close to the size of a C_{60} molecule (Iijima 1987). Growth of such a multi-shell structure is a key to understand the C_{60} molecule formation (Kroto 1988).

MULTI-SHELL CARBON NANOTUBES

Search for the multi-shell graphite particles leads to unexpected discovery of carbon nanotubes which grow on a cathode in a carbon-arc chamber for the C_{60} production (Iijima 1991). HRTEM images of carbon nanotubes tell us their diameters and the number of shells (Fig. 2a). The fact that basal plane lattice images

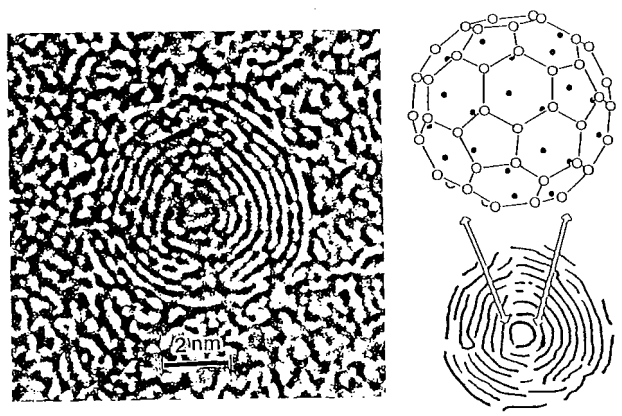

Fig. 1. A HRTEM image of a carbon particle of multi-shelled spherical shape. The most inner shell diameter is 0.7nm, corresponding to the size of the C_{60} molecule (indicated in the illustration).

are always seen independently in the tubule orientations suggests that the graphitic shells are nesting tubes rather than a scroll. In this case the HRTEM enables us to deduce tubule's 3-D structures, Cylindrical crystals are found commonly in living cells but rarely in inorganic structurcs. Atomic arrangements on the tubules are studied by examining their electron diffraction patterns. This was carried out by the micro-beam diffraction mode in the TEM. The method enables us to examine a tubule structure on the basis of an single atom sheet. The analysis of the diffraction patterns results in finding a helical arrangement of carbon hexagon rings on each cylinder (Fig. 2b). Helicity is a popular structure in biological substances such as micro-tubulines and a tobacco-mosaic virus.

SINGLE-SHELL CARBON NANOTUBES WITH ABOUT ONE NANOMETER DIAMETER

Electronic band structure calculations of nanotubes (Hamada et al. 1992) predict a semiconductive nature of the tubules when they are less than 2nm in diameter and single-shelled tubes. Such an ideal nanotube has been prepared successfully in a carbon-arc deposition by feeding metal catalyst (Iijima et al. 1993, Bethune et al. 1993). The thinnest

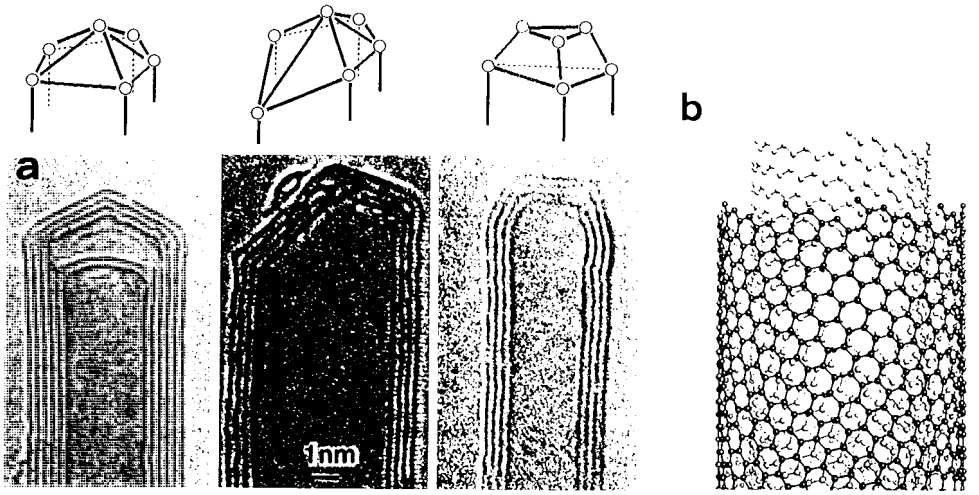

Fig. 2. (a) HRTEM images of multi-shelled carbon nanotubes with caps which contain pentgonal carbon rings as indicated by open circles in illustrations. (b) and idealized 3-D model of a nesting carbon nanotube.

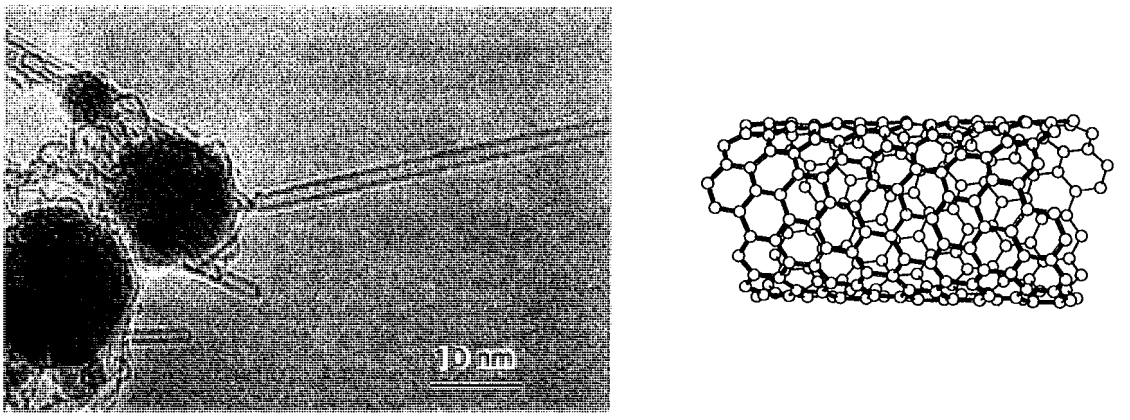

Fig. 3. A model for a single-shelled and helical carbon nanotube with a diameter of 0.9nm whose existance has been confirmed experimentally.

tubuic was only 0.7nm in diameter which is the same as that of C_{60}. An electron diffraction pattern recorded from such an individual tubule shows the 2mm symmetry, which confirms the presence of the helicity in carbon hexagon arrangements (Fig. 3). The spiral pitches are different from tublue to tubule.

MORPHOLOGY AND NON-HEXAGON CARBON RINGS

The role of pentagons in fullerene molecule structures is to introduce positive gaussian curvatures into a flat carbon hexagon network. A completely closed cage structure needs twelve pentagons according to the Euler theorem. The rule is applied equally to morphologies of tubules and their caps (Iijima et al. 1992). A variety of cap shapes are attributed to a distribution of six pentagons on the tip (Fig. 2a). A similar packing geometry is known in spherical viruses. A negative curvature which is caused by heptagons or octagons is observed often in our nanotubes. Non-hexagon carbon rings were found to be more reactive in oxidation than hexagon rings (Ajayan et al. 1993, Ajayan et al. 1993). This observation is suggestive in the characterization of activated carbon.

GROWTH OF CARBON NANOTUBES

It is needed to measure well-defined tubules in the characterization of their electronic properties since they are critically dependent on their structures. Tubule morphologies are associated with their growth and thus their analysis is important (Iijiman 1993). The effort is now in progress. Our strategy is to under-stand the growth mechanism of tubules and to control it to produce any desired morphology. In the single shelled tubule production th metal particles act as growth centers but their details need further study (Iijima 1994).

REFERENCES

Ajayan PM, S Iijiman. 1993. Capillarity induced filling in carbon nanotubes. Nature **361:** 333-334.

Ajayan PM, TW Ebbssen, T Ichihashi, S Iijima, K Tanigaki, H Hiura. 1993. Opening carbon nanotubes with oxygen and implications for filling. Nature **362:** 522-523 (1993).

Bethune DS, C-H Kiang, MS deVries, G Gorman, R Savoy, J Vazques, R Beyers. 1993. Cobalta-catalysed growth of carbon nanotubes with single-atomic-layer walls. Nature **363:** 605-606.

Iijima S. 1980. Direct observation of the tetrahedral bonding in graphitized carbon black by high resolution elecron microscopy, J. Cryst. Growth **50:** 657-683.

Iijima ST, T Ichihashi. 1986. Structural instability of ultrafine particles of metals. Phys. Rev. Lett. **56:** 616-619.

Iijima S, 1987, The C60-carbon cluster has been revealed! J. Phys. Chem., **91:** 3466-3467.

Iijima S, T Ichihashi, Y Ando. 1992. Pentagons, heptagons and negative curvature in graphite microtubule growth. Nature **356:** 776-778.

Iijima S. 1993. Growth of carbon nanotubes. Mat. Sci. & Enign, **B19:** 172-180.

Iijima S, T Ichihashi. 1993. Single shell carbon nanotubes of one nanomcter diameter. Nature **361:** 603-605.

Iijima S. 1994. Carbon nanotubes. MRS Bulletin, **XIX:** 43-49.

Iijima S. 1991. Helical micro-tubules of graphitic carbon. Nature **354:** 56-58.

Hamada H, S Sawada, A Oshiyama. 1992. New one-dimcnsional conductors; Graphitic microtubules. Phys. Rev. Lett. **68:** 1579-1581.

Kroto HW, JR Heath, SC O'Brien, RF Curl, RE Smalley. 1985. C60:Buckminsterfullerene. Nature **318:** 162-163.

Kroto HW. 1988. Space, Stars, C_{60}, and Soot. Science **242:** 1139-1145.

Zoological Studies 34, Supplement I (1995)

Zoological Studies

Selective Imaging of Multiple Probes Using Fluorescence Lifetime Contrast

R. Sanders[1], A. Draaijer[2], H.C. Gerritsen[1] and Y.K. Levine[1]

[1]*Debye Institute, Department of Molecular Biophysics, Utrecht University, P.O. Box 80.00, 3508 TA Utrecht, The Netherlands*

[2]*TNO Institute for Environmental Sciences, P.O. Box 6011, 2600 JA Delft, The Netherlands*

The most common technique in Fluorescence microscopy for discriminating between distinct fluorescent species relies on differences in their emission spectra. Thus experiments using multiple labels utilize spectral filters to produce fluorescent images corresponding to the distribution of each probe. However, in many instances the fluorescent probe molecules which need to be employed exhibit overlapping emission bands and cannot be distinguished spectrally. Nevertheless, a discrimination between them can be achieved by the simple stratagem of exploiting the differences in their intrinsic fluorescence lifetime. Moreover, this contrast mechanism can also be used for suppressing the autofluorescence background from the images. The method effectively imposes a lifetime filter on the intensity image.

Several techniques are currently employed for the measurement of fluorescence lifetimes of fluorophores in bulk samples. The techniques may be subdivided into frequency domain (e.g. phase fluorometry) and time domain methods (time-gating, time correlated single photon counting). Both types of technique have been implemented for fluorescence lifetime imaging in wide field as well as confocal microscopes. Here we shall present applications of time-gated detection combined with confocal imaging for the acquisition of selective images in multilabelling experiments.

We have implemented a time-gated detection scheme in a commercially available confocal laser scanning microscope (CLSM). The setup utilizes a low-power CW Ar-ion laser equipped with an electro-optical chopper producing nanosecond pulses with a repetition rate of up to 25 MHz . The fluorescence emission excited by every light pulse is acquired in two consecutive time windows. In the simplest scheme, the first window is opened straight after the excitation pulse while the second is opened immediately after shutting the first window. Both windows have identical widths (several nanoseconds) and the fluorescence lifetime information is obtained on taking the ratio of the accumulated intensities.

Almost all of the fluorescence is detected in the two time-windows after each light pulse. This makes the method very efficient in terms of the number of photons required to determine the fluorescence lifetime. Only 200 detected fluorescence photons are necessary to achieve an accuracy of 10% in the lifetime. In addition the simultaneous acquisition in the two windows makes the method insensitive for photo bleaching. Experience has shown that this time-gated detection technique enables the measurement of the fluorescence lifetime of a pixel in 40 μs.

For a mono-exponential fluorescence decay, the decay time τ can be calculated from the ration of the intensities recorded in the time windows (I_A/I_B):

$$\tau=\Delta t/\ln(I_A/I_B)$$

with Δt the width of the windows. This equation is only valid for windows of equal width and provided the excitation pulse is short compared to the decay time. The two channel time-gated detection affords the determination of only a single decay time. Consequently, it determines an effective lifetime if the fluorophores exhibit a multi-exponential fluorescence intensity decay. This limitation can be overcome by adding more detection windows.

The potential of fluorescence lifetime contrast for selective imaging in multilabelling experiments will be illustrated using Sertoli cells stained with three different probes: Syto 13, $DiOC_6$ and Nile Red. These vital staining probes are commonly used for

staining the nucleus, the cytoplasm and lipid droplets respectively. The probes are cell permeable and spread through the cell by diffusion. The overlap of the emission spectra of the probes makes it difficult to distinguish these probes by their emission spectra. However, since the probes have different fluorescence lifetimes (the lowest being Nile Red, the middle $DiOC_6$ and the highest Syto 13) it is possible to separate them by their lifetime.

The fluorescence intensity image of a layer of Sertoli cells stained with Syto 13, $DiOC_6$ and nile Red shows a wide distribution of fluorescence intensities, which cannot be related to the morphology of the cells in a straightforward way. On the other hand, the fluorescence lifetime image of the same cells exhibits three distinct lifetime components, each of which corresponds to the individual probes. The image can now be subdivided in three different lifetime ranges by imposing lifetime masks on the image (thresholding), with each mask corresponding to one of the probes.

The maximal number of probes which can be distinguished in this way depends on both the lifetime range and lifetime resolution of the instrument. In principle it should be possible to perform multi-labelling experiments with 10 or more different probe molecules and this number can probably be doubled on combining the lifetime contrast method with spectral filtering techniques.

We gratefully acknowledge financial support by the Technical Foundation (STW) of The Netherlands, grant number UNS00.2225.

Zoological Studies 34, Supplement I (1995)

Zoological Studies

The Cubic Gyroid-based Membrane Structure of the Chloroplast in *Zygnema (Chlorophyceae zygnematles)*

Yuru Deng and Tomas Landh

Departments of Biophysical Sciences and Biomaterials, State University of New York at Buffalo, Buffalo, NY 14214, USA

Green algae do not form true grana. Instead the chloroplast membrane(s) tend to form more complex morphologies than the simple "lamellar-like" structures usually associated with cell organelles. One of us has recently shown that the chloroplasts of the green alga *Zygnema* form a 3-D structure described as a ***cubic membrane***, i.e. a triply self intersection-free membrane structure based on the family of periodic surfaces with cubic symmetries (Landh 1994). Accordingly, analysis of previously published electron micrographs reporting "lamellar lattices" in the *Zygnema revealed* them to be a primitive cubic membrane. This particular structure is, however, composed of several, approximately parallel, bilayers. Such a construction represent a multicontinuous cubic membrane described as foliated periodic cubic surfaces (PCS) each differing only in the magnitude and sign of their mean curvature. By definition such a multimembranous structure partitions space into n+1(where n equals the number of membranes) physically distinct, intertwined, but separate subspaces.

Due to the very complex geometries and symmetries of cubic membranes, their projected electron densities, as produced in transmission electron microscopy (TEM), are inherently difficult to decipher. However, the more complex the symmetries, the fewer number of projections are actually needed to recover the 3-D structure. Continuous membranes with cubic symmetries have in fact, recently been shown by one of us to be described by PCS's whose mathematical expressions are well known (Landh 1994). We have developed a template-correlative matching procedure in which mathematical simulations of projected electron density maps of PCS's are matched, through cross-correlation calculations, to the experimental TEM micrographs. As a part of this work a "library" of theoretical projections have been calculated as function of their potential, crystallographic direction, and section thickness.

We have observed cubic chloroplast membranes in TEM experiments using a sample preparation protocol following a modification of that previously published. Briefly, *Zygnema* (LB 923, UTEX) filaments from cultures grown under a 16-18 hr. light (3200 lux)-dark cycle were embedded in agar, fixed with 2% glutaraldehyde: formaldehyde (1:1) in 0.1 M cacodylate buffer containing 2.5% sucrose, washed, and postfixed in 2% osmium tetroxide.

A chloroplast membrane with cubic symmetry was observed in culture LB 923 after approximately 41 days of culture (Fig. 1a). In addition to the cubic membrane, there were a small, but significant, amount of lamellar-like morphologies "dispersed" throughout the cubic membrane morphology. As is seen in Figures 1 and 5 the membrane(s) of the lamellar configuration is continuous with those of the cubic, thus giving further evidence for the continuous membrane folding model put forward earlier. Utilizing the above mentioned technique we show that the chloroplasts of *Zygnema* terminal to their log phase of growth display a cubic membrane with gryoid-based morphology (Figs. 1b, 2, and 3). Furthermore, these chloroplast membranes seem to be continuous with the membranes inside the pyrenoid body through stalk lamellar-like morphologies. Inside the pyrenoid body the membranes refold into another gyroid-based cubic membrane (Fig. 4).

Intriguingly, we observe both single (Figs. 1, 2 and 3) and double gryoid-based membrane morphologies (Figs. 5 and 6), but no primitive-PCS based multicontinuous morphology as was identified in earlier publications. The basis of such a seemingly

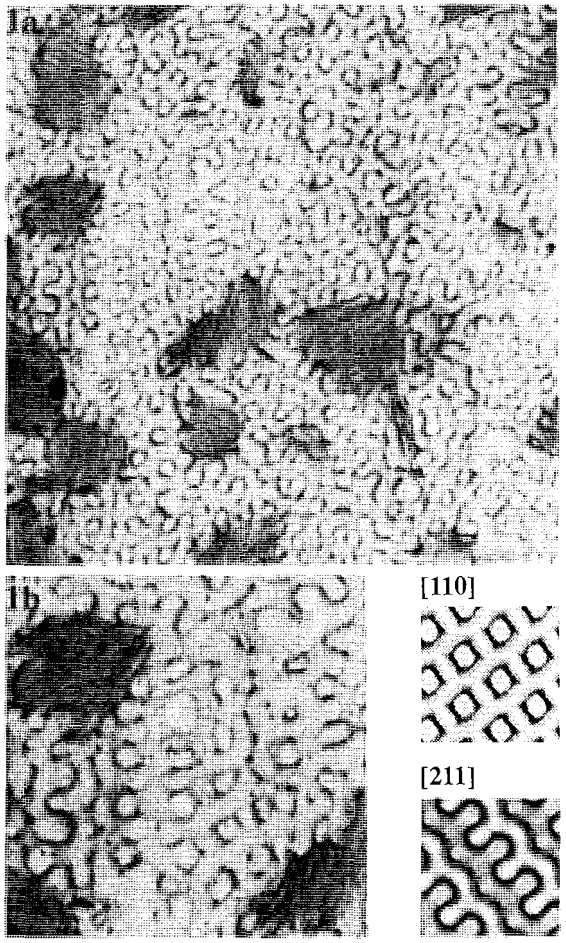

Fig. 1. TEM micrographs showing the gryoid cubic membrane morphology of a chloroplast in *Zygnema* (LB 923) (a) Overview. Note the continuous folding of the membrane between the lamellar-like and gryoid-based morphologies. Thus, while both structures, define, at least locally, two subspaces in the chloroplast, this can only be directly proven (by projections) through the study of the cubic membrane (b)Detail of the cubic membrane of which several regions can be matched to the theoretical projections a single membrane gryoid structure. The gryoid membrane has very close to zero potential i.e., an average mean curvature of zero, and the section is approximately a unit cell thick. Note the very well preserved details of the pro-jected electron density as compared to the theoretically determined expectation. Regions of the projection along the [211] and the [110] directions are indicated.

structural invariant choice is currently unknown. However, in the case of the invariant choice of the double diamond cubic membrane morphology of the prolamellar body of etiolated chloroplasts in higher plants, the underlaying structure-functional reason seems to be fulfilling a particular need-

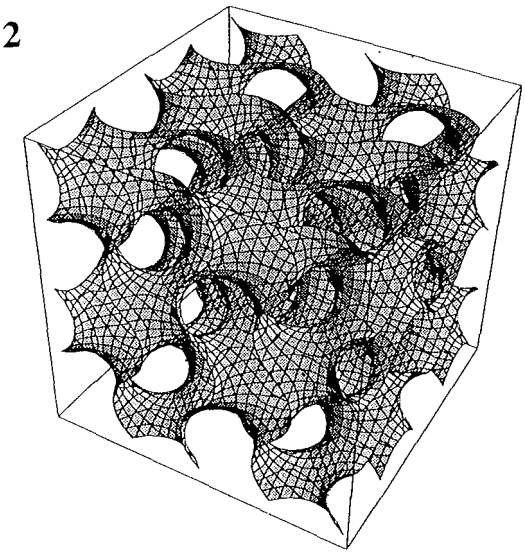

Fig. 2. The G-PCS (eight unit cells) shown as based on its nodal surface representation[1]. The group/subgroup relation is $Ia3d/I4_132$. Naturally, the space group of the cubic membranes must be that of the sugroup of type 2, i.e., the black-and-white subgroup, since the membrane is compositionally asymmetrical and thus lacks the mirror symmetry creating the invariance of the Ia3d spacegroup of the gyroid.

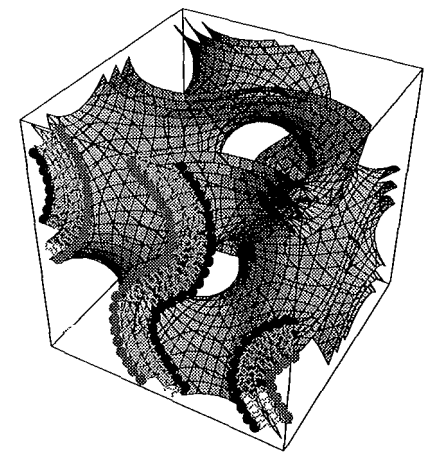

Fig.3. Three parallel G-based surfaces (one unit cell)of which the centered is the nodal (zero-potential), and the other two parallel surfaces are the constant surfaces (equi-potential). The potential differs only with respect to the sign. These parallel surfaces can be used to describe either: a single membrane, in which case the centered surface is the "imaginary" midbilayer surface and the two parallel surfaces are the two apolar/polar surfaces; or they can describe multimembranous (three membranes in this case) arrangements in whcih each surface describes the midbilayer surface of each membrane (see Figure 5 for examples depicting two membranes).

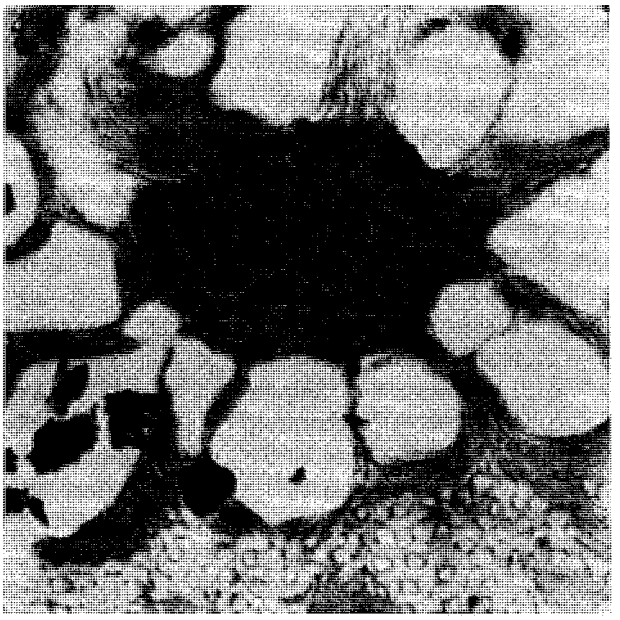

Fig. 4. G-PCS membrane in the pyrenoid body surrounded by starch granules (electron transparent). Note the folding of the cubic to lamellar-like morphology which forms a connective bundle or stalk of membrane into the pyrenoid body. (a≈500 nm)

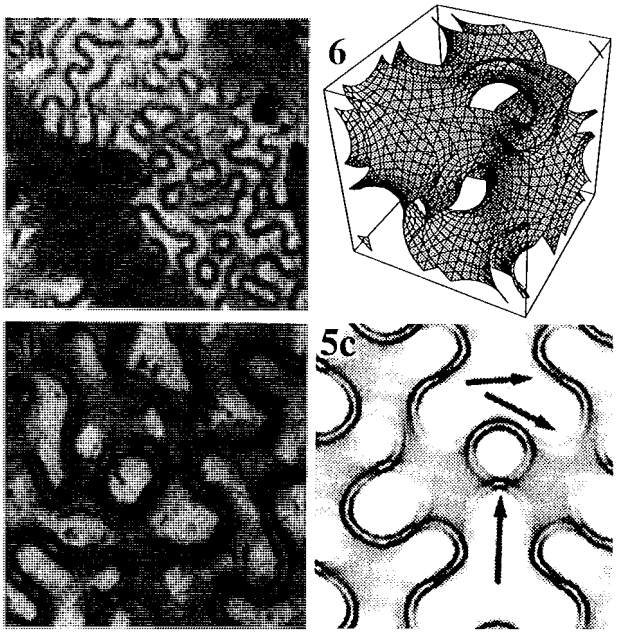

Fig. 5. Analysis of the double G-CPS based cubic morphology of *Zygnema* (LB 923). (a) Overview showing lamellar-like andcubic mor-phologies. Comparison between a enlarged view (b) of the doble G-PCS and its theoretical projection (c) along the [221] direction. Note the minute preser-vation of the fine details of the projected electron density (arrows) proving the double membrane structure.

namely, that of capturing photons.

The reason for the existence of multiple separate subspaces in organelles is currently unknown, but several theories have been put forward (Landh 1994, Landh and Deng).

Fig. 6. One unit cell of the double membrane gyroid. Note that even though this structure define three subspaces of divergent volume of the chloroplast, it has the same symmetry as the colored single membrane, i.e., $I4_132$.

REFERENCES

Landh, T. 1994. Cubic bilayer membrane systems described by periodic minimal surfaces: from reversed cubic phases to cytomembranes. in Fundamentals of Medical Cell Biology (E.E. Bittar, ser. ed.): Structural and Biological Roles of Lipids forming Non-lamellar Structures (R.M. Epand, ed.) JAI Press, Greenwich.

McLean RJ, CF Pessoney. 1970. J. Cell Biol. **45**, 522.

De Rosier DJ, A Klug. 1968. Nature **217**, 130.

Landh T, M Mieczkowski. 1995. J. Mol. Biol. In press.

Starr RC, JA Zeikus. 1993. J. Physcol. **29**, Suppl. 2, I..

Landh T, Y Deng. to be submitted.

Zoological Studies 34, Supplement I (1995)

Zoological Studies

A Versatile 2π Tilting Device for Conventional Light – and Confocal Laser Scanning Microscopy

J. Bradl[1], B. Schneider[1], B. Rinke[1], E. H. K. Stelzer[2], M. Durm[1], M. Hausmann[1] and C. Cremer[1]

[1]*Institute of Applied Physics, University of Heidelberg, D-69120 Heidelberg, F.R.G.*

[2]*Light Microscopy Group, European Molecular Biology Laboratory, D-69117, Heidelberg, F.R.G.*

A tilting device for full rotation (0-360°) of biological specimens has been built on the basis of the 3D-system described by Bradl et al. 1992 and Bradl et al. 1994. The main feature of this device is a quartz glass capillary (diameter 0.2mm, length 75mm) containing cells or cell nuclei of interest. The axis of rotation is perpendicular to the optical axis, and can be oriented on the microscope stage parallel to the x- or y-axis. Different optical and imaging effects (e.g. refraction index matching, object position in the capillary) were analyzed by means of test objects and computer simulation.

The three-dimensional image-forming properties of fluorescent beads in the capillary system were experimentally examined using an inverse confocal laser scanning microscope. The results were compared to measurements obtained from the same microscope with the standard stage for plane slides with cover glasses. The measured point spread function suggested that in spite of the a berration effects, the optical arrangement used allows a gain in the 3D resolution by tilting the object.

We have adapted this device to a Zeiss Standard 25 microscope, equipped with a step motor controlled xy-table with a z-focus unit. The specimen images are registered by a cooled black/white CCD camera CF 8 RCC. All components are controlled by a 80486/50 MHz MS-DOS computer with a frame grabber board under Windows 3.1, with the image acquisition and analyzing software Optimas. With this setup, 3D imaging after optical sectioning of objects in the capillary was performed. To get an optimal perspective of the objects, the capillary can be tilted automatically under any angle desired. For example, this has the advantage to acquire optical sections of an object, rotate this object by 90°, and register an additional set of optical sections. If both sets of sections are merged in an appropriate way, an improved spatial resolution can be obtained (e.g. as described by Shaw et al. 1989) (equal resolution in all three directions x, y, z). Rotating by further 90°C may also be helpful to discriminate shading effects of high absorbing regions in the object.

The device can also be adapted to other conventional microscopes and to confocal laser-scanning microscopes (CLSM). We have been able to combine the tilting device successfully with the following microscopes:

Leitz Orthoplan, Leica TCS 4D, Zeiss Axiophot, Zeiss LSM 10 and 310, Zeiss Standard 25, and with the inverse CLSM at the EMBL described by E.H.K. Stelzer, 1990) In those cases where an automated xy-movement of the microscope table and automated z-focusing were not available, a modification of the basic device for manual tilting was used. Results from cell nuclei with chromosome regions labeled by fluorescence in situ hybridization show that the tilting approach is suitable to improve 3D distance measurements.

For visual analysis, optical sections of two fluorescent beads were recorded by CLSM. One bead of 5.85 μm diameter showed a light microscopically observable internal structure. The other, smaller one had a diameter of 3μm. At tilting angles of 0°, 10°, 20°,..., 360° the image planes located centrally in the larger bead were registered. After alignment, the entire series was animated on a 80486/50 MHz PC (under the Linux operating system). The online visualization ("movie") of rotating objects indicated the feasibility of this procedure for 3D inspection.

A modification of the tilting device was performed applying glass-fibres instead of capillaries. This has the advantage that the biological objects can be fixed onto the fibre instead of sucking in a suspension into the capillary. The fibres can easily be manufactured with different diameters, and

glass types of different Prefractive indices can be used for appropriate matching to different buffer solutions. During reparation, the biological objects are mounted into a specially designed device which has the same dimensions as a microscope slide. Standard preparation techniques can be applied so that *in situ* hybridization has not to be performed in su-spension. If by any reason the refractive index of the glass-fibre and the buffer medium cannot be matched in an accurate way, the object can be tilted until it is located at its nearest position to the objective. From there, 2D- as well as 3D- images of the object can be acquired under rotation angles of ±40° without major image distortions caused by the refractive index mismatch. It is possible to work either with or without a standard coverslip, which is located between the objective and the glass-fibre. With the coverslip, the immersion oil for different objectives can be used while the object can be mounted into buffer solutions in a similar wayas in the conventional microscopical setup, We thank Dr. T. Cremer and Dr. P. Lichter Heidelberg, for access to the Leica TCS 4D, the Zeiss Axiophot, and the Zeiss LSM, respectively.

REFERENCES

Bradl J. et al. 1992. J. Microsc. **168:** 47-57.
Bradl J. et al. 1994. J. Microsc. **176:** 211-221.
Pawley JB. 1990. Handbook of Biological Confocal Microscopy, Plenum Press, New York , pp 93-103.
Shaw P. et al. Biophys. J. **55:** 101-110.
Dietzel S. et al. submitted.
Stelzer EHK. 1990. Handbook of Biological Confocal Microscopy, (ed by J.B. Pawley) pp. 93-103, Plenum Press, New york.

Zoological Studies 34, Supplement I (1995)

Zoological Studies

The Optical Fractionator

Susana Maria Guimarães Antunes
Abel Salazar Institute for Biomedical Sciences - M. Sc. in Immunology Largo Abel Salazar, 2 - 4050 Porto - Portugal

Stereological methods are precise tools which gives us information about three-dimensional (3D) objects from essentially flat two-dimensional (2D) images, which may be physical or optical slices (Gundersen et al. 1988b, Mayhew 1992). To use these techniques, a rigorously defined and uniform random sampling must be executed, giving every element of the object under investigation the same chance of being selected. This is the only way of ensuring an unbiased sample (Mayhew 1992). Systematic sampling is frequently used in biology and materials science, and it has been found to be much more efficient than simple random sampling (Gundersen and Jensen 1987, Thioulouse et al. 1993). It provides an "unbiased" and "efficient" estimator, which mean respectively "without systematic deviation from the true value" and "with low variability after spending a moderate amount of time" (Gundersen et al. 1988b). "New stereology" does not rely on the use of simplistic models of real objects and makes no assumptions about object shape, size and orientation (Mayhew 1992).

Stereological methods can be applied to all levels of organization, estimating numbers of particles, lenghts, surface areas and volumes. The stereological estimators can be divided into two groups, according to the necessity of randomizing only the location of the section planes (volume, number) and also the orientation (surface, area, lenght, particle spacing, layer thickness) (Cruz-Orive and Weibel 1990, Gundersen et al. 1988a and b, Mayhew 1992).

PARTICLE NUMBER

Number is a dimensionless quantity, so counting particles is essentially equivalent to counting points. Particle number in 3D cannot be estimated unless a 3D probe is used (Cruz-Orive and Weibel 1990, Gundersen et al. 1988a).

THE DISECTOR

The disector (Sterio 1984) is a probe which samples isolated objects or particles with a uniform probability in 3D space, irrespective of their size and shape. This device counts particles between randomly positioned pairs of parallel slice planes separated by a known distance. Complete transects (one or more profiles in the same particle) are sampled if they appear in an unbiased counting frame on one slice plane (the "reference plane") but not on its partner (the "look-up plane") (Fig. 1). The number (**N**) of particles so counted ($\mathbf{Q^-}$) is contained within a volume (**V**) equal to the area of the counting frame (A), multiplied by the distance between the upper (or lower) faces of the slices **(d): est. N/V = Q^-/(A.d)**

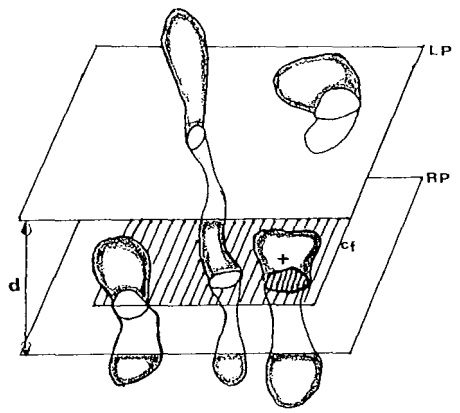

Fig. 1. The disector counts particles between randomly positioned pairs of parallel slices separated by a known distance (d). Particle labeled + is counted because it is hit by reference plane (RP), its transects are captured by the unbiased counting frame (cf), and it is not hit by look-up plane (LP). The other particles are not counted because they do not fulfil these requirements. Direct estimate of N/V is obtained by dividing the number of particles counted (Q-) by the volume (V) , which is equal to the area of the counting frame (A) multiplied by the distance between the planes: est. N/V = Q^- / (A.d).

THE OPTICAL

Disector the ordinary or "physical" disector requires cutting at least two sections, measuring their thickness accurately and using two microscopes to observe the reference and the look-up sections simultaneously. By taking a reletively thick section (25-50 mm) and using optical sections planes by moving the focal plane up or down these problems can be avoided, and much labour can be saved (Gundersen et al. 1988a).

Optical sectioning will be at its best when used on a confocal microscope; if the particles exhibit fluorescence or reflectance they can be counted using un unbiased counting brick (Howard et al. 1985, Petran et al. 1968). However a conventional light microscope, modified in various ways, can be used when working with thick plastic sections.

The two main modifications are an electronic microcator which has been fitted to the microscope to measure the movements of the stage in the z-axis with high precision and that the microscope is fitted with a projection arm (or a television monitor). It is essential to use high numerical aperture, oil-immersion objectives, so that movements in the z-direction reported by the microcator represent the true distance moved by the focal plane through the thick section (Gundersen et al. 1988a) and also that the optical section thickness is tolerably thin (about 0.5 μm for a 1.4 NA lens). The use of glycol methacrylate as an embedding medium permits optical sectioning in thick sections (25 mm) to be performed with minimal shrinkage effects (Bjugn 1993, Braendgaard et al. 1990, Jensen and Pakkenberg 1993, Korbo et al. 1993, West and Gundersen 1990, West et al. 1991). The importance of preparation artefacts such as fixation shrinkage is due to the fact that the disector yelds numerical density, N/V, rather than N itself. However, when combined with Cavalieri estimates of volume, these difficulties can be circumvented.

THE OPTICAL FRACTIONATOR

A recent development involving the combination of the optical disector with a fractionator sampling scheme, referred as the Optical Fractionator (West et al. 1991), involves counting particles with optical disectors in a uniform and systematic sample, that constitutes a known fraction of the region to be analysed. It is unnafected by tissue shrinkage or expansion, and makes possible the analysis of frozen, vibratome, celloidin and paraffin sections.

The **fractionator** (Gundersen 1986) is an application of systematic sampling. To estimate some quantity within an object we may cut it into a few fragments. If we pick every f^{th} fragment, with random start between **1** and **f**, and measure for all these fragments the quantity of interest, then we only need to multiply this measured quantity by **f** to obtain an unbiased estimate of the total quantity in the whole object. This can be extended to several subsampling stages; every $\mathbf{f_1}^{th}$ fragment of the first fractionation step is cut into subfragments, of which every $\mathbf{f_2}^{th}$ fragment is picked, and so on. To obtain the total quantitiy we seek, the last $(\mathbf{k^{th}})$ subsample is multiplied with $\mathbf{f_1 . f_2 . (...) . f_k}$ (Cruz-Orive and Weibel 1990, Gundersen et al. 1988a, Mayhew 1992).

West et al., in 1991, estimated the total number of neurons in the subdivisions of the rat hippocampus using the optical fractionator. After an exhaustive sectioning of the hippocampus, a random systematic sampling of the sections was executed. In each sampled section, counts of neurons were made with optical disectors at regular predetermined x,y positions within the subdivisions, again after random placement of the first counting frame within the first x,y interval, moving each section in a raster pattern with stepping motors. The area of the unbiased counting frame of the disector, a(frame), was known relative to the area associated with each x,y movement, a(x,y step). The latter was calculated from the size of the step movements made on x and y axes (dx.dy = a(x,y step)). The area sampling fraction (asf) was then a(frame) / a(x,y step). The height (h) of the disector was known relative to the thickness of the sections (t) - mean thickness estimated with a microcator - as was the section sampling fraction (ssf). The number of neurons in the subdivisions (N) was estimated as:

$$\text{est } N = \bar{SQ} \cdot t/h \cdot 1/asf \cdot 1/ssf$$

$\bar{SQ}$ refers to the total number of neurons actually counted in the disectors that fell within the sectional profiles of the subdivisions seen on the sampled sections (Fig. 2).

OPTIMIZING THE SAMPLING SCHEME

One of the most valuable features of this metod is that the evaluation of the precision of the individual estimates, the coefficient of error

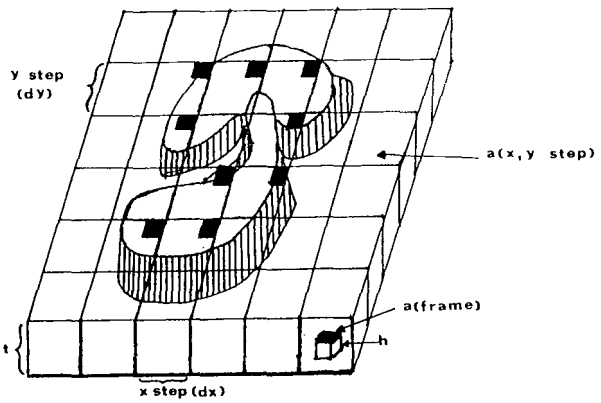

Fig. 2. Hippocampal section, sampled by the fractionator technique. Each section is moved in a raster pattern with stepping motors, so that in the center of the field viewed on a video monitor we see those positions indicated by the intersections of the lines of the sampling lattice. An unbiased counting frame (black square) is superimposed on he video image, and at positions where it falls over the neurons of a subdivision, samples of neuron number are made with an optical disector (Q^-). Area of the sampling fraction is the area of the counting frame, a (frame), relative to the area assoicated with each step of the stepping motors, a (x, y step): asf=(a (frame)/a (x,y step)). The thickness sampling fraction is the height, h / t. Adapted from West et al. 1991.

(CE), provides the information necessary for determining whether or not a particular sampling scheme is appropriate for a particular study. In this case, in order to do a complete study, the sampling must be organized into a hierarchy of levels such as individuals, sections, and disector samples. The variance of the estimates at each level contributes to the overall variance of the estimate at the top level. For biological material, the level that usually contributes most to the total variance is exactly the biological variance between individuals at the top level. This can be easily solved by using larger experimental groups. The strategy for effecting optimal sampling is to ensure that the variance of the estimate at a particular level (j), contributed by the variance of the estimate at the next lower level (j + 1), is a minor part of the variance observed at level j.

It should also be pointed out that although the sampling and the estimates described for the optical fractionator are unbiased, the CEs used in the evaluation of the efficiency of the sampling scheme are aproximations. Exact CEs can only be obtained with simple random sampling schemes (the expected CE for n independent observations made from a Poisson distribution is 1/ n), a procedure impossible to realize in 3D space. The method currently used to to estimate the CE (or the precision of the estimate of **N**) uses the quadratic approximation formula described in Gundersen & Jensen (1987). This approach to estimating CE has been improved and provided with a more thorough theoretical background by Cruz-Orive (1990) and Thioulouse et al.(1993).

REFERENCES

Bjugn R. 1993. The use of the optical disector to estimate the numbers of neurons, glial and endothelial cells in the spinal cord of the mouse - with a comparative note on the rat spinal cord. Brain Research. **627:** 25-33.

Braendgaard H, SM Evans, CV Howard, HJG Gundersen. 1990. The total number of neurons in the human neocortex unbiasedly estimated using optical disectors. J. Microsc. **157:** 285-304.

Cruz-Orive LM. 1990. On the empirical variance of a fractionator estimate. J. Microsc. **160:** 89-95.

Cruz-Orive LM, ER Weibel. 1990. Recent stereological methods for cell biology: a brief survey. Am. J. Physiol. 258 (Lung Cell. Mol. Physiol. 2): L148-L156. Gundersen HJG. 1986.

Stereology of arbitrary particles. A review of unbiased number and size estimators and the presentation of some new ones, in the memory of William R. Thompson. J. Microsc. **143:** 3-45.

Gundersen HJG, P Bagger, TF Bendtsen, SM Evans, L Korbo, N Marcussen, A Møller, K Nielsen, JR Nyengaard, B Pakkenberg, FB Sørensen, A Vesterby, MJ West. 1988a. The new stereological tools: Disector, fractionator, nucleator and point sampled intercepts and their use in pathological research and diagnosis. APMIS. **96:** 857-881.

Gundersen HJG, TF Bendtsen, L Korbo, N Marcussen, M Møller, K Nielsen, JR Nyengaard, B Pakkenberg, FB Sørensen, A Vesterby, MJ West. 1988b. Some new, simple and efficient stereological methods and their use in pathological research and diagnosis. APMIS. **96:** 379-394.

Gundersen HJG, EB Jensen. 1987. The efficiency of systematic sampling in stereology and its prediction. J. Microsc. **147:** 229-263.

Howard CV, S Reid, A Badeley, A Boyde. 1985. Unbiased estimation of particle density in the tandem scanning reflected light microscope. J. Microsc. **138:** 203-212.

Jensen GB, B Pakkenberg. 1993. Do alcoholics drink their neurons away? The Lancet. **342:** 1201-1204.

Korbo L, BB Andersen, O Ladefoged, A M Møller. 1993. Total number of various cell types in rat cerebellar cortex estimated using an unbiased stereological method. Brain Research. **609:** 262-268.

Mayhew TM. 1992. A review of recent advances in stereology for quantifying neural structure. J. Neurocytol. **21:** 313-328.

Petran M, M Hadravsky, MD Egger, R Galambos. 1968. Tandem - scanning reflected - light microscope. J. Opt. Soc. Am. **58:** 661-664.

Sterio DC. 1984. The unbiased estimation of number and sizes of particles using the disector. J. Microsc. **134:** 127-136.

Thioulouse J, JP Royet, H Ploye, F Houllier. 1993. Evaluation of the precision of systematic sampling: nugget effect and

covariogram modelling. J. Microsc. **172:** 249-256.

West M J, HJG Gundersen. 1990. Unbiased stereological estimation of the number of neurons in the human hippocampus. J. Comp. Neurol. **296:** 1-22.

West MJ, L Slomianka, HJG Gundersen. 1991. Unbiased stereological estimation of the total number of neurons in the subdivisions of the rat hippocampus using the optical fractionator. Anatomic. Record. **231:** 482-497.

Zoological Studies 34, Supplement I (1995)

Zoological Studies

Simultaneous Blur and Image Restoration in 3-D Optical Microscopy

Gopal B. Avinash

Noran Instruments, Inc., 2551 W. Beltline Highway, Middleton, WI 53562, USA

The point spread function (PSF) in three-dimensional (3-D) optical microscopy including widefield and confocal (fluorescence, brightfield reflective and transmission) is spatially variant especially in the axial direction. Further, the PSF depends upon various parameters such as the refractive indices of the materials along the light path, wavelength of the light and the depth of the volume of interest from the coverslip (Hell et al. 1993). Even though empirically derived PSF is an estimate of the true PSF, one must be aware of the caveat that it may not be an accurate estimate when optical conditions change. Rather than depending on an unreliable, empirically determined PSF, a type of image restoration called blind deconvolution has been developed and introduced in the literature (Holmes 1992, Krishnamurthy et al. 1992). In this paper, we present a novel, iterative algorithm for simultaneous blur and image restoration (SBIR) in 3-D optical microscopy. The method described here requires fewer iterations than those published in literature without sacrificing numerical accuracy of the results. Moreover, all the constraints necessary for the restoration are derived from the data itself.

The process begins by sectioning data into overlapping volumes so that overlap save method of convolution can be performed (Oppenheim and Schafer 1975). Since the PSF changes rather slowly in the axial direction but never abruptly, it can be modeled as spatially shift invariant within a given subvolume, but shift variant across subvolumes. Each subvolume can be processed independently as follows: The desired result is initialized to the observed data while the PSF is initialized to the Dirac delta function. Next, the input image subvolume is examined to determine the constraints on the PSF. The spatial extent of the PSF is usually overestimated in x-, y-, and z-directions. The spatial extent of the image subvolume is limited to the non-zero voxel intensities within the volume after background subtraction. The spatial frequency bounds are determined by examining sections of the 3-D power spectrum (periodogram) of the data in three mutually orthogonal directions. This estimation is possible since it is the PSF and not the true specimen which determines the bandlimits. The bandlimit estimation is done as follows: First we notice the lowpass nature of the power spectral sections. The magnitude function pertaining to extreme high frequency portions of the plotted spectral sections can be assumed to represent underlying noise processes and the bandlimit at each of the axis is determined by locating the point where the image frequency content drops off to the noise content as one traverses from low frequency end to the high frequency end. Generally, we overestimate this cut-off frequency since significant artifacts can result if the bandlimits are underestimated.

The iterative SBIR algorithm uses a generalized Landweber-type method (Strand 1974) for both the PSF and the image update in the Fourier domain. Each iteration begins by computing a PSF estimate in the Fourier domain given a specimen estimate. Bandlimit constraints estimated from the observed data are applied to the PSF in the frequency domain. The PSF estimates are further constrained to have unity gain with numbers being non-imaginary and positive in the spatial domain. Next the specimen update is obtained in the frequency domain by using the PSF estimate from the previous step. Constraints such as spatial bounds and positivity are applied in spatial domain. Acceptable results can usually be obtained within ten such iterations.

The SBIR algorithm was validated using simulated 3-D images. Test images were obtained by using a known computer generated specimen which was corrupted by convolving with a known PSF and by adding Gaussian noise. Blur and noise

variances were varied to simulate different conditions generally encountered in practice. Blurry and noisy images were then restored with the SBIR algorithm and the quality of restoration was studied using a normalized mean squared error criterion. Next fluorescent latex beads of known diameter were used for the validation of the SBIR algorithm under more realistic conditions. The test specimen consisted of spherical fluorescent beads of 4μm diameter (hollow) and 1μm diameter (solid). These beads were next to each other in the axial direction. From the raw data, one could not resolve these two beads nor determine that the 4μm bead was hollow. In the processed data, both these limitations were resolved as both lateral and axial resolution of the image were improved. Finally, the algorithm was applied to unknown specimens. The preliminary results have shown that successful restorations could be obtained using the SBIR algorithm even when the specimen is located deeper in the tissue.

In conclusion, the SBIR algorithm improved lateral and axial resolution for different kinds of specimens. Since all the constraints were based only on the observed image data, the proposed algorithm was applicable for improving the quality of images at arbitrary depths. The algorithm provided acceptable results in fewer iterations than the methods described in literature. Furthermore, this procedure has potential to become a turnkey system to deblur images in 3-D optical microscopy.

REFERENCES

Holmes TJ. 1992. Blind deconvolution of quantum limited incoherent imagery: Maximum likelihood approach, J. Opt. Soc. Am. A. Vol. **9:** 1052-1061.

Krishnamurthy V, YH Liu, B Roysam, JN Turner, TJ Holmes. 1992. Blind deconvolution of 2D and 3D fluorescent micrographs. Biomedical Image Processing and Three-Dimensional Microscopy. SPIE, **1660:** 95-102.

Hell S, G Reiner, C Cremer, EHK Stelzer. 1993. Aberrations in confocal microscopy induced by mismatches in refractive index. J. of Microscopy, Vol. **160:** 391-405.

Oppenheim AV, Schafer RW. 1975. Digital Signal Processing, 113-114 Prentice-Hall, Inc., New Jersey.

Strand ON. 1974. Theory and methods related to the singular-function expansion and Landweber's iterations for integral equations of the first kind. SIAM J. of Num. Ana., VOl. **11:** 798-825.

Zoological Studies 34, Supplement I (1995)

Zoological Studies

Confocal Microscopy with Electronic Pinholes

P. A. Benedetti, V. Evangelista, D. Guidarini and S. Vestri
Istituto di Biofisica - CNR, Via S. Lorenzo 26, 56127 Pisa, Italy

PROBLEMS IN BIOLOGICAL CONFOCAL MICROSCOPY

Especially in the biomedical field, the accurate imaging of tiny three-dimensional structures and the measurement of time-evolving microscopical phenomena, generally require that the specimen is irradiated in a spectrally adequate and non-invasive way. Unfortunately, current confocal microscopes give their best results in materials research applications on reflecting specimens in which spectral requirements, irradiation damage and saturation are of minor or no importance.

Actually, the design of most confocal microscopes, is based on the use of laser sources in a confocal-point (CP) scanning, epi-illumination configuration. On one hand, in fluorescence analysis, this imposes scarce flexibility and relatively high costs in the selection of a source being suited to a particular chromatophore. On the other hand, in many cases, specimen damage due to the high instantaneous irradiation doses and fluorescence saturation effects can't be tolerated (Wells et al. 1990, Visscher et al. 1994). Moreover, instrumentation in the latter class is substantially unsuited to transmitted-light confocal analysis that is very important in many branches of the biological and medical investigation.

In order to overcome some of the cited limitations, confocal microscopes have been proposed, based on multi-confocal-points (MCP) scanning approaches, with the use of revolving spatial modulators (Egger and Petran 1967, Kino and Xiao 1990, Lichtman and Sunderland 1989) or on confocal-line (CL) illumination and detection methods (Benedetti et al. 1992, Brakenhoff and Visscher 1992). Conventional sources can be more favorably adopted in these cases and the instantaneous irradiation dose on the sample is substantially reduced, due to parallel operation. When observing specimens of small or moderate thickness, the spatial resolution performance of MCP instruments essentially corresponds to that of CP instruments, but unfortunately the construction is even more complicate and costly, the versatility is scarce and the epi-illumination configuration prevents any practical possibilities for the study of the light-absorbing properties of the specimens. On the other hand, the CL methods existing offer interesting capabilities, but their spatial resolution performance remains inferior to that of CP and MCP techniques (Benedetti et al. 1994, Sheppard et al. 1991).

OPTICAL OR ELECTRONIC FILTERING ?

In current confocal instrumentation, most of the light available from the specimen is deliberately thrown out (Wells et al. 1990) by the spatial selectivity of the detection pinhole (optical filtering). Consequently, in many applications, such as in the detection of low fluorescence signals but even in the case of three-dimensional reconstructions (Hiraoka et al. 1990), an extensive part of microscopical activity is presently performed with the aid of non-confocal microscopes, using high performance image sensors and computer deconvolution of spatial data (electronic filtering). While affected by intrinsic limitations in the ultimate resolution performance, if compared to the confocal techniques (Frieden 1967, Streibl 1985, Carringhton et al. 1990, Sandison and Webb 1994), the latter approach can be more sensitive and offer a higher signal-to-noise ratio, along with a higher biological compatibility. Also, the experimental setup is more adaptable to a variety of microscopies and different analytical requirements, due to the

use of the conventional instrument, associated to an advanced image sensor with relatively powerful data processing devices and consequent programming flexibility.

A MORE RADICAL SOLUTION

As a further improvement to the performance of the current methods discussed above, the authors have devised and experimentally implemented a novel microscopical imaging technique aimed to combine advantages of confocal and non-confocal microscopies, called Electronic Multi Confocal Points (EMCP) microscopy (Benedetti et al. 1995). The method is based on a substantially unmodified microscope design and can achieve conventional, partly-confocal or confocal imaging performance in several configurations including reflection, fluorescence, transmission, etc. Any imaging activity is performed with the aid of an image sensor fitted to the photographic tube of the microscope (Fig. 1).

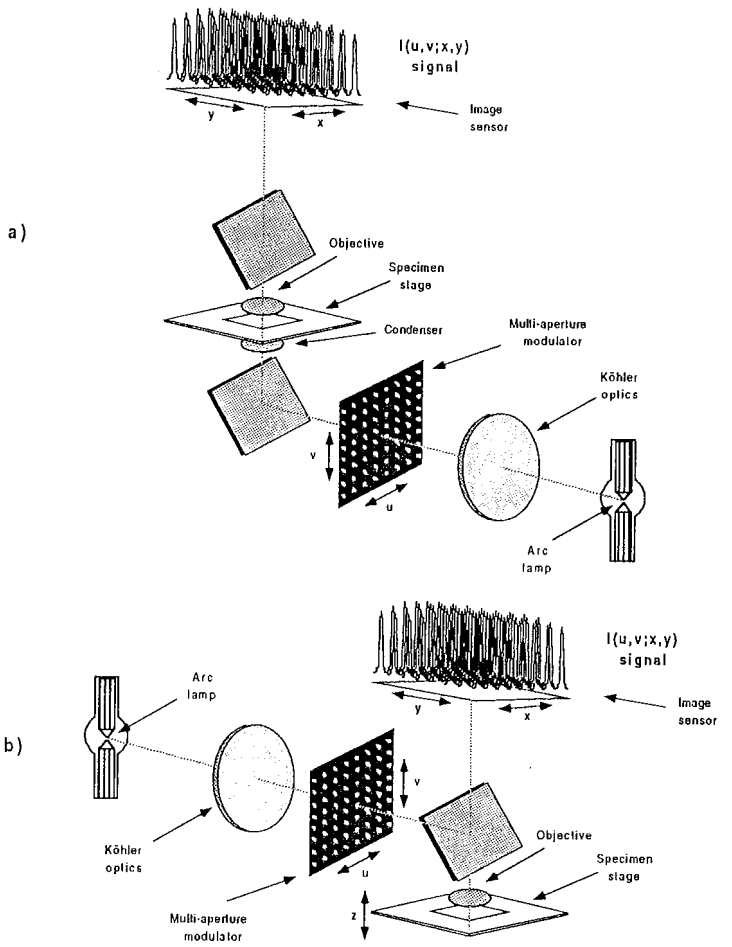

Fig.1. The EMCP optical setup. a) transmission configuration, b) epi-illumination configuartion

In cases in which the confocal imaging performance is desired, a multi-point spatial modulator (hole-pattern) is placed in an image plane along the illumination path of the microscope. As a consequence, the specimen is Koehler illuminated by the multitude of spots that corresponds to the demagnified pattern of the modulator. The image sensor is equally used for the detection, but a spatial filtering process, conjugated to the illumination spots, is performed here at the electronic level, selecting only those pixels that correspond to the illumination spots. Spot positioning, on the detector surface, is obtained during a preliminary reference measurement. A set of subsequent images is collected while the modulator is scanned in its plane in steps capable of covering the full object by means of interleaved spot positions. The summation of the images collected in this way, represents the confocal image of the object.

The method is closely related to other MCP techniques, with the important difference that critical opto-mechanical parts are substituted by more reliable opto-electronic processes, taking advantage of modern technology.

The optical and mechanical characteristics of the spatial modulator are not particularly demanding in EMCP and the size of the illumination spots, their distribution and the fill-factor can be easily changed with the simple substitution of the modulator itself. The latter capability is very important to optimize the multi-point operation to the specific characteristics of the sample. The initial reference measurement provides to adapt the data collection process to the characteristics of the particular modulator selected and also to correct a relatively wide class of imperfections due to modulator manufacturing.

CONCLUSIONS

The EMCP method is simple and the resulting instrumentation, compared to existing confocal systems, is relatively simplified since it requires only modest opto-mechanical additions to a normal research microscope and an accurate image sensor followed by suitable components for electronic data processing.

As a result, the most salient features of EMCP microscopy are:

a) The instantaneous irradiation doses are orders of magnitude less than in CP microscopy, resulting in lower specimen damage, improved spatial resolution and linear photometric characteristics. The latter aspect is specially important when spatial deconvolution procedures are employed on image data.

b) Conventional light sources can be used with substantial advantages in spectral flexibility, simplified design and low cost.

c) The method is adaptable to different microscopies and offers improved peculiarities, over existing approaches, in the measurement of space and time dependent phenomena.

REFERENCES

Benedetti PA, V Evangelista,Guidarini D Vestri S. 1992. Confocal line microscopy. J. Microsc. 165, 119-129.

Benedetti PA, V Evangelista, Guidarini D, Vestri S. 1994. Achieving confocal-point performance in confocal-line microscopy. Bioimaging **2:** 122-130 .

Benedetti PA, V Evangelista, Guidarini D, Vestri S. 1995. Electronic multi-confocal-points microscopy. SPIE/IS&T's Electronic Imaging: Science & Technology Conference (in press).

Brakenhoff GJ. K Visscher. 1992. Confocal imaging with bilateral scanning and array detectors. J. Microsc. **165:** 139-146.

Carrington WA, KE Fogarty, L Lifschitz, FS Fay. 1990. "Three-dimensional imaging in confocal and wide-field microscopy," in Handbook of Biological Confocal Microscopy, I. B. Pawley, ed. (Plenum, New York), Chap. 14.

Egger MD, Petran M. 1967. New reflected light microscope for viewing unstained brain and ganglion cells. Science **157:** 305-307.

Frieden BR. 1967. Optical transfer of the three-dimensional object. J. Opt. Soc. Am. **57:** 56-66 .

Hiraoka Y, JW Sedat, DA Agard. 1990. Determination of three-dimensional imaging properties of a light microscope system. Biophys. J. **57:** 325-333 .

Kino GS, GQ Xiao. 1990. "Real-time scanning microscopes" in Confocal Microscopy, T. Wilson, ed. (Academic, London), 361-387.

Lichtman JW, WJ Sunderland. 1989. High-resolution imaging of synaptic structure with a simple confocal microscope. New Biologist **1:** 75-82 .

Sandison DR, WW Webb. 1994. Background rejection and signal-to-noise optimization in confocal and alternative fluorescence microscopes. Appl. Opt. **33:** 603-615 .

Sheppard CJR, CJ Cogswell, M Gu. 1991. Signal strength and noise in confocal microscopy: factors influencing selection of an optimum detector aperture. Scanning **13**, 233-240.

Streibl N. 1985. "Three-dimensional imaging by a microscope," J. Opt. Soc. Am. A **2:** 121-127.

Visscher K, GJ Brakenhoff, TD Visser. 1994. Fluorescence saturation in confocal microscopy. J. Microsc. **175** Pt. 2, 162-165.

Wells KS, DR Sandison, J Strickler, WW Webb. 1990. In Handbook of Biological Confocal Microscopy,Pawley I. B., ed. (Plenum, New York), 27-39.

Zoological Studies 34, Supplement I (1995)

Zoological Studies

Multi-colour Confocal Microscopy by Means of Intensity-Modulated Multiple-beam Scanning (IMS)

Erik M.M. Manders, Ardan Patwardhan, Anders Lijeborc and Kjell Carlsson
Physics IV, The Royal Institute of Technology, S-100 44 Stockholm, Sweden

For the analysis of the spatial relationship between different biological structures in the same preparation, dual-colour confocal microscopy (Carlsson, 1990) has proven to be a successful technique. For example: experiments where DNA double labelling techniques were combined with accurate distance measurements in dual-colour confocal images have shown that DNA replication is a dynamic process (Manders et al. 1992, Manders et al. submitted) . However, it is impossible to prove the existence DNA move-ment during the replication process by using a confocal microscope equipped for the detection of only two colours. A third (FISH; fluorescent *in situ* hybridization) label should be used to investigate the DNA-replication process in more detail. Also, in many other biological and biomedical applications the recording of more than two different fluorophores in the same preparation (Multi-colour confocal microscopy) is an urgent need. Therefore, we built a confocal microscpe for the voxel-simultaneous detection of three or four fluorophores.

Major interfering effects in multi-colour confocal micrscopy (Brelje et al. 1993) are: 1) *cross-talk* between the fluorescence signals and 2) positional*shift* between the colour components of an image. To minimize the latter effect, all fluorescence signals should be recorded during one scan (exact repositioning of the scanning table is difficult) and UV-excitation of one of the fluorophores should be avoided (large differences of excitation wavelengths will generally spoil the alignment of the fluorescence signals). To minimize the amount of cross-talk we applied a new technology, Intensity-modulated Multiple-beam Scanning (IMS) (Carlsson et al. 1994), that drastically reduces the cross-talk between the fluorescence signals.

In this study we investigated the possibility to use the fluorophores FITC, Texas Red and Cy-5 for voxel-simultaneous scanning. For the excitation of these fluorochromes we used an Argon laser tuned to 488 nm and a Krypton laser in multi-line mode. From the Kr-laser the wavelengths 568 nm and 647 nm were selected and subsequently separated (Fig. 1). The three wavelengths predominantly excite one fluorophore each. The three laser beams were intensity-modulated by three electro-optical modulators (EOMs) tuned to different frequencies in the MHz region, and combined before entering the confocal microscope. The emitted light was spectrally separated and detection was performed by three photomultiplier tubes (PMTs) with filters for green (500-550 nm), red (580-630 nm) and far-red (665-695 nm). The outputs of the PMTs were connected to three lock-in amplifiers, each tuned to the modulation frequency of the corre-sponding laser beam. The signals from the three lock-in amplifiers were sampled voxel-simultaneously and subsequently digitized and stored. The recorded (full-colour) images can be displayed during scanning.

In our experiments we used preparations of pure fluorochromes, fluorochrome-conjugates and microbeads coated with fluorochromes. All measurements were performed with, and without the lock-in detection technique in order to determine the effect of the lock-in technique on cross-talk quantities. In addition to the described triple-colour set-up, we have investigated the use of a fourth fluorophore, without using an additional laser-line or an additional PMT for this purpose we tested the excitation and emission quantities of PerCP (Beckton Dickinson). This fluorophore can be excited with 488 nm and emits in the far-red region. By using an extra lock-in amplifier connected to the 'far-red PMT' and tuned at the modulation frequency of the 488-nm-beam, we managed to separate the PerCP-fluorescence signal from other

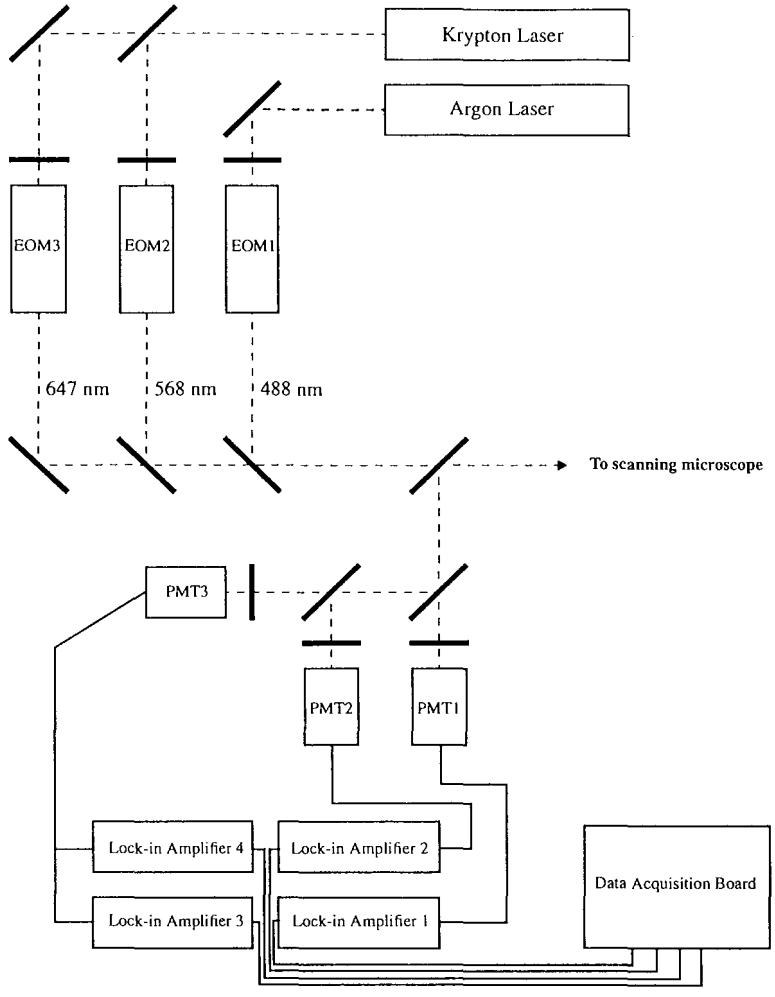

Fig.1. The three colour IMS set-up. As shown, the set-up is con-figured for scanning four fluorophores using two lasers three detectors and four lock-in amplifiers.

fluorescence signals. In this manner, the IMS technique can be used for the application of an extra fluorophore (instead of cross-talk reduction).

This study was supported by the Netherlands Organization for Scientific Research (NWO) and the Göran Gustafsson Stiftelse.

REFERENCES

Brelje TC, MW Wessendorf, RL Sorenson. 1993. Multicolour laser scanning confocal immunofluorescence microscopy: Practical application and limitations. Methods in Cell Biology **38:** 97-181.

Carlsson K, N Aslund, K Mossberg, J Philip. 1994. Simultaneous confocal recording of multiple fluorescent labels with improved channel separation. J. Microsc. **176:** 286-299.

Carlsson K. 1990. Scanning and detection techniques used in a confocal scanning laser microscope. J. Microsc. **138:** 21-27.

Manders EMM, J Stap, GJ Brakenhoff, R van Driel, JA Aten. 1992. Dynamics of three dimensional replication patterns during the S-phase analysed by double labelling of DNA and confocal microscopy. J. Cell Sci. **103:** 857-862.

Manders EMM, J Stap, R van Driel, J Strackee, JA Aten, Spatial progression of DNA replication in the cell nucleus. Submitted to J. Cell Sci.

Zoological Studies 34, Supplement I (1995)

Zoological Studies

A Sensitive Method for Measurements of Luminescence in Single Cells

Martin Köhler[1], Svante Norgren[1], Bertil B. Fredholm[2], Olof Larsson[1], Holger Luthman[1] and Per-Olof Berggren[1]

[1]*The Rolf Luft Center for Diabetes Research, Department of Molecular Medicine, Karolinska Institute, Karolinska Hospital, S-171 76 Stockholm, Sweden*

[2]*Department of Physiology and Pharmacology, karolinkska Institute, S-171 77 Stockholm, Sweden*

A method was developed to monitor changes in cytoplasmic ATP concentration in intact living insulin-producing cells. Luciferase was introduced into HIT M2.2 cells (Santerre e al. 1981, Edlund et al. 1985) by transient expression of firefly (*Photinus* pyrialis) luciferase cDNA (de Wet et al. 1987). In transfected cells, extracellular addition of luciferin increased the luminescence signal to a mixiumum within 50 to 120 seconds. Addition of 0.3, 3, and 30 mM azide (NaN_3) decreased the luminescence in a dose-dependent manner; this effect was completely reversed upon withdrawal of the compound. Changes in the luminescence signal were parallelled by changes in cellular ATP, ADP, and AMP contents and in activity of the ATP-sensitive K^+channel (K_{ATP} channel).

This method may be used to monitor changes in cytoplasmic ATP in real time and thereby to assess the role of ATP in different key regulatory steps of the simulus-secretion coupling in the insulin secreting β-cell. Thus, in the future it should be possible, using imaging techniques, to monitor local changes in ATP concentration in well defined areas of the cell.

For optimization of transfection, luciferase activity was quantified in extracts from transfected cells using a liquid scintillation counter. As means of transfection, calcium phosphate precipitation, lipofectin, and electroporation were tested. In our hands, electroporation produced the highest and most reproducible expression. The choice of heterologous promotor to drive the luciferase cDNA was based on analysis of CAT reporter gene constructs driven by the rat, human insulin, SV40 and RSV promotors. This demonstrated that the relative promotor activities were approximately 80, 1, 20 and 100, respectively. We therefore used the RSV-driven luciferase construction (pRSVL).

Cells attached to coverslips were superfused in a custom built open chamber with a flow rate of 0.1 ml/min. The chamber was mounted on an inverted microscope (Zeiss Axiovert 135TV, Zeiss, Germany) equipped with a photon-counting photometer tube, chilled to between -30 and -25°C with a custom made water cooled peltier element. Lenses were Zeiss Achrostigmat 40x/1.30 Oil and, for imaging, Zeiss Fluar 40x/1.30 Oil. Data acquisition was performed with hardware from Spex Industries (Edison, NJ). Integration time was 5 seconds per time point and background (dark) signal was in average 2.5 counts per second (cps). Acquisition of images was done with a cooled CCD (Charge Coupled Device) camera (CH50 with KAF 1400, Photometrics Ltd., Tucson, AZ) connected to an imaging system (Inovision Corp., Durham, NC). Integration time used for images was 300 seconds. Temperature during experiments was 33°C. In order to quantify the effect of azide on luminescence, linear functions were curve fitted to the trace before, during, and after the lowering effect of the metabolic inhibitor was detected. Curve fitting was necessary because of the decay of luminescence and the signal to noise ratio. As shown in Figure 1E, we denote the endpoints of the fitted functions S_1, S_2, S_3, and S_4. These endpoints were corrected for background (dark counts) in respective experiment. The effect on luminescence (Δ-luminescence) was then calculated as $(S_2\text{-}S_1)/S_1$ (Fig. 1F), and the degree of recovery after withdrawal of azide was calculated as $\{(S_4\text{-}S_3)/S_4\}/\{(S_2/S_1)/S_1\}$ (Fig. 1G). Only experiments in which the background was lower than 4 cps were included in the calculations.

To investigate the correlation between changes in ATP concentration and changes in lumi-

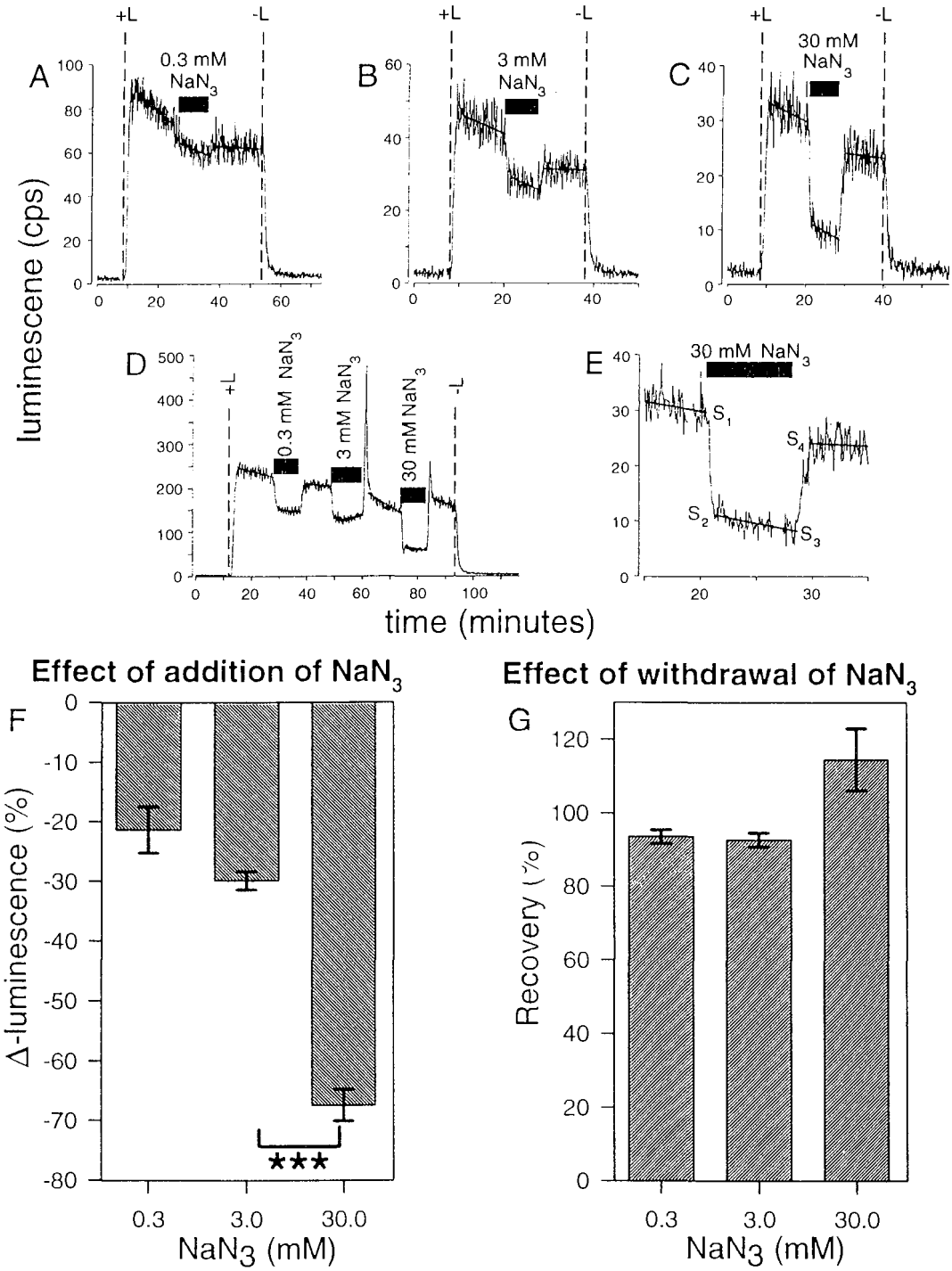

Fig. 1. Luminescence detected from groups of luciferase expressing HIT M2.2 cells (20-30 in the measuring field), during exposure to 0.1 mM D-luciferin added to theextracellular medium. Addition of azide (0.3, 3, and 30 mM), as indicated in the figure, was accompanied with a decrease in luminescence. The linear fitted functions to the traces before, during and after azide exposure are included in the figure, was accompanied with a decrease in luminescence. The linear fitted functions ot the traces before, during and after azide exposure are included in the figure. Due to light artifacts short segments of the trace were excluded when changing perifusion buffers. **A-D:**"+L" denotes addition of D-luciferin and "-L" denotes withdrawal of D-luciferin. **E:** Part of Figure C showing the endpoints (S_1, S_2, S_3 and S_4) of the linear functions fitted to the luminescence traces, before, during and after the response to azide. **F:** The luminescence effect in response to azide (Δ-luminescence) given in percent (%) and calculated as $(S_2-S_1)/S_1$. Effects of 0.3, 3, and 30 mM azide are plotted as mean ±SEM(n=5, 10, and 6, respectively). The effect at 30 mM azide is significantly lower than at 3 mM of the metabolic inhibitor (***$p<0.001$), as calculated with Student's unpaired t-test. **G:** The recovery of luminescence afte withdrawal of azide, given in percent (%) and calculated as $\{(S_4-S_3)/S_4\}/\{(S_2-S_1)\}$.

nescence, we exposed cells to 0.3, 3, and 30 mM sodium azide (NaN_3), a mitochondrial electron transport inhibitor of cytochrome a_3. We then compared theresponses in luminescence with two other methods of ATP detection: K_{ATP} channel activity and total ATP content.

The luminescence from 10-40 transfected cells, in the same field of view, was measured in the microscopic system. Addition of 0.1 mM D-luciferin to the extracellular medium resulted in an increase in signal, which reached a maximal value within 50 to 120 s. Thereafter luminescence decayed, with slightly varying kinetics in the different experiments. In response to addition of azide, a decrease of the luminescence signal was recorded and could be reversed by withdrawal of the inhibitor. The relative decrease of luminescence (Δ-luminescence) depended on azide concentration (Fig. 1). Luminescence from a field of cells, as well as distribution in single cells, was monitored with image acquisition by a CCD camera. The fraction of cells expressing luciferase was small at the time of the experiment and the degree of expression was quite variable (Fig. 2). However, luminescence was apparently evenly distributed within each cell.

K_{ATP} channel activity is regulated by cytosolic ATP (Cook and Hales 1984, Ashcroft et al. 1984) and this channel will thus serve as a biosensor of the ATP concentration in the submembrane space. We used the patch-clamp technique to study changes in membrane potential and K_{ATP} channel activity in response to azide. The electrophysiological experiments show a similar temporal and quantitative response to azide as the luminescence measurements. Azide (3 mM) hyperpolarizes the cell within 30 s from the plaeau potential of -50 mV to approximately -80 mV. Withdrawal of the compound induces depolarizationof the cell and concomitant reappearance of overshooting action potentials. In parallel experiments, we recorded whole-cell K_{ATP}-currents by alterna-tively stepping the potential to -60 and -80 mV, repeatedly, from a holding potential of -70 mV. Following 3 mM azide, an aproximately 5-fold increase in channel activity was observed. In order to more directly study the effects of azide on the K_{ATP}-channel current, we recorded single-channel activity using the cell-attached patch configuration. In the presence of 3 mM glucose, little channel activity was observed. The number of channel openings dramatically increased upon exposure to 3 mM azide. In the presence of 30 mM azide, the channel activity was further increased and the opeings were more prolonged. These effects were fully reversed by withdrawal of the metabolic inhibitor.

The K_{ATP} channel activity is inhibited by ATP but stimulated by ADP. In fact the ATP/ADP ratio, rather than the ATP concentration *per se*, is considered the actual parameter controlling channel activity (Ashcroft and Rorsman 1989). In order to further verify that the actual exposure to azide indeed decreased both the ATP concentration and the ATP/ADP ratio, we measured the total content of ATP, ADP, and AMP in our cells, using HPLC analysis. The ATP content, following addition of azide, was decreased in a dose-dependent manner (significant changes between

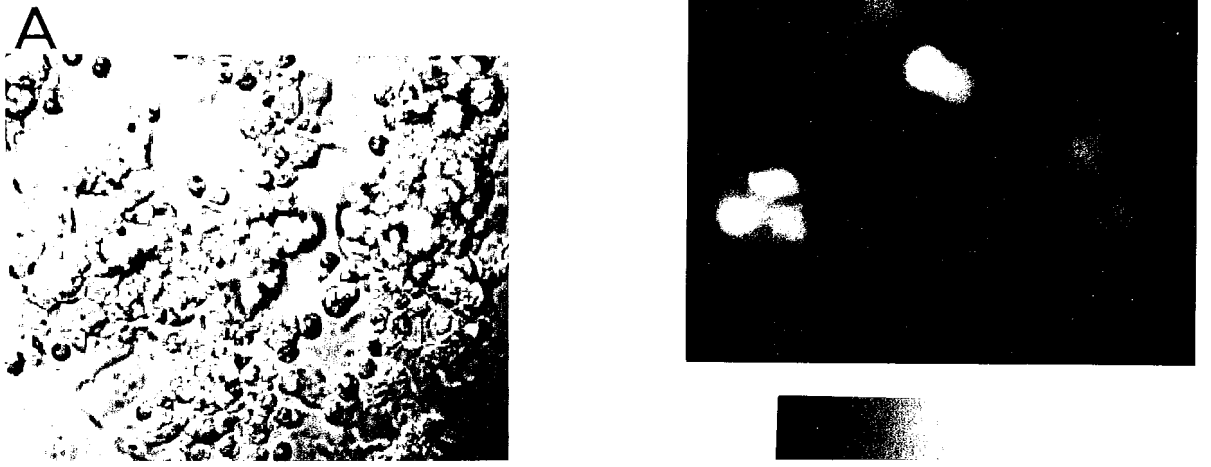

Fig. 2. A: Luciferase expressing HIT M2.2 cells visualized with DIC (differential interference contrast).
B: The same field (and the same focus) as in A shwing luminescence when the cells are exposed to 0.1 mM D-luciferin.

0.3 and 3 mM azide as well as between 3 and 30 mM of the metabolic inhibitor). Also the ATP/ADP ratio was decreased (significant between 0.3 and 3 mM as well as between 3 and 30 mM azide), as well as the total adenine nucleotide content (significant between 3 and 30 mM azide).

REFERENCES

Santerre RF, RA Cook, RMD Crisel, JD Sharp, RJ Schmidt, DC Williams, CP Wilson. 1981. Proc. Natl. Acad. Sci. USA **78:** 4339-4343.

Edlund T, MD Walker, PJ Barr, WJ Rutter. 1985. Science **230:** 912-916.

de Wet J, KV Wood, M DeLuca, DR Helinski, S Subramani. 1987. Mol. Cell. Biol. **7:** 725-737.

Cook DL, CN Hales. 1984. Nature **311:** 271-273.

Ashcroft FM, DE Harrison, SJH Ashcroft. 1984. Nature **312:** 446-448.

Ashcroft FM, P Rorsman. 1989. Prog. Biophys. Mol. Biol. **54:** 87-143.

Zoological Studies 34, Supplement I (1995)

Zoological Studies

Analysis and Utility of Chromosome Information 75. Semi-automatic Image Analysis for Small Plant Chromosomes

S. Nakayama[1], P. Wankling[2], E. Takagawa[2], T. Koga[2] and K. Fukui[3]
[1]*National Institute of Agrobiological Resources, Tsukuba 305, Japan*
[2]*Carl Zeiss Vision, Tokyo 160, Japan*
[3]*Hokuriku National Agricultural Experiment Station, Joetsu 943-01, Japan*

Plant chromosomes are categorized into two groups. One group consists of large chromosomes represented by the genera *Triticum* and *Hordeum*. The other is small represented by the genera *Oryza* and *Brassica*, etc. It had been difficult to identify the small chromosomes, because of the similarity in the morphology at the *mitotic* metaphase stage. Moreover the band patterns are simple and it is even possible that there are no bands on the chromosomes after the banding treatments. The small plant chromosomes, however, show on uneven condensation pattern along the chromosomes especially at the prometaphase stage of the mitosis. The condensation pattern, CP, which appears as darkly and lightly stained regions along a chromosome at the prometaphase stage of small plant chromosomes was first defined by Fukui and Mukai (1988). All the rice chromosomes have been identified based on the condensation pattern (Fukui and Iijima 1991). Moreover it has been shown that the CP is a representative characteristic of the chromosome morphology in plants since all the rice chromosomes have been semi-automatically identified using only the information of CP (Kamisugi et al. 1993). For quantitative analysis of the CP, image analysis has been employed. Quantitative maps of small plant chromosomes have thus been obtained based on the CP. In this paper, we present new imaging methods that enable us to obtain numerical data of the CP as the grey value profile and to generate a quantitative chromosome map based on the CP.

Two photographs, under- and normal exposure, of the same chromosomal image have been employed for image analysis. The under-exposed photograph has higher resolution in grey levels at the condensed or darkly stained region of chromosomes (Iijima and Fukui 1991). This is used for the precise determination of the density distribution of the chromosomes. The normally exposed photograph is suitable for the determination of chromosomal areas. Thus this photograph is used to discriminate the chromosomal regions.

The imaging programs that enable us to obtain the quantitative map based on the CP are divided into the six parts. The procedures for standardization of the CP and the outlines of the programs are as follows;

1. Under-exposed chromosome images are captured into the image memories. Using the contour lines of the normally exposed chromosome images, the background of the under-exposed image is masked in preparation for the analysis.

2. Light deflection of the image is adjusted by standardization of the grey values. i.e., the minimum and maximum grey values of the chromosomal area within a plate are extended from grey value, 1 to grey value, 255. Thus all the grey values in the chromosomal area within the plate are distributed between the grey values 1 and 255.

3. Each chromosomal region is extracted from the image and each of their grey values are measured. Chromosomal constriction(s) is/are interactively marked and the grey value profiles under the mid-lib lines of the chromatids are read digitally.

4. The minimum and maximum grey values of the homologous chromosomes in the plate are adjusted to the average grey values of all the plates measured.

5. The length of each chromosome arm is adjusted to the average length of the arm of homologous chromosomes of all the plates by an affine transformation.

6. The standard greygram of the chromosome

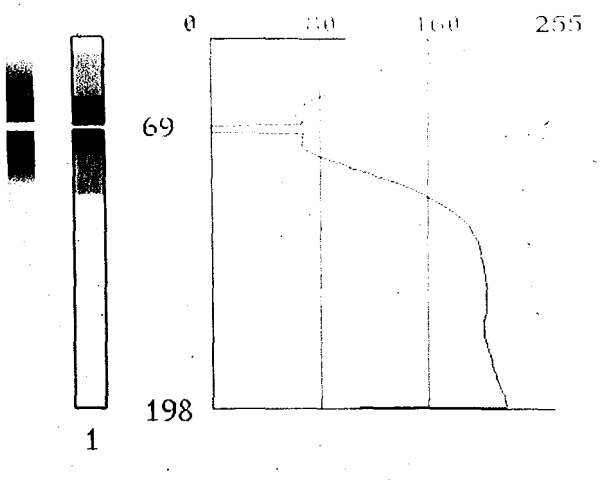

Fig. 1. Standard greygram, idiogram and grey value profile of chromosome 1 of *Brassica nigra* constructed by the semi-automatic imaging programs.

is constructed from the average grey value. The darkly, intermediately and lightly stained areas of the standard greygram are decided, interactively. The quantitative idiogram is developed by setting two thresholds on the standard greygram. The standard grey value profile of each chromosomes represents well the characteristics of the condensation pattern of the chromosomes.

The image analysis and processing programs constructed are semi-automatic. Some procedures in the standardization procedures have already been automatized. For example, the grey values of all the chromosome images within the plate have been measured and standardized automatically. The adjustments after the measurement of the grey value profile of each chromosome are also automatic.

The adjustments after measurement of the grey gram profiles are also automatized. The remaining two interactive steps in the imaging program will be automatized. One is the automatic positioning of the under exposed images to the contour of the normal exposed ones for capturing images to image memories. The other is the automatic determination of the mid-lib lines of two chromatids for measuring the grey value profiles from the chromosomes. Although the mapping of small plant chromosomes based on the CP had taken long time and required an image analysis expert, the fast and easy mapping is enabled by the semi-automatic imaging programs.

REFERENCES

Fukui K, K Iijima. 1991. Somatic chromosome map of rice by imaging methods. Theor. Appl. Genet. **81:** 589-596.

Fukui K, Y Mukai. 1988. Condensation pattern as a new image parameter for identification small chromosomes in plants. Jpn. J Genet. **63:** 359-366.

Iijima K, K Fukui,. 1991. Clarification of the conditions for the image analysis of plant chromosomes. Bull. Natl. Inst. Agrobiol. Resour. **6:** 1-58.

Kamisugi Y, N Furuya, K ijima, K Fukui. 1993. Computeraided automatic identification of rice chromosomes by imaging parameters. Chromosome Res. **1:** 189-196.

Zoological Studies 34, Supplement I (1995)

Zoological Studies

Design and Development of Soft X-ray Imaging System at Taiwan Light Source

G.J. Jan[1,3], K.T. Hsu[1,3], K.T. Pan[1,3], C.S. Chen[1,3] and P.K. Tseng[2]

[1]*Department of Electrical Engineering, Institute of Electro-Optical Engineering, National Taiwan University, Taipei, Taiwan, R.O.C.*

[2]*Department of Physics, National Taiwan University, Taipei 10764, Taiwan, R.O.C.*

[3]*Synchrotron Radiation Research Center, Shin-Chu Science Based Industrial Park, Hsin-Chu 30377, Taiwan, R.O.C.*

The third generation synchrotron radiation light source at Synchrotron Radiation Research Center (SRRC, Taiwan Light Source) has been constructedin Hsin-Chu since 1993. Taiwan Light Source could provided an ideal light source which is a high brilliance, low emittance and excellent photon source in soft ray energy range. It is well suited to set up an experimental facilities for a biological microscopy at SRRC. Currently, it is an extremely powerful and useful research tool for the research of the life science around the world. The imaging microscope will operate in a real time mode and recording the entire image at the well spatial resolution. Imaging x-ray microscope (XM) which receive radiation from an adjacent bending magnet. XM has been initiated as a development high resolution zone plate microscope. This x-ray microscope will open a new experimental technique to study the biological specimens in the domestic area and development tool to investigate the ray optics as well as the characterization system of the key component.

A preliminary layout for the x-ray microscope from the SRRC bending magnet is shown in figure 1. An illustration of the main features of XM is shown in figure 2. It uses a first mirror to reject unwanted short wavelength radiation, a condenser zone plate and aperture that serve as a modest resolution linear monochromator and as the sample illuminator. The remainder of the XM consists of the sample chamber and high precision translational stage, a high resolution micro zone plate as an objective lens, and photoresist contact image plate or a soft x-ray sensitive charge couple device (CCD) image array detector. The condenser len is being provided through a collaboration with the University Gottigens institut fur Rontegenphysik. The condenser micro zone plate will include and derived by the translation stage with some motion in this XM to enhance uniformity of illumination in the desired field of view. Anticipated performance of XM is summarized in table 1.

In order to optimum the parameters of the x-ray

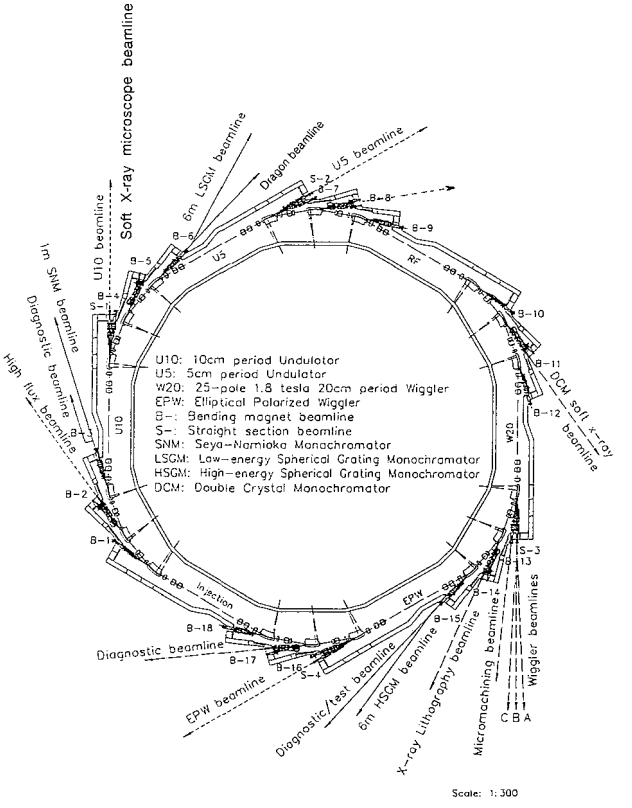

Fig. 1. Beamlines on the SRRC experimental floor.

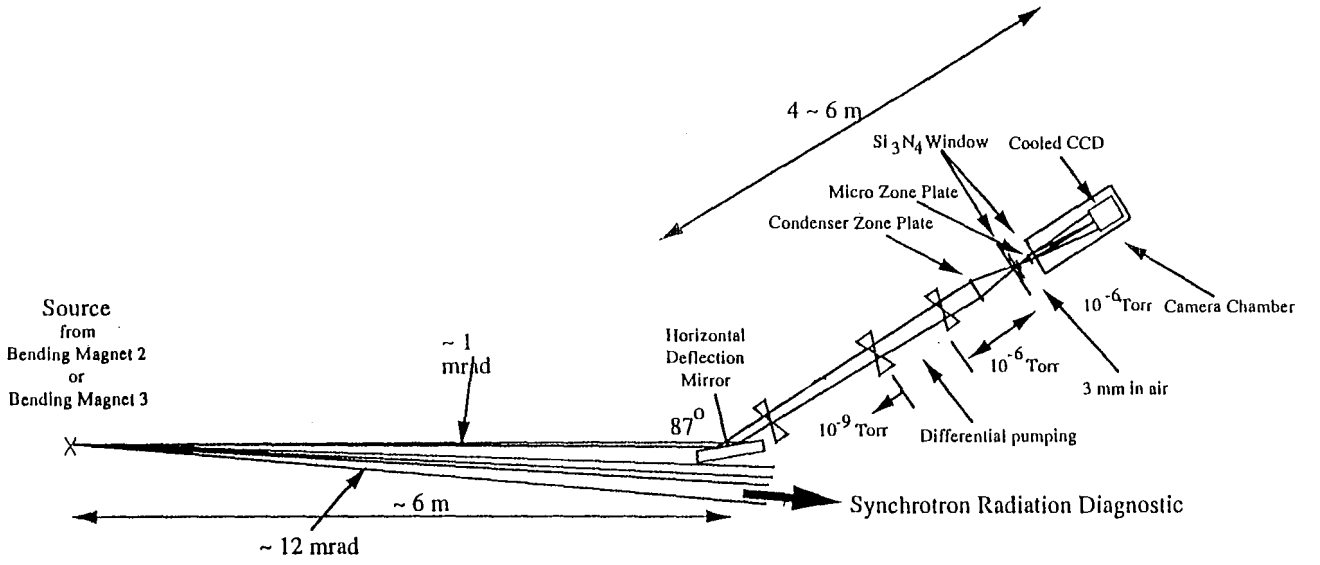

Fig. 2. Soft x-ray microscopy beamline conceptual layout

optics to use a micro zone plate as an image element for a high resolution x ray microscope, the theoretical calculation that is referred to, Thieme 1983, are performed and an optical system are also designed and specified. The key components, such as reflected mirror, micro-zone plate and two dimensional CCD image sensor are ordered from abroad and will be installed from the radiation source of the bending magnet at TLS Beam line. The CCD camera is thinned and back-illuminated device same as Advanced Light Source (ALS) used in Berkeley. All components and XM imaging system are underway and will be characterized later on. The detailed results and status will be reported on the conference meeting.

Table 1. Specification of x-ray contact imaging system from the beinding magnet at Taiwan Light Source

Operational	Summer, 1986
Objective lens	Zone plate
Outermost zone-width	300 Å
Nominal depth of focus	1 mm
Exposure time	10 sec
30 nm, 1000 counts/pixel	300
Monochromator	20-50 Å
(spectral resolution)	contrast in transmission
Tuning range (nominal)	and reflection
Ondependent visible light	Piezo-actuator &
microscope	mm translational stage
Translational stage	Normal enviroment or
Sample cell	in high vacuum chamber

REFERENCES

SRRC design handbook, 1992.

Schmahl G, D Rudolph, P Guttmann, O Christ. 1984. Zone plates for x-ray microscopy. X-Ray microscopy 63-74, ed. G Schmahl and D Rudolph, Berlin: Springer-Verlag.

Thieme J. 1984. Construction of condenser zone plates for a scanning X-ray microscope. X-Ray microscopy 91-96, ed. G Schmahl and D Rudolph, Berlin: Springer-Verlag.

Zoological Studies 34, Supplement I (1995)

Zoological Studies

Three Dimensional Reconstruction of Histological Sections from the Region of the Porta Hepats of a 11 Week Human Foetus

Vijayalaxmy Vijayan and Carolyn E. L. Tan

Department of Paediatric Surgery, Singapore General Hospital, Singapore 0316

INTRODUCTION

The biliary tree forms an intricate system of drainage ducts through which bile is transported from the liver to the small intestine. Essentially it consists of two parts: the intrahepatic (within the liver) and the extrahepatic (outside the liver). The biliary tree literally resembles the tributaries of a river, where smaller ducts join to form larger and larger ducts, the smallest of which is in contact with the liver cell, while the largest drains into the small intestine. Bile, which is produced by the liver cell flows through this intricate system of ducts to reach the small intestine.

The development of the biliary system in the foetus has fascinated embryologists for many years. It has been suggested that the intrahepatic and extrahepatic biliary system develop separately and connect at the porta hepatis region of the liver. However more recent evidence suggests that the intrahepatic and extrahepatic systems are in communication throughout gestation. Through an active remodelling process certain intrahepatic ducts are selected for development while the others are deleted. This process occurs at the porta hepatis region of the liver between 11 and 13 weeks of gestation and leads to the creation of an effective biliary drainage system. Errors in this remodelling process may be the cause of the condition called biliary atresia which results in improper biliary drainage, jaundice and later liver fibrosis in infants.

The porta hepatis is the region of the liver where the extrahepatic biliary tree ceases and continues as the intrahepatic. As this is a very important region in its development, we performed 3 dimensional reconstruction of the biliary tree in this region. As our work mainly involves histological techniques, in this project we have used images from such techniques to perform 3 dimensional reconstructions.

Three dimensional reconstruction of histological sections poses problems that do not arise with images of tomograms. One of the main problems is to align the sections so that the structures fall one behind the other in a natural order. Another difficulty is differences in staining intensity which affect the brightness of the images. The aim of this project is to study the feasibility of using simple serial, histological sections to construct a 3 dimensional image that will show the true situation within the organ.

MATERIALS

The paraffin embedded whole liver of an 11 week normal human foetus was serially sectioned at a thickness of 5 μ. The porta hepatis region was identified and every third section was routinely stained with hematoxylin and eosin. Thirty nine sections were included in the 3 dimensional reconstruction covering an area of 585 μ.

IMAGE PROCESSING

The sections were viewed under a Carl Zeiss (Germany) AXIOPHOT upright microscope. Images were obtained through a PROGRESS 3012 camera using the PROGRESS software option.

Alignment was done using a RGB monitor connected to the VIOB output of the IBAS 2.5 system (Kontron Elektronik, Germany). In order to align an image, the preceding image was converted to overlay and the current image aligned according to the overlay. Alignment was done at low magnifications of 2.5 using the outline and other clearly

visible structures in the image as references. Images were obtained at a magnification of 5. Eight bit images were obtained at a size of 1024 X 1024 and stored for later use.

After the alignment all further work with the images was done on the HDD monitor (FLEXSCAN F760i.W). Working with the IBAS, the images were reduced to a size of 512 X 512. Uneven intensities in the images were observed due to differences in staining which were corrected in by using the function normalize. The ducts in the biliary system were selected manually using the eraseoutside function in each image. The images thus obtained by selecting the ducts was stored as a separate sequence. As the stain used did not preferentially stain the ducts there was no difference in grey values between the ducts and other structures. In order to create the difference, the original images and the images of ducts alone were scaled differently and combined as in the following macro:

```
for i=1; i<40; i=i+1                    #i=image number
eraseoutside i, i+40, 300, 0            #selects the ducts
subtract 300, i, i+80, 2                #removes ducts from the
                                          original image
scalim i+80, i+120, 1,255,1,170,1,170,1
                                        #scales background to
                                          lower grey levels
scalim i+40, i+160, 1,225, 200, 255, 200, 255, 1
                                        #scales the ducts to
                                          higher grey levels
orim i+160, i+120, i                    #combines the two
                                          showing a difference
                                          in grey values between
                                          the ducts and other
                                          structures
```

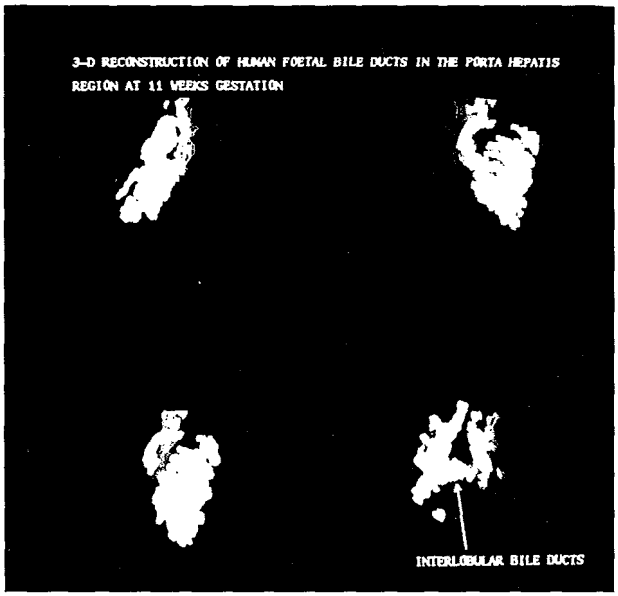

Fig. 1.

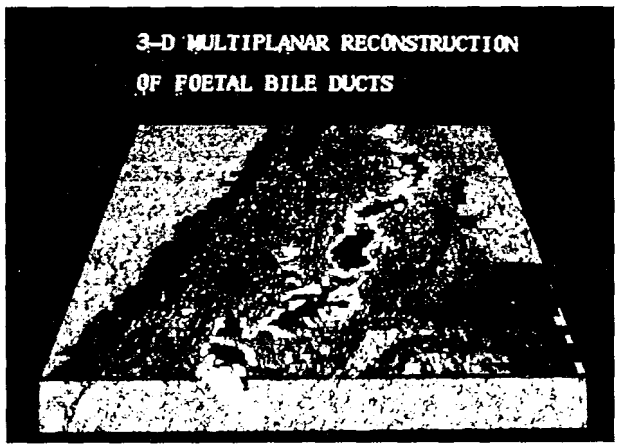

Fig. 2.

THREE DIMENSIONAL RECONSTRUCTION

Mipron system version 2.0 (running on the Ibas computer) (Kontron Elektronik, Germany) was used for 3 dimentional work. Thirty nine images were used for the reconstructions shown in figures 1 and 2. Voxel size of the images were 1.08 μ in the X, 1.04μ in the Y and 15μ in the Z direction.

Surface distance shading was used for the images containing only the ducts without the background structures.(Fig. 1) The following parameters were used for the reconstruction:

Rotation X: 0.0 Increment 5.0
Rotation Y: 0.0 Increment 20.0
Rotation Z: 0.0 Increment 0.0
view Point: 1000
Grey Threshold: 100-255
Output Resolution: 1.08

The 4 images in a clockwise direction from top left, show the following rotations:

1: X 0, Y 0,Z 0
2: X 10, Y 40, Z 0
3: X 15, Y 60, Z 0
4: X 50, Y 200, Z 0

Using the images which were created to show a grey level difference between the ducts and background structures multiplanar reconstruction was done using the same parameters as above. (Fig. 2) A cutplane has been used to show the continuity in

the lumen of the biliary system which is not seen in the other planes.

CONCLUSION

The 3 dimemsional reconstruction of this image sequence shows that by using very simple histological techniques in serial sections it is possible to study the behaviour of the object of interest in the real three dimensional situation. In this series we were able to show that many of the ducts led to dead ends, while one continued, maintaining an open tract from the first to the last section. Extension of the reconstruction in either direction, which we are currently pursuing, will add to the picture and provide useful information.

REFERENCES

Desmet VJ. 1985. Intrahepatic bile ducts under the lens. J Hepatol. **1:** 427-447.

Tan CEL, GJ Moscoso. 1994. The developing human biliary system at the porta hepatis level between 29 days and 8 weeks of gestation: A way to understanding biliary atresia: Part 1. Pathol International. **44:** 29-40.

Zoological Stufies 34, Supplement I (1995)

Zoological Studies

Soft X-ray Microscopy Project at NSRL

Xingshu Xie[1,2], Chengzhi Jia[1], Yongfei Zhao[1], Lei Shang[1], Jiangyang Zhang[1], Xiangtung Xu[2] and Xhiping Jiang[2]

[1]*Center for Fundamental Physics*

[2]*National Synchrotron Radiation Laboratory, University of Science and Technology of China, Hefei 2300226, China*

The Hefei Synchrotron Radiation Facility, a national synchrotron radiation source was operated and available for experiments at the end of 1991. This 800 Mev storage ring produces the synchtotron radiation in the spectral range from infared to VUV and soft x-ray microscopy has been planned at Hefe National Synchrotronyn Radiation labortory (NSRL) since 1984 (Xie et al.) The aims of our soft x-ray microscopy project are the construction of a soft x-ray scanning microscope, development of soft x-ray scaning microscope, development of soft x-ray scanning microscope, development of soft x-ray contact imaging techniques and demonstration of the unique capabilites of soft x-ray microscopy in high resolution, element-specific studies of biological specimens. We also begin the project of other types soft x-ray imaging study, e.g. x-ray holography.

A Prototype scanning transmission x-ray microscope has been installed in beamline U12A. In the first generation of our instrument the x-ray probe is formed by a 2μm pinhole. We have tested this scanning x-ray microscope and obtained the real time x-ray image using synchrotron radiation. The specimen on stage is mechanically scanned across the x-ray spot. The continuous scan (50μm × 50μm) is generated by a pair of PZTs and the fast scan direction is horizontal. The PZTs ar driven by fast, high voltage (1000) operational amplifiers which are controlled by low voltage signals from a CAMAC DAC. The position is sensed by a pair of LVDTs, the outpu of which is converted to a voltage by a high gain signal processor and inputted to two channels of a CAMAC ADC. The x-rays transmitted by specimen are detected by a flow gas proportional counter which is fabricated in our lab. The x-ray micrograph is displsyed on a color monitor via the video display interface and can be stored on a hard disk or diskette. Simple image processing can be done in thses stored images including changing contrast and color level, pixel size and starting position (Xie et al.). The effort of constructing a new x-ray scaning microscope is undertaken. In the next generatio of the instrument a high resolution micro zoneplate with outermost zonewidth 45 nm which was fabricated at IBM (Anderson et al.) will be used to focus the x-rays. An improved scanning stage and an x-ray image processing system also will be made.

Studies of soft x-ray contact microscopy have been performed using ysnchrotron radiation. We designed and built a prototype device for doing the specimen exposure with synchtotron radiation. This device is vacuum compatible and convenient for the specimen handling. Typical time to reach pressure of the order of 10-5 torr is about 10 minutes. The specimen holder consists of five holes in which one is painted on P-31 phosphor for beam alignment and others hold specimen-resist assembly. The holder can be moved toexact position through a linear feedthrough. We also developed and tested a wet specimen chamber. A Si3N4 window of thinkness 1000Å is used to seperate the beamline vacuum ad the expasure area. The Si3N4 windows which is fabricated in our laboratory has been used with-out breaking and leaking. Exposures in a broad-hand beam and monochromatic beam have been made. Simple grid and some biological specimens have been chosen for examination and demonstration (Jia et al.).

ACKNOWLEDGMENTS

We are grateful to Dr. E. Anderson and Prof. D.

Attwood of Center for X-Ray Optics at LBLand Prof. J. Kirz of SINY at Stony Brook for their help and suport to our x-ray microsocpy project and to our colleagues in China for their continuous help and contributions.

REFERENCES

Anderson E, D Kern. 1992. Nanofabrication of zone plates for x-ray microsocpy. In X-Ray Microscopy III, ed. by AG Michette, GR Morrison, CJ Buckley. Berlin, Spinger-Verlay, pp75-78.

Buckley J. Berlin, springer-Verlay, pp75-78.

Jia C, X Xie, Y Zhao. Studies of soft x-ray contact microscopy performed with synchrotron radiation at NSRL. Annual Report 1992-1993, NSRL, 50.

Xie X, S Kang, C Jia, T Jin. 1986. Soft x-ray microsocpy at the Hefei Synchttron Radiation Laboratory. Nucl. Inst. Meth. phys. Res. **A246:** 698-701.

Xie X, C Jia, Z Zhou, Y Zhang, Y Zhao, M Wang. 1992. Progress of the soft x-ray microscopy project at Hefei, In X-Ray Microscopy III, ed. by AG Michette, GR morrison, CJ Buckley. Berlin. Springer-Berlay. pp. 157-159.

Zoological Studies 34, Supplement I (1995)

Zoological Studies

Near-Field Scanning Optical Microscopy Imaging of Individual threading Dislocations on Relaxed Ge_xSi_{1-x} Films

J.W.P. Hsu[1], E.A. Fitzgerald[2], Y.H. Xie[2] and P.J. Silverman[2]
[1]*Department of Physics, University of Virginia, Charlottesville, VA 22901, USA*
[2]*AT&T Bell Laboratories, 600 Mountain Ave., Murray Hill, NJ 07974, USA*

Using a near-field scanning optical microscpe (NSOM), we investigate defects and morphology on the surface of relaxed GeSi films that arise from the strain release caused by lattice mismatch between the heteroepitaxial films and the Si substrates. Threading dislocations are identified by simultaneously imaging the surface topography and the photoelectric signals. Characterization using an electron microscope is commonly used for this type of defect imaging. Images based on photoelectrical contrast is analogous to electron beam induced current (EBIC) imaging. The resolution achieved with a NSOM it ten times higher than with conventional far-field optical techniques, and similarto that of EBIC. We will present results of surface morphology and photoelectic response near threading dislocations, as well as compare our results with EBIC results.

The ability to integrate devices made of different materials is the key to advancing modern electronic and optoelectronic technologies. Thus, the growth of good quality films having bulk properties on lattice mismatched substrates and the characterizations of such flms have been major area of study in material science. We will rport the use of a novel optical technique, the near-field scanning optical microscope (NSOM), to simultaneously study, with spatial resolution better than 100 mm, the surface morphology and electric-optical activity of individual threading dislocations on relaxed Ge_xSi_{1-x} films. Because the size of each crystalline defect is much smaller than the diffraction limit of visible light, such defect characterization has been limited until now to electron microscopy techniques. This study also demonstrates the power of the NSOM, which achieves a more than tenfold increase in spatial resolution from conventional far-field optical methods. The capability to simultaneously study morphology and photoresponse of the same defect structure is the major advantage of the NSOM over electron microscopy.

The NSOM used in this experiment operates in reflection mode, and was modified from a commercial scanning force microscope (PSI BD-2). The tips were tapered, Al-coated optical fibers similar to those reported in Betzig et al. 1991. Shear force feedback (Betzig et al. 1992, Burrato et al. 1994) was used to regulate the tip-sample separation between 10 and 20 nm. Topographic images are generated by applying a voltage to the z piezo scanner to keep the shear force signal constant, while the spatially resolved near-field photoresponse is measured simultaneously.

Samples studied in this experiment are grown by molecular beam epitaxy and consist of a uniform Ge_xSi_{1-x} cap layer of ~1μm on top of a compositionally graded layer on Si (100) substrates. They are completely relaxed, exhibiting bulk Ge_xSi_{1-x} optical properties. (Fitzgerald et al. 1991, Xie et al. 1992) Typicaly, these graded films have threading dislocation densities $\leq 5 \times 10^6$ cm^{-2}. This was determined with electron beam induced current (EBIC) (Fitzgerald et al. 1992) because the density is too low to be detected by transmission electron microscopy. Fig. 1 shows side by side (a) topographic and (b) photovoltage images in a 10.9 μm x 10.9 μm area taken simultaneously. In Fig. 1b, three threading dislocations are easily identified by the three dark spots in the image. The corresponding topographic image (Fig. 1a) is dominated by the cross-hatch pattern that is due to the underlying misfit dislocation network characteristic of these graded samples. Nevertheless, three shallow depressions corresponding to the region of reduced photoresponse can be identified. These electrically-active shallow depressions are individual

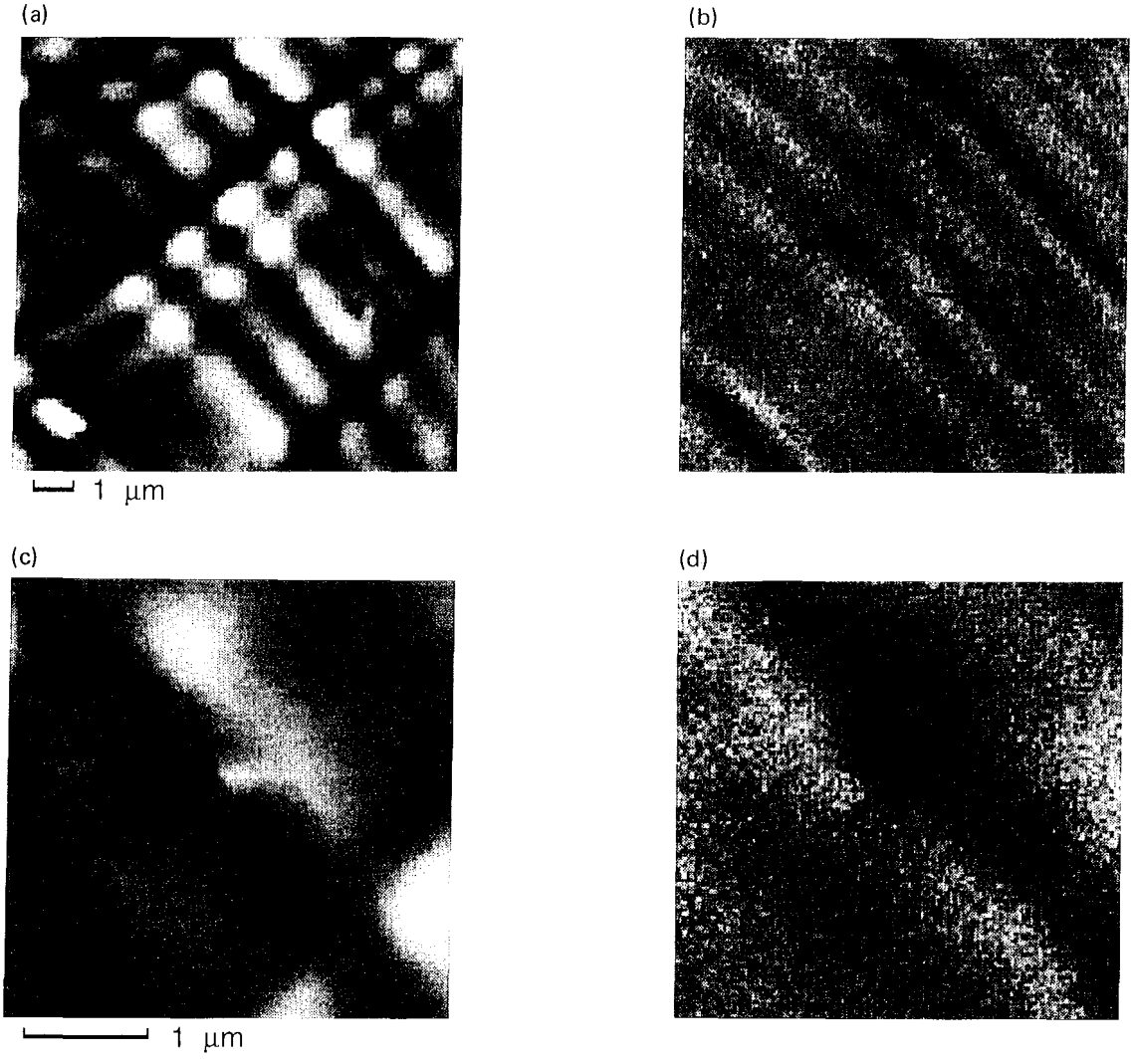

Fig. 1. (a) Topographic and (b) photovoltage images taken sim-ulateously of a 10.9 μm x 10.9 μm area. (c) Topographic and (d) photovoltage images of a 3.6 μm x 3.6 μm area near dislocation #1, indicated in (b). The full gray scale for (a) & (c) represent 100 Å and for (b) & (d) correspond to a 10% change.

defects since their photoresponse is similar in both magnitude and spatial extent to their morphoogy. Fig. 1c and d show topography and photoresponse near threading dislocation #1 from Fig. 1a and (b) with higher manification (3.6 μm x 3.6 μm). It is now clear that these threading dislocations display a distinctive morphology as reported in Hsu et al. 1992 and act as carrier recombination centers. The average spatial extent of the photovoltage reductionfor a threading dislocation is (0.66±0.16) μm, larger than that of the depressions, (0.39±0.11) μm. This is because the electrical activity length scale is determined by carrier diffusion length,which can be large in good materials, as well as aperture size. EBIC images of threading dislocations in these samples show dark spots with ~1 μm diameters. The full scale of Fig. 1b and d represents a 10% change about the average photovoltage. Typical reduction of threading dislocation photoresponse is measured to be 5 ~ 10%. A few precent change is also what is observed in EBIC.

REFERENCES

Betzig E, JK Trautman, TD Harris, JS Weiner, RL Kostelak. 1991. Breaking the diffraction barrier: optical microscopy on a nanometric scale. Science **251:** 1468-1470.

Betzig E, PL Finn, JS Weiner. 1992. Combined shear force and near-field scanning optical microscopy. Appl. Phys. Lett. **60:**

2484-2486.

Burrato SK, JWP Hsu, JK Trautman, E Betzig, RB Bylsma, CC Bahr, MJ Cardillo. 1994. Imaging InCaAsP Quantum Well Lasers Using Near-Field Scanning Optical Microscopy. J. Appl. Phys. **76:** 7720-77025.

Fitzgerald EA, YH Xie, ML Green, D Brasen, AR Kortan, J Michel, YJ Mii, BE Weir. 1991. Totally relaxed Ge_xSi_{1-x} layers with low threading dislocation densities grown on Si substrates. Appl. Phys. Lett. **59:** 811-813.

Fitzgerald EA, YH Xie, D Monroe, RJ Silverman, JM Kuo, AR Kortan, FA Thiel, BE Weir. 1992. Relaxed Ge_xSi_{1-x} structures for III-V interation with Si and high mobility two-dimensional electron gases in Si. J. Vac. Sci. Technol. B. **10:** 1807-1819.

Hsu JWP, EA Fitzgerald, YH Xie, PJ Silverman, MJ Cardillo. 1992. Surface morphology of relaxed Ge_xSi_{1-x} films. Appl. Phys. Lett. **61:** 1293-1295.

Xie YH, EA Fitzgerald, PJ Silverman, AR Kortan, BE Weir. 1992. Fabrication of relaxed GeSi buffer layers on Si(100) with low threading dislocation density. J. Mat. Sci. Eng. B. **14:** 332-335.

Zoological Studies 34, Supplement I (1995)

Zoological Studies

Biological Application of a Projection X-ray Microscope

T. Horikoshi[1], H. Chiba[1], K. Takahashi[1], W. Hiraoka[1], T. Mitsui[1] and K. Yada[2]

[1]*Department of Physics, School of Science and Technology, Meiji University, Higashimita, Tama-ku, Kawasaki 214, Japan*

[2]*Aomori Public College, Yamazaki, Goshizawa, Aomori 030, Japan*

A projection X-ray microscope was constructed by modifying a scanning electron microscope, HITACHI S-2500CX, using a transmitting X-ray target (Fig. 1). A LaB_6 cathode was adopted to get good resolution. The resolving power of the microscope was better than those of optical microscopes, as was revealed by X-ray photographs of diatom: structures close to 0.1μm were observed fairly clearly. Thin films of gold and germanium of the thickness of 0.1-1μm were used as the target. Gold was used for relatively hard X-rays (1-6Å) and germanium for relatively soft X-rays (1-10Å). We used an imaging plate and photographic films as a detector. The former is better in time resolution but worse in space resolution than the latter. We were interested in high-resolution images and used the films in taking the images reported here. A projection X-ray microscope has advantages of very large focal depth and easiness in taking stereo-pair photographs as described, for instance, by Yada and Takahashi(1989). Hence one can inspect three-dimensional internal structures of thick specimens up to a few mm. We took stereo-pair photographs in most cases.

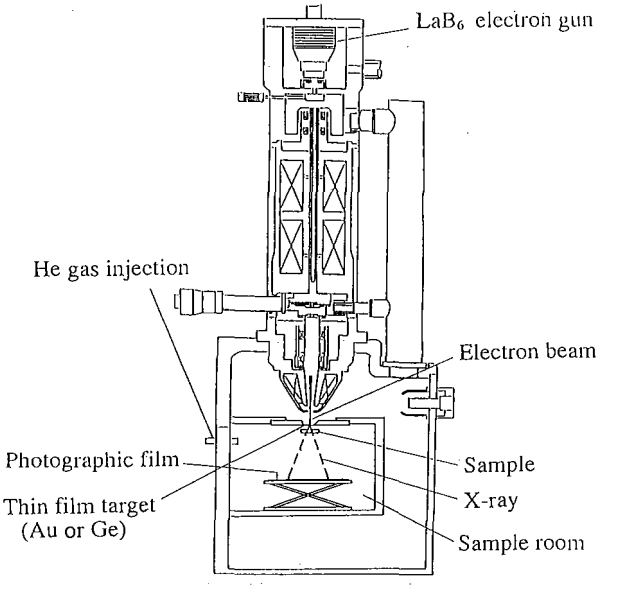

Fig. 1. Structure of the projection X-ray microscope. Height is 1.7m.

We can see inside of optically opaque samples with the X-ray microscope. It is known that an aphid is apt to be suffered by a parasititic small bee. Our inspection of hypertrophic aphides clearly showed existence of a parasitic bee in each aphid. Some bees appeared to be a larva and some an imago. Sometimes an aphid was just an empty body with a large hole on the back from which presumably a bee got out.

By a roentgenograph, one can see bones and lungs of human beings as a high and low electron density parts in body, respectively. The projection X-ray microscope can be looked upon as an instrument to get enlarged roentgenographs. As is well known, bones in animals are formed after chondrogenesis. An intermediate stage from cartilage to hard bone was observed in paw of new born (one day old) rat. As the lung of human being, tracheae of insects are filled with air and we could observe them even through the cuticula shell with X-ray microscope. We tried to observes organs other than bone and trachea in living insects treated by anesthesia. It was possible to see some internal structures by selecting suitable X-ray wave length for each specimen, but generally it was difficult to get very clear images. The critical-point drying is widely used in preparation of specimens for electron microscope. This method was tried in order to get more distinct images of organs in small animals such as ants and water bears (a small aminal of the size of less than lmm: cf. Mathews 1937). Arrangement of muscle

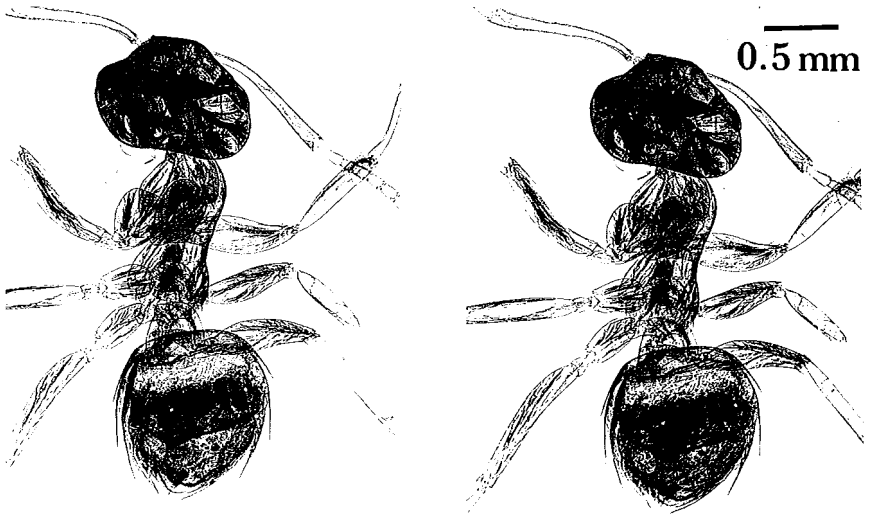

Fig. 2. X-ray image of ant treated by the critical-point drying method. Target: Au(about 0.2 μm thick). Acceleration voltage of electrons: 10kV. Atmosphere in the sample room: He gas. Exposure time: 10 min.

fibres was clearly observed in ants as shown in Fig. 2. Some organs (brain and digestive organ, etc.) were seen in bodies of water bears.

A projection X-ray microscopy is a useful tool in histology in medicine especially because one can easily get stereo-pair photographs of as thick sections as a few hundred μm compared to about 1μm in ordinary electron microscopes and about 5μm in high-voltage electron microscopes. Yada and Takahashi (1989) presented stereo-pair X-ray images of Golgi-stained sections of rat brain. We continued the study and could clearly see three-dimensional network of nerve fibres with spines in Golgi-stained sections of rat brain. As the sections were thick, we could observe arrangement of capillary vessels and some spiral structure around the vessel. Recently, Wake and Sato (1993) studied three-dimensional structure of stellate cells in porcine liver in connection with their functions by means of optical and electron microscopes. We took stereo-pair X-ray photographs of Golgi-stained sections of porcine liver supplied by Prof. Wake. Many section photographs were needed to reconstruct three dimensional structure in the case of optical and electron microscopes, whereas one stereo-pair photographs were good enough to see three-dimensional structure of stellate cells and network of bile canaliculi (capillary bile ducts) in the liver sections with the X-ray microscope.

We wish to thank Prof. K. Hama for supplying Golgi-stained sections of brain, and Prof. K. Wake for Golgi-stained sections of porcine liver and Prof. K. Utsugi for water bears.

REFERENCES

Yada K, S Takahashi. 1989. Target materials suitable for projection X-ray microscope observation of biological samples. J. Electron Microscope **38:** 321-331.

Mathews, GB. 1937. The Tardigrada or water bear, China Journal **26:** 97-105.

Wake K, T Sato. 1993. Intralobular neterogeneity of perisinusoidal stellate calls in porcine liver, Cell Tissue Res. **273:** 227-237.

Zoological Studies 34, Supplement I (1995)

Zoological Studies

Constructions and Applications of a Simple Optical Tweezers

Y.C. Jong[1], H.M. Chen[1], J.H. Hsu[1] and W.S. Fann[2]

[1]*Department of Physics, National Taiwan University, Taipei, Taiwan, R.O.C.*

[2]*Institute of Atomic and Molecular Sciences, Academia Sinica, Taipei, Taiwan, R.O.C.*

The combination of laser with optical microscope provides the exciting possibility of not only observing small objects but also trapping or even manipulating them. "A Single Beam Gradient Force Trap", also called "Optical Tweezers", uses a strongly focused laser beam to create a trapping zone, which is stable in all three dimensions. (Ashkin 1986) The axial stability of the trap is derived from the large axial gradient in light intensity near the focus. It gives rise to a gradient force (also called " negative radiation pressure"), capable of pulling a particle back into the trapping zone (the largest light intensity area), even against the direction of light propagation. (Block) In the aqua, optical tweezers had been demonstrated to trap dielectric particles with dimensions between 25 nm to 10 μm. (Ashkin et al. 1986) It has been used to manipulate small objects such as motile bacteria and sperm cells, to move eurkaryotic cells through the fluid, and to displace certain vesicles and organelles within larger cells. (Ashkin et al. 1987, Block et al. 1989) Recently, optical tweezers has been applied to study the DNA dynamics. (Perkins et al. 1994).

The schematic of our optical tweezers is shown in Fig. 1. In order to ensure enough gradient force, it is necessary to have a large gradient field around the trapping zone. This is accomplished by focusing the laser beam by a large N.A. objective. A trapping zone is formed near, but not at the focus. In addition, the same microscope is used to observe the trapping phenomena. The laser is an Argon laser operated at 514.5nm and the microscope is the Nikon Optiphot-2. The microscope has two auxiliary ports: the video output port, and the epi-fluorescence attachment port. For precisely adjustments and measurements, the video monitor is more helpful than the eyepieces. The laser beam is injected into the microscope through the epi-fluorescence attachment port. The microscope objective is a 100×ELWD Plan Achromat with N.A. 0.8.

Some modifications are made to the Nikon Optiphot-2 microscope. (Afzal 1989) The laser beam passes through a positive lens before entering the epi-fluorescence attachment port to insure the focus falling onto the object plane of objectives.

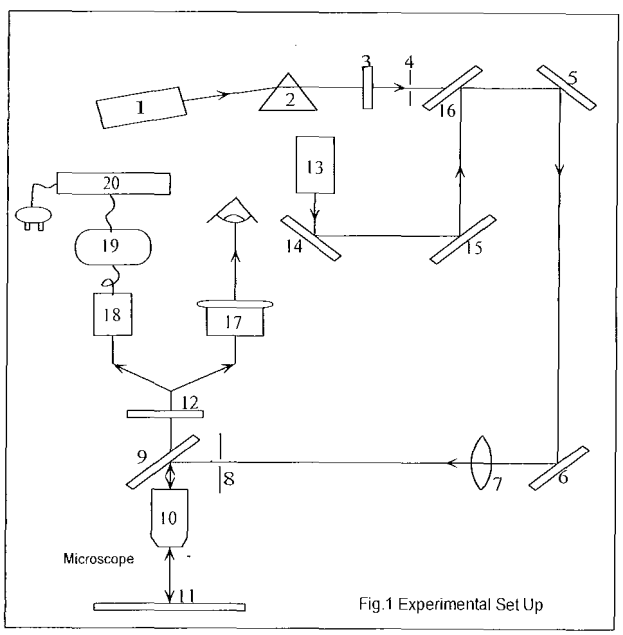

Fig. 1. The experimental set up contains two parts: Part (I) the optical tweezers and Part (II) the observation System.

Part (I)
1.Argon laser
2.Prism
3.ND filter
4.Iris
5.Reflection mirror
6.Reflection mirror
7.Positive lens
8.Epi-fluorescence attachment port
9.Dichroic mirror
10.Objective
11.Stage
12.Color filter
13.He-Ne laser
14.Reflection mirror
15.Reflection mirror
16.Slide glasses

Part (II)
17.Eyepieces
18.CCD camera
19.Monitor
20.Video recorder

This allows simultaneously observation of both objects and laser spot. In addition, the laser spot could be minimized by adjusting the position of this lens. To reflect the laser beams down to the objectives, a dichroic mirror is placed between the epi-fluorescence attachment port and the objectives. This dichroic mirror allows some portion of white light from microscope going through, preserving the original function of the microscope. A long-pass color filter is added to block the laser light from saturating the CCD camera. A low power He-Ne laser is collinear with the Argon laser to serve as the indicator for the laser focus.

Polystyrene latex is chosen to test the optical tweezers because of its spherical shape and uniform size. Trapping of 4μm polystyrene latex could be obtained using power as low as 1mW, and the trapped polystyrene latex can be pulled freely within the field of view. We have estimated the trapping force by the following method. By moving the stage of the microscope continuously, we observed that other objects moved rapidly with respect to the trapped particle. The velocity of this motion enabled us to estimate the trapping force because most of the trapping force is used to overcome the viscous force of water. The viscous force of water can be obtained from the Stock's law $f = 6\pi\eta Ur$, where η is the viscosity of water, U is the velocity of the trapped particle, and r is the radius of the particle. By putting proper numbers into the formula, the trapping force is estimated to be on the order of 0.1 to 0.01 μdynes. However, because of the difficulties in measuring the actual velocity, the trapping force should be larger than the above estimations. In addition, since a polystyrene latex with diameter 1.05 g/cm^3 will experience a gravity of 0.03 μdynes. Thus, the trapping force is hard to overcome the gravity. This helps to explain why the optical tweezers need to work in the aqua.

We had also used the optical tweezers to study Euglena. The Euglena, which belongs to the Mastigophora of the Protozoa, has the dimensions about 2×4 μm and one flagella. It can swim freely in the fluid. The optical tweezers can trap a Euglena with laser power about 100mW. In addition, the trapped Euglena could be pulled freely by the tweezers.

Other unconventional ways of constructing optical tweezers as well as the possibility of integrating the optical tweezers with scanning probe microscope and confocal optical microscope will also be discussed.

REFERENCE

Block SM. Noninvasive Techniques in Cell Biology, Chap.15, pp. 375-402.

Ashkin A, et al. 1986. Observation of a single-beam gradient force Trap for dieletric particles, Optical Letters. Vol 11.

Perkins TT, et al. 1994. Relexation of a single DNA molecule observed by optical microscopy. Science Vol 264.

Ashkin A, et al. 1987. Optical trapping and manipulation of viruses and bacteria. Science Vol 235.

Block SM, et al. 1989. Compliance of Bacterial Flagella Measured with Optical Tweezers. Nature 338.

Afzal RS, EB Treacy. 1992. Optical tweezers using a diode laser, Rev. Sci. Instrum. 63(4).

Zoological Studies 34, Supplement I (1995)

Zoological Studies

Electron Microscopy Imaging and "3D" Reconstruction of Crystal Surfaces [1]

Tung Hsu

Material Science Center, National Tsing-Hua University, Hsinchu, 30043, Taiwan, R.O.C.

While normally operated in transmission mode, the transmission electron microscope (TEM) can be operated to collect the electrons reflected off the crystal surfaces for forming the real space images of these surfaces. This technique, called reflection electron microscopy (REM) [2, 3, 4] is an extension of a more familiar technique, reflection high energy electron diffraction (RHEED). In REM, high energy electrons are reflected off the surface of the specimen to form the RHEED pattern. A high intensity spot in the RHEED pattern is then selected with the objective aperture. Electrons passing the aperture go through the lens system and form an image on the view screen of the electron microscope.

The REM image of the surface is a foreshortened picture equivalent to viewing the surface at a glancing angle of no more than 5°. The power of REM lies in its capability of detecting single defect, such as dislocation, stacking fault, atomic step, etc., on the crystal surface. It is also useful in imaging the non-uniform distributions of these defects, domains of reconstructions, and the periodic structure of surperlattices.

All images are two dimensional. REM images are no exceptions, but when the surface fluctuation is more than a few atomic layers, the reflected electron intensity may be affected by mor-phology. Consequently, the REM image may appear to be 3D although it is actually still a density distribution in the plane of the picture. Then the 3D model of the surface can be reconstructed from one or more REM images, based on information on the crystalline structure of the surface extracted from the sim-ultaneous RHEED data. This process usually requires modeling on a computer and may require more than one REM image of the same surface area.

Fig. 1. This REM image of a polished α-$A1_2O_3$(1100) surface appears 3D and is actually constructed with two types of facets unparallel to each other.

Spatial resolution of REM is about 1 to 2 nm, which lies between that of STM and SEM. In the surface normal direction, REM is capable of detecting one atom high steps. Since contrast of REM comes from diffraction, the technique is very sensitive to crystalline structure of the surfaces. Geometry of the surface can be precisely measured from REM and RHEED.

This work is supported by NSC grant 84-2112-M-007-047.

REFERENCES

Microscopy Research and Techniques, 20/4 1992. A special issue on current research on reflection electron microscopy, guest ed. T. Hsu.

Ultramicroscopy, 48/4 1993. A special issue featuring invited papers for an REM symposium at the 5th Asian Pacific Electron Microscopy Conference, Beijing, China, 1-6 August, 1992, guest eds. L-M Peng and K.H. Kuo

K. Yagi. 1993. Surface Sci. Reports. **17:** 305-362.

Zoological Studies 34, Supplement I (1995)

Zoological Studies

Hydathodes in *Ficus Formosana* Maxim Form. Himadai Hay

Chyi-Chaunn Chen and Yung-Reui Chen
Department of Botany, National Taiwan University, Taipei, Taiwan, R.O.C.

Leaf blades of *Ficus formosana* Maxim form. Shimadai Hay were cut into small cubes in fixation buffer containing 2.5% glutaraldehyde. These cubes were transfered to a fresh fixation buffer for 2h, postfixed in 1% osmium tetraoxide for 4h, dehydrated through an ethanol series, and then infiltrated and embedded in Spurr's resin. Sections in golden color were collected on grids, doubly stained with uranyl acetate and lead citrate, and observed with a Hitachi H-600 transmission electron microscope (TEM). Thick sections, 1 mm in thickness, were stained with Toludine blue and photographed with a Zeiss Photomicroscope III. For surface observation, samples were critical-pointly dried after dehydration with ethanol, coated with gold in an ion sputter and examined with a Hatachi S-520 scanning electron microscope (SEM).

Hydathodes of *Ficus formosana* unexceptionally distrubute on the adaxial surface of leaf blade, whereas stomata are always on the abaxial side. They arrange parallelly in two rows along the axis of leaf blade and one on each side of the midrib. The number of hydathodes on leaf surface is closely related to successive appearance in phylotaxy, and is determined in young extended leaf and independent of leaf developmental stage. The passive hydathodes consist of numberous water pores and enclosed by a distinct trichome and several cellular glands which involve in active secretion. Water pores are preferentially located within the regions of sunken hydathodes and their number per each hydathode are around 60. The openings of water pores are much smaller than that of stomata. They are hydropassive and release water passively under the control of root pressure. Mineral crystals, bacterial sludges and fungal mycelia are often oberved on the surface of hydathodes. The complex hydathodes of this fig contain five parts: water pores, enclosed by two peripheral cells; subaperature chamber, bounded by 2 layers of parenchymatous cells which are larger than that of epithem; epithem proper, consisted of a group of thin-walled and more or less elongated smallest cells; sheath layer, extend from vascular bundles is 1-2 celled in thickness surrounding the epithem proper; vascular endings, contacted with epithem proper. Ultrasctructural studies show that: peripheral cells of water pore contain amyloplasts and employ with the partially wall-thickening around pores; the pattern of their wall thickening is differerent from that in guard cells in stoma complex. Epithemal cells are surrounded by the waveringly wall-thickening and irregular in shape. Cells in sheath layer are characterized by the centrifugal location of plastids which is in intermediate type mediated between mesophyllous cells and epithemal cells. Tracheid with distinct secondary wall are found in vein ending contact with epithem.

Two major ways of water discharge from plant leaves are vapour transpiration and liquid guttation through stomata and hydathodes, respetively. Besides pure water, guttation fluid also contains various minerals, sugars and other organic substances which cause injury to plants or microbial infections through their accummulation on leaf surface. Functionally, hydathodes not only play an important role on water excretion but also on retrieval minerals. Their structure are different from those of stomata, even though both have same phylogenic origin. *F. formosana* Maxim form. Shimadai Hay. are small shrubs in height of 1-2 m and grow in the regions near the creeks or beneath the large trees in the leeward-slope of low mountains. They like low light intensity, high humicity and non-windy weather condition. The distribution and structure of hyperdermal hydathodes and hypodermal stomata could be fiffted with the habitation of the shrubs. Moreover, the observations of the complex passive hydathodes at ultrastruc-

tural level are certainly limited. Epithemal cells with special wall inward-growth referred as transfer cells were reported in some plant species. Sheath cells tightly contacted each other with cutinized adjacent cells were also observed before. However, epithemal cells only with wave-formed wall pattern and sheath cells without cutinization on cell wall were observed in this studies.

Zoological Studies 34, Supplement I (1995)

Zoological Studies

Applications of X-ray Microscopy with Hydrated Specimens in Biomedical Research

H. Spring[1], P. Guttmann[2], D. Rudolph[2], G. Schneider[2], G. Schmahl[2] and M.F. Trendelenburg[1]

[1]*Biomedical Structure Analysis Group, German Cancer Research Center (DKFZ), Im Neuenheimer Feld 280, D-69120 Heidelberg, Germany*

[2]*Institute of X-Ray Physics, University of Göttingen, Geiststr. 11, D-37073 Göttingen, Germany*

INTRODUCTION

In the last years, the development of zone plates with high efficiency as optics for high resolution X-ray microscopy of hydrated specimens has undergone great steps towards an application of such a microscope in biomedical research. Concomitant with the development of zone plates for high resolution and high magnification it was also necessary to develop stable environmental ('wet') chambers as support for the hydrated specimen during observation. With such an equipment we were able to observe different biomedical specimens at high resolution in the hydrated state using amplitude contrast and/or phase contrast X-ray microscopy.

MATERIALS AND METHODS

For the experiments described, we used the Göttingen X-ray microscope situated at the BESSY (Berlin, Germany) electron storage ring facility operated with a wavelength of 2.4 nm (for more details, see Rudolph et al. 1984, Niemann et al. 1994). Different zone plates as objective lenses were constructed with electron beam lithography (David et al. 1992) and had outermost zone widths in the range of 50-20 nm and numerical apertures of NA 0.06, thus allowing theoretical resolutions of up to 25 nm and primary magnifications of up to 2400 X. The specimens were observed in special environmental chambers (Schneider and Niemann 1992, see also Rudolph et al. 1992) consisting of polypropylene foils with a layer of polyimide and a stabilizing layer of silicon H evaporated on the surface (for the 'slide' foil) and a layer of aluminium oxide (for the 'coverslip' foil). The metal carrier rings of the foils were separated by a spacer ring and due to a special syringe evacuation system the distance of the foils could be calibrated to produce an inner chamber width of about 10 μm or less for sufficient transmission of the X-rays and structural preservation. Such foils could be sterilized by immersion into 70% ethanol before the cultivation of cell culture cells on the surface of the foil acting as the 'microscope slide'. We used PTK2 epithelal cells grown on the foil for 24 hours. In other experiments we used freshly isolated nucleoli and nuclear contents of oocytes of the newt Pleurodeles waltlii or a dispersal of a culture of E. coli bacteria. All specimens were slightly fixed with a solution of 1-2.5 % glutaraldehyde made up in appropriate buffers. After fixation the specimen chamber was closed with the spacer ring and the second plastic foil and mounted into a special holding system (for details, see Schneider and Niemann 1992) for observation in the X-ray microscope. Prior to the observation the thickness of the chamber was adjusted and calibrated with syringes to obtain a chamber of about 10 μm in depth. Interesting regions of the specimen could be selected by a built-in light microscope (Carl Zeiss, Oberkochen/Jena, Germany) and prefocussed for X-ray microscopy to minimize H radiation damage. Specimen images generated by the microscope were taken with a high resolution CCD-camera with a thinned backside illuminated chip. They were stored on magneto-optical disks and photographed and printed with appropriate equipment.

RESULTS AND DISCUSSION

Fig. 1 shows an image of a PTK2 cell culture cell as seen in the X-ray microscope in the slightly fixed hydrated state using the phase contrast mode. The nucleus and especially the densely packed nucleolus are clearly visible. At closer inspection also the nuclear membrane and some cytoplasmic structures like vesicles, mitochondria and stress fibers can be detected. Fig. 2 gives an example of a cell division in a PTK2 cell at metaphase with the amplitude contrast mode of the X-ray microscope. The paired chromosomes and one centriole (arrow) are in the focal plane. Numerous microtubules (some are denoted by arrowheads) are connecting the chromosomes with the centrioles. Fig. 3 gives an example of nuclear contents of the oocyte of the newt Pleurodeles waltlii as seen in amplitude contrast. Three individual nucleoli can be seen in the image. Interestingly, the internal structure of the nucleoli with more ore less densely packed constituents and nucleolar caverns can easily be detected, even though the average of diameters of such nucleoli is 12-15 μm. In other images (data not shown) we could observe parts of the lampbrush chromosomes with the characteristic transcriptional aspects of the individual genes. Further experiments will also deal with spread defined amphibian oocyte ribosomal genes located in the nucleoli (for images of such genes in light and electron microscopy, see Spring and Trendelenburg 1990). Fig. 4 gives an example of hydrated Escherichia coli bacteria. Individual flagella as well as the bacterial nucleoid can be detected.

In summary we can show, that the X-ray microscope is a useful tool to investigate biomedical hydrated specimens, especially for observations at resolutions higher than offered by light microscopy . It should be noted, that the exposure time of the images we have shown was in the range of several seconds. Further investigations with

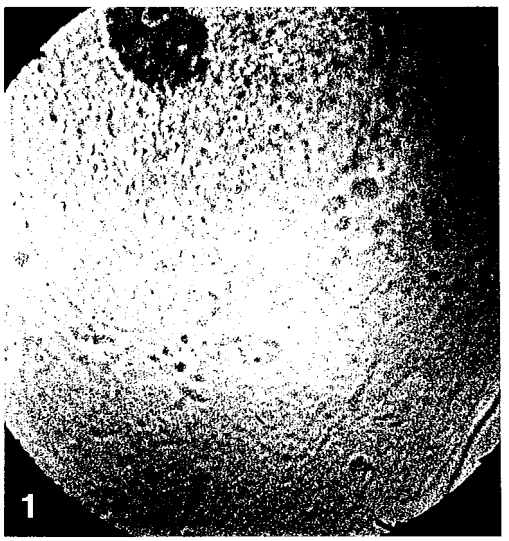

Fig. 1. PTK2 cell in interphase as seen in the phase contrast imaging mode of the X-ray microscope in the wet chamber.

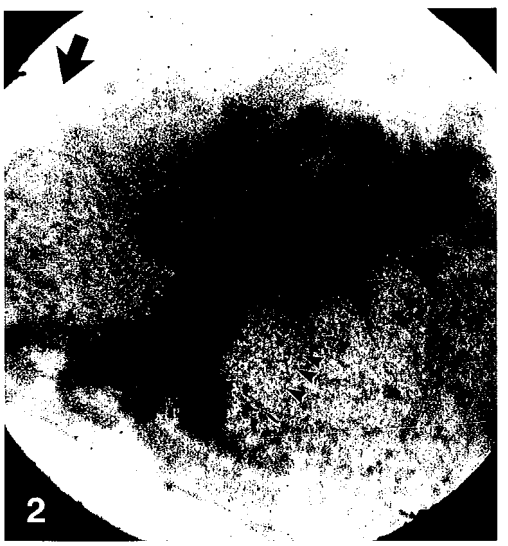

Fig. 2. PTK2 cell in metaphase of mitosis imaged in amplitude contrast. The arrow denotes the centriolar region, several microtubules are demarcated by arrowheads.

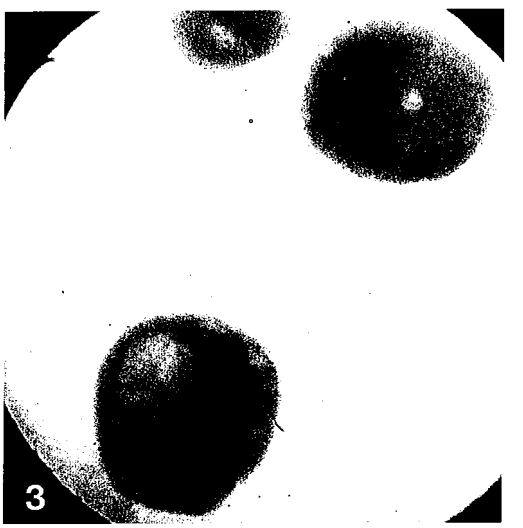

Fig. 3. Nucleoli from the nuclear contents of the oocyte of the newt Pleurodeles waltlii. Note that even from such thick specimens (10-15 μm) a transmission of the beam can be achieved.

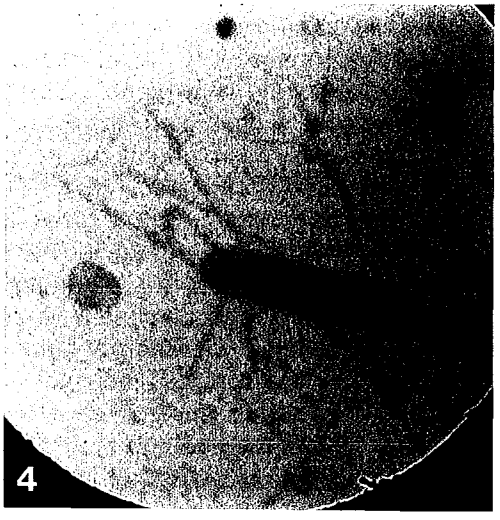

Fig. 4. Bacterial suspension of a culture of Escherichia coli. Numerous bacterial flagella as well as the nucleoid can be seen.

hydrated biomedical specimens will be undertaken with a laboratory X-ray microscope with a plasma X-ray source (for details see Schmahl et al. 1992) with the advantage of short beam exposure times avoiding image blurring due to molecular (Brownian) movements in the specimens. It will also be possible to observe living, unfixed cells.

REFERENCES

David C, J Thieme, P Guttmann, G Schneider, D Rudolph, G Schmahl. 1992. Electron-beam generated x-ray optics for high resolution microscopy studies. Optik **91:** 95-99.

Niemann B, G Schneider, P Guttmann, D. Rudolph, G Schmahl. 1994. The new Göttingen x-ray microscope with object holder in air for wet specimens. In: X-Ray Microscopy IV, V.V. Aristov, AJ Erko, eds.; Bogorodski Pechatnik Publishing, Moscow, in press.

Rudolph D, B Niemann, G Schmahl, O Christ. 1984. The Göttingen x-ray microscope and x-ray microscopy experiments at the BESSY storage ring. In: X-ray Microscopy, Springer Series in Optical Sciences, Vol. 43, pp 192-202, G.Schmahl, D. Rudolph, eds.; Springer-Verlag Berlin.

Rudolph D, G Schneider, P Guttmann, G Schmahl, B Niemann, J Thieme. 1992. Investigations of wet biological specimens with the x-rax microscope at BESSY. In: X-Ray Microscopy III, Springer Series in Optical Sciences, Vol. 67, pp 392-396; AG Michette, GR Morrison, CJ Buckley, eds.; Springer-Verlag Berlin.

Schmahl G, B Niemann, D Rudolph, M Diehl, J Thieme, W Neff, R. Holz, R Lebert, F Richter, G Herziger. 1992. A laboratory x-ray microscope with a plasma x-ray source. In: X-Ray Microscopy III, Springer Series in Optical Sciences, Vol. 67, pp 66-69; A.G. Michette, G.R. Morrison, C.J. Buckley, eds.; Springer-Verlag Berlin

Schneider G,, B Niemann. 1992. Environmental chamber for x-ray imaging of wet biological specimens. In: X-Ray Microscopy III, Springer Series in Optical Sciences, Vol. 67, pp 350-354; AG Michette, GR Morrison, CJ Buckley, eds.; Springer-Verlag.

Spring, H., MF Trendelenburg. 1990. Towards light microscopic imaging of hydrated 'native' ribosomal RNA genes. J. Microscopy **158:** 323-333.

Zoological Studies 34, Supplement I (1995)

Zoological Studies

Imaging X-Ray Microscope with Zone Plates and Its Application to Biological Specimens at UVSOR

N. Watanabe[1], S. Aoki[1], Y. Shimanuki[2], K. Kawasaki[2], M. Taniguchi[3], E. Anderson[4], D. Attwood[4], D. Kern[5], S. Shimizu[6], H. Nagata[6], Y. Horikawa[7], S. Mochimaru[7] and H. Kihara[8*]

[1]*Institute of Applied Physics, Tsukuba University, Tsukuba 305, Japan*
[2]*Department of Oral Anatomy, Tsurumi University, Yokohama 230, Japan*
[3]*Department of Physics, Nagoya University, Nagoya 464, Japan*
[4]*Lawrence Berkeley Laboratory, Berkeley, CA, USA*
[5]*IBM Research Center Yorktown Heights, NY, USA*
[6]*Nikon Corp., Nishi-ooi, Shinagawa-ku, Tokyo 140, Japan*
[7]*Olympus Optical Co. Ltd., Hachioji-shi, Tokyo 192, Japan*
[8]*Physics Laboratory, Kansai Medical University, Hirakata 573, Japan*

INTRODUCTION

Soft x-ray microscopes offer observation methods for wet biological specimen with higher resolution than that of optical microscopes (Sayre et al. 1977, Rudolph et al. 1992). We have been assembling imaging microscopes with zone plates at UVSOR BL8A [synchrotron radiation facility (750 MeV, 200mA) at Institute for Molecular Science, Okazaki, Japan] (Watanabe et al. 1992).

In our previous report, a 63nm line and space pattern could be resolved, and dry biological specimen could be observed (Watanabe et al. in press). As a next step, an environmental chamber (wet cell) was made and wet biological specimens were observed at 2.4nm. In the present microscope, the numerical aperture of a condenser zone plate (CZP) was much smaller than that of an objective zone plate (OZP). To adjust both the numerical apertures, an ellipsoidal condenser mirror system was made and imaging test was performed at 3.2nm.

OPTICAL SYSTEM

The optical arrangement is shown in Fig.1. The characteristics of the zone plates are CZP (diameter: 4.3mm, outermost zone width: 0.25μm, material: Au 0.2μm, support: SiN 0.1μm) and OZP (diameter: 50μm, outermost zone width: 45nm, zone material: Ni 0.13μm, support: SiN 0.1μm) (Anderson et al. 1992), respectively. Characteristics of the other optical elements are the filter (SiN 0.1μm and Ti 55nm), the mask (a 90% transparent Ni mesh of which the ϕ 2.4mm area is covered with Al foil), and the pinhole (ϕ 20μm).

The CZP monochromatized the soft X-ray and condensed it at the properly placed pinhole. A wavelength of 3.2nm was selected for imaging test. The third order radiation of the CZP was used, because the size of the source image at 3.2nm by the first order radiation was large compared with that of the pinhole. The calculated monochromaticity was 108 from the relationship $\lambda/\Delta\lambda = D/2d$, where λ: wavelength, D: a diameter of CZP, d: a larger diameter between that of the pinhole and the image of the source (Niemann et al. 1974).

The specimen was imaged by OZP. The magnification ratio was 740. The image was focussed at the outside of the zero-th order radiation of OZP. A film (Kodak T-max 400) and a microchannel plate (MCP) were set at an image plane. When the MCP was used, images were converted to visible ones by a fluorescent plate (FP), and monitored by a SIT camera(C2400, Hamamatsu Photonics K.K.). The images from the SIT camera were digitized, accumulated, subtracted the background data (accumulated records of the same number of frames without x-ray illumination) and then stored

*To whom correspondence should be addressed.

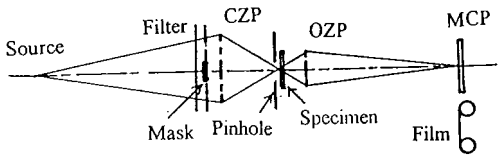

Fig. 1. Schematic of the microscope
CPZ: condenser zone plate, OZP: objective zone plate.

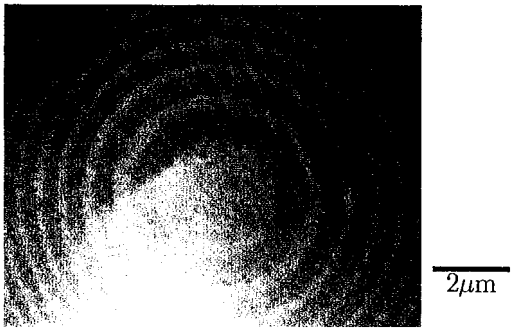

Fig. 2. Zone plate image at 3.2nm.
MCP and SIT camera, accumulation: 8s.

on floppy disks using an image processor (ARGUS-100, Hamamatsu Photonics K.K.). The images of these data were re-displayed on a monitor and were photographed. Sliding the MCP perpendicularly to the optical axis, the film could be used as a detector.

The optical performance was estimated using a zone plate as a specimen. The characteristics of the zone plate was the same with the OZP. Figs.2 and 3 show images of the zone plate at 3.2nm. Almost the outermost zone of 45 nm width can be resolved in Fig. 3.

OBSERVATIONS OF WET BIOLOGICAL SPECIMENS

For observation of wet biological specimens, an environmental chamber (wet cell) with SiN (0.1μm thickness) windows was made as shown in Fig.4. Imaging tests were performed at 2.4 nm with the magnification ratio of 570. Fig. 5 shows an image of a wet lettus protoplast. Fig.6 shows an image of Deinococcus radiodurans strain.

ELLIPSOIDAL CONDENSER MIRROR SYSTEM

In the present microscope, the numerical aper-

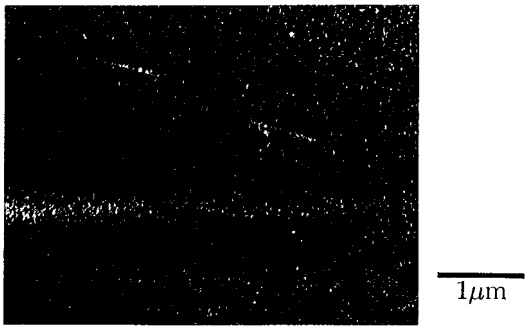

Fig. 3. Zone plate image at 3.2nm.
Film(T-max 400) used as a detector, exposure: 2min.

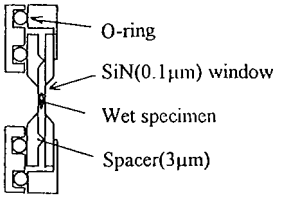

Fig. 4. Schematic of the wet cell.

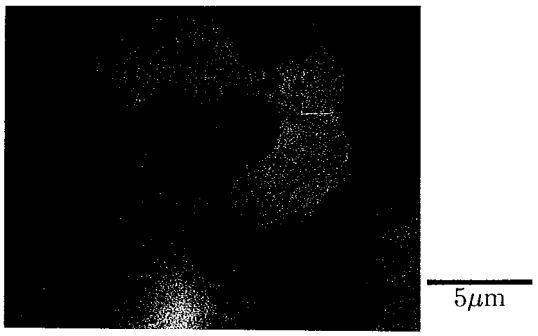

Fig. 5. Lettus protoplast image at 2.5 nm.
Film (T-max 400) used as a detector, exposure: 5min.

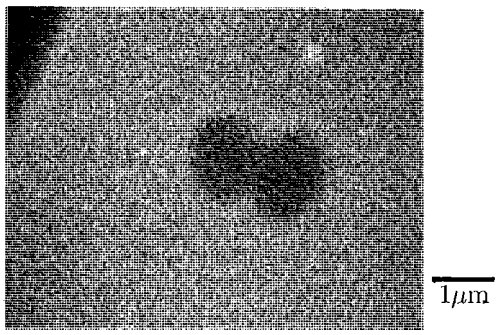

Fig. 6. Deinococcus radiodurans strain image at 2.5 min.
Film (T-max 400) used as a detector, exposure: 2min.

ture of CZP was much smaller than that of OZP. To adjust both the numerical apertures, CZP with the same outermost zone width of OZP has to be made. It is difficult to manufacture such a zone plate with a large diameter. Then an ellipsoidal condenser mirror system was designed (Fig.7), and imaging test was performed at 3.2nm. A magnification ratio of soft x-ray was 320. Fig. 8 shows an image of Cu mesh (#2000).

DISCUSSION

The theoretical resolution of OZP is 55nm (1.22 × the outermost zone width). The experimental resolution is worse compared with the theoretical one. This is probably due to low monochromaticity of illumination and the second order radiation of CZP.

In the observation of Deinococcus radiodurans strain (Fig.6), specimens moved to the outside of the imaging field during soft x-ray illumination, and specimens that maybe died could be imaged.

It is necessary to stop its motion for observations of such a motile biological specimen. It is possible to substitute the ellipsoidal mirror condenser system for a condenser zone plate to adjust both the numerical apertures of a condenser and OZP.

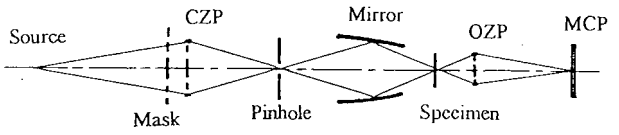

Fig. 7. Ellipsoidal condenser mirror system.
CZP: condenser zone plate, OZP: objective zone plate.

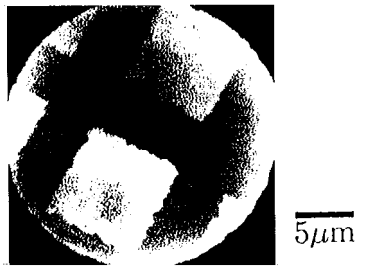

Fig. 8. Cu #2000 mesh image.
MCP and SIT camera, exposure: 16s.

ACKNOWLEDGEMENTS

The authors are gratefull for the help and encouragements from A. Prof. M. Kamada, Mr. K. Sakai and other staffs of the Institute for Molecular Science.

REFERENCES

Anderson EH, D Kern. 1992. Nanofabrication of Zone Plates for X-Ray Microscopy. In X-Ray Microscopy III, eds. A G Michette, G. R. Morrison, C. J. Buckley. Berlin: Springer-Verlag, pp. 75-78.

Niemann B, D Rudolph, G Schmahl. 1974. Soft X-Ray Imaging Zone Plates with Large Zone Numbers for Microscopic and Spectroscopic Applications. Opt. Commun. **12:** 160-163.

Rudolph D, G Schneider, P Guttmann, G Schmahl, B Niemann, J Thieme. 1992. Investigation of Wet Biological Specimens with the X-Ray Microscope at BESSY. In X-Ray Microscopy III, eds. AG Michette, GR Morrison, C J Buckley. Berlin: Springer-Verlag, pp. 392-396.

Sayre D, J Kirz, R Feder, DM Kim, E Spiller. 1977. Transmission Microscopy of Unmodified Biological Materials: Compararive Radiation Dosages with Electrons and Ultrasoft X-ray Photons. Ultramicroscopy **2:** 337-349.

Watanabe N, M Taniguchi, Y Shimanuki, K Kawasaki, Y Watanabe, Y Nagai, H Kihara. 1992. Soft X-Ray Microscopy with Zone Plates at UVSOR. In X-Ray Microscopy III, eds. AG Michette, GR Morrison, CJ Buckley. Berlin: Springer-Verlag, pp. 147-150.

Watanabe N, S Aoki, Y Shimanuki, K Kawasaki, M Taniguchi, E Anderson, D Attwood, D Kern, S Shimizu, H Nagata, H Kihara. 1995. Soft X-Ray Imaging Microscopee with Sub-optical Resolution at UVSOR. In X-Ray Microscopy IV, eds. Al Erko and V V Aristov. Chernogolovka, Moscow Region: Bogorodski Pechatnik Publishing Company (in press).

Zoological Studies 34, Supplement I (1995)

Zoological Studies

The Ultrastructural Examination of Spray-dried Microalgal Cells with Low Vacuum Scanning Microscopy and X-ray Microanalysis

Liang P. Lin and Ching B. Liu

Electron Microscopy Laboratory, Department of Agricultural Chemistry, National Taiwan University, Taipei, Taiwan 106, R.O.C.

A green alga, *Chlorella* is cultivated on large scales in Taiwan. Commercially, the harvested *Chlorella* cells are dehy-drated by spray dryers and dried products are sold as the health foods. The microstructure of this powder reflects an important factor for the health food industry. This research was performed by using a low vacuum scanning electron microscope (LV SEM) with x-ray energy dispersive microanalyzer (EDX) as the important instrument to determine the fine structures and chemical elements of spray-dried microalgal cells. We mainly focused on the outer surface and inner structure of particles, and also determined the existence of some chemical elements.

Spray-dried *Chlorella* powders were mounted on an aluminum specimen stage (stub) by pressing on a double stick of 3M Scotch adhesive tape. The prepared specimens were examined in a JEOL JSM-5400LV at an accelerating voltage of 2 to 15 kV, and specimen chamber pressure of 14 to 140 Pa (0.1 to 1 Torr). The analysis of chemical ions was performed by a JEOL "Mini Cup" energy dispersive x-ray micro-analyzer. Most of the spray-dried cells showed the range of 20 to 60 μm in diameter with an irregular spherical shape (Fig. 1). At the higher magnification, it revealed that wrinkled surface structure possessing a smooth appearance (Fig. 2). This phenomenon was produce by elevated temperature treatments during the degradation and dehydration processes. The higher temperature was used, the more alteration was induced on the morphology of the particles. On some samples, the ash-like materials were clearly distributed on the surface of particles owing to unsuitable heat treatments. These results were not observed in our previous experiment (Lin 1985

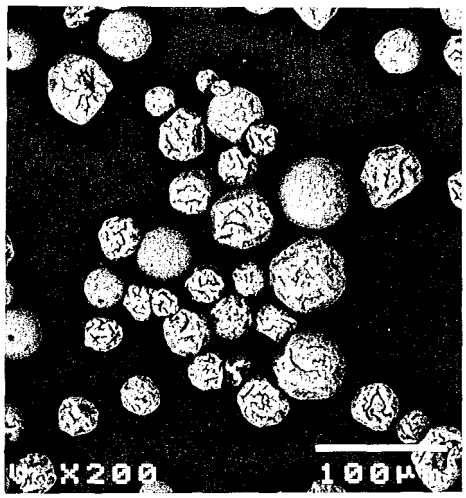

Fig. 1. A LV SEM photograph of spray-dried *Chlorella* cell-granules (particles).

Fig. 2. A spray-dried *Chlorella* particle, showing a fused appearance.

Food Mic-rostruc. 4:341-348) by using the conventional SEM.

Some particles possessed the hole structure inside. This structure was formed during the evaporation of water from an algal droplet surface by spray-drying. The powder-particles of an acceptable for commercial uses were 50 to 80 μm in size with suitable hardness and dispersibility for tablet properties. Fig. 2. A spray-dried Chlorella particle, showing a fused appearance. Fig. 1. A LV SEM photograph of spray-dried Chlorella cell-granules (particles).

The x-ray microanalysis spectra indicated that Cu, Si, Mg, P, S, K, Ca, and Fe ions were present in the powders. There were no indications of heavy metal ions existing in significant amounts. Elemental analyses were carried out without interference of coating materials as used in conventional SEM. The serious health effects from food stuffs and drinking water contaminated by heavy metals, such as lead (Pb) and arsenic (As) have become one of the major concerns of the people of Taiwan. The Pb and As contents of Chlorella powders examined in our laboratory by atomic absorption spectrometry were about 1 to 3 ppm and less than 0.5 ppm respectively. This content is in the safe level of food standards.

In conclusions, the LV SEM and x-ray micr-oanalyzer provide us to observe fine structure and elemental analysis for the food quality control. This method also allows us to observe specimens without any particular preparation, such as drying and coating required by the conventional SEM.

Zoological Studies 34, Supplement I (1995)

Zoological Studies

Development of a Zone Plate Soft X-ray Microscope at the TRISTAN Accumulation Ring

J.-D. Wang[1], Y. Kagoshima[1], T. Miyahara[1], M. Ando[1], S. Aoki[2], E. Anderson[3], D. Attwood[3] and D. Kern[4]

[1]*Photon Factory, National Laboratory for High Energy Physics, Tsukuba, Ibaraki 305, Japan*

[2]*Institute of Applied Physics, University of Tsukuba, Tsukuba, Ibaraki 305, Japan*

[3]*Center for X-ray Optics, Lawrence Berkeley Laboratory, Berkeley, CA 94720, USA*

[4]*Institut für Angewandte Physik, Universität Tübingen, Auf der Morgenstelle 12, Tübingen 1, FRG*

INTRODUCTION

In a zone plate soft x-ray microscope, the zone plate must be used with monochromatic illumination because of the strong chromatic aberration. A typical microscope employs a linear monochromator consisting of a zone plate and a pinhole (Niemann et al. 1983), which spectral resolution depends on the dimensions of the zone plate and the pinhole (Niemann et al. 1974). However, since such a linear monochromator can provide an appropriate spectral resolution only when the zone plate has a larger dimension and is illuminated effectively, it is suitable for radiation with a relatively large angular divergence such as from a bending magnet but may not be suitable for radiation with a small divergence such as from an undulator as well as the future light sources with a very low emittance such as the 3rd generation synchrotron radiation.

In addition, the object distance of a high resolution zone plate is very close to its focal length which is usually shorter than 1 mm, its focal depth is only several microns. The sizes of optical elements and objects are also very small. Therefore, it is very difficult to find a correct focus of a zone plate and align the x-ray optical system precisely without any auxiliary implement.

On the basis of the above consideration, we have introduced a grating monochromator and constructed a zone plate microscope associated with a visible light pre-focus unit. Here, we would briefly describe the optical system of the microscope and the visible light pre-focus unit. Some experimental results are also presented.

BEAMLINE, THE SOFT X-RAY MICROSCOPE AND THE VISIBLE LIGHT PRE-FOCUS UNIT

The microscope has been developed at the beamline NE1B of the 6.5-GeV TRISTAN accumulation ring (AR) in KEK, National Laboratory for High Energy Physics, where circularly polarized soft X rays are produced by a helical undulator (Yamamoto et al. 1989, Kitamura 1992). The wavelength of its first harmonic can be tuned from 0.8 nm to 5 nm. The NE1B is equipped with a 10 m vertical-dispersion grazing incidence spherical grating monochromator and a post-focusing mirror (Kagoshima et al. 1995). Fig. 1 shows the schematic diagram of the optical arrangement of the NE1B together with the soft x-ray microscope. The spectral resolution of the monochromator, $\lambda/\Delta\lambda$, is estimated to be about 280 ~ 290 at λ=2.37 nm and meets the monochromaticity requirement of the zone plate we used.

The optical system of the microscope consists of a ϕ500 μm pre-pinhole, a condenser zone plate (CZP), a ϕ20 μm pinhole, and an objective zone plate (OZP). The pre-pinhole placed at the focus of the post-focusing mirror is used as a monochromatic secondary source. The CZP generates a reduced image of the pre-pinhole in an object plane through the ϕ20 μm pinhole. The OZP generates a magnified image of the object in an image plane.

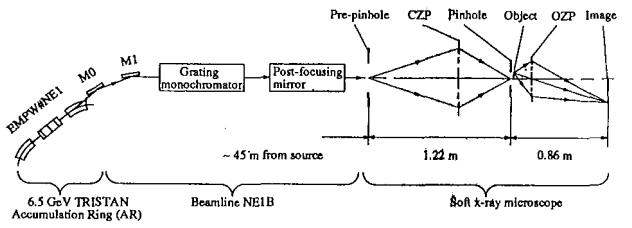

Fig. 1. Schematic diagram of the optical arrangement of the beamline NE1B and the soft x-ray microscope.

The x-ray image can be recorded directly with photographic film or converted into a visible image by using MCP. The numerical parameters of the zone plates are summarized in Table 1. The CZP was fabricated by NTT (Sekimoto et al. 1988), while the OZP was fabricated by IBM as a collaboration between LBL and IBM (Anderson et al. 1992).

Fig. 2 shows the visible light pre-focus unit. The unit works as a reflected illumination visible light microscope consisting of two objectives inside a vacuum chamber for the x-ray microscope and common eyepieces outside the chamber. One of the objectives is perpendicular to the x-ray axis and provides a relatively low magnification (10 ×). It is called coarse adjustment objective and is used to monitor an adjustment of the OZP, an object and the pinhole in its view field (~ ϕ1 mm) and to avoid any collision between them. Another objective is on the x-ray axis and provides a relatively high magnification (20 ×). It is called fine adjustment objective and is used to measure an object distance of the OZP and a distance between the pinhole and an object precisely along the x-ray axis. One of the two optical paths of the objectives can be selected by using a change-over splitter. The fine adjustment objective has a ϕ2 mm central hole to make x rays pass through.Its focal depth is designed to be about ±1.5 μm. Since that is less than the focal depth of the OZP, the object distance can be measured precisely. The working distance of the fine adjustment objective is designed as long as 10 mm. The distance between the pinhole and an object can also be measured. Therefore, the x-ray optical system of the microscope can be adjusted easily, quickly, and precisely by using the unit.

RESULTS

A spatial resolution test has been performed at λ=2.37 nm to evaluate performance of the micro-

Table 1. Parameters of zone plates

Parameters	CZP	OZP
Radius of the innermost zone	15.8 μm	1.41 μm
Number of zones	1000	200
Width of the outermost zone	0.25 μm	0.05 μm
Numerical aperture	0.048	0.24
Focal length (1st order at λ=2.37 nm)	105 mm	0.84 mm
Focal depth		±2.1 μm
Zone material	500 nm Ta	100 nm Ni
Supporting material	300 nm Si_3N_4	100 nm Si_3N_4

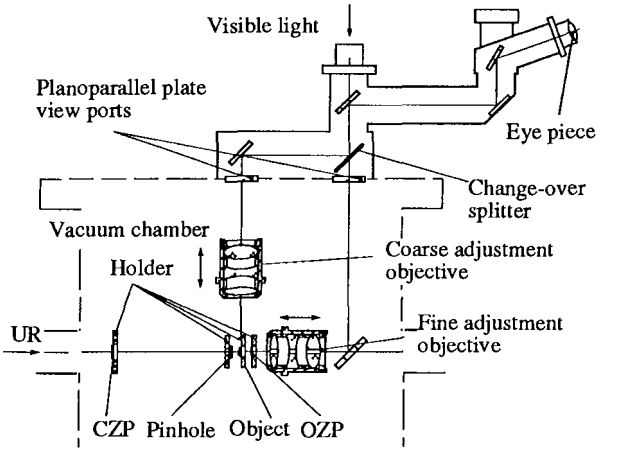

Fig. 2. Schematic diagram of the visible light pre-focus unit.

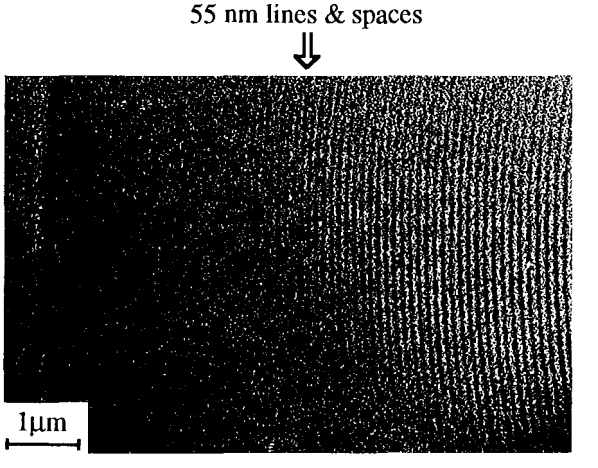

Fig. 3. An x-ray magnified image of the outer region of the zone plate test pattern. X-ray magnification ~ 1020.

scope. The test pattern is a zone plate with finer structures than the OZP. The diameter of this zone plate is 49 μm and its innermost radius is 1.5 μm. The width of the outermost zone is 45 nm. Here the test pattern serves as an object and is imaged by the microscope at a magnification of 1020. Fig. 3 shows a magnified x-ray image of the outer region of the zone plate. It is taken by Kodak T-Max 3200 Professional Film with an exposure time of 3 minutes. The small widths of zones down to 55 nm are successfully resolved. According to Rayleigh's criterion, the spatial resolution of a zone plate microscope is comparable to the width of the outermost zone. Since that width of the OZP is 50 nm, we would believe that the resolution of our microscope has almost reached its diffraction limit.

Some dry biological specimens, diatoms, have been clearly observed by the microscope. Fig. 4 shows their x-ray images. It has been confirmed that the microscope is applicable to biology.

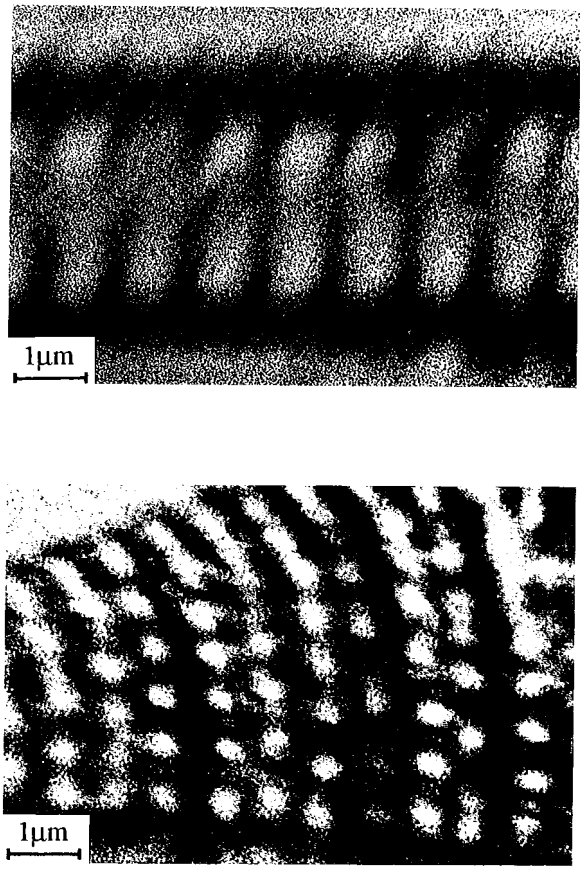

Fig. 4. X-ray magnified images of the diatoms.

FUTURE EXPERIMENTS

Some attempts will be performed in the future. First, an environmental chamber should be developed to observe biological specimens in their natural state. Second, since the circularly polarized soft x rays are available at the beamline NE1B, helical structures which are much attractive in biology may be observed by using circularly polarized soft x rays (Kagoshima et al. 1992, Keller et al. 1985). Thus we may obtain much novel information about helical structures using circularly polarized light which is unobtainable using non-circularly polarized light.

REFERENCES

Anderson E, D Kern. 1992. Nanofabrication of zone plates for x-ray microscopy. in X-Ray Microscopy III, edited by A G Michette, G R Morrison, C J Buckley (Springer-Verlag, Berlin), pp. 75-78.

Kagoshima Y, T Miyahara, M Ando, S Aoki. 1992. Present status and future plan of soft x-ray microscopy at the Photon Factory. Rev. Sci. Instrum. **63:** 605-608.

Kagoshima Y, T Miyahara, S Yamamoto, H Kitamura, S Muto, S-Y Park, J-D Wang. 1995. Construction and performance of the beamline NE1B for circularly polarized soft x-rays in the TRISTAN Accumulation Ring. Rev. Sci. Instrum. **66:** (in press).

Keller D, C Bustamante, M F Maestre, I Tinoco, Jr. 1985. Imaging of optically acitve biological structures by use of circularly polarized light. Proc. Natl. Acad. Sci. USA **82:** 401-405.

kitamura H. 1992. Production of circularly polarized synchrotron radiation. Syn. Rad. News Vol. 5, No. **1:** 14-20.

Niemann B, D Rudolph, G Schmahl. 1974. Soft x-ray imaging zone plates with large zone numbers for microscopic and spectroscopic application. Opt. Commun. **12:** 160-163.

Niemann B, D Rudolph, G Schmahl. 1983. The Göttingen microscopes. Nucl. Instrum. and Methods. **208:** 367-371.

Sekimoto M, A Ozawa, T Ohkubo, H Yoshihara, M Kakuchi, T Tamamura. 1988. X-Ray Zone Plate with Tantalum Film for an X-Ray Microscope. In X-Ray Microscopy II, edited by D Sayre, M Howells, J Kirz, H Rarback (Springer-Verlag, Berlin), pp. 178-181.

Yamamoto S, H Kawata, H Kitamura, M Ando. 1989. First production of Intense circularly polarized hard x-rays from a novel multipole wiggler in an accumulation ring. Phys. Rev. Lett. **62:** 2672-2675.

Yamamoto S, T Shioya, S Sasaki, H Kitamura. 1989. Construction of insertion devices for elliptically polarized synchrotron radiation. Rev. Sci. Instrum. **60:** 1834-1837.

Zoological Studies 34, Supplement I (1995)

Zoological Studies

A Compact Multi-channel Laser Scanning Confocal Optical Microscope

Guoqing Xiao and Horst Groneberg
Technical Instrument Co., USA

INTRODUCTION

Confocal scanning optical microscopes have become important imaging tools for, engineers and scientists. However, their high cost, difficulty to use and lack of portability greatly limit their aplications. We have design a laser point scanning confocal optical microscope based on a new optical design to overcome some of the drawbacks of the existing confocal microscopes.

OPTICS DESIGN

The most important feature of our confocal microscope is its unique arrangement of the illumination pinhole and detection pinhole. Instead of placing the two pinholes at two conjugate planes, as is usually done in conventional confocal microscopes, our design combines the two pinholes together, thus completely eliminating the need of aligning the two pinholes to each other. This design significantly simplifies the alignment procedure of the microscope. It makes it possible to change the excitation filters, barriner filters and even the primary dichroic mirror and pinholes without need of re-alignment. The user can easily check the alignment condition of the microscope by simply inspecting the output laser beam from an empty objective port.

Another important feature of this microscope is its compactness. The portion of optics that has to be directly mounted to the microscope contains only two scanning mirrors, filters, beamspliters, confocal pinholes and a scanning lens, whereas the more bulky components, such as photomultiplier tubes (PMT), laser sources and electronics are mounted outside the optics module. The optical signal from the sample is collected through high transmission multi-mode optical fiber to the PMTs, and the excitation light is introduced through a single-mode optical fiber from one or multiple remote laser sources. The multi-mode fibers have a measured transmission effciency of more than 91% without coatings at the ends, and with anti-reflection coatings, the transmission ef-ficency can be easily raised to 98%. the laser coupling optics averages a 70% overall efficiency, depending greatly upon the beam quality of the lase source.

ELECTRONICS DESIGN

The electronics of the system can be divided into four major parts; scanner control electronics, light detection electronics, digitizing electronics and focus control electronics. The scanner control electronics includes a closed-loop scanner driver and a programmable raster scan generator. The raster scan generator generates the driving signals for the two scanning mirrors, and the scanner driver moves the mirrors to the specified positions. The closed-loop feeback circuity of the scanner driver automatically compensates the inertia effect and other nonlinear effects of the scanning mirror assemblies.

The light detection eectronics consists of a programmable high voltage power supply to the PMT, a matched PMT pre-amplifier, a low noise integration amplifer with a protection circuitry to shut off the PMT voltage when the input light is too intense. The selection of either the integration amplifier or the track/hold amplifier, the setting of PMT voltage and the adjustment of image black level can all be

carried out through software controls. The amplified signal from the light detection electronics is then digitized by a high performance multi-channel digitizing board. The digitized data can be processed, stored in the computer, or displayed as an image. The digitizing board has an EISA bus interface, which can support a data transfer rate of more than 10 MByte/sec. between the digitizing board and the host computer.

The focus control electronics drives a DC servo motor with a 10,000 count/revolution rotary encoder which is directly coupled to the fine focus shaft of the microscope. For a typical 100 micron/ revolution fine focus mechanism, the theoretical resolution is 0.1 micron; however, since all focus mechanism has much greater backlash and exhibits uneven friction, the actual focus resolution is between .1 to .5 micron, depending upon the condition of the fine focus mechanism.

The electronics layout is completely modularized: each functional unit is put on a circuit board, self-contained and independent of each other. The electronics chassis can house up to three PMT boards and an optional photo detector board to simultaneously detect three fluorescence Channels and one transmission channel. This modular electronics design makes the system much more flexible and expandable.

SYSTEM TESTS

We have built several systems to test our design. The test systems have two simultaneous fluorescence channels, two sizes of pinholes and three built-in dichroic mirrors and use a green HeNe laser and Agron Ion laser as a source. After having gone through more than half a year of operation and multiple times of packing, shipping and reinstalling at different locations, they all demonstrate good stability. No extra alignment is need. We hae also tested several key opto-mechanical components, especially the pinhole assembly. We built a mechanism to switch between the two pinholes. After 10,000 cycles, the pinholes were still in good alignment. We have manually operated the beamsplitter assembly and fiber-optical coupling mechanism for more than half a year. No additional adjustment is required. With the laser-to-fiber coupling optics pre-aligned and installed to the laser source, we can easily switch between different laser sources without any alignment and still have a coupling efficiency of around 50%. One of the key tests of they system integrity is the vibration control. Since the system is built from a solid metal frame, and has a very low profile, it demonstrates very good vibration-damping capability, even on a relatively weak microscope stand without additional support. For critical imaging applications, we have found that a table top vibration isolation bench is effective against most ambient disturbances.

We have tested the image resolution using different fluorescence samples. Good depth and transverse resolution are obtained with the small pinhole (20 microns), whereas the large pinhole (50 microns) yield much brighter images but with lower resolution. To check the system optical signal to noise ratio, we measured the total internal light scattering. The combination of special optical arangement and filter selection reduces the total system internal light scattering to such a low level that the reflection from the objective lens becomes the dominant source of background light. Further reducing the background light will require careful selection, or special design of the objective lens.

CONCLUSION

We have developed a high performance compact multi-channel laser scanning confocal optical microscope. The system is capable of producing up to three channel simutaneous fluorescence images and one optional transmission channel. The system is very easy to set up, align, and operate. It is ultra compact and has a light weight (the optics module measures 3.5 "X6.5" X8.5" and weighs less than 8 1b). It can be readily fitted on most upright and inverted microscopes.

Zoological Studies 34, Supplement I (1995)

Zoological Studies

Spatial Filtering in Microscopy: The Use of Matched Filters to See Further in Time and Space

J. Rudi Strickler, Dana Ono and John Reimer

Center for Great Lakes Studies, University of Wisconsin - Milwaukee Milwaukee, WI 53204, USA

1958 Zernike described a set of optical experiments in microscopy which are based on modifying the optical properties of the backfocus planes of both the condenser and the objective. Since the introduction of the Phase Contrast Microscope in 1955 (Science 121: 345-349), few improvements have been made despite a plethora of technical advances in optics (e.g. coherent light). The use of matched filters in the planes of spatial filtering (= backfocus; Figs. 1 and 2) allowed us to observe biological events with an extended range in time and space (Fig. 3).

The introduction of a density gradient in the plane of the object as an additional optical element resulted in seeing hydrodynamic disturbances caused by moving objects (e.g. animals, mouthparts, swimming appendages, Fig. 4). Furthermore, we can observe chemical gradients and their temporal

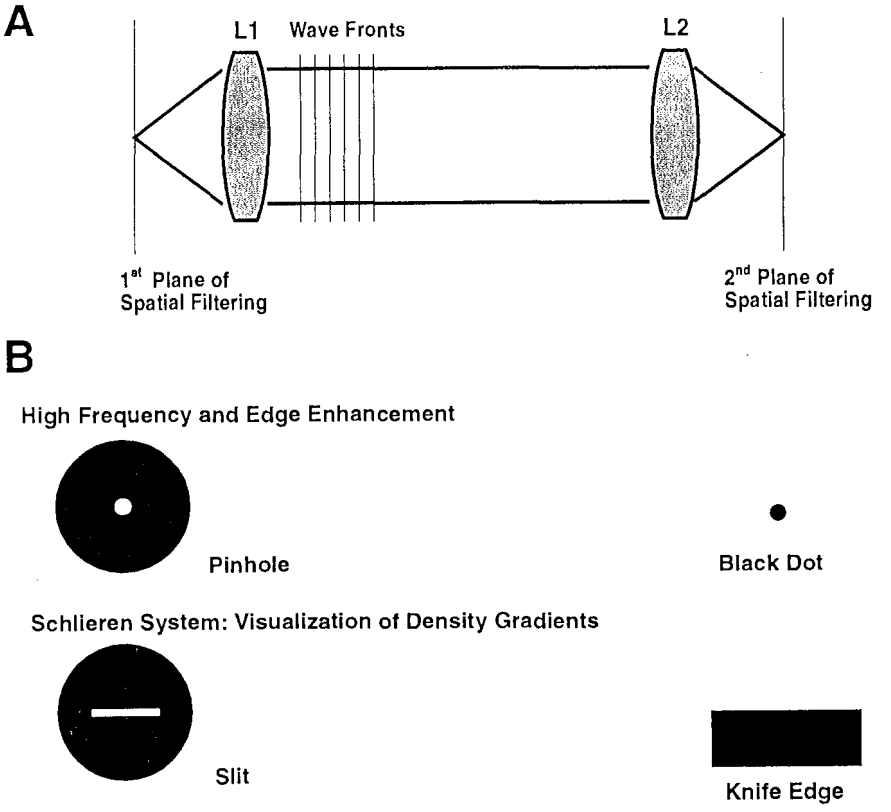

Fig. 1. Schematics of the principle of matched filters in the optical design of observational set-up. A) Production of plane wave fronts and position of spatial filters. B) Two examples of matched filters, one for high frequency and edge enhacement, the other for visualization of density gradients perpendicular to the knife edge.

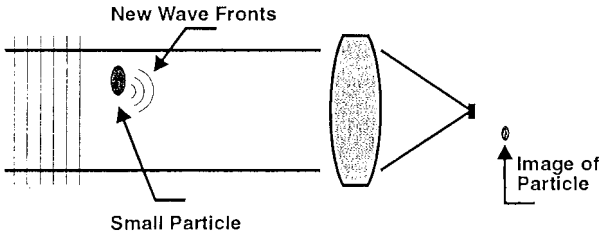

Fig. 2. Schematics of image formation in matched filter optical design of observational set-up. Small particles and focus is given because particles distort wave fronts anywhere within the collimated and expanded laser beam. Very small particles form new centers of light emission and are visible even if their sizes do not allow image formation.

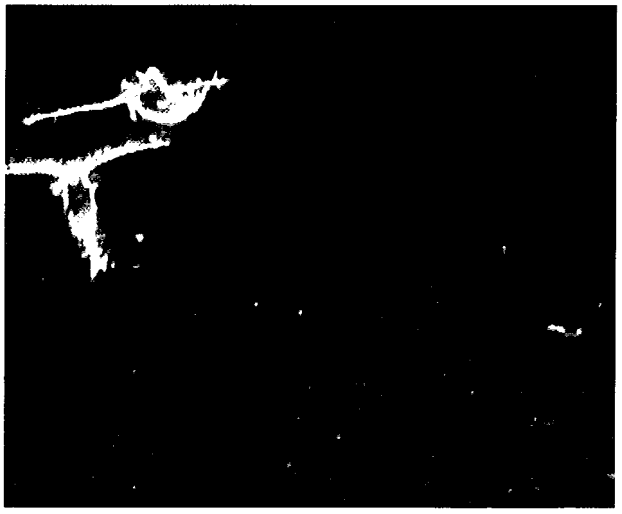

Fig. 3. One frame from a video observation of the feeding behaviors of *Diaptomus minutus*. The two animals are separated in the dimension of the optical axis by 1 cm. Upper animal is in focus. The behavior patterns of the lower animal can still be evaluated with the same temporal resolution as the ones of the upper animal. Visualization of the feeding current can only be performed with animals in optical focus. The suspended particles are algae in the size range of 5 to 10 microns.

behavior which either are created or modified by live animals. We use this optical approach to study zooplankton of a size range of 50 microns to one centimeter.

Well tuned optical systems allow us also to observe ecological interactions between aquatic

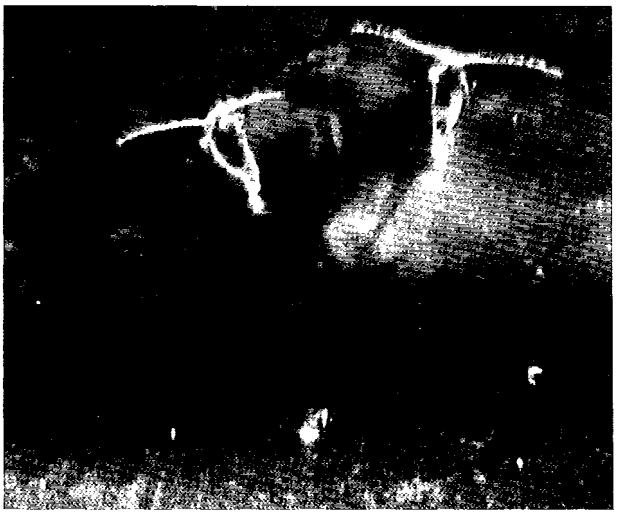

Fig. 4. One frame from a video observation of the creation of hydrodynamic disturbances by feeding and swimming calanoid copepods (*Diaptomus minutus*). Animal on the left glides capturing algae. Animal on the right entered the picture from the left, avoided encountering the animal on the left by executing three short hops and creating three vortex rings in the water. Body lengths on both animals are 1 mm. With this technique of adding a density gradient as an optical element we can observe very fast events like escapes at 500 body lengths per second because we can trace the hydrodynamic disturbances rather than film at high frame rates (over 10,000 frames per second would be necessary, at times of random escapes).

predators and their prey with a resolution of five microns in a field of view and a depth of focus of one centimeter. To date, the largest set-up allowed us to observe, in three dimensions, interactions between zooplankters (e.g. mating) within a vessel of one liter with a resolution of 50 microns. These observations were possible because we used carefully matched filters (Fig. 1A) which canceled all distortions of the wave fronts that we did not perceive as informative.

REFERENCE

Zernike, F. 1958. The wave theory of microscopic image formation. In: Concepts of classical optics (J. Strong, ed.), Appendix K, 525-536.

Zoological Studies 34, Supplement I (1995)

Zoological Studies

A Novel Idea in Confocal Scanning Microscopy

Zhihua Ding, Guiying Wang, Zhifeng Fan and Zhijiang Wang
Shanghai Institute of Optics and Fine Mechanics, Academia Sinica, People's Republic of China

The techniques that, by virtue of their capability for producing superior resolution, fall into two classes. The first involves the use of shorter wavelength radiation, such as in electron or x-ray microscopy, The second includes the various forms of scanning probe microscopy, of which scanning tunneling microscpy is the best known example. That these methods have not already largely supplanted optical microscopy is attributable to the fact that, in the request for higher resolution, a fustian bargain has been struck so that in each method, several of the attractive features of optical microscopy have been sacrificed such as nondestructiveness, low cost, high speed, reliability, versatility, accessibility, ease of use, and informative contrast. In this paper we describe a novel confocal scanning optical microscopy, perhaps it is a promising microscopy in the area of higher resolving power microscopes.

It is exciting if we can diminish the Airy central core to some degree by apodization, for example, one tenth of the origial width, then the ony question that remains in getting superior resolution details is its low contrast owing to large diffraction effect, but this can be overcomed by confocal technology. When a pupil coating is applied to a diffraction limited pupil of modest aperture, it causes the point amplitude diffraction pattern to collapse inward, as if the resultant pupil were still clear and diffraction limited but now with a predetermined times larger aperture. Thus the image is formed as the coating had physically extended the given aperture outwards in space, and by a designed amount. It accomplishes this by diffracting outside the field of view all light which would otherwise tend to broaden the pattern into an ordinary airy disk. If a lense of this kind is used solely, the imaging quality can nt be good enough, because all light that diffracting outside the view becomes a strong background and degrades the image contrast. But we can suppress the background by another diffraction limited lens just as the setup in confocal microscopy. So we put forward the idea of implementation of apodization in confocal system, perhaps it is a practical way to solve the problem of bargain between higher resolution and attractive features of optical microscopy.

The theoretical development and calculated results are depicted thoroughly in this paper, in addition to comparision with results obtained by inserting annualar pupls.

Zoological Studies 34, Supplement I (1995)

Zoological Studies

Possible Effects of Fluorescence Bleaching/Saturation on the Definition of the Paper Surface in CLSM Measurements

Odd Løvhaugen
The Norwegian Pulp and Paper Research Institute, Norway

We have observed that scanning a paper surface with a low f-number objective (10×0.3) in the "reflection mode" at 488 nm on our Leica TCS4D, an ambiguous definition of the paper surface may occur, when using a modified centre of mass algorithm for detection of the surface. This ambiguity depends among other things on the laser power, and it manifests itself both in the texture of the SFP images, and in the calculation of surface roughness parameters. But as this "reflection" mode also includes the fluorescent emission of the object we tend to interpret the result as an effect of fluorescence bleaching and saturation (Visscher et al. 1994).

We have several indications for this.

1) a given laser power seems to give a repeatable result for the surface roughness. This means that a measurement of laser power P3 gives approximatly, the same result as a measurement of laser power P1 if P3=P1, even if a measurement of power P2 at a higher power level than P3 has been made in between. All measurements are made over exactly the same area.

2) the short time fluctuations in laser power seems to be insignificant, when tested using a flat mirror.

3) the effect depends on the averaging mode. Line averaging gives a stronger effect than frame averaging for the same energy exposure. The repetition frequency experienced by each voxel is in order 0.001 s for line average and 0.1 s for frame average.

POSSIBLE MECHANISMS

This inconsistency may come from one or more of several sources.

-the topography of the paper surface may change mechanically due to the exposure of the laser.

-the optical properties of the upper surface layer may change due to the laser light.

-the laser radiation may be erratic itself creating high frequency laser power fluctuations.

-electronic or digital noise from the recording and an imperfect optical impulse response function of the objective may give random errors in detection of the surface.

-the surface detection algorithm may be instable or there are some error in the software.

Having analyzed these factors, a change in the optical properties of the surface layer may be the most likely, as the constitutents of paper may have optically unstable properties in the 480-500 nm region. These instabilities show up as photo yellowing, changes in the luminescent absorption and emission spectra and fluorescent bleaching (Olmstead and Gray 1993). Athough the paper may be very inhomoge-neous with fines and fibre parts in the sub resolution regime which could change form during exposure, the scattering cross section of these are so small that topological change in these would be less likely to cause the observed changes.

MAGNITUDE OF THE EFFECT

For the laser power high (3-5 mW), medium (1-2 mW) and low (<1.0 mW) with line averaging (8 x), the calculated roughness parameter Ra. (average magnitude of height deviation from mean height) was respectively 1.3μm, 1.6μm and 2.3μm. Whereas for 8x frame and average medium laser power the calculation gave Ra=1.3μm. Apart from the change in laser power and averaging method and proper adjustment of the dynamic range, all other sampling parameters were equal. Sampling distance in z-direction was 1.0 μm. The variation in the 1 μm

range are to be compared with the FWHH of 4. μm in the axial resolution curve. Even without centre of mass calculation of the surface position, the numeric noise contribution to Ra should be approximately: 1μm/512*512=0.002 μm.

IMPACT

We feel that a qualified answer to the cause of the observed deficiency is not yet found. Alterations in the fluorescence absorption, and thus the reflection properties of the fluorphores may influence their measured spatial distribution. The surface roughness measurements of papers by use of confocal microscopes as well as by laser profilometers must be closely examined, if a deficiency relating to fluorophore properties can be confirmed.

REFERENCES

Visscher K, GJ Brakenhoff, TD Visser. 1994. Fluorescence saturation in confocal microscopy. J. of Microscopy **175:** 162-165.

Olmstead JA, DG Gray. 1993. Fluorescence emission from mechanical pulp sheets. J. Photochem. Photobiol. A: Chem. **73:** 59-65.

Zoological Studies 34, Supplement I (1995)

Zoological Studies

Get Nano-information by Nano-pinhole in X-ray Holography

Zhihua Ding, Cuiying Wang, Zhifeng Fan and Zhijiang Wang
Shanghai Institute of Optics and Fine Mechanics, Academia Sinica, People's Republic of China

It is well known that from the invention of Scanning-Tunneling-Microscopy (STM) by binning et al., the ero of nanotechnology is coming. Many members of Probe-Scanning-Microscopy family have obtained information of nanometer-resolution, the key of these successes lies in the usage of nano-probe as their detectors. In recent years, scientists contribute more and more interesting to the spectrum of x-ray, especially of the soft-x-ray (1-30nm). The move is driven particulary by the fact that biologists may hope to see a nearnative aqueous environment structural features.

If we focus x-ray energy by a fresnel lens onto a pinhole plane, then the diameter of the pinhole determines the lateral resolution of Non-Redundant holography (Stroke holography). So the difficulty in fabrication of fresnel lens now transfers to the problem of fabrication of a pinhole with nanometer radius. By the fabrication of a nano-pinhole we may hope to get nanometer-scale information in the x-ray region.

It is posible for us to get small pinhole, such as using taper hollow fiber as small hole, using e-beam of scanning electron microscope to fabricate this nano-pinhole, and shrinking the pinhole of thin film by electroplating, and so on. Here we put forward a new idea of nano-pinhole fabrication by STM system.

By appling voltage pulse between tip and substrate of STM system operated in constant current mode, leads to the transition of work station from tunneling to field emission. A factor of 10^2-10^3 increase in current between tip and substrate may occur in some typical experiments, and high-field strength (~1GV/m) may be achieved. Furthermore, the close proximity of tip and substrate adds some additional effects as exchange correlation and screening, which must be considered in the explanation of fabrication mechanism. Due to these characteristics high current with nanometer spatial resolution, high field between nanometer gap between tip and substrate, close proximity of tip and substrate of STM system, we conclude some methods and mechanisms in nano-fabrication as below:

NANOMETER-SCALE EXPLOSIVE THERMAL MELTING

A sudden burst of tunneling current (due to an instantaneous increase in bias voltage) from a STM operated in the constant-current mode. The high current density of injected electrons localized to a small region of substrate by the STM tip gives rise to an explosive event which may be reponsible for the electro-etching of substrate or thermal melting of substrate in nano-region.

FIELD-INDUCED ATOMIC EMISSION

If we position the tip of STM within nanometers of a substrate, high-field strength can be achieved with substantially lower voltage for the small gap between tip and substrate. Furthermore, the close proximity of tip and substrate causes overlap of atomic potencials, which can lead to a lowering of the energy barrier for field evaporation. By using tungsten as tip in gold substrate (the threshold for field evaporation is significantly lower in gold than in tungsten, 3.5V/A in FIM experiments for gold versus 5.7V/A for tungsten). One would expect some of gold removed from the substrate to be transferred to the tip.

STM ELECTRON BEAM EXPLOSURE

In classical electron beam fabrication the high-energy (~10KeV) electron beam causes an im-

portant scattering of the electrons in the resist layer as well as in the substrate, which leads to a lowing in resolution of fabrication beam. This proximity effect can be avoided when a low-energy (~10eV, but energetic enougy to cause bond scission in resist such as PMMA) electron beam leaving the STM tip is used for the explosure. After explosure and development a mask with a nano-pinhole is achived, then by reactive ion eching below substrate of anisotropical material, this leading to a bigger hole in substrate, and by metaling the hole from the back side of substrate, causing the shrinking of hole in substrate. In this way we would expect to fabricate a pinhole whose diameter is determined by that in mask.

All methods that can be used to obtain nano-information may also can be used as a method in nano-fabrication, for they are the two aspects of one problem. So we put forward the idea of nano-fabrication by STM system. Because nano-fabrication and imaging can be done in the same device, it is convenient for hole location and likely to solve the problem of nano-pinhole fabrication. By focusing x-ray energy onto this nano-pinhole to form point source in Non-Redundant holography we may envision to get nano-information in the x-ray region.

REFERENCES

Binning G, H Rohrer, Ch Gerber, E Weibei. 1992. Phys. Rev. Lett. **49:** 57.

Wang ZJ. 1993. Academia Bulletin. **38(23):** 2205.

Attwood D. 1992. Phys. Today. **45:** 24.

Li YZ, L Vazquez, R Piner, RP Andres, R Reifenberger. 1989. Appl. Phys. Lett. **54:** 1424.

Mamin HJ, PH Guether, D Rugar. 1990. Phys. Rev. Lett. **65(19):** 2418.

Stockman L, C Van Haesendonck, Y Bruynseraede. 1993. Appl. Phys. Lett. **62:** 2935.

Lewis A. 1984. Ultramicroscopy. **13:** 227.

Zoological Studies 34, Supplement I (1995)

Zoological Studies

Migratory History Recorded in Otoliths of the Japanese Eel, *Anguilla Japonica*, Elvers as Revealed from SEM and WDS Analyses

Wann-Nian Tzeng

Department of Zoology, College of Science, National Taiwan University, Taipei, Taiwan 106, R.O.C.

The environmental history of the Japanese eel, *Anguilla japonica* (Temminck & Schlegel), during its migration from the spawning ground to the rivers of Taiwan, was studied by examining otolith microstructure with SEM, and the strontium (Sr) and calcium (Ca) contents measured from wavelengths of x-rays emitted from the otoliths with WDS (Wavelength dispersive spectroscopy). The Sr/Ca changes in the otoliths in relation to environmental and physiological changes of the fish are discussed.

LIFE HISTORY OF THE EEL

The Japanese eel is one of the most important culture species in Taiwan. Large numbers of eel elvers are caught for cultivation from November to March during their upstream migration in estuaries (Tzeng 1985). The eel is a catadromous fish, spawning in the North Equatorial Current west of the Mariana Islands (15°N, 140°E) during the period from June to July (Tsukamoto 1992). The eel larvae, a willow-leaf-shaped leptocephali, drift with the current from their oceanic spawning ground, and metamorphose into transparent glass eel, or elvers, before entering the estuaries. After upstream migration, the elvers become young eels and live in the rivers for 5-20 years. During late autumn, the maturing eel migrates downstream to the ocean to spawn.

OTOLITH MICROSTRUCTURE AND DAILY AGE

Since Pannella (1971) discovered primary growth increments in otoliths of fish, ageing technique by examining daily growth increments in otoliths has been applied widely to study the age of ths fish (Campana and Neilson 1985). There are three pairs of otoliths in fish's otic vesicles, functioning as hearing and body balance of the fish. Otolith is a biogenic aragonite, alternatively consisted of a calcium-rich incremental zone and an organic-rich discontinuity zone. When otoliths are ground with fine mesh polishing paper, polished with alumina paste, and etched with 5% EDTA (ethylene diamine tetra-acetate; pH adjusted with NaOH to 7.4). The above-mentioned two zones become the "crest and trough" on the polished otolith, which could then be viewed under SEM (Fig.1). The otolith incremental and discontinuity zones are deposited on a daily basis (Tzeng and Yu 1988). This permitted the time required for migration of the eel larvae from the spawning ground to the coasts, and the spawning season of the eel, to be estimated (Table 1).

OTOLITH MICROCHEMISTRY AND MIGRATORY HISTORY

Recent studies have indicated that past environmental history of the fish can be reconstructed from analysis of the ratio of trace element, especially Sr, incorporated during the process of otolith growth (Radtke et al. 1990, Secor 1992). Sr can inter-change with Ca in otoliths during the depositional process because Sr has the same valence as Ca, as well as a similar ionic radius (Amiel et al. 1973). The Sr content in the otolith of diadromous fish was found to differ between freshwater and seawater phases (Casselmam 1982, Radke et al. 1988, Kalish 1990). The incorporation of Sr into the otolith is a physiological process controlled by many interactive factors including temperatrue, salinity, ontogeny and migration (Kalish 1989, Sadovy and Severin 1992, Smith et al. 1979,

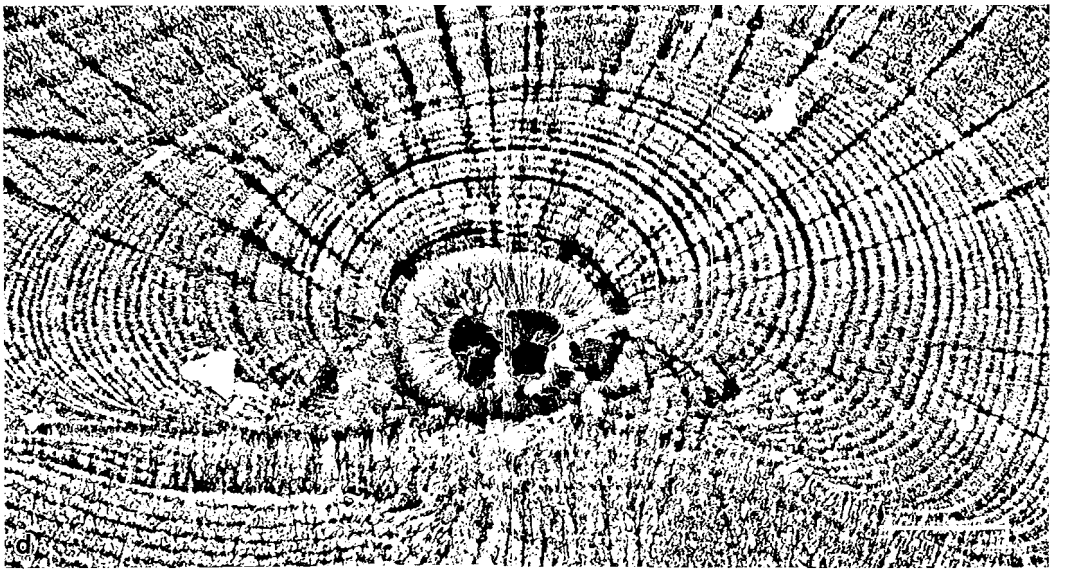

Fig. 1. SEM micrograph illustrating daily growth incremental (light band) and discontinuity zones (dark band) in otolith of a 56.0 mm TL elver. Scale bar = 10 μm. (from Tzeng 1990).

Table 1. Daily ages and birth date of elvers collected from four estuaries (SA, SL, LS and TK) in the eastern and western coasts of Taiwan on 22 December 1989 and 22 and 23 January 1990. (from Tzeng and Tsai 1992)

Sampling site	Sampling date	Sample size	Total length (mm)	Otolith radius (μm)	Age (days)	Birth date
SA	22 Dec. 1989	9	56.39±1.39	141.25±8.85	169.3±14.9	18 June-24 July
SL	22 Jan. 1990	5	56.66±2.84	129.44±10.21	175.6±27.8	26 June-9 Sept.
LS	22 Jan. 1990	5	56.20±2.21	56.20±2.21	165.6±22.6	10 July-3 Sept.
TK	23 Jan. 1990	6	56.80±2.15	56.80±2.15	171.7±26.2	7 July-22 Sept.

Townsend et al. 1992, Tzeng 1994). Quantitative measurements of the concentration of Sr in otolith relative to that of Ca was made using a WDS for the elver collected in a river estuary of northern Taiwan.

The Sr/Ca concentration ratio was lower in the primordium of the otolith, then increased gradually and reached a maximum at an area approximately two-thirds of the otolith radius from the primordium, and dramatically decreased to a low level at the otolith edge during the fish migrated to the freshwater (Fig. 2). The otoliths of freshwater fishes typically have lower Sr levels than those of seawater fishes (Odum 1975). The low Sr content in the primordium, probably due to the sources of deposition, were of maternal or freshwater origin of the oocyte. The dramatic decrease in Sr/Ca ratio most likely corresponds to the period when leptocephalus metamorphoses into an elver. When finishing metamorphosis, the fish will migrate from the strong Kuroshio Current into coastal waters. Leptocephalus is known to contain extensive amounts of gelatinous extracellular matrix composed of sulfated glycosaminoglyscans (GAG) which are broken down during the process of metamorphosis (Pfeiler 1984). Since GAG indicates an affinity to alkali earth elements, particularly high to Sr (Nishizawa 1978). GAG breakdown may reduce the absorption Sr from seawater and result in a drastic decrease of otolith Sr content and, consequently, Sr/Ca ratios (Otake et al. 1994).

In conclusion, otoliths are like a biological CD ROMs recording information about the environment the fish experienced and about how the fish lived. The information on them is never lost and can be retrieved potentially in any temporal sequence.

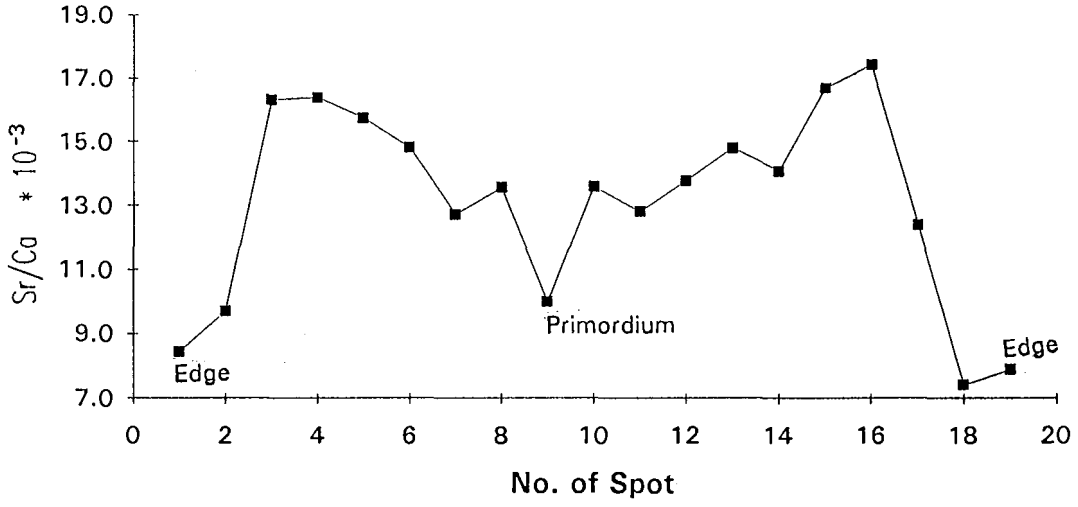

Fig. 2. Changes in strontium/calcium concentration ratio measured through the maximum edge-primordium-edge axis (spots 1-19) of a sectioned otolith of a 56.2 mm TL elver with a maximum otolith diameter of 142 μm, collected in a river estuary of northern Taiwan on 22 January 1990. (from Tzeng and Tsai 1994)

REFERENCES

Amiel AJ, GM Friedman, DS Miller. 1973. Distribution and nature of incorporation of trace elements in modern aragonite corals. Sedimentol. **20:** 47-64.

Campana SE, JD Neilson. 1985. Microstructure of fish otoliths. Can. J. Fish. Aquat. Sci. **42:** 1014-1032.

Casselman JM. 1982. Chemical analyses of optically different zones in eel otoliths. In Proceedings of the 1980 North American Eel Conference (Loftus KH. ed.). Ontario Fish. Tech. Rep. Ser. **4:** 74-82.

Kalish JM. 1989. Otolith microchemistry: validation of the effects of physiology, age and environment on otolith composition. J. Exp. Mar. Biol. Ecol. **132:** 151-178.

Kalish JM. 1990. Use of otolith microchemistry to distinguish the progeny of sympatric anadromous and non-anadromous salmonids. Fish. Bull. U.S. **88:** 657-666.

Nishizawa K. 1978. Marine algae from a viewpoint of pharmaceutical studies. Jap. J. Phycol. **26:** 73-78.

Odum HT. 1957. Biochemical deposition of strontium. Texas Univ. Inst. Mar. Sci. **4:** 39-114.

Otake T, T Ishii, M Nakahara, R Nakamura. 1994. Drastic changes in otolith strontium/calcium ratios in leptocephali and glass eels of Japanese eel *Anguilla japonica*. Mar. Ecol. Prog. Ser. **12:** 189-193.

Pannella G. 1971. Fish otolith: daily growth layers and periodical patterns. Science, N.Y. **173:** 1124-1127.

Pfeiler E. 1984. Glycosaminoglycan breakdown during metamorphosis of larval bone fish *Albula*. Mar. Biol. Lett. **5:** 241-249.

Radtke RL, DW Townsend, SD Folsom, MA Morrison. 1990. Strontium: calcium ratios in larval herring otoliths as indicators of environmental histories. Environ. Biol. Fish. **27:** 51-61.

Radtke RL. DJ Shafer. 1992. Environmental sensitivity of fish otolith microchemistry. Aust. J. Mar. freshw. Res. **43:** 935-951.

Secor DH. 1992. Application of otolith microchemistry analysis to investigate anadromy in Chesapeake Bay striped bass *Morone saxatilis*. Fish. Bull. U.S. **90:** 798-806.

Sodovy Y, KP Severin. 1992. Trace elements in biogenic aragonite: correlation of body growth rate and strontium levels in the otoliths of the white grunt, *Haemulon plumieri* (Pisces: Haemulidae). Bull. Mar. Sci. **50:** 237-257.

Smith SV, RW Buddemeier, RC Redalje, JE Houck. 1979. Strontium-calcium thermometry in coral skeletons. Science **204:** 404-406.

Townsend DW, RL Radtke, S Corwin, DA Libby. 1992. Strontium: calcium ratios in juvenile Atlantic herring *Clupea harengus* L. otolith as a function of water temperature. J. Exp. Mar. Biol. Ecol. **160:** 131-140.

Tsukamoto K. 1992. Discovery of the spawning area for Japanese eel. Nature **356:** 789-791.

Tzeng WN. 1985. Immigration timing and activity rhythms of the eel, *Anguilla japonica*, elvers in the estuary of northern Taiwan with emphasis on environmental influences. Bull. Jap. Soc. Fish Oceanogr. **47/48:** 11-28.

Tzeng WN 1990. Relationship between growth rate and age at recruitment of *Anguilla japonica* elvers in a Taiwan estuary as inferred from otolith growth increments. Mar. Biol. **107:** 75-81.

Tzeng WN. 1994. Temperature effects on the incorporation of stontium in otolith of Japanese eel, *Anguilla japonica* Termminck & Schlegel. J. Fish Biol. **45:** 1055-1066.

Tzeng WN, YC Tsai. 1992. Otolith microstructure and daily age of *Anguilla japonica* elvers from the estuaries of Taiwan with reference to unit stock and larval migration. J. Fish Biol. **40:** 845-857.

Tzeng WN, YC Tsai. 1994. Changes in otolith microchemistry of the Japanese eel, *Anguilla japonica*, during its migration from the Ocean to the rivers of Taiwan. J. Fish Biol. **45:** 671-684 .

Tzeng WN, SY Yu. 1988. Daily growth increments in otolith of milkfish, *Chanos chanos* (forsskal), larvae. J. Fish Biol. **32:** 495-504.

Zoological Studies 34, Supplement I (1995)

Zoological Studies

Visualization of Cell Adhesion Molecules on Cardiovascular Cells by Confocal Microscopy

P. Pietsch, M. Braun, S.B. Felix and G. Baumann
Medizinische Klinik Universitätsklinikum Charité Humboldt-Universität D-10098, Berlin, Germany

Cell adhesion molecules (CAM) are important glycoproteins which mediate cell-cell interactions. The expression of these molecules are modulated by a variety of mediators engaged in cell activation.

Common methods applied for the detection of CAM are cell ELISA, FACS or radioactive binding studies. All these methods summarize the expression on a great number of cells and do not visualize CAM on single cells. The quantitative detection of CAM expression on cultured cells by conventional epifluorescence microscopy is difficult because of the rapid photobleaching of the fluorescent dye. We established a method to visualize CAM on single cells using confocal microscopy.

MATERIALS AND METHODS

Human coronary and pulmonary smooth muscle cells were cultured on 3well glass-slides (DMEM-medium with 15% FCS). At cell-confluency, medium was changed to 1% FCS for 48 hours in order to synchronize the cell cycle. Cells were fixed with ice-cold methanol (10 min) and incubated with monoclonal antibodies against I(nter) C(ellular) A(dhesion) M(olecule)-1 and V(ascular) C(ell) A(dhesion) M(olecule)-1 (Dianova, 1:50, 60 min). The antigen-antibody-complexes were detected by a second antibody coupled with Cy-3 (Dianova, 1:50, 60 min). Immunofluorescence measurements were performed with the confocal laser scan microscope Odyssey XL (Noran instruments) using the inverted microscope Diaphot 200 (Nikon). Specimen were studied with the 60x oil-imersion objective (NA 1,4). Probes were excited with the 515 nm line of a 10 mW multiline Argon ion laser and Cy-3 emission was detected at wavelengths >550 nm after passage through a 10 μm slit aperture. Cells were localized at a framerate of 30/sec and pictures of individual cells were taken by averaging 120 frames. CAM expression was determined by two different ways: a) mean fluorescense intensity (from 3 to 255 arbitrary units) of the pixels forming single cells and b) the sum of the pixel intensities per cell area. We analyzed 10 cells per well and determined the mean value for each individual cell preparation.

RESULTS

Under basal conditions there was a low expression of CAM on vascular smooth muscule cells. The mean fluorescence intensity of basal expression amounted to 7 ± 2 (ICAM-1) and 6 ± 1 (VCAM-1) (n=3 coronary cell preparations). Control experiments with an indirect cell ELISA also showed very similar basal expression values of both ICAM-1 and VCAM-1.

CAM are regulated by cytokines on endothelial cells as well as smooth musle cells (Carlos and Harlan 1994, Couffinhal et al. 1993). Using the ELISA technique we observed a marked stimulation of CAM expression with TNFα (10 ng/ml; 15 h) on a confluent cell monolayer (4-fold increase in optical density units). This stimulating effect

Correspondence to: Dr. Peter Pietsch Universitätsklinikum Charité Kardiologisches Forschungslabor Ziegelstra βe 5-9 D-10117, Berlin, Germany

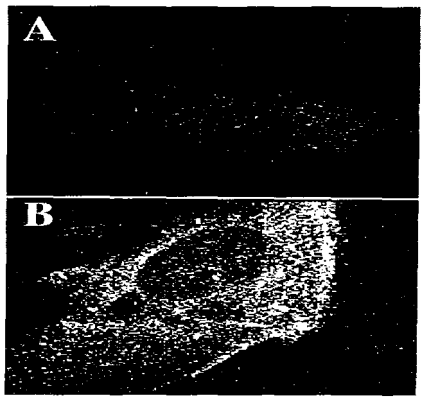

Fig. 1. ICAM-1 expression on single pulmonary SMC.

ICAM-1 expression on single human pulmonary SMC aunder conditions (IA) and mulet with TNF α 10 ng/ml

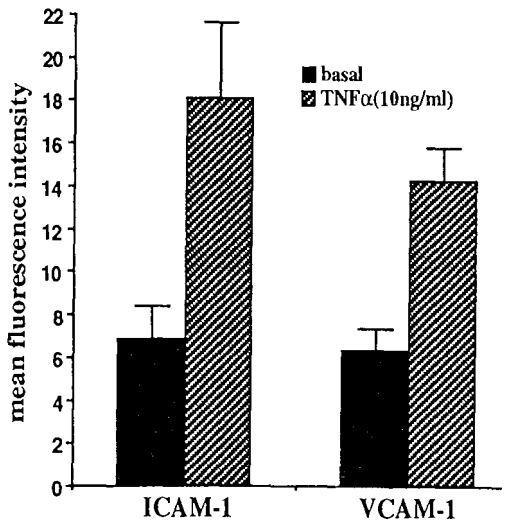

Fig. 2. Effects of TNFα on CAM expression of coronary SMC.

ICAM-1 and VCAM-1 expression (mean fluorescense intensity) on human coronary SMC under basal conditions (■)and after stimulation with TNFα (10 ng/ml, ■) for 15 hours (n=4-5).

of TNFα was detectable on single cells by confocal microscopy. The mean fluorescence intensity amounted to 18 ± 4 (ICAM-1) and 14 ± 4 (VCAM-1) (n=3) (Figs. 1 and 2)

The stimulation of CAM expression induced by TNFα is based on de novo synthesis of the glycoproteins. Measurements with the ELISA technique showed that the stimulation could be abolished by preincubation of the cells for 3 hours

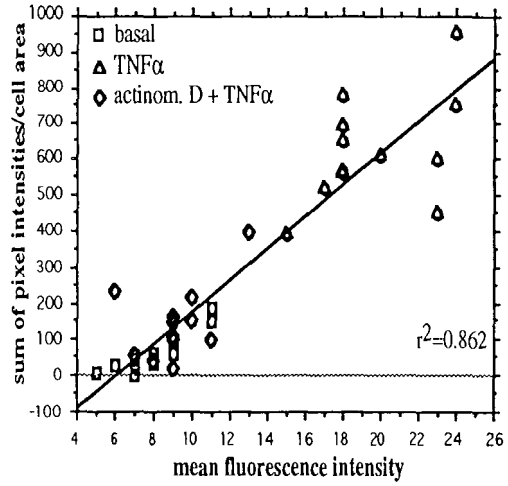

Fig. 3. ICAM-1 expression: correlation between mean fluorescence and the sum of fluorescence intensities per cell area.

ICAM-1 expression on human coronary SMC. Results from 34 individual cells under basal conditions (❑), stimulated with TNFα (10 ng/ml, 15 h, Δ) and stimulated with TNF after preincubation with actinomycin D(1 μg/ml, 3h. ◊)are shown.

with the transcription-inhibitor actinomycin D (1 μg/ml) or cycloheximid (10 μg/ml), an inhibitor of protein biosynthesis. These inhibitory effects were also detectable on single cells by confocal microscopy. Fig. 3 demonstrates CAM expression on pulmonary smooth muscle cells under basal conditions, after TNFα-stimulation with and without actinomycin D preincubation. There is a good correlation between the two different detection methods we used to visualize CAM on single cells.

These data demonstrate that CAM expression could be visualized on singe cells by confocal microscopy. The method is sensitive to detect low levels of basal expression and the effects of exogenously added substances could be demonstrated onsingle cell level. This method will provide a new technique to study the modulation of CAM expression on different cell types.

REFERENCES

Carlos TM, JM Harlan. 1994. Leucocyte-endothelial adhesion molecules. Blood. **84:** 2068-2100.

Couffinhal T et al. 1993. Regulation of vascular cell adhesion molecule-1 and intercellular adhesion molecule-1 in human vascular smooth muscle cells. Circ. Res. **74:** 225-234.

Zoological Studies 34, Supplement I (1995)

Zoological Studies

Mitochondria-rich Cells in Gills of the Euryhaline Teleost, *Oreochromis Mossambicus*

Tsung-Han Lee[1,2], Hui-Chen Lin[3], Ming-Jiunn Yu[4,2], Fore-Lien Huang[1] and Pung-Pung Hwang[2,4]

[1]*Institute of Zoology, National Taiwan University, Taipei, Tiawan 107, R.O.C.*

[2]*Institute of Zoology, Academia Sinica, Nankang, Taipei, Taiwan 115, R.O.C.*

[3]*Department of Biology, Tung-Hai University, Taichung, Taiwan 400, R.O.C.*

[4]*Institute of Fisheries Science, National Taiwan University, Taipei, Taiwan 107, R.O.C.*

The gill is considered as one of the most important osmoregulatory organs in teleostean fish. There are four pairs of gill arches. Each of the arches has two rows of filaments and leaf-like lamellae protrudes along both side of each filament. The epithelium of gill filaments has at least four morphologically different cell types, each with different functions : the pavement cells; the mitochondria-rich (MR) cells; the mucus cells and the undifferentiated cells Mitochondria-rich cells are responsibile for ionic exchanges required for teleosts (Pisam and Rambourg 1991).

Ultrastructural features of gill mitochondria-rich (MR) cells in euryhaline tilapia, *Oreochromis mossambicus*, were studied with scanning and transmission electron microscopy. MR cells distribute mostly on the filamental epithelium and very rarely on the lamellar epithelium. SEM studies presented three types of apical surfaces of the MR cells — wavy convex, shallow basin and deep hole — on the afferent side of gill filaments (Fig. 1). TEM observations revealed that all three types of MR cells were characterized in the cytoplasm with numerous mitochondria and the labyrinth-like tubular system. However, other characteristics like leaky junctions and intercellular digitations only occurred between deep holes but not between wavy convexes and shallow basins. Experiments on the adaptation to various milieux proved that the size and density of MR cells altered abruptly within 24 hours following transfer. Hence various types of MR cells were correlated to diverse ion changes in the environments.

Na, K-ATPase, the membrane-bound enzyme responsible for the energy dependent exchange of cytoplasmic Na^+ for extracellular K^+ in most animal cells, plays a critical role in salt secretion of euryhaline teleost. Immunocytochemical studies with a monoclonal antibody demonstrated that the gold particles representing Na, K-ATPase α-subunit were distributed along the membrane-formed tubules in the gill MR cells, but not in other epithelial cells. Na, K-ATPase has also been found to localize in different types of MR cells (Fig. 2).

To sum up, (1) changes in shape and amount of mitochondria-rich cells in gills of euryhaline tilapia with different environmental ions implies the correlations between distinct MR cell types and ions; (2) alteration of MR cells occurred within 24 hours after transfer of the fish to different milieux and (3) exhibition of Na,K-ATPase in the cytoplasm of all types of MR cells indicate that branchial MR cells of euryhaline teleost may transform interchangeably within a short period of time to ensure the survival of the fish.

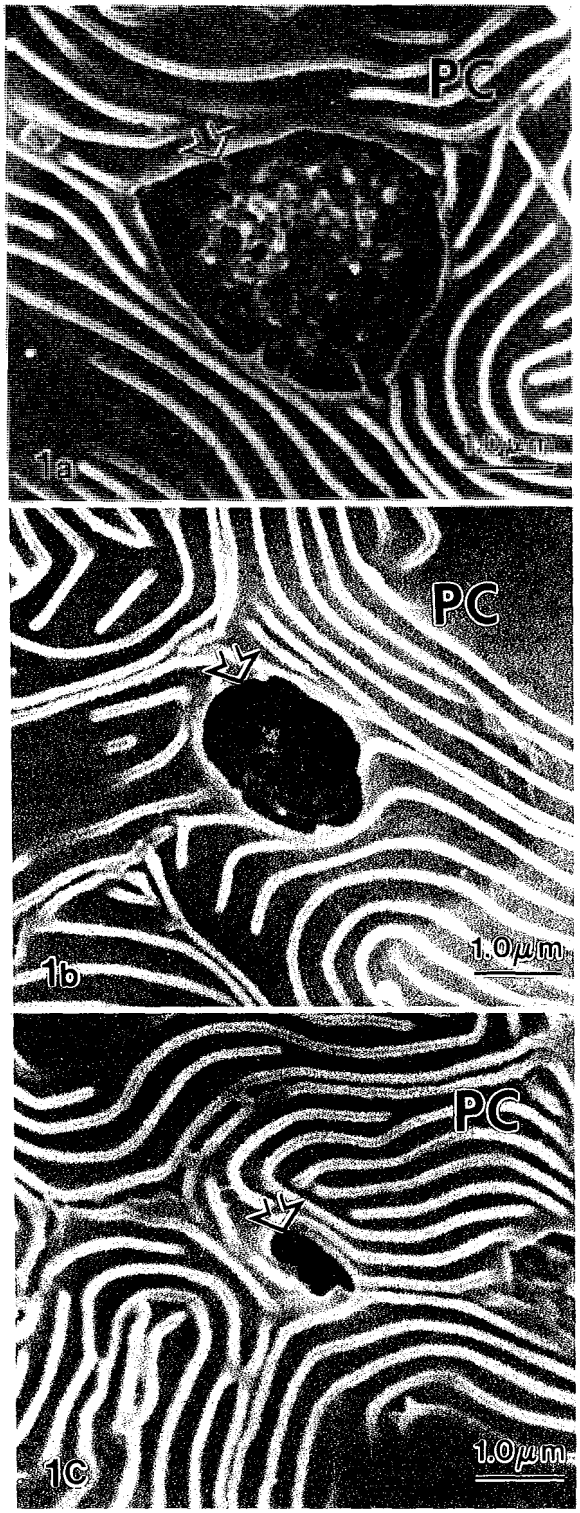

Fig. 1. SEM pictures show three types of apical surfaces (arrows) of mitochondria-rich (MR) cells on gill epithelium of euryhaline teleost, *Oreochromis mossambicus*. a-wavy convex; b-shallow basin; c-deep hole. PC, pavement cells.

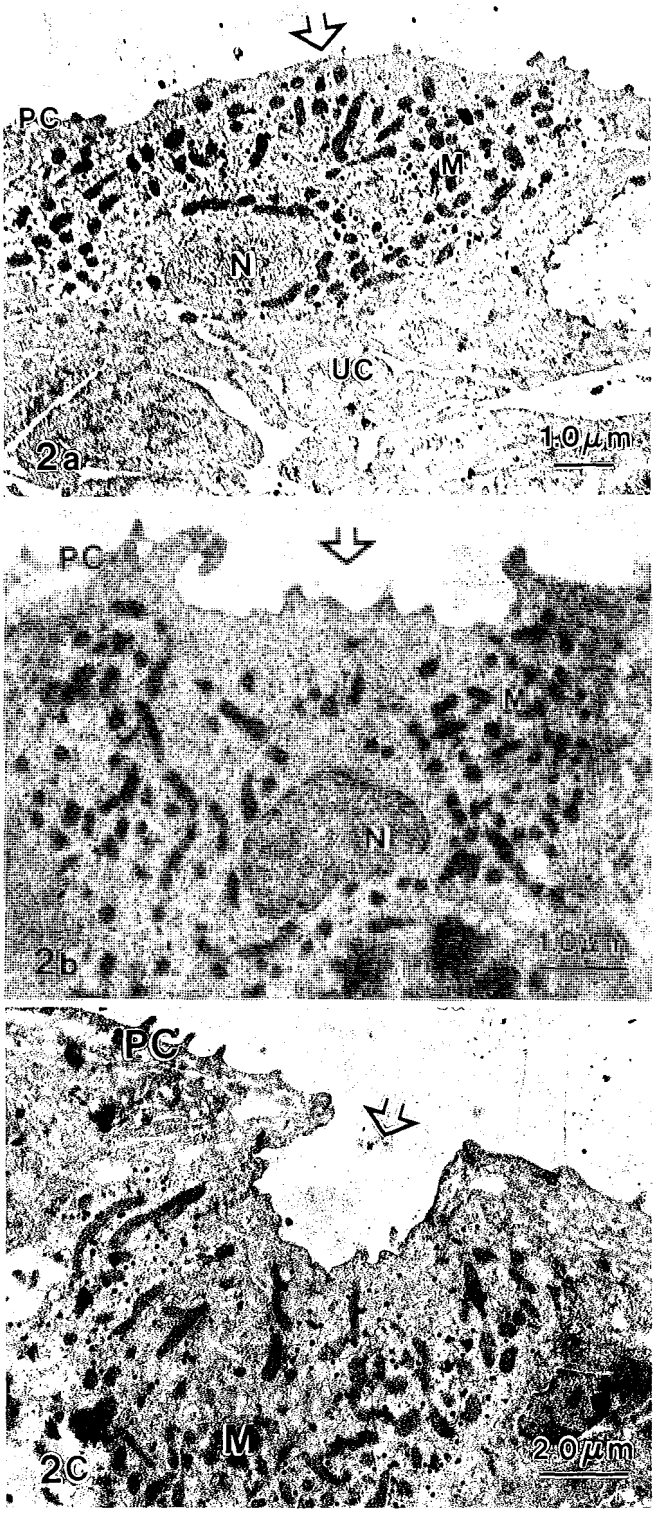

Fig. 2. TEM pictures show immunocytochemical localization of Na, K-ATPase (presented as gold particles) in the cytoplasm of three types of gill MR cells. a-wavy convex; b-shallow basin; c-deep hole. Arrows, apical surface of MR cells; M, mitochondria; N, nucleus; PC, pavement cells; UC, undifferentiated cells.

Zoological Studies 34, Supplement I (1995)

Zoological Studies

Structure Defining Functions of Cell Membrane Morphologies with Cubic Symmetry

Tomas Landh

Departments of Biophysical Sciences and Biomaterials, State University of New York at Buffalo, Buffalo, NY 14214, USA

Cell membranes, particularly the smooth endoplasmic reticulum (SER), have long been recognized to form highly interconnected and convoluted morphologies. The true 3-D structure is, however, yet to be fully understood, and most models describe the SER as an irregular arrangement of tubules. In addition to this traditional model of the SER there are numerous reports dealing with various, hitherto puzzling, membrane morphologies such as the "paracrystalline", "undulating", "honeycomb", "cotte de maile" to mention a few forms of the SER, as well as of other cell membranes. These 3-D membrane morphologies were recently shown to represent the same basic morphology and to be exactly described by the so called periodic cubic structures (PCS) (Landh, in press) well known to mathematicians and phycisists in the form of periodic minimal and/or nodal surfaces (Nitche 1990, Dierkes et al. 1992, Schnering and Nesper 1991, Andersson et al. 1995). These membranes were hence named Cubic Membranes (CM), of which, to date, three fundamental forms have been identified (Fig. 1). These intricate continuously folded membranes are, among other things, optimal space partitioners in which capacity they divide space into at least two physically distinct but highly intertwinned supspaces. Thus CM's in a closed form are in keeping with the well known barrier function of cell membranes. Most intriguingly, CM's occur in conjunction with numerous cell types, from all kingdoms, and in virtually any cellular membrane, including the SER, inner nuclear membrane (INE), plasma membranes, inner mitochondrial membrane, and Golgi apparatus (Landh, in press). Altogether we have to date cataloged some one thousand published and unpublished transmission TEM electron microscopy micrographs of both normal and pathological tissues in which CM's can be identified (representative examples are tabulated in ref 1.)

In projection, like those produced in TEM experiments, the patterns of which profiles of CM's often show, due both to their symmetry and the fact that they are necessarily continuous membranes, an extraordinary complexity. While this

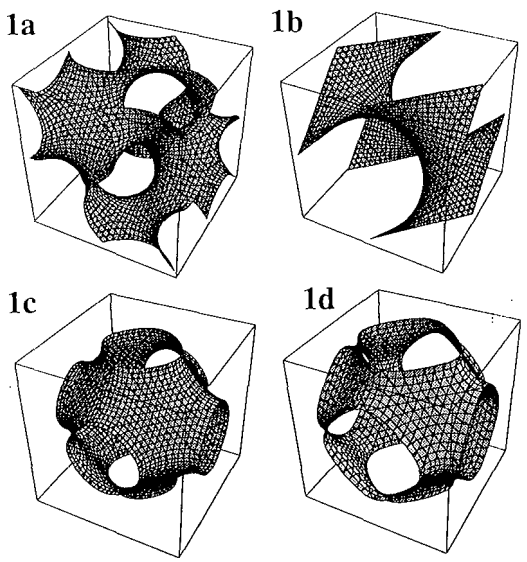

Fig. 1. The three fundamental cubic membranes represented as periodic nodal surfaces with zero potential (a-c). One unit cell is shown. The surfaces describes the mid-membrane surface (see Deng and Landh elsewhere in this volume). (a) The G-PCS with spacegroup $I4_132$. Since each side of the membrane must be, at least, chemically different the space group of the CM's is that of the subgroup of type 2 as compared to the congruent case. Thus the structure of the CM's are conventiently represented by differently colored sides of the membrane. (b) The D-PCS with spacegroup Fd3m. (c) The P-PCS with spacegroup Pm3m. (d) Example of a periodic equipotential (nonzero) P-surface in which the subspace volume relation is approximately 1:3.

has, on the one hand, made the them perplexing and puzzling to researchers for 35 years, it is, on the other, what makes them uniquely identifiable. This can, however, on the basis of information theory, only be realized once we know what we are looking at. CM's thus seems to stand alone since it is the only conserved 3-D continuous cell membrane morphology that can be close to exactly determined and usually easily recognized. Through the knowledge of the base-structure; i.e., its crystallography and the subspace volume relation (potential); of these PCS's we have established a "library" of computer generated projections simulating the appearence of CM's in TEM micrographs. These computer generated theoretical projections are then matched to experimental projections through a direct template-correlative method (Landh in press, Mieczkowski and Landh in prss). With this method, examplified in Figures 2-4, the three fundamental families of PCS's have been identified: the gyroid (G) of Schoen (Schoen 1990) (Figs. 1a and 2), Schwarz' double diamond (D) (Figs. 1b and 3) and primitive (P) (Figs. 1c and 4) surfaces (Schwarz 1890). In addition, we have from biology learned about a new type of PCS's form. Namely their multicon-tinuous forms which are based on multiple parallel membranes in which each membrane is described by a PCS with a particular potential. Thus these morphologies separate space into n+1 spaces, where n is the number of membranes in the structure. The multicontinuous surfaces seem to be as widespread in nature as the single PCS's, and all three of the fundamental PCS's above have been found to form them (see Fig. 4 for an example).

The formation of CM's is believed to take place through a intersection-free membrane folding process schematically shown in Fig. 5 (Landh, in press). However, the driving force for this is currently unknown, as is the topology of the initial and final states of the membrane(s). Several additional intriguing questions such as: What governes the selection of a particular CM type? Why are these more than two spaces in conjunc-

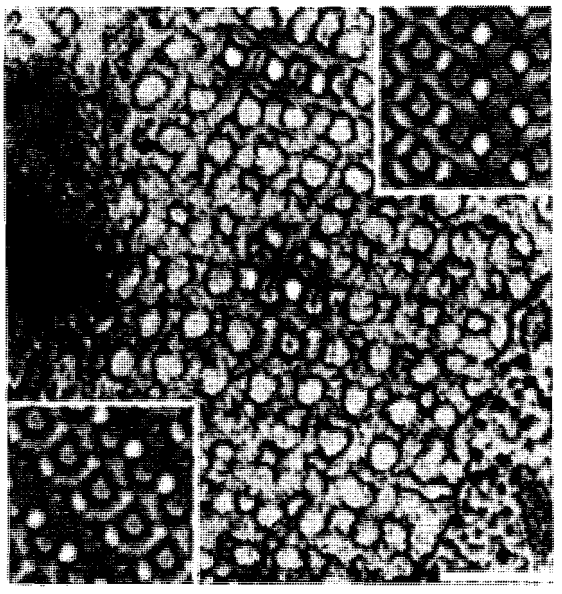

Fig. 2. Example of a G-based CM identified in cultured skeletal muscle cells of thick embryos in which the t-tubule invaginate to form the G-GM. Two areas is matched correponding to projections of a G-PCS along the [320] (upper) and [331] directions with close to zero potential (minimal surface area) and with a sample thickness af about half a unit cell. The unit cell size is approximately 100 nm. The insets shows projections generated from 5 unit cells. Bar, 200 nm, Adopted from reference 1 and 7 (Whitford & Landh).

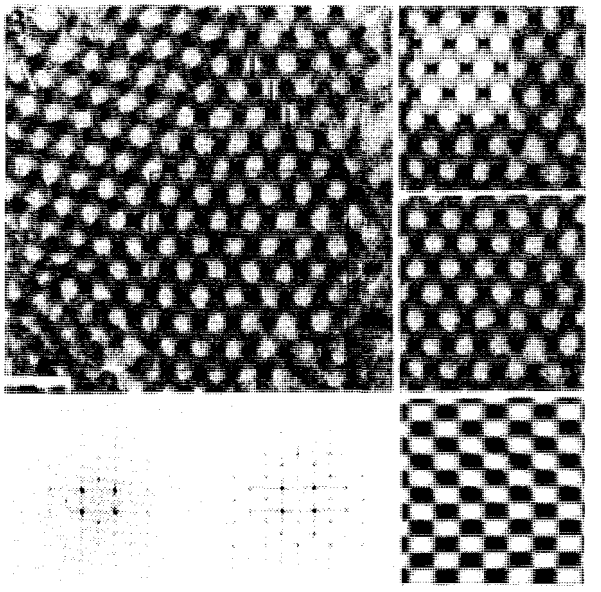

Fig. 3. Example of a D-based CM of the PLB in etiolated leaves of squash. The TEM projection corre[ond to the projected electron density of the D-PCS along the [110] direction. The computer generated projection is matched to the micrograph before (upper right) and after contrast adjustment and introduction of random noice (mid-right). The power spectrum (calculated on the boxed area in the micrograph (upper left) of the TEM (lower left0 and that of the computer computer generated projection (lower center) conrrespond very well as is seen in their cross-correlation (lower right). The specimen thickness is approximately a quarter of a unit cell. The PLB D-PCS has a constant potential corresponding to a subspace volume relation of about 1:4. Bar, 100 nm. Adopted after reference 3.

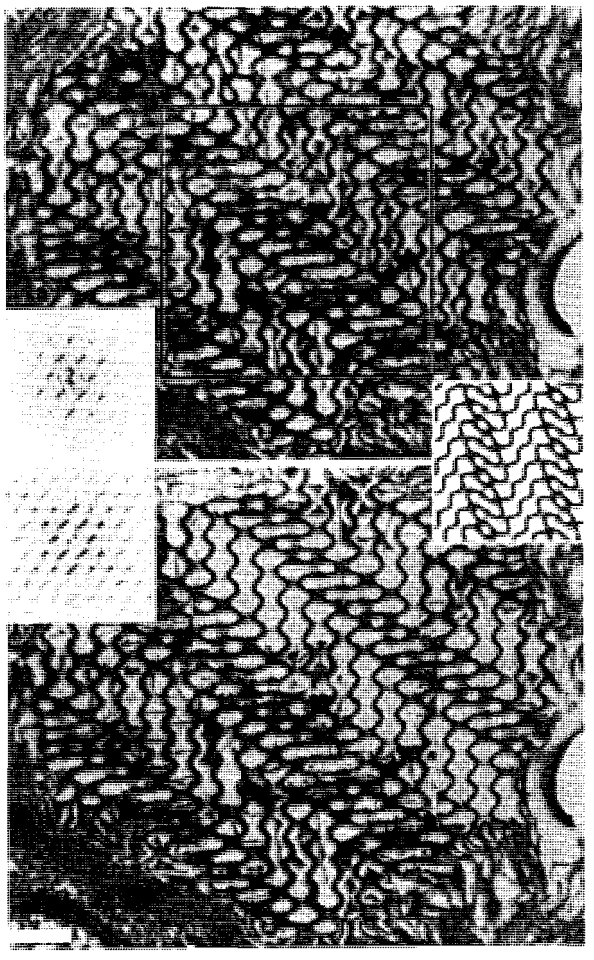

Fig. 4. Example of a P-based multimembranous CM identified in cholorplasts of the green algae Zygnema. This complex projected membrane pattern corrspond to the the projection of ten individual membranes, hence the large thickness. Its symmetry and pattern can, however, be simulated by a single PCS. The projection can be identified as the [751] projection of P-PCS as is shown in the matched areas in the lower micrograph (note that there are several areas matched), and the specimen thickness correspond to approximately a quarter of a unit cell which is about 300 nm. The power spectrum (upper) calculated on the boxed area of the micrograph correspond well to the theoretical (lower). The computer generated projection inset shows 12 unit cells. Bar, 150 nm. Adopted after reference 1.

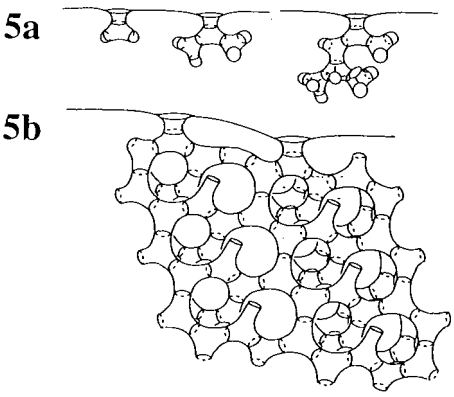

Fig. 5. Schematics of the membrane folding process. (a) The first stages of the development of a cuic membrane with global spherical topology, but with a local topology defined by the specific cubic structure. To the right is shown a tentative model for the continuous cubic-to-cubic (G-to D-PCS) membrane transformation which also is intersection-free. (b) A G-CM which is continuous with two pores. It is thus topologically identical to the torus assuming that its ends are spherically connected. Note that the ends of the gyroid cubic membrane has intentionally been kept open to the interior of the cell, linking the outside with the inside, to show the large number of pores created relative to the number of unit cells. Adopted after reference 1.

tion with the multicontinuous CM's, particularly in the ER and mitochondria? How are these physically distinct spaces formed and maintained? etc. are currently being considered/investigated.

The identification of a crystallographically defined 3-D membrane morphology allows for the application of structure-functional relationships. In particular, we have identified several types of CM's which are structurally invariant with respect to specie. An example is the prolamellar body (PLB) formed during development or in etiolated states of chloroplast membranes in the leaves of higher plants. Its structure belongs to one of the most studied 3-D membrane morphologies and it has been suggested to exhibit various cubic symmetries by several contributors (Gunning and Seer 1975, Wehrmeyer 1965, Murakami et al 1985, Larsson 1980, Lindstedt and Iijenberg 1990). We have recently shown that the PLB is invariantly described by a D-PCS with a rather constant potential (subspace volume relation) and lattice size (Mieczkowski and Landh). This lead to the suggestion that this particular structure might be selected to fulfill a specific purpose based on the physical properties of the structure and its crystallographic space group. In late 1992 I became aware of the striking similarity between the structure of the PLB and certain experimentally produced dielectrics with cubic symmetry which acts as wave blockers through the existence of band gaps. Thus it was suggested (see e.g. Science News 145, 266-268, 1994) that the D-PCS-based morphology of the PLB was selected due to its efficiency in "capturing" certain photons with the wavelength necessary for the conversion of

protochlorophyll to chlorophyll. Even though this theory remains to be ex-perimentally proven, it introduces the concept of crystallographically determined structure-functional aspects of cell membranes which is a new functional attribute of cell membranes. Similar concepts are currently being explored/applied to several other membrane systems in our laboratory (Landh and Whitford, Landh and Deng).

REFERENCES

Landh T, Cubic bilayer membrane systems described by periodic minimal surfaces: From reversed cubic phases to cytomembranes. In: Structural and Biological Roles of Lipids forming Non-lamellar Structures (Epand RM, ed.) JAI Press, Greenwich, (in press).

Nitche JCCC, 1990. Lectures on Minimal Surfaces. Cambridge University Press, Cambridge.

Dierkes U, S Hildebrandt, A Küster, O Wohlrab. 1992. Minimal Surfaces. Vol. I-II, Springer-Verlag, Berlin.

Schnering von HG, R Nesper. 1991. Nodal surfaces of Fourier series: fundamental invariants of structured matter. Z. Phys. **B 83:** 407-412.

Andersson S, Z Blum, S Hyde, T Landh, K Larsson, S Lidin, B Ninham. 1995. The Language of Shape. Elsevicr, Amsterdam

Mieczkowski M, & T Landh. The periodic cubic surface of the prolamellar body. J. Mol. Biol. (in press).

Schoen AH. 1990. Infinite Periodic Minimal Surfaces without Self-intersections. NASA Techn. Note D-5541, Washington, D.C, USA.

Schwarz HA. 1890. Gesammelte matermatische abhandlung. Vol. 1. Springer, Berlin.

Gunning BES. 1965. The greening process in plastids. 1. The structure of the prolamellar body, Protoplasma, **60:** 111-130.

Gunning BES, MW Seer. 1975. Ultrastructure and the biology of plant cells, pp. 111-115, 254-257, Amold Publisher, London.

Wehrmeyer W. 1965. Zur Kristallgitterstruktur der sogenannten Prolamellarkörper in Proplastiden etiolierter Bohnen. II. Zinkblendegitter als Muster tubulärer Anordnung in Prolamellarkörper. Z. Naturforschg. **20b:** 1278-1288.

Murakami S, N Yamada, M Nagano, M Osumi. 1985. Three-dimensional structure of the prolamellar body in squash etioplasts. Protoplasma, **128:** 147-156.

Larsson K, K Fontell, N Krog. 1980. Structural relationships between lmellar, cubic and hexagonal phases in monoglyceride water systems. Possibility of cubic structures in biological systems. Chem. Phys. Lipids, **27:** 321-328.

Lindstedt I, C lijenberg. 1990. On the periodic minimal surface structure of the plant prolamellar body, Physiol. Plantarum, **80:** 1-4 .

Landh T, W Whitford. Foldings of T-tubules described by the gyroid morphology. J. Mol. Biol. (Submitted).;

Landh T, Y Deng. Periodic cubic surface morphologies of chloroplast membranes in Zygnema (Chlorophyceae, Zygenematales). J. Mol. Biol. (submitted);

Deng Y, T Landh, elsewhere in this volume.

Zoological Studies 34, Supplement I (1995)

Zoological Studies

Using Search Algorithms for Automating Alignment of Radiographs for Subtraction Radiography

Chandima Edirisinghe[2], Jagath Samarabandu[2], Kristin M Allen[1], Ernest Hausmann[1] and Raj Acharya[2]
[1]*Department of Oral Biology, State University of New York at Bufalo, NY, USA*
[2]*Department of Electrical & Computer Engineering State University of New York at Buffalo, NY, USA*

Subtractions of serial radiographic images of unchanged structures should in theory be uniformly grey. In practice, one observes in such subtractions varying sized and shaped aggregates of pixels which are lighter or darker than the remainder of the pixels in the subtraction image. Such aggregates are called structured noise and could be misinterpreted to represent anatomical change. The appearance of structured noise in a subtraction image may occur when there is lack of correspondence between the two images for a single or combination of reasons: non- uniformity in film processing producing differences in film contrast ; variation in film position and/or discrepancy in projection geometry of x-ray beam to anatomical structures of interest; misalignment of radiographic images wheng enerating the subtraction image; or different "best-appearing"alignments of images with discrepant geometry.

Even though the best presently available techniques for obtaining standardized radiographs for subtraction are utilized, there may still be pairs of radiographs with significant geometric discrepancy. This results in a problem more difficult to correct and/or manage. For such images there is no perfect alignment. Utilization of different reference areas for alignment, local or global could result in different alignments and consequent differences in the quality and/or quantity of structured noise. Even theuse of the same manual alignment procedure used repeatedly by the same aligner may produce different alignments on repeated attempts. An automated alignment procedure would enable one to achieve a reproducible alignment for pairs of radiographs with imperfect geometry.

Radiographs which served as the basis for digital subtraction images were taken at 32 alveolar crestal sites on 16 dried human skulls. The radiographs used represented an anterior and posterior mix of maxillary and mandibular crestal sites with 1/4 inch or 1 inch thickness of simulated soft tissue covering the range of cheek thickness anticipated in a group of adult subjects. A pair of x-rays was taken at each designated site. The angle difference between the pairs was experimentally controlled to be 2 degrees in the vertical direction. The x-rays were taken by placing a skull in a holding device, which is fixed to a sleeve in which the x-ray collimator fits. The 2 degree vertical angle discrepancy of the x-ray beam between two radiographs was obtained by moving the skull in the holding device relative to the fixed x-ray collimator in a vertical direction. The film was maintained at right-angles to the beam. This produces changes similar to those observed in clinical serial radiographs.

Subtraction images were obtained from 32 pairs of radiographs. Two sets of subtraction images were created. For one set, the pairs were manually aligned and for the other set, the pairs were automatically aligned utilizing the algorithm presented in this paper. Alignment was done using a locally defined procedure. A window was outlined with a cursor just apical to the crestal area of interest on the subtraction image. This window includes the subcrestal alveolar bone and the interface between the tooth root and the bone. For a given pair of radiographic images, the same window was used to achieve the desired alignment for manual and automatic alignment method. For the purpose of manual alignment, the aim was to minimize the range of gray levels in the window by subjective assessment.

The algorithm used in this study addressed the problem of fine alignment.The task of the automated alignment procedure was to shift (both vertically and horizontally) and rotate one of the images

so that the anatomical structures within the window of interest are aligned as well as possible with those of the other image. The amount of shift was limited to a translation of ± 20 pixels and a rotation of ± 5 degrees, made in 0.2 degree increments. The criterion for evaluating the quality of the match was the edges of difference (EOD), which is determined as the best method after evaluating several other methods. The position which produced the minimum edges of differences was considered the best alignment.

To evaluate the best alignment position we needed to search all the possible18,491 (41 vertical translations x 41 horizontal translations x 11 rotational translations) image positions which takes about 15 hrs. when we used a sun4/160 work station. Rather than exhaustively search all possible image positions, the algorithm proceeded in 2 stages. The coarse alignment was done on 1/4 scale images, searching ± 5 pixels and ± 5 degrees at 1 degree increments requiring 1331 (11x11x11) evaluations. Fine alignment was thencarried out in a search space of pm 5 pixels and ± 1 degree at 0.2 degree increments. This required another 1331 (11x11x11) evaluations, giving an effective rate of 2662 evaluations per image pair which consumes only 3 hrs.of calculation time.

In this case we have used the downhill simplex method. After giving three randomly selected shift positions, this method automatically converges the results to a minimum value point. In this particular situation we could not use the simplex method directly because of the possibility of converging to a local maxima instead of the true solution. Once a solution is achieved,another starting point was randomly selected (which is ± 1 pixel and ± 1 degree shifted from the solution) and the process is repeated until we achieve the same results three times in a row. This method gives the results in less than 45 minutes and has the same accuracy as the method 1.

For 24 observers the preference for automated alignment ranged from 19% to 91% of 32 observations. For the 32 subtraction pairs the preference for automated alignment ranged from 12% to 87% of 24 observations. The mean percentage of preference for the automatically aligned images for 24% observers was 49% with a standard error of 4%. Within 95% confidence limits it was calculated that the true mean must lie somewhere between 41% and 57%.

The results of this study indicate that automated alignment of pairs of radiographs produces subtractions which are indistinguishable in quality from subtractions aligned manually by an experienced aligner. In developing the algorithm for automated alignment, care was taken that the criteria used for establishing a window appropriate for testing the quality of alignment were the same for both alignment techniques. It should be noted that no claim is made that the algorithm corrects for the angle discrepancy between the pairs of images, but rather that it merely seeks to find the best possible alignment for a specific inter-proximal bone site.Furthermore, since at low resolution, the procedure is using the root edge as the primary feature, it did not miss the global minimum at high resolution with the given search space. Figure 3 shows the performance of the matching criteria for a typical radiograph.

This automated alignment procedure represents one step towards our present goal to completely automate this procedure. Two further steps must be automated: 1) placing completely unaligned images into approximatealignment 2) defining an alignment window for the procedure implemented in this study. This would permit identical alignment for any pair of images in different laboratories. Such uniformity of technique would allow for more effective comparison of results of digital subtractions performed in different laboratories.

REFERENCES

Allen K, Hausmann E, Carpio L, Loza J, Kutlubay E, Wobshall D. Comparison of 2 methods for standardizing radiographs. J dent. Res. 1993; **72:** Abstract 1221.

Mc Henry K, Hausmann E, Wikesjo U, Dunford R, Lyon E, Christersson L. Methodological aspects and quantitative adjuncts to computerized subtraction radiography. J Periodont. Res. 1987; 22: 1987.

Webber RL, Ruttimann UE, Groenhuis RAJ. Computer Correction of Projective Distortions in Dental Radiographs. J Dent Res. 1984; 63: 1032-1036.

Jeffcoat MK, Jeffcoat RL, Williams RC. A new method for the comparison of bone loss measurements on non-standardized radiographs. J Periodontal Res. 1984; **19:** 434- 440.

Benn DK. Limitations of the digital image subtraction technique in assessing alveolar bone crest changes due to misalignment errors during image capture. Dentomaxillofac Radiol 1990; **19:** 97- 104.

Jeffcoat MK, Reddy MS, Webber RC, Ruttimann UE. Extraoral control of geometry for digital subtraction radiography. J. Periodont. Res. 1987; **22:** 396-402.

Zoological Studies 34, Supplement I (1995)

Zoological Studies

The Microscopist Facing Uncertainty

Sterling P. Newberry
CBI Labs, 11 S. Westcott Road Schenectady, NY 12306, USA

With tight budgets and political uncertainty world wide, microscopists indeed face uncertainty, which is worthy of our concern. However, it is the uncertainty principle of physics which is the primary concern here.

In the early days of electron microscopy, it was believed that the ultimate resolution capability would be useless once we could reach a resolution some what less than the cross section of a single atom, since the outer electrons would reveal no detail and the nucleus is so much smaller than the outer electron orbits, that even full theoretical resolution by electron waves could not hope to resolve the nucleus. Your author did not accept this view and talked privately with his colleagues concerning it. There was always the tantalizing wonder of whether we could at least see the electron's average positions in the so called "orbits" similar to the hydrogen orbitals as calculated using the Schroedinger Equation.

With our improved resolution and computing power today we now look at the electron microscope image at highest resolution, not as a true likeness of the subject but as a wave pattern from which we can hope to calculate the true image within the limits of the uncertainty principle. Also with better understanding of the uncertainty principle, we realize that by sacrificing the certainty about other dimensions, we can greatly enhance the measurement in one dimension. Furthermore Scanning Probe Microscopy has been able to sense the electric fields of orbitals in shared bonds. We have only seen the beginning of the fruitful results which will be gained by this combined use of improved microscope and computer. Possibly those actively engaged in this field should try to project what the next steps to improve these techniques will be.

For my part I wish to propose a new approach, which to my knowledge has not yet been proposed, or perhaps, not even conceived by any one else. It concerns how Electron Microscopy may be a help in studying the basic laws of physics but in a less direct manner than currently employed. Microscopes have helped physics in the past. Contrast the discovery of Brownian movement which was direct observation, with the indirect method in the oil drop experiment to determine the charge on the electron.

In objective study we must constantly avoid the human tendency to judge time and space by our own size and speed of sensory comprehension and our human reluctance to work outside the confines of our own laboratory space. As we know, progress in science is usually initiated by experiments which are in conflict with our theories, while understanding has almost always come from indirect measurements; long before we have the experimental capability to do the direct measurements required. What I am proposing is that we use the Electron Microscope's image field as a new vantage point for launching indirect measurements of the interactions of fundamental particles. This is the next logical extension in freeing ourselves from the confines of our environment since we have already created a new vantage point in astronomy by sending probes and telescopes into Outer-Space, beyond earth's atmospheric confines for studies of fundamental physics. With the Electron Microscope we can do more than just interpret observations, we should be able to establish a vantage point for indirect measurements in Micro-Space below the resolution limit of the microscope where the region of nuclear particles is found.

It is my hope that a dialogue can be started among microscopists, especially those who are also physicists, for the possibility of such experiments. Let me offer some opening suggestions of techniques available for such measurements. Annihilations can be used as the driving force for these experiments. Annihilations can be made to occur in large numbers, in a controllable, small area; as is now done experimentally for cancer treatment

with anti-protons. Can we reduce and control this area well enough to get a high probability of annihilations occurring in the field of view of the electron microscope; probably so. Furthermore those neutrinos which are thought to carry charge, are also believed to be very plentiful in free space. Do they effect an electron wave pattern? Can Holographic Electron Microscopy detect such interaction? Also, as we go to press we are told of apparent success in detection of the Top Quark in free space(1). These quarks are thought to have a dumbbell shape and if separated to immediately recombine with other released Quarks or with other nuclear particles. Here the "Nuclear Glue" force appears to be exhibiting itself on atomic dimensions. Because of the Top Quark's short half life in free space, it is very rare to find one in experiments on a scale of meters, as need be employed in the high energy machines. Is it not possible, that we may be able to provoke a constant supply of free quarks at near nuclear dimensions and are they not likely to have disturbing effects on the atoms and electrons we observe in the electron microscope? An interesting suggestion that quarks hold protons and neutrons together by acting like shared bonds, which we find at the molecular level, was expressed in an interview with John Domingo to a science editor recently(2). This report is a good summary for the non-physicists which explains why it would be advantageous to be able to observe events in the region close to the nucleus because the particles found by high energy experiments, appear to show their complete characteristics only in association with the nuclear environment. In the past I initiated a call for us to use the power of Electron Microscopy to explore "Micro-Space" as the space to hold our growing information files, today I ask you to consider the possibility of using the power of the Electron Microscope to establish a laboratory in the vicinity of the nucleus.

REFERENCES

Associated Press Release, Batavia, Ill. March 3, 1995.

Flam, Faye (Ed) 1995. "A New Accelerator Explores The Social Life of Quarks", Science V. 267 p 1266-7.

Zoological Studies 34, Supplement I (1995)

Zoological Studies

Can X-ray Photometry Be Applied to 3-D images?

Sterling P. Newberry
11 S., Westcott Road Schenectady, NY 12306, USA

STATEMENTS OF PROBLEMS

X-Ray Microscopes which do not use the brilliance of the synchrotron are deficient by comparison to those which do use synchrotron x-rays on two counts. They have far less intensity in the very soft region and they cannot have continuously variable, monoenergetic illumination which is so helpful in chemical identification. However, they have two important advantages over synchrotron illuminated microscopes. They are small enough to be fitted into an ordinary laboratory space and they are far less expensive. Since these smaller microscopes produce very useful images for a large range of subjects, and can be made available to a wider user group, it behooves us to look for ways to enhance their performance in these two areas. In this paper we shall narrow the scope of the paper to the Shadow Projection type of microscope, which is still the most attractive of the laboratory source illuminated instruments.

BACKGROUND EXPERIENCE

Our experience has shown that thickness sensitivity has not been a problem due to the use of 5 kV and higher beam energy. Thin organic films, smoke from oil fires, charcoal, and plastic foams are easily imaged. Difficulty arises in getting image contrast in very uniform mixtures of organic materials. Computer enhancement has been of considerable help here. What is most troublesome is the inability to distinguish between materials of very nearly the same atomic weight. Past work on this latter problem has concentrated on the use of two line sources on either side of a prominent absorption edge to identify a component. While this has had some application in micro-radiography where one may easily select line radiation from white radiation by Bragg reflections it is less convenient for projection images. It also suffers from lack of generality.

SUGGESTION TO EMPLOY X-RAY PHOTOMETRY

Another attractive approach would be to use x-ray photometry since the absorption characteristics of all the elements are cataloged and the absorption of compounds can be calculated or measured in pure samples. Photometry has long been used for samples such as thin sections in which the material is the same, in a given area, through out the thickness of the sample. It has not been used with thicker samples if the material varied in the Z direction. With tomography, the absorption of individual voxels can be measured and thus in principle photometry can be applied to determine the composition of small regions even if the sample is not homogenous in the Z direction. Using the same principles, can the voxel absorption be determined in the much more convenient 3-D display?

In visual examination of 3-D displays one can easily see a small region of different density even though it lies in a plane between regions of yet other densities. We generally record 3-D images with photographic material which complicates photometry but does not preclude it. With CCD or other electronic image detectors now available the photographic material need not be used. Areal mapping techniques can identify planes of constant Z value and thus identify conjugate voxels in the two stereo views. The basic question is whether two views are adequate for calculating the x-ray density of a voxel. With the larger number of views in tomography it is reasonable to assume that the path overall density

variations average out. Visually the 3-D views appear to do the same. The question remains, however, that the human brain, which is such an efficient tomographic computer, may be deceiving us with respect to the absolute value of the voxels. As we know the human visual system is a sensitive ratio detector but tends to ignore the back ground level. I shall argue that for 3-D views in which the small details have good contrast, a measurement of the photons in an x-ray pencil corresponding to one voxel's back projected area, compared with the average of back projected voxels which surround the border of the small detail, will give the true absorption of that small detail. Furthermore, that the quality of a given small detail for analysis can be selected automatically so that only the better voxels are included in an analysis.

SUGGESTION FOR CHEMICAL CONTRAST ENHANCEMENT

There is still the question of whether we can hope to distinguish chemically different materials which appear to have equal absorbing power in an image. That is can we find a general way to accomplish what the two exposures which straddle the critical absorption edge have done in a few favored cases. For this final problem I shall propose a method which can be used in conjunction with the determination of voxel density by 3-D analysis. The idea is to compare three sets of pictures taken by three different narrow band exposures. Here we can expect that since the absorption coefficients vary so rapidly with wave length, that in those cases where the compounds to be expected are known, one can distinguish between closely related compounds. As a matter of experience we have found that the likely components in a sample are generally known. An unexpected component becomes obvious by comparison, and once identified in space, can be studied by other analytical methods.

1. The author is grateful to Professor P.C. Cheng for useful discussions concerning these problems.

Zoological Studies 34, Supplement I (1995)

Zoological Studies

What Happened to Marton's Dream of a Field Emission X-ray Microscope?

Sterling P. Newberry
CBI Labs, 11 S. Westcott Road Schenectady, NY 12306, USA

INTRODUCTION

In 1951 at a symposium on Electron Physics, L. Marton gave a very enthusiastic appeal for the development of a Shadow Projection x-Ray Microscope employing a field emission electron source. At that time he was envisioning exposure times so short as to permit full speed x-ray microscopic movies in a resolution beyond the optical microscope. Two and one half years later, when the proceedings finally appeared, Marton was less optimistic (Electron Physics 1954). His written paper addressed the many problems and his predictions were considerably lowered. However, he never lost hope that the much higher brightness of the field emitter would eventually be made available for x-Ray Microscopy. Marton passed away about ten years ago without his dream being realized.

Today, despite the many improvements in field emission, few workers are looking to it for x-ray microscopy. The purpose of this paper is to examine its possible role for x-ray microscopy.

THE FAMILY OF X-RAY MICROSCOPES

Already we see a proliferation of models of the x-Ray Microscope and can expect more with maturity of our field. In attempting to classify and compare the known possible approaches to x-ray microscopy, we find the source of x-ray illumination to be the most distinguishing feature. The following sources have been used: thermionic electron impingement, Synchrotron radiation, variously excited plasma, and true x-ray lasers.

The opportunity to use field emission would most likely be as a replacement for thermionic electron sources in direct production of x-rays. The joint abilities to pulse field emission and to employ multiple sources in parallel may provide high total currents which could possibly make field emission useful in plasma generation. Electron impingement and plasma have a very important advantage for work with higher energy x-rays over the powerful synchrotron based microscopes, in that they can be used in an ordinary laboratory space at much less cost. Their disadvantage lies in their low intensity in the water window and their lack of a general monochromator for chemical identification. Some possible ways to overcome these disadvantages are discussed by the author in another paper at this conference, i.e. "Can x-ray photometry be applied to 3-D Images?".

SCOPE OF THIS PAPER

In this paper we shall limit our discussion to ways in which field emission might produce a smaller, more productive, direct electron impact, type microscope based on the classical Shadow Projection principle. This choice does not imply that larger direct impact type microscopes based on a scanning electron microscope structure with ultra thin targets have no place in the family of x-Ray Microscopes, but rather that field emission is less attractive than the more robust lanthanum hexaboride cathodes for these instruments.

The approach which I favor, should employ the recently developed atomic sized tip which Scheinfein et al have shown to indeed have two orders of magnitude more brightness than the larger tip sources (Scheinfein et al. 1993) and Spence et al have applied to electron shadow imaging (Spence et al. 1993). These tips require very low extraction voltages and thus can be made immune to ion destruction even in a 10^{-6} Torr surrounding. Because

of their small physical size it is possible to consider a table top configuration. Furthermore a sealed envelope with built in holding pump is practical in the 10 kV range (Newberry 1993) which eliminates a bulky and expensive demountable pumping system. A suggested layout for such a system will be discussed. It will be appropriate for opaque samples in the thickness range of confocal microscopy. Sealed sources for more penetrating radiation would be better served by dispenser cathodes. Thus at least two versions of the sealed Shadow Projection x-Ray Microscope can be expected along with the SEM demountable vacuum version.

The author is grateful to Professor John Spence, of Arizona State University, for discussions of the current status of Low-Voltage Projection Microscopy studies.

REFERENCES

"Electron Physics", National Bureau of Standards Circular 527, issued March 17, 1954, (Proceedings of the Semicentennial Symposium on Electron Physics, held at the NBS on Nov.5-7, 1951, Bureau of Standards, L. Marton Chairman).

Scheinfein MR, W Qian, JCH Spence. 1993. "Brightness Measurements of Nanometer-sized Field-Emission Tips", MSA Proceedings 1993 p 632-3.

Spence JCH, W Qian, J Liu, W Lo. 1993. "Experimental low-voltage point projection microscopy", MAS Proceedings p 1060-1.

Newberry S.P, 1993. "Is a aealed ahadow projection x-ray microscope possible?". To be published in Proceedings of XRM'93, Moscow.

Zoological Studies 34, Supplement I (1995)

Zoological Studies

NORAN Odyssey XL/Super Video Rate Confocal System

Bruce E. Batten
Noran Instruments, Inc., 2551 West Beltline Hwy, Middleton, WI 53562, USA

In late 1993 NORAN introduced a new version of the Odysey, called the Odyssey XL which added variable rate scan control features and fast digital image processing hardware. While the Odyssey XL is based on the same optical layout used in the Odyssey, the XL's new Dynamic Scan Control hardware was added to provide greater control over the Odyssey's point scanning mechanism as incroporate important video rate image processing features like background subtraction and averaging. Image scan rates, resolution, and pixel dwell time can be controlled to tailor the Odyssey XL's image capture and preprocessing facilities for later acquisition and analysis one the host computer scan parameter options available with the Odyssey XL.

The pixel dwell time is defined as the period of time during which excitation and detection occur for each point scanned in the active scan area (Odyssey field of view). The Odyssey XL pixel dwell time can vary from 100 nanoseconds up to 6.4 microseconds whereas the original Odyssey has a fixed pixel dwell time of 100 nanoseconds. ADC sample rates are adjusted according to the pixel dwell time. For slower dwell time (greater than 800 nanoseconds) the PMT signal is directed to an integrator stage prior to the ADC to accumulate over the entire dwell time; ie. lossless data acquisition.

In the Odyssey the analog signal generated by the PMTs is fed immediately to an output stage where it is translated into a RS-170 compatible video signal for output to a framegrabber in a host computer or to a video monitor for direct viewing. The Odyssey XL operated differently in that it digitized the PMT signal and can optionally perform arithmetic functions directly on the image data at video rates prior to sending the image to an output stage. The Odyssey XL video output stage includes both a CCIR 601 compatible digital video output and a RS-170 analog video output. The Dynamic Scan Control hardware embeds control information into each video frame that describes key scanning parameters and data organization. Acquisition software executed on the host computer interprets this control information and then as a results decides how to process, display, and store the ac-

Table 1.

Image Size	Frame Rate	Scan Time Per Image	Pixel Dwell Time
320×120	240	4.1 milliseconds	100 nanoseconds
320×240	120	8.3 milliseconds	100 nanoseconds
320×240	30	33.3 milliseconds	400 nanoseconds
640×480	30	33.3 milliseconds	100 nanoseconds
640×480	15	66.7 milliseconds	200 nanoseconds
640×480	7.5	133.3 milliseconds	400 nanoseconds
640×480	3.7	266.7 milliseconds	800 nanoseconds
640×480	1.8	533.3 milliseconds	1600 nanoseconds
1280×960	1	1.0 seconds	800 nanoseconds
1280×960	0.5	2.1 seconds	1600 nanoseconds
1280×960	0.2	4.3 seconds	3200 nanoseconds

quired data.

The Dynamic Scan Control hardware is based on a dual TMS34020 graphics system processor (GSP) architectur which also includes a separate fast arithmetic logic unit (ALU). Acquisition memory is 512×512×16 bits deep and is used to store data digitized by 10 MHz 8-bit ADC. The ALU can do background subtraction, accumulation (summing), and averaging operations on data in the acquisition memory at video rate. Results from an ALU operation are stored in display memory at video rate. Results from an ALU operation are stored in display memory at video rate. Results from an ALU operation are stored in display where it is staged for eventual output in either digital or analog video formats.

The display memory is controlled by a dedicated TMS34020 GSP which enables the Dynamic Scan Control hardware to decouple acquisition timing requirements from display and RS-170 video synchronization requirements. Thus even if the Odyssey XL is scanning at the slowest possible rate it is still maintaining an RS-170 compatible video output.

References (e.g. background) images can be captured and stored locally for subsequent ALU operations. Like acquisition memory, data stored in the background memory can be transferred to the display memory for output. This makes it possible for the Odyssey XL operator to switch between different displayed (output) images interactively.

This pressention will focus on how this new hardware can be utilized for diverse biological applications. Further the issue of dwell time and photo damage will also be addressed.

Index to Authors

Indexed/Abstracted in:
Biological Abstracts
Chemical Abstracts
Current Contents
Zoological Record

Zoological Studies

Vol. 34, Supplement I
April, 1995

國際立體顯微科技學會第八屆年會論文集